Studies on Silk-based Bionanocomposites

Thesis submitted in partial fulfilment of the requirements for the degree of

DOCTOR OF PHILOSOPHY

by

RAHUL PATWA

(Roll No.: 126107030)

Department of Chemical Engineering

Indian Institute of Technology Guwahati

Guwahati-781039, Assam, India

June, 2018

Dedicated to

My Family

for their

Unconditional Love, Support and Encouragement

INDIAN INSTITUTE OF TECHNOLOGY GUWAHATI

Guwahati- 781039, Assam, India

Department of Chemical Engineering

STATEMENT

This is to certify that the research work in the thesis entitled **"Studies on Silk-based Bionanocomposites"**, is carried out by me at the Department of Chemical Engineering, Indian Institute of Technology Guwahati, under the supervision of **Dr. Vimal Katiyar** and **Dr. Amit Kumar**. The results documented in this thesis are achieved by me and have not been submitted to any other University or Institute for the award of any degree or diploma.

(Rahul Patwa)

Roll No.: 126107030

Department of Chemical Engineering

Indian Institute of Technology Guwahati

Guwahati- 781039, Assam, India.

Guwahati, June 2018.

INDIAN INSTITUTE OF TECHNOLOGY GUWAHATI

Guwahati- 781039, Assam, India

Department of Chemical Engineering

CERTIFICATE

This is to certify that the thesis entitled **"Studies on Silk-based Bionanocomposites"**, being submitted by **Rahul Patwa** for the award of Ph.D. degree has been carried out by him at the Department of Chemical Engineering, Indian Institute of Technology Guwahati, under our guidance and supervision. The work documented in this thesis has not been submitted to any other University or Institute for the award of any degree or diploma.

(Dr. Vimal Katiyar)
Associate Professor
Department of Chemical Engineering
Indian Institute of Technology Guwahati
Guwahati- 781039, Assam, India.

(Dr. Amit Kumar)
Associate Professor
Department of Chemical Engineering
Indian Institute of Technology Guwahati
Guwahati- 781039, Assam, India.

Acknowledgement

"Starting something can be easy, it is finishing it that is the highest hurdle."
–Isabella Poretsis

The journey of doctoral study is always a difficult and challenging task. Throughout this long journey, I have gained a lot of learning to persevere despite hardships. I would never have successfully completed this research work without the assistance of numerous people who have helped me directly or indirectly, I would like to acknowledge them all. First and foremost, I would like to express my special appreciation and gratitude to both my supervisors Dr. Vimal Katiyar and Dr. Amit Kumar, who have been tremendous mentor for me. I appreciate their contributions of time, ideas and funding to make my Ph.D. experience productive and stimulating. I am fortunate to have advisors who encouraged my research, allowing me to grow as a researcher by training me to develop my technical, writing and communication skills, but also supported me emotionally whenever I needed them. A special mention to Dr. Katiyar, the joy and enthusiasm he has for his work was contagious and motivational for me, even during the tough times in my Ph.D. pursuit. I offer my sincere thanks to my doctoral committee members, Professor Mihir Kumar Purkait, Professor Gopal Pugazhenthi (Department of Chemical Engineering), Dr. Kalyan Raidongia (Department of Chemistry), for their insightful comments, suggestions and valuable criticism during all review assessments of my Ph.D. programme which helped me to improve the quality of my research work. I have been privileged to attend many International conferences and workshops during my Ph.D. tenure where I got the opportunity to meet and interact with the prominent scientists across the globe. I would like to express my sincere thanks to Professor Shinichi Sakurai at Department of Bio-based Material Science, Kyoto Institute of Technology (KIT), Kyoto, Japan, for his motivation and valuable suggestions when I met him in ASP-2014, Guwahati and also during my two month internship at KIT, Japan. I am thankful to the Central Library, Central Instruments facility (CIF), Centre of Excellence for Sustainable Polymers (CoE-SusPol), and Department of Chemical Engineering at IIT Guwahati for providing me a research-friendly atmosphere with up-to-date research facilities. Sincere thanks to the all the technical and non-technical staff particularly Dr.Kula Kamal Senapati, Mr. Chandan Borgohain, Mr. Madhurjya Borah, Mr. Kishor Talukdar and Mr. Milan Mahadani (from CIF), Ritumoni Kalita, Harsaraj Biswanath, Dr. Lukumoni Borah, Debajit Borah, Dipak

Kumar Barman, Jayanta Kumar Mout, Pankaj Sekhar Baruah, Deep Jyoti Sinha, Sailen Das, Bhagya Boro, Lakhyadhar Boro and Jyotish (from chemical department) for providing me all help and assistance for the completion of my work. I also thank Indian Institute of Technology Guwahati for providing me the fellowship and such a good accommodation in this scenic campus.

"A good companion shortens the longest road." I have been fortunate to be surrounded by some amazing friends both at campus and at home. I owe my sincere gratitude to Dr. Arvind Gupta, SurendraSingh Gaur, Umesh Bhardwaj, Anup Ashok, Dr. Prodyut Dhar, Siddharth Mohan Bhasney,Narendren Soundararajan,Dr. Melakuu Tesfaye,Monika, Neha Mulchandani, Tabli Ghosh, Shivkumar Venkatachalam, Kartik Sharma, Gourhari Chakraborty, Medha Mili, ShasankaSekhar Borkotoky, Naba Kumar Kalita, Debashis Tarafdar, Ananya Das, Amit Pandey, Arbind Prasad, Kiran Kumar Gali, Khalid Wani, Munmi Das, Pankaj Baruah, Dr. Purabi Bhagabati, Dr. Valapa Ravi Babu, Dr. Prasanta Baishya, for all kinds of help, moral support and research related discussions which made my stay in lab cheerful and productive. I have these six gems in my life Ritesh, Navneet, Ravi, Yogesh, Pradhyumn and Aditya who have constantly made fun of my research, making me feel lighter, I feel lucky to have all of them.

"The love of a family is life's greatest blessings". I am blessed to have a wonderful family, which includes my parents, in-laws and my wife. In this precious moment of my life. I would like to express my deep sense of gratitude to my parents Narendra and Manju Patwa for their unconditional love, countless sacrifices and endless encouragement, which made it possible for me to reach this stage in my life. I would like to attribute all my success to them. I thank my wife Minal who dealt with me during my frustrations, motivated me to continue all the way. I would also like to thank my sister Vinita, brother-in-law Abhimanyu and my nephew Darsh for their love and best wishes. Finally, I owe it all to the almighty God for being all in all and enabling me to the completion of the doctoral work. Where this work succeeds I share the credit, where it errs I alone accept the responsibility.

Rahul Patwa

Abstract

Environmental hazards caused by conventional plastics having fossil-fuel origin have aroused interest in bio-based polymers. Poly(lactic acid) (PLA) has rapidly gained popularity in the past decade as potential replacement for petroleum-based plastics. Attributes like biodegradability, recyclability, compostability, biocompatibility and non-toxicity is what makes PLA the eco-friendly alternative. However, several drawbacks are associated with PLA such as brittle nature, slow crystallization and poor gas barrier properties which avert its utilization for food packaging applications to its full potential.An effort has been undertaken in the current doctoral research work to address these limitations by fabrication of PLA based bionanocomposites.

In the current work, the effect of novel discotic bio-filler crystalline silk nano-discs (CSNs) on the structural, morphological, thermo-mechanical, optical and barrier properties of PLA is investigated. CSNs are extracted from waste Muga silk through novel hydrolysis cum sonication route providing an effective strategy for upconversion of 'waste to wealth'. The physico-chemical, structural and morphological properties of the isolated CSNs are studied. The CSNs are having a predominant β-pleated sheet conformation which was confirmed using FTIR, Raman and NMR studies. The average diameter and thickness of CSNs calculated using AFM, TEM and FESEM is 49.1±12 nm and 3.1±0.9 nm, respectively. Amino acid analysis shows that CSNs are mainly composed of alanine, serine and glycine which are 83.8%, 6.8% and 6.1%, respectively which makes CSNs hydrophobic in nature. X-ray diffraction studies disclose that CSNs are highly crystalline nanoparticles with ~93.7% percentage of crystallinity. Thermal analysis reveals that they have superior thermal stability of 310 °C., respectively. Furthermore, surface of CSNs are modified using iron-oxide nanoparticles to fabricate magnetic CSNs through one-step reduction reaction. TEM analysis reveals that MGCSNs have diameter and thickness of 58.2 ± 4.6 nm and 16.0 ± 2.6 nm, respectively. Subsequently, CSNs are used as reinforcement material in the poly(lactic acid) (PLA) matrix to fabricate biopolymeric/ crystalline silk nano-discs (CSNs)-based "green" bionanocomposites through melt-extrusion for potential high temperature engineering and food packaging applications. At optimum loadings of 1 wt. %, show well-dispersed CSNs covering the entire matrix, corroborated through morphological analysis, leads to significant improvement in intrinsic characteristics such as thermal, mechanical, barrier, and processing capabilities. Thermo-gravimetric analysis confirms the role of CSNs in enhancing melt stability of

PLA, as that the decomposition temperature for the PLA bionanocomposite with 1wt. % CSN content is increased by ~10 °C over neat PLA, when onset of decomposition is takenas point of comparison. Due to enhanced crystal nucleation density, water-vapor and oxygen permeability reduced by ~28 and ~70%, respectively. Enhancement in toughness, percentage elongation and tensile strength up to ~65%, ~40% and ~10%, respectively is obtained. These favorable properties along with their non-toxicity, sustainability and complete biodegradability makes the PLA/CSN bionanocomposites-based packaging a promising candidate to replace non-degradable fossil-based plastic packaging.

Further, the influence of CSNs on crystallization behavior of melt-extruded PLA was investigated to measure the thermodynamic parameters which are essential during processing of polymers. The crystallization behavior is studied using non-isothermal cold crystallization and isothermal melt crystallization using differential calorimetry. Both the phenomenon are also studied through spherulite morphology and growth rate using polarizing microscopy. Crystallization data was analyzed by Jeziorny, Liu-Mo and Tobin models to determine useful crystallization information. Incorporation of CSNs facilitates the crystallization process. Addition of CSNs in PLA matrix results in lower cold crystallization temperatures (T_{cc}) and shorter crystallization half-time ($t_{0.5}$) with enhanced growth rates. It was found that CSNs act as heterogeneous nucleating agents, hence improve non-isothermal crystallization kinetics of PLA. Spherulitic morphology and growth of spherulites in case of PLA and PLA/CSN are observed over a wide range of crystallization temperatures (90-120 °C) using polarized optical microscopy (POM).Improvement in crystal nucleation density is observed as CSNs contribute towards new nano-nucleation sites. With incorporation of CSN, the crystallization kinetics were modified, the overall isothermal melt crystallization rates of PLA/CSN increased, however the crystallization mechanism remained unaltered. The apparent activation energy and surface energy barrier for crystallization process decreased upon addition of silk nano-discs. Decreasing crystallization temperatures decreased growth rates of PLA spherulites. Both PLA and PLA/CSN exhibited highest crystallization rates ~107 °C.

In addition to this, effect of CSNs on the thermal degradation kinetic studies for PLA and PLA/CSN are carried out using thermogravimetric analysis (TGA) at various non-isothermal heating rates. The apparent activation energies (E_a) of bionanocomposites, determined from model free (Flynn-Wall-Ozawa, Kissinger-Akahira-Sunose method) and

model fitting (Coats-Redfern method) approach, increased in comparison to pure PLA which inform that CSNs impede the thermal degradation process. A possible mechanism is proposed for the thermal degradation process of PLA/CSN bionanocomposites using Criado method. Hyphenated TGA-Fourier transform infrared (FTIR) analysis is utilized to identify the evolved gaseous products of untreated muga, CSNs, PLA and PLA/CSN bionanocomposites. For untreated muga and fabricated CSNs various volatile species were released such as different amide containing products, carbon dioxide (CO_2), carbon monoxide (CO) while in case of PLA and PLA/CSN bionanocomposites similar type of major products such as CO_2, CO, cyclic oligomers, lactide, hydrocarbons and aldehydes were detected. Furthermore, the hydrolytic degradation behavior of PLA and PLA/CSN were studied at different incubation temperatures (37 and 60 °C) and pH (acidic, neutral and alkaline) conditions. The results demonstrate that hydrolytic degradation rate of bionanocomposites was slower as compared to PLA in acidic, neutral and alkaline media at pH=2, 7 and 12, respectively due to hydrophobic nature of CSN and pH. This work provides valuable insight for the application and reclamation of PLA/CSN bionanocomposites in moist and wet working environments.

Further, fabricated CSNs and MGCSNs are utilized for preparation of biocompatible nanofiber based scaffolds by melt blending with poly(lactic acid) (PLA) followed by electrospinning. The prepared scaffolds are characterized for morphological, structural, thermal and mechanical properties. We assessed release behavior of these scaffolds using curcumin, a naturally occurring anticancer drug, curcumin and found effective towards sustained release over 25 days which also shows effective cytotoxicity against human cervical cancer cells. Interestingly, alignment of CSN derived magnetic nanoparticles due to effective fiber drawing process during electrospinning could improve cytocompatibility against BHK-21 cells. In vitro cell cytocompatibility studies show improved cell adhesion and proliferation on the surface of the developed bionanocomposites scaffolds which support its biocompatible nature. Combined effect of curcumin and hyperthermia reduced the growth to ~57%. Therefore, this doctoral thesis focusses on utilization of CSNs and its magnetic derivative, MGCSNs as a novel bio-filler for PLA based bionanocomposites for potential food packaging and cancer therapeutics which has been summarized in eight chapters and explained in detail in subsequent sections.

भारतीय प्रौद्योगिकी संस्थान गुवाहाटी
Indian Institute of Technology Guwahati

Contents

भारतीय प्रौद्योगिकी संस्थान गुवाहाटी • Indian Institute of Technology Guwahati •

List of Figures

List of Tables

List of Tables

Nomenclature

Abbreviations

1D	One dimensional
2D	Two dimensional
3D	Three dimensional
4D	Four dimensional
AFM	Atomic force microscopy
Ala	Alanine
ALP	Alkaline phosphatase
AMF	Alternating magnetic field
Asp	Aspartic acid
ASTM	American society for testing and materials
ATR	Attenuated total reflectance
BET	Brunauer Emmett Teller
BHK	Baby hamster kidney
CCD	Charge-coupled device
CHN	Carbon hydrogen nitrogen
CI	Crystallinity Index
CIE	International Commission on Illumination
CIF	Central Instruments facility
CNC	Cellulose Nanocrystals
CNT	Carbon Nanotube
CO	Carbon monoxide
CO_2	Carbon di-oxide
CoE-SusPol	Centre of Excellence for Sustainable Polymers
C-R	Coats-Redfern
CSB	Central silk board
CSN	Crystalline silk nano-discs
DAPI	4’, 6-diamidino-2-phenylindole dilactate
DCPC	Department of Chemicals and Petrochemicals
DLS	Dynamic light scattering
DMEM	Dulbecco´s modified Eagle's medium
DMSO	Dimethyl sulfoxide

Abbreviations

DRS	Diffuse reflection spectroscopy
DSC	Differential scanning calorimetry
DTG	Differential thermo-gravimetric
ECM	Extracellular matrix
EDX	Energy dispersive X-ray spectroscopy
FBS	Fetal bovine serum
FDA	Food and drug administration
Fe_3O_4	Magnetite/ iron oxide
$FeCl_3$	Ferric (III) chloride
FESEM	Field emission scanning electron microscope
fps	Frames per second
FTIR	Fourier transform infrared spectroscopy
F-W-O	Flynn-Wall-Ozawa
Glu	Glutamic acid
Gly	Glycine
GmbH	GesellschaftmitbeschränkterHaftung
GPC	Gel permeation chromatography
GS	Gram-Schmidt
H_2SO_4	Sulfuric acid
HCl	Hydrochloric acid
HDPE	High density polyethylene
HDT	Heat deflection temperature
HeLa	Henrietta lacks
HPLC	High performance liquid chromatography
HR-TEM	High resolution transmission electron micrographs
K-A-S	Kissinger-Akahira-Sunose
KBr	Potassium bromide
LCA	Life Cycle Assessment
LDPE	Low density polyethylene
mf	Incubated under static magnetic field
MFI	Melt flow index
MGCSN	Magnetic crystalline silk nano-discs

Abbreviations

MMA	Methyl methacrylate
MRI	Magnetic resource imaging
Mt	Metric ton
MTT	3-[4,5-dimethyltriazol-2-y1]-2,5-diphenyl tretrazolium
MW	Molecular weight
MWCNT	Multi-walled carbon nanotube
N_2	Nitrogen
Na_2CO_3	Sodium carbonate
$NaBH_4$	Sodium borohydride
NCCS	National centre for cell science
OD	Optical density
OP	Oxygen permeability
OTR	Oxygen gas transmission rate
OWRK	Owens, Wendt, Rabel and Kaelble
PBAT	Butylene adipate-co-terephthalate
PBS	Phosphate-buffered saline
PBS	Polybutylene succinate
PBSA	Poly(butylene-succinate-co-adipate)
PC	Polycarbonates
PCL	Polycaprolactone
PDI	Polydispersity index
PE	Polyethylene
PEA	Polyester amides
PEG	Polyethylene glycol
PEO	Polyethylene oxide
PET	Poly(ethylene terepthalate)
PHAs	Polyhydrohyalkanoates
PHB	Polyhydrohybutyrate
PHBV	Poly(3-hydroxybutyrate-co-3-hydroxyvalerate)
PLA	Poly(lactic acid)
PLAA	PLAMGCSN electrospun under external magnetic field
PLA/CSN	Poly(lactic acid)/crystalline silk nano-discs

PLA/MGCSN	Poly(lactic acid)/magnetic crystalline silk nano-discs
PLAN	PLAMGCSN electrospun without magnetic field

Abbreviations

POM	Polarizing optical microscope
PP	Polypropylene
PPC	Poly propylene carbonate
PPG	Polypropylene glycol
ppm	Parts per million
PS	Polystyrene
PTFE	Polytetrafluoroethylene
PU	Polyurethane
PVA	Polyvinyl acetate
PVC	Polyvinyl chloride
RH	Relative humidity
ROP	Ring opening polymerization
rpm	Rounds per minute
SAED	Selected area electronic diffraction
SEM	Scanning electron microscope
Ser	Serine
SF	Silk fibroin
SFE	Surface free energy
SFNs	Silk fibroin nanoparticles
SS	Stainless steel
SSF	Spider silk fiber
ss-NMR	Solid state Nuclear magnetic resonance
TEM	Transmission electron microscope
TGA	Thermogravimetric analysis
TOC	Total organic carbon
TS	Tensile strength
UK	United Kingdom
USA	United States of America
UTS	Ultimate tensile strength
UV	Ultraviolet

v/v	Volume by volume
VSM	Vibrating sample magnetometer
w/v	Weight by volume
WD	With drug
wt. %	Weight percentage
WVP	Water vapor permeability
WVTR	Water vapor transmission rate
XRD	X-ray diffraction
YAG	Yttrium aluminium garnet
ZP	Zeta potential

Notations

A	Pre-exponential factor (s^{-1})
A	Absorbance
a^*	Greenness
a_0	Unit cell dimension of PLA (Å)
b^*	Yellowness
b_0	Distance between two nearby fold planes (Å)
c.a.	Approximately
d	Interlayer spacing (nm)
D_a	Dalton
E	Activation energy (kJ/mol)
E	Young's modulus (GPa)
$E´$	Dynamic storage modulus (MPa)
Ea	Average Activation energy (kJ/mol)
E_a	Apparent activation energy (kJ/mol)
f	Correction factor
$F(T)$	Heating rate to reach a defined degree of crystallinity at unit crystallization time (°C min^{-1})
$f(\alpha)$	Differential form of kinetic model function
G	Growth rate (min^{-1})
G_0	Pre-exponential term (min^{-1})
k	Arrhenius rate constant
k_b	Boltzmann constant

Nomenclature

K_g	Nucleation constant
K_T	Tobin rate constant
l	Average film thickness (mm)
L^*	Lightness/darkness
M_n	Number average molecular weight (D_a)
M_w	Weight average molecular weight (D_a)
n	Avrami exponent
P	Partial pressure (kPa)
q	Work for chin folding (kJ/mol)
R	Universal gas constant (J/mol.K)
R^2	Regression co-efficient
t	Crystallization time (min)
T	Absolute temperature(K)
T_0	Onset crystallization temperature(°C)
$t_{0.5}$	Crystallization half time (min)
T_∞	Imaginary temperature below which viscous flow is expected to be ceased(K)
T_c	Instantaneous crystallization temperature(°C)
T_{cc}	Cold crystallization temperature (°C)
T_e	End crystallization temperatures(°C)
T_f	Final decomposition temperature (°C)
T_g	Glass transition temperature (°C)
T_i	Initial decomposition temperature (°C)
T_m	Melting temperature (°C)
T_m^0	Equilibrium melting temperature (K)
T_{max}	Temperature of maximum degradation(°C)
T_{onset}	Onset of degradation temperature
T_p	Peak degradation temperature (°C)
T_s	Reference temperature (°C)
U^*	Diffusion activation energy (cal/mol)
w_0	Initial mass of the sample (mg)
w_f	Final mass of the sample (mg)
W_R^{400}	Weight percentage of the residue at 400 °C

w_t	Actual mass of the sample (mg)
X_c	Degree of crystallinity (%)
X_T	Relative crystallinity
Z_c	Modified Avrami rate constant
Z_t	Avrami rate constant
ΔE_{ab}	Total color difference
ΔH_{cc}	Enthalpy of crystallization (J/g)
ΔH_f^0	Heat of fusion for fully crystalline PLA (J/g)
ΔH_m	Enthalpy of melting (J/g)

Greek letters

γ_s	Total surface energy (kJ/mol)
γ^D_L	Dispersive surface energy component of liquid(kJ/mol)
γ^P_L	Polar surface energy component of liquid(kJ/mol)
γ_L	Liquid surface tension (kJ/mol)
γ^P_S	Polar surface energy component of solid surface(kJ/mol)
γ^D_S	Dispersive surface energy component of solid surface(kJ/mol)
σ	Lateral surface free energy(kJ/mol)
α	Degree of conversion
β	Heating rate (°C min^{-1})
θ	Diffraction angle (°)
λ	Cu-Kα radiation wavelength (nm)
ε_b	Percentage elongation at break (%)
ϕ	Nucleation activity
Ω	Ohm
σ_e	Binding surface free energy (kJ/mol)

Chapter 1

Introduction and Literature Review

This chapter provides a brief outline on the environmental hazards caused by conventional plastics having fossil-fuel origin. The benefits, limitations and applications of bio-based non-toxic and biodegradable polymers as potential alternatives for replacement of conventional plastics are discussed. A brief summary of basic fundamentals and terminologies about bioplastics, biopolymers and more emphasis on technological practices for overcoming limitations associated with biopolymers to achieve key target properties are discussed. The chapter also provides overview of the origin, chemical structure, properties, challenges and applications of bio-based polymers and proteins. This chapter mainly focuses on discussing various aspects of poly(lactic acid) and silk, especially muga silk. Some major outcomes reported so far on extraction, modification and utilization of silk with poly(lactic acid) in the area of packaging of food products, wound dressing scaffolds, cancer therapeutics and others are highlighted. Thereafter, the chapter presents the objectives of the doctoral thesis followed by organization of the thesis.

Parts of this chapter are published as book chapters

- Vimal Katiyar, Neelima Tripathi, **Rahul Patwa** and Prakash Kotecha, Environment friendly packaging plastics (CRC Press, Taylor & Francis Group, 2013).
- Arvind Gupta, Akhilesh Kumar Pal, **Rahul Patwa**, Prodyut Dhar and Vimal Katiyar, Green Composites Films with Excellent Barrier Properties (John Wiley & Sons, 2017).
- Akhilesh Kumar Pal, Neelima Tripathi, **Rahul Patwa**, Tabli Ghosh, Prodyut Dhar, Medha Mili, and Vimal Katiyar, Bio-based sustainable polymers for Food Packaging Applications (Smithers Rapra, 2017).

1.1 Introduction

Plastics play a major role in industrial growth of developing economies such as India. They have potential applications in market sectors such as transportation, construction, electronics, packaging and biomedical **(Geyer et al., 2017)**. This is due to their favorable characteristics such as low cost, easy processability, light weight, durability and storage efficiency. The conventional plastics are primarily derived from petrochemical feedstock and their widespread use has made us dependent on petrochemical sources **(Hopewell et al., 2009)**. Out of the total plastic production, packaging remains as the major market sector in which huge volumes of plastics are utilized worldwide (Figure 1.1). As per the data of 2015, around 381 million tons of plastic was produced worldwide, which is estimated to cross over 400 million metric tonnes by 2020 **(Fornasiero and Graziani, 2011)**.

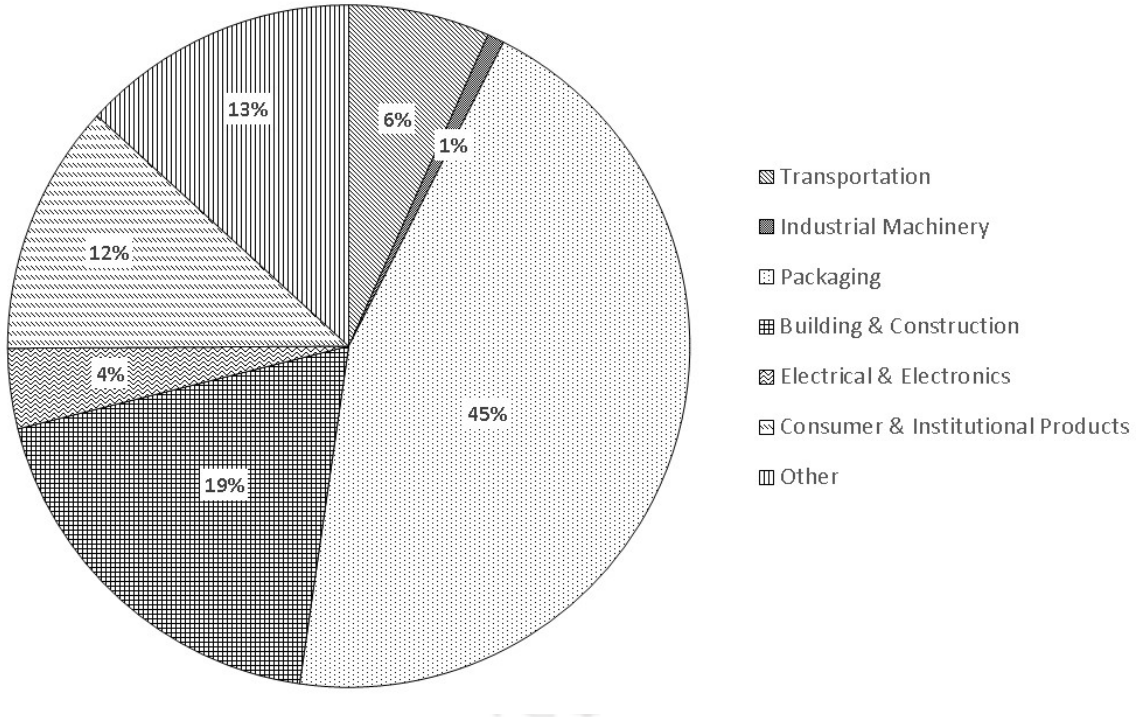

Figure 1.1: Percentage consumption of plastics for different applications (taken from (**(Geyer et al., 2017)**).

At present, majority of plastics used for packaging sector are fossil fuel-based such as polyethylene terephthalate (PET), polypropylene (PP), polyvinyl chloride (PVC), high density polyethylene (HDPE), low density polyethylene (LDPE) and polystyrene (PS) **(Sogancioglu et al., 2017)**. Each of the above-mentioned plastics have distinct characteristics to address specialized packaging applications. For example, PET is optically

clear and possesses high tensile strength making it suitable for transparent packaging. PVC has higher elongation which makes it suitable for production of pipes and sheets. PP and HDPE are used for production of firm and clouded containers respectively, by injection molding. LDPE, which possesses excellent stretchability, is ideal choice for storage bags. PS is mainly used for manufacturing Styroform®, which is an ideal shock-proof and insulating packaging material. The key thermal mechanical and barrier properties of different conventional polymers discussed above are presented in Table 1.1.

Table 1.1: Properties of different conventional polymers compared to PLA (taken from **(Crompton, 2012)** and **(Shogren, 1997)**).

Properties	**PC**	**PET**	**PVC**	**PP**	**HDPE**	**LDPE**	**PS**	**PLA**
Tensile Strength (MPa)	50	55	51	26	32	10	34	53
Percentage Elongation (%)	200	300	60	80	150	400	1.6	6
Young's Modulus (GPa)	2.1	2.3	3	2	1.25	0.25	3	3.5
Max. serviceable Temperature (°C)	110	115	70	135	120	80	90	55
Thermal Conductivity (W/m.K)	0.22	0.15	0.25	0.11	0.47	0.33	0.13	0.13
Oxygen Transmission Rate (cc.cm/sq. cm. s. cm Hg × 10^{10})	1.4	0.035	0.045	1.2	0.3	2.2	3.4	0.26
Water vapor Transmission Rate (cc.cm/sq. cm. s. cm Hg × 10^{10})	1400	130	275	35	9	68	1400	3.2

Despite the considerable benefits that the fossil fuel-based conventional plastics have, the depleting fossil fuel reserves and the environmental pollution caused by conventional plastics has become a major concern of our modern day society. Out of the total plastic produced, around 60% is discarded after first use, which is either incinerated or goes into the landfills which ultimately goes to the oceans and gets accumulated there forever. So far, a total of 8300 million metric tons (Mt) of plastics has been produced and 6300 Mt of plastic waste has been generated out of which only 9% goes to recycling, 12% is incinerated and 79% is dumped at landfilling sites **(Geyer et al., 2017)**. As a result of this, large amounts of pollutants are released into the environment adding to the carbon footprint. All the three alternatives for disposal of plastic waste have their shortcomings. Incineration is the less favored option as it leads to emission of huge amounts of carbon dioxide and other toxic green-house gases, which results in global warming. Landfilling is often discouraged due to dwindling landfilling sites and leachates ultimately polluting

water bodies. Out of the three, recycling seems to be an appropriate option to deal with the plastic waste generated. However, recycling is an energy-intensive process with several pre-treatment steps prior to reprocessing into final end product. In addition to this, the final product lacks in terms of overall quality when compared to fresh manufactured item. Due to such alarming issues, it is the need of the hour to develop bio-based materials having similar or better properties than petroleum-based products for a sustainable future. At present, bio-based plastics are being studied extensively to improve their properties and make their production more cost-effective to replace petroleum-based plastics. The bio-based polymers derived from biomass or obtained from the derivatives of biomass which can be processed to finished products are known as bio-based plastics **(Pilla, 2011)**.

1.1.1 Biopolymers

Biopolymers are basically polymers that are bio-based, biodegradable or both **(Imre and Pukánszky, 2013)**. Biopolymers are considered to be environment friendly, as carbon atoms in these materials originate from atmospheric carbon dioxide fixed by plants during photosynthesis. If incinerated these materials do not produce any extra carbon dioxide, thus keeping greenhouse gases under check. **Kfoury et al. (2013)** divided biodegradable polymers into two broad categories viz. natural and synthetic biodegradable polymers (Figure 1.2(a)). These can be further classified as:

(i) Natural biodegradable polymers
   (a) Polymers obtained from agro-based resources.
   (b) Polymers obtained through microbial fermentation processes.

(ii) Synthetic biodegradable polymers
   (a) Polymers synthesized by conventional methods using bio-derived monomers.
   (b) Polymers synthesized by conventional method using monomers derived from petrochemical resources.

Major biodegradable polymers include poly(lactic acid) (PLA), poly(hydroxybutyrate) (PHB), poly(ε-caprolactone) (PCL), polypropylene carbonate (PPC) etc. The production of bio-based polymers in 2011 was 3.5 million tonnes which is estimated to shoot up to 12 million tonnes in 2020, with an annual 15% growth till 2015 already observed. As shown in Figure 1.2(b), the packaging sector accounts for up to 66.5% consumption of bio-based polymers, based on the data of year 2016. PLA is a versatile and promising bio-based,

renewable and biodegradable thermoplastic polyester derived from lactic acid which can be used for food packaging **(Ramos et al., 2014; Rhim et al., 2013)**.

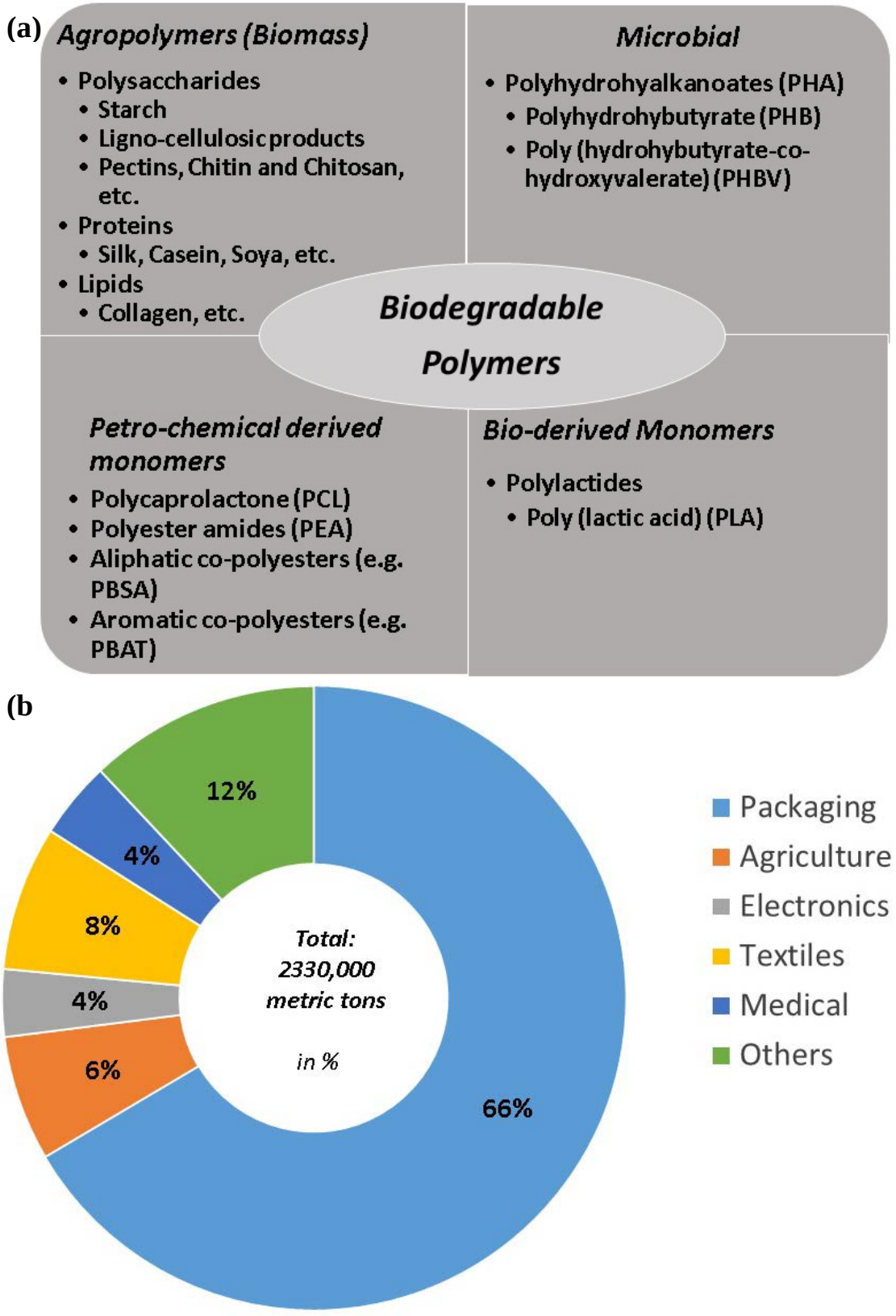

Figure 1.2: (a) Classification of biodegradable polymers and (b) global consumption of biodegradable plastics**.**

1.1.2 Poly(lactic acid)

PLA is a linear, aliphatic, thermoplastic polyester that can be produced from L-lactic acid or D-lactic acid monomers. These monomers are obtained from natural resources like corn, sugar beet, sugar feedstock and wastes from food and agriculture industry through fermentation **(Bocchini et al., 2010)**. The monomer unit of poly(lactic acid) is 2-hydroxy propionic acid. PLA is widely used in various biomedical applications such as sutures, drug delivery, tissue engineering as scaffolds, orthopedic implants, etc. Another potential application is in packaging sector, especially food packing industry. PLA is commercially available in various grades and has been approved by the food and drug administration (FDA). PLA degrades slowly by simple hydrolysis of the ester bonds to harmless products like carbon dioxide and water **(Drumright et al., 2000)**. The life cycle of PLA along with its chemical structure is shown in Figure 1.3. PLA can be synthesized by various polymerization routes viz. polycondensation, azeotropic dehydrative condensation polymerization, ring opening polymerization (ROP) and solid state polymerization of low molecular weight PLA **(Lunt, 1998)**.

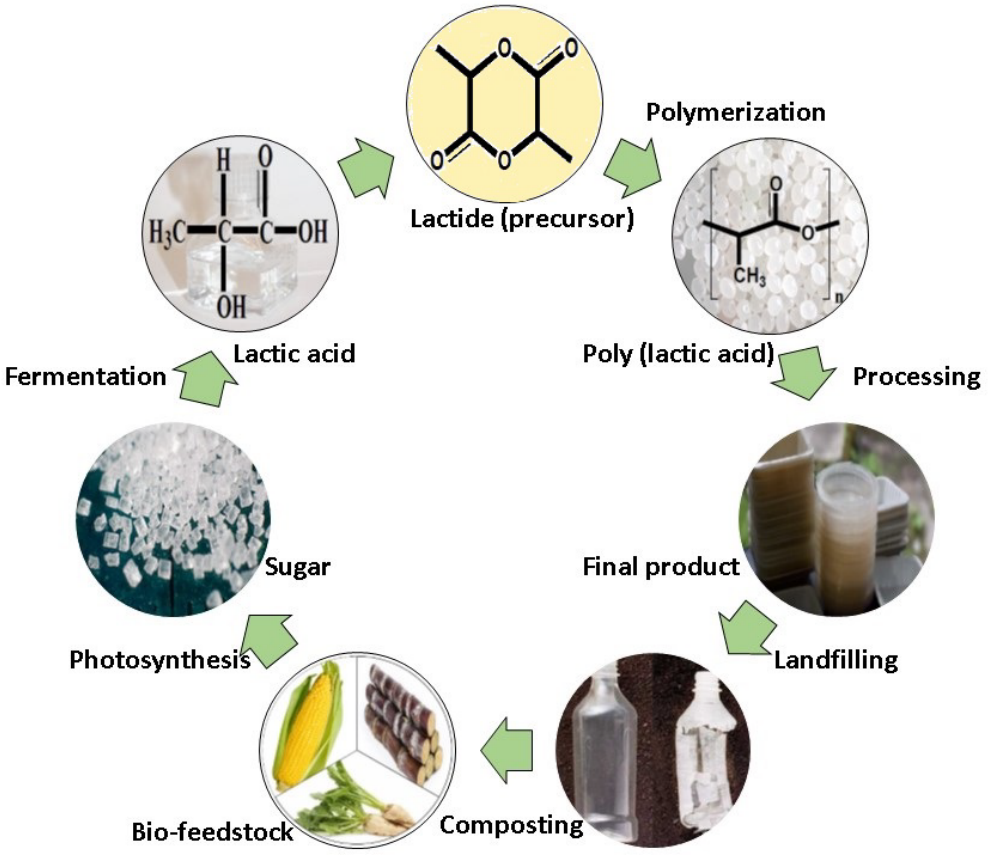

Figure 1.3: Life cycle of poly(lactic acid) (taken from **(Gironi and Piemonte, 2011)**).

1.1.3 Properties of poly(lactic acid)

In this section, thermophysical, mechanical, barrier, and rheological properties, and solubility and degradation characteristics of poly(lactic acid) are presented. Attributes such as biodegradability, recyclability, compostability, biocompatibility and non-toxicity make PLA an eco-friendly alternative to conventional petroleum-based plastics. During processing, PLA consumes around 25% lesser energy as compared to petroleum-based polymers **(Rasal et al., 2010)**. PLA is a transparent, colorless, stiff and glossy thermoplastic with physical properties quite similar to polystyrene. Pure PLA enantiomer exhibits semicrystalline nature and different phases with melting point (T_m) ranging from 160–175 °C, glass transition temperature (T_g) ranging from 55–70 °C and cold crystallization temperature (T_{cc}) ranging from 90–125 °C. The melt enthalpy for completely crystallized PLA is estimated to lie between 93–148 Jg^{-1} **(Miyata and Masuko, 1998)**. PLA has a slow crystallization rate even at optimum temperature range 110–130 °C. **Huang et al. (1998)** reported the spherulite growth rate to be ~4 μm/min at 125 °C. Mechanical properties of PLA are highly dependent on molecular weight and degree of crystallinity. Accordingly, amorphous PLA can be soft and elastic while crystalline PLA can be stiff. Semicrystalline PLA displays a balance of the desired mechanical properties such as tensile strength ranging from 50–70 MPa, tensile modulus reaching to 3 GPa and elongation at break roughly around 4% **(Södergård and Stolt, 2002)**. Upon annealing, the tensile strength and impact resistance increase due to crosslinking of crystalline segments and stereo-regularity, respectively **(Farah et al., 2016)**. Stereocomplexation leads to superior mechanical properties due to intermolecular crosslinking **(Gupta and Katiyar, 2017)**. Barrier properties too are highly dependent on PLA crystallinity. Gas transmission rates increase with increasing temperatures. PLA displayed a water vapor transmission rate (WVTR) of 82 and 172 g/m^2.day for crystalline and amorphous forms, respectively **(Shogren, 1997)**. Oxygen permeability of PLA at 30 °C and 50% relative humidity (RH) is around 500 cm^3/m^2.day.0.1MPa **(Narayanan et al., 2017)**. PLA, being a thermoplastic polymer, is found to have non-Newtonian characteristics with pseudoplastic nature. High viscosity linear PLA is observed to exhibit zero shear viscosity around 1000 Pa.s at 190 °C which is expected to decrease with reduction in molecular weight **(Dorgan et al., 1999)**. PLA is highly soluble in chloroform, dichloroacetic acid, acetonitrile, dioxane, methylene chloride, 1,1,2-trichloroethane whereas it is sparingly soluble in acetone, toluene, ethyl benzene and tetrahydrofuran. PLA is insoluble in water, alcohols such as ethanol, methanol

and other unsubstituted hydrocarbons **(Lasprilla et al., 2012)**. PLA can degrade in natural environments such as soil and composts via hydrolytic and enzymatic degradation pathways. During hydrolytic degradation, water seeps in and cleaves the ester bonds by random scission. This results in production of oligomers thus resulting in reduction in molecular weight. When the molecular weight of fragments approaches to 10–20 kg/mol, the microbes present in the soil consume them and convert to carbon dioxide and water. Therefore, hydrolytic degradation takes place initially followed by microbial degradation.

1.1.4 Limitations of poly(lactic acid)

Although PLA has comparable thermal, mechanical and barrier properties which makes it a promising candidate for replacement of conventional plastics, it suffers from some limitations which restrict its applications **(Armentano et al., 2013)**. PLA has a brittle nature which is undesirable in flexible packaging. It is not fit for high temperature and high strength applications due to its weak mechanical properties and poor heat stability. PLA has a slow crystallization rate which poses difficulties during processing. PLA has poor barrier properties which make its applicability to food packaging very limited. It cannot hold hot beverages due to its low heat deflection temperature. PLA has a short working lifetime which prevents its use in engineering applications requiring longer workability **(Carrasco et al., 2010)**.

1.1.5 Applications of poly(lactic acid)

PLA has a wide range of applications owing to its comparable material properties to conventional plastics. The three important sectors where PLA has major application are packaging, textiles and bio-medical. According to the **Grand view research, 2017** market survey report published in May, 2017, packaging sector accounted for the maximum share of 59.1% in 2016 due to increasing awareness towards green packaging. Notably, as PLA is biocompatible and biodegradable, it can be used for biosorbable sutures and implants, eliminating the need to operate on the body for removal. Other areas where PLA finds application are building and construction, agriculture, electronics etc.

1.1.6 Polymer nanocomposites

In order to improve material properties of biopolymers, they are filled with nanoparticles of other materials to yield nanocomposite materials. Nano-fillers can have organic or inorganic origin. Inorganic fillers at some stage from production to end-of-use pose

environmental or health hazards **(Fawell, 1993)**. Hence, it is wiser to opt for organic nano-fillers to ensure sustainability. Combining nano-fillers into PLA/PCL matrix to form nanocomposite material has been explored as an innovative and effective approach to achieve superior thermomechanical and barrier properties than each of the constituent material. These nano-fillers are added at small loadings. Due to dimensions at the nanoscale, the filler has high surface area and can interfere with polymer chain movement. This brings about a change in matrix properties; thus improved material properties can be achieved. The improvement in material properties depend upon the extent of dispersion and chemical/physical interactions between nano-fillers and the polymer matrix. Conventionally, there are four ways to prepare polymer nanocomposites viz. solution casting-cum-evaporation technique, melt extrusion, electrospinning and in-situ polymerization method, which are described next: **(Dhar et al., 2017; Gupta et al., 2017; Suwantong et al., 2012)**.

1.1.6.1 Solution casting-cum-evaporation technique: This method involves the dissolution of polymers in an appropriate solvent, after which the nano-fillers are usually added in the polymer-solvent mixture. After appropriate mixing, the mixture is allowed to relax and the trapped air bubbles are allowed to escape. The solution is poured onto non-sticky flat surfaces like glass or Teflon and solvent is allowed to evaporate **(Jamshidian et al., 2012)**.

1.1.6.2 Melt compounding method: This technique involves the melt-integration of polymers with reinforcement directly without the use of harmful solvents making it a real 'green processing' technique. The materials are mixed at temperatures slightly higher than the melting temperature of polymer **(Monika et al., 2017)**.

1.1.6.3 Electrospinning: In this process, voltage is applied to polymer solution to overcome its surface tension which causes the formation of nanofibers, whose dimensions can be fine-tuned depending upon process conditions such as voltage, rotating speed, injection speed. The nanofibers possess high porosity, large surface area and high gas permeation rates **(Suwantong et al., 2012)**.

1.1.6.4 In-situ polymerization method: In this method, the nanomaterials are well dispersed in the monomer solution, which is subsequently polymerized in the presence of fillers **(Tesfaye et al., 2017)**.

1.1.7 Biofiller-reinforced poly(lactic acid)

To retain biodegradability and non-toxicity, PLA can be mixed with biofillers, i.e. nano-fillers from natural polymeric materials such as cellulose, chitosan, gums, silk etc. **(Gupta and Katiyar, 2017; Pal and Katiyar, 2016; Tripathi and Katiyar, 2016)**. They offer a lot of advantages such as abundancy, low-cost and sustainability. However, biofillers have high density of functional (polar) groups on their surface which restricts proper dispersion. Surface modification of the biofiller may be required to achieve good dispersion.

1.1.8 Silk: nature's nylon

The term silk refers to the wide range of continuous filaments spun by several insect species of Lepidoptera and Arthropoda. It has excellent strength which is comparable with Kevlar. Silk is produced by specialized glands which are stored in the lumen sac until it is spun into silk fibers. However, it still remains a mystery to researchers as to what happens on the molecular scale at the spinning duct that converts the silk dope present in the sac initially in liquid form to fibers of such high strength. The taxonomic classification can be seen in Figure 1.4(a) **(Sonthisombat and Speakman, 2003)**. They have a range of purposes ranging from cocoons which provide protective casing for eggs/pupa to draglines which hold the spider orbs against impact from prey and are also used for escape. Silks are hierarchically arranged from the amino-acid level up to micro and macroscopic structures. It is evident that both types of silks (spider and silkworm) do not have any common lineage. Furthermore, their amino acid composition is also different. On weight basis, silk is five times stronger than steel **(Keten et al., 2010)**, but at the same time is as tough and extendable as synthetic rubber. Silks' discovery dates back to around 3000 B.C. in China where cultivation was closely guarded and was limited to aristocratic use, but attempts to do the same with spiders have proven unsuccessful because of their territorial and cannibalistic nature. According to Central Silk Board (CSB) **(Natesh, 2011)**, total production of silk in India as per 2010–11 data is 20,410 Mt consisting of all four major varieties of silk produced in India viz. Mulberry, Tasar, Eri and Muga shown in Figure 1.4(b–e). Out of these, silk produced by *Bombyx mori*, also known as the mulberry silk amounts to ~80%, i.e. 16,360 Mt whereas the share of the other three varieties, collectively termed as Vanya silks, is mere ~20%, i.e. 4550 Mt, with Muga silk having even lesser share of just 0.6%, i.e. 124 Mt **(Natesh, 2011)**. Silk fiber is constructed with two proteins namely, fibroin and sericin. Silk production has a minimal wastage as compared to other synthetic alternatives. The byproducts during silk production are unused parts of pupa and

cocoon. The major source of silk waste is from pierced cocoons and left over cocoons from silk reeling process, called the reeled cocoons. Silk fiber is hydrophobic, renewable, biodegradable and biocompatible, making it a valuable resource. Utilizing waste silk-reinforced polymer bionanocomposites can be very cost-effective especially for packaging and bio-medical applications.

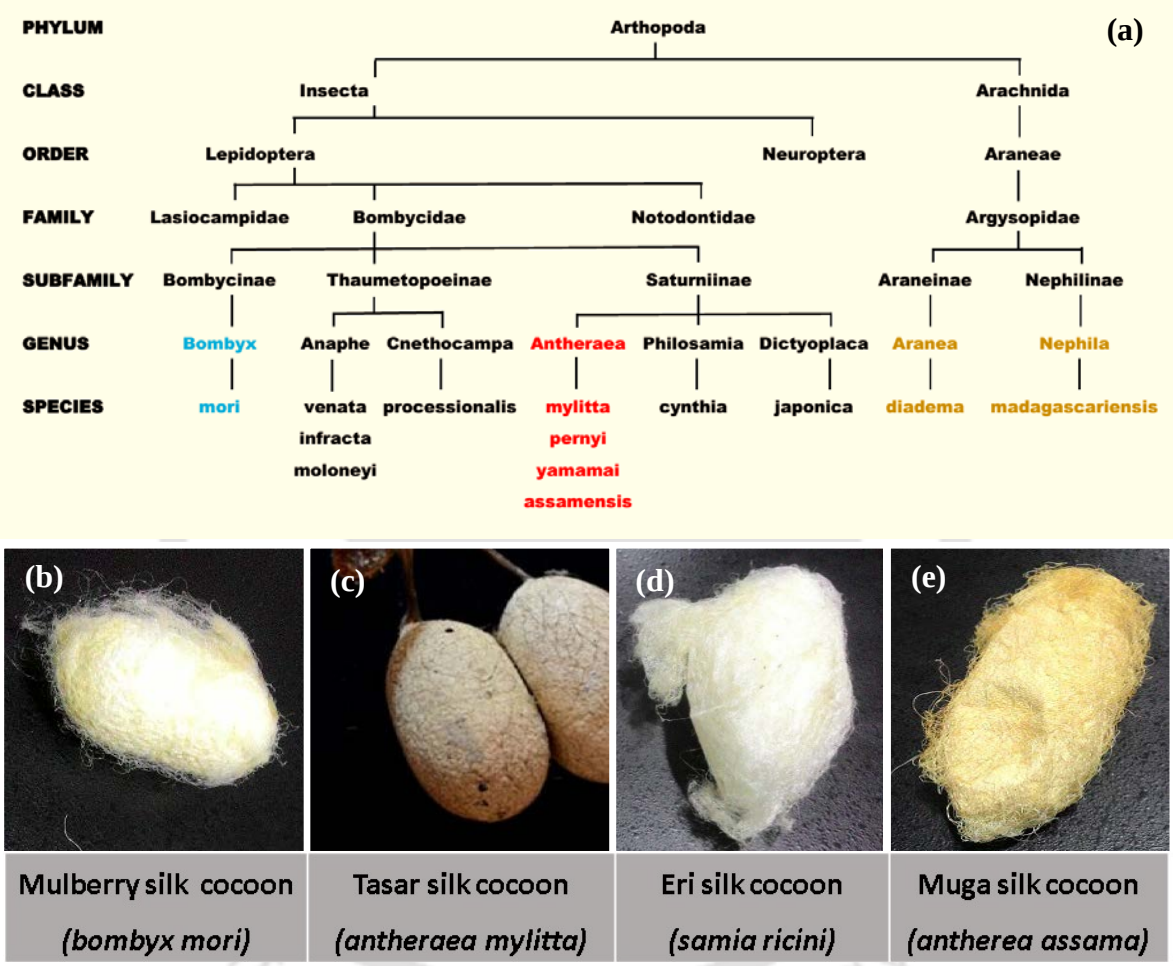

Figure 1.4: (a) Taxonomic classification of silks and (b-e) visual appearance of different varieties of silk cocoons available in India (taken from **(Sonthisombat and Speakman, 2003)**)

1.1.9 Structure of silk

As illustrated in Figure 1.5, all silks irrespective of their origin are thought to consist of a protein core and a protective coating. The core which contains the fibroin, is made up of two protein mono-filaments called brins (extruded from two silk glands) which are embedded inside sericin, a hydrophilic glycoprotein which needs to be removed by a process known as degumming **(Gulrajani, 1992)**. Sericin forms 25–30% weight of the silk fiber, and is rich in amino acid serine. It is rich in carotenoids which are responsible for

pigmentation of cocoons. Sericins are UV resistant and are difficult to digest by microbes or insects. Sericin is known to generate immune response that is why silk needs to be properly degummed prior to use in biomedical applications. The brins are made up of bundles of nanofibrils, which are arranged parallel to the axis of the fibre. The nanofibrils bundles are grouped together to form microfibrils which combine to form brins.

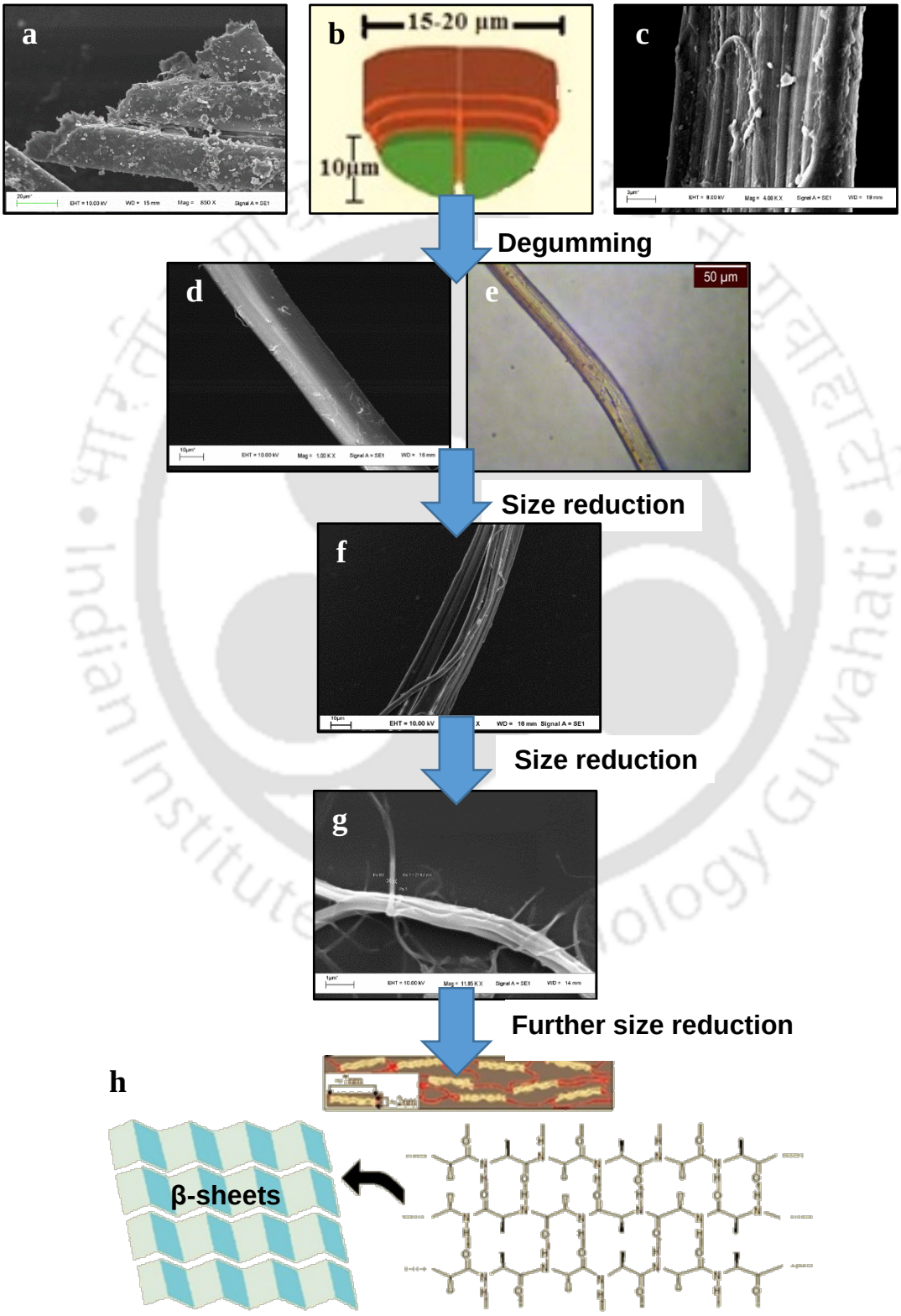

Figure 1.5: Molecular arrangement of silk fiber. (a) microscopic view of degummed silk fiber showing two brins, (b) microscopic view of silk fiber showing ~20 μm with sericin outer layer, (c) microscopic view of raw silk fiber with calcium oxalate crystals over surface, (d) degummed silk fiber, (e) optical microscope image of raw silk fiber showing high shimmer under light due to its high refractive index (f) microfibrils from silk fiber, (g) nanofibrils from silk microfibers and (h) the nanostructured arrangement of hydrophilic and hydrophobic domains, where hydrophobic domains are organized into β-sheets adapted from (**(Sonthisombat and Speakman, 2003)**).

1.1.9.1 Molecular structure of silk

To know more about the microstructure of silk proteins, various sophisticated techniques such as nuclear magnetic resonance (NMR) spectroscopy, X-ray diffraction (XRD) and transmission electron microscopy (TEM) have been utilized **(Barghout et al., 1999; Plaza et al., 2012)**. Silk proteins are supposed to be a matrix of rubbery polypeptide which imparts elasticity with small, rigid, inextensible β-sheet crystallites embedded in it imparting strength. Silk structure can be simplified into primary and secondary structures for a clearer understanding.

1.1.9.1.1 Primary structure of silk

Primary Structure of silk comprises highly repetitive sequences which give rise to very regular conformations as shown in Figure 1.6. It is known that these amino acids are grouped together in many fibroins; e.g., there is evidence for long sequences of glycine, alanine, and serine in *Bombyx mori* fibroin, and for poly(alanine) sequences (12-13 residues) in the non-mulberry silk followed by glycine-rich domains containing bulky residues, which closely resemble to that of primary structure of spider silk (5-7 residues) **(Ayoub et al., 2007; Plaza et al., 2012)**. The hydrophobic domains are mainly composed of charge carrying amino acids such as glycine, alanine, serine, threonine and valine repeats which can form anti-parallel β-sheets . The hydrophilic units are smaller and more complex that consist of bulky and polar side chains which make up the amorphous portion of silk, imparting elasticity. Non-mulberry silks possess higher alanine to glycine ratio and poly-alanine blocks which form β-sheets **(Lucas et al., 1960)**.

AAAAAAAAAAAAAGS GSGGYGGYGGYG SAAAAAAAAAAA SAGG GGGYGWGDGGY SAAAAAAAAAA

Figure 1.6: Typical amino acid sequences of repetitive core of wild silk (genus: *Antheraea*) fibroin. The highlighted regions are definite β-sheet forming segments. The sequence is for *Antheraea pernyi* fibroin (accession number: O76786) (adapted from **(Fu et al., 2011)**).

1.1.9.1.2 Secondary structure of silk

Silks are two-phased semicrystalline biopolymers having both amorphous and crystalline regions. The silk proteins are essentially block copolymers with alternate arrangements of hydrophobic (crystalline) and hydrophilic (amorphous) regions. Crystalline regions are composed of β-pleated sheets of polyalanine repeats in case of spiders and wild silks, and polyglycylalanine for mulberry silks. The hydrophobic domains are assembled in the form of nanocrystallites which are highly conserved amino acid sequences, with crystal size around 2 × 5 × 7 nm as measured using XRD **(Riekel and Vollrath, 2001)**. Nanocrystals contribute to superior mechanical properties of silk **(Keten et al., 2010)** and are mostly insoluble in all major solvents including water. **Nova et al. (2010)** used molecular modelling approach to study the interplay between amorphous regions and nanocrystals. They observed that the amorphous regions unravel first which impart the silk its extensibility while nanocrystals are responsible for ultimate tensile strength by forming interlocking regions that transfer the load. The amorphous regions have random coil arrangements. The ultimate tensile strength is directly related to the size of nanocrystals. The ratio of crystalline to non-crystalline domains is different in spiders and silkworms. The β-pleated sheets are formed by intermolecular forces such as H-bonding, one of the weakest chemical bonds known with typical bond energies around 5 kcal/mol. It has been found that the intrinsic weakness of H-bonds when grouped in clusters of around 4, upon breaking of a single bond does not result in breakdown of entire system. In addition to that, hydrogen bonds can reform upon breaking, contributing to exceptional toughness of silk **(Shao and Vollrath, 2002)**. Furthermore, β-sheets in silk are aligned parallel to fiber axis unlike amyloid protein aggregates responsible for Alzheimer's, Parkinson's and Huntington's diseases which are known to form cross beta sheets. This compels force to propagate along the strand, requiring higher force to dissociate all inter-strand hydrogen bonding at once **(Du et al., 2006)**. The beta sheet structure of silk is quite similar to Nylon 6 except that the hydrogen bonding is much higher. This results in higher degradation temperature of silk as compared to other aliphatic polyamides **(O'Brien et al., 1998)**. Beta sheets have dimensions of a few nanometers and constitute roughly 10-15% of the silk volume for spiders and silkworm silks **(Keten et al., 2010)**.

1.1.10 Difference between mulberry and non-mulberry silk

Both mulberry and non-mulberry silkworms belong to the Bombycidae family as shown in the tree diagram in Figure 1.4(a). The former belongs to the Bombicinae subfamily while

the latter belongs to the Saturniinae subfamily. This naturally makes their silk fibroins quite different in the amino acid sequence, composition, their arrangement as well as structure **(Devi et al., 2011; Lucas et al., 1958)**. *B. mori* contains alternate glycine and alanine in their consensus amino acid sequence, i.e. (Gly-Ala-Ser-Gly-Ala-Gly)~Tyr, while *A. assama* contains multiple repeats of alanine in their consensus amino acid sequence. *B. mori* contains a higher percentage of glycine than alanine while *A. assama* contains a higher percentage of alanine than glycine **(Devi et al., 2011)**. In *B. mori* the distance between beta sheets is alternatively 3.79Å and 5.27Å while in wild silkworms it is a uniform 5.27 Å **(Kaplan et al., 1993)**.

1.1.11 Properties of silk

This section briefly discusses the physical, chemical, mechanical, degradability and other properties of silk. Silk fibers generally have a triangular cross-section with rounded corners and elongated wedge shape for wild silk varieties. The surfaces reflect light at many angles giving silk a shimmering appearance. Silk has a smooth and soft texture, and loses around 20% of its strength when wet. Silk is a poor conductor of electricity but displays static effect during manual handling. The silk fibroin protein of non-mulberry silkworm is a homodimeric protein of 395 kDa, with each monomer approximately 197 kDa **(Datta et al., 2001)**. Silk is resistant to most mineral acids, except sulfuric acid which dissolves the silk. Mulberry silk is soluble in chaotropic solvents such as lithium bromide, lithium thiocyanate, calcium chloride solution in ethanol etc. at temperatures above room temperature. Non-mulberry silks are only partially soluble or non-soluble in such solvents due to increased hydrogen bonding. Regenerated or reconstituted silk which is essentially in random coil conformation and is converted to β-form by annealing (steam or water), treatment with methanol or ethanol. Most products fabricated from regenerated silk are weak and brittle with only around 1–2% of mechanical strength of original form. **Koh et al. (2015)** have compared the mechanical properties of natural and synthetic fibres. Spider silks are comparable to commercially available synthetic fibres as seen in Table 1.2. Through *in vivo* experiments on rats and pigs, silk is found to be biocompatible after proper degumming and sterilization **(Fan et al., 2009)**. Silk can be degraded by enzymes such as α-chymotrypsin and protease **(Shaw, 1964)**; **(Srihanam and Simchuer, 2009)**. Silk can be effectively used as implants over polylactides or polyglycolides, as it does not degrade into acidic fragments which decrease the pH of surrounding. The degradation of silk can be controlled by varying the content of β-sheets.

1.1.12 Muga silk

Muga silk, which is geographically tagged to the state of Assam in the year 2007, is obtained from Muga (A*ntheraea assama*) silkworm which is a wild/semi-domesticated, multivoltine (i.e. breeds many times a year), non-mulberry species belonging to the family Saturniidae (superfamily Bombycoidea) **(Unni et al., 2009)**. These silkworms are raised on aromatic leaves of Som (*Machilus bombycina*) and Soalu (*Litsaea polyantha*) plants. Cocoons are large (about 5 × 2.5 cm in size) and exhibit a bright brown color.

Table 1.2: Mechanical properties of silk compared to other materials (adapted from **(Koh et al., 2015)).**

Source	Tensile strength (MPa)	Toughness ($MJ \cdot m^{-3}$)	Elongation (%)	Modulus (GPa)
B. mori silk	300–740	70–78	4–26	10–17
A. assama silk	440–620	84–149	33-45	3.8–5.8
Dragline silk	875–1300	200	16.7–38	10
Collagen	0.9–7.4	-	24–68	0.0018–0.046
Wool	200	60	50	0.5
Rayon	685	-	12	13
Nylon	430–950	80	18	1.8–6
Kevlar	3600	50	2.7	154
Steel	1500	6	0.8	209
Natural rubber	22–32	-	700	0.0015–0.0025

It is found only in the Brahmaputra valley situated in the north eastern region of India, especially Assam state from which it gets its name '*assama*'. The word 'Muga' in Assamese language means amber brown which indicates the golden color of silk fiber. *A. assama* is a promising candidate as a biocompatible, biomimetic, and biodegradable biomaterial of natural origin for applications in tissue engineering and regenerative medicine **(Kasoju et al., 2009)**. The unit cell dimensions for wild silk are a = 10.6 Å (side-chain), b = 9.44 Å (H-bond) and c = 6.95 Å (fiber axis) **(Warwicker, 1960)**. Linear density, refractive index, density and birefringence of Muga silk is around 2.3 dtex, 1.536, 1.308 g/cm^3 and 0.040, respectively **(Rajkhowa et al., 2008)**.

1.2 Literature review

1.2.1 Synthesis/preparation of silk nanoparticles

This section shows key representative literature on synthesis and preparation of silk nanoparticles using various methods used so far by various researchers.

Rajkhowa et al. (2008) prepared ultra-fine silk particles from three silk varieties, viz. Mulberry, Muga and Eri. The silk fibers were chopped into snippets and then pulverized using rotary and planetary ball mill. They studied the effects of degree of degumming, size of milling media, water and lubricant amount on particle size. They found that effective degumming reduces milling time but severe degumming prevents effective size reduction due to particle aggregation. A volume based median particle size (d (0.5)) of around 200 nm was achieved. Size reduction occurred by separation of micro and nanofibrillar structures. It was found that planetary ball mill was more efficient than rotary milling, and wet milling was more effective than dry milling. Non-mulberry silk showed higher fragmentation rate than mulberry silk. For ball milling, material-to-water ratio by weight was 1: 10–15, rotating speed was 200 rpm, milling media was ziralumina 10 mm balls. For further size reduction 0.5–5 mm balls were used once size reached 10-12 μm.

Kundu et al. (2010) prepared silk nanoparticles from silk fibroin solutions of non-mulberry Tasar silkworm using desolvation technique, dimethyl sulfoxide (DMSO) as desolvating agent. The fibroin was collected from silk glands of silkworms. The particle size was around 157–168 nm with spherical shape and negative surface charge -5.06 to -25.15 mV. The particles possessed a β-sheet structure. Cytotoxicity was assessed against L929 fibroblast cells, which indicated that silk nanoparticles are relatively non-toxic to the cells. *In vitro* release of growth factors was achieved without initial burst, releasing ~35% up to 5 days followed by a more sustained release ~1% per day after that. The silk fibroin nanoparticles were developed for cancer diagnostics and therapeutics.

Zhang et al. (2007) prepared silk fibroin nanoparticles (SFNs) using regenerated silk (8–200 kDa) by rapidly introducing liquid silk into water miscible protonic solvents. Well dispersed, stable and insoluble nanoparticles were obtained which were globular in shape with sizes in the range of 35–125 nm. The size and morphology was confirmed using TEM, scanning electron microscopy (SEM), atomic force microscopy, (AFM) and dynamic light scattering (DLS). The conformation change of silk from random coil to β-

sheet structure was confirmed by infrared, Raman, and NMR spectroscopy. It was observed that nanoparticles prepared using acetone showed 20 times more UV resistibility than native silk powder. *E. coli* and *B. subtilis* could not grow in solutions containing silk nanoparticles. The X-ray diffraction curves showed the crystallinity to be about four-fifths of native fiber. The silk nanoparticles were generated by rapid dispersing which resulted in instant dehydration and denaturing internally and externally. The SFNs were biocompatible, easy to functionalize and suitable for application as medical biomaterials and in drug delivery.

Lammel et al. (2010) prepared silk fibroin particles (500 nm–2 μm) by salting out using potassium phosphate (> 0.75 M). Secondary structure, size and zeta potential of prepared nanoparticles could be controlled by varying the pH. The size and yield of nanoparticles increased as the pH was increased. Nanoparticles fabricated through salting out process using 1.25 M potassium phosphate at pH 6 showed β-pleated structures whereas particles produced at pH 9 had a mainly random coil structure. The reported silk fibroin nanoparticles could be loaded with drug by simple absorption based on electrostatic interactions and were used for controlled release of hydrophobic model drug (rhodamine B) which released quickly with high burst release in the first 3 hours.

Wang et al. (2010) prepared silk spheres with controllable size and shape using aqueous-based preparation method. The method involves phase separation between silk fibroin and polyvinyl alcohol (PVA) at a weight ratio of 1:1 and 1:4. The nanospheres were obtained by dissolution of previously air-dried blend solution in water; the residual PVA was removed by centrifugation. The spheres had around 30% beta content and less than 5% residual PVA. The study also discusses obtaining spindle-shaped particles by stretching the films prior to dissolving in water. The sphere sizes could be controlled by varying the concentration of PVA, silk fibroin solution or by applying ultrasonication. The porous nature of nanoparticles and amphiphilic nature of silk facilitated the loading of a variety of drugs with different zeta potentials and hydrophobicities, which can lead to different drug release profiles. Silk nanospheres can be utilized as drug delivery carriers in a variety of biomedical applications.

Gupta et al. (2009) prepared pure silk fibroin or silk fibroin and chitosan nanoparticles with varying ratios (<100 nm) fabricated using capillary-microdot technique. The drug (1

mg) was added to silk fibroin solution (100 µl) and was dispensed on glass slides via micro capillary, which was frozen overnight and later lyophilized. Dry dots were scraped off and were subjected to crystallization by suspending the nanoparticles in methanol for 15 minutes. After crystallization phosphate buffered saline (PBS) washing was done and the nanoparticles were stored until further use. Particle size was determined using transmission electron microscopy. The prepared nanoparticles were loaded with curcumin and release profiles were studied. It was found that nanoparticles derived from pure silk fibroin showed highest drug entrapment, drug release and highest efficacy against breast cancer cells.

1.2.2 Extraction of crystalline silk

This section discusses current know-how about the isolation/extraction of crystalline portion of silk from native silk fibers.

Drucker and Smith (1950) and **Drucker et al. (1953)** dissolved silk fibroin in cupri-ethylenediamine, which was followed by neutralization and dialysis. The regenerated solution was subjected to tryptic hydrolysis. This led to formation of a precipitate, whose amino acid composition was determined using hydrochloric acid digestion. The precipitate consisted of glycine, alanine and serine in the ratio 3:2:1. The trypsin hydrolysis liquor on the other hand showed the presence of bulky amino acids such as tyrosine, valine, leucine, arginine, phenylalanine, aspartic acid, glutamic acid and proline. The molecular weight of portion consisting of bulky side-chains was estimated to be 5000 units whereas the molecular weight of the precipitate was estimated to be around 7000 units. The fibroin molecular weight was reported as 33000 units. To form a complete silk molecule, three straight chain sections of molecular weight (MW) 7000 each are linked by two regions of bulky amino acids having total MW of 5000 each. These findings were correlated with X-ray diffraction patterns of fibroin, which showed that crystalline portion consists of glycine alternating with alanine or serine.

Shaw and Smith (1961) obtained residues by treatment of various silk fibroins with acid, alkali and oxidation using hydrogen peroxide. The residues were identified using column chromatography. The wild silk residues upon acid treatment had higher amounts of alanine (71.8%), glycine (9.4%) and serine (8.5%) than untreated fibroins which have alanine (36.9%), glycine (23.5%) and serine (9.8%). The yield with acid (10N HCl), alkali (4N NaOH) and oxidation (3% w/v, pH 5) was 39%, 47% and 48% after 70, 95 and 45 h, respectively. They further performed X-ray diffraction studies to observe that the crystal

structure of residues was almost identical to the crystal structure of unmodified fibroins, except residues had sharper intensities.

Bhat and Nadiger (1980) carried out partial acid hydrolysis of four Indian varieties of silk viz. Mulberry, Tasar, Eri and Muga using hydrochloric acid at 40 °C. Hydrolysis of mulberry silk was carried out using 6N acid for 48 h while wild silk varieties were subjected to 8N acid strength for 96 h. The partial acid hydrolysis yielded a chemically resistant portion which is supposed to be mostly crystalline. The percentage crystallinity was determined using electronic diffraction and infrared spectroscopy. For mulberry silk, absorption bands at 975 and 998 cm^{-1} are present and become stronger upon hydrolysis. These bands are Ala-Gly linkages. In addition to that, peaks at 1015 and 975 cm^{-1} were absent which are designated for Gly-Gly and Ala-Ala linkages, respectively. The reverse was the case for wild silk varieties. This led to the understanding that mulberry silk is a copolymer of glycine and alanine, whereas wild silks have Ala-Ala linkages in their crystalline portions. The crystallite size for (002) reflection for mulberry silk increases from 10 to 20 while for Muga it shows considerable increase from 32 to 60. Reflection 002 arises from planes whose normal are in direction of side chains of amino acid residues. Due to the presence of Ala-Ala linkages in crystalline part in the wild silkworms, the crystallite size is bigger as compared to mulberry silks which contains alternate Ala-Gly linkages. It was observed that wild silks have around 60% crystalline fraction which was confirmed from the ratio intensity of 1265 and 1235 cm^{-1}.

Numata et al. (2010) investigated the anti-parallel β-pleated sheet structure of silk and found that they are fully degradable and non-toxic structures in biology. They also showed the beta sheets from silkworm are structurally different from amyloid structures formed during disease conditions and show no cytotoxicity. The enzymatic degradation was carried out on beta sheets using protease XIV (300 μg/mL) and alpha-chymotrypsin (300 μg/mL) in 0.1 M PBS at 37 °C for 24 h. It leads to fibrils and subsequently to nanofilaments (2 nm thickness and 160 nm length) as observed by AFM. The degradation products produced by Protease XIV were beta-sheet structures with 37% beta-strand and 50% unordered whereas those for α-chymotrypsin were 5% beta-strand and 57% unordered. Hence, protease degradation was found to be faster than alpha-chymotrypsin. They reported that dimension of one beta-sheet layer is 1 nm thick and 56–212 nm long.

Alpha-chymotrypsin results in loosely-packed chains around tightly packed chains generating soluble fractions with random coil and few beta sheets.

Tao et al. (2012) prepared crystalline silk fibroin (CSFs) nanoparticles, a kind of natural protein nanocrystals using sulfuric acid (64 wt%). The treatment periods were varied and optimum results were obtained at 2 h and 45 °C. TEM microscopy showed that CSFs existed as short-rod like fragments and spherical particles. After treatment, the crystallinity improved from 53.9% to 78.7% and β-sheet content increased. The CSFs showed reduction in molecular weight from 34.6×10^5 g/mol to 11.5×10^5 g/mol. The glass transition temperature and degradation temperature showed an upward shift from 179 and 293 °C to 216 and 320 °C, respectively. These nanoparticles were mixed with high strength polyurethane and showed improvement in mechanical properties such that elongation at break improved from 1070 to 2370%, tensile strength increased from 0.6 to 2.2 MPa whereas Young's modulus improved from 0.3 to 4.0 MPa.

1.2.3 PLA/silk nanocomposites

This section shows main available literature related to nanocomposite preparation using PLA and silk in various physical forms.

Cai et al. (2002) modified the surface of poly(lactic acid) with silk fibroins of different molecular weights, and assessed functions of rat osteoblasts cultured *in vitro*. The PLA films were prepared by solvent casting technique using chloroform as solvent which were acid and base-treated to cap them with carboxylic group. The silk fibroin solution with different molecular weights was obtained by treating reconstituted silk with 0.2N NaOH at 45, 85 and 95 °C for 30 minutes. The PLA-COOH films were soaked in silk fibroin solutions and after immobilization were washed with PBS buffer. The surface of modified PLA was investigated by contact angle and electron spectroscopy. It was observed that by using silk fibroin, the hydrophilicity (wettability) and availability of nitrogen atoms on the surface can be incorporated to PLA surface. The study revealed that silk fibroin-modified PLA surface can improve the interaction between osteoblasts and the PLA films which was confirmed by cell proliferation, MTT assay or alkaline phosphatase (ALP) assessment.

Cheung et al. (2010) prepared silk/PLA composite material for biodegradable implants. With the reinforcement of tussah silk fiber, enhancement in stiffness and ductility of PLA in addition to faster biodegradation rate (approximately 4 months) was observed. Silk fiber

was cut into snippets of 5 mm and mixed with PLA in ratio of 5:95 wt% and extruded at 180 °C at 100 rpm and 10 minutes residence time which were then injection molded to form dumbbell shaped biocomposite samples. The biodegradability was assessed for 4 months in PBS solution at pH 7.4. The biodegradation of silk/PLA implants did not show large increment in acidity and thus would not affect the *in vivo* environment. The materials started to show translucent/milky coloration due to increased crystallinity. The incorporation of silk fibers resulted in porous structure due to higher water uptake of silk fibers as a result of their strong hydrophilic ability. Such biodegradable implants with controllable biodegradability can match with neo-tissue regeneration rate and reduce the need of second operation for implant removal.

Wang et al. (2009) prepared tubular porous-structured scaffold using electrospinning having PLA fibers as outside layer and fibroin/gelatin as inside layer. Biocompatibility of these implants was examined, in particular by *in vitro* and *in vivo* cell culture and subcutaneous implantation test. The lyophilized reconstituted silk sponges and gelatin were dissolved in formic acid to obtain 13 wt% solution while PLA was dissolved in acetone: chloroform (1:2) to obtain 5 wt% solution which were used for electrospinning. The scaffolds were immersed in ethanol for 15 min to impart strength and stability. The tubular scaffolds showed around 82% porosity, breaking strength of 2.21 MPa, elongation (pliability) of 61% and suture retention strength of 4.58 N. The burst pressure strength obtained was 1596 mmHg which was much higher than native vessels. The scaffolds were insoluble in water and biocompatible with both mouse fibroblasts and human endothelial cells. In addition, upon subcutaneous implantation they did not result in any macrophages and lymphocytes proving that they can be an ideal candidate for tissue engineering blood vessels.

He et al. (2011) prepared electrospun nanofibers of tussah silk fibroin/poly(lactic acid) composites by dissolving in 1,1,1,3,3,3-hexafluoro-2-propanol in the ratio of 90:10 by weight. Addition of 10% PLA led to decrease in average nanofiber diameter from 583 nm to 178 nm. XRD and infrared studies showed that upon addition of PLA, the conformation of silk changed from random coil and α-helix to β-sheet. The breaking stress and breaking strain improved from 1.158 MPa and 4.05% to 2.727 MPa and 4.39%, respectively. Upon increasing PLA content, beta content of silk decreased and phase separation was observed with increase in average diameter.

Zhao et al. (2010) prepared silk fiber/PLA biocomposites using melt compounding methods for environment engineering applications. The effect of silk fiber on the structural, thermal, dynamic mechanical properties and enzymatic degradation behavior of the PLA matrix was investigated. Incorporation of silk fibers in PLA matrix resulted in improvement in stiffness, confirmed by increased storage modulus (E´) values, but thermal stability was lowered. The enzymatic degradation enhanced upon addition of silk fibers. The crystallization temperature (T_{cc}) decreased on addition of silk fiber, suggesting that silk fibers can be used as effective nucleating agents. The improved enzymatic degradation (improved weight loss and water absorption) can be attributed to the hydrophilicity of silk fibers. The authors suggested 5 wt% silk fiber as optimum loading for silk/PLA nanocomposites.

1.2.4 Packaging application of bio-based materials

This section presents known works related to food packaging which use silk as one of the components.

Ma and Song (2005) prepared films from regenerated silk fibroin (SF) using plasticizers and their physical properties were evaluated. The various plasticizers used were polyethylene glycol (PEG), polypropylene glycol (PPG) and glycerol. It was found that glycerol-laden films showed the least strength of 14.24 MPa albeit with highest % elongation 184.44%. PEG and PPG films showed tensile strength and % elongation of 23.71 MPa, 7.23% and 24.52 MPa, 2.51%, respectively. Water vapor permeation (WVP) of SF films varied with addition of plasticizers, with the values being 4.12, 3.92 and 1.32 ng.m/m^2s.Pa for glycerol-SF, PPG-SF and PEG-SF, respectively and these WVP values were found to be lower than that of pure silk fibroin films. The Hunter color parameter revealed no difference in L (~95–96) values but a (-0.38 to -0.7) and b (3.38–4.07) values were higher than silk fibroin. These films could be used for food packaging applications, especially PEG-SF with respect to WVP, tensile strength and % elongation.

Singha and Kapoor (2014) prepared films by solvent casting method where silk particles and methyl methacrylate (MMA) grafted silk particles with varying concentrations (10, 20, 30 and 40 wt%) were used as reinforcements for starch and PVA. The films were assessed for improvement in mechanical and water-resistant properties. The composites were plasticized using citric acid and cross-linked using glutaraldehyde. The films showed increment in tensile strength and decrease in elongation at break. The biocomposites were

found to be biodegradable and possess anti-bacterial properties. Citric acid reduced the tensile strength and increased % elongation due to improved hydrogen bonding as a result of its multi-carboxylic structure, whereas glutaraldehyde resulted in improvement in tensile strength and decrease in % elongation. Incorporation of silk particles in PVA matrix resulted in better interfacial adhesion between particle and matrix. The optimum particle loading was found to be 20 wt% beyond which particle-particle aggregation was observed.

Kweon et al. (2001) prepared silk fibroin (5% w/v)/chitosan (5% w/v) blends by dissolving in formic acid and solvent casting, which showed no phase separation. The dried films were treated with methanol prior to analysis. The chitosan content was varied (0–100%) in the blends and physical and mechanical properties were investigated for feasibility of using these films as artificial skin and wound dressing. These films showed improved mechanical properties and high water vapor and oxygen permeability making them ideal for wound dressing and artificial skin. The swelling was around 150–210% when chitosan ratio was 10–20%, but above 40% there was not much variation and was around 120–140%. The addition of chitosan (10–40 wt%) results in flexibility (5–10 MPa) of highly stiff silk films (~35MPa). The 20% chitosan resulted in 90% elongation. Addition of chitosan content increased the water vapor permeability (WVP) from 1.2×10^{-8} g.cm.cm^{-2}.s^{-1} (1037 g/m^2.day) towards 2.4 g.cm.cm^{-2}.s^{-1} (2074 g/m^2.day), which is the WVP for chitosan. The oxygen permeability coefficient at 50:50 ratio of fibroin and chitosan was 0.579 cm^3(STP).cm/ cm^2. s.cmHg $\times 10^{10}$.

Fernandez and Ingber (2012) fabricated a bioinspired material that reproduces the chemical composition and phase separated structure of insect cuticle by laminar arrangement of chitosan and fibroin. The designed material showed outstanding strength and toughness similar to aluminum alloys but was half in density. The strength and toughness was ten times that of unstructured component blend and twice of chitosan. This can be used to replace plastics in consumer products, as well as medical applications, as both chitosan and fibroin are biodegradable and biocompatible. Around 12 μm thick chitosan film was cast on glass substrate and treated with sodium hydroxide, over which fibroin was cast and treated with methanol to induce insoluble β-sheet structure. This laminate structure was called ‘Shrilk’ which exhibited ultimate tensile strength (UTS) of 119 MPa, at a 1:2 chitosan-to-fibroin ratio. The toughness of ‘Shrilk’ is 1.5 times that of

pure chitosan. The stiff material can be made flexible by controlling the amount of hydration.

Doblhofer et al. (2016) processed cationic recombinant spider silk protein, eADF4 together with synthetic lysine treated layered silicate sodium hectorite through drop casting. The resulting films were both thermally and chemically stable and completely water insoluble. The internal structure showed that spider silk was well-oriented and self-assembled on the nanoclay surface yielding high oxygen and water vapor barrier properties. It was observed that spider silk occupied the interlayer spaces between clays as confirmed by X-ray studies. The beta content was found to be ~28% as opposed to ~18% for neat silk films. The composite showed a decomposition temperature of 327 °C. The films were found stable against humidity, acidity and sterilizing environment more than 7 days. The mechanical properties of the biocomposite were superior to recombinant spider silk alone; the modulus, UTS and toughness were 1682 MPa, 100 MPa and 1.0 MJ/m^3, respectively. The gas (oxygen) and water vapor transmission rates of the bionanocomposite were reported to be 3.87 $cm^3.\mu mm^{-2}day^{-1}.bar^{-1}$ and 0.28 $g.\mu mm^{-2}day^{-1}.bar^{-1}$, respectively. The bionanocomposite showed better barrier performance than poly(vinylidene chloride) and poly(ethylene terephthalate (PET) by 60-fold and 600-fold, respectively. The material showed good biocompatibility and hence can be used for green, flexible packaging applications.

1.2.5 Tissue engineering application of bio-based materials

This section discusses key literature available in the area of biomedical devices, tissue-engineering and allied fields where silk has been utilized as one of the components.

Wharram et al. (2014) prepared electrospun scaffolds from silk fibroin/ polyethylene oxide (PEO) (2:1 or 4:1) blended materials and assesses them for feasibility towards biomedical applications such as wound healing. The electrospun scaffolds (20–80 μm) showed adequate moisture and oxygen transmission rates, biodegradability, absorption (460%) to be utilized for wound dressings. The prepared mats were subjected to alcohol treatment to induce conformational change followed by dissolution of PEO in water which resulted in interconnected porous structure. Active agents like therapeutic drug can also be added to the blend mixture. The composite showed 86% weight reduction in 14 days. The achieved oxygen gas transmission rate (OTR) was about 15460 $cm^3/m^2/day$ and WVTR was 1934 $g/m^2/day$.

Singh et al. (2015) prepared bionanocomposite of spider silk fibers using neoteric solvents, both ionic liquids (ILs) and deep eutectic solvents. Hydrated tetrabutylammonium hydroxide (TBAH) was used to disperse 7.5 mg/ml of spider silk. Spider silk was collected from the surroundings, washed multiple times to remove dust; this was later degummed using sodium bicarbonate (0.5% w/v) at 100 °C for 30 min. Quaternary ammonium IL was used for fabrication of magnetite-functionalized bionanocomposite. Iron oxide nanoparticles were prepared separately by co-precipitation method which were ultrasonicated for 30 min, washed and vacuum dried. The degummed silk fibers (5 mg) were dispersed in 1mL of IL at room temperature for 2 h to obtain dispersion of spider silk fibers (SSF) into which 5 mg of iron oxide powder was added and ultrasonicated for 30 min. The material was lyophilized to obtain dry powder. Attachment of iron oxide nanoparticles on the surface of spider silk was confirmed by TEM and energy dispersive X-ray spectroscopy (EDX) which showed presence of 14.72% of Fe on silk surface and chemical structure was confirmed using Fourier transform infrared spectroscopy (FTIR). The prepared bionanocomposite showed antibacterial properties and allowed growth of mammalian cells (human lung carcinoma A549) *in vitro*. The material can be used for therapeutic applications.

Lian et al. (2014) prepared nanofibrous scaffolds by electrospinning using silk fibroin (SF)/poly(L-lactic acid-co-ε-caprolactone) (P(LLA-CL)) in the ratio 1:1. The conformational change from random coil to β-sheet structure was achieved by treating with 75% ethanol vapor. The blends were loaded with curcumin and scaffolds showed controlled release, antioxidant and antimicrobial activities, and free radical scavenging activities. The curcumin-loaded scaffolds inhibited S. aureus growth (< 95%). The authors showed that curcumin-loaded SF/ (P(LLA-CL)) scaffolds can be effectively used as potential candidates for wound healing and tissue engineering scaffolds. The nanofiber size varied from 293–497 nm. It was ethanol treatment and not curcumin incorporation which brings change in conformation. At 6 wt% curcumin loading, increase in the diameter of nanofibers was observed which resulted in increment in percentage elongation (117.44%) and tensile strength (5.27 MPa). The scaffolds showed 12 h initial burst and a sustained release over 72 h.

1.2.6 Outcome of literature review

The detailed literature survey discussed above reveals the continuing efforts focused on improving the thermal, mechanical and barrier properties of PLA. In this regard, the present doctoral work focuses on the fabrication of PLA-based nanocomposites by incorporation of a novel nano-biofiller, namely crystalline silk nano-discs (CSNs), in the PLA matrix and on understanding the influence of the reinforcement on the thermal, mechanical and barrier properties of PLA. Crystalline silk is selected as reinforcement due to the following advantages possessed by the filler: stable in suspension, renewability, low-cost, easy availability, biocompatibility, ease of functionalization, thermal stability, slow biodegradability. The nanoparticles possess high surface area which allows for better adhesion with PLA matrix leading to improvement in strength. The nanoparticles have a high aspect ratio which results in providing a tortuous diffusion path leading to enhanced gas barrier properties. Highly crystalline and thermally stable hydrophobic silk can be dispersed in hydrophobic PLA in order to significantly enhance the mechanical and barrier properties, crystallization characteristics and thermal stability along with processability of PLA. Especially, for food packaging applications, it is important to understand both mechanical and barrier properties of filler materials as well as their compatibility with food during storage.

1.2.7 Gaps in the prior art

Extensive literature survey revealed that very few studies have been conducted on exploring the use of crystalline silk-based fillers for food packaging and wound healing applications. The strength of silk is due to the crystalline domain, present in the form of β-sheet crystallites, which can be utilized as PLA reinforcement. It has been found that although silk can be reconstituted from cocoons and also extracted directly from silk glands, and has film forming ability, it still has random coil conformation which even after treatment to obtain β-sheet structure lacks strength and toughness. This inhibits its usage in packaging and other applications. Hence, researchers have found different ways such as utilizing silk fibers or obtaining silk nanoparticles and using them as reinforcements to avoid such limitations. It has also been inferred from literature survey that the use of silk nanoparticles in wound healing applications has not been explored in detail.

Based on the literature survey, it was observed that no work has been published (to the best of our knowledge) on: (a) preparation of silk nano-discs with high crystallinity using Muga silk, (b) use of silk nano-disc-based bionanocomposite for food packaging applications, and (c) use of silk nano-disc-based bionanocomposite for wound healing applications.

Therefore, the present doctoral work focuses on two applications, namely (i) packaging application and, (ii) wound healing application. In packaging application, the hydrophobic silk nano-discs are utilized as filler in the PLA matrix to improve the characteristic properties of PLA. Further, the prepared silk nano-discs are functionalized with iron nanoparticles and electrospun with PLA and tested for wound healing applications.

1.2.8 Motivation & hypothesis

Completely green packaging is of interest worldwide as it is environment-friendly and can be manufactured from combination of renewable resources. In the case of PLA/silk nanocomposite, abundantly available agricultural crop waste and waste silk can be used for producing PLA and silk nano-discs respectively. Such bio-based, biodegradable materials have the potential to meet environmental and health requirements along with the required necessary properties for food packaging and wound healing applications such as barrier, mechanical and thermo-physical properties.

The aim of current work is to develop PLA/silk nano-disc based food packaging films with necessary barrier, mechanical and thermal properties to overcome the limitation of conventional bio-based PLA. The nanoscale reinforcement due to silk is expected to improve the mechanical and thermo-physical properties of PLA. This novel formulation can be used to produce bionanocomposite films by melt extrusion technique, which will provide cost-effective process production of films. Therefore, the objectives of the doctoral work are framed as follows:

1.2.9 Objectives of the research

- Isolation of crystalline silk nano-discs from *Antheraea assama* and their detailed characterization.
- Preparation of PLA/silk bionanocomposites and detailed characterization of the bionanocomposites for improvement in mechanical, thermal and barrier properties.
- Investigation of thermal and hydrolytic degradation, and crystallization kinetics of the prepared bionanocomposites.
- Fabrication of scaffolds using electrospinning for tissue engineering application and checking for biocompatibility.

1.2.10 Outline of doctoral thesis

This doctoral thesis provides fundamental and applied research and analysis of a biodegradable polymer nanocomposite, namely PLA/silk nano-disc which is described systematically in the following chapters and schematic representation is shown at the end of this chapter:

Chapter 1: Introduction and Literature Survey

In this chapter, a comprehensive literature of published articles related to the broad theme of the thesis are reviewed. Gaps in knowledge are determined, and objectives are formulated.

Chapter 2 Materials and Methods

In this chapter, the materials used, experimental procedures followed, and the characterization techniques and equipment used are described in detail.

Chapter 3 Isolation of crystalline silk nano-discs (CSN) from Muga silk, preparation of magnetic CSN (MGCSN) and their detailed characterization

In this chapter, isolation of crystalline silk nano-discs (CSNs) from *Antheraea assamensis* (Muga) silk fibroin is discussed. The isolated CSNs were thoroughly characterized on mainly morphological, structural and conformational fronts. As a continuation of this work, the isolated CSN were modified using magnetic nanoparticles which were electrostatically adhered to the $–NH_2$ moieties of the CSN to prepare magnetic silk nano-discs (MGCSNs). The MGCSNs are characterized with respect to their morphology, magnetic moment, structure, etc.

Chapter 4 Studies on poly(lactic acid)/crystalline silk nano-discs based 'green' bionanocomposite for food packaging applications

This chapter describes the fabrication of biopolymeric/CSN-based "green" bionanocomposite films using bio-based polylactic acid (PLA) for potential food packaging applications. The formation of network-like structure of CSNs in PLA matrix, corroborated through morphological analysis, leads to significant improvement in structural, crystallization and thermal properties. The melt extruded films showed high resistance to oxygen gas and water vapor permeation, which were within the limits as per standard legislations. These favorable properties along with their non-toxicity, sustainability and complete biodegradability makes the PLA/CSN bionanocomposites suitable for food

packaging applications

Chapter 5 Influence of crystalline silk nano-discs (CSNs) on the crystallization behavior of melt extruded PLA films

Crystallization studies are very important for improvement of various properties essential for stringent food packaging applications.
The effect of silk nano-disc content on crystallization behavior of PLA/CSNs is assessed by isothermal and non-isothermal crystallization kinetics. Polarizing optical microscope (POM) analysis suggested that the spherulite growth of PLA is improved significantly with the addition of silk nano-discs.

Chapter 6 Thermal degradation kinetics and hydrolytic degradation studies of PLA/CSN bionanocomposites

The influence of crystalline silk nano-discs (CSNs) on thermal stability and evolved gas characteristics of PLA is discussed with the help of thermal gravimetric analysis coupled with Fourier transform infrared spectroscopy (TG-FTIR). Different models from isoconversional and model fitting techniques are used to evaluate the degradation kinetics. Moreover, mechanism of thermal degradation is predicted by Criado method. In addition, the materials are also evaluated for hydrolytic degradation behavior with respect to molar mass, morphology, residual weight, etc.

Chapter 7 Preparation and characterization of PLA/CSN and PLA/MSCSN bionanocomposites with and without anticancer drug (Curcumin) by electrospinning, and evaluation for cytotoxicity and anti-cancer activity

This chapter discusses the utilization of CSNs and MGCSNs for preparation of bionanocomposite scaffolds using electrospinning. The morphological, structural, thermal and mechanical properties of the prepared scaffolds are characterized. Drug encapsulation ability and release kinetics are also evaluated. This chapter assesses the biocompatibility of silk nano-disc-based polymeric materials for suitability towards food packaging applications. The silk nano-disc-filled electrospun polymeric scaffolds are evaluated for proliferation of fibroblasts. The drug-loaded scaffolds are assessed for anti-cancer activity due to sustained drug release, magnetic hyperthermia or concomitant effect.

Chapter 8 Conclusions & Future Directions

This chapter summarizes the conclusions of major findings of all the chapters and highlights the important technical and fundamental issues addressed in each chapter. The structural, morphological, conformational and other aspects of prepared silk nano-discs are summarized and discussed. The application of silk nano-discs, developed and demonstrated in the thesis, are also highlighted including use in PLA-based packaging material, wound healing, targeted drug delivery, and magnetic hyperthermia. Based on the general conclusions of the work presented in the thesis, some suggestions for future work are made on the development of silk nano-disc-based functional materials for high performance applications.

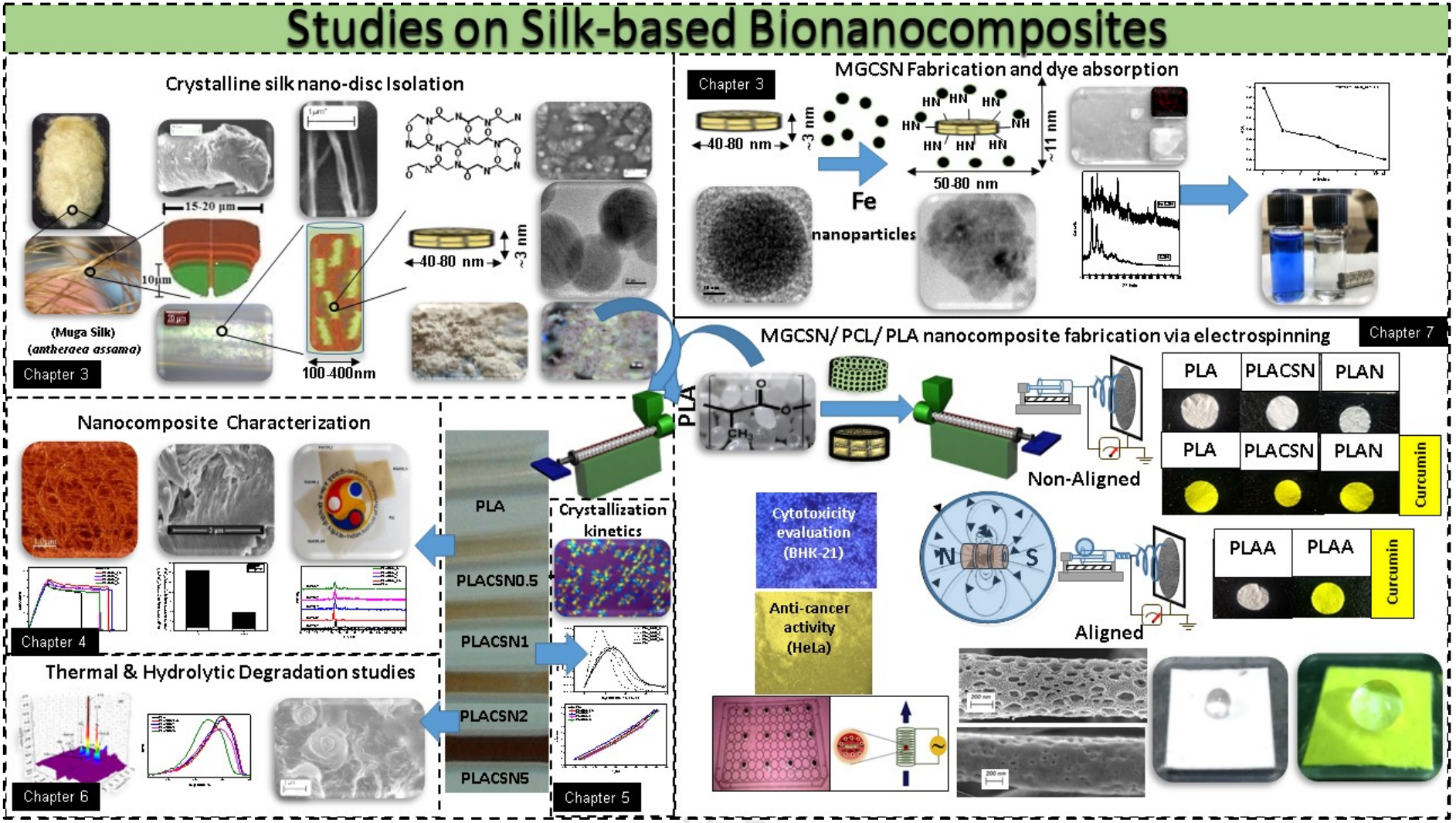
Studies on Silk-based Bionanocomposites
Crystalline silk nano-disc Isolation
15-20 µm
10µm
(Muga Silk)
(antheraea assama)
Chapter 3
100-400nm
40-80 nm
~3 nm
MGCSN Fabrication and dye absorption
Chapter 3
40-80 nm
~3 nm
~11 nm
50-80 nm
Fe
nanoparticles
MGCSN/ PCL/ PLA nanocomposite fabrication via electrospinning
Chapter 7
PLA
Non-Aligned
PLA
PLACSN
PLAN
PLA
PLACSN
PLAN
Curcumin
Nanocomposite Characterization
Chapter 4
PLA
PLACSN0.5
PLACSN1
PLACSN2
PLACSN5
Crystallization kinetics
Chapter 5
Cytotoxicity evaluation (BHK-21)
Anti-cancer activity (HeLa)
N
S
Aligned
PLAA
PLAA
Curcumin
Thermal & Hydrolytic Degradation studies
Chapter 6

Chapter 2

Materials and Method

This chapter provides details of the materials and reagents used and protocols followed for performing various experiments in this research work. Extraction of crystalline silk nano-discs (CSNs) from Muga silk using sulfuric acid as hydrolyzing agent has been discussed. Surface modification of CSNs with iron-oxide nanoparticles to fabricate Fe_3O_4-CSNs has been discussed in detail. Processing of CSN-based polymeric bionanocomposites through different approaches such as melt extrusion, solvent casting and electrospinning has been reported. The fabrication of electrospun nanofibers under the influence of magnetic field has been explained. The calculation methodology for converting raw experimental data into appropriate results has been elaborated. The analytical instrumentation and experimental procedure followed for the characterization of aforementioned nanoparticles and bionanocomposites have also been discussed in this chapter.

2.1 Materials

Poly L-lactic Acid (PLA) granules (grade: 2003D MFI of 6.0 g/ 10 min at 210 °C) were purchased from NatureWorks® LLC, USA. The weight averaged molecular weight (M_w), number averaged molecular weight (M_n) and polydispersity index (PDI) were ~250,000 *Da*, ~135,000 *Da* and 1.82, respectively and content of L-lactic acid/D-lactic acid was 98.6/1.4. Sodium carbonate (>97%) (analytical grade) used for degumming of silk was purchased from Merck, India. Fabrication of crystalline silk nano-discs (CSNs) was carried out using sulfuric acid (>99%) as hydrolyzing agent which was purchased from SISCO Research Laboratories (SRL Chemicals, India) (analytical grade). Waste pierced Muga (*Antheraea assama*) cocoons were supplied by Regional Muga Research Station (RMRS), Central Silk Board (CSB), Boko, Assam, India. For gel permeation chromatography (GPC) analysis, the reagent chloroform (Merck, high performance liquid chromatography (HPLC) grade) was used. For the fabrication of iron-oxide supported CSNs, chemicals required such as ferric (III) chloride ($FeCl_3$) (96%), sodium borohydride ($NaBH_4$) (95%), sodium hydroxide (NaOH) (>97%), curcumin (>95%) (analytical grade) were received from SISCO Research Laboratories (SRL Chemicals, India). Diiodomethane (Sigma Aldrich, India) was used for contact angle measurements. All solvents such as chloroform, dimethylformamide, methanol, acetone and ethanol were purchased from Merck, India. Ultrapure water was obtained from a Milli-Q filtration unit Millipore® (TOC <10ppb,

particles <0.22 μm/ml, resistivity: 18.2 MΩ.cm at 25 °C) was used as solvent for all the experiments reported in the thesis.

2.2 Methods

2.2.1 Fabrication of crystalline silk nano-discs (CSNs) through sulfuric acid as hydrolyzing agent

2.2.1.1 Degumming Process (Sericin removal)

CSNs are fabricated through the traditional route of sulfuric acid-based hydrolysis with waste pierced Muga silk cocoons as fibroin precursor. The waste silk contains fibroin as main ingredient in which sericin is present as protective protein coat. The extraction of purified fibroin was carried out through degumming; the step-wise procedure is shown in Figure 2.1. Firstly, silk cocoons are chopped into small pieces and cleaned to remove eggs, plant debris, dirt and foreign impurities. Degumming of silk was carried out with 0.02 M Na_2CO_3 at 98 °C for 30 min **(Rockwood et al., 2011)**. The fibroin was filtered out and washed with copious amount of Milli-Q water three times to remove trace amount of sericin and subsequently the fibroin was dried in oven at ~80 °C to remove moisture.

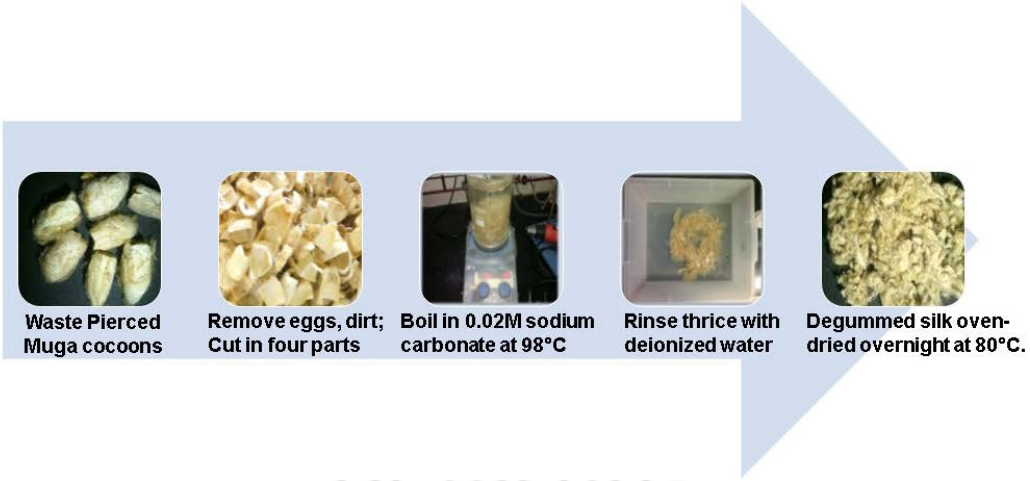

Figure 2.1: Step-wise degumming procedure **(Rockwood et al., 2011)**.

2.2.1.2 Isolation of CSNs

The stretched and dried degummed silk fiber (~5 g) was hydrolyzed with sulfuric acid (64 wt%, 50 ml) under combined mechanical stirring (~500 rpm) and sonication (~40 kHz) for 2 h, at 45 °C as shown in Figure 2.2(a). Subsequently, equal volume of chilled deionized water was added to stop the reaction. The CSN suspension was centrifuged (Remi, India) at 10,000 rpm for 20 min and the precipitate was transferred to cellulose acetate dialysis

membrane with a cut-off molecular weight 12–14 kDa (Sigma Aldrich) to achieve neutral pH. Further, the neutralized pH suspension was collected as pellet upon centrifugation followed by lyophillization after quench freezing with liquid nitrogen (at ~ -110 °C) (Scanlaf, Denmark) and dried CSN was stored in inert atmosphere as shown in Figure 2.2(b).

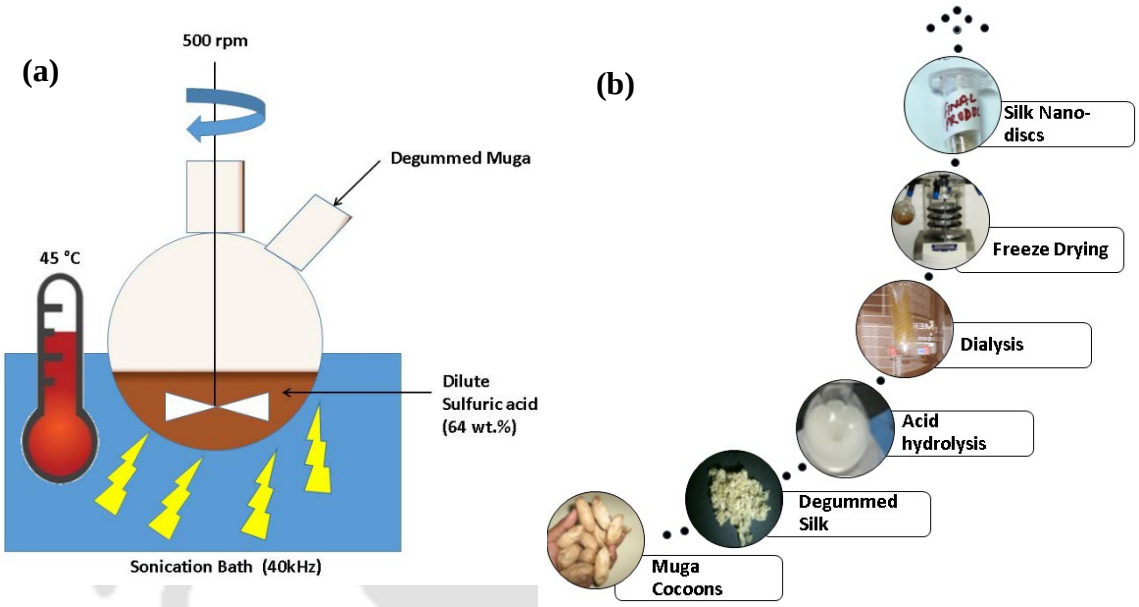

Figure 2.2: (a) Hydrolysis setup and (b) overall experimental representation for preparation of crystalline silk nano-discs (CSNs).

2.2.2 Fabrication of Fe_3O_4-adsorbed crystalline silk nano-discs (MGCSNs)

The iron oxide (Fe_3O_4) nanoparticles were adsorbed onto the CSN surface by chemical reduction method. The reaction setup is depicted in Figure 2.3. CSN (70 mg) was uniformly dispersed in 50 ml deionized water followed by ultrasonication (3000MP, Biologics, USA) at 30% amplitude for 2 min. Subsequently, $FeCl_3$ (30 mg) salt was dissolved in CSN suspension, and pH was adjusted to ~5.0 using 0.1N NaOH under inert atmosphere (by continuously purging with inert gas). The contents were vigorously stirred (at ~1000 rpm). For the fabrication of Fe_3O_4 nanoparticle-adsorbed CSNs (MGCSNs), 500 mg $NaBH_4$ in 10 ml solution was added dropwise into the iron salt-CSN solution at 65 °C and stirred for 2 h; suspension turned black immediately with evolution of hydrogen gas bubbles. The MGCSNs were separated from the solution using permanent magnets and washed three times with water and ethanol to remove impurities. Finally, the MGCSNs were centrifuged, dried at 50 °C and crushed into fine powder using mortar.

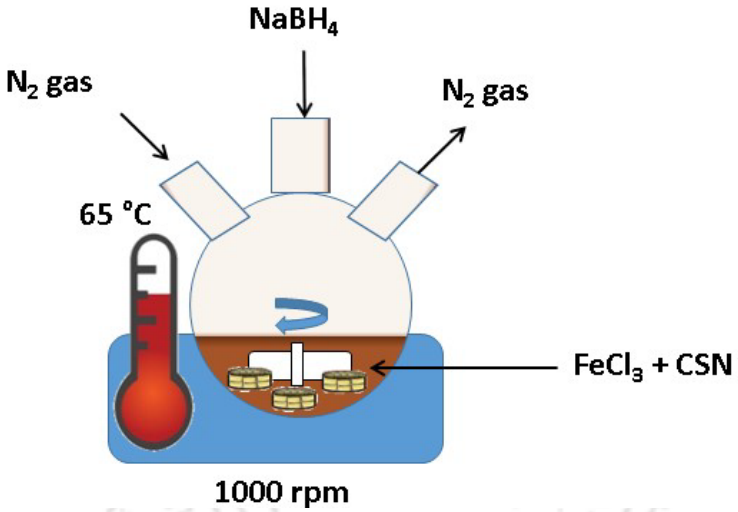

Figure 2.3: Reaction setup for fabrication of magnetic crystalline silk nano-discs (MGCSNs).

2.2.3 Dye adsorption studies

Adsorption of aniline blue (AB) was carried out to evaluate the adsorption activity of the fabricated iron oxide-adsorbed CSNs. The adsorption was carried out using 1000 ppm of aniline blue (20 ml) at room temperature with a fixed amount of synthesized nanoparticles (10 mg). A small amount of sample mixtures (200 µl) was pipetted out at various time intervals (30s–30 min) and diluted depending upon the initial dye concentration. The calibration curve shown in Figure 2.4 for aniline blue was plotted for at 598 nm with R^2= ~0.98. The MGCSNs were removed from the supernatant using a permanent magnet, followed by filtration using 0.2 µm syringe filters and concentration was evaluated.

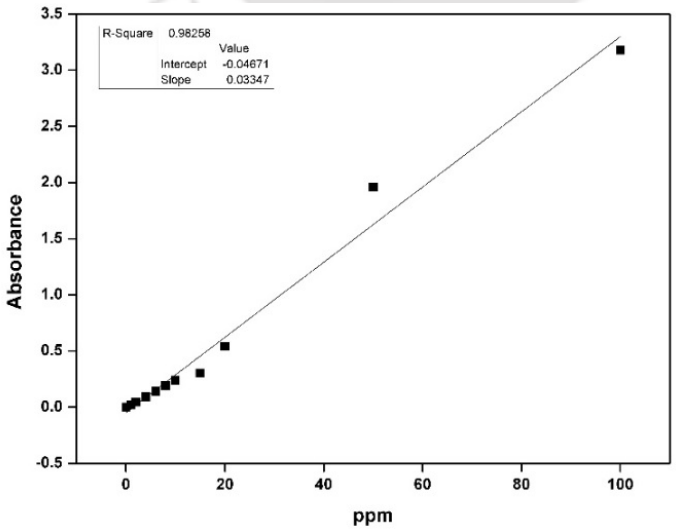

Figure 2.4: Calibration curve for aniline blue at 598 nm.

2.2.4 Fabrication of bionanocomposites using melt-extrusion

2.2.4.1 Poly(lactic acid) (PLA)/ crystalline silk nano-discs (CSNs) bionanocomposites

PLA/CSN bionanocomposites were fabricated by melt compounding with a twin screw micro extruder (Haake™ MiniLabII, Thermo Scientific, Germany) shown in Figure 2.5(a). Miniextruder is first heated to ~300 °C to stabilize the instrument. Initially neat PLA is extruded at a processing temperature of 210 °C to remove any leftover impurities, obtain uniform temperature throughout the barrel and also to check for initial leakages. The screw rotation and the residence time were set to 100 rpm and 1 min, respectively. Before extrusion, PLA granules were dried overnight at 80 °C in an oven. The PLA granules (~7 g) and freeze dried CSNs were pre-mixed at four different weight ratios 0.5, 1, 2 and 5 wt% followed by vacuum drying at 40 °C (for 24 h) to remove the adsorbed moisture. Bionanocomposites of PLA with different CSN content were extruded by introducing into the closed loop (recycle mode) for proper melt mixing of materials under inert environment. After 1 min, the loop was opened to obtain bionanocomposites in the form of strips having dimensions ~ 5 mm (width) × 0.5 mm (thickness) as shown in Figure 2.5(b). Control (PLA 2003D) was also manufactured using the same conditions, so that there would be no difference in the thermal history between manufactured samples. Hereafter, the extruded strips with the CSNs produced from sulfuric acid over the loading range 0.5–5 wt% are represented as PLACSN0.5– PLACSN5, as summarized in Table 2.1.

Table 2.1: Composition of PLA/CSN bionanocomposites.

Codes of samples	PLA (wt%)	CSN (wt%)
PLA	100	0
PLACSN0.5	99.5	0.5
PLACSN1	99	1
PLACSN2	98	2
PLACSN5	95	5

Standard dumbbell shaped specimens (Figure 2.5(c)) as per ASTM D638 were prepared by injection molding machine (Haake™ Minijet Pro, Thermo Scientific, Germany). The injection barrel and the mold were pre-heated to desired temperature of 200 and 45 °C, respectively. The dumbbells are removed from the mold after 10 s.

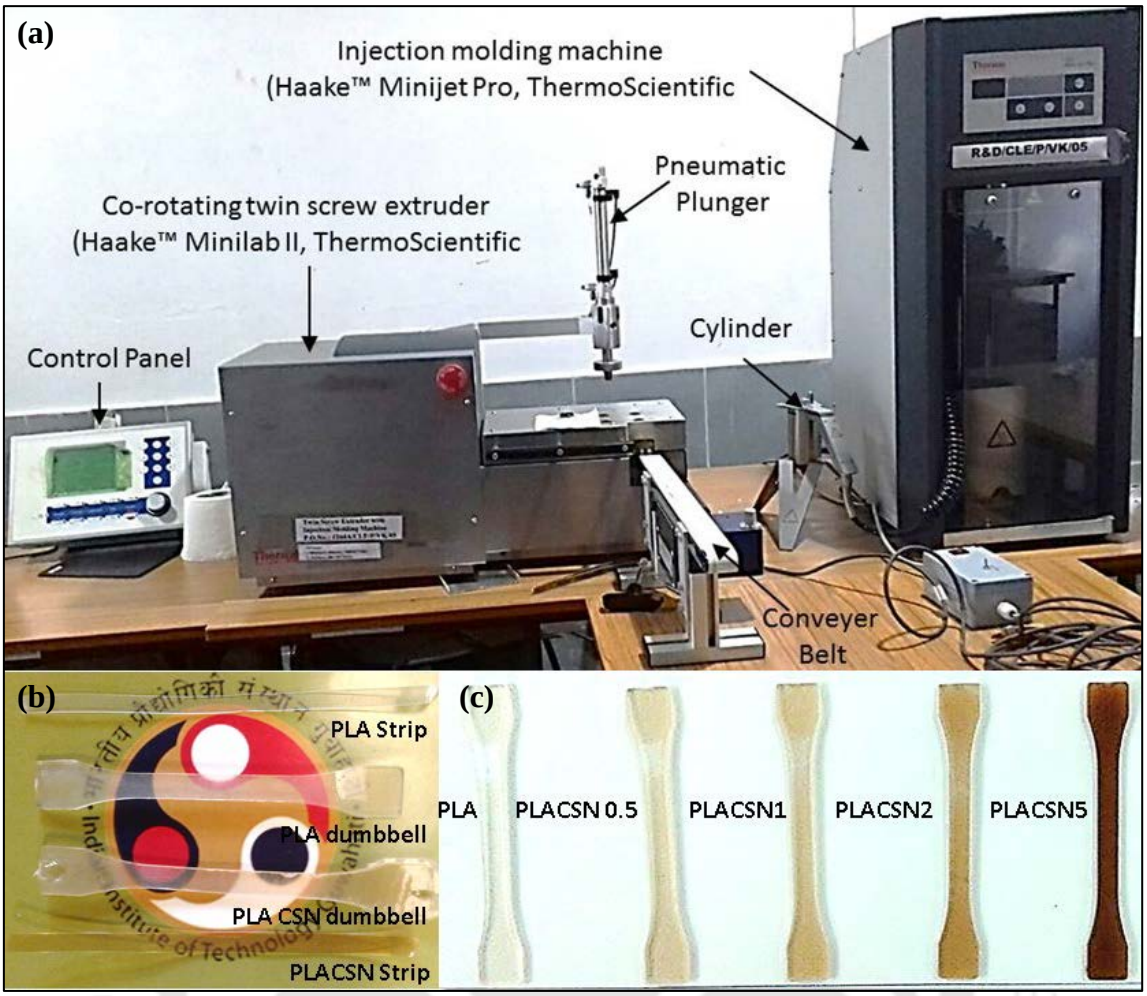

Figure 2.5: (a) Co-rotating twin screw extruder and injection molding machine, (b) fabricated PLA strip**,** PLA dumbbell, PLA/CSN strip (1 wt%)**,** PLA/CSN dumbbell (1 wt%) and (c) neat PLA and PLA/CSN bionanocomposite dumbbells with different CSN loading from 0.5–5 wt%.

2.2.5 Preparation of PLA and PLA/CSN bionanocomposite films

Films (~ 100 μm) from melt extruded samples were prepared by simple solution casting method and are shown in Figure 2.6 which clearly display the film formability of PLA/CSN bionanocomposites. First, PLA (~2 g) was dissolved in 50 ml of HPLC grade chloroform with continuous stirring (~500 rpm) for 2 h in order to completely dissolve PLA. Thereafter, the stirring was stopped and solution was allowed to sit to get rid of trapped air bubbles. Finally, the solution was cast on Teflon petriplates (~15 cm diameter) and allowed to dry in fume hood for 12 h. The dried films were peeled off carefully from the petriplates and dried under vacuum at 40 °C for another 12 h. The films were stored in zip lock bags and kept in desiccator until further use. These solvent cast films were used

for estimation of barrier properties, transparency, color and for investigation of hydrolytic degradation.

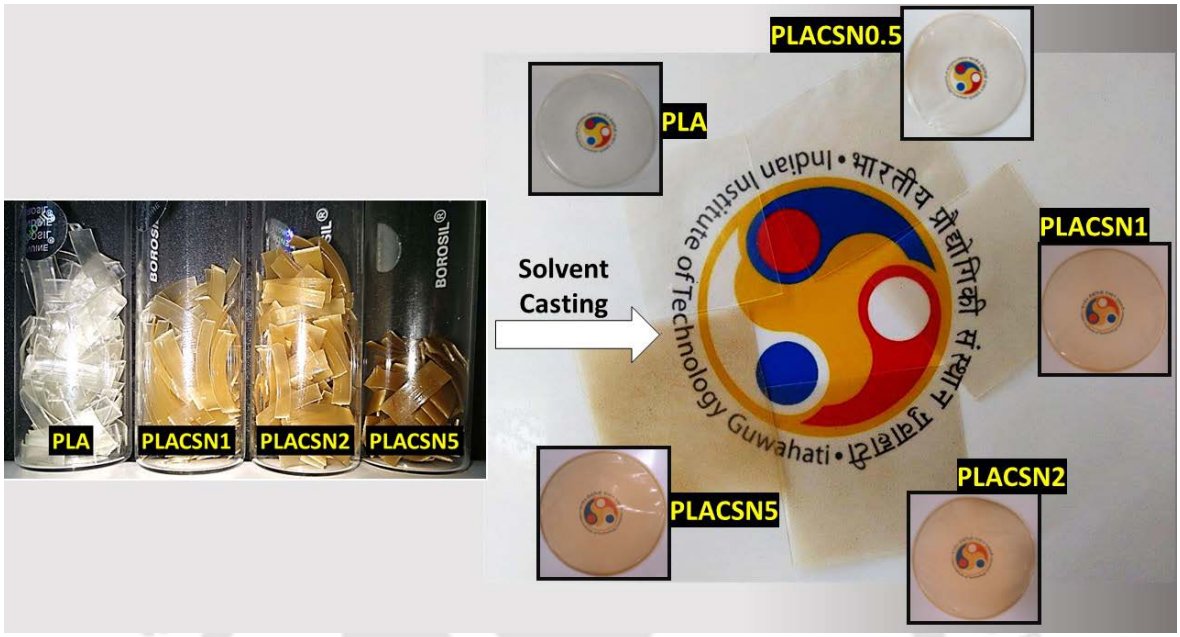

Figure 2.6: Fabrication of PLA and PLA/CSN films by solution casting method.

2.2.6 Hydrolytic degradation measurements

For hydrolytic degradation investigations, samples (30 × 20 mm^2) were cut from solvent cast films of thickness 100 ± 10 μm. To prepare films, calculated amounts (~2g) of melt-compounded samples were dissolved in chloroform under stirring (500 rpm) for around six hours. After complete dissolution, solution for poured onto PTFE petriplates and finally films were obtained after evaporation of solvent. Study was carried out at 37 and 60 °C under three hydrolytic mediums, viz. alkaline condition (NaOH solution, pH= 12), acidic condition (HCl solution, pH=2) and neutral condition (distilled water, pH=7). Prior to immersion, weight of the initial sample (dried under vacuum at 37 °C) was carefully measured. After being placed into the solution for a defined time period, the sample was taken out, washed with fresh water and dried at 37 °C for 24 h to ensure complete removal of water. Subsequently, the residual weight of the hydrolyzed sample was carefully measured to know the weight loss of the sample during the hydrolytic degradation process. The residual weight fraction, ϕ, was determined using the following expression **(Girdthep et al., 2016)**:

$$\phi = \frac{W_t}{W_o} \times 100 \qquad (2.1)$$

where, W_o and W_t refer to the dry weight (g) of the sample, prior to and after certain time (t) of the hydrolytic degradation process, respectively. The hydrolytic degradation rate (R, %/day) was defined according to the following relation **(Fernández and Fernández, 2017)**:

$$R = \left(\phi_{before} - \phi_{after}\right)/t \quad (2.2)$$

where, ϕ_{before} and ϕ_{after} are the residual weight fractions of sample before and after being hydrolyzed for a certain time *t*. Samples subjected to hydrolytic degradation were coded as PLA_pH_T and PLACSN_pH_T, where pH can be basic (B), neutral (N) and acidic (A), depending upon the hydrolytic degradation medium used. The symbol *"T"* refers to the temperatures, either 37 or 60 °C, used in this particular study.

2.2.7 Fabrication of electrospun bionanocomposite scaffolds

2.2.7.1 Normal electrospinning

The melt extruded strips were dissolved in a binary solvent of chloroform: dimethylformamide (9:1) to obtain 10% (w/v) solution. The solutions were stirred overnight and were used for production of nanofibers via electrospinning using a standard electrospinning setup (E-spin, Nanotech, India). The polymer solution was taken into a 5 ml plastic syringe with a 20G SS needle. The solution was pumped with a flowrate of 0.8 ml/h with a positive voltage of 6 kV to the needle. The collector to needle distance was maintained at 15 cm. A flat plate collector was used to collect the scaffold of randomly oriented fibers at 23 °C under 35% relative humidity. A schematic of the electrospinning setup is shown in Figure 2.7(a). Electrospun scaffolds containing anticancer drug curcumin (5 wt%) were also prepared in similar manner. Images of electrospun samples are shown in Figure 2.7(b).

2.2.7.2 Magnetic field-assisted electrospinning

Apart from standard procedure, magnetic field-assisted electrospinning was carried out with a small modification in the setup (Figure 2.7(c)). Three tubular neodymium magnets (10 mm × 5 mm) attached back to back (Figure 2.7(d)) with central opening of around 5 mm were used. The electrospinning needle was passed through these magnets without touching them with 10 mm of needle tip protruding outside from the magnets (Figure 2.7(e)). The applied voltage was 12 kV whereas all other parameters were maintained the same as that in the absence of magnetic field. PLA/MGCSN with and without curcumin

were prepared separately under identical conditions and termed as PLAA (Figure 2.7(f)). The as-formed PLA-CSN/MGCSN bionanocomposite scaffolds were oven dried for 24 h at 50 °C before using for further analysis.

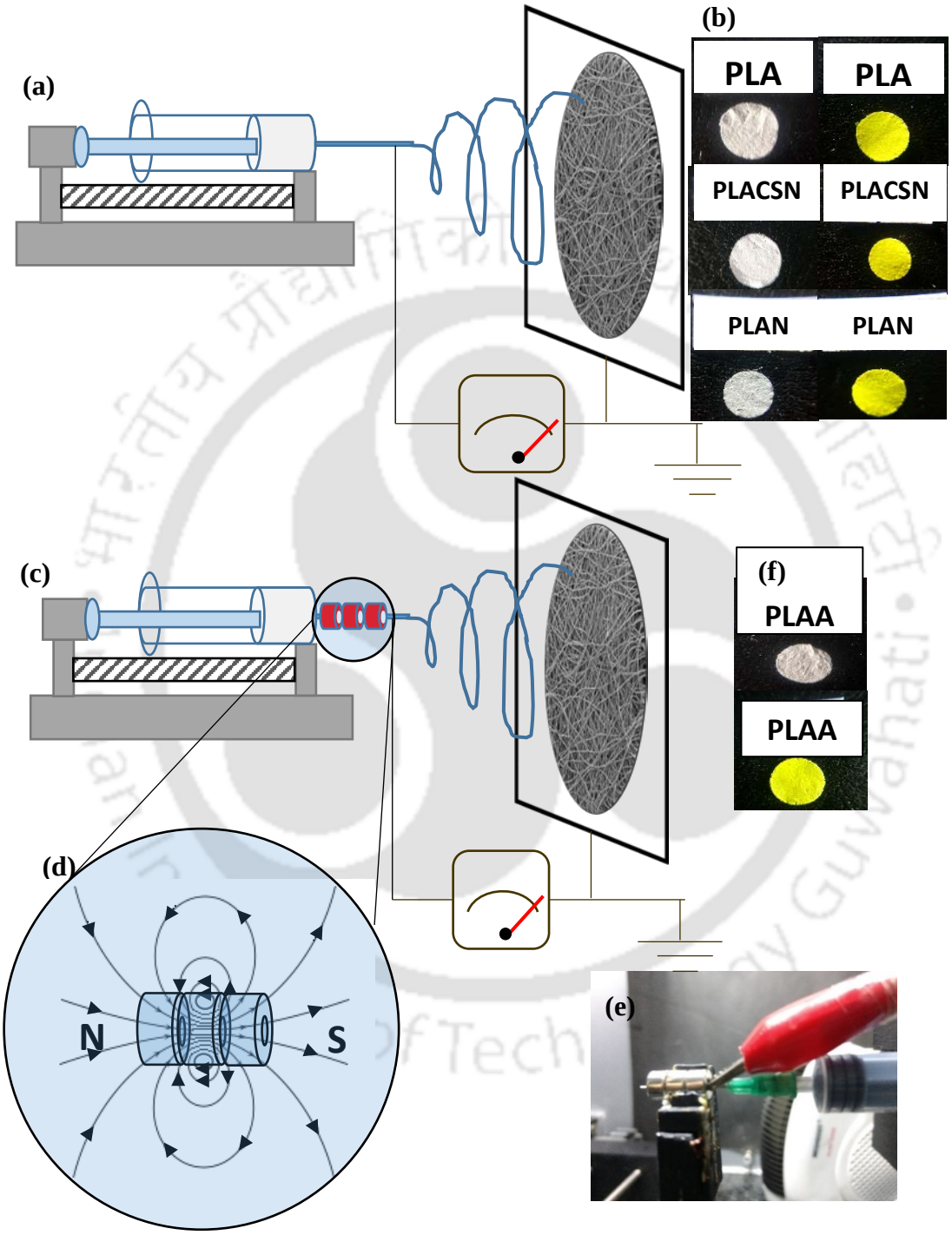

Figure 2.7: (a) Normal electrospinning setup, (b) PLA-based electrospun scaffolds with and without curcumin, (c) magnetic field-assisted electrospinning setup, (d) magnetic field diagram of the magnetic assembly, (e) visual appearance of magnetic field-assisted

electrospinning setup and (f) PLA-based electrospun scaffolds under the influence of magnetic field with and without curcumin.

2.2.8 Swelling properties

The swelling behavior of electrospun scaffolds was determined by dipping the samples in phosphate-buffered saline (PBS) at pH 7.4 for 24 h. After this duration, the samples were taken out, washed with deionized water, surface dried using blotting paper and weighed. The gain in weight percentage is reported.

2.2.9 In vitro curcumin release

Prior to release studies, entrapped drug amount was calculated. The drug loading was estimated by dissolving 1 × 1 cm^2 pieces of prepared materials in 1ml dichloromethane followed by addition of 1ml methanol to precipitate the polymer matrix. The precipitate was removed by centrifugation (10000 rpm, 30 min). The supernatant was filtered using polytetrafluoroethylene (PTFE) syringe filters and the drug content was estimated by UV-Vis at 425 nm. The calibration curve is shown in Figure 2.8(a)). Release profile of anti-cancer drug was studied *in vitro* by immersing the electrospun nanocomposite scaffolds loaded with curcumin in 30 ml glass vial containing 10 ml solution maintained at a pH ~7.4 for 37 °C, 150 rpm, kept in orbital shaker-cum-incubator. The solution consisted of PBS containing Tween-80 (5 % v/v) because curcumin is sparingly soluble in PBS alone. At predetermined times, sample solution (~1 mL) was taken and replaced back with equal quantity of fresh solution. The released curcumin in the sample solution was analyzed using UV-Vis spectrometer at 425 nm by plotting a calibration curve (Figure 2.7(d)). Release studies were carried out in triplicates where sample dimensions were 1 × 1 cm^2. Average values were reported as percentage cumulative drug release as a function of time.

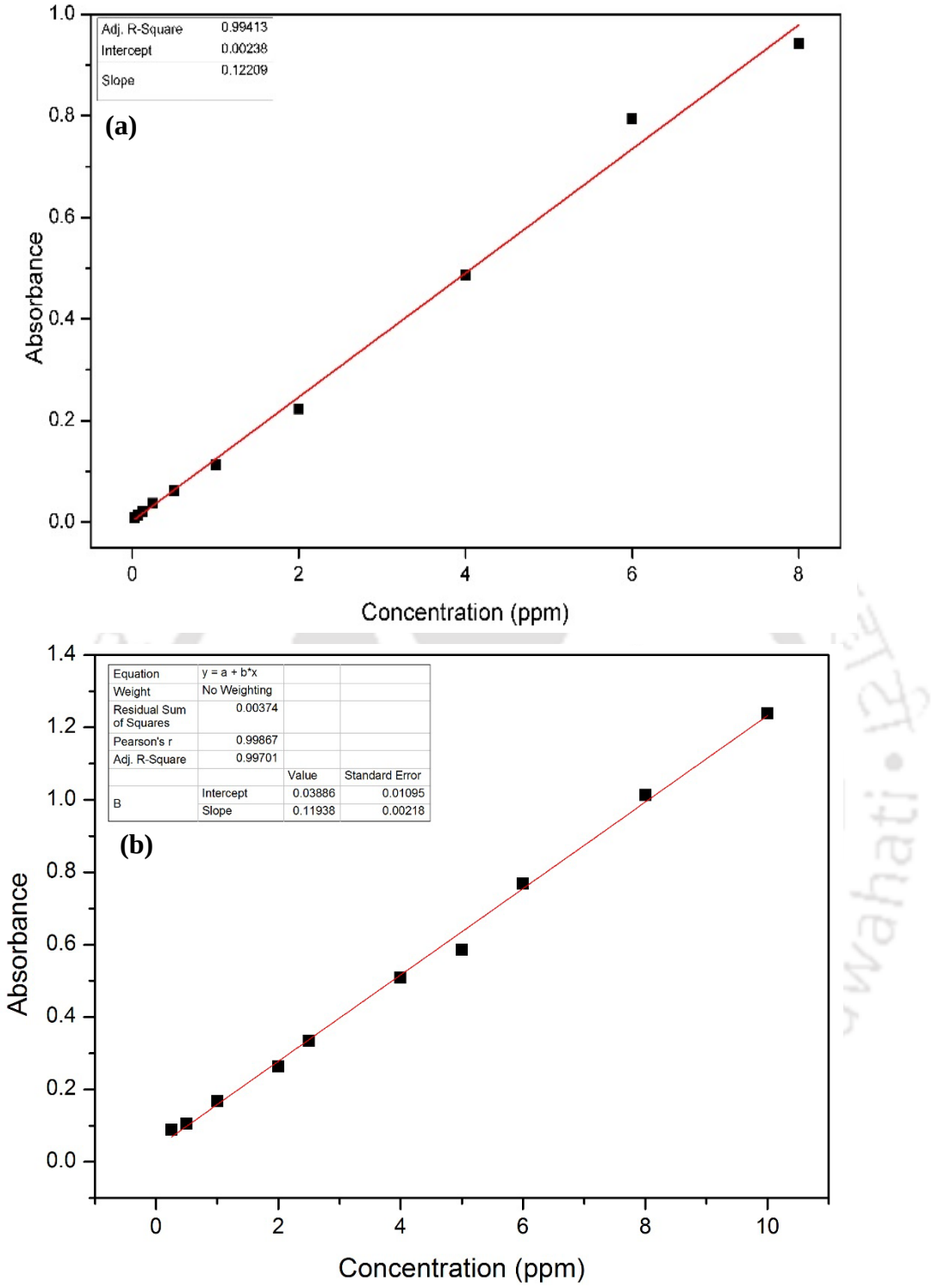

Figure 2.8: (a) Calibration curve for curcumin dissolved in DCM: MeOH (1:1) at 425nm and (b) calibration curve for curcumin dissolved in PBS/Tween 80 at 425 nm.

2.2.10 Cell culture experiments

Baby hamster kidney (BHK-21) fibroblast cells and human cervical cancer cells (HeLa) (National Centre for Cell Science (NCCS), Pune, India) were used for biocompatibity

studies on electrospun scaffolds. The cells were cultured in 75 cm^2 T25 tissue culture flasks using Dulbecco's modified Eagle's medium (DMEM) (Invitrogen, USA) supplemented with 10% fetal bovine serum, 1% penicillin-streptomycin, 1% L-glutamine, and 1% pyruvate (Invitrogen, USA). The cells were cultured in a standard incubator with humidified atmosphere and 5% CO_2 at 37 °C. The cells were further recultured and maintained for cell adhesion and proliferation assay. The cells were stained with trypan blue (SRL) and counted using automated cell counter (Countess® II FL, Thermo Fisher Scientific). In the present work, for the bionanocomposite scaffolds containing MGCSN (electrospun with and without magnetic field), neodymium magnets (N52, 5 mm × 1.5 mm) were applied under culture plate wells as shown in Figure 2.9 to investigate the cell growth under magnetic field.

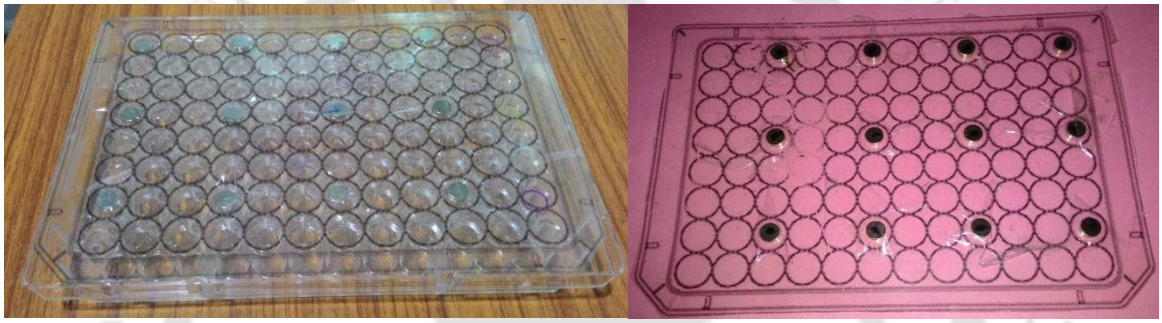

Figure 2.9: Twelve (12 nos.) neodymium magnets arranged onto 96-well culture plate.

In the present work, six groups (I- VI) of scaffolds were studied for cell viability which are summarized in Table 2.2.

Table 2.2: Composition of electrospun samples.

S.No.	Group Name	Details
Group I	PLA	Neat PLA
Group II	PLA/CSN	PLA filled CSN 5 wt%
Group III	PLAN	PLA filled MGCSN 5 wt%
Group IV	PLAA	PLA filled MGCSN 5 wt% electrospun under external magnetic field
Group V	PLAN (mf)	PLA filled MGCSN 5 wt% incubated under static magnetic field
Group VI	PLAA (mf)	PLA filled MGCSN 5 wt% electrospun under external magnetic field; incubated under static magnetic field

Nanofiber mats were cut to fit into individual wells of a 96-well plate (Nunc, USA) in the form of circular discs (~6 mm diameter) and were sterilized for 30 min in ultraviolet light.

Prior to cell seeding, 0.1 ml of complete culture medium containing 2 x 10^5 cells/well was added to each well with polystyrene (PS) as control. All the studies were carried out in triplicates and average values with standard deviations are reported.

2.2.10.1 Alternating magnetic field (AMF)-induced heating of magnetic scaffolds

The heat generation properties of magnetic nanoparticles were utilized by applying alternating magnetic field (AMF) with an alternating magnetic field generator (Ambrell, U.S.A.) at room temperature. The strength and frequency of the magnetic field were kept at 12.57 kA/m and 293 kHz, respectively to maintain an optimum temperature for hyperthermia **(Sasikala et al., 2016)**. In a typical procedure, the well plates containing scaffolds and culture media which were under incubation for 48 h were placed at the center of the coil. 48 h time point was selected as optimum growth period for any noticeable cell count differences. During experiment controls (cells grown without mats) and electrospun mats of PLAA, i.e. group IV (in Table 2.2) and curcumin-loaded PLAA were seeded with HeLa cells and cultured in DMEM medium in a 5% CO_2 incubator at 37 °C in humidified environment. All samples were taken in triplicates. For application of hyperthermia, AMF was turned 'on' for 15 min after placing the samples in the center of the coil. After the hyperthermia treatment, samples were allowed to incubate for 24 h and then checked for effect of hyperthermia on cell viability using MTT assay.

2.2.11 Cell proliferation and morphological characterization

Cell attachment and proliferation were studied using a combination of MTT assay and fluorescence microscopy (Nikon, H600L, Japan). Proliferation was assessed at 8, 16, 24, 48, 72 and 96 h from the start of experiment. Mitochondrial activity of BHK-21/HeLa cells seeded onto electrospun scaffold was measured by enzymatic conversion of tetrazolium dye MTT (Sigma-Aldrich, USA). MTT reagent was made by adding 5 mg of MTT in 1 ml PBS. After every measurement (at aforementioned times), 10 μl of MTT was added to the wells followed by 3 h of incubation at 37 °C. Subsequently, the MTT reagent was discarded and 100 μl of dimethyl sulfoxide (Merck) was added to dissolve the formazan crystals. Absorbance at 570 nm was measured using plate reader (Thermo Fisher Scientific, USA) with reference value 650 nm. For cells to be fixed for morphological study using fluorescence microscopy, BHK-21/HeLa cell nuclei were stained with DAPI (4', 6-diamidino-2-phenylindole dilactate) (Sigma Aldrich, USA). DAPI stock solution (5 mg/ml) was prepared in water and diluted to 1:2500 in 1% PBS solution. The culture

medium was removed completely from the wells and washed thrice with PBS. The cells were fixed with 4% formaldehyde, incubated for 10 min and then washed thrice with PBS. The cells were then permeabilized using 0.2% Triton X-100, kept for 5 min and washed thrice with PBS. DAPI (300 μl) was added to the wells and incubated in dark for 15 min, followed by discarding of stain and washing thrice with PBS. Fluorescence was captured by exciting DAPI with ultraviolet light and detecting through a blue/cyan filter. The images were captured using fluorescence optical microscope at 10x resolution.

2.3 Analytical instrumentation and characterization

From the synthesis to final decomposition, the nanoparticles, polymer and nanocomposites, need to be characterized in detail and various properties such as morphological, thermal, mechanical, optical, barrier etc. need to be measured. It is very crucial to have a proper understanding of the working principle of all the characterization techniques utilized for polymers. A number of characterization techniques are utilized in this study and are described in detail nextx.

2.3.1 Transmission electron microscopy (TEM)

TEM is a powerful microscopic technique to obtain microscopic and electronic diffraction information about the specimen. A very narrow and intense electron beam is focused with the help of magnetic lenses and the image is formed by the electrons transmitted through the specimen. Sample thickness for TEM should be as small as possible allowing more electrons to pass through it and form image with minimum energy loss. The samples were uniformly dispersed using sonication (~30 min) in water at a concentration of ~0.01 wt% followed by drop casting onto the carbon-coated grids (Pacific Grid, USA) and vacuum drying at 60 °C. Images were acquired using TEM (JEM-2100, JEOL, USA) at an accelerating voltage 200 kV, and dimensions of prepared nanoparticles were determined (using Image J software, version 1.42) and reported as average values.

2.3.2 Scanning electron microscopy (SEM)

SEM images of degummed and native silk fibers were analyzed by scanning electron microscope (1430vp, LEO, USA), operated at a voltage of 10 kV with 15 mm working distance. A small fiber piece is mounted on aluminum stubs over carbon tape. Further, a thin gold layer was coated on the samples under vacuum using sputter coater (SC7620, Quorum) to increase the conductivity of the samples.

2.3.3 Field emission scanning electron microscopy (FESEM)

FESEM is used for acquiring surface morphological and elemental composition information about the specimen. An electron beam generates electrons which are accelerated using a high electric field gradient. This beam is focused using electronic lenses to develop a narrow beam. The collimated electrons are bombarded on the specimen, the emitted secondary electrons are detected by detector and electric signals are generated which are amplified and transformed into images. The angle and velocities of secondary electrons determine the shape and size of specimen.

To make samples conductive, the samples are coated with a thin layer of gold or platinum using plasma sputtering method. To examine the surface morphology, samples were well-dispersed in water with the help of sonication (~30 min), drop cast on aluminum foil, placed over double sided carbon tape and dried under vacuum overnight. For examining variation in surface morphology of PLA films with an increase in filler loading, small pieces of film samples were dipped in liquid nitrogen and taken out after bubbling stopped and broken immediately. The broken samples were mounted on aluminum stub with carbon tape. To make specimen conducting, ~5 nm gold coating was done under vacuum by using sputter coater (SC7620, Quorum). For electrospun scaffolds, a small piece was cut and placed on Al stub over carbon tape. The analysis was performed using FESEM (Sigma, Zeiss) at accelerating voltage of 2–5 kV.

2.3.3.1 Energy dispersive X-ray (EDX) spectroscopy

Energy dispersive X-ray analysis (EDX) (Oxford Instruments, UK) was used to investigate the elemental composition and to carry out mapping of the nanocomposites. The accelerating voltage of 20 kV is used and sample analysis is done using Aztec software.

The composition analysis and mapping of bionanocomposite was carried out using energy dispersive X-ray analysis (EDX) (Oxford Instruments, UK) at an accelerating voltage of 20 kV and analyzed using Aztec software.

2.3.4 Atomic force microscopy (AFM)

AFM is a microscopic technique which can develop three-dimensional image of the sample at nanoscale. A mechanical probe moves over the surface and due to forces between sample and probe, the probe deflects as per Hooke’s law. These deflections change the reflections of the laser focused on the probe and are recorded by a detector. The surface

topography and morphology of CSNs were assessed using AFM (Agilent, Model 5500 series) with silicon cantilever having a spring constant of 42 N/m at a resonance frequency of 320 kHz. The samples were prepared by drop casting CSN suspension in water (0.01 wt%) on sonicated silica substrates (1 cm × 1 cm) and dried overnight under vacuum. AFM images and 3D morphologies were analyzed with the WSxM software (version 5.0). To examine the dispersion of CSN in PLA matrix, PLA and PLA/CSN bionanocomposites were dissolved in HPLC chloroform and drop cast.

2.3.5 Polarizing optical microscopy (POM)

POM is a type of optical microscope used for crystallization studies of small individual crystals of polymers and to obtain important information such as spherulite morphology, spherulite growth rate and spherulite density. During crystallization process, the formed crystals rotate the polarized light in particular direction and develop birefringence due to difference in refractive index. The growth of PLA spherulites in PLA and PLA/CSN bionanocomposite films were observed using POM (Eclipse LV100N POL, Nikon Co., Japan) supplied with a Linkam TST350 hot stage (Linkam Scientific Instrument, UK). The samples (~ 20 μm) were placed in between the glass slides and rapidly heated to 190 °C at a heating rate of 50 °C/min to obtain a thin slice. This was followed by a 3 min isothermal hold to remove the thermal history. Thereafter, the samples were rapidly cooled down to the crystallization temperature at a cooling rate of 50 °C/min (using liquid nitrogen) and maintained at isothermal condition for 30 min (until complete crystallization). The radius of the PLA spherulites at different time intervals were recorded using a stationary CCD camera and images were analyzed using J software. Nucleation density was obtained by counting the number of crystals in a particular area. Growth rate (G) of spherulite was estimated from the slope of the straight line plots of spherulitic radius (R) versus time of crystallization (t) as per the following expression.

$$G = \frac{dR}{dt} \tag{2.3}$$

To investigate the cold crystallization morphology, the PLA and PLA/CSN samples were investigated using POM. The crystallization process during the second heating cycle at the rate of 2.5 °C/min was recorded, till the final temperature was about 120 °C, which is lower than the T_m. The cell proliferation studies were carried out using optical microscope with fluorescent lens attachment; the stained cells appeared blue and could be detected

well through a blue/cyan filter. The images were captured using fluorescence optical microscope at 10x resolution.

2.3.6 X-ray diffraction (XRD)

This characterization technique allows identification of different phases of semi-crystalline polymer and unit cell dimensions of the crystalline phase. All possible diffraction directions are detected by scanning the sample through a range of 2θ angles. XRD studies were carried out using D8 Advance diffractometer (Bruker, Germany) equipped with θ-θ goniometer and Ni-filtered Cu-K_α radiation (λ=0.1541 nm). X-ray generator was operated at 40 kV and 40 mA. The 2θ range for the analysis was chosen from 10 to 50° with a continuous scan speed and an increment of 2 s/step and 0.05°/s, respectively. The powdered samples were dried under vacuum at 60 °C whereas the film samples were annealed at 80 °C for 2 h before analysis. The interlayer spacing (d) was calculated by Eq. 2.4 **(Warwicker, 1960)**:

$$d = \frac{\lambda}{2sin\theta} \tag{2.4}$$

where λ is the wavelength of incident radiation, and θ is half the Bragg's angle corresponding to the crystalline peak. The degree of crystallinity was determined using OriginPro® software version 8.5. The program deconvoluted the XRD data to remove the background noise and calculated the degree of crystallinity from the difference in area of crystalline peak to amorphous region which is based on Eq. 2.5:

$$I_c = \frac{\sum Area_{crystalline}}{\sum Area_{Amorphous+crystalline}} \times 100 \tag{2.5}$$

2.3.7 Fourier transform infrared spectroscopy (FTIR)

Fourier transform infrared spectroscopy (FTIR) of prepared nanoparticles, i.e. CSN and MGCSN, and PLA/CSN bionanocomposite was carried out using FTIR spectrophotometer (Frontier1, PerkinElmer, USA). The powdered samples pelletized with KBr (in ratio 1:100) were investigated in diffuse reflectance spectroscopy (DRS) mode using dried KBr as background. Before analysis, the samples were kept in hot air oven at 60 °C overnight. The polymeric films were scanned in attenuated total reflectance (ATR) mode in the spectral range 400–4000 cm^{-1} and a minimum of 64 scans with a resolution of 4.0 cm^{-1}.

2.3.8 Raman spectroscopy

Raman spectroscopy, unlike FTIR spectroscopy, uses monochromatic light in the visible and near-IR to illuminate the samples. The spectra are obtained from scattering of light by vibrating molecules, unlike from absorption of light by vibrating molecules as in FTIR spectroscopy. Secondly scattered light is observed at right angles to the direction of the incident beam whereas in case of FTIR the absorption signal is measured in the same direction as the incident beam. Raman spectra were measured using Horiba Jobin Yvon Raman spectrometer (Labram HR, France) equipped with a 1W, 1064 nm Nd: YAG diode-pumped laser at an excitation wavelength of 514 nm. 1024 scans were accumulated with the use of a double-sided forward-backward scanning mode. The finely ground powdered sample was placed on a glass slide and spectra was collected at different locations viewed through an attached microscope.

2.3.9 ^{13}C-Solid state nuclear magnetic resonance spectroscopy (ss-NMR)

NMR is an analytical technique used for the determination of atomic arrangement of molecule, purity of substance, chemical composition etc. It is based on the fact that when a population of nuclei is exposed in an external magnetic field, the nuclei turn out to be aligned either with the magnetic field (alpha orientation) or against the field (beta orientation). This process generates fluctuation in magnetic field known as resonance. This resonance can be detected and converted into peaks. Conformational studies for isolated CSN were performed on ^{13}C solid-state nuclear magnetic resonance (NMR) spectrometer (Bruker Avance 500 MHz) with resonance frequency of 59.6 MHz for ^{13}C, and chemical shifts were referenced to tetramethylsilane.

2.3.10 Ultraviolet-visible (UV-Vis) spectroscopy

For estimation of dye adsorption activity, the concentration of samples taken at different time intervals in quartz cuvette was measured. The characteristic peaks for aniline blue were taken and transparency of the films was determined using a UV-Visible spectrophotometer (Labmda 25, PerkinElmer, Germany). The wavelength range for the measurement was kept between 190 to 1100 nm with a scan rate of 50 nm/min and 2 nm of spectral bandwidth. The transparency measurements were carried out with films of dimension 20 × 10 mm. Transparency of the films was calculated using Eq. 2.6 **(Bhasney et al., 2017)**:

$$Transparency = \frac{A_{600}}{X} \quad (2.6)$$

where A_{600} and X are the absorbance at 600 nm and the film thickness (mm), respectively. Results are based on a mean of three measurements.

2.3.11 Differential scanning calorimetry (DSC)

The polymer sample absorbs or releases energy when undergoing endothermic or exothermic phase transitions. The change in heat enthalpies can be used to determine the temperatures corresponding to different phase transitions in polymer samples such as glass transition, crystallization and melting. Similarly, heat capacity, heat of fusion etc. can be determined directly whereas degree of crystallinity can be determined indirectly. Using DSC data and applying various theoretical models, one can study kinetics of crystallization which is a critical aspect of polymer processing. The thermal properties of the bionanocomposites were characterized with DSC 204 F1 Phoenix® (Netzsch, Germany) under inert nitrogen flow (~60 ml/min). The instrument was pre-calibrated with Indium standards. Platinum-Rhodium (Pt-Rh) crucible was used for the tests with sample weight ~6–8 mg and an empty crucible made of the same material was used as reference. Phase transition information (i.e. glass transition, T_g; cold crystallization, T_{cc}; enthalpy of cold crystallization, ΔH_{cc} and enthalpy of fusion, ΔH_f) is obtained by scanning at a rate of 10 °C/min with temperature varied from 25 to 190 °C followed by 3 min isothermal hold at 190 °C. After erasing the processing history in the first heating cycle, samples were cooled to 25 °C and then second heating cycle was used for recording the information. The percentage crystallinity (% X_c) of PLA was calculated according to the Eq. 2.7:

$$\%X_c = \left(\frac{(\Delta H_m - \Delta H_{cc})}{\Delta H_m^{\circ} \times \left(1 - \frac{wt\%\ filler}{100}\right)}\right) \times 100 \qquad (2.7)$$

where ΔH_m and ΔH_{cc} are the enthalpies of fusion and crystallization, respectively, ΔH_m° is the enthalpy of fusion of 100% crystalline polymer matrix (93.0 J/g for PLA) and wt% filler is the filler weight percentage **(Dong et al., 2011)**. To better understand the crystallization phenomenon and evaluate various kinetic parameters related to process of crystallization, both non-isothermal and isothermal crystallization kinetics were studied. For non-isothermal crystallization kinetics, the film samples were scanned at varying rates of 5, 7.5, 10 and 12.5 °C/min. In order to cancel the effect of thermo-mechanical histories, the samples were heated from room temperature and held at 190 °C for 3 min. Subsequently, the samples were cooled to room temperature and again heated to 190 °C at the predetermined rates. For investigation of isothermal crystallization kinetics, the film

samples were heated from 25 to 190 °C at a scanning rate of 50 °C/min followed by holding the samples for 3 min to eliminate remaining nuclei which may function as seed crystals. Thereafter, the samples were rapidly quenched from 190 °C to the respective crystallization temperatures of 90, 95, 100, 105, 110, 115 and 120 °C at a cooling rate of 50 °C/min. The temperature was maintained until the crystallization process was completed.

2.3.12 Thermogravimetric analysis (TGA)

TGA can determine the thermal transitions (onset of degradation, T_{onset}; degradation temperature, T_{max}) by measuring the mass change (loss or gain) and rate of the change with respect to increase in temperature or time in a controlled environment due to absorption/desorption of volatile components, oxidation/reduction or decomposition of the sample. TGA can be used to determine the thermal and oxidative stability of the material and also composition of the material. Thermogravimetric analysis for the bionanocomposites (~6 mg sample weight) was performed using TGA (TGA-4000, PerkinElmer, USA) under nitrogen atmosphere (at a flow rate of 250 ml/min) from 30 to 600 °C at a heating rate of 10 °C/min. The experimental data were evaluated through Pyris-1™ Thermal Analysis Software. The non-isothermal degradation kinetics for PLA/CSN bionanocomposite films was studied in the temperature range of 30–600 °C at three different heating rates of 10, 20 and 30 °C/min. The activation energy (E_a) and mechanism for thermal degradation of the PLA/CSN bionanocomposite have been measured by applying various theoretical models.

2.3.12.1 Hyphenated thermogravimetric-Fourier transform infrared spectroscopy (TG-FTIR)

Hyphenated TG-FTIR analysis was carried out to investigate the mass loss of PLA, PLA/CSN bionanocomposite films (~9 mg) and online, real-time investigation of evolved gaseous products. A thermogravimetric analyzer (TGA-4000, PerkinElmer, USA) coupled with Fourier transform infrared spectrophotometer (Frontier-1, PerkinElmer, USA) was used in the temperature range of 30–700 °C at a heating rate of 5 °C/min under the flow of nitrogen gas at 50 ml/min. The start time difference between FTIR and TG was about 2 min which was due to the time required for the nitrogen gas to fill the cell volume of the spectrophotometer. The isothermal condition was maintained at 700 °C for 1 min. TGA was coupled to FTIR using an interface line having gas transfer tube and gas cell. The interface line was heated up to 260 °C to avoid condensation of the evolved gases from

TGA instrument. The FTIR scanning range was set to be 4000-450 cm^{-1} at a resolution of 8 cm^{-1} with 4 scans.

2.3.13 Mechanical testing using universal testing machine (UTM)

UTM is used for determining tensile strength of the polymer films. In this technique, samples are prepared as per ASTMD638 standard for the analysis. The mechanical properties (tensile strength, elastic modulus, toughness and elongation at break) of the prepared dumbbells using injection molding machine as per ISO-527-2-1BA standard (5 mm width, 2 mm thickness and 25 mm gauge length) were measured using a universal tensile testing machine (8801J4051, Instron, U.S.A.) equipped with a 100 kN load cell at a constant cross-head speed of 5 mm/min. The samples were equilibrated in an environmental chamber at 25 °C ± 5 °C and 50 ± 5% relative humidity (RH) for 48 h prior to testing. Five replicates of each sample were tested and the mean of the obtained results was reported along with standard deviation.

2.3.14 Micro-tensile testing

The mechanical properties of CSN/MGCSN-filled electrospun scaffolds were measured with the micro-tensile stage (Linkam, TST 350) built in 200 N load cell with micro-Newton resolution. Samples with an average thickness of ~50 μm were stretched at a constant speed of 3 mm/min under standard condition following ASTM D638-03 Type I, scaled down by a factor of 3. The measured width and gauge length of the sample were 7 and 15 mm, respectively. Stage is controlled by system controller PE95/T95 with system software Linksys 32. Three replicates of each sample were tested and the average results are reported with standard deviation.

2.3.15 Dynamic mechanical analysis (DMA)

In this test, the specimen is subjected to dynamic force with progressive increase in temperature to measure viscoelastic behavior, i.e. loss and storage modulus of the polymer with known geometry either in tensile or compression mode. DMA can be used to measure glass transition temperature (T_g) as well as heat deflection temperature (HDT). The thermo-mechanical analysis of PLA and PLA/CSN bionanocomposite dumbbells cut to 10 × 5 × 2 mm^3 was carried out with DMA 242E Artemis (Netzsch, Germany) in tensile mode under a dynamic force of 2N, oscillation amplitude of 20 μm at a frequency of 10 Hz. Samples were heated from 25 to 100 °C at a heating rate of 3 °C/min in 100 ml/min nitrogen gas flow.

2.3.16 Shore hardness test

The shore hardness tests of melt blended PLA and PLA/CSN bionanocomposite dumbbells were carried out using Durometer (GGR-30, Hiroshima) based on ASTM D2240 under atmospheric conditions. The average hardness value was reported by performing the measurement at five different positions for each composition.

2.3.17 Oxygen permeability (OP)

Oxygen gas transmission rate (OTR) measurements of PLA and PLA/CSN bionanocomposite films were made using a Perme® OX2/231 oxygen permeability tester (Labthink International Inc., Medford, Massachusetts, U.S.A). OTR measurements were carried out at 23 ± 0.1 °C, maintained by temperature controller (Labthink, model TC-01), on circular films having an area 50 cm^2 according to ASTM D3985 standard at 0% relative humidity using oxygen gas of high purity (>99.95%). The samples were conditioned in diffusion cell by purging with nitrogen gas (~99.9995% purity) for a minimum of 24 h under equilibrium humidity. During test, pure oxygen at pressure 0.5 bar and a flow rate of 20 ml/min was introduced into the upper half of the sample chamber while nitrogen gas was injected into the lower half of the chamber. Analysis was performed for at least 6 h until steady state value was achieved and OTR (cm^3/m^2.day) values were recorded. The oxygen permeability (OP) coefficient was calculated by Eq. 2.8:

$$OP = \frac{OTR}{\Delta p} \times l \qquad (2.8)$$

where Δp is the difference in partial pressure of the oxygen gas in the test chamber and l is the average film thickness measured with digital coating thickness meter (6156, Indi, India). The thickness of each sample was determined at 10 different locations and the average value was considered.

2.3.18 Water vapor permeability (WVP)

Water vapor transmission rates (WVTR) of nanocomposite films was recorded using a water vapor permeability tester (Permatran-W® 1/50G, Mocon, U.S.A.) as per ASTM E398-03. Prior to the analysis, the samples were conditioned at 25 ± 5 °C and 50% RH for 48 h. Three samples each of 50 cm^2 were examined at 37.8 ± 0.1 °C and 90% RH. Pure nitrogen (~99.9%) at a pressure of 30-35 psig was used for purging. Tests were carried out in continuous mode and continued until ten successive readings showed only a 5% deviation from the average value for each sample, which was considered its WVTR value.

Moisture permeability through the electrospun bionanocomposite scaffolds was measured as per ASTM standard E-96 where specimen was sealed over an open mouth of a vessel containing water and the assembly was placed in a controlled atmosphere (35 °C and 65% RH). The test unit was weighed periodically and the weight was plotted as a function of time for a period of 24 h. Further, water vapor transmission was measured as the slope of the curve (in the linear region) divided by the area of the vessel mouth. The water vapor permeability (WVP) coefficient was determined using Eq. 2.9:

$$WVP = \frac{WVTR}{\Delta p} \times l \tag{2.9}$$

2.3.19 Wettability studies: Contact angle measurement (CA)

The contact angle is defined as the angle between materials' surface and tangent to the point of contact with the test droplet. It is used for estimation of surface properties, i.e. hydrophilic or hydrophobic nature. It is also used to measure the interfacial tension between solid and liquid. Contact angle measurements for PLA and PLA/CSN were carried out on goniometer (DSA 25, Kruss, Germany). Two different liquids namely water (Milli-Q) and diiodomethane were used for contact angle measurements. A sessile drop of the liquid (~2 μl) was released on the sample surface and geometry of the droplet was evaluated with a CCD camera operating at a recording speed of 50 frames per second (fps). Measurements at temperature of 25 °C were taken after 1 min in order for the contact angle to stabilize. Averages of three values along with standard deviation were reported. The surface free energy (SFE) for the samples was calculated by the method of Owens, Wendt, Rabel and Kaelble (OWRK). The surface tension γ_L of the reference liquids along with disperse γ_L^D and polar fractions γ_L^P were taken from the literature and are summarized in Table 2.3.

Table 2.3: Surface tension values of the test liquids used in this study.

	Surface Tension (γ_L) (*mN/m*)	Disperse (γ_L^D) (*mN/m*)	Polar (γ_L^P) *(mN/m*)
Water	72.8	21.8	51.0
Diiodomethane	50.8	50.8	0.0

The contact angles (θ) of the reference liquids on bionanocomposites was used to plot a straight line as per Eq. 2.10, from which polar and disperse contributions of the SFE were determined as slope and intercept.

$$\frac{1}{2}(1+cos\,\theta)\frac{\gamma_L}{\sqrt{\gamma_L^D}} = \sqrt{\gamma_S^P}\sqrt{\frac{\gamma_L^P}{\gamma_L^D}} + \sqrt{\gamma_S^D} \quad (2.10)$$

where, γ_s is the surface free energy of a solid. The surface wettability of the electrospun scaffolds was determined using Milli-Q water with drop size of 2 µl. The measurements were taken in triplicates and results were reported as average values.

2.3.20 Gel permeation chromatography (GPC)

GPC, also known as size exclusion chromatography, is a type of high performance liquid chromatography (HPLC). The weight average molecular weight (M_w), number average molecular weight (M_n) and polydispersity index (PDI) for PLA and PLA/CSN bionanocomposite films and electrospun scaffolds were determined using GPC. The molecular weight is determined on the basis of the hydrodynamic volume of the molecule. The molecular weights of the prepared samples were measured using the gel permeation chromatography (GPC) system (auto sampler SIL-20A HT; liquid chromatograph, LC-20AD; degassing unit, DGU-20A_{3R}; refractive index detector, RID-10A; Agilent two PL gel 5 µm MIXED-D column in series with column oven, CTO-20A) (Shimadzu, Japan) at 40 °C. HPLC grade chloroform was used as an eluent with a flow rate of 1.0 ml/min. Narrow molecular weight standard of polystyrene samples from ~144-400 kDa were used for calibration. Prepared bionanocomposites (30 mg) were dissolved in 1.5 ml HPLC chloroform and filtered through 0.2 µm PTFE syringe filters before analysis.

2.3.21 Melt flow Index (MFI)

Melt flow index (MFI) was calculated by Melt Flow Indexer (at 210 °C, load 2.16 kg) (International Equipment Company, India) according to the ASTM standard D1238 using Eq. 2.11:

$$MFI = 600\frac{W}{t} \tag{2.11}$$

where W is the extruded weight (g) and t is the test time (s).

2.3.22 Color and Haze measurements

Psychometric chroma co-ordinates such as L^* (0: black; 100: white), a^* (+ve: redness,-ve: greenness), and b^* (+ve: yellowness, -ve: blueness) of PLA and PLA/CSN film samples were measured using a Chromameter (Datacolor® 550, Datacolor Technology Suzhou Co. Ltd., China) based on ISO 9001:2008 standard. The chromameter was calibrated on the CIE L^*, a^*, and b^* scale before each measurement using a white ceramic (serial no. 8812351; L^*= 89.35, a^*= -0.22, and b^*= +4.79) at 23.8 °C and 46% RH. The illuminated area of film samples was lesser than the exposed area to avoid edge effects. Three specimens of each film sample were used for analysis and average values are reported. The total color difference (ΔE^*) between control PLA and PLA/CSN bionanocomposite films was calculated as per the Eq. 2.12:

$$\Delta E^* = \sqrt{(\Delta L^*)^2+(\Delta a^*)^2 + (\Delta b^*)^2} \tag{2.12}$$

where ΔL^*, Δa^* *and* Δb^* are the change is lightness, redness/greenness and yellowness/blueness, respectively.

The Chroma (C*) value is defined as relative purity or saturation of a color and is determined by using Eq. 2.13 **(Rotabakk et al., 2006)**:

$$C^* = \sqrt{(\Delta a^*)^2 + (\Delta b^*)^2} \tag{2.13}$$

Haze in conformance with ASTM D1003. Haze measurements require two readings. One reading is taken with the calibrated white tile at the reflectance port and next one is taken with the black trap at the reflectance port. Prior to analysis of samples, instrument is calibrated with white tile and black light trap individually without any samples. Haze values are reported in percentage.

2.3.23 Vibrating sample magnetometer (VSM)

The magnetic properties of the fabricated CSN, MGCSN were analyzed at room temperature with a vibrating sample magnetometer (VSM) (Lakeshore, 7410 series). The powdered samples (~10 mg) were wrapped in Teflon tape prior to analysis.

2.3.24 Amino acid analysis (AAA)

Amino acid composition of isolated CSN and Muga silk was determined using an amino acid analyzer (AminoQuant II, Hewlett Packard, USA) equipped with auto-sampler for automated sample handling, derivatization and injection into the liquid chromatograph column. The samples were hydrolyzed with 6N hydrochloric acid (HCl) at 110 $^{\circ}$C for 24 h.

2.3.25 Elemental/Ultimate (CHN) analysis

Carbon, hydrogen and nitrogen content of isolated CSN were measured using CHNS Elemental analyzer (Eurovector, EA3000). The sample was heated at 600 °C for 1 h and the residual weight was calculated to find out the quantity of inorganic materials.

2.3.26 Real-time particle size analysis

The particle size distribution of isolated CSN was recorded using real time dynamic light scattering instrument (Malvern, Nano-Sight NS300). The data was analyzed using nanoparticle tracking analysis software.

2.3.27 Zeta potential (ZP)

Zeta Potential (ZP) measurements were carried out using a dynamic light scattering (DLS) instrument (Delsa™ Nano C, Beckman Coulter, Germany) following Smoluchowski's theory. Extracted CSNs were suspended in Mili-Q water at 0.1 wt% and sonicated for 2 min at ambient temperature.

2.3.28 Surface area measurements

The Brunauer-Emmett-Teller (BET) surface area of the samples was assessed from N_2 isotherms at 77 K using a surface area analyzer (Beckman Coulter SA 3100, USA). Prior to nitrogen physisorption, samples were degassed at 393 K for 2 h.

2.3.29 Optical polarity measurements

The specific rotations of the PLA and PLA/CSN bionanocomposite with different CSN loadings were determined with self-calibrated Autopol® II polarimeter (Rudolph Laboratory, USA) at a wavelength of 589 nm where ~200 mg sample was dissolved in 20 ml chloroform and filtered to remove the interference of CSNs during analysis.

2.3.30 Acid value measurements

Titration measurements were carried out to calculate the acid value (acid end groups – COOH) of neat PLA and PLA/CSN bionanocomposites. Solutions were prepared by dissolving ~1 g of samples in 20 ml of chloroform. The solution was titrated against potassium hydroxide solutions prepared in methanol of 0.0208 mol/L strength. Acid value is calculated using Eq. 2.14:

$$AV = \frac{V_e \times C \times M}{m} \tag{2.14}$$

where V_e (ml) is the volume of KOH used to achieve corresponding equilibrium pH, C (mol/L) is the concentration of KOH, M is molecular weight of KOH and m (g) is weight of sample dissolved in chloroform.

2.3.31 Intrinsic viscosity measurements

Intrinsic viscosity investigations were performed on temperature controlled Ubbelholde-type viscometer. PLA and PLA/CSN bionanocomposite samples were prepared in different concentrations such as 2.25, 3.33, 5.0 and 6.67 mg/ml by dissolving in chloroform. The biofiller was filtered using 0.2 μm syringe filters. The intrinsic viscosity ([η]) was determined by extrapolation of reduced viscosities to zero concentration. Specific viscosity (η_{sp}) and relative viscosity (η_{rel}) of the samples were calculated using Eq. 2.15 and 2.16:

$$\eta_{red} = \frac{\eta_{sp}}{C} = \frac{1}{C}\left(\frac{t-t_0}{t_0}\right) = [\eta] + K'[\eta]^2 C \tag{2.15}$$

$$\eta_{inh} = \frac{ln(\eta_{rel})}{C} = \frac{1}{C}\left(ln\frac{t}{t_0}\right) = [\eta] + K''[\eta]^2 C \tag{2.16}$$

where η_{red} and η_{inh} are reduced and inherent viscosities, respectively. t and t_0 are the flow times of solution and pure solvent, respectively, and K' and K'' are the Huggins and Kramer constants, respectively. Intrinsic viscosity can be related to Mark-Houwink-Sakurada equation which relates viscosity and average molecular weight ($\overline{M_v}$) through Eq. 2.17:

$$[\eta] = B(\overline{M_v})^{\nu} \tag{2.17}$$

where B and ν for PLA are 0.005 and 0.73, respectively. To evaluate degradation through reduction in molecular weight, degradation constant (K) is calculated from reciprocal of intrinsic viscosity **(Zhou and Xanthos, 2009)**.

Chapter 3

Isolation of Crystalline Silk Nano-discs (CSNs) from Muga Silk, Preparation of Magnetic CSNs (MGCSNs) and Their Detailed Characterization

*This chapter focuses on isolation and characterization of crystalline silk nano-discs (CSNs) from Muga silk through novel hydrolysis-cum-sonication route, and the physico-chemical, structural and morphological properties of the CSNs obtained. Utilization of waste silk for production of discotic CSNs provides a strategy for upconversion of 'waste to wealth'. The extracted CSNs from Muga silk have a yield of ~13 wt%. Analytical techniques such as Field emission scanning electron microscope (**FESEM**), Atomic force microscopy (**AFM**), Transmission electron microscopy (**TEM**) and dynamic light scattering (**DLS**) were employed to calculate the CSN diameter and the values obtained were 48.15±12.7, 49.1±12 nm, 49.4 ± 17.6 nm and 89±37 nm, respectively. The thickness of CSNs as determined by AFM and TEM was found to be around 3.1±0.9 nm and 3.38±0.5 nm, respectively. The extracted CSNs show higher percentage crystallinity and superior thermal stability of ~93.7% and 310 °C, respectively. Furthermore, surface of CSNs was modified using iron-oxide nanoparticles to fabricate MGCSNs. Through one-step reduction reaction, monodisperse spherical iron-oxide nanoparticles (~5 nm) were adhered onto the entire CSN surface. Amine groups on CSN remain anionic at close to neutral pH, and the addition of positively charged iron salt (Fe^{3+}) led to strong electrostatic interaction with negatively charged amine groups of CSNs forming a uniformly dispersed iron salt-CSN solution.TEM analysis revealed that MGCSNs have diameter and thickness of 58.2 ± 4.6 nm and 16.0 ± 2.6 nm, respectively.*

The work in this chapter is accepted as:

- R. Patwa, N. Soundararajan., N. Mulchandani, S. M. Bhasney, M. Shah, S. Kumar, A. Kumar and V. Katiyar, "Silk nano-discs: A natural material for cancer therapy," *Biopolymers*, DOI: 10.1002/bip.23231. (Accepted).

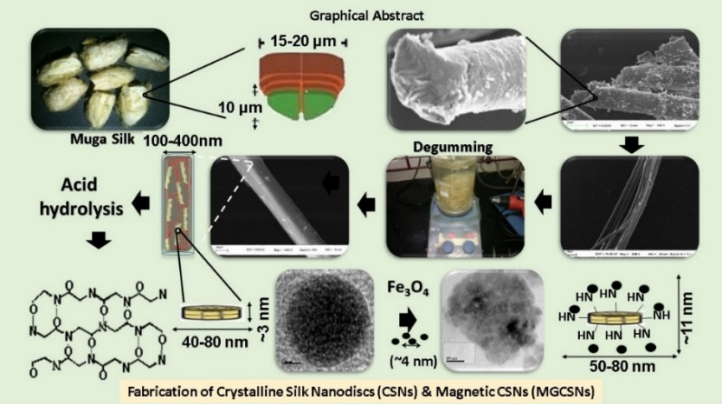

3.1 Introduction

Silk is a fibrous protein known for its excellent mechanical properties such as combined tensile strength and stretchability, which makes it one of the toughest materials known to mankind **(Keten et al., 2010)**. The term silk refers to the wide range of continuous filaments spun by several species of Lepidoptera and Arthropoda such as silkworms and spiders. Its role is to protect the pupa during metamorphosis by forming a protective outer layer known as cocoon. Spiders use it for various functions such as preying, building their web, building egg sac, etc. **(Babu, 2016)**. However, despite years of research, it is still impossible to mimic silk's unique properties which are a result of controlled self-assembly of the domains at nanoscale precision **(Keten et al., 2010)**. Silk fibers mainly consist of proteins which amount to 95% of its content while other impurities namely waxes, mineral salts such as calcium oxalate crystals and ash constitute about 4–5%. Silk spun by silkworms contains two major proteins namely fibroin and sericin whose amount ranges from 80–86 wt% and 12–16 wt%, respectively **(Basu, 2015)**. Presence of gummy layer of sericin needs to be removed by a process known as degumming **(Gulrajani, 1992)**. Chemically fibroin is composed mainly of three major amino acids namely alanine, glycine and serine. These three simple amino acids occur as long sequences of glycylalanine repeats in mulberry silks whereas they occur as polyalanine in non-mulberry species **(Acharya et al., 2009)**. The combined composition of alanine and glycine is ~80% in both mulberry as well as non-mulberry silk but wild silks have high alanine content while domesticated silks have high glycine content **(Kumar and Kundapur, 2015)**. Moreover, silk possesses environmental stability, ease of functionalization, favorable oxygen/water permeability, minimal antigenic response, biocompatibility, morphologic flexibility and better mechanical properties in comparison to globular proteins **(Altman et al., 2003; Babb et al., 2017; Jo et al., 2017; Rockwood et al., 2011; Shimanovich et al., 2017)**. These properties make silk a viable entity in various fields of biomedical applications such as for developing sutures, controlled drug delivery, cancer therapeutics, wound healing, etc. **(Darshan et al., 2017; Jo et al., 2017; Min et al., 2017; Yan et al., 2016)**. Although a major confusion lies regarding its degradable nature, various reports suggest that silk can be degraded by proteolytic enzymes *in vivo* which over the time gets absorbed slowly **(Cao and Wang, 2009)**. To utilize the superior properties of silk stored in its molecular structure, nano-level formulations of silk can be exploited using various routes **(Nova et al., 2010)**. Nanoparticles of silk fibroin can be obtained through emulsion-solvent

evaporation, phase separation, self-assembly, rapid expansion of supercritical solution, spray drying, electro-gelation, and salting out proteins **(Rockwood et al., 2011)**. The above procedures utilize reconstituted silk having random coil structures which need to be reconverted to pleated structures; hence material properties are compromised **(Rousseau et al., 2004)**. Interestingly, silk's original properties can be retained through direct utilization of silk post-degumming using mechanical attrition. Silk principally consists of antiparallel β-sheets that are stacked together to create highly ordered β-sheet nanocrystals which are embedded in semi-amorphous matrix consisting of less ordered β-structures, 3_{10} helices and β-turns **(Keten et al., 2010)**. Additionally, β-sheet nanocrystals reinforce the macromolecular chains by forming interlocks between the chains which allows the amorphous domains to extend significantly upon stretching **(Nova et al., 2010)**. Silk nanocrystals are thermally stable due to high crystallinity, hydrophobic nature and extensive hydrogen bonding **(Altman et al., 2003; Buehler, 2010; Hu et al., 2006)**. Crystalline portion of silk can be isolated by partial acid hydrolysis, enzymatic digestion, oxidative degradation and alkali treatment **(Numata et al., 2010; Shaw, 1964; Tao et al., 2012)**. Silk nanocrystals have been isolated from *Bombyx mori* as nanofilaments of 2 nm diameter and 160 nm length by digestion with enzymes **(Numata et al., 2010; Tao et al., 2012)**. Similarly, treatment of mulberry silk with acids yielded silk nanocrystals which are irregularly shaped with few spheres **(Numata et al., 2010; Tao et al., 2012)**. To improve the case for use of silk nano-discs for drug delivery and cancer therapeutics, magnetic functionalization is desired. Iron oxide nanoparticles can be prepared by various methods such as co-precipitation, non-aqueous and aqueous sol-gel, hydrothermal/solvothermal, micro-emulsion, and precipitation using reducing agents like $NaBH_4$ **(Yathindranath et al., 2011)**. There are few reports on magnetizing nanoparticles obtained from naturally occurring fibers. Recently, magnetite nanoparticles supported on cellulose nanocrystals were prepared for high performance applications **(Dhar et al., 2016)**. Further, silk microspheres/fibers-supported Fe_3O_4 composite materials have been explored for anti-cancer drug delivery **(Singh et al., 2015; Zhang et al., 2014)**.

The novelty of the present work is preparation of discotic silk nanoparticles which are highly crystalline, hydrophobic and can readily be functionalized through amine, carboxyl and hydroxyl functionality. These nanoparticles are isolated from waste pierced cocoons which are low-cost and easily available natural source of silk and are abundantly available in the north eastern region of India. The present investigation outlines the formation of

nano-discs, their functionalization, and detailed characterization. To the best of our knowledge, there is no study available in literature on the isolation of crystalline silk nano-discs by acid hydrolysis of Muga silk fibroin (*Antheraea assama*) and fabrication of magnetic nano-discs by adhering magnetite nanoparticles on the disc surface.

3.2 Results and discussion

3.2.1 Degumming of Muga cocoons

The Muga fibers were observed to be around ~40 μm in diameter as seen in Figure 3.1(a). The fiber is made up of two brins which are sealed together by sericin and has a uniform distribution of calcium oxalate crystals. Fibroin has a high refractive index, due to which it gives a shimmer when illuminated under optical microscope, as seen in Figure 3.1(b) where the sericin outer layer appears as dark shadow. The silk brins (see Figure 3.1(c)), are approximately 20μm in diameter each. The uniform sericin layer on the fiber is clearly visible in Figure 3.1(d) where sericin layer (depicted in gray dotted lines) can be seen at the edge due to the angle at which the fiber was cut. Degumming was done to remove the sericin from the fibers. Improper degumming temperature, low amount of base, excess amount of silk can all lead to improper degumming, as seen in Figure 3.1(e) where the sericin coating can be observed in patches (shown in white arrows) even after degumming. After degumming, the degummed fibers were subjected to high speed grinder which resulted is the fibers breaking up into microfibrils (Figure 3.1(f)) and nanofibrils (inset of Figure 3.1(f)).

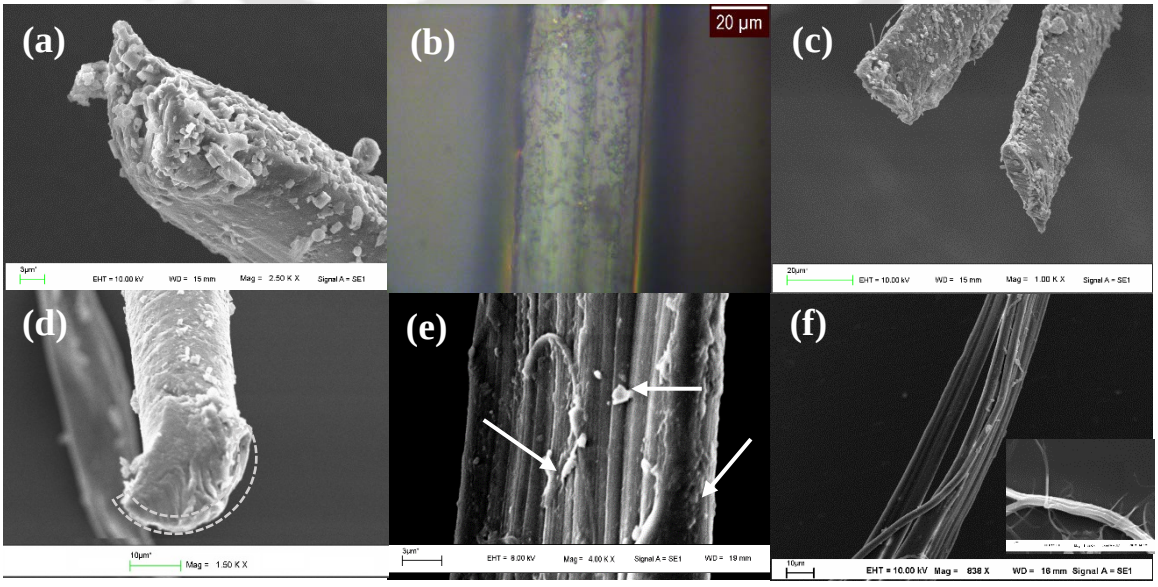

Figure 3.1: Muga silk (a) SEM micrograph showing uniform distribution of calcium

oxalate crystals, (b) optical micrograph, (c) fibers made up of two brins, (d) uniform sericin coating (edge shown in dotted lines), (e) improperly degummed fiber (sericin shown with arrows) and (f) silk microfibrils (inset: silk nanofibrils).

The waste pierced cocoons were cleaned by removing twigs, eggs and other plant debris, cut into dime-shaped pieces and dried. The amount of dried cocoon pieces was found to be ~95% of initial weight. After degumming, the amount of dried Muga silk fibroin was ~ 76% of initial weight, which shows that the sericin content of Muga silk was ~24 wt%. Sericin is a hydrophilic protein which readily dissolves in hot water; sodium carbonate makes sericin swell, then emulsifies it in degumming bath resulting in its removal from the filaments. **Sonwalkar (1993)** has suggested that the sericin content of Muga silk is ~25 wt%, which confirms that the degumming process was quite efficient, which can be seen by sericin-free silk fiber as shown in Figure 3.2.

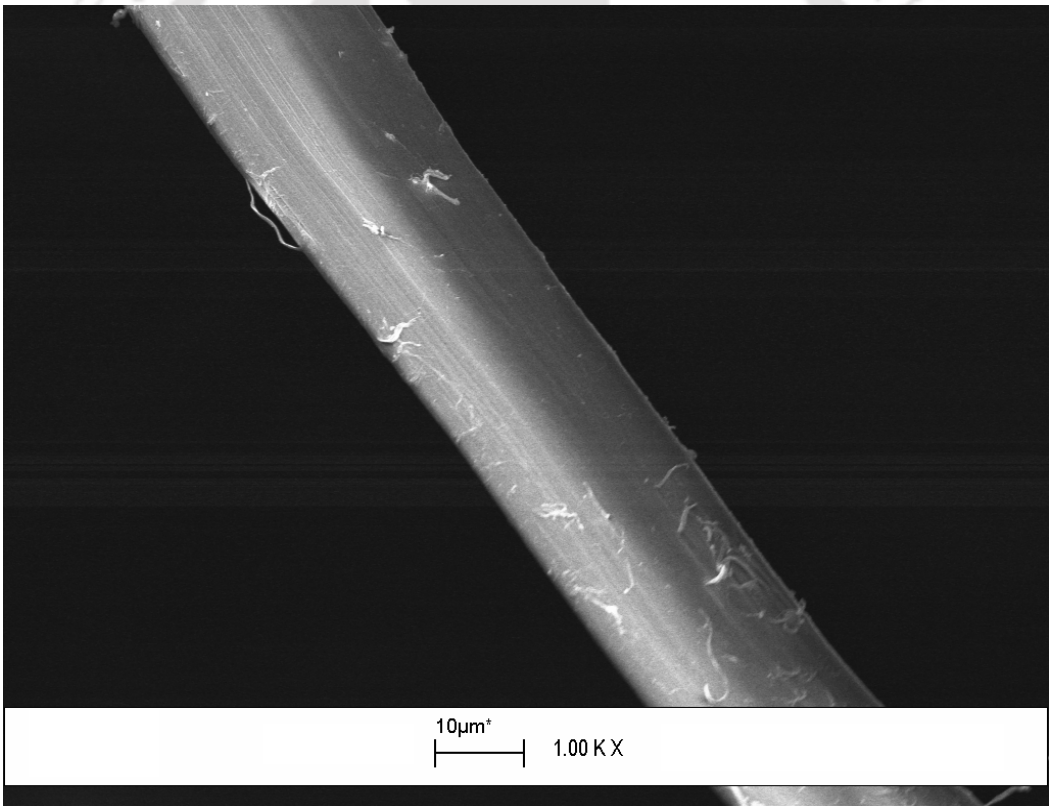

Figure 3.2: Silk fiber without sericin coating after efficient degumming process.

3.2.2 Fabrication of crystalline silk nano-discs (CSNs) from degummed Muga silk

Crystalline silk nano-discs (CSNs) were fabricated from degummed waste Muga silk. After degumming of the waste pierced Muga, the amount of degummed fibroin obtained was ~80 wt%, indicating the sericin content of Muga silk to be ~20 wt%, which matches with

the findings of **Sonwalkar (1993)** and is found to be lower than the ~20–30% sericin content of mulberry silk **(Yukseloglu and Canoglu, 2016)**. This weight loss can be attributed to the removal of not only sericin, but also inorganic minerals such as calcium oxalate crystals on the fiber surface, waxes and other water soluble impurities which are found in trace amounts. The degummed silk can be stored at room temperature **(Rockwood et al., 2011)**.

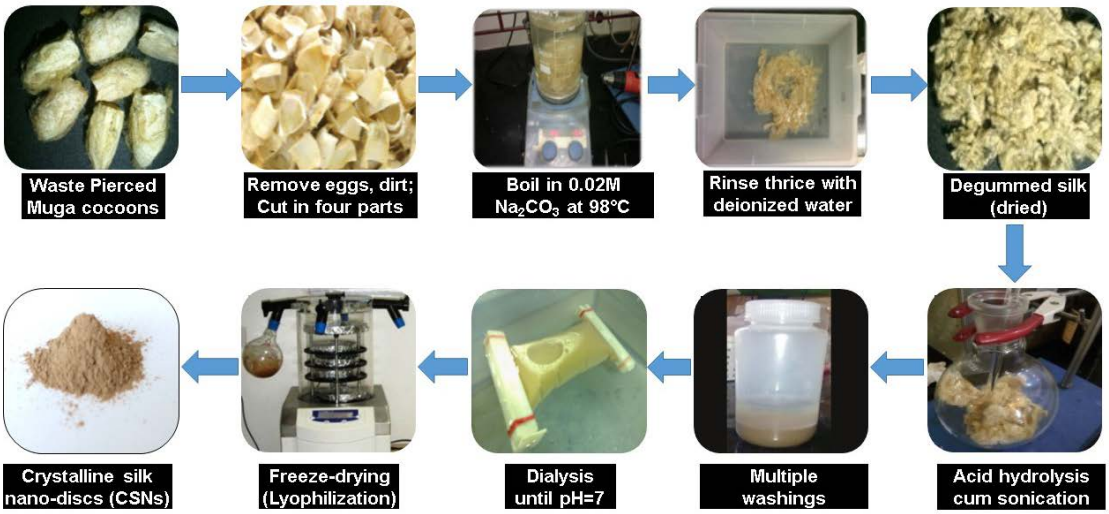

Figure 3.3: Step-wise representation of isolation of crystalline silk nano-discs (CSNs) from Muga silk.

After removal of sericin, the degummed silk was subjected to acid hydrolysis in the presence of ultrasonication and overhead mechanical stirring. The yield of CSNs was ~15% of the weight of degummed silk; the remaining amorphous and loosely packed crystalline domains were selectively dissolved, as the reaction progressed. The overall procedure of fabrication of CSNs is depicted in Figure 3.3. The freeze-dried powder was used for characterization, except for techniques which required aqueous suspensions in water.

3.2.3 Physico-chemical and structural properties of fabricated CSNs

3.2.3.1 Attenuated total reflectance-Fourier transform infrared spectroscopy (ATR-FTIR)

FTIR analysis was carried out to understand the structural differences arising out of the fibroin chain rearrangements during alkali and acid-based treatments. Absorption bands which are conformationally sensitive can be detected in silk proteins at spectral regions

like amide I, II, III and V **(Freddi et al., 1994)**. For untreated raw Muga silk, absorption bands at 1660 cm^{-1} shows the vibration of amide I band (C = O stretching) which confirms the presence of random coil conformation or α-helix as shown in Figure 3.4. The other absorption bands observed at 1260 cm^{-1} and 669 cm^{-1} in untreated silk are characteristic signature peaks for amide III and amide V, respectively. These peaks also show that raw silk is not entirely in β-form **(Freddi et al., 1997)**. After acid hydrolysis, the above-mentioned peaks disappear and shift to new positions. The amide spectral bands appear at 714 cm^{-1} (amide V), 1221 cm^{-1} (amide III) and 1630 cm^{-1} (amide I). The reason for shift in peak positions is that major portion of silk attains β-sheet conformation in the CSNs obtained after acid hydrolysis. This result is consistent with similar distinct peaks at 700 cm^{-1}, 1230 cm^{-1} and 1630 cm^{-1}, respectively reported by **Tsukada et al. (1995)** for β-sheet structure of Tussah silk. The effectiveness of degumming process can be confirmed by observing the IR bands at 1069 cm^{-1} (broad peak) and 1316 cm^{-1} (sharp peak), which denote the presence of sericin and calcium oxalate crystals in untreated samples, respectively. These peaks do not show up in CSN spectrum confirming that fibroin has been properly degummed **(Teramoto and Miyazawa, 2003; 2005; Teshome et al., 2014; Zhang and Wyeth, 2010)**. As observed by previous researchers, the crystalline portion of non-mulberry silk is essentially composed of alanine and glycine **(Kumar and Kundapur, 2015)**. Peaks at 965 cm^{-1} and 1047 cm^{-1} in Figure 3.4 have become significantly sharp for CSNs which indicates that alanine and glycine are major amino acids present in CSNs **(Fang et al., 2017)**.

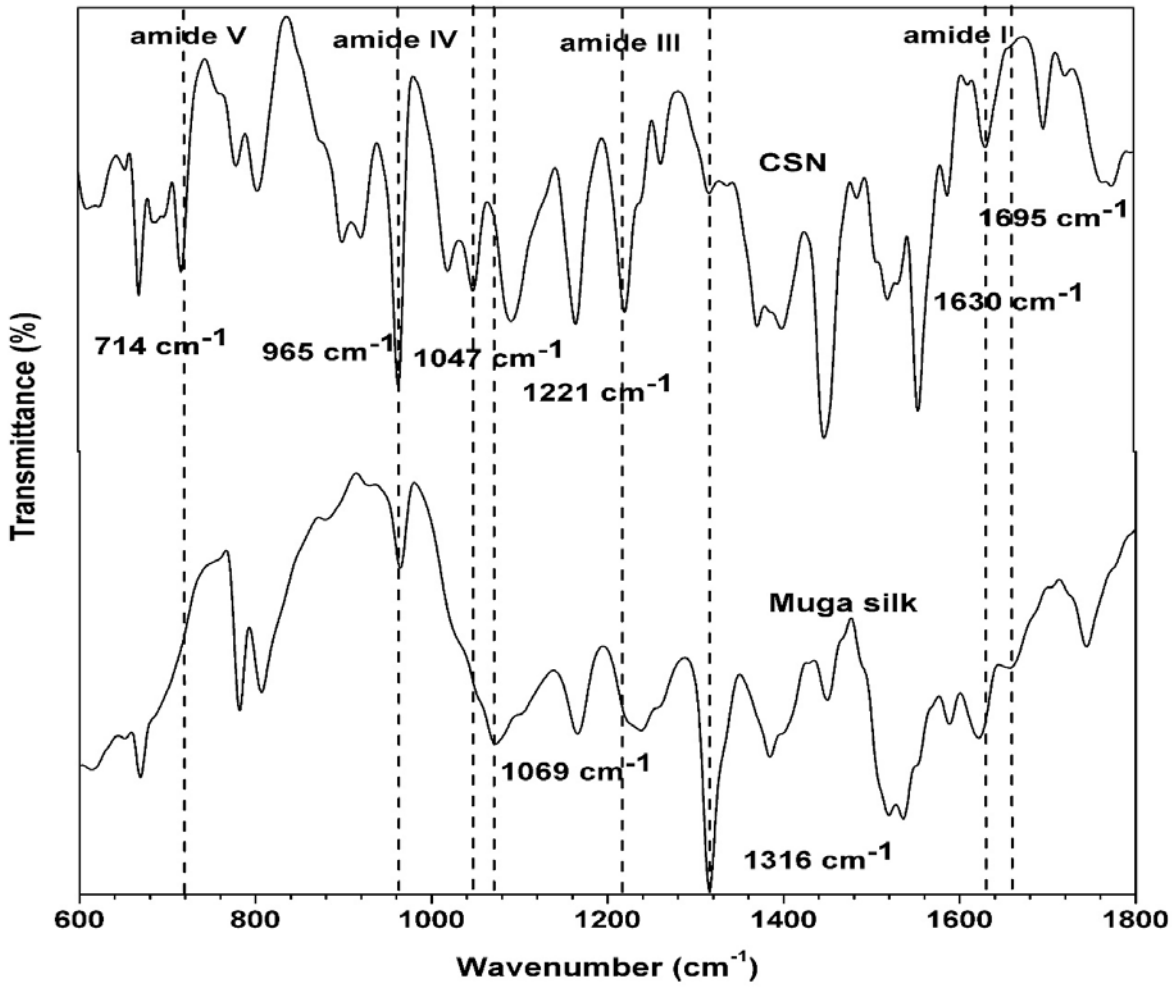

Figure 3.4: FTIR analysis of untreated Muga silk and crystalline silk nano-discs (CSNs) in the range of 600 to 1800 cm^{-1}.

3.2.3.2 X-ray diffractometry (XRD)

The XRD diffraction patterns of untreated Muga silk, degummed fiber and acid-hydrolyzed silk nano-discs (CSNs) were captured to identify type of conformation and crystallinity. The crystallinity index (CI), d-spacings and diffraction planes were calculated, and are shown in Figure 3.5 and summarized in Table 3.1. It can be observed that peak intensity and sharpness increases with each treatment step which means that the crystallinity has increased, without significant shift in peak position. Untreated Muga silk shows well-resolved peaks but with low intensity, which indicates the semicrystalline nature of Muga silk.

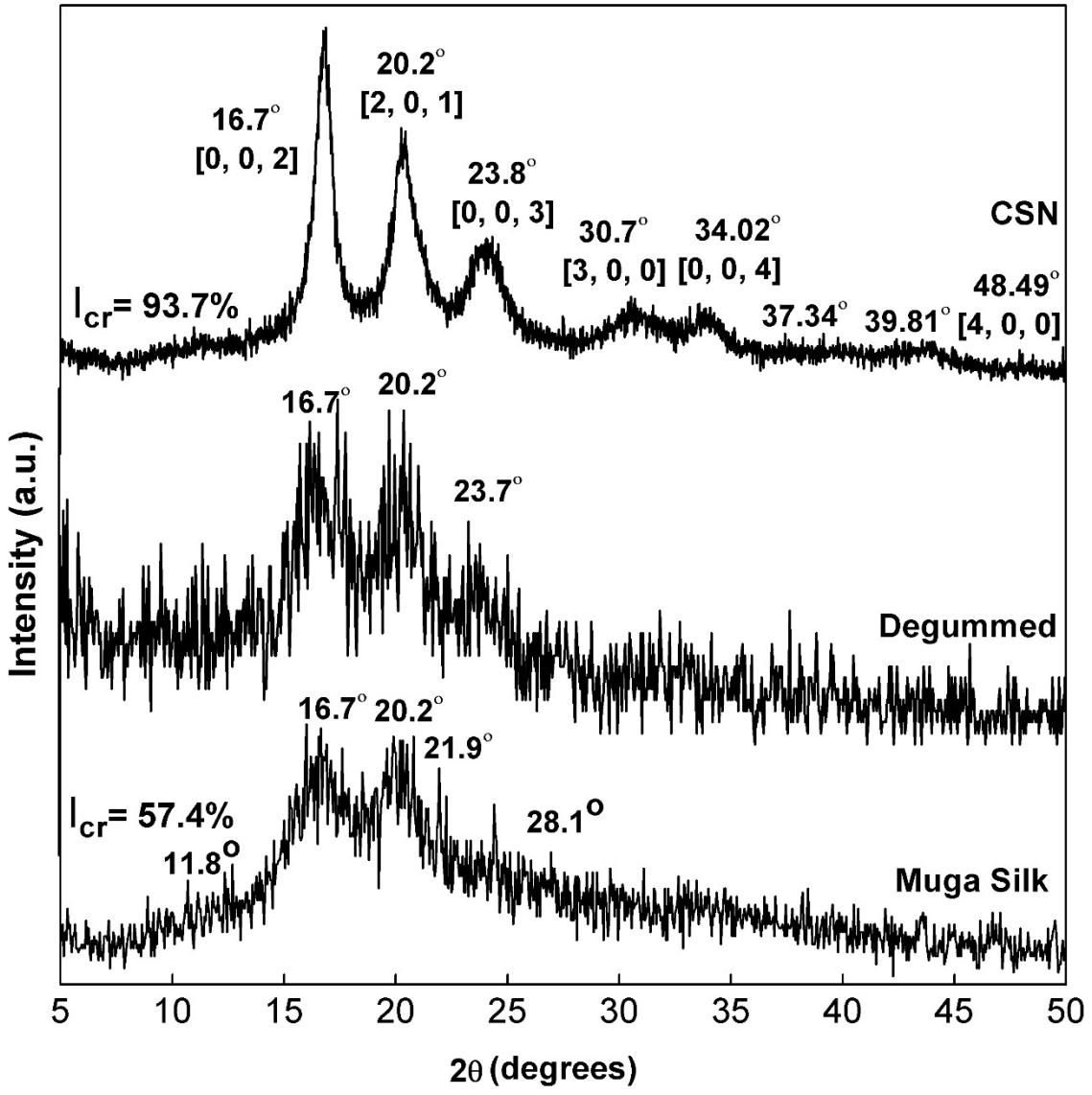

Figure 3.5: XRD analysis of untreated Muga silk, degummed silk and fabricated CSNs from Muga silk.

The crystallinity index (CI) of raw Muga was found to be ~57.4% which matches well with reported values of 60% **(Babu, 2013; Bhat et al., 1980; Devi et al., 2011)**. Muga silk has β-form of crystal fraction predominantly. However, three small peaks of low intensity at 11.8°, 21.9° and 28.1° are present in raw Muga silk diffractogram, which are absent in CSNs, indicate the presence of the α-form. This implies that Muga silk consists of both α- and β-form of crystalline secondary structures **(Kweon and Park, 2001)**. The degumming process resulted in removal of sericin outer protective coating which is mainly amorphous **(Rocha et al., 2017)**. Devoid of sericin, the degummed silk showed enhanced crystallinity with increased peak intensities. It can also be noticed that the peaks for α-form are either missing or reduced in intensity. The reported values of crystallinity index (CI) for

degummed silk is ~73.6% as compared to 63.8% for the degummed silk in our study **(Devi et al., 2011)**. Upon acid hydrolysis, CSNs displayed several sharp peaks at 16.7°, 20.2°, 23.8°, 30.7°, 34.0 and 48.5° which are characteristic peaks for β-sheet structure of silk. The lattice planes viz. (002), (201), (003), (300), (004) and (400), respectively.

Table 3.1: Crystallographic information derived from XRD diffractogram of CSNs.

2θ (degrees)	d-spacing (Å)	Lattice Plane			FWHM
		H	k	l	
16.7	5.28	0	0	2	0.799
20.2	4.39	2	0	1	1.107
23.9	3.72	0	0	3	0.931
30.7	2.90	3	0	0	-
34.02	2.63	0	0	4	-
48.49	1.87	4	0	0	-

The diffraction peaks were observed to be in line with reports in the literature **(Bhat et al., 1980; Siddaraju et al., 2012)**. The crystallinity index (CI) for isolated nano-discs increased from 57.4% for raw Muga silk to 93.7%, which indicates that CSNs are highly crystalline in nature. Acid hydrolysis leads to the removal of unordered amorphous domains resulting in closer packing of crystalline domains, and strain-free and less distorted crystallites.

3.2.3.3 ^{13}C-solid-state nuclear magnetic resonance (^{13}C-ss-NMR) spectroscopy

The ^{13}C-NMR chemical shifts of carbon atoms in proteins are sensitive to the secondary structure **(Mielke and Krishnan, 2009)**, and this makes ^{13}C-NMR an effective tool for analyzing the secondary structure of isolated CSN. The ^{13}C chemical shifts of the alpha (-C_α), beta (-C_β) and carbonyl (-C=O) carbon give us information about the conformation of isolated CSN, are shown in Figure 3.6.

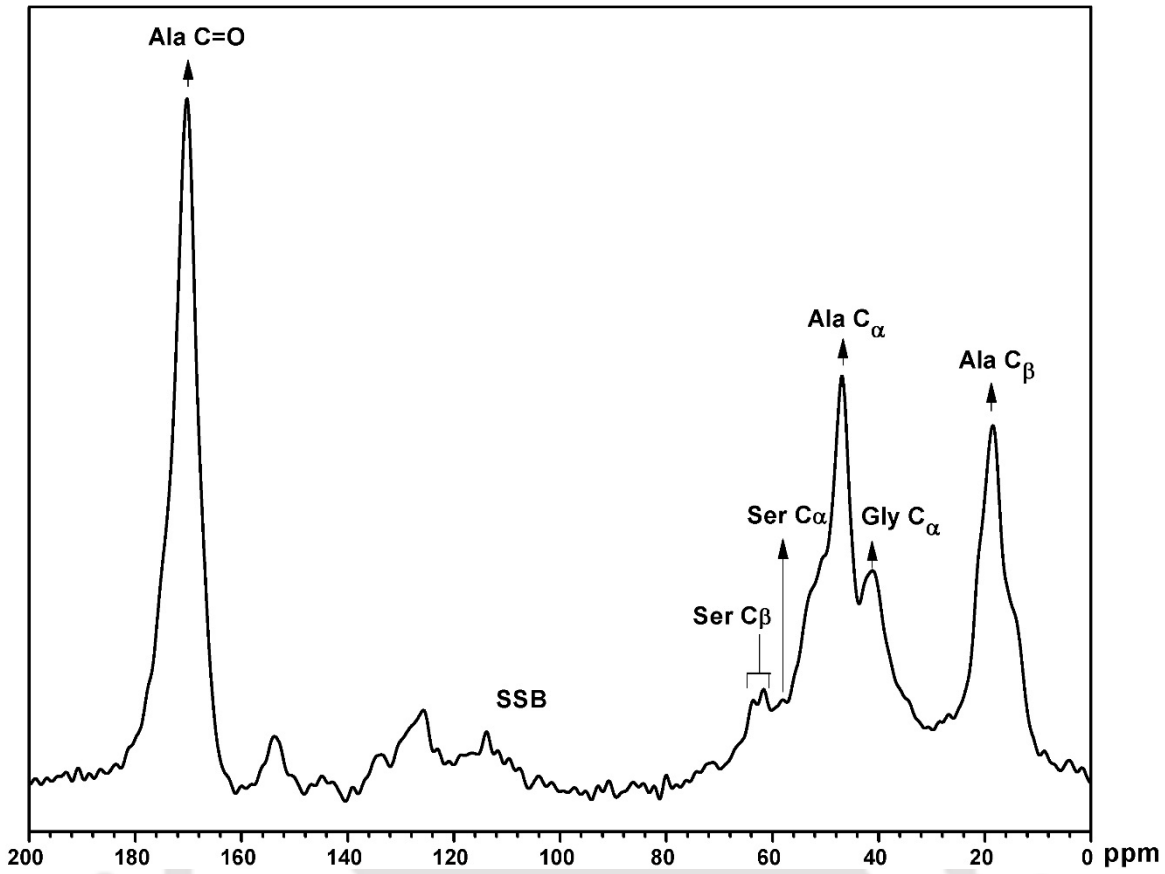

Figure 3.6: ^{13}C-ss-NMR spectra of fabricated silk nano-discs (CSNs), SSB stands for the spinning side bands.

The chemical shifts for alanine (C_α, C_β and C=O) and glycine C_α, are observed at 46.9, 18.5, 170.4 and 41.3 ppm, respectively owing to β-sheet conformation of CSN. The chemical shifts for β-sheet conformation for alanine (Cα, C_β and C=O carbon) and glycine Cα reported in literature are at 48.8, 20, 171.9 and 42 ppm, respectively **(Addison et al., 2013; Asakura et al., 2006; Nakazawa and Asakura, 2002)**. The chemical shifts found in the region 80 to 140 ppm are for the spinning side bands. It can be seen that very low intensity chemical shifts for serine are observed at 61.7, 63.8 (C_β) and 58.1 (C_α) ppm which indicates that serine residues occur as both α-helix and β-sheet conformation. The comparison of chemical shifts of CSN and model polypeptides is shown in Table 3.2.

Table 3.2: Comparison of ^{13}C chemical shifts observed from CSNs and from model polypeptides with known secondary structures **(Nakazawa and Asakura, 2002).**

Residue	Random coil (ppm)	α-helix (ppm)	β-sheet (ppm)	CSN (ppm)	Conformation
Ala C=O	175.5	176.4	171.9	170.4	β-sheet
Ser C_β	61.3	60.7	63.4	61.7, 63.8	α-helix, β-sheet
Ser C_α	56.6	59.2	55.2	58.1	α-helix
Ala C_α	50	52	48.8	46.9	β-sheet
Gly C_α	43.4	46	42	41.3	β-sheet
Ala C_β	16.6	15.8	20	18.5	β-sheet

3.2.3.4 Raman spectroscopy

To identify the conformation of CSN, Raman spectra was recorded. The comparative Raman spectra (800–1700 cm^{-1}) for untreated raw Muga silk and CSNs is shown in Figure 3.7. As confirmed by diffraction studies, untreated Muga silk consists of both α- and β-crystalline forms. The fibroin is coated with a gummy sericin coating, which leads to very low signals. After acid hydrolysis, the CSNs acquire a predominant β-sheet conformation. Muga silk has a small portion of crystalline domain which exists in the form of α-helix, as discussed in XRD in section 3.2.3.2. Therefore, Raman shifts around 1657 cm^{-1} characteristic of amide I (C=O stretching) can be observed. The peak has a very low intensity and are difficult to differentiate from the noise. Upon fabrication of CSNs, the β-form becomes predominant and shows strong peaks at 1667 cm^{-1} (amide I), 1242 cm^{-1} (amide III), 1093 cm^{-1} (amide IV) and 908 cm^{-1} (amide IV) regions which correspond to C=O stretching, N-H in-plane bending, CH_3 rocking and C^α-C stretching, respectively **(Rousseau et al., 2009; Rousseau et al., 2004)**. These peaks appeared as low intensity peaks in the spectrum for raw Muga silk.

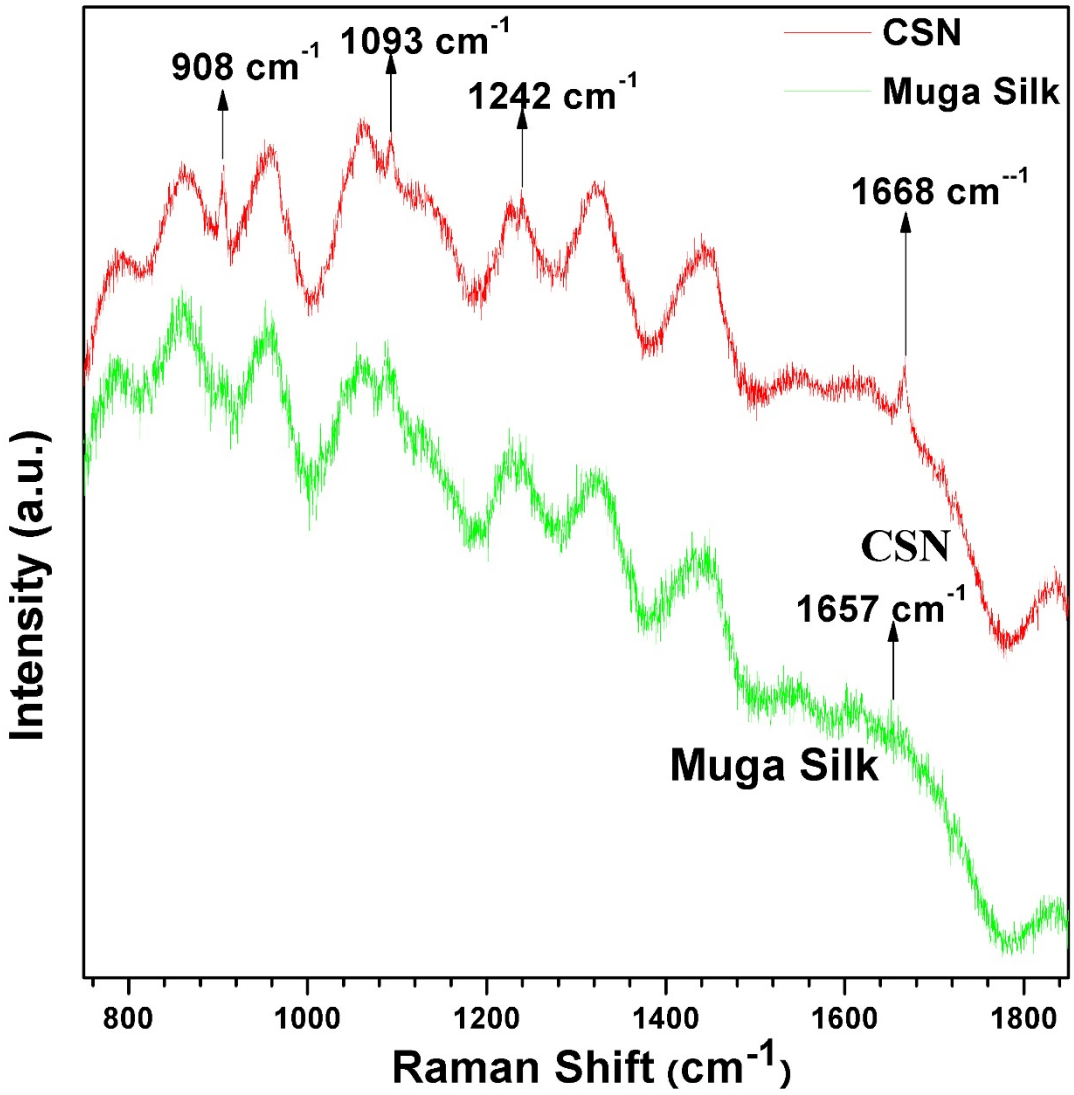

Figure 3.7: Raman analysis of untreated Muga silk and crystalline silk nano-discs (CSNs) in the range of 800 to 1700 cm^{-1}.

3.2.4 Morphological analysis of fabricated CSNs

3.2.4.1 Polarized optical microscopy (POM)

After fabrication, the CSNs were initially observed under polarized light in optical microscope before investigating using sophisticated imaging techniques such as atomic force microscopy (AFM), transmission electron microscopy (TEM) and field emission scanning electron microscopy (FE-SEM). Polarized light can effectively allow to observe the crystalline portion in the sample. Therefore it can easily depict if there is any modification in the crystalline part of silk. Crystalline parts get illuminated and show birefringence. Polarized image of silk fibers are shown in Figure 3.8(a) where crystalline regions, which are entrapped within the amorphous part, reflect the incident polarized light

and are indicated with black arrows. In contrast, the fabricated silk nano-discs appear to completely reflect the incident polarized light, as shown in Figure 3.8(b) where the sample shows bright clusters which are fully illuminated as compared to silk fibers, indicating that acid-hydrolysis has effectively dissolved away the amorphous regions, leaving behind only the crystalline regions.

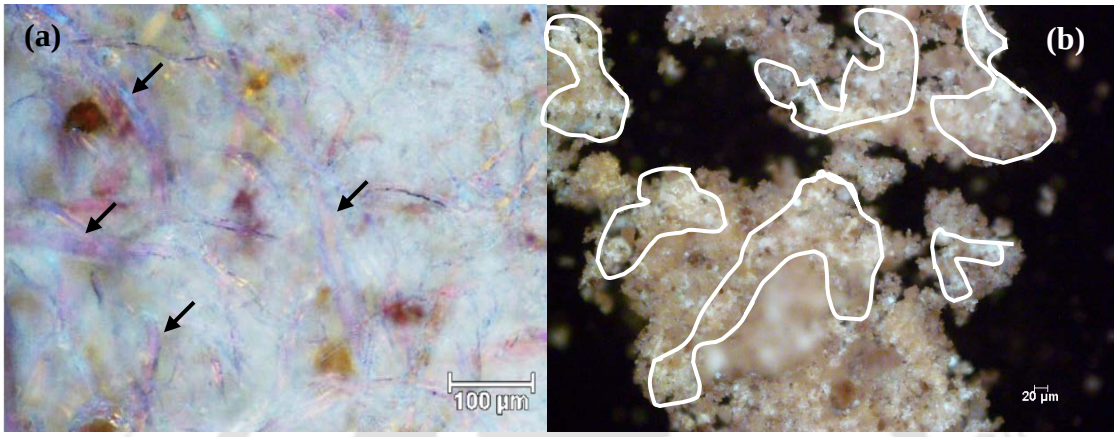

Figure 3.8: Comparative polarized optical micrographs for (a) Muga silk (crystalline domains shown with black arrows) and (b) CSNs (bright clusters shown in white).

3.2.4.2 Atomic force microscopy (AFM)

The morphology and topology of CSN is investigated by using AFM. In the AFM micrograph (XY-axes) of a 500 × 500 nm^2 area, shown in Figure 3.9(a), CSNs appear to have a circular cross-section and a narrow size distribution with an average diameter of 49.1±12 nm. CSNs appear to have a uniform and homogeneous dispersion without any sign of agglomeration. To estimate the thickness and overall shape of the nanoparticles, the height profile was studied. The height profile (Z-axis) of AFM micrograph is shown in Figure 3.9(b), which indicates that the thickness of the fabricated nanoparticles is <2 nm, much less than the diameter of CSNs. This proves that the CSNs have a discotic morphology. The 3-D elevated AFM image of the selected area is shown in Figure 3.9(c). It shows that the thickness varies from 0–4.4 nm. Using this information, the thickness distribution of CSNs is determined as shown in Figure 3.9(d) and the average thickness was calculated to be approximately 3.1±0.9 nm.

3.2.4.3 Field emission scanning electron microscopy (FE-SEM)

The morphology and average size distribution of CSNs was confirmed using FESEM. The silk nano-discs shown in Figure 3.9(e) appear to be spherical nanoparticles with narrow

particle size distribution, having an average particle size of 48.15±12.7 nm. It is noteworthy to mention that the CSNs have a dimension of ~50 nm diameter and ~3.1 nm thickness. At low magnifications of ~75000x the CSNs cannot be resolved properly and appear to be more like spherical nanoparticles rather than disc. For better understanding of the shape of CSNs, higher magnifications should be used such as ~200,000x as shown in Figure 3.9(f) where CSNs can be seen embedded at different angles.

भारतीय प्रौद्योगिकी संस्थान गुवाहाटी • Indian Institute of Technology Guwahati •

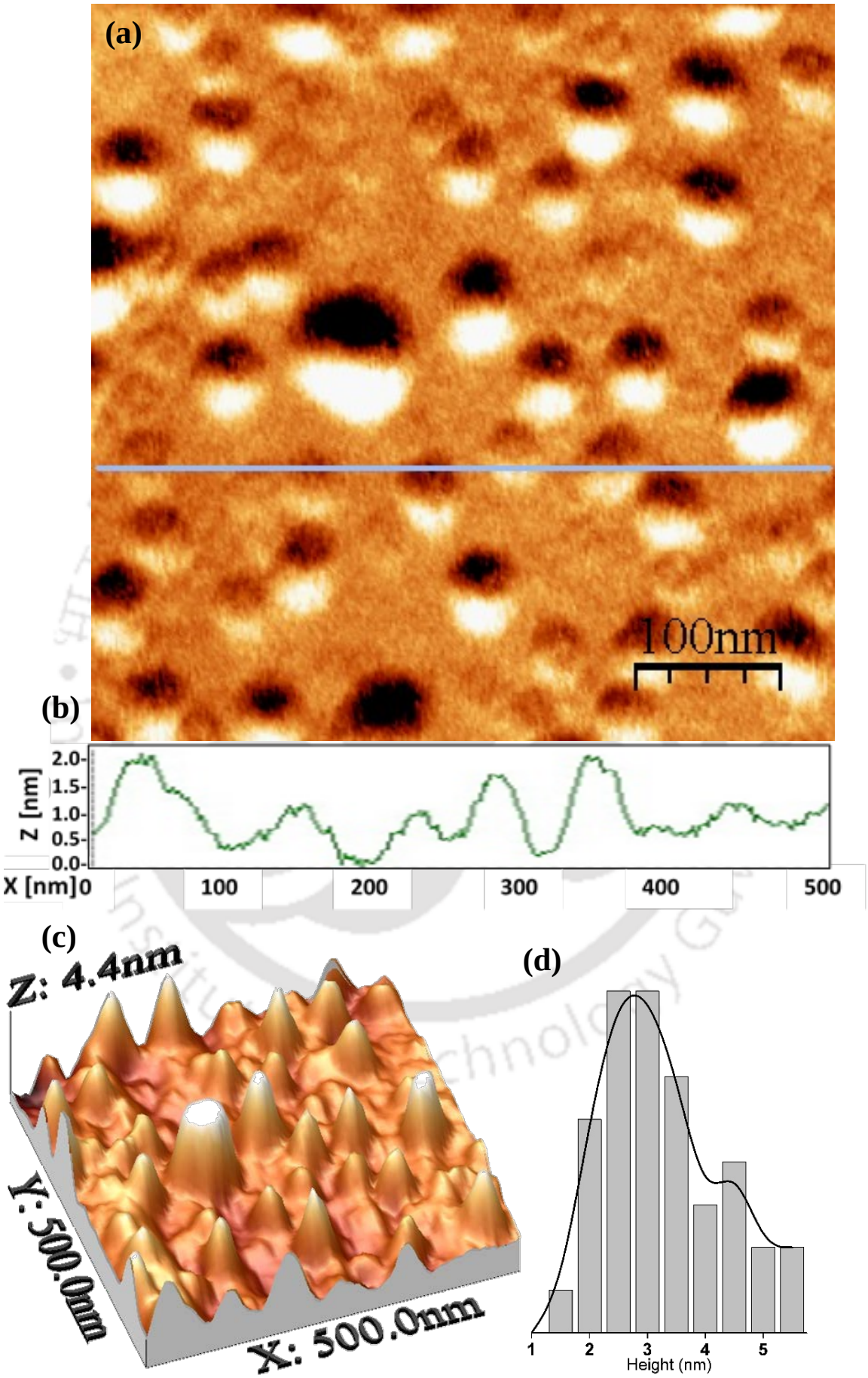
(a)
100nm
(b)
Z [nm]
2.0
1.5
1.0
0.5
0.0
X [nm]0
100
200
300
400
500
(c)
Z: 4.4nm
Y: 500.0nm
X: 500.0nm
(d)
1
2
3
4
5
Height (nm)

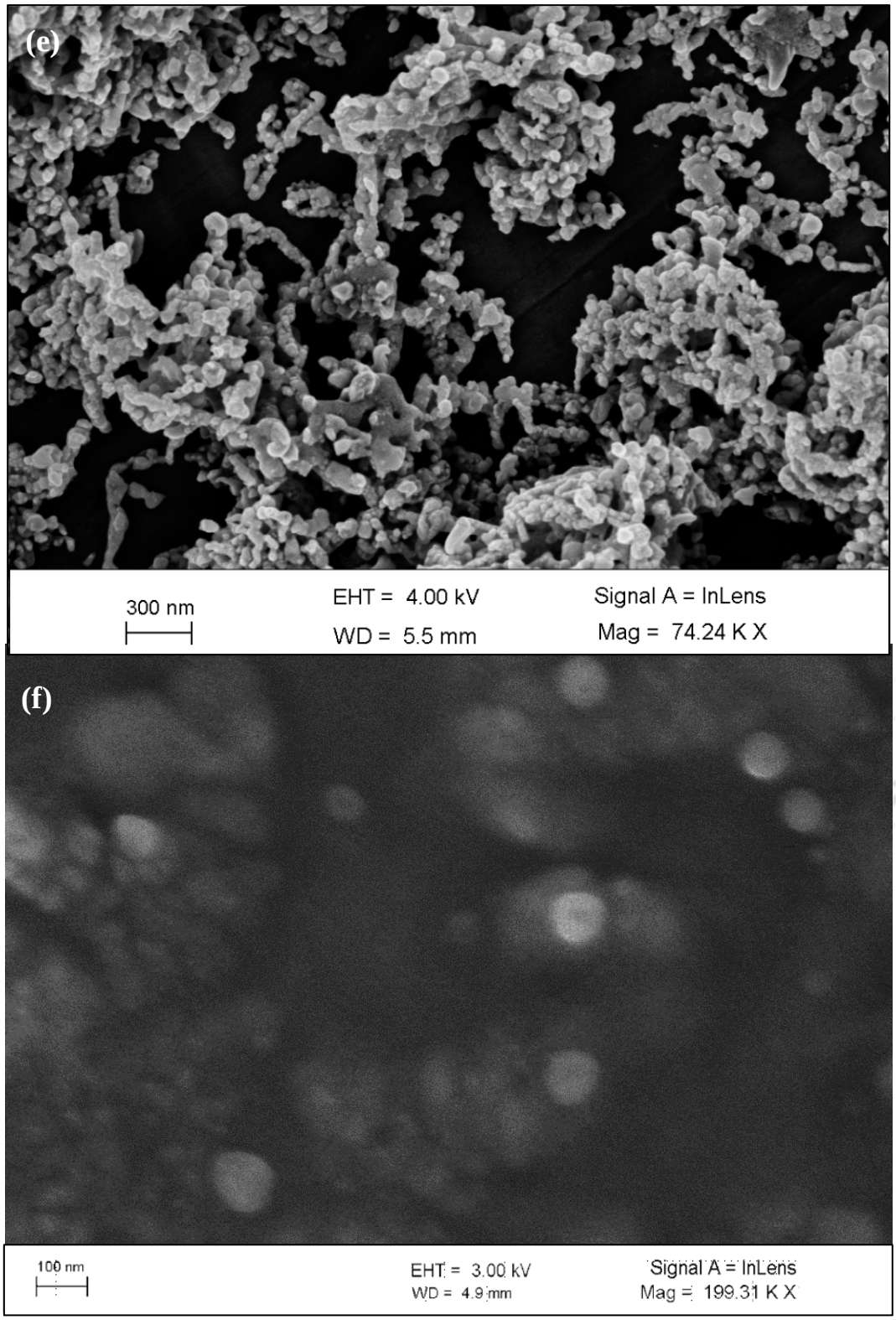

Figure 3.9: Morphological studies on laboratory fabricated CSNs, (a-d) AFM analysis (a) AFM micrograph (500 × 500 nm^2) showing diameter of fabricated CSNs, (b) height profile (along green line) to assess the thickness of fabricated CSNs, (c) 3D-elevated height profile and (d) particle thickness distribution and (e-f) FESEM micrographs at magnification, (e) ~75,000 x (scale: 300 nm) and (f) ~200,000x (scale: 100nm).

3.2.4.3.1 Elemental composition by energy dispersive X-ray (EDX) spectroscopy and ultimate (CHN) analysis

To investigate the elemental composition, energy dispersive x-ray spectroscopy (EDX) was performed. The energy spectra of CSN shown in Figure 3.10 shows the presence of carbon (49.9 wt%), oxygen (21wt%) and nitrogen (19.6 wt%). Remaining amount is expected to be hydrogen that cannot be detected by EDX. It was interesting to find that elemental percentages matched closely with the assumption that major component of the crystalline part of Muga silk is alanine (see Table 3.3). To estimate the amount of hydrogen, ultimate analysis was carried out which showed the presence of hydrogen along with carbon and nitrogen. Elemental analysis was used to measure the elemental composition (C, H and N wt%) of untreated Muga, degummed silk and fabricated CSNs. The average weight percentages (wt%) of N, H and C for untreated Muga silk were found to be 13.3, 5.07 and 38.4 wt%, respectively and for degummed silk to be 16.3, 5.7 and 42.6 wt%, respectively. The average weight percentage of N, H and C for CSNs was 14.3, 5.4 and 38.2 wt%, respectively. Thus, the elemental composition of the three materials did not show much difference. A comparison of the elemental compositions obtained from CSN analysis, EDX analysis and theoretical considerations (assuming CSNs to be composed of alanine only) is shown in Table 3.3. The nitrogen and carbon percentage values of silk cocoon membrane of *Antheraea mylitta* reported by **Tulachan et al. (2014)** were 13.4 and 42.6 wt%, respectively, which matched closely with our obtained values.

Table 3.3: Elemental composition (wt%) of silk-nanodiscs, calculated by CHN analysis, EDX analysis and from theoretical considerations.

Elements	**Ultimate (CHN)**	**EDX**	**Theoretical[a]**
Carbon (C)	38.2	49.9	49.7
Nitrogen (N)	14.3	19.6	19.3
Oxygen (O)	-	21	23.9
Hydrogen (H)	5.4	-	7.1

[a]polyalanine repeats (ala=12) for non-mulberry silks.

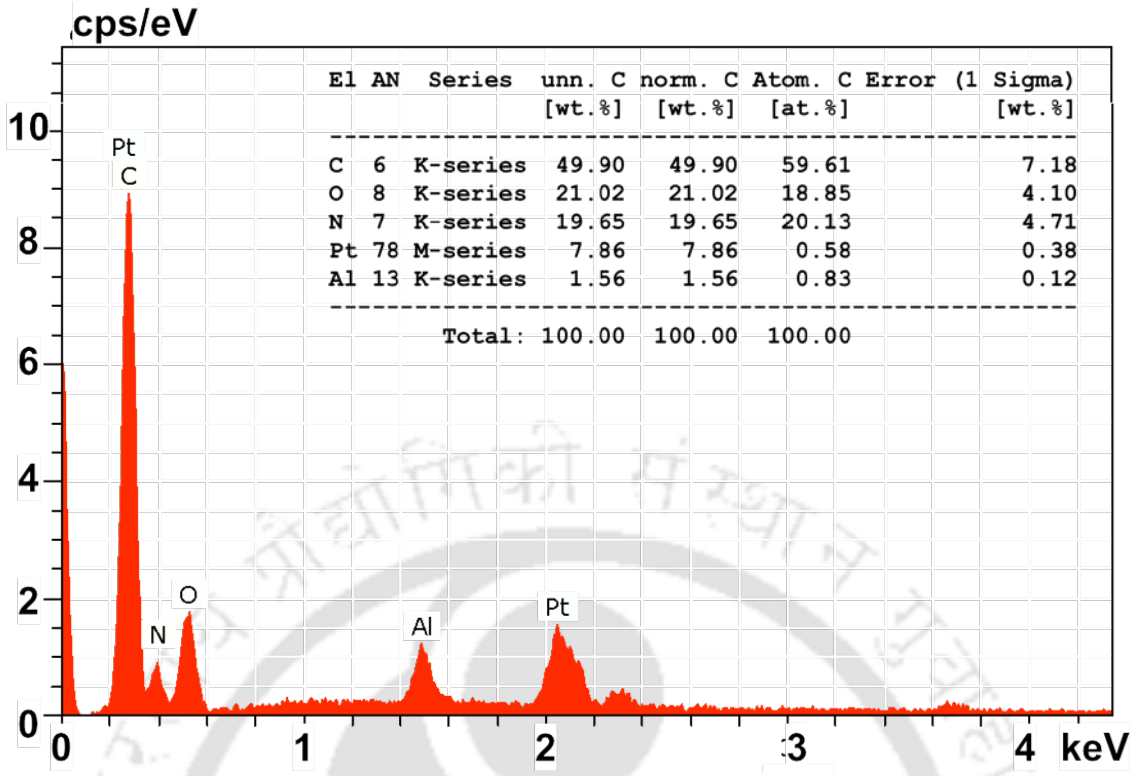

Figure 3.10: Elemental composition analysis of CSN by EDX spectroscopy.

3.2.4.4 Transmission electron microscopy (TEM)

TEM micrographs provided clear insight into the CSN morphology, as can be seen in Figure 3.11. The images reveal that silk nano-discs have a discotic morphology (Figure 3.11(a)) with average diameter of 49.4 ± 17.6 nm, as obtained by analysis using ImageJ® image processing tool, and a narrow size distribution (Figure 3.11(a) inset). The average size obtained was consistent with the observations made by AFM (49.1±12 nm) and FESEM (48.15±12.7 nm). Upon closer examination, it was observed that the underlying nanocrystals could be seen through nanocrystal situated over them (see Figure 3.11(b)), which is a clear indication that the thickness of these particles is much less compared to their diameter, thus suggesting a disc-like shape of fabricated CSN . In another view (Figure 3.11(c)), transverse view of CSNs could be seen in which CSNs are dispersed uniformly in various orientations. The average disc thickness (inset of Figure 3.11(c)) was calculated to be around 3.38 ± 0.5 nm, which was very similar to the thickness estimated using AFM.

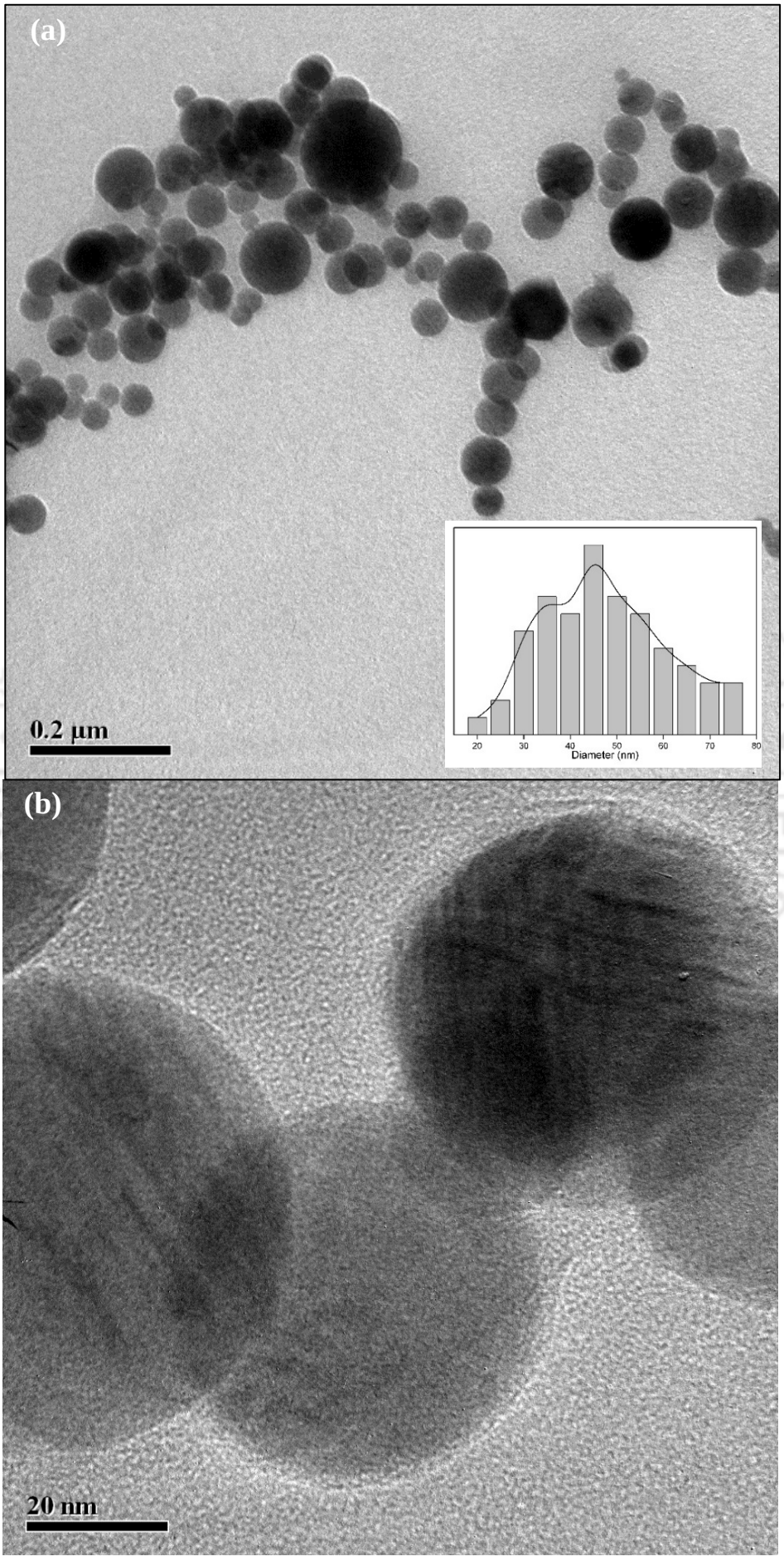
(a)
0.2 µm
20
30
40
50
60
70
80
Diameter (nm)
(b)
20 nm

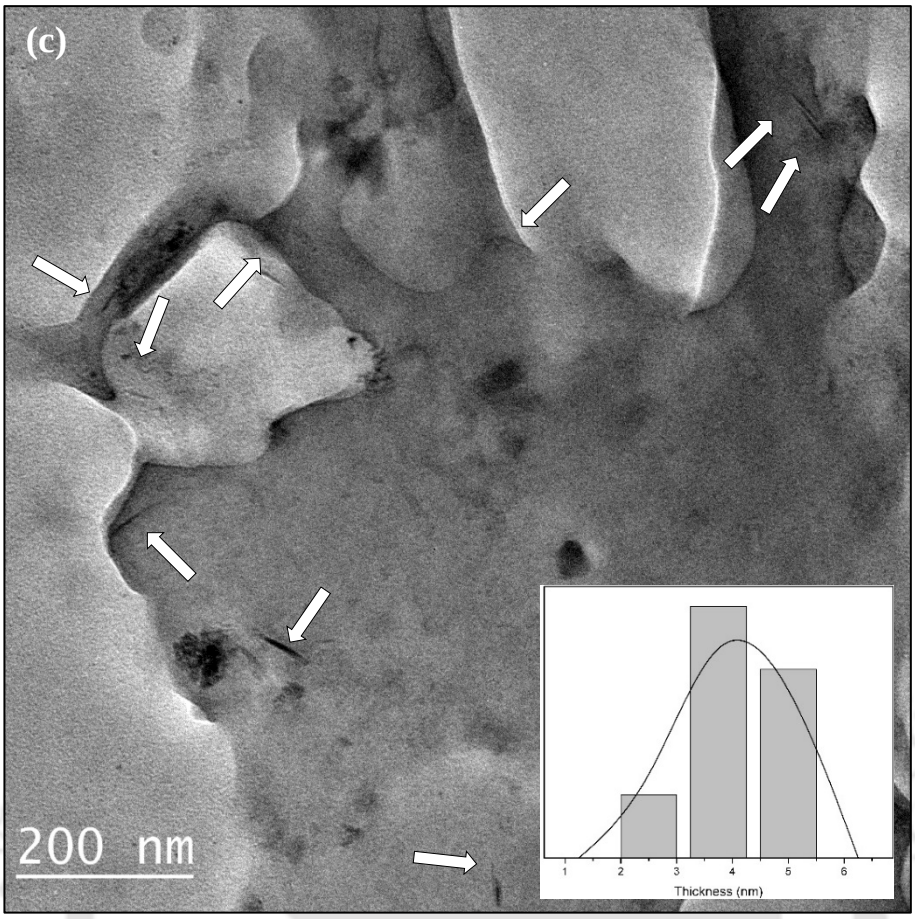

Figure 3.11: TEM micrograph of fabricated CSNs (a) low magnification, scale: 200nm, (inset: particle size distribution), (b) higher magnification, scale: 20 nm and (c) evidence of disc-like morphology of CSNs (inset: particle thickness distribution).

3.2.4.4.1 Selected area electron diffraction (SAED) pattern

To determine the ordering within the fabricated CSNs, diffraction patterns were obtained. The crystalline components of CSNs produce diffraction spots of high intensity and brightness which are well-spaced and well-oriented, whereas the amorphous regions produce halos **(Li et al., 2013)**. As shown in Figure 3.12(a), the CSNs dispersed in water (TEM image shown in Figure 3.12(b)) exhibit diffraction pattern in the form of sharp discontinuous spots, which indicates strong alignment of β-sheet crystallites. The better the alignment among β-sheets, higher will be the crystallinity and hence, the number of rings with the shape of the rings being sharper and well defined. The reason for such rigid β-sheet assembly could be almost complete degradation of amorphous regions in the wild silk fibroin which allowed more mobility to the polypeptide chain.

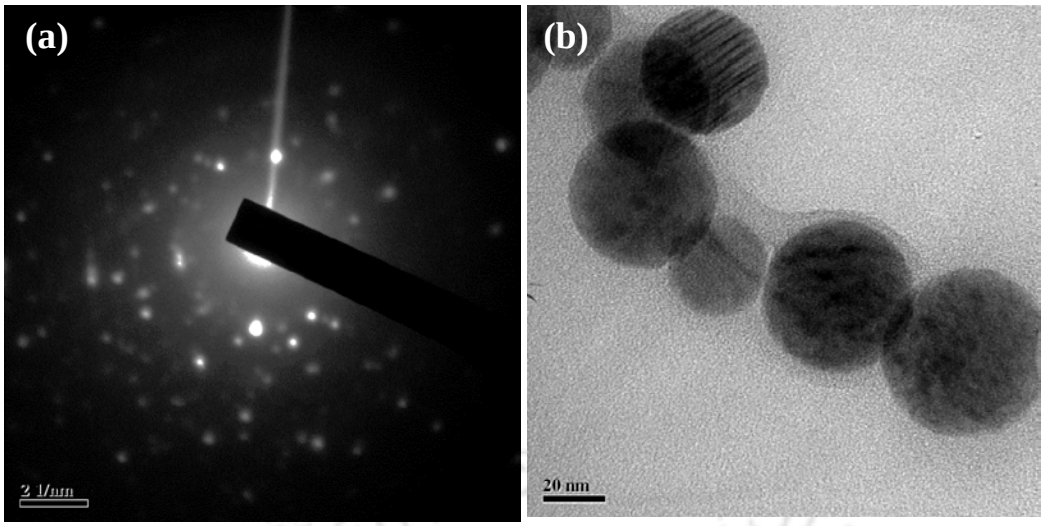

Figure 3.12: (a) SAED pattern of fabricated CSNs and (b) corresponding TEM micrograph for which SAED pattern has been recorded.

3.2.4.4.2 Corroboration of electronic and X-ray diffraction pattern of isolated CSNs

This corroboration was done to confirm that peaks from XRD and bright spots from SAED are of the same material, i.e. CSNs. Initially, d-spacings of XRD peaks (Figure 3.13(a)) are calculated. Subsequently, the scale bar of the SAED pattern (Figure 3.13(b)) was measured using ImageJ® and multiplication factor was obtained which was then multiplied with reciprocal of d-spacings. Finally, the product of the two gives the distance from the center on electronic diffractogram where the bright spots should be located. We observed that all the XRD peaks have their imprint on the SAED pattern, the calculations for which are shown in Table 3.4.

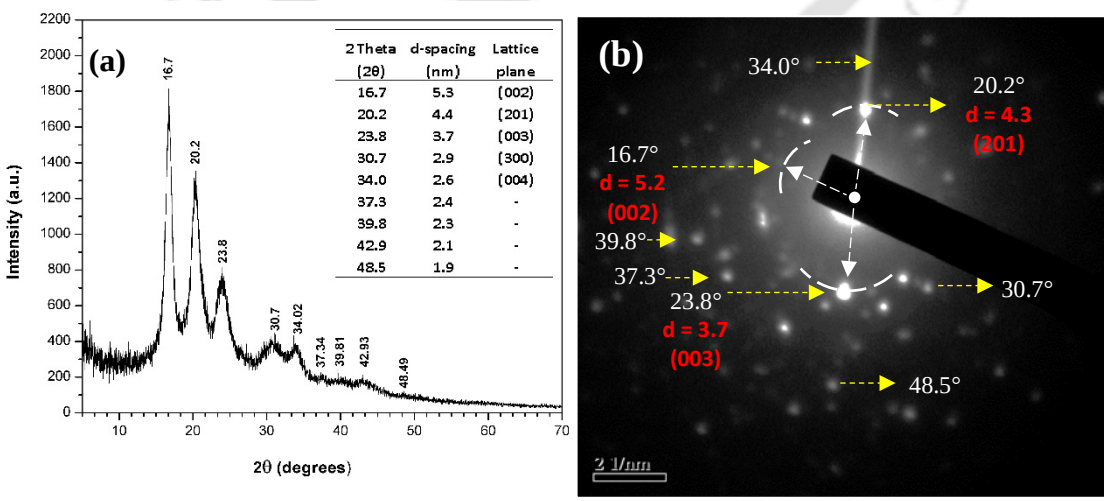

Figure 3.13: (a) Calculations for XRD diffraction peaks and (b) Calculations for SAED bright spots.

Table 3.4: Calculations for corroboration of XRD peak positions and SAED bright spots for fabricated CSNs.

X-ray diffraction(XRD)			Selected area electronic diffraction (SAED)	
Peak position (2θ°)	**Peak d-spacing (nm)**	**Peak [1/(d-spacing)] (nm^{-1})**	**Multiplication factor* [Scale= 1.3cm/2 nm^{-1}] (cm.nm)**	**Spot distance from centre* (cm)**
16.79	0.53	1.89		1.23
20.22	0.44	2.28		1.48
23.88	0.37	2.68		1.74
30.70	0.29	3.44		2.23
34.02	0.26	3.80	0.65	2.47
37.34	0.24	4.16		2.70
39.81	0.23	4.40		2.86
42.93	0.21	4.75		3.09
48.49	0.19	5.33		3.47

Image dimensions on print: 263 × 241 pixels

3.2.4.5 Dynamic light scattering (DLS)

The average particle size was also calculated by dynamic light scattering with real time nanoparticle tracking (Figure 3.14(a)). The average particle size of 89±37 nm was significantly higher than those obtained from previous analyses. The probable reason for increased average size could be agglomeration of the particles. Real time nanoparticle tracking was done and particle size distribution for a frame taken at a random time is shown in Figure 3.14(b).

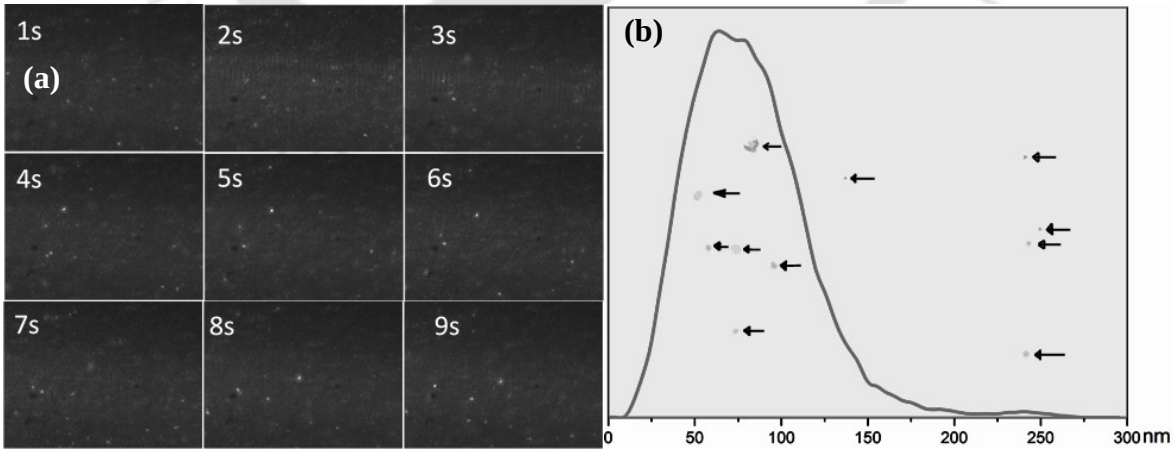

Figure 3.14: (a) Real time nanoparticle tracking 0–9 s, and (b) particle size distribution for a frame taken at a random time

.

3.2.4.6 Thermogravimetric analysis (TGA)

Thermal stability of CSNs is important for their application in different fields such as melt-processing of polymer nanocomposites. As shown in Figure 3.15(a) the CSNs have a higher thermal stability than Muga silk upto 333 °C and lose only 19% of the mass till this temperature. Beyond this temperature it is observed that the CSNs have a lower thermal stability compared to Muga silk. The loss of 50% mass is seen in the first degradation stage from 260–406 °C with the remaining mass loss occurring in the second degradation stage from 406–605 °C, as shown in Figure 3.15(b). It was observed that CSNs were more thermally stable than Muga silk upto 333 °C due to increased crystallinity and removal of amorphous portion. It should be noted that it is imperative for a filler to have a comparable thermal stability to PLA. CSNs can be easily used as a biofiller along with PLA for various PLA-based applications as PLA can be processed at ~200 °C and the serviceable temperature of PLA-based applications lies below 100 °C. Therefore, lower thermal stability of CSN as compared to Muga silk above 330 °C is not much of a concern as processing and targeted applications are at temperatures below 330 °C.

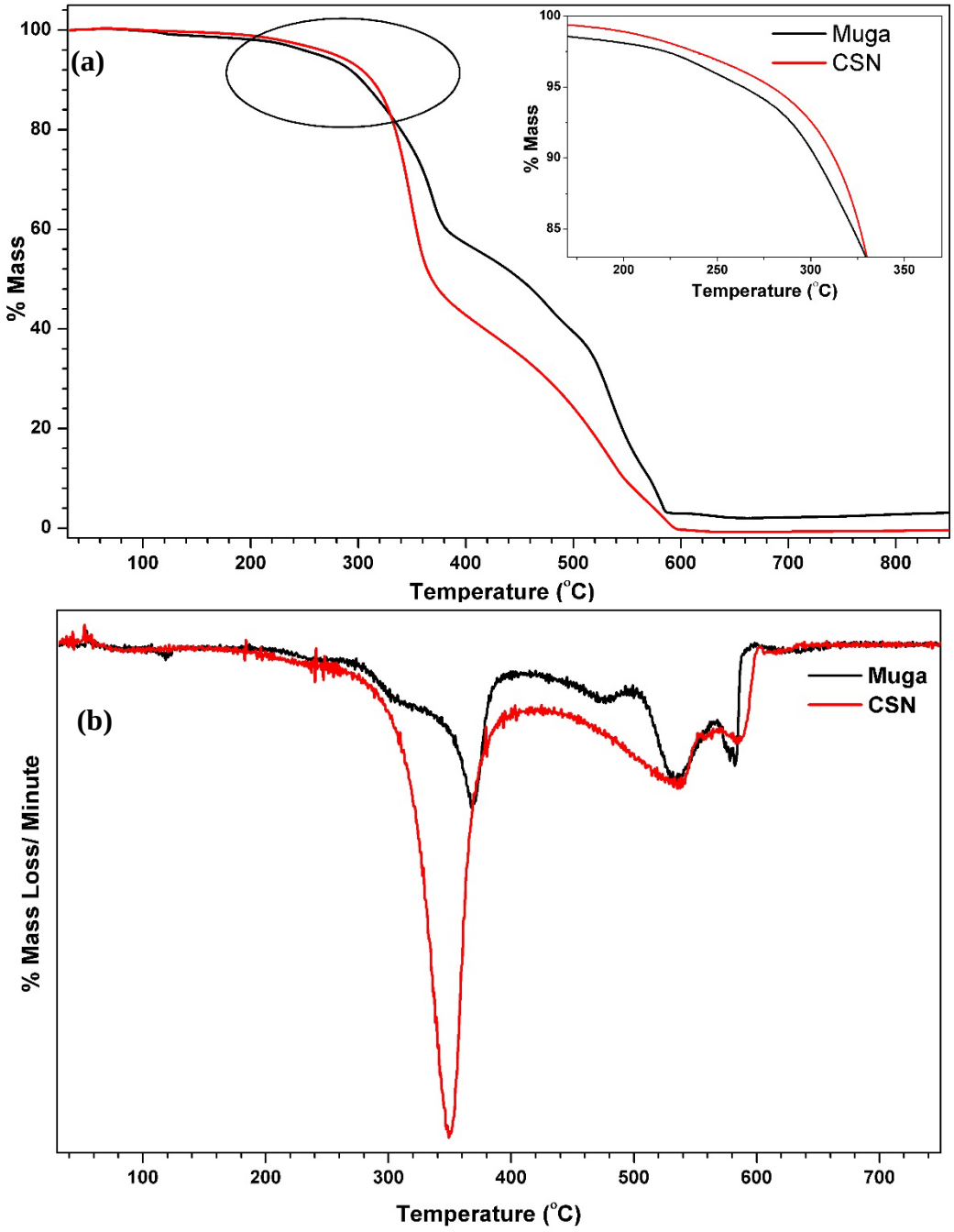

Figure 3.15: (a) TGA thermograph of fabricated CSNs and (b) DTG profile of CSNs.

3.2.4.7 Amino acid analysis (AAA)

Amino acid analysis of CSN and Muga (see Table 3.5) was carried out to know the effect of acid hydrolysis. Alanine, glycine and serine content in Muga silk was found to be 33.3, 30.4 and 13.2%, respectively which matched closely with previously reported values of 28.4, 34.7 and 9.11%, respectively **(Sen and Babu, 2004)**. Upon acid hydrolysis, hydrophobic amino acids which are not labile to dissolution by acids form the crystalline domains while the amount of other amino acids is significantly reduced **(Keten et al.,**

2010). CSNs were found to consist of alanine, glycine and serine as major constituents with 83.8% alanine, 6.1% glycine and 6.8% serine, respectively, which make up the β-sheet crystallites. This data closely matches with the crystalline repeat sequence of another wild silk, *Antheraea pernyi* which shows alanine content as high as ~84% **(Sezutsu and Yukuhiro, 2000)**. This data is also corroborated by the FTIR data which shows sharp alanine peak at 965 cm^{-1}.

Table 3.5: Comparison of amino acid composition of Muga silk and CSN.

Amino Acids	Muga silk	CSN
Aspartic acid	6.1%	1.2%
Glutamic acid	2.1%	0.1%
Serine	13.2%	6.8%
Glycine	30.4%	6.1%
Alanine	33.3%	83.8%
Histamine	1.4%	0.2%
Threonine	1.6%	0.0%
Arginine	3.1%	1.5%
Tyrosine	5.7%	0.1%
Valine	0.7%	0.0%
Methionine	0.0%	0.0%
Phenylalanine	0.4%	0.0%
Isoleucine	0.3%	0.0%
Leucine	0.4%	0.0%
Lysine	0.3%	0.0%
Proline	0.7%	0.1%
Total	100%	100%

3.2.4.8 Zeta potential (ZP)

It is important to mention that it is not just the shape and size of the nanoparticles that influence its resultant properties; the surrounding environment also plays an important role. The average zeta potential (ζ-potential) value of silk nano-discs dispersed in water at 25 °C was found to be ~ -34 mV. Intense charges on the nanoparticle surface leads to repulsive forces among them allowing for stable dispersions. It is known that an absolute value of 30

mV shows solution stability, which suggests that CSNs should have a good dispersion ability **(Lizundia et al., 2017)**.

3.2.5 Fabrication of magnetic crystalline silk nano-discs (MGCSNs)

The iron-oxide (Fe_3O_4) nanoparticles were adsorbed onto the CSN surface by chemical reduction method using sodium borohydride ($NaBH_4$) as the reducing agent (Figure 3.16). CSN (70 mg) was uniformly dispersed in 50 ml deionized water followed by probe ultrasonication for 2 min (amplitude ~30%). Subsequently, $FeCl_3$ (30 mg) was added to the CSN suspension and pH was adjusted to ~5 using 0.1N NaOH under inert atmosphere (by continuously purging with argon gas). The contents were vigorously stirred at ~1000 rpm. For the fabrication of Fe_3O_4 nanoparticle-adsorbed CSNs (MGCSNs), 500 mg $NaBH_4$ in 10 ml solution was added drop-wise into the iron salt-CSN solution at 65 °C and suspension turned black immediately with evolution of hydrogen gas bubbles. After stirring for 2 h, the MGCSNs were separated from the solution using permanent magnets and washed three times with water and ethanol to remove impurities. Finally, the MGCSNs were centrifuged out, dried at 50 °C and crushed into fine powder using mortar.

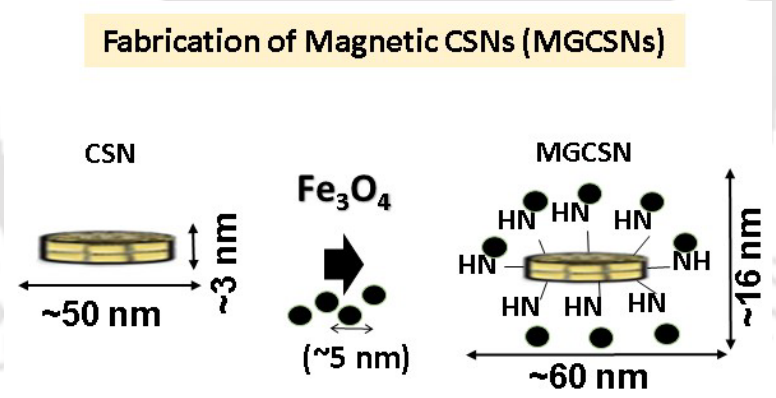

Figure 3.16: Overall scheme of preparation of magnetic crystalline silk nano-discs (MGCSNs) from Muga silk.

3.2.6 Morphological studies on fabricated MGCSNs

3.2.6.1 Field emission scanning electron microscopy (FE-SEM)

Monodisperse Fe_3O_4 nanoparticles were adsorbed onto surface of CSNs through one-step chemical reduction method. After the reduction reaction, spherical iron oxide nanoparticles with average size of ~5 nm were adhered on the CSN surface, covering the whole surface of CSNs, as seen in the high-resolution scanning electron micrographs in Figures 3.17(a)

and (b), forming a densely packed structure with 'nonpareil cookie' like morphology where the white arrows mark the edge of the silk nano-discs. Homogeneous ~5nm particles are formed because rapid stirring results in anomalous diffusion of particles resulting in slow growth kinetics leading to smaller particles.

3.2.6.1.1 Elemental composition of fabricated MGCSNs

Mapping of MGCSNs (Figure 3.17(c), (d)) shows that magnetite nanoparticles are homogeneously dispersed on CSN surface with the presence of iron, carbon, oxygen and chlorine. Traces of chlorine could be due to incomplete removal upon washing of fabricated MGCSNs. Oxygen and iron were mapped, and it was found that iron oxide nanoparticles are homogeneously dispersed on CSN surface as seen in Figure 3.17(e). Elemental composition is shown in Figure 3.17(f), where Fe content of ~38 wt%, corresponds to the Fe_3O_4 nanoparticles adsorbed onto CSNs. Higher loadings (~ 51 wt%) of magnetite onto cellulose nanocrystals have been reported due to –OH clusters by **(Dhar et al., 2016)**.

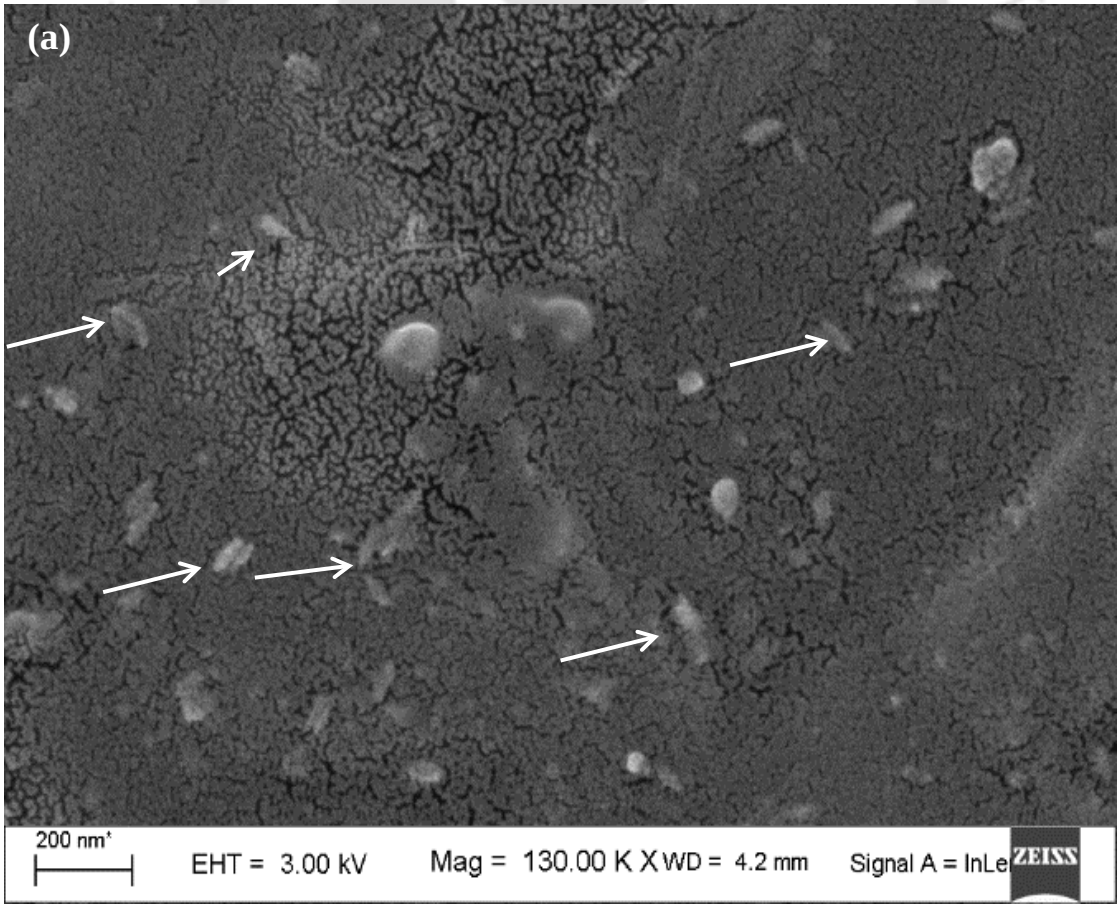

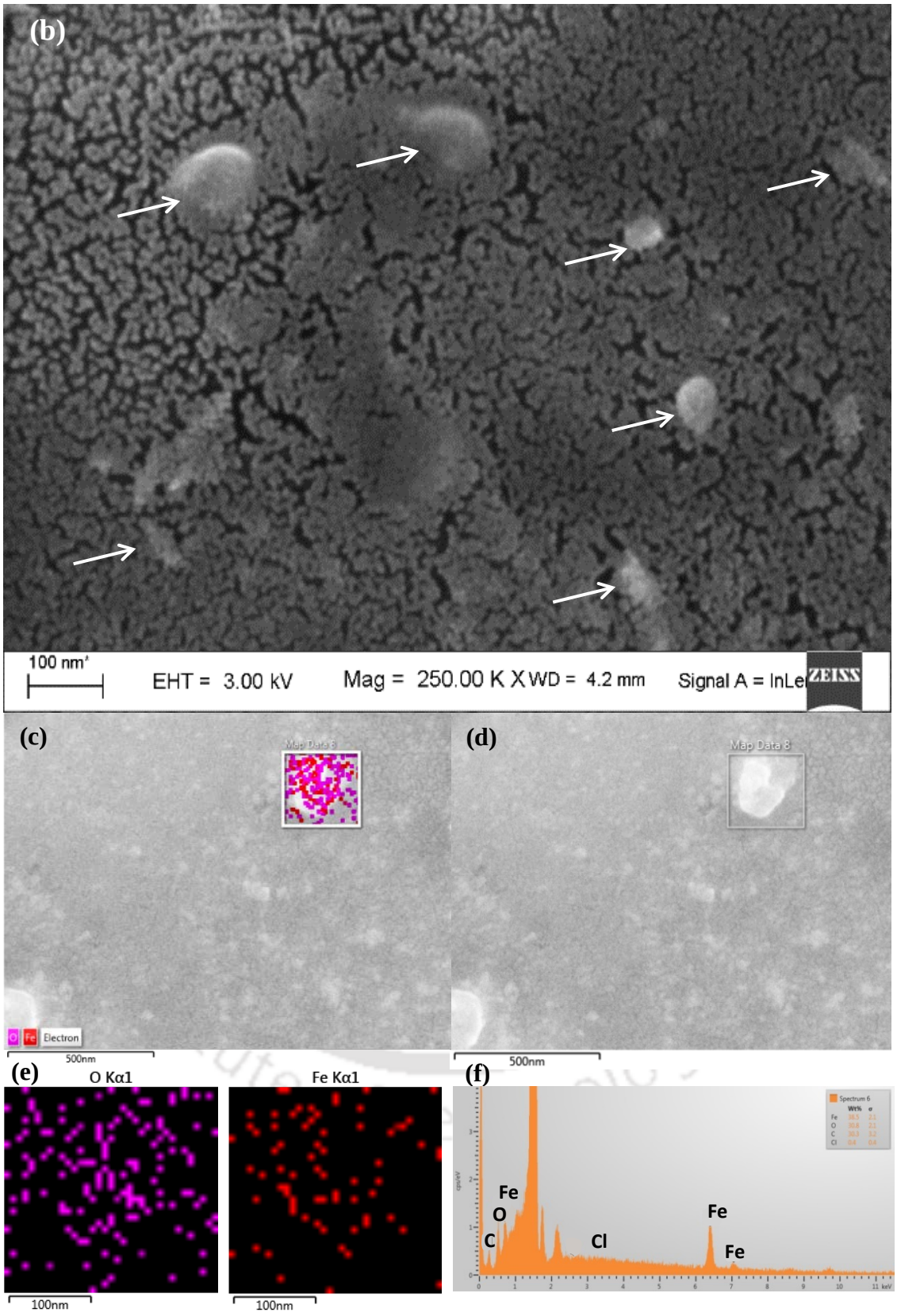

Figure 3.17: FESEM micrographs of fabricated MGCSNs: (a) 130,000x magnification, (b) 250,000x magnification, (a, b) white arrows mark the edge of the silk nano-discs, (c)

micrograph used for elemental analysis, (d) original mapped area, (e) mapped oxygen and iron, and (f) elemental composition.

3.2.6.2 Transmission electron microscopy (TEM)

The TEM images (Figure 3.18(a)) show that MGCSNs have diameter of 58.2 ± 4.6 nm and thickness of 16.0 ± 2.6 nm. The amine groups act as site for precipitation of magnetite nanoparticles during reduction, which possibly increased the dimensions of MGCSNs as compared to CSNs. Absence of nascent Fe_3O_4 nanoparticles indicates that they strongly interact with CSN surface and could not be separated even after sonication process which was done prior to microscopic analysis. SAED pattern (inset of Figure 3.18(a)) displays a second ring indexed to (002) plane of CSN; all other rings matched with cubic Fe_3O_4 while HRTEM lattice spacings of 0.48 nm (Figure 3.18(b)) corresponds to (111) spacing of cubic Fe_3O_4 **(Fu et al., 2015)**.

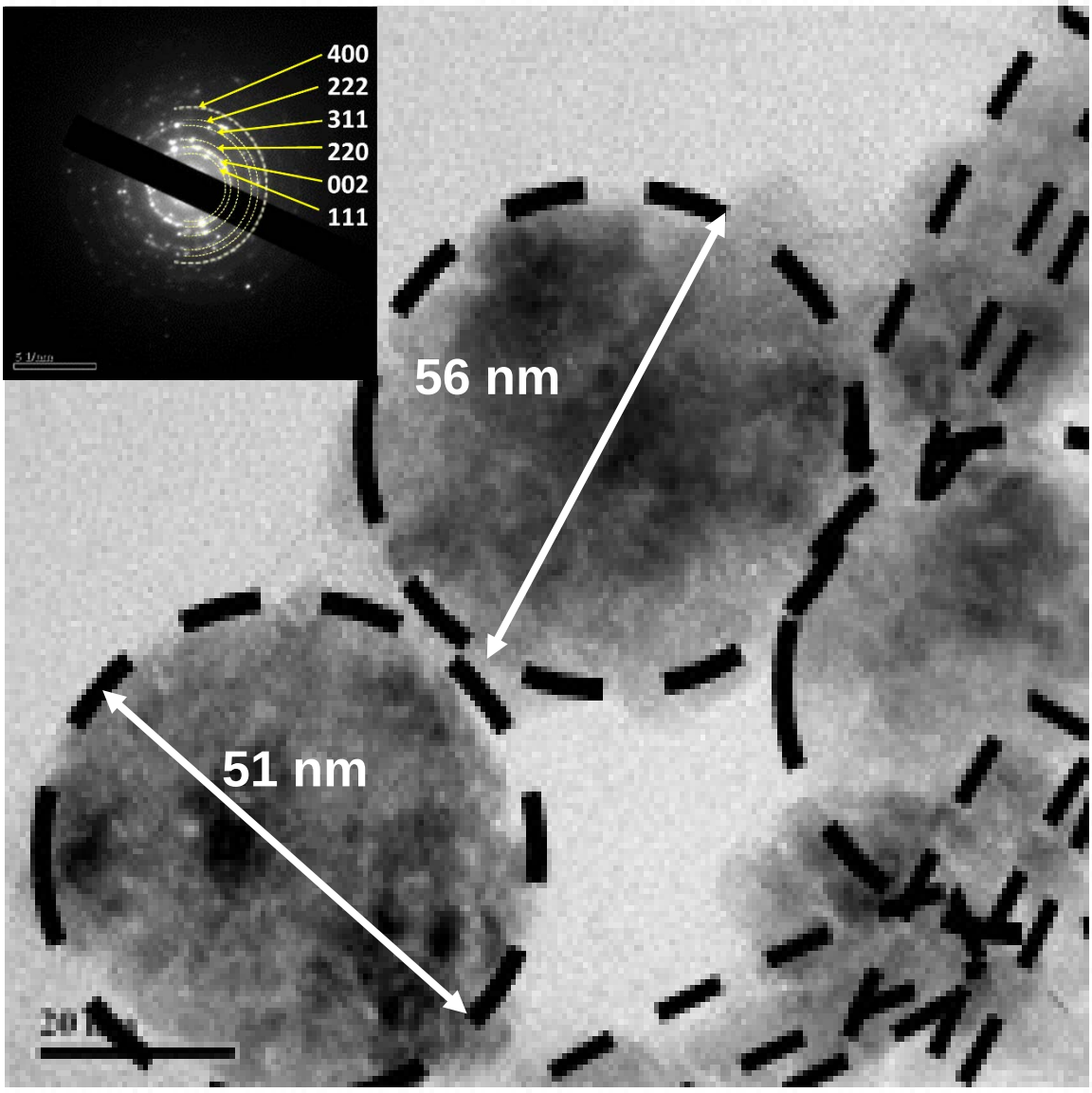

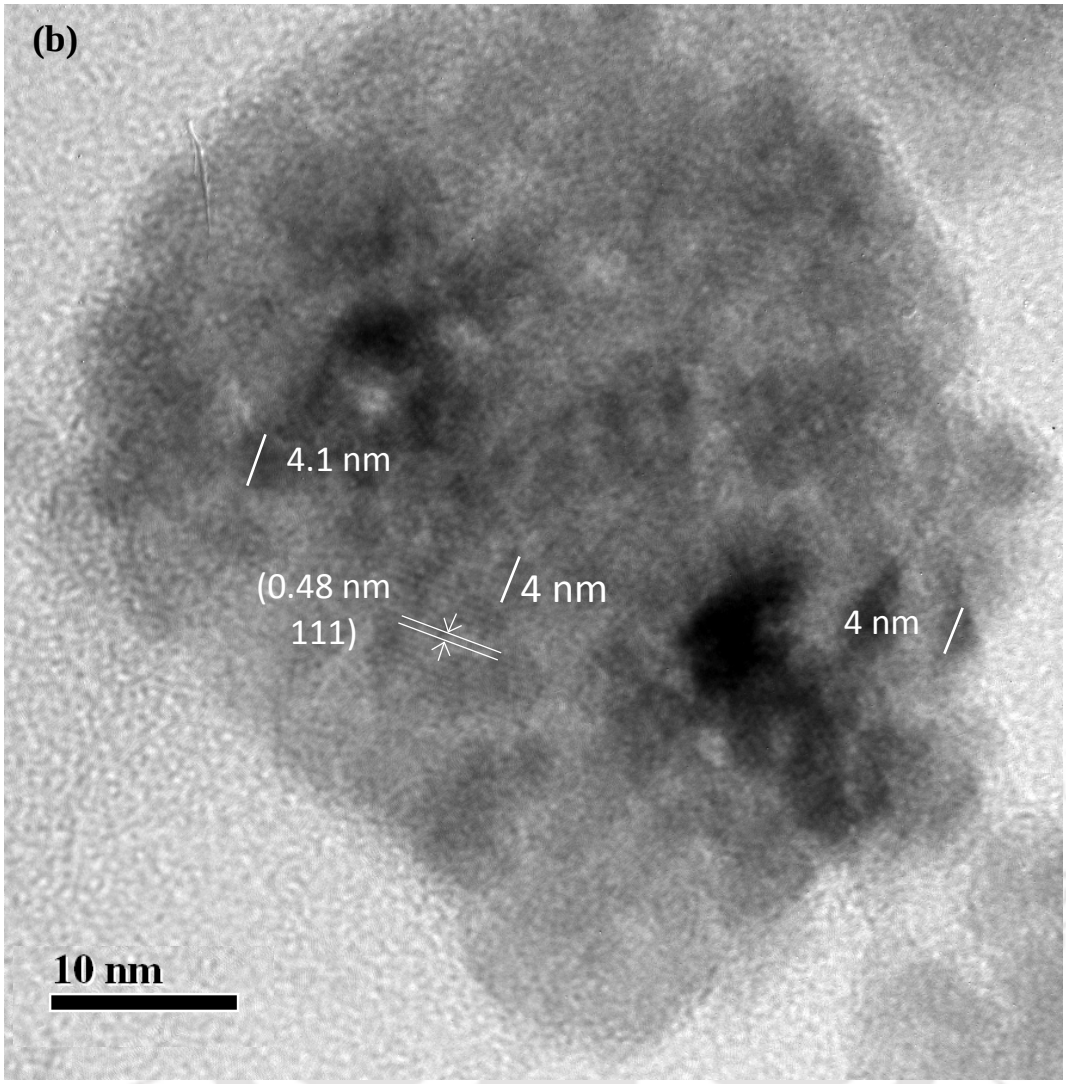

Figure 3.18: (a) TEM micrographs of fabricated MGCSNs, scale bar: 20 nm, (inset: SAED pattern for the MGCSNs) and (b) HRTEM image of the fabricated MGCSNs.

3.2.7 Physico-chemical and structural properties of fabricated CSNs

3.2.7.1 Fourier transform infrared spectroscopy (FTIR)

The FTIR spectrum (Figure 3.19) of CSN showed representative peaks at 3268, 1629, 1535, 1224, 1160, 695 and 701 cm^{-1} corresponding to -NH stretching, -C=O stretching, -NH deformation or -CN stretching, -CH stretching or -NH in-plane bending, -OH bending, -NH rocking, and N-C=O in-plane bending respectively, which are characteristic 2° (secondary) amine signature peaks of silk. MGCSNs showed all these characteristic peaks, albeit with subdued intensities because of the immobilization of Fe_3O_4 nanoparticles onto the CSN surface. Furthermore, MGCSNs show new peak and shoulder at ~685 and 620

cm^{-1} respresenting bending and stretching vibrations of Fe-O, respectively, which can be attributed to the formation of iron oxide nanoparticles **(Dhar et al., 2016)**.

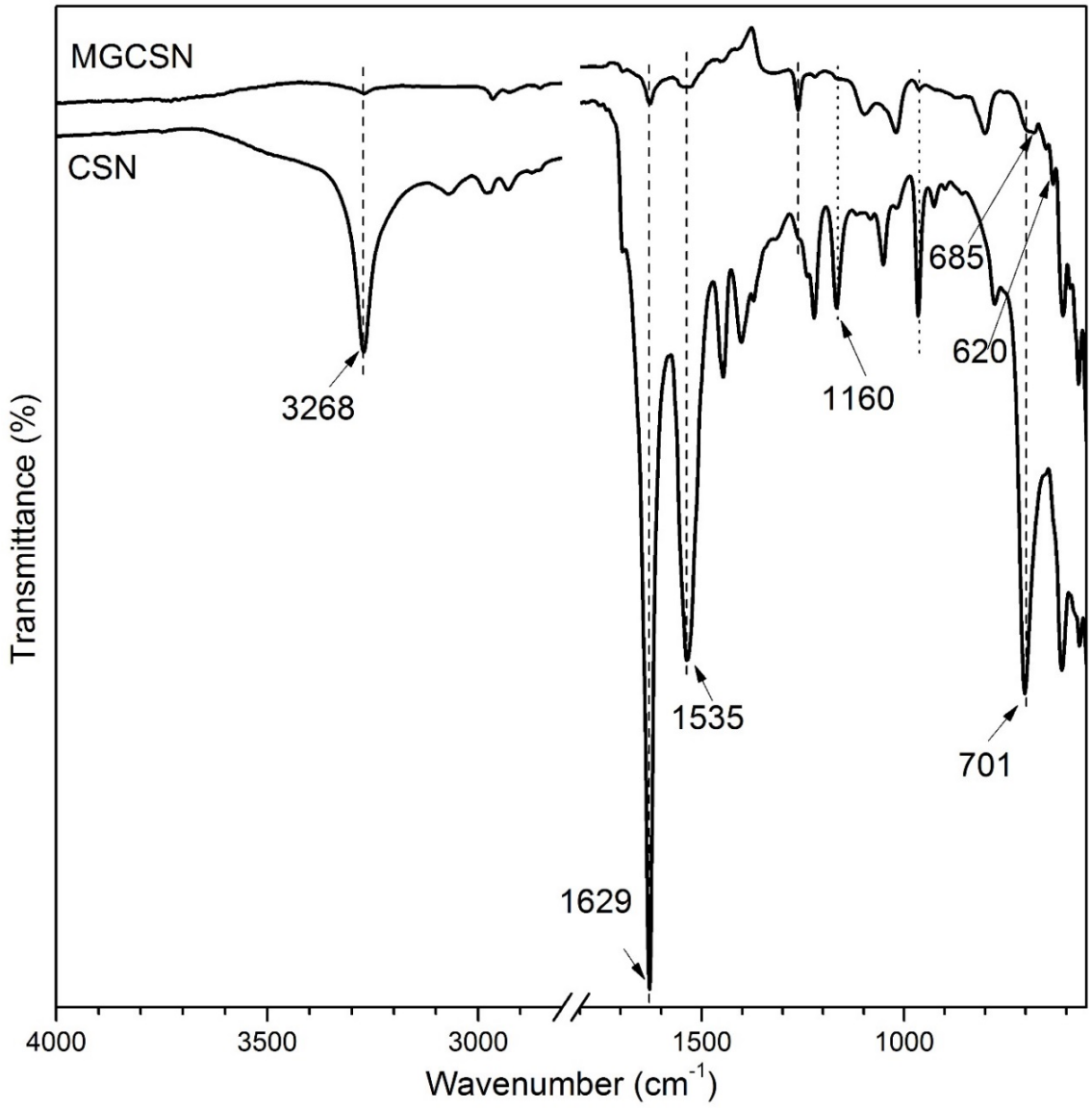

Figure 3.19: FTIR spectra for MGCSNs and CSNs.

3.2.7.2 X-ray diffractometry (XRD)

The XRD pattern for MGCSNs (Figure 3.20) shows new diffraction peaks at 2θ values of 30.4° (220), 35.6° (311), 43.4° (400), 53.6° (422), 57.4° (511) and 63.5° (440) corresponding to reflections of Fe_3O_4 nanoparticles **(Dhar et al., 2016)**. The peaks at 16.7° (002), 20.2° (201) and 23.8° (003) confirmed the presence of CSNs (inset of Figure 3.20). The average crystallite size of Fe_3O_4 nanoparticles adhered onto the CSN surface, calculated by Scherrer's formula, was found to be ~4.14 nm which corresponds to the peak at 2θ = 35.5° (311) and matches with the size range ~4–5 nm measured from

TEM/FESEM. Therefore, crystallographic studies confirmed that MGCSNs retained CSN crystal structure and magnetic nanoparticles anchored onto the CSN surface.

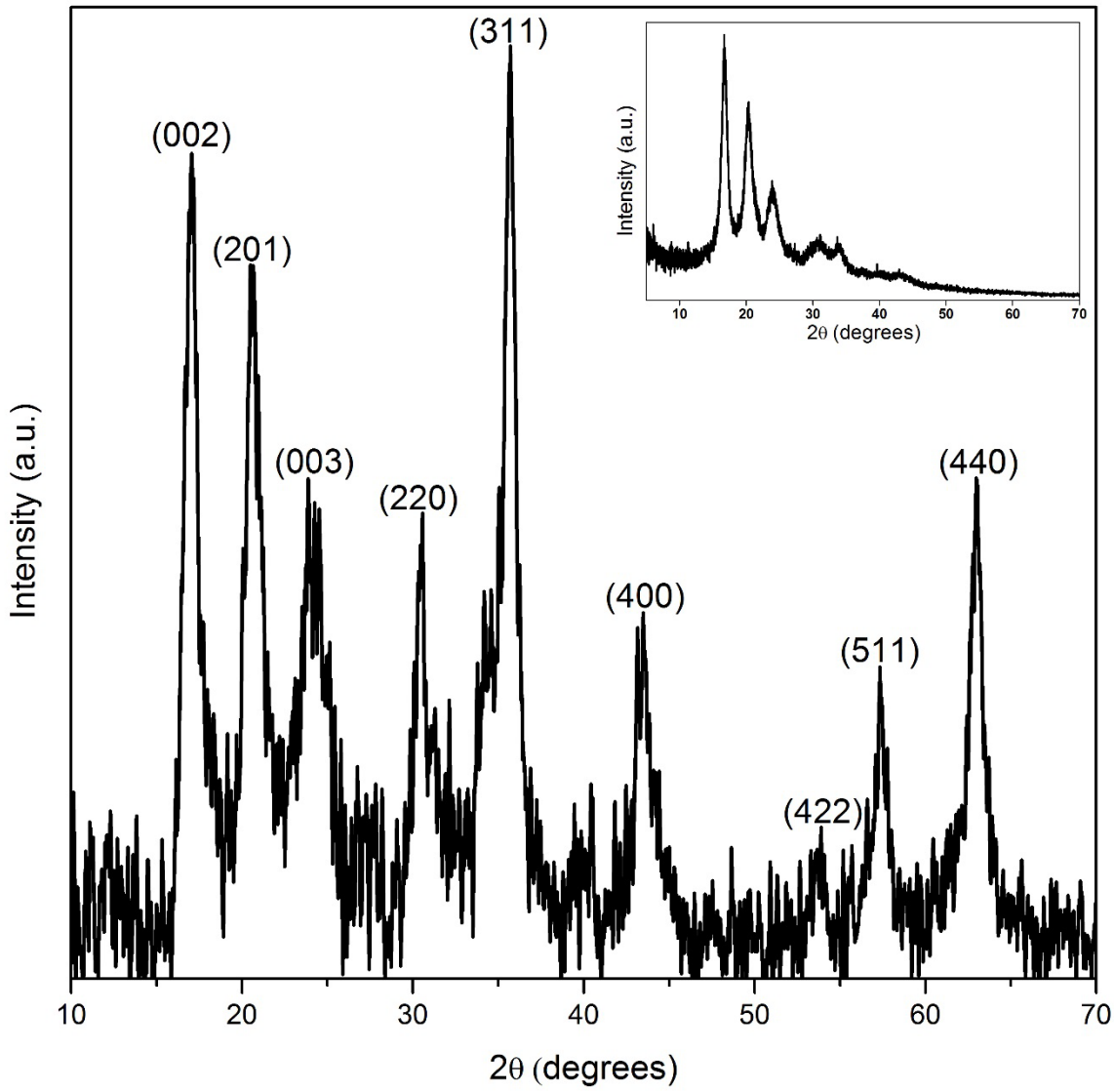

Figure 3.20: XRD diffractogram for MGCSNs, inset: XRD diffractogram of CSNs.

3.2.7.3 Raman spectroscopy

The CSNs show characteristic Raman peaks (see Figure 3.21) at 905, 965, 1093, 1224 and 1669 cm^{-1} corresponding to the –CN stretching, -CH_3 rocking, -C_α-C_β stretching, -NH in-plane bending and C=O stretching, respectively **(Freddi et al., 1997)**. The sharp peaks at 219, 283 and 670 cm^{-1} for MGCSNs confirm the presence of iron oxide nanoparticles **(Dhar et al., 2016)**. The precipitation of Fe_3O_4 nanoparticles onto the CSNs led to the disappeareance of absorption bands at 1242 and 1667 cm^{-1} due to –NH bending and –C=O stretching, respectively. MGCSNs show the presence of few peaks, albeit with reduced intensity, such as 905, 1095 and 1224 cm^{-1} and new peaks at 376, 1106, 1265 and 1545 cm^{-}

[1] corresponding to amine signatures of CSN which act as nucleation sites for iron oxide nanoparticles.

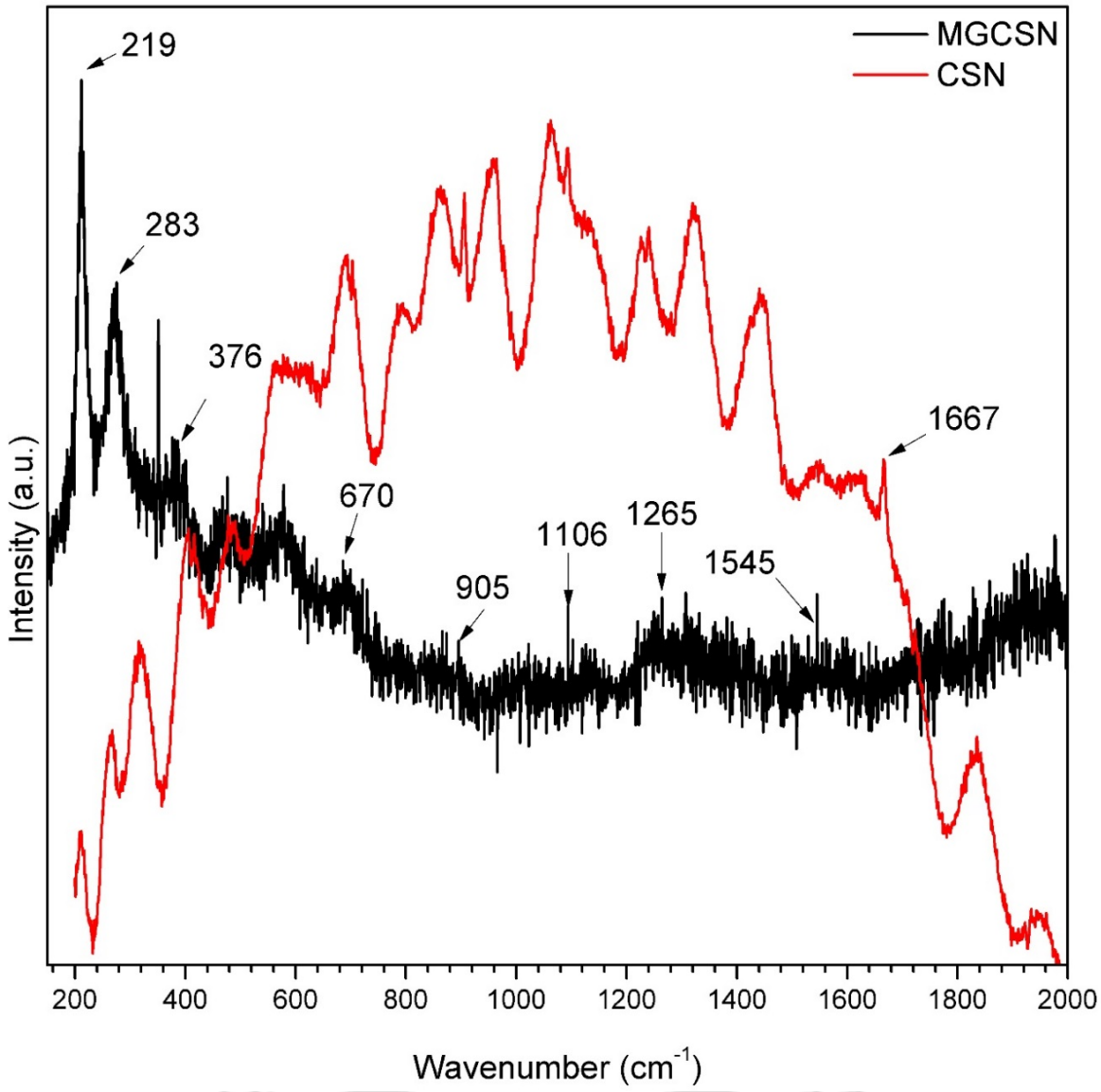

Figure 3.21: Raman spectra for MGCSNs and CSNs.

3.2.7.4 Vibrating sample magnetometer (VSM)

The magneto-responsive behavior of dried CSN and MGCSN powdered samples was evaluated using VSM. Figure 3.22 shows that CSNs display diamagnetic behavior with very low magnetization value whereas MSCSNs exhibit low coercivity without hysteresis and remanence, confirming the presence of superparamagnetic Fe_3O_4 nanoparticles with a magnetization value of ~33 emu/g. The low values of magnetization can be attributed to low iron content in MGCSNs **(Dhar et al., 2016)**.

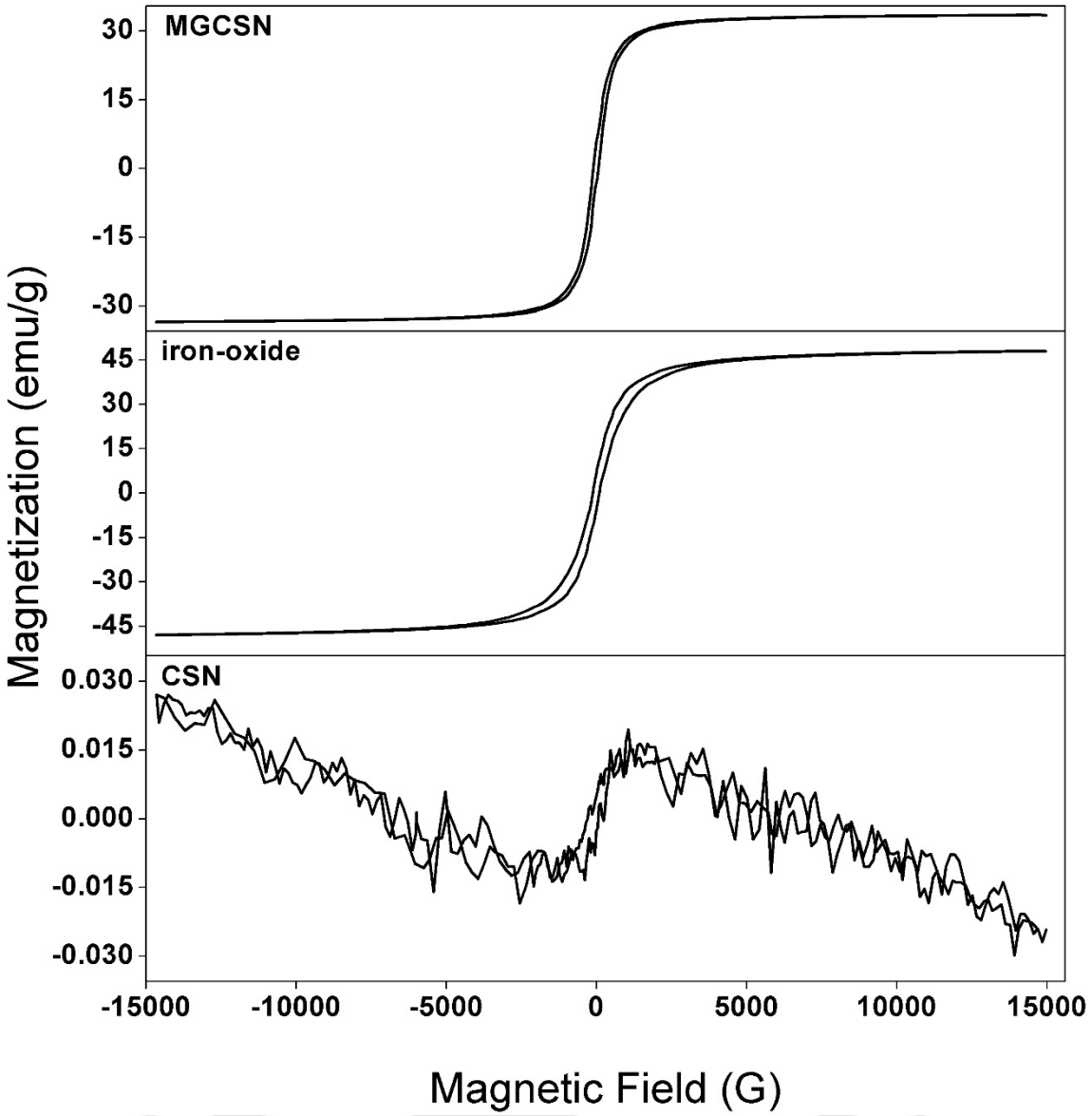

Figure 3.22: Magnetization values for MGCSNs compared with iron-oxide nanoparticles and CSNs.

3.2.7.5 Thermogravimetric analysis (TGA)

As can be seen in Figure 3.23, the thermal stability of magnetic discs is lower than CSNs in the range of 120-330 °C. It should be noted that at PLA processing temperature i.e. 210 °C ca. the magnetic discs show only ~7% weight loss, which is not a major issue. Furthermore, MGCSN are used for biomedical applications which do not require high temperature exposure upon fabrication. At ~600 °C, the percentage weight loss difference for both the materials was estimated to be ~65 wt% due to the amount of Fe_3O_4 on the CSN surface, which was consistent with the EDX results (~35% Fe content in MGCSNs).

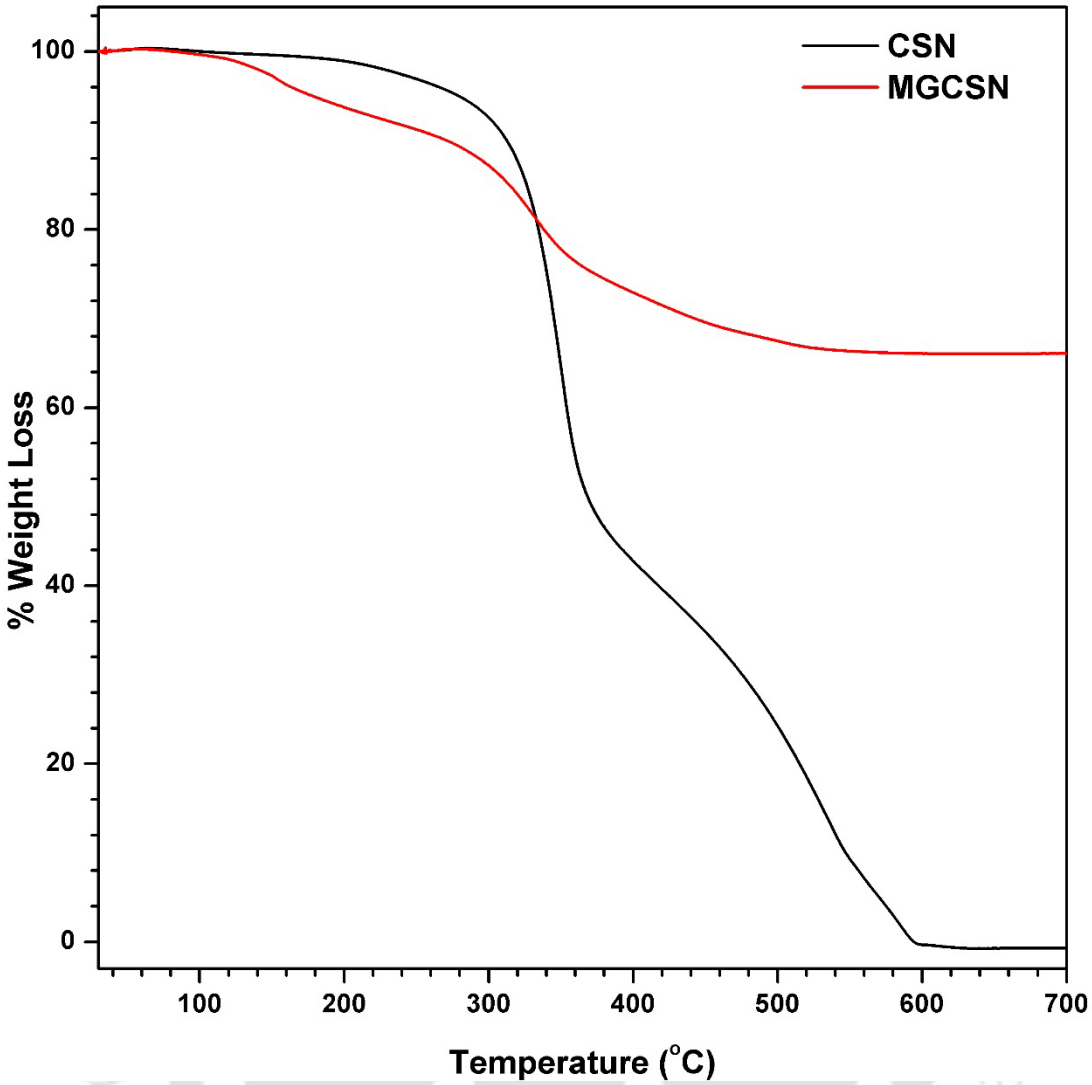

Figure 3.23: Thermal degradation profile for MGCSNs compared with CSNs.

3.2.7.6 Surface area analysis by Brunauer Emmett Teller (BET) analysis

As summarized in Table 3.6, CSNs posses a low BET surface area of ~ 3.9 m^2/g as they are hard, non-porous material, whereas their functionalized form, i.e. MGCSN, exhibits ~20 fold increase to 83.2 m^2/g, suggesting the adsorption of iron nanoparticles onto the surface of CSN.

Table 3.6: Surface area analysis of fabricated nanoparticles.

Material	BET surface Area (m^2/g)	Average pore size (nm)	Pore volume (cc/g)
CSN	3.977	1.872	0.014
Iron-oxide	77.731	3.808	0.420
MGCSNs	83.155	3.773	0.212

3.2.7.7 Dye adsorption properties of MGCSNs: A sustainable adsorbent for waste-water remediation

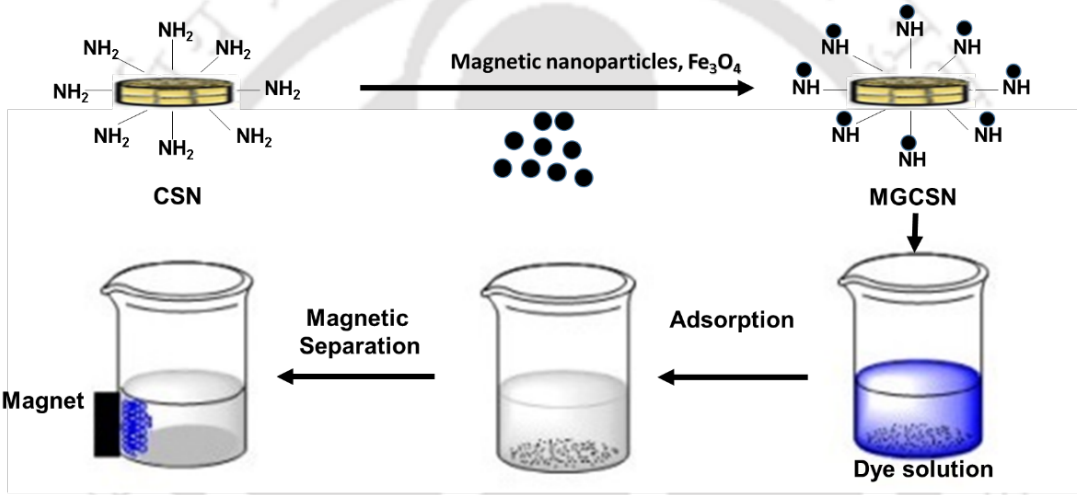

Figure 3.24: Dye adsorption using MGCSNs.

Magnetic nanoparticle-adsorbed CSNs have potential application in the bioremediation of wastewater. Here we report the use of magnetic CSNs as efficient material for dye removal, with the overall process illustrated in Figure 3.24. Aniline blue (AB), $C_{37}H_{27}N_3Na_2O_9S_3$ (Figure 3.25(a) inset) is a high molecular weight (~799.8 g/mol), water soluble dye which belongs to triphenylmethane class of dyes. It is highly soluble in water, which is the reason for its long residence time in water. To measure the effectiveness of these silk-based magnetic nanoparticles in wastewater remediation, adsorption of AB was carried out in the presence of MGCSNs. The adsorption of AB was visually examined as a blue-colored solution turned transparent and spectroscopically monitored through the continuous decline of the peak intensity at 598 nm in the UV-vis spectrum **(Pare et al., 2008)**. With the addition of a small amount (10 mg) of MGCSNs, the dye got adsorbed immediately, indicating that the fabricated MGCSNs were highly effective in AB

adsorption. Figure 3.25(a) shows the degradation profiles of 100 ppm dye with respect to time, where a gradual reduction in the intensity of the 598 nm peak of the UV-visible spectra can be observed. The gradual decolorization of AB solution with time was also observed visually (inset of Figure 3.25(b)). This decolorization was possibly due to the high surface area of iron nanoparticles resulting in effective adsorption of the dye. The AB adsorption is an instantaneous and fast process and a comparative plot of A_t/A_0 against time for MGCSNs and magnetic nanoparticles is shown in Figure 3.25(b), indicating that MGCSNs takes almost similar time to achieve the final adsorption levels as achieved by pure magnetic nanoparticles. A_t and A_0 are the absorbance at time 't' and at initial time t = t_0.

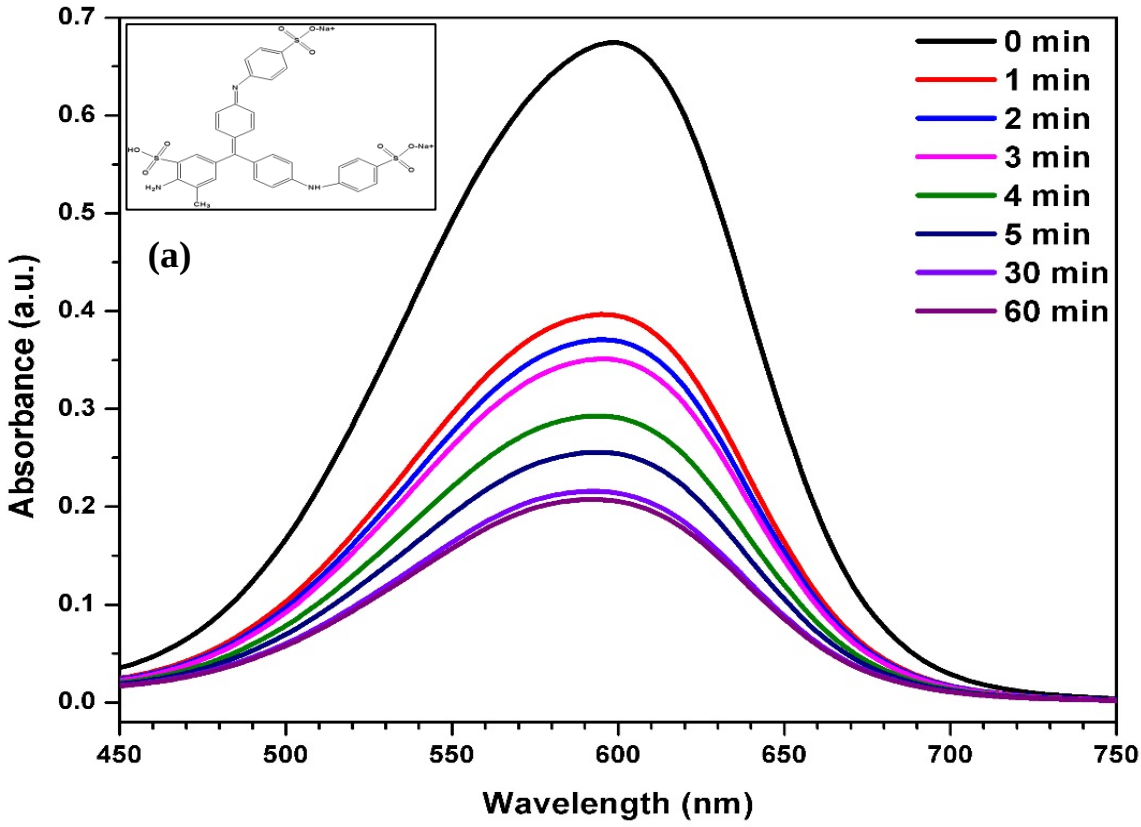

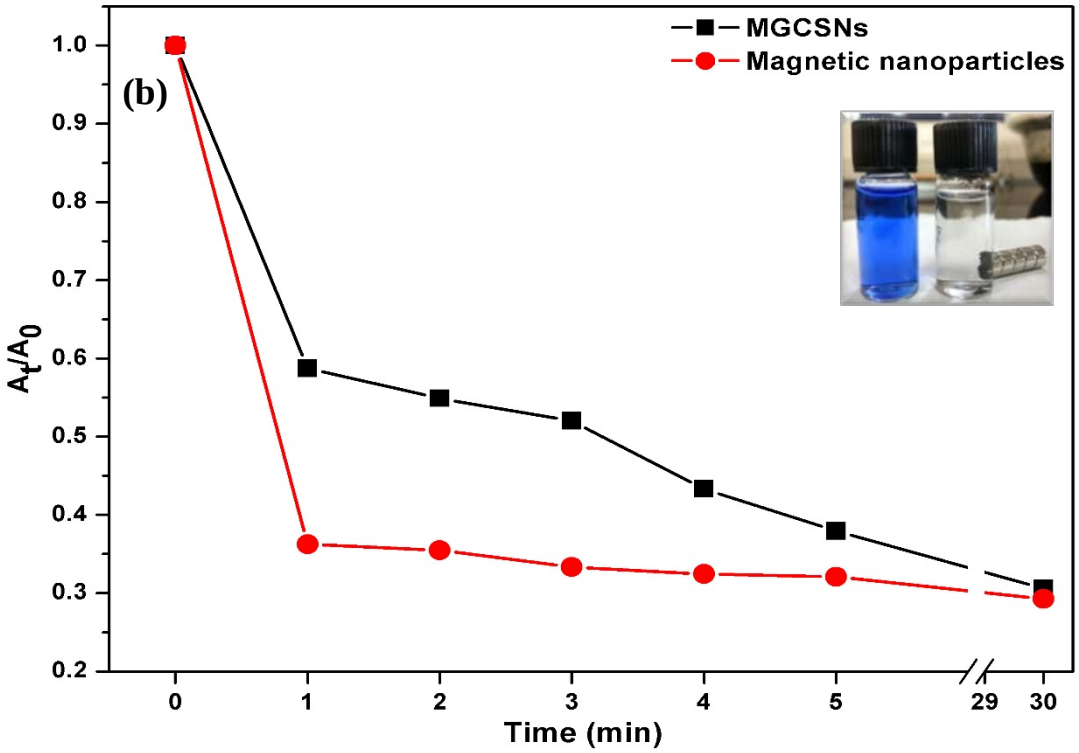

Figure 3.25: (a) UV-visible spectra of AB solution (100 ppm) containing MGCSNs at different times, (inset: chemical structure of aniline blue), and (b) plots of A_t/A_0 against time for MGCSNs and magnetic nanoparticles (inset: visual decolorization of AB with MGCSNs after 5 min).

3.3 Summary

The renewable waste such as Muga silk cocoons can be effectively converted into crystalline silk nano-discs (CSNs) and their derivatives through strategic pretreatment and acid hydrolysis route. The CSNs fabricated from Muga silk show distinct discotic morphology confirmed by TEM, SEM and AFM. The average size of the CSNs as analyzed from AFM was found to be 49.1±12 nm (in diameter) and 3.1±0.9 nm (in height). CSNs are found to consist of crystallites having β-sheet conformation, which was established by FTIR and ss-NMR. The amino acid analysis confirmed the presence of alanine (~80%), glycine (~6%) and serine (~6%) by weight in the CSNs, indicating their hydrophobic nature. The X-ray diffractograms and SAED patterns show that the CSNs are highly crystalline (crystalline index ~90%). Magnetic CSNs (MGSCNs) are fabricated using borohydride reduction method and are characterized by XRD, FTIR, TEM and SEM analysis. The TEM images show that MGCSNs have diameter of 58.2 ± 4.6 nm and thickness of 16.0 ± 2.6 nm. The MGCSNs are found to have good dye adsorption ability.

Moreover, CSNs with functional groups show tunable surface behavior, as demonstrated by the fabrication of superparamagnetic nano-crystalline discs (i.e., MGCSNs) having non-toxic characteristics, which are quite promising for applications in biomedical sciences as novel bioferrofluids for drug delivery vehicles (studied in detail in Chapter 7 and as MRI agents.

Chapter 4

Studies on Poly(lactic acid)/Crystalline Silk Nano-discs Based 'Green' Bionanocomposite for Food Packaging Applications

In this chapter, crystalline silk nano-discs (CSNs) which was isolated successfully from waste Muga silk via acid hydrolysis, are used as reinforcement material in the poly(lactic acid) (PLA) matrix to investigate the influence of CSNs on the structural, morphological, thermal, optical, mechanical and barrier properties of PLA bionanocomposites. Melt extrusion, a facile, solvent-free approach is employed for the fabrication of biopolymeric/ crystalline silk nano-discs (CSNs)-based "green" bionanocomposite films utilizing the bio-based poly(lactic acid) (PLA) for potential high temperature engineering and food packaging applications. At optimum loadings of 1 wt%, the CSNs are well dispersed covering the entire matrix, corroborated through morphological analysis, leads to significant improvement in intrinsic characteristics such as thermal, mechanical, barrier and processing capabilities. Due to enhanced crystal nucleation density, water vapor and oxygen permeability reduced by ~30 and ~70%, respectively. Enhancement in toughness, percentage elongation and tensile strength by up to ~65%, ~40% and ~10%, respectively is obtained. Onset of thermal decomposition for the PLA/CSN improved up to ~10 °C, confirming the role of CSN in enhancing melt stability. These favorable properties along with their non-toxicity, sustainability and complete biodegradability make the PLA/CSN bionanocomposites promising candidates to replace non-degradable fossil fuel-based plastics in packaging applications.

The work in this chapter is accepted as:

- R. Patwa, A. Kumar, and V. Katiyar, Effect of silk nano-disc dispersion on mechanical, thermal and barrier properties of poly(lactic acid) based bionanocomposites," J. Appl. Polym. Sci. ., DOI: 10.1002/app.20180102

4.1 Introduction

Rising apprehensions regarding the ecosystem, carbon footprint and human health have resulted in increased interest in bio-based materials, such as green and sustainable biodegradable polymers, as alternatives to fossil fuel-based plastics for various applications. Among the diverse synthetic biodegradable polymers available in the current scenario, only a few such as poly(ε-caprolactone) (PCL), poly(lactic acid) (PLA) and polyhydrohybutyrate (PHB) are suitable for melt processing for manufacture of commodity articles. However, these biopolymers are yet to prove themselves in terms of processability, durability, recyclability, etc. They suffer from inferior gas barrier properties, poor melt strength, slow crystallization rate and somewhat lower glass transition temperature in comparison to conventional plastics, which limit their utilization for engineering applications to their full potential. In pursuance of enhancing their properties, various strategies such as blending two or more polymers, stereocomplexation, inclusion of micro or nanofillers, plasticizers etc. have been adopted by research fraternity across the world.

Poly(lactic acid) has comparable gas barrier, optical and thermomechanical properties along with enough durability to maintain these properties, is regarded as the worthy candidate to substitute petroleum- based plastics. PLA is an aliphatic bio-based polyester synthesized from lactic acid as monomer, which can be derived from fermentation of glucose-rich sources such as beet, corn, etc. PLA can be processed through several methods such as solution-casting, melt processing, electrospinning, etc. **(Hao et al., 2016; Valapa et al., 2015a; Xiang et al., 2009)**. Melt processing of PLA severely affects the molecular weight due to high shear and temperature conditions, resulting in poor melt strength and mechanical properties inadequate for commodity applications **(Tesfaye et al., 2017)**. PLA-based nanocomposites, obtained by incorporation of nano-sized fillers in the PLA matrix, have been reported to show enhanced properties for wide range of potential applications such as biodegradable packaging, biocompatible scaffolds in tissue engineering and theranostics **(Lasprilla et al., 2012; Muller et al., 2017)**. Incorporation of small amounts of nanofillers can lead to significant improvement of the desired properties, which are substandard in PLA.

Researchers have carried out a large number of studies on PLA composites with enhanced properties. Addition of inorganic fillers with high aspect ratio such as graphene platelets **(Gao et al., 2017)**, carbon nanotubes **(Wang et al., 2016a)**, layered silicate

(Krikorian and Pochan, 2003) and silica nanoparticles **(Hao et al., 2016)** have showed superior mechanical properties. Wang and coworkers reported improved tensile strength from ~51 MPa to ~68 MPa due to high aspect ratio and uniform dispersion of CNT with 3 wt% loading **(Wang et al., 2016a)**. Addition of silica nanoparticles provided improved thermal stability (8000 s, ~60% improvement) and viscoelastic properties of PLA with ~2.8 vol% addition **(Hao et al., 2016)**. Addition of ~15 wt% Cloisite 30B clay results in ~60% enhancement in storage modulus and optically transparent composites **(Krikorian and Pochan, 2003)**. In another study using Cloisite 30B clay, it was found that low amount of layered silicates (~0.8 wt%) results in ~20% reduction in oxygen permeability **(Koh et al., 2008)**. Such significant improvement in material properties make the composites ideal for high performance applications; however, in regard to food packaging, greater emphasis is needed on understanding the interaction of the polymer composites with food upon contact. Accordingly, in the search for ideal fillers, non-toxicity and human compatibility becomes top priority. In contrast to inorganic fillers, reports on fabrication of PLA-based composites using bio-based fillers are relatively recent. However, the interest in these materials is growing as they have the potential to be fully bio-based, biodegradable, non-toxic alternative to conventional plastics. The influence of different bio-fillers such as cellulose **(Gupta and Katiyar, 2017)**, starch **(Muller et al., 2017)**, cellulose nanocrystals **(Dhar et al., 2015b)**, chitosan **(Pal and Katiyar, 2016)**, gum **(Tripathi and Katiyar, 2016)** and sucrose palmitate **(Valapa et al., 2015b)** on the thermomechanical and permeation properties of PLA have been examined.

Silk is a fibrous protein spun by silkworms and spiders. Silk fiber is composed of a fibrous protein core known as fibroin and protective coat protein termed sericin which binds everything to form cocoons. To obtain continuous silk fibers, sericin needs to be removed by a process called degumming **(Rockwood et al., 2011)**. The remarkable strength, biocompatibility, prolonged biodegradability and ease of modification makes silk stand out from other available animal fibers. Silks' excellent mechanical properties are by virtue of well-ordered structures called β-nanocrystals, made up of highly crystalline hydrophobic domains **(Keten et al., 2010)**. Lately, truncated silk fibres have been utilized as reinforcing material for polymer matrix of poly(lactic acid) (PLA) , polypropylene (PP) and poly(butylene succinate) (PBS) **(Alam et al., 2011; Chen et al., 2017; Hinchcliffe et al., 2016)**. Owing to their biocompatibility and biodegradability, silk nanoparticles have been an ideal choice for biomedical applications such as controlled drug delivery and

tissue engineering applications **(Maitz et al., 2017; Mottaghitalab et al., 2017; Ping et al., 2017)**. Silk nanoparticles have not been explored fully as polymer matrix reinforcements. Therefore, the work presented in this chapter mainly focuses on enhancing the morphological, thermal, mechanical, barrier and optical characteristics of a new fully biodegradable and sustainable bionanocomposite fabricated by dispersing laboratory-fabricated hydrophobic crystalline silk nano-discs (CSNs) from waste Muga silk fibroin into hydrophobic PLA matrix via melt extrusion. The present chapter also reports on the influence of this eco-friendly biofiller on PLA bionanocomposites for potential application in food packaging.

4.2 Results and discussion

4.2.1 Poly(lactic acid)/crystalline silk nano-discs bionanocomposites: Morphological investigations

PLA/CSN bionanocomposites were prepared by melt extrusion at various CSN loadings (0.5–5 wt%) in the PLA matrix. Fracture morphology of PLA and PLA/CSN bionanocomposites was examined using FESEM to understand the dispersion and interaction of hydrophobic filler and matrix. PLA micrographs obtained from FESEM, shown in Figure 4.1(a), reveal smooth polymer matrix with no distinct structures. PLA/CSN bionanocomposites are shown in Figure 4.1(b–f), which shows homogeneous dispersion of CSN (at ~1 wt% loading) on a smooth polymer matrix surface, where a large fraction of bio-filler is embedded in the polymer, thus providing more contact surface area. The addition of CSN leads to some structural features which are not observed in the micrographs of pure PLA. These are probably because of the physico-chemical interaction between CSN and PLA matrix which is able to reinforce the bionanocomposite upon mechanical load. Figure 4.1(d) shows the PLA/CSN bionanocomposite at 1 wt% loading at higher magnification (75,000x) which clearly shows small polymer chains (~50 nm diameter) can be observed (shown with white arrows). This could be due to the proper dispersion of CSNs in the matrix which results in reinforcing effect. This signifies strong attractive interaction between hydrophobic CSNs and hydrophobic PLA matrix. However, at higher loadings (>2 wt%), CSNs start to agglomerate in the form of clusters on the polymer surface, the particle-particle interaction overcomes the polymer-particle interaction. Therefore, dispersion is affected resulting into CSNs forming aggregates. This results in reduced interfacial area of contact between polymer and biofillers at higher

concentrations. The average cross-sections of voids calculated were 223±39 nm and 517±143 nm, for loadings of 2 and 5 wt% CSNs respectively.

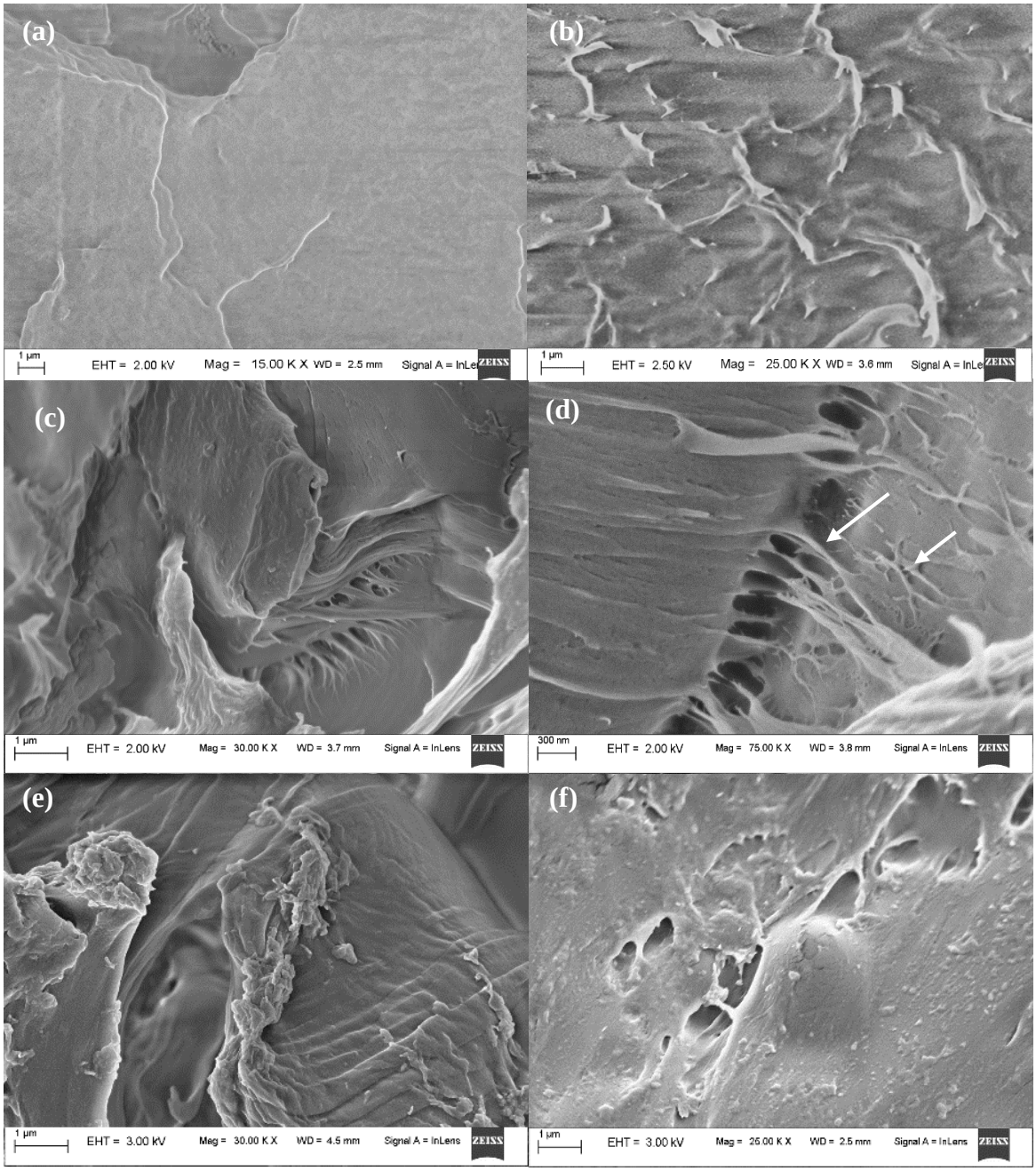

Figure 4.1: FESEM micrographs of pure PLA and PLA/CSN bionanocomposite films: (a) pure PLA, (b) PLACSN0.5, (c) PLACSN1 (30,000x), (d) PLACSN1 (75,000x) (polymer fibrils shown with white arrows), (e) PLACSN2 and (f) PLACSN5.

AFM micrographs Figure 4.2(a–e) show the well dispersed CSN into the PLA matrix. Neat PLA (Figure 4.2(a–b)) appear smoother as compared to PLA/CSN (1 wt%) bionanocomposites. The AFM micrographs of PLACSN1 (Figure 4.2(c–d)) show CSNs

embedded in between the polymer chains; a pictorial representation is also shown in Figure 4.2(e). TEM micrograph (Figure 4.2(f)) shows the CSNs well-dispersed in the PLA matrix.

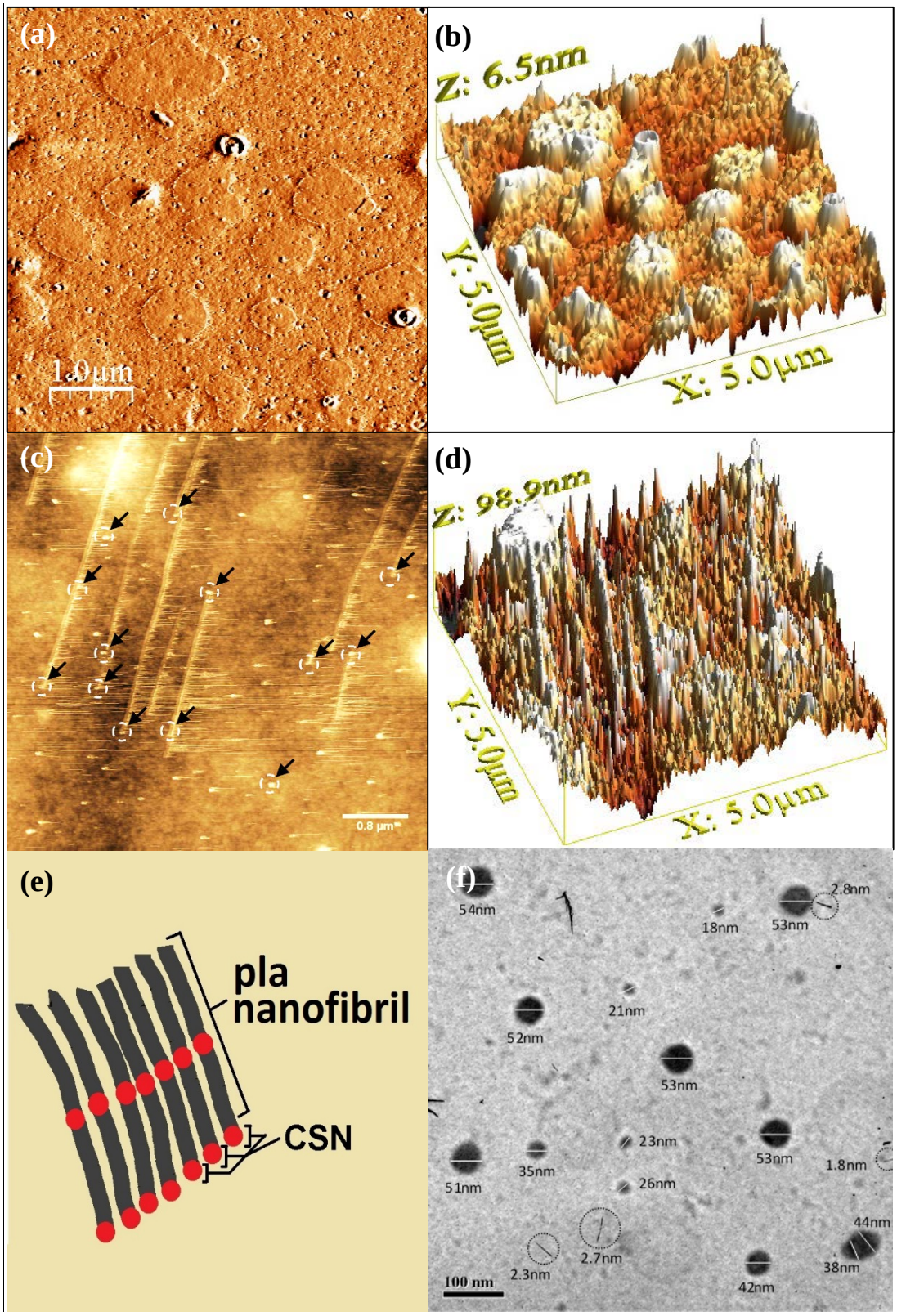

Figure 4.2: AFM micrographs of the PLA and PLACSN1 bionanocomposite films: (a) neat PLA (5 × 5 μm), (b) 3-D micrograph of neat PLA, (c) PLACSN1 (CSNs shown in

black arrows), (d) 3-D micrograph of PLACSN1, (e) cartoon depicting the dispersed CSN in polymer matrix, and (f) TEM micrograph of PLACSN1.

4.2.2 Dispersion of CSNs in PLA matrix: A mechanistic understanding

The interaction between CSNs and PLA matrix (at low CSN loading ~1 wt%) is understood through XRD and FTIR studies. X-ray diffraction patterns along with characteristic lattice planes for fabricated CSNs, PLA and PLA/CSN bionanocomposites with different CSN loadings are shown in Figure 4.3. CSNs show the presence of three distinct peaks at 16.8°, 20.2° and 23.9° representing the orthorhombic β-sheet crystal structure with (002), (201) and (003) lattice planes respectively **(Bhat and Nadiger, 1980)**. The diffraction patterns for the acid-derivatized CSNs show the presence of β-sheet structure similar to initial fibroin precursor used (degummed Muga fibers) as shown in Figure 3.5, suggesting that hydrolysis using acids did not alter the inherent silk structure. The CSN showed higher crystallinity value of ~93% with the crystallite size dimension of 8.2 nm corresponding to the peak at 16.8° (002).

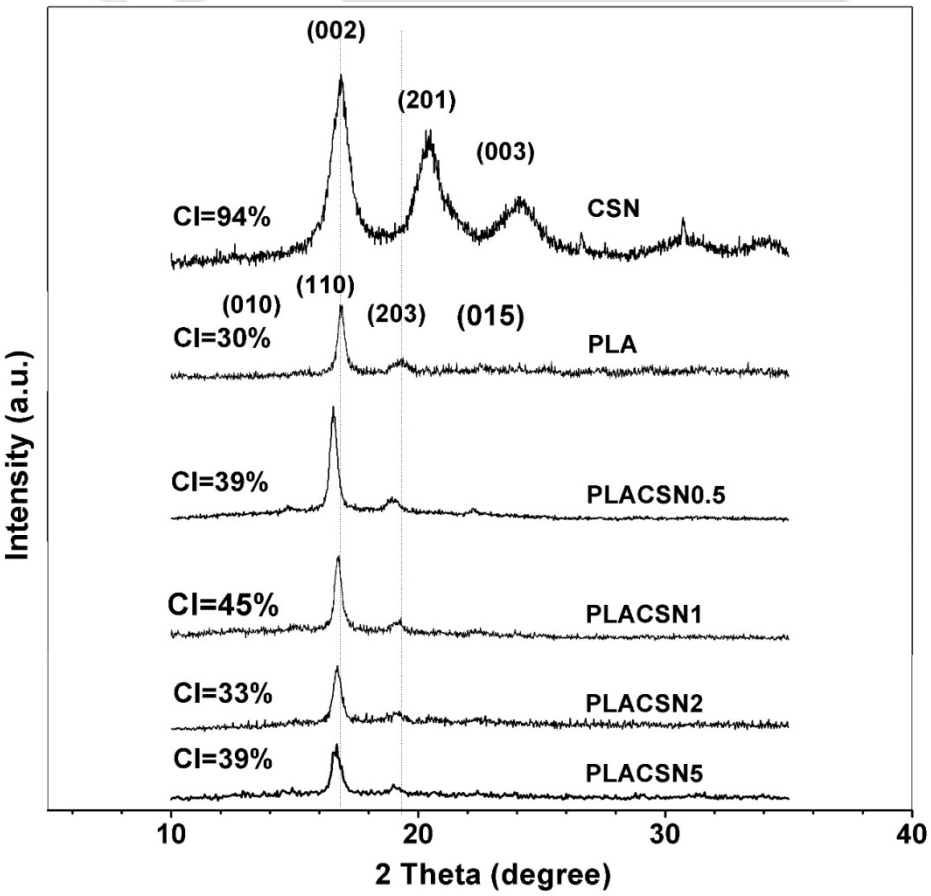

Figure 4.3: XRD diffractograms for PLA, CSN and PLA/CSN bionanocomposites at various CSN loadings.

Lattice reflection peak of PLA can be clearly seen in the diffraction spectra with peaks at 14.9°, 16.8° and 19.9° **(Gupta and Katiyar, 2017; Pal and Katiyar, 2016)**. It can be observed that upon 0.5 wt% CSN loading a slight peak shift is observed. For all other concentrations there is no peak shifting which shows that upon incorporation of CSN no change takes place in the crystal structure. The percentage crystallinity for PLA/CSN bionanocomposites is higher as compared to PLA i.e. ~45% for PLACSN1. It is noteworthy to mention that PLA and CSN show an intense peak in the XRD diffraction pattern at $2\theta_{PLA}$=16.5° and $2\theta_{CSN}$=16.8°, respectively. For PLA/CSN bionanocomposites it results in overlapping of PLA and CSN peaks thus resulting into one single peak. Due to lower concentration of CSN in bionanocomposites, other less intense peaks of CSN are not observed. Since the CSN peak is broader than PLA peak which is narrow, we observe that as the CSN concentration is increased, the peak around 16.5 gets broader and lower in intensity due to increasing content of CSN **(Dhar et al., 2015a)**.

The FTIR spectra along with characteristic absorption bands for fabricated CSNs, PLA and PLA/CSN bionanocomposites with different CSN loadings are shown in Figure 4.4. Absorption bands at 754 cm^{-1} corresponds to the –CH- bending of the PLA molecule which represents the crystalline phase of PLA. The peak at 870 cm^{-1} can be seen in all the samples except CSN which depicts –C-C- stretching representing the amorphous phase of PLA, denoting the semi-crystalline nature of PLA and bionanocomposites. The bands at 1082 and 1182 cm^{-1} are characteristic bands for –C-O- stretch of PLA molecules and biocomposites.

The intense and sharp absorption band of –C=O (carbonyl stretching) valence vibration at 1752 cm^{-1} can be noticed for all the samples except CSN where these peaks are missing. In addition, amino-acids present in silk show strong absorption bands of amide I and II which depict –C=O stretching and -N-H bending, respectively are observed at 1630 and 1530 cm^{-1} in CSN and bionanocomposites. These bands are missing completely in PLA. Nonetheless, these bands appear with low intensities in bionanocomposite films due to low CSN content, i.e. 0.5, 1, 2 and 5 wt% in PLA/CSN bionanocomposites. Hence, the presence of CSN is confirmed in bionanocomposite films. The band at 1630 cm^{-1} for CSN has shifted to 1668 cm^{-1} and appears as a shoulder for bionanocomposite films, which is a clear indication that PLA matrix and CSN molecularly interact with each other. It can be presumed that intermolecular hydrogen bond formation can occur by interaction possibly

between hydroxyls of amino acids (serine, aspartic acid and glutamic acid) present in CSN and the carbonyls on the PLA chain.

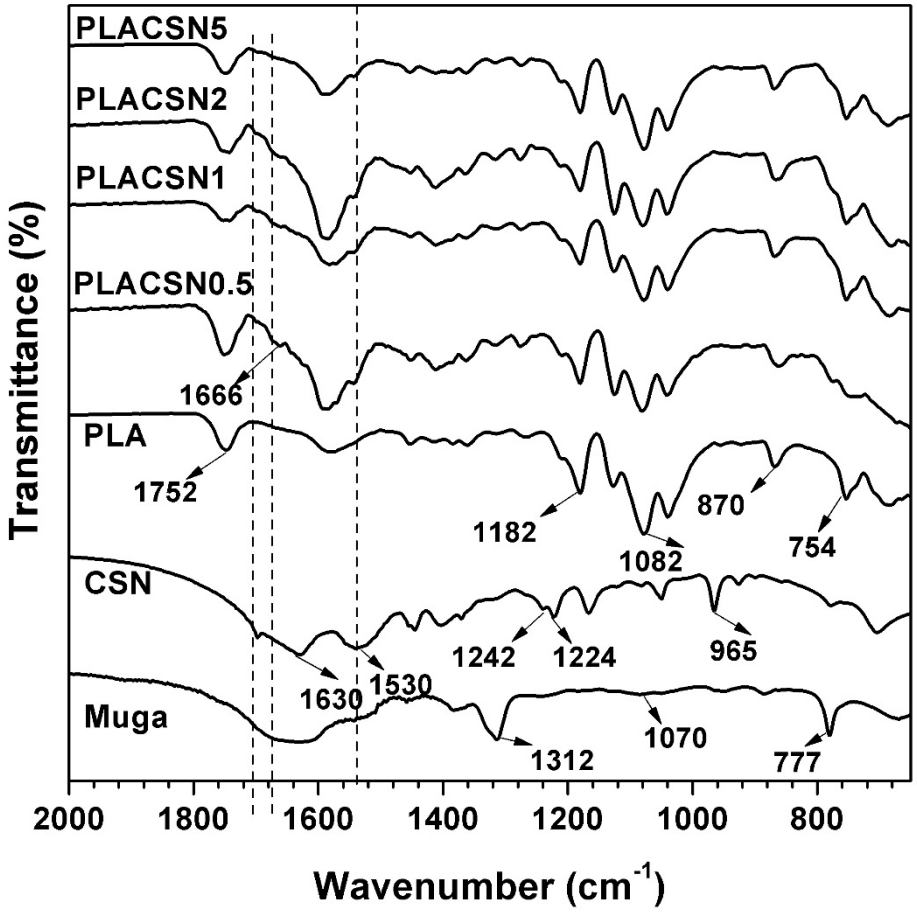

Figure 4.4: FTIR spectrograms for PLA, CSN and PLA/CSN bionanocomposites at various CSN loadings.

4.2.3 Thermal characteristics of PLA/CSN bionanocomposites

Differential scanning calorimetry (DSC) studies were conducted to understand the change in crystallization and melting behavior of PLA upon incorporation of silk nano-discs. DSC second heating thermograms for PLA and PLA/CSN bionanocomposites at a heating rate of 10 °C/min are shown in Figure 4.5. Three thermal events namely glass transition (T_g), cold crystallization (T_{cc}) and melting (T_m) temperature were observed upon analysis. The melting region for all bionanocomposites show a unimodal endothermic peak (T_m = 152.2 °C) which is identified as the α-crystalline form of PLA, and which matches with the XRD results discussed in section 4.2.2. It can be seen that PLA shows a T_g around 60 °C, as also listed in Table 4.1. Single T_g for all bionanocomposites confirms the uniform dispersion of

CSN in PLA matrix with no phase separation. Upon incorporation of 1 wt% CSN, all transition temperatures (T_{cc} and T_m) decreased. The heat of fusion (ΔH_m) is higher in the case of PLA/CSN bionanocomposites as compared to neat PLA which can be attributed to the increment in nucleating sites and possible attractive interaction between PLA and CSN resulting in enhanced percentage crystallinity ($\%X_c$). Higher T_{cc} values for other loadings suggest that presence of CSNs suppress the diffusion rate leading to slower migration of the polymer chains to the surface of the nucleus **(Katiyar et al., 2010)**.

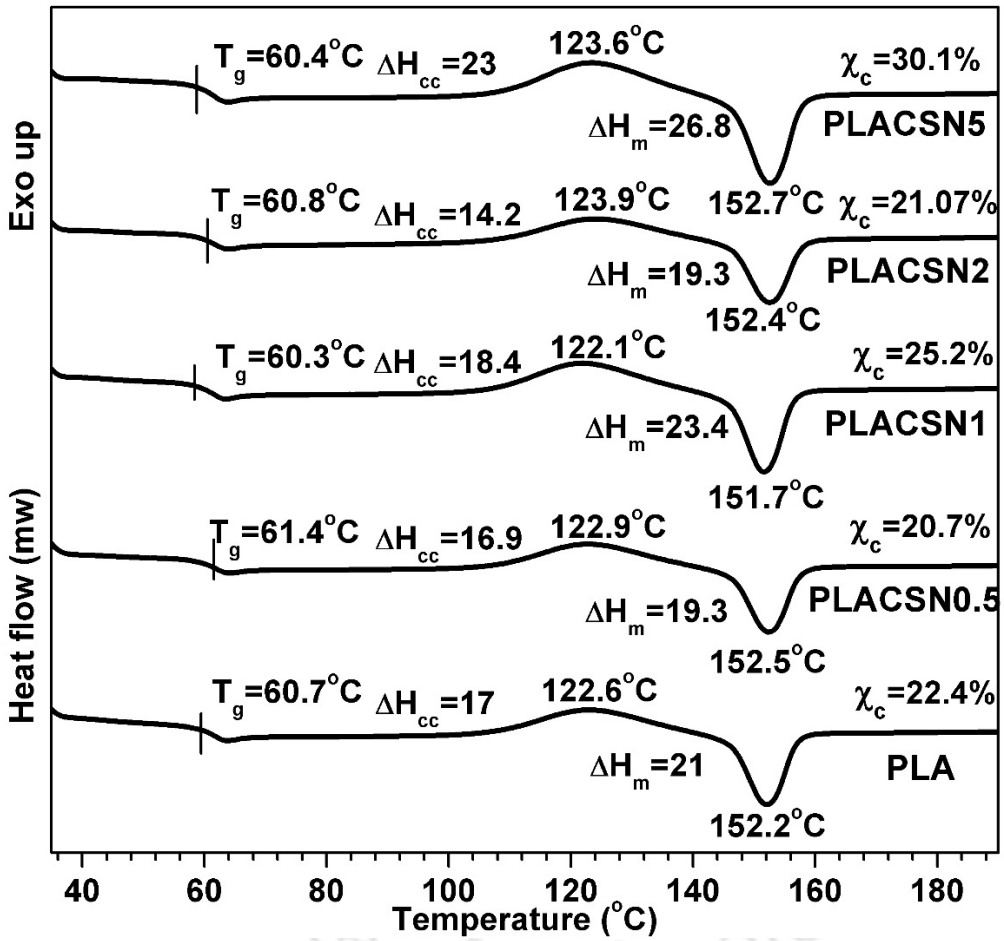

Figure 4.5: Various thermal phase transitions of PLA and PLA/CSN bionanocomposites films during DSC analysis.

Thermogravimetric analysis (TGA) is an effective way for evaluation of the thermal stability of bionanocomposites. Figure 4.6(a) shows the TGA thermographs (30 °C to 600 °C) of CSN and PLA bionanocomposites with different CSN loadings obtained at a heating rate of 10 °C/min. All the bionanocomposites were thermally stable in the region between 30 to 310 °C. The major weight loss for PLA and bionanocomposites occurs in the range of 310 – 390 °C which is related to the backbiting or the transesterification reaction of PLA

(Garlotta, 2001; Monika et al., 2017). The CSN started to lose mass when the temperature exceeded 310 °C. CSN shows two-step degradation, with two stages of decomposition evident at 350 and 534 °C. The first mass loss region reflects the thermal degradation of highly oriented β-sheet configuration **(Cho et al., 2015)**. This region experiences ~45% of mass loss. The second region is a sluggish degradation step from 421 °C right down to 600 °C which corresponds to carbonization of the protein. The T_{onset} values of PLA, PLACSN0.5, PLACSN1, PLACSN2 and PLACSN5 were seen to be 308, 316, 318, 312 and 311 °C, respectively whereas the T_{max} values as obtained from Figure 4.6(b) for PLA, PLACSN0.5, PLACSN1, PLACSN2 and PLACSN5 are 380, 382, 381, 378 and 369 °C, respectively. It can be seen that incorporation of 1 wt% CSN into PLA matrix enhances the T_{onset} by 10 °C, whereas the temperature of maximum degradation, T_{max} is slightly higher than PLA.

Table 4.1: Thermal analysis (DSC and TGA) of the pure PLA and PLA/CSN bionanocomposites.

CSN loading (wt%)	T_g (°C)	T_{cc} (°C)	ΔH_{cc} (J/g)	T_m (°C)	ΔH_m (J/g)	X_c (%)	T_{onset} (°C)	T_{end} (°C)	T_{max} (°C)	Wt Loss at T_{max} (%)	W_R^{400} (%)
0	60.7	122.6	17	152.2	21	22.4	307.7	398.7	379.9	62.0	1.7
0.5	61.4	122.9	16.9	152.5	19.3	20.7	315.7	401.0	381.8	66.0	1.7
1.0	60.3	122.1	18.4	151.7	25.2	25.2	317.8	404.7	380.5	67.0	2
2.0	60.8	123.9	14.2	152.4	19.3	21.1	312.0	397.6	378.0	65.0	2.3
5.0	60.4	123.6	23	152.7	26.8	30.1	310.6	394.6	369.0	52.0	4.3

T_g, T_{cc} and T_m are glass transition, cold crystallization and melting temperatures, respectively and ΔH_{cc} and ΔH_m are enthalpies of cold crystallization and fusion, respectively. T_{onset}: onset degradation temperature, T_{end}: end temperature of degradation peak, T_{max}: maximum temperature of the DTG curves, W_R^{400}: residual weight at 400 °C.

As mentioned in Table 4.1, the weight loss % at T_{max} was found to be ~62%, ~66%, ~67%, ~65% and ~52% for PLA, 0.5, 1, 2 and 5 wt% CSN loadings, respectively. Based on the T_{max} and T_{onset} information for PLA bionanocomposites, one can conclude that PLACSN0.5 and PLACSN1 has improved thermal stability as can be seen from the higher temperature for onset of thermal degradation as compared to bionanocomposites with higher loadings. Although incorporation of biofillers usually leads to reduction in thermal

stability **(Zhao et al., 2010)**, in the present case, addition of CSN nanofiller into the PLA matrix improved the thermal stability. This can be attributed to the attractive interaction of CSNs with the PLA chains that leads to their arrangement in micro-chains resulting in a "labyrinth"-like structure due to better strong favorable interaction between CSN and PLA, thereby restricting the thermal motion of polymer domains. Similar findings are reported by **Leszczyńska et al. (2007)** where MMT clay nanoparticles dispersed in polymer matrices such as polypropylene (PP), polyamide (PA) and poly (methyl methacrylate) (PMMA) showed restricted diffusion of oxygen molecules into polymer matrix which causes pyrolytic conditions inside nanocomposites. However, at high loadings the CSNs form agglomerates resulting in poor thermal stability **(Corcione and Frigione, 2012)**. As the biofiller content increases, the number of acidic sites generated during the degradation of CSN in the PLA matrix also increases which reduces the thermal stability at high CSN loadings **(Pal and Katiyar, 2016)**. The residual weight percent values at 400 °C for PLACSN0.5, PLACSN1, PLACSN2 and PLACSN5 were 1.7, 2.0, 2.3, 4.3% respectively compared to 1.7% for neat PLA.

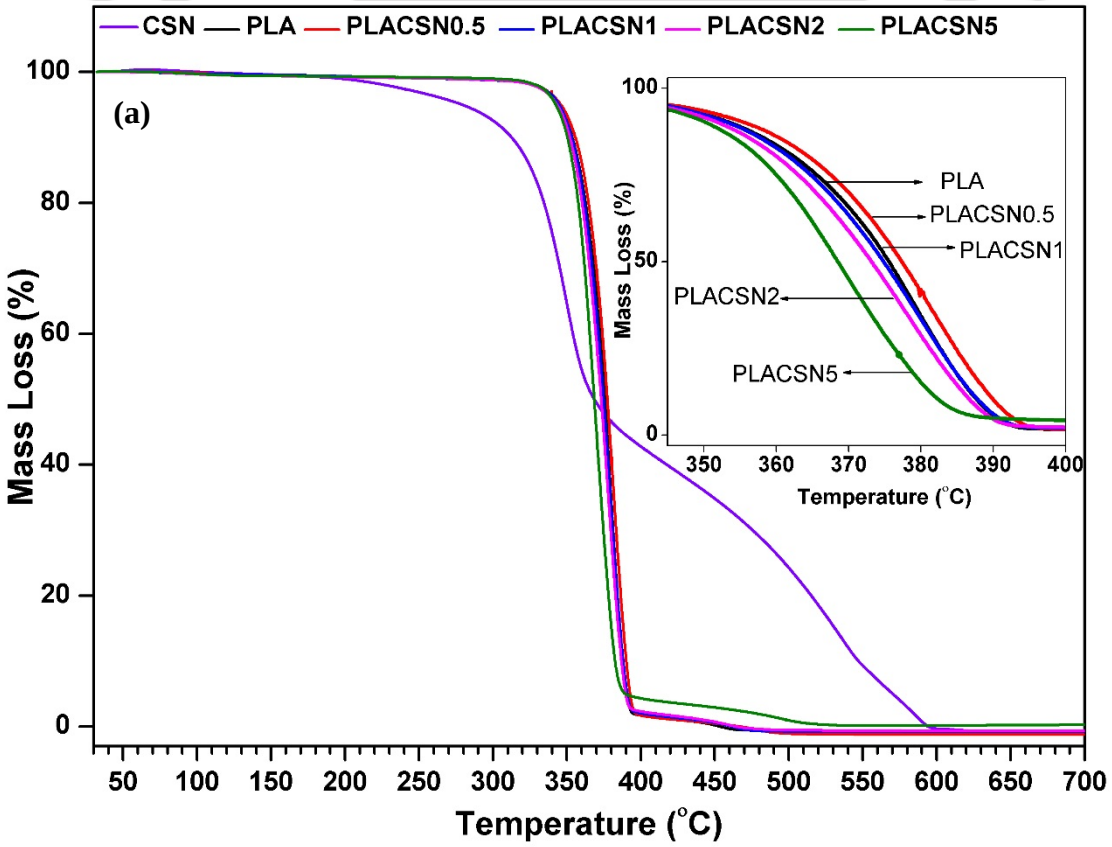

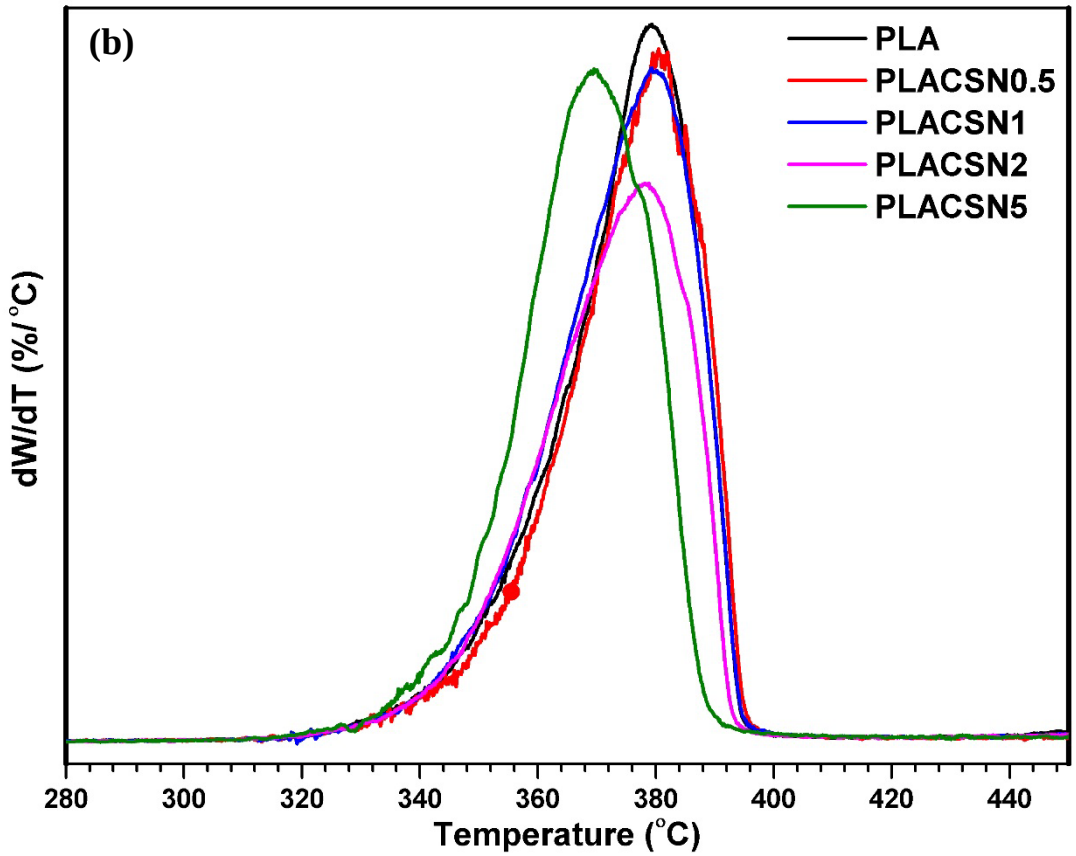

Figure 4.6: (a) TGA, inset: enlarged view of the temperature range 345-400 °C and (b) DTG thermograms of CSN, PLA, PLA/CSN bionanocomposites at heating rate of 10 °C/min.

4.2.4 Molecular weight studies

The number average molecular weight (M_n) and weight average molecular weight (M_w) of virgin PLA granules was ~183 000 Da and ~335 000 Da, respectively. The effect of various loadings of CSN on the values of M_n, M_w and polydispersity index (PDI) of PLA during melt extrusion technique are shown in Figure 4.7. It can be seen that incorporation of CSN leads to reduction of molecular weight and increasing in polydispersity index, which is especially pronounced at higher CSN loadings (> 1%). Interestingly, the molecular weight at 1% loading showed the lowest reduction (~10%) in number average molecular weight. This is possibly due to proper dispersion of CSNs into the PLA matrix, which delay the molecular chain movement during melt processing. At higher loadings (5 wt%), the values of M_n and M_w showed a reduction of ~55%, which can be attributed to CSN acid groups along with lactic acid which catalyze polymer degradation causing reduction in polymer chain lengths. The formation of agglomerates at high CSN loadings

further lowers polymer-filler interaction, resulting in increased thermal degradation during processing and consequent reduction of molecular weight. Similar results have been observed by **Pluta et al. (2002)** for PLA/montmorillonite-based nanocomposites prepared by melt compounding.

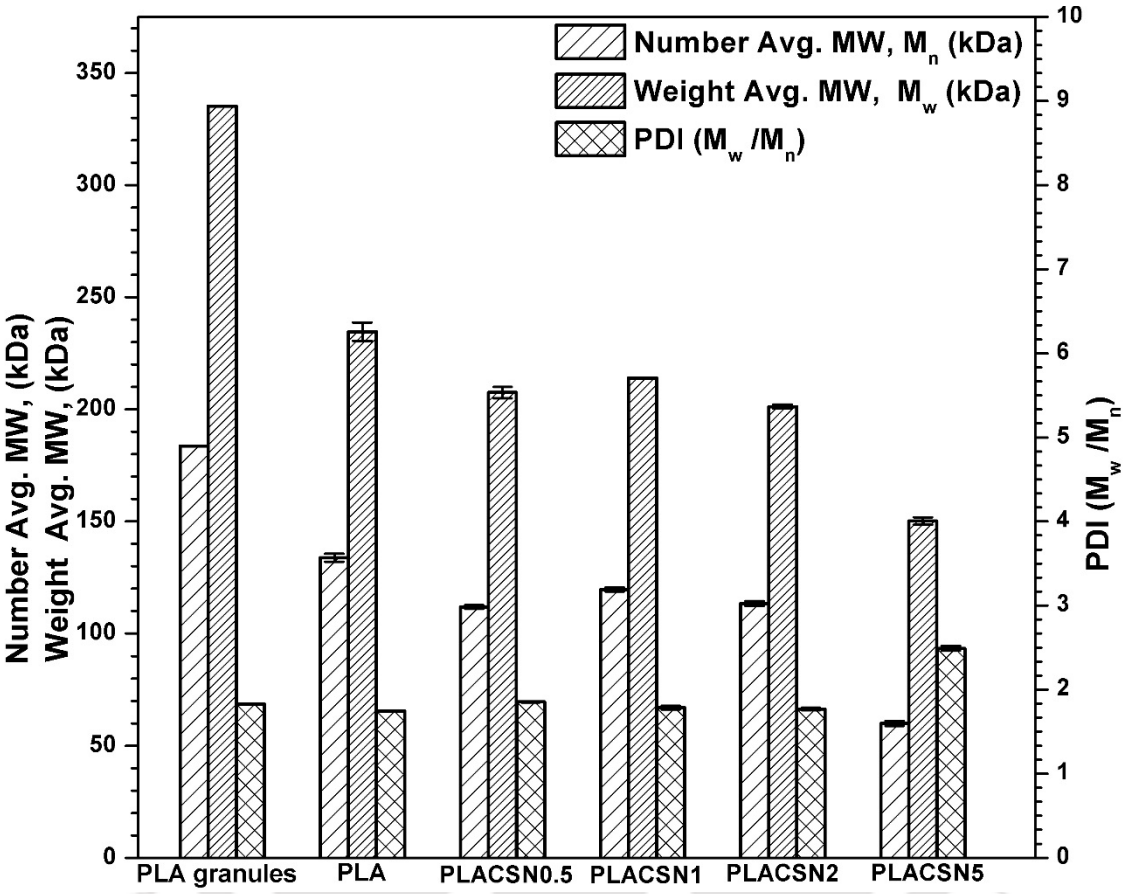

Figure 4.7: Molecular weight distribution in melt-extruded PLA and PLA/CSN bionanocomposites with (0.5–5 wt%) CSN loadings.

4.2.5 Mechanical analysis of PLA/CSN bionanocomposites

The effect of biofiller content on mechanical properties of PLA/CSN was investigated using universal testing machine (UTM) and dynamic mechanical analysis (DMA). The ultimate tensile strength (UTS) (MPa), percentage elongation at break (%), Young's Modulus (GPa), toughness (kJm^{-3}) and shore hardness values of the samples are presented in Table 4.2. The UTS of PLA without filler was 56.3 MPa which was increased to 62.2 MPa (enhancement ~10%) in case of PLACSN0.5. Increment in the tensile strength can be ascribed to the interaction of PLA chains with the CSN which hinder the movement of the chains, which ultimately increases the resistance to the mechanical pull. As observed from the stress-strain curves illustrated in Figure 4.8(a), a plateau region joining strain at peak

stress and break strain is formed. This plateau is much smaller in case of PLA as compared to bionanocomposites. It shows that silk nano-discs can prolong the fracture process in bionanocomposites by initiating interlock mechanism inside the PLA matrix, thus contributing to the toughness.

Table 4.2: Mechanical properties of pure PLA and PLA/CSN bionanocomposites with % improvement (over pure PLA) shown in parenthesis.

CSN (wt%)	Yield strength (MPa)	Percentage elongation at break (%)	UTS (MPa)	Young's Modulus (GPa)	Toughness (kJm^{-3})	Shore D Hardness
0.0	41.8 ± 2.2	9.5± 2.5	56.3± 2.3	1.67 ± 0.19	4.2 ± 0.11	83.5±2.7
0.5	43.5 ± 5.0 (4.1)	13.2± 1.9 (38.6)	62.2± 2.0 (10.5)	1.78 ± 0.02 (6.5)	6.9 ± 0.06 (64.2)	85.2±1.6 (2.0)
1.0	43.9 ± 5.0 (4.9)	13.7± 1.8 (43.4)	59.7± 1.8 (6.0)	1.78 ± 0.09 (6.4)	6.3 ± 0.08 (50.0)	85.5±1.0 (2.3)
2.0	42.9 ± 3.1 (2.5)	12.3± 2.5 (29.3)	58.0± 1.1 (2.9)	1.82 ± 0.05 (8.8)	5.3 ± 0.11 (26.2)	82.5±2.2 (-1.3)
5.0	40.2 ± 4.3 (-3.9)	12.0± 1.4 (25.8)	54.9± 1.5 (-2.6)	1.82 ± 0.05 (8.9)	4.9 ± 0.06 (16.7)	82.3±1.4 (-2.3)

Toughness and percentage elongation at break for PLACSN0.5 showed increment of ~64% and ~39%, respectively as seen in Figure 4.8(b). The percentage elongation at break and **Young's** modulus of elasticity for PLACSN1 showed ~43% and ~6% improvement respectively, showing increment in ductility with not a drastic increase in stiffness of the bionanocomposite, which is essential for flexible packaging. The mean hardness value of melt blended PLA is measured as ~83.5±2.7 which is close to values reported previously **(Bhasney et al., 2017)**. Upon addition of ≤ 1 wt% CSN the hardness value shows improvement of 2.3%. Uniformly dispersed CSNs in the polymer matrix contribute towards the improvement in the above-mentioned mechanical properties.

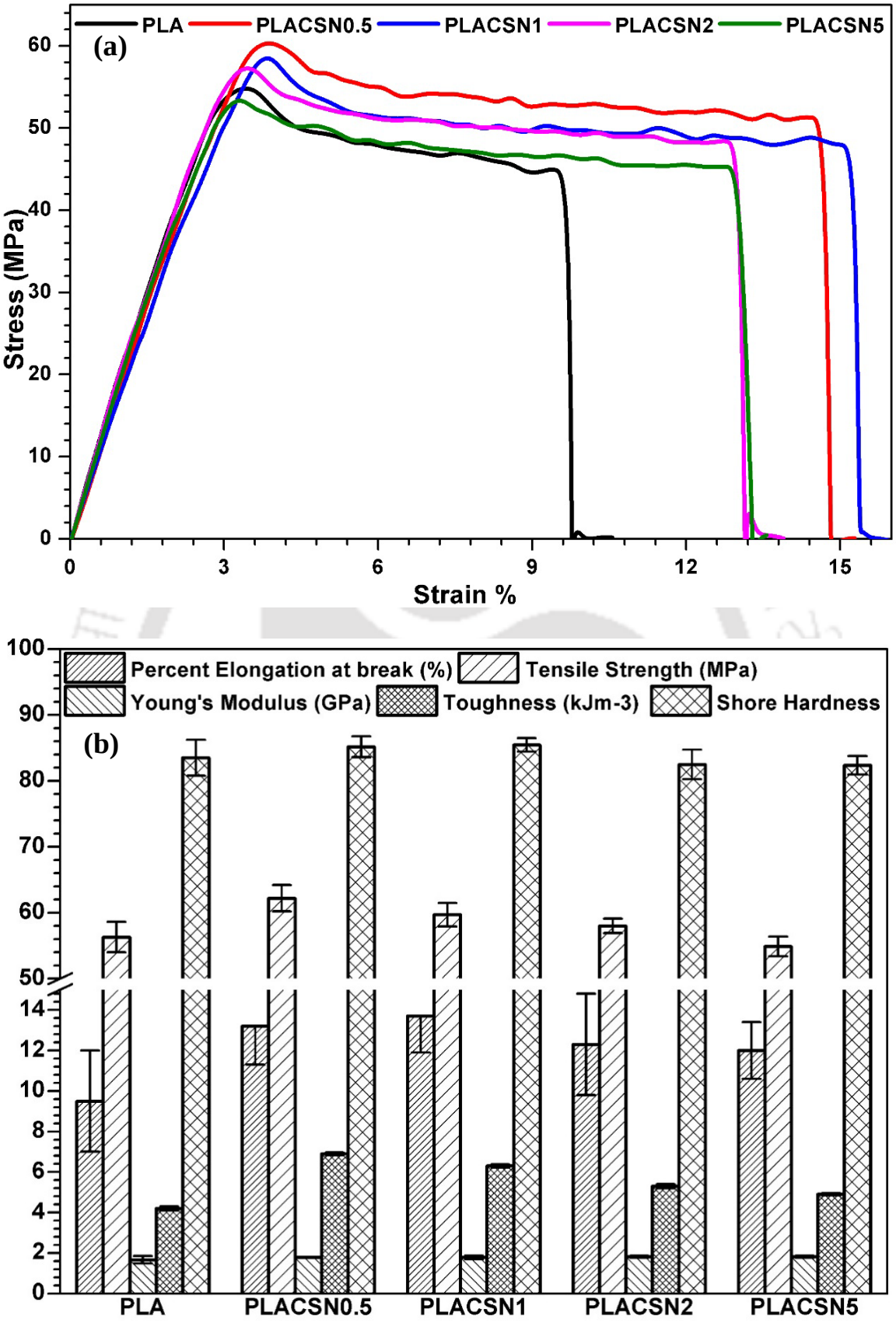

Figure 4.8: (a) Stress-strain curves and (b) mechanical properties of PLA and PLA/CSN bionanocomposites.

Presence of filler exerts a substantial impact on thermo-mechanical properties of PLA bionanocomposites. For practical purposes, it is imperative to determine the dynamic properties of polymeric bionanocomposites over a range of temperatures and frequencies. The dynamic storage modulus (*E´*) provides information about the load-bearing capability of the bionanocomposites. Generally, *E´* decreases gradually upon heating and shows a sharp drop around the glass transition region. DMA of the bionanocomposites suggests improvement in the thermo-mechanical properties. The storage modulus thermograph is shown in Figure 4.9(a). It was found that the *E´* at ambient temperatures improved by more than 500 MPa (~11%) in case of PLACSN1 compared to pure PLA indicating mechanical reinforcement introduced by the silk nano-discs thus allowing transfer of load to both filler and matrix **(Zhao et al., 2010)**. However, reinforcement by CSN cannot suppress molecular chain mobility at elevated temperatures; hence, the difference in modulus values at elevated temperatures is much less compared to room temperature. Thus, PLA/CSN biocomposites display enhanced overall mechanical characteristics which were confirmed by the tensile and thermomechanical tests. This can be explained by the proper dispersion of CSN nanoparticles in the PLA matrix.

The tan δ value, also known as the mechanical loss factor or damping factor, is calculated as the ratio of viscous modulus to elastic modulus. The maxima at a particular temperature corresponds to the glass transition temperature of polymer. The values of temperatures corresponding to maxima in tan δ denote the glass transition temperatures of particular polymer samples, which are close to those obtained from DSC analysis. The peaks of tan δ curves for PLA, PLACSN0.5, PLACSN1, PLACSN2 and PLACSN5 are observed at 70.8, 69.7, 71.1, 70.8 and 70.5 °C, respectively as depicted in Figure 4.9(b). It can be observed that T_g values show slight increment at 1 wt% at which the CSN are well-dispersed in the matrix which created hindrance for polymer chain mobility. Whereas as the CSN content is increased it results in formation of agglomerates resulting in easy movement of polymer chains therefore, the Tg is lowered.

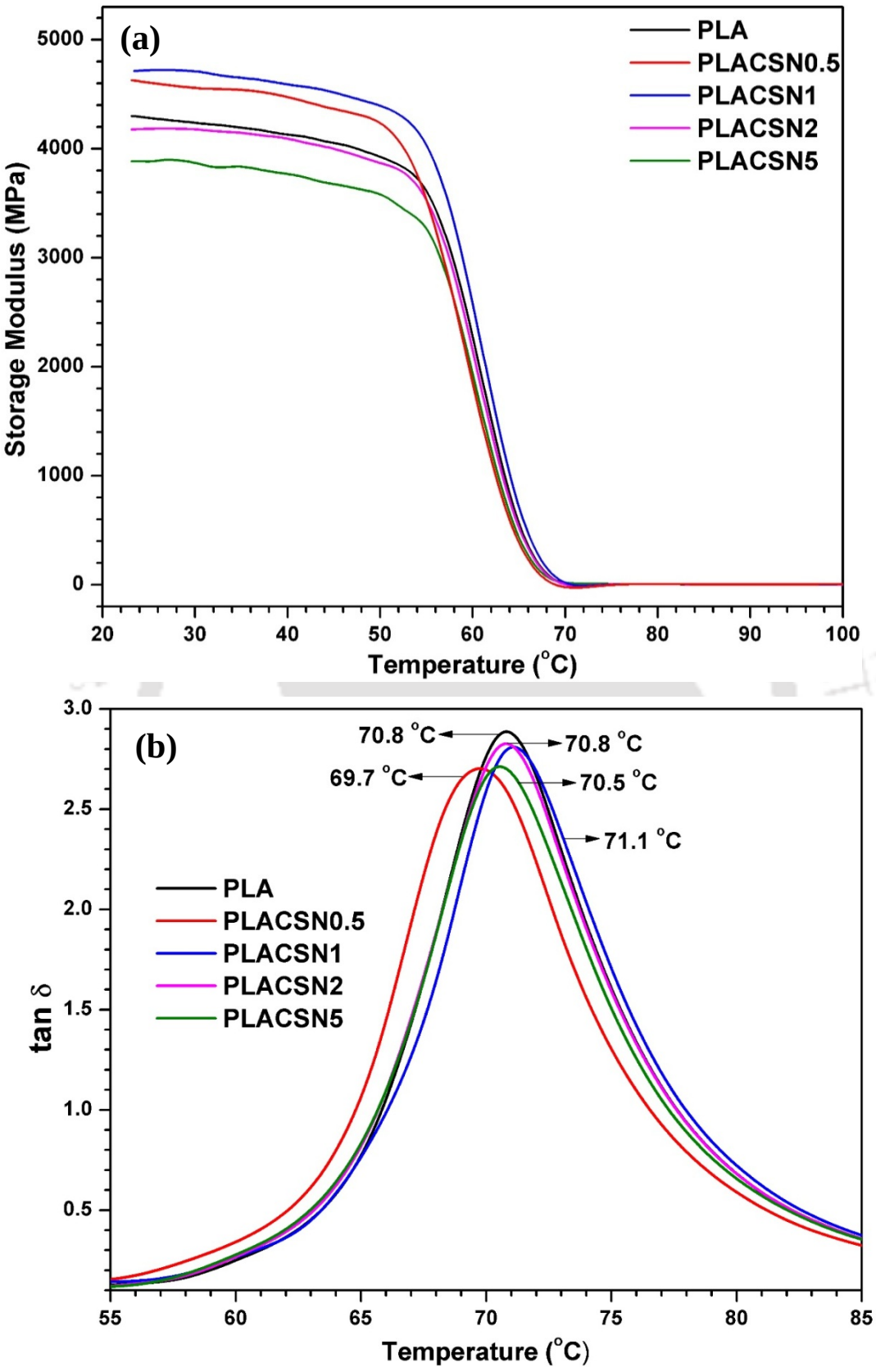

Figure 4.9: (a) Storage modulus (E′) and (b) damping factor (tan δ) curves against temperature for PLA and PLA/CSN bionanocomposites.

4.2.6 Gas barrier properties of PLA/CSN bionanocomposites

One of the indispensable requirements of a bio-based food packaging film is to prevent moisture and oxygen from outside into the packaged food item. In view of this, the water vapor and oxygen permeability should be as low as possible. Measurements of the water vapor permeability (WVP) and oxygen permeability (OP) of the films formed from different samples were carried out to determine the effect of CSN loading on the permeability properties of PLA/CSN bionanocomposites as shown in Figure 4.10. The WVP values of the neat PLA film is in agreement with the reported values in the literature **(Jamshidian et al., 2012)**. Decrease in WVP was observed when silk nanodiscs were incorporated into the polymer matrix. The reduction in water vapor permeability for PLACSN0.5 and PLACSN1 was observed to be around ~33% and ~28% respectively. At higher loadings of CSN, the reduction in permeability was less pronounced due to increase in agglomeration of filler particles. Therefore, the hydrophobic nature of both PLA and CSN, their physico-chemical interactions and proper dispersion, may be responsible for improved water vapor barrier properties

A significant decrease in oxygen gas transmission was observed upon addition of silk nano-discs to PLA. The PLA/CSN bionanocomposites showed improved barrier effect due to their good dispersion in PLA matrix, confirmed through the electron micrographs shown in Figure 4.1(d). OP values for pure PLA closely matched with the reported values **(Narayanan et al., 2017)**. PLA/CSN films with 0.5, 1, 2 and 5 wt.% showed ~53%, ~72%, ~57% and ~70%, reduction in oxygen gas permeability values with respect to the pure PLA films. Due to strong PLA/CSN, the PLA/CSN nanocomposites provide labyrinth-like pathways for permeating oxygen molecules. Further, the presence of well- dispersed, non-porous CSN and physico-chemical interaction between CSN and PLA reduced the number of active sites for sorption of oxygen molecules into the PLA matrix **(Dhar et al., 2015a)**. Hence, the decrease in oxygen permeability in the presence of CSN can be attributed to increased tortuosity of diffusion pathways. However, for 5wt%, slight decrease in oxygen permeability is observed which is possibly due to improvement (increase) in the degree of crystallinity upon higher loading of CSNs which is discussed in XRD in Section 4.2.2. It is known that the crystalline regions are inaccessible to permeating gas molecules.

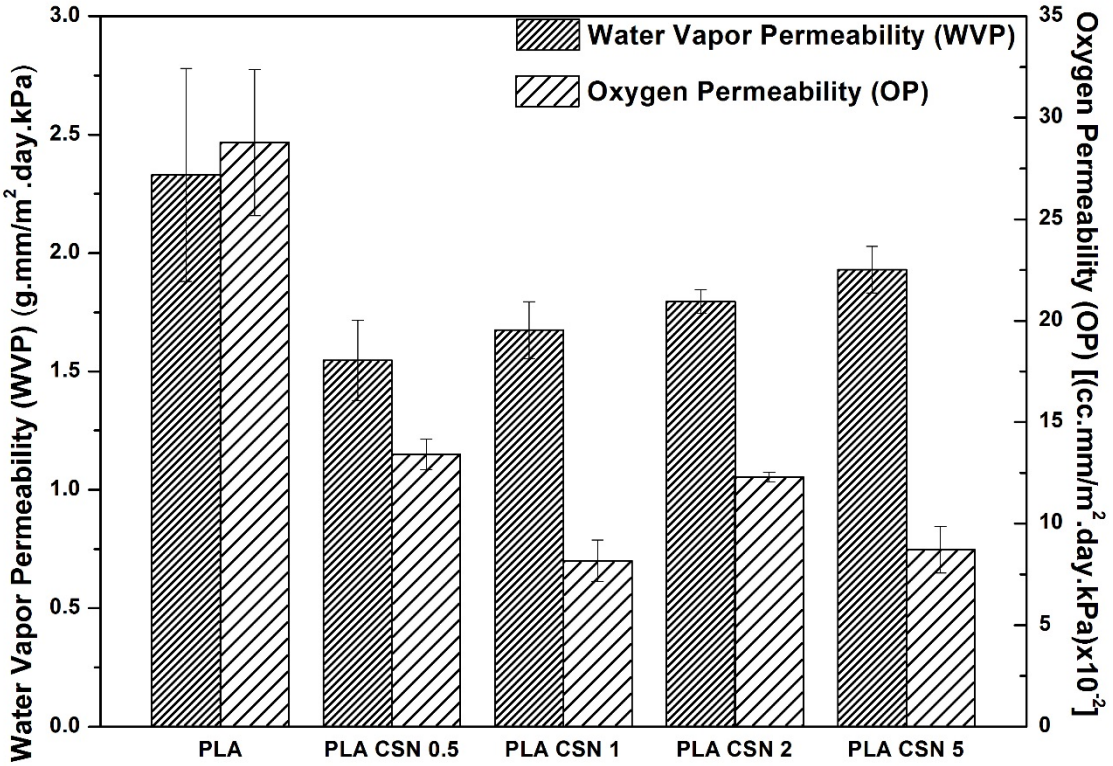

Figure 4.10: Water vapor and oxygen permeability values for PLA and PLA/CSN bionanocomposites.

4.2.7 Optical properties of PLA/CSN bionanocomposites

CSNs are uniformly dispersed throughout the PLA matrix at various loadings and melt extruded. PLA/CSN bionanocomposites having CSN content above 1 wt% displayed agglomeration due to poor dispersion. Furthermore, optical transparency of bionanocomposite films measured in the visible range (see Figure 4.11(a)), were found to have reduced transparency from 2.95 mm^{-1} for PLA to 3.18 mm^{-1} at 1 wt% CSN loading. Nonetheless, at higher loadings, film transparency is drastically affected as a result of strong agglomeration of CSNs. Haze value for PLA was around 8.8%, similar to haze value of 6.71% reported in literature **(Hughes et al., 2012)**. Low haze value of PLA is due to the clarity, or in other words lack of impurities in the matrix. It can be observed that as the CSN content increases, the haze values increase due to reduced transparency of films. The transparency and Haze values of PLA and PLA/CSN bionanocomposites are listed in Table 4.3.

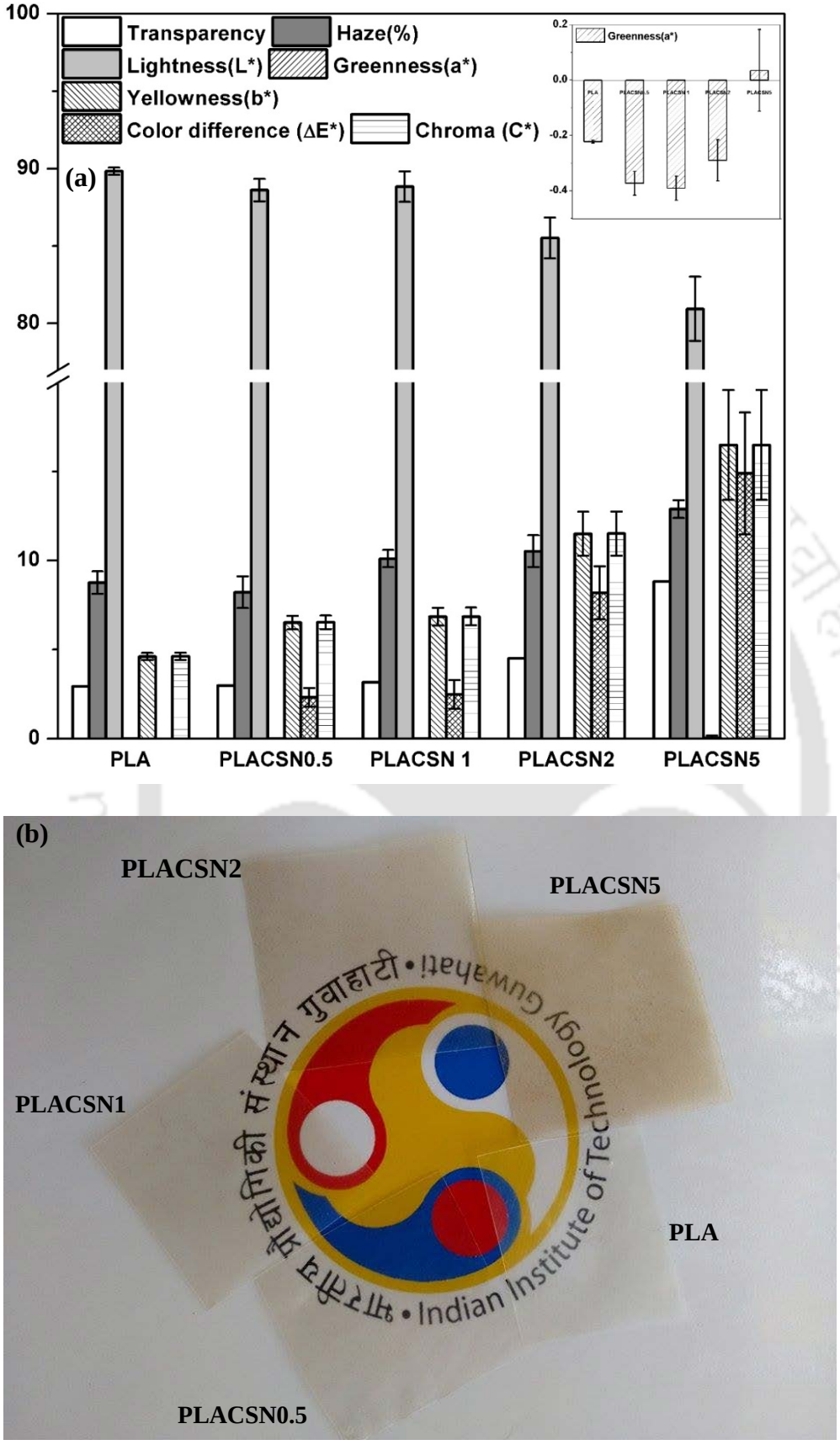

Figure 4.11: (a) Transparency, haze and color parameters, inset: greeness values and (b) visual photographs for PLA and PLA/CSN bionanocomposites.

The films' color CIE values (L^*, a^*, and b^* color values) and total color difference (ΔE_{ab}) are shown in Figure 4.11(a) and summarized in Table 4.3. The incorporation of CSNs at low loadings slightly decreased L^* and at higher loadings (> 2 wt%) decreased L^* values considerably which indicates an increase in film darkness. The L^* values for PLA is measured as 89.83±0.2 whereas on incorporation of filler at 0.5, 1, 2 and 5 wt%, the L^* values decreased to 88.61±0.7, 88.84±1.0, 85.52±1.3and 80.94±2, respectively. The brownish color of the bio-filler imparts color to the films leading to reduction in whiteness. Bionanocomposite films showed a greenness increment initially which decreases again at higher loadings. PLA/CSN bionanocomposites showed a yellowness intensification by a significant increase in b^* values when compared to PLA films. The values of a^* increase at higher loadings and are measured to be more than PLA indicating that the films show increase in redness. The yellowness (b^*) values increased from ~4.6 to ~16.5. In general, PLA bionanocomposites appeared darker, greener, and yellower as compared to PLA, and these changes were directly dependent on CSN loading. The higher yellowness values for bionanocomposites are in agreement with visual observations, as shown in Figure 4.11(b).

ΔE^* values showed that incorporation of CSNs affected total color differences. Similar changes in film CIE values have been reported previously **(Molinaro et al., 2013)**. The color difference may be due to the degree of dispersion of the filler in the PLA matrix which depends on surface hydrophobicity. Higher ΔE^* values were due to incomplete dispersion of CSN which bring about significant change in color between PLA and PLA/CSN bionanocomposite films. The C^* increases from 4.62±0.2 to 16.49±3.08 with increase in CSN loading indicating the increase in saturation of colors.

Table 4.3: Various optical parameters such as transparency, haze and color measurements for PLA and PLA/CSN bionanocomposites.

CSN (wt%)	Film Thick-ness (µm)	Trans-parency (mm^{-1})	Haze (%)	Lightness (L*)	Greenness (a*)	Yellow-ness (b*)	Color difference (E*)	Chroma (C*)
0	93.15	2.95	8.76±0.63	89.83±0.2	-0.22±0.01	4.61±0.20	-	4.62±0.20
0.5	106.86	2.99	8.22±0.89	88.61±0.7	-0.37±0.04	6.52±0.38	2.32±0.52	6.53±0.39
1	100.79	3.18	10.11±0.49	88.84±1.0	0.39±0.04	6.85±0.50	2.49±0.80	6.86±0.50
2	101.97	4.51	10.53±0.89	85.52±1.3	0.29±0.08	11.51±1.23	8.19±1.49	11.51±1.23
5	98.35	8.82	12.89±0.50	80.94±2.1	0.04±0.15	16.49±3.08	14.90±3.42	16.49±3.08

4.2.8 Surface wetting properties of PLA/CSN bionanocomposites

Wetting behavior of the biocomposites, such as contact angle and total surface free energy, was analyzed using water and diiodomethane as polar and non-polar liquids, focusing on the effect of filler loading. The hydrophobicity of the films becomes more prominent upon addition of fillers. The increase in contact angle with water and decrease with diiodomethane shows an increasing hydrophobic character of the bionanocomposites. The hydrophobicity as well as the dispersion of fillers influence the contact angle of the bionanocomposites. The contact angles (see Figure 4.12(a)) increase initially and are highest for PLACSN1 but decrease upon futher increase in CSN loading, which indicates agglomeration **(Palakattukunnel et al., 2011)**. Surface energy is related to the interface between two phases. Variation of surface free energy of the PLA and PLA/CSN films can be seen from the Figure 4.12(b). Surface free energies for all filled bionanocomposites are lower than that of PLA with the lowest value observed for PLACSN1, indicating that less wetting of liquids is experienced compared to neat PLA specimens. For bionanocomposites, total energy first decreases then increases which shows that the nature of forces acting on the composite surface is different **(Palakattukunnel et al., 2011)**. Hydrophobicity is indicated by higher contact angle and smaller surface energy **(Adamson and Gast, 1997)**. As a result of increase in hydrophobicity, the dispersive component decreases and polar component increases. As the contact angle increases, the surface free energy shows a decreasing trend and vice-versa **(Neumann et al., 1974)**.

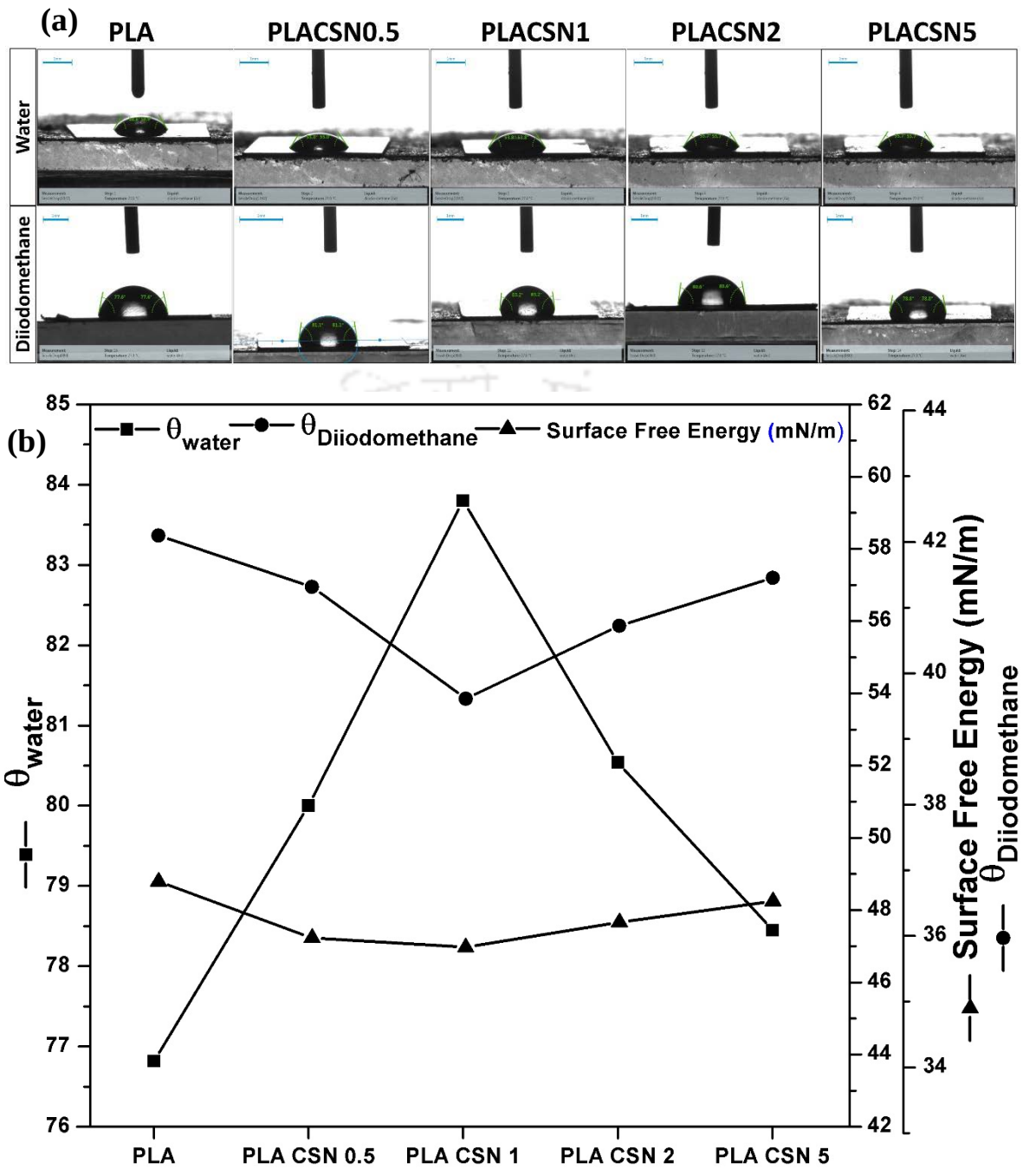

Figure 4.12: (a) Contact angles with water and diiodomethane and (b) surface free energy (SFE) and contact angles for PLA and PLA/CSN bionanocomposites used in this study.

4.2.9 Melt flow index (MFI) for PLA/CSN bionanocomposites

The melt flow index (MFI) value for PLA obtained was ~6, which is close to the values reported in literature **(Zhou and Xanthos, 2009)**. The melt flow characteristics summarized in Table 4.4 shows that the bionanocomposites have a reduced viscosity which improves the flow properties due to slippage of molecular chains over the filler

materials. The increase in MFI can also be attributed to similar reduction in intrinsic viscosity values. The increased MFI values show reduction in viscosity resulting from degradation due to shear stresses during melt processing.

Table 4.4: Melt flow, intrinsic viscosity, acid value and specific rotation values for PLA and PLA/CSN bionanocomposites.

Material	Melt flow index	Intrinsic Viscosity (ml/g)	Molecular Weight (Mv)	Acid value (mg KOH/g polymer)	Specific rotation (°)
PLA	6.0	172.20	70030	1.60	-156.13
PLACSN0.5	9.0	171.74	69775	0.82	-152.37
PLACSN1	12.7	174.87	71521	1.61	-156.89
PLACSN2	16.1	171.18	69464	1.76	-151.49
PLACSN5	20.9	157.86	62166	2.22	-138.71

4.2.10 Intrinsic viscosity measurements for PLA/CSN bionanocomposites

Intrinsic viscosity measurements were carried out to understand the structural changes taking place due to incorporation of CSNs in PLA matrix. Measurements were performed for sample dissolved in chloroform using a temperature controlled Ubbelholde-type capillary viscometer. The concentration range was between 2.25 to 6.67 mg/ml, and temperature was maintained at 25 °C. The biofiller was filtered using 0.2 μm syringe filters. As can be seen from Figure 4.13(a–b) the correlation (R^2) values for Kraemer and Huggins plots for PLA and PLA/CSN bionanocomposites are close to 0.95. Intrinsic viscosity values summarized in Table 4.4 show reduction, as the CSN loadings increase. The calculated intrinsic viscosity and viscosity average molecular weight values for PLA were 172.2 g/ml and 70030 Da, respectively. Similar values have been previously reported in literature **(Zhou and Xanthos, 2009)**. After addition of CSN, the nanocomposites showed lower values, except at 1 wt% CSN loading, which shows improvement in intrinsic viscosity and molecular weight (174.87 g/ml and 71521 Da, respectively). Interestingly, PLACSN1 shows increase in intrinsic viscosity, which is due to the improved attractive interaction between filler and matrix resulting in reinforcement effect.

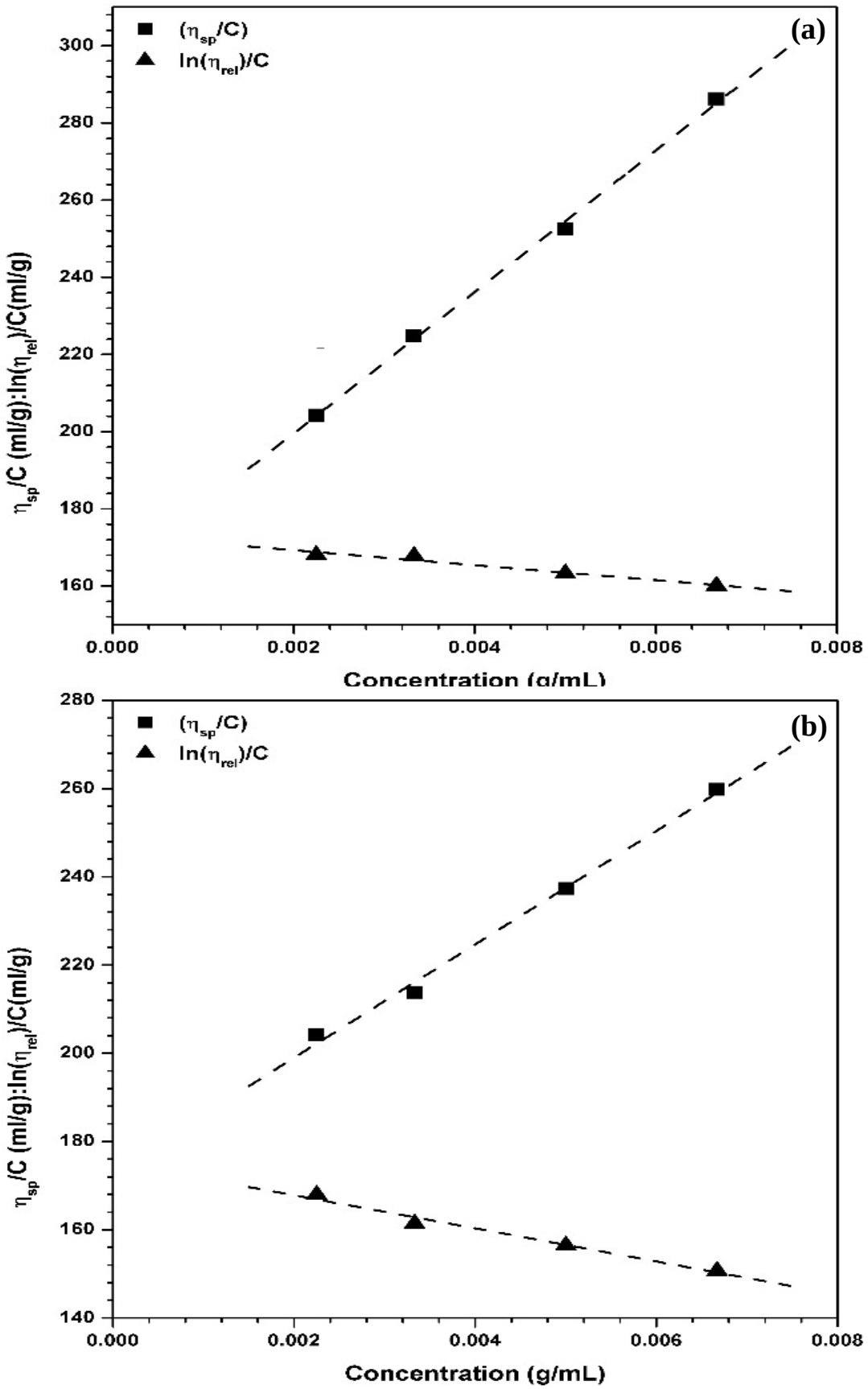

Figure 4.13: Intrinsic viscosity plots (Huggins and Kraemer plots) for (a) PLA and (b) PLACSN1 bionanocomposite.

4.2.11 Acid value (AV) investigations

Acid value is a measurement of the carboxyl and hydroxyl end groups, which increase due to various degradation reactions such as β-scission, hydrolysis, and trans-esterification reactions. As seen from values in Table 4.4, the acid values increase with increase in CSN loading. Interestingly, the acid value is lower or similar to pure PLA up to 1 wt% CSN addition which shows that lower loadings of CSN do not affect the thermal stability of the bionanocomposite.

4.2.12 Specific rotation analysis

The specific rotation of PLA is observed at -156.13°, as presented in Table 4.4. Similar results are reported for PLA by **Katiyar and Nanavati (2011)**. The specific rotation values of PLA remain unaltered upon addition of CSN up to 2 wt%, which means that optical purity of PLA (98.6% L form) remains unaltered even after addition of CSN.

4.3 Summary

Silk nano-discs (CSNs) have been extracted from waste Muga silk through a facile one-step acid hydrolysis process and melt processed with PLA in various ratios at laboratory scale using co-rotating mini twin-screw extruder. Melt processing has been adopted as a solvent free approach to disperse CSN into the PLA. Various analytical techniques relating to structural, thermal, surface, mechanical and barrier properties of bionanocomposites were employed. XRD confirms increase in crystallinity from 30 to 45% and CSN intercalation in the PLA matrix while FTIR studies showed amide peak shift confirming the physico-chemical interaction between CSN and PLA. CSN due to its hydrophobic nature, is well dispersed in the PLA system. This improved dispersion of filler has a positive influence on the thermal properties; DSC analysis shows that at optimum loading of 1 wt% CSN, T_{cc} and T_m are decreased and the heat of fusion ΔH_m is higher as compared to neat PLA suggesting increment in nucleating sites and possible physico-chemical interaction between PLA and CSN. The thermal stability of PLA/CSN bionanocomposites, studied using TGA, was improved by ~10 °C. For 1 wt% filler loading, the film showed improvement in toughness, percentage elongation and improved storage modulus by ~70%, ~ 40% and ~12% respectively (over neat PLA) as a result of effective reinforcement of PLA by CSN biofiller. By the uniform dispersion of CSNs in PLA matrix, the gas barrier properties viz. oxygen and water vapor permeability values were reduced by ~70% and ~28%, respectively. It is observed that presence of nanofiller at low loadings lowers

the transparency marginally (~8%). To conclude, significant property enhancements are observed upon addition of small amounts of CSN in the PLA matrix. Moreover, both CSN and PLA are obtained from renewable natural resources that are abundant, non-toxic and in true sense, fit well in the class of ‘green’ bioplastics for food packaging applications.

Chapter 5

Influence of Crystalline Silk Nano-discs (CSNs) on the Crystallization Behavior of Melt-extruded PLA Films

This chapter demonstrates the influence of novel biofiller crystalline silk nano-discs (CSNs) on crystallization behavior of melt-extruded PLA to measure the thermodynamic parameters which are essential during processing of polymers. The study of crystallization behavior is also equally important for improvement in properties of nanocomposite to be suitable for various value added products. The crystallization behavior is studied using non-isothermal cold crystallization and isothermal melt crystallization using differential calorimetry. Both the phenomena are also studied through spherulite morphology and growth rate using polarizing microscopy. Avrami equation was used to calculate nucleation parameter and crystallization rate constant. Crystallization data is analyzed by Jezioney, Liu-Mo and Tobin models to determine useful crystallization information. Incorporation of CSNs facilitates the crystallization process. Addition of CSNs in PLA matrix results in lower cold crystallization temperatures and shorter crystallization half-time with enhanced growth rates. It is found that CSNs act as heterogeneous nucleating agents, hence improve non-isothermal crystallization kinetics of PLA. Spherulitic morphology and growth rates were examined over a wide range of crystallization temperatures (90-120 °C). Improvement in crystal nucleation density is observed as CSNs contribute towards new nano-nucleation sites. With incorporation of CSN, the crystallization kinetics were modified, the overall isothermal melt crystallization rates of PLA/CSN increased, however the crystallization mechanism remained unaltered. The apparent activation energy and surface energy barrier for crystallization process are decreased upon addition of silk nano-discs. At lower isothermal crystallization temperatures (T_c) viz. (90-100 °C), reduced growth rates of PLA spherulites is observed. Both PLA and PLA/CSN exhibited highest crystallization rates ~107 °C.

The work in this chapter is published as:

- R. Patwa, A. Kumar and V. Katiyar, "Isothermal crystallization kinetics and hydrolytic degradation studies of poly (lactic acid)/crystalline silk nano-discs based bionanocomposites," J. Appl. Polym. Sci., vol. 135, pp. 46590-46618, May 2018, DOI: 10.1002/app.46590.
- R. Patwa, Monika, A. Kumar and V. Katiyar, "Thermal stability and non-isothermal crystallization kinetics of silk nano-discs reinforced poly (lactic acid) bionanocomposites," Polym. Bull. (Under review).

5.1 Introduction

PLA suffers from various natural drawbacks like low glass transition temperatures, poor thermal stability, high costs, slow crystallization rate and brittle nature have obviated its widespread commercial usage. The crystallization of polymer affects the material properties and also process control which is indispensable part of polymer processing. Physical characteristics of PLA decides the product performance which largely depend on crystallization behavior. Kinetic analysis can provide information on energy barriers and mechanisms of crystallization. Crystallization phenomenon occurs during manufacturing process mainly extrusion and injection molding, a faster crystallization rate would reduce fabrication time leading to reduced cost of final product. Non-isothermal crystallization studies can be more meaningful than isothermal ones as they can help mimic the conventional industrial processing **(Pivsa-Art et al., 2016)**.

Consequently, different strategies have been employed to enhance the crystallization rate by incorporation of nucleating agents such as fillers, polymer blending and stereocomplexation, etc. Among these, the use of micro or nano-fillers as nucleating agents has been considered the most venerable approach. Most routine examples include clay, talc, carbon black, etc. **(Lee et al., 2008; Pivsa-Art et al., 2016; Su et al., 2009b; Tesfaye et al., 2017)**. Of late, the culpability of inorganic fillers in polluting ecosystem from their production till end-use has been established **(Albrecht et al., 2006)**. An ideal filler material should essentially be non-toxic as well as biodegradable, if the biocomposites is intended for sustainable food packaging applications because of their direct contact with the food items **(Tan et al., 2015)**. In view of this, much scientific research is being carried out towards exploring non-toxic fillers for PLA based nanocomposites **(Claramunt et al., 2016; Thakur et al., 2016)**. Green fillers such as cellulose nanocrystals, chitosan, sucrose palmitate, etc. **(Dhar et al., 2017; Pal and Katiyar, 2016; Valapa et al., 2016)** are low cost, abundant, light-weight, biodegradable and biocompostable, etc.

The use of silk based organic fillers for PLA generates a new class of complete biodegradable composites making it a suitable reinforcement for PLA due to its superior mechanical properties, biocompatibility and biodegradability. Silk has a morphologic flexibility which has opened new avenues for applications like high engineering materials, tissue engineering, food packaging, biomedical engineering etc. Silk can be used as a PLA reinforcement in form of fibers, blends and nanoparticles, etc. Very few have reported the

impact of silk or silk derivatives on crystallization properties of PLA **(Qiao et al., 2009)**. **Tesfaye et al. (2017)** have performed investigations on the isothermal crystallization kinetics and thermal degradation of PLA/silk nanocrystals nanocomposites under repetitive extrusion process. Another modification of silk is the crystalline silk nano-discs (CSNs), which are highly crystalline nanoparticles having a well-defined disc--type morphology. Such materials have not been reported so far to the best of our knowledge. In this investigation, the influence of silk nano-discs (CSNs) loading on crystallization behavior, kinetics of PLA/CSN bionanocomposites has been investigated using various techniques. The crystallization behavior is studied using non-isothermal cold crystallization and isothermal melt crystallization using differential calorimetry. Both the phenomenon are also studied through spherulite morphology and growth rate using polarizing microscopy. It is expected that the research reported herein can allow for enhancing the crystallization behavior of the system to decide for potential applications.

5.2 Theoretical considerations for non-isothermal crystallization kinetic computations

5.2.1 Relative degree of crystallinity

The relative crystallinity for PLA and PLA bionanocomposites can provide useful information about the influence of additives/fillers on non-isothermal crystallization behavior. From the DSC thermograms, the temperature (T) dependent relative crystallinity (X_T) for different heating rates is obtained as per Eq. (5.1):

$$X_T = \frac{\int_{T_0}^{T_c}\left(\frac{dH}{dT}\right)dT}{\int_{T_0}^{T_e}\left(\frac{dH}{dT}\right)dT} \quad (5.1)$$

Where, T_c, T_0 *and* T_e are the instantaneous, onset and end point of crystallization temperatures, respectively. dH /dT denotes the heat flow rate. Temperature dependent values $X(T)$ can be changed to time scale (X_t) by the following Eq. (5.2):

$$t = \frac{(T - T_o)}{\beta} \quad (5.2)$$

Where, T is the crystallization temperature at time t, and β is the heating rate. Relative crystallinity (X_t) is the most important measurement for analyzing the crystallization behavior, it can also be expressed as a function of time (t) by Eq.(5.3) **(Ding et al., 2015)**:

$$X_t = \frac{\int_{t_0}^{t_c}\left(\frac{dH}{dt}\right)dt}{\int_{t_0}^{t_e}\left(\frac{dH}{dt}\right)dt} \quad (5.3)$$

The experimental data from DSC analysis were further analyzed using several mathematical models which are described below in detail.

5.2.2 Modified Avrami analysis or Jeziorny's model

Avrami equation **(Avrami, 1940)** is generally applied to understand isothermal crystallization phenomenon, the changes in relative crystallinity can be related with time as per the following relation Eq. (5.4):

$$1 - X(t) = exp(-Z_A t^{n_A}) \tag{5.4}$$

Where, X_t is the relative crystallinity at crystallization time t, n_A is the Avrami exponent which gives information about nucleation behavior and geometry of crystals and Z_A is the crystallization rate constant which involves both nucleation and growth rate parameters. To apply for the non-isothermal crystallization behavior, **Jeziorny (1978)** incorporated the heating rate β into the crystallization rate parameter.

$$\ln Z_c = \ln Z_A/\beta \tag{5.5}$$

Where, Z_c is the modified Avrami rate constant. Taking double natural logarithm of the Eq. (5.4), the obtained expression Eq. (5.6) can be used to analyze experimental data.

$$\ln(-\ln(1 - X_t)) = n_A \ln t + ln\ Z_c \tag{5.6}$$

Where, straight line plots can be obtained between $\ln(-\ln(1 - X_t))\ vs.\ \ln t$, n_A values decrease as the heating rate is increased. Furthermore, half-time of crystallization can be measured from kinetic parameter using Eq. (5.7):

$$t_{0.5} = \left(\frac{\ln 2}{Z_A}\right)^{(1/n_A)} \tag{5.7}$$

5.2.3 Liu & Mo analysis

Liu et al. (1997) developed a new method to describe non-isothermal crystallization which is combination of Avrami and Ozawa equation. The various physical variables involved are heating rate β, relative degree of crystallinity (X_t), temperature of crystallization *T*.

$$\log(Z_t) - n \log t = \log K(T) - m \log t \tag{5.8}$$

Rearranging, Eq. 5.8 into the following form:

$$\log \beta = \log F(T) - \alpha \log t \tag{5.9}$$

The expression Eq. (5.9), gives straight lines whose slopes and intercept provides useful kinetic parameters such as $[F(T) = [K(T)/k_A]^{1/m}]$ defined as heating rate to reach a defined degree of crystallinity at unit crystallization time, α = n/m which is ratio of Avrami to Ozawa exponent. This method can be used to plot $\log \beta \; vs. \log t$, for a certain degree of crystallinity. The values of *F(T)*, increases with increasing relative crystallinity.

5.2.4 Tobin analysis

Avrami theory ignores the effects of growth site impingement and secondary crystallization to ensure simplicity. **Tobin (1974)** proposed a theory for phase transformation kinetics which consider effects of growth site impingement, relative crystallinity/time relation is expressed as Eq. (5.10):

$$X(t) = \frac{(k_T t)^{n_T}}{1+(k_T t)^{n_T}} \tag{5.10}$$

The above expression can be modified, to obtain Eq. (5.11):

$$\log\left(\frac{X_t}{1-X_t}\right) = \log k_T - n_T \log t \tag{5.11}$$

Where, X_t is relative crystallinity at time t, n_T and k_T are Tobin exponent and Tobin crystallization rate constant, respectively. The value of n_T need not necessarily be an integer and depends on nucleation and growth mechanisms, its value deceases with increasing heating rate. The values of n_T are larger than n_A, though both have similar physical meanings.

5.2.5 Crystallization activation energy

5.2.5.1 Kissinger method

The non-isothermal crystallization is greatly influenced by heating rates. To evaluate the overall effective energy barrier (*ΔE*), **Kissinger (1956),** proposed a method based on variation of crystallization peak temperature (T_p) with heating rate (β).

$$\frac{d[ln(\beta/T_p^2)]}{d[(1/T_p)]} = \frac{-\Delta E}{R} \tag{5.12}$$

Where, β is the heating rate, R is the universal gas constant and T_p is peak crystallization temperature and *ΔE* is the effective energy barrier (kJ/mol).

Plots of $\left[ln\left(\beta/T_p^2\right)\right] vs. \left[\left(1/T_p\right)\right]$ will generate straight line plots. The negative slope values suggest that crystallization rate increases with increasing temperature.

5.2.5.2 Takhor method

Similarly, **Takhor (1971)** suggested another model:

$$\frac{d\left[ln\left(\beta/T_p\right)\right]}{d\left[\left(1/T_p\right)\right]} = \frac{-\Delta E}{R} \tag{5.13}$$

Where, β is the heating rate, R is the universal gas constant and T_p is peak crystallization temperature and ΔE is the effective energy barrier (kJ/mol).

5.2.6 Nucleation activity

Dobreva and Gutzow (1993) calculated nucleating activity. For homogeneous nucleation as well as heterogeneous cooling rate can be expressed using Eqns. (5.14 & 5.15):

$$\ln \beta = A - \left(\frac{B}{2.303\ \Delta T_p^2}\right) \tag{5.14}$$

$$\ln \beta = A - \left(\frac{B^*}{2.303\ \Delta T_p^2}\right) \tag{5.15}$$

Where, β is the heating rate, A, B and B^* are constants and $\Delta T_p = T_m - T_p$, ψ is the nucleation activity defined by:

$$\psi = \frac{B^*}{B} \tag{5.16}$$

As per above expression, if filler is an active nucleating agent ψ value is close to 0, if it is inert, values approach to 1. The plots of $\ln \beta\ vs. \left(1/\Delta T_p^2\right)$ gives straight lines.

5.3 Theoretical considerations for isothermal crystallization kinetic computations

5.3.1 Relative degree of crystallinity

The relative crystallinity (X_t) of PLA and PLA based bionanocomposite film provides understanding about the effect of CSN on nucleation phenomenon during isothermal melt crystallization. The relative crystallinity in terms of heat flow per gram of the sample (dH) as a function of crystallization time (X_t) can be expressed as Eq. (5.17):

$$X_t = \frac{\int_{t_0}^{t} (dH/dt).dt}{\int_{t_0}^{t\infty} (dH/dt).dt} \tag{5.17}$$

Where, dH/dt is the heat evolution rate, t_0 and t_∞ are the initial and ending crystallization times. The relative crystallinity (X_t) is calculated by integrating the area under the exothermic peak during the isothermal crystallization period during the DSC experiments. The induction times of isothermal crystallization at each crystallization temperatures were considered. The crystallization process occurs in two steps viz. primary and secondary crystallization. The primary crystallization refers to the linear portion whereas the secondary crystallization refers to the impingement crystallization which occurs in later stages and appears as non-linear portion. To, obtain kinetic parameters, relative crystallinity data in the primary crystallization region were used.

5.3.2 Avrami theory

To evaluate relevant parameters for characterizing isothermal melt crystallization kinetics, Avrami analysis is the most convenient methodology. It assumes that X_t increases with *t* as per Eq. (5.18) **(Avrami, 1941)**:

$$1 - X_t = exp(-Kt^n) \tag{5.18}$$

Where, X_t, *n, K, and t* stands for the relative crystallinity of polymer as a function of fractional crystallinity at time 't', Avrami exponent, crystallization rate constant and period of crystallization process, respectively. The Avrami exponent (n) which gives information about the crystallization mechanism and *K* takes into account the nucleation as well as crystal growth phenomenon. Usually n values are non-integer due to constant growth of crystals. Avrami equation is based on the assumption that the growth takes place radially at a constant rate, phase change does not encounter any change in volume and secondary crystallization is not considered. As per Eq. (5.19), the slope and intercept of the plot of log [-log (1-X_t)] against log (t) allows for estimation of *n* and *K* values, respectively. Other important parameters that can be derived from Avrami theory are the crystallization half time ($t_{0.5}$) and growth rate (G) that can be calculated from the Eqns. (5.20 & 5.21). The crystallization half-time ($t_{0.5}$) refers to the time consumed by the sample to reach 50% relative crystallinity. The values of ($t_{0.5}$) can effectively give the initial viewpoint about the crystallization rate. The calculated theoretical values from Avrami theory can be compared to experimental half-time values from DSC data.

$$log[-log\,(1 - X_t)] = n \log t + \log K \tag{5.19}$$

$$t_{0.5} = \left(\frac{\ln 2}{K}\right)^{1/n} \quad (5.20)$$

$$G = \left(\frac{1}{t_{0.5}}\right) \quad (5.21)$$

The isothermal crystallization behavior of PLA and PLA/CSN bionanocomposites can be estimated by calculating the apparent activation energy (ΔE_a) which can be estimated from the Arrhenius Eq. (5.22) **(Arrhenius, 1889)**:

$$\left(\frac{1}{n}\right) \ln K = \ln K_0 + \left(\frac{\Delta E_a}{RT_c}\right) \quad (5.22)$$

Where, K_0 denotes the pre-exponential factor which is temperature independent, K stands for crystallization rate constant, T_c is the crystallization temperature, R is universal gas constant. ΔE_a can be estimated from the slope straight lines obtained from plots of (*1/n*) *ln K* versus $1/T_c$.

5.3.3 Hoffman-Lauritzen nucleation theory

The Hoffman-Lauritzen theory is based on nucleation and growth phenomenon which occurs during crystallization. Crystal growth theory of is applied to determine the thermodynamic parameters pertaining to crystallization process. Growth rate (G) of spherulite was estimated from the slope of the straight line plots of spherulitic radius (R) versus time of crystallization (t) as per Equation (5.23). Nucleation density was obtained by counting the number of crystals in a particular area.

$$G = \frac{dR}{dt} \quad (5.23)$$

Temperature dependence on the growth rate (G) of a linear polymer crystal with fold chains can be expressed as Eq. (5.24) **(Hoffman et al., 1976)**:

$$G = G_0 exp\left[\frac{-U^*}{R(T_c - T_\infty)}\right] exp\left[\frac{-K_g}{f T_c \Delta T}\right] \quad (5.24)$$

Where, G_0 denotes a pre-exponential term, the first exponential part representing the growth while second exponential part representing the nucleation. 'U^*'is the diffusion activation energy required for mobility of crystallizable segment at interface, U^*= 1500 cal/mol for PLA, T_∞ is the imaginary temperature at which chains are motionless i.e. T_∞= T_g - 30K, $f = 2T_c(T_m^0 + T_c)$ is the correction factor, T_c is the crystallization temperature, ΔT is the degree of super-cooling ($\Delta T = T_m^0 - T_c$), T_m^0 is the equilibrium melting temperature,

calculated from the intersection of the lines $T_m = T_c$ and extrapolated lines of plots of T_m against T_c for PLA and PLA/CSN bionanocomposites obtained from DSC data analysis. The Eq. (5.23) can be rearranged to get the following expression Eq. (5.25):

$$\ln G + \frac{U^*}{R(T_c - T_\infty)} = lnG_0 - \left[\frac{K_g}{fT_c\Delta T}\right] \quad (5.25)$$

The nucleation constant (K_g) can be calculated from slope of plots of $\left[\left(\ln G + (U^*/R(T_c - T_\infty))\right)\right]$ against $(1/fT_c\Delta T)$. The K_g is dependent on surface free energies and expressed as Eq. (5.26) **(Zhang et al., 2002)**:

$$K_g = \frac{mb_0\sigma\sigma_e T_m^0}{k_B\Delta H_f^0} \quad (5.26)$$

Where, b_0 is space between two neighboring fold planes, σ_e and σ are the binding (basal) and lateral (interfacial) free energies of the lamellae per unit area, k_B stands for the Boltzmann constant, m is a crystallization regime dependent factor. The value of m for regime I (low temperatures) and regime III (high temperature) should be 4 and for regime II (intermediate temperatures) it should be taken as 2. The lateral surface energy (σ), can be determined using Thomas-Stavaly Eq. (5.27) **(Thomas and Staveley, 1951)**:

$$\sigma = \alpha\Delta H_f^0\sqrt{a_0 b_0} \quad (5.27)$$

Where, α=0.25, a constant for high melting polyesters, '$a_0.b_0$' are chain cross-sections of PLA crystal the dimensions of PLA crystal i.e. 5.17 and 5.97 Å, respectively. ΔH_f^0 is the equilibrium enthalpy of fusion, 1.11 x 10^8 J/m^3, i.e. product of equilibrium melting enthalpy ($\Delta H_m^0 = 93.7\ J/g$) and density (ρ_c= 1.25 g/cm^3). Using Eq. (5.26), the lateral surface free energy was calculated and came out to be 15.4 J/m^2. Same σ values were used for PLA as well as PLA/CSN bionanocomposites as incorporation of CSN do not alter the crystalline structure of PLA. Work of chain folding (q) was determined from the following relation Eq. (5.28):

$$q = 2a_0 b_0 \sigma_e \quad (5.28)$$

Where, q is the work for chain folding. The crystallization half-time estimated from Avrami theory (by DSC experiments) can also be used to replace the spherulite growth rate (G). Therefore, Eq. (5.25) can be modified Using Eq. (5.29), as follows:

$$ln\frac{1}{t_{0.5}} + \frac{U^*}{R(T_c - T_\infty)} = ln\left(\frac{1}{t_{0.5}}\right)_0 - \left[\frac{K_g}{fT_c\Delta T}\right] \quad (5.29)$$

5.4 Results and discussion

5.4.1 Influence of crystalline silk nano-discs (CSNs) on the non-isothermal cold crystallization kinetics of PLA

5.4.1.1 DSC analysis

Figure 5.1 shows the total DSC thermogram for PLACSN1 which shows no significant exothermic/endothermic events during the cooling cycle other than T_g (glass transition temperature). This indicates that it is hard to melt crystallize during the non-isothermal quenching process, thus amorphous PLA matrix is obtained. Hence, a second heating cycle was performed and all three thermal events T_g, T_{cc} and T_m (glass transition temperature, cold crystallization and melting points) were obtained from the second scanning. The non-isothermal crystallization and melting behavior studies of neat PLA and PLA/CSN biocomposites was investigated by scanning at various heating rates of 5.0, 7.5, 10.0 and 12.5 °C/min. To remove any thermo-mechanical histories, the samples were heated from ambient temperature and held isothermally at 190 °C for 3 min. Subsequently, the samples were cooled back to room temperature and again heated to 190 °C at the predetermined rates. The experimental data were analyzed through Proteus™ Thermal Analysis Software (version 6.0).

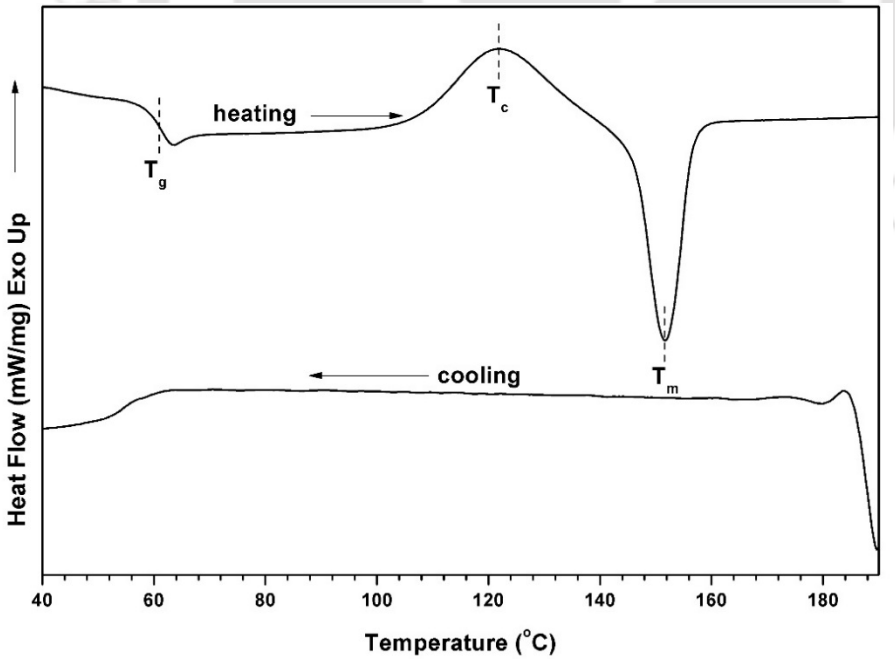

Figure 5.1: DSC thermogram of PLACSN1 at 10 °Cmin^{-1}.

5.4.1.2 Influence of CSN on thermal properties of PLA

The glass transition (T_g), cold crystallization (T_{cc}) and melting temperatures (T_m) of PLA and PLA/CSN bionanocomposites are determined using differential scanning calorimetry (DSC) are mentioned in Table 5.1.

Table 5.1: Thermal proprties of PLA and PLA/CSN bionanocomposites recorded at second heating cycle at varying heating rates.

	CSN (%)	T_g (°C)	T_{cc} (°C)	T_m (°C)	ΔH_m (J/g)	X_c (%)		CSN (%)	T_g (°C)	T_{cc} (°C)	T_m (°C)	ΔH_m (J/g)	X_c (%)
5 °C/min	0	58.7	111.7	149.4	28.6	30.6	**10 °C/min**	0	60.7	122.6	152.2	21.0	22.4
	0.5	59.9	111.5	149.5	25.8	27.7		0.5	61.4	122.9	152.5	19.3	20.7
	1	58.7	110.8	149.2	31.2	33.7		1	60.3	122.1	151.7	23.4	25.3
	2	58.8	112.6	149.9	25.8	28.1		2	60.8	123.9	152.4	19.3	21.0
	5	58.4	112	149.8	36.8	41.4		5	60.4	123.6	152.7	26.8	30.1
7.5 °C/min	0	59.8	117.9	151.1	26.0	27.8	**12.5 °C/min**	0	61.5	126.9	152.9	14.7	15.7
	0.5	59.9	118	151.1	24.0	25.8		0.5	62.6	126.2	153.4	14.3	15.4
	1	58.3	116.8	150.6	27.6	29.8		1	61.1	126.4	152.5	17.2	18.6
	2	59.9	118.7	151.5	24.4	26.6		2	61.6	127	153.4	13.3	14.5
	5	59.4	118.5	151.3	33.1	37.2		5	61.2	127.1	153.5	18.8	21.1

As predicted, cold crystallization temperature (T_{cc}) shows shifting to elevated temperatures with increasing heating rates, this can be due to the smaller supercooling phenomenon at higher heating rates as PLA has a lower heat conductivity **(Ravari et al., 2013)**. Second heating scans of neat PLA and PLA/CSN bionanocomposites obtained at various heating rates (5, 7.5, 10 and 12.5) are shown in Figure 5.2. It can be noted that for each heating rate, T_{cc} and crystallization exotherm broadness of PLACSN1 are lower and narrower, respectively in comparison to PLA. This implies that crystallization rate at 1 wt. % CSN loadings is faster than PLA suggesting that CSN act as nucleating sites for PLA crystallization. On the contrary, reverse phenomenon is observed at higher loadings, the possible reason for this could be CSN agglomerates acting as obstacles for polymer chain diffusion to nucleus surface resulting in slower motion **(Katiyar et al., 2010)**. The melting endotherm for PLA and PLA/CSN bionanocomposites show a unimodal peak ~150 °C exhibits the α-crystalline form of PLA **(Pal and Katiyar, 2016)**. A trend similar to the cold crystallization is observed for the T_m upon incorporation of 1 wt. % CSN, which validates

its nucleating ability. It can be seen that the T_g (PLA, 60.7 °C) remains unchanged for PLA/CSN bionanocomposites suggesting that the incorporation of CSN did not lead to the formation of shorter chain **(Lv et al., 2017)**.

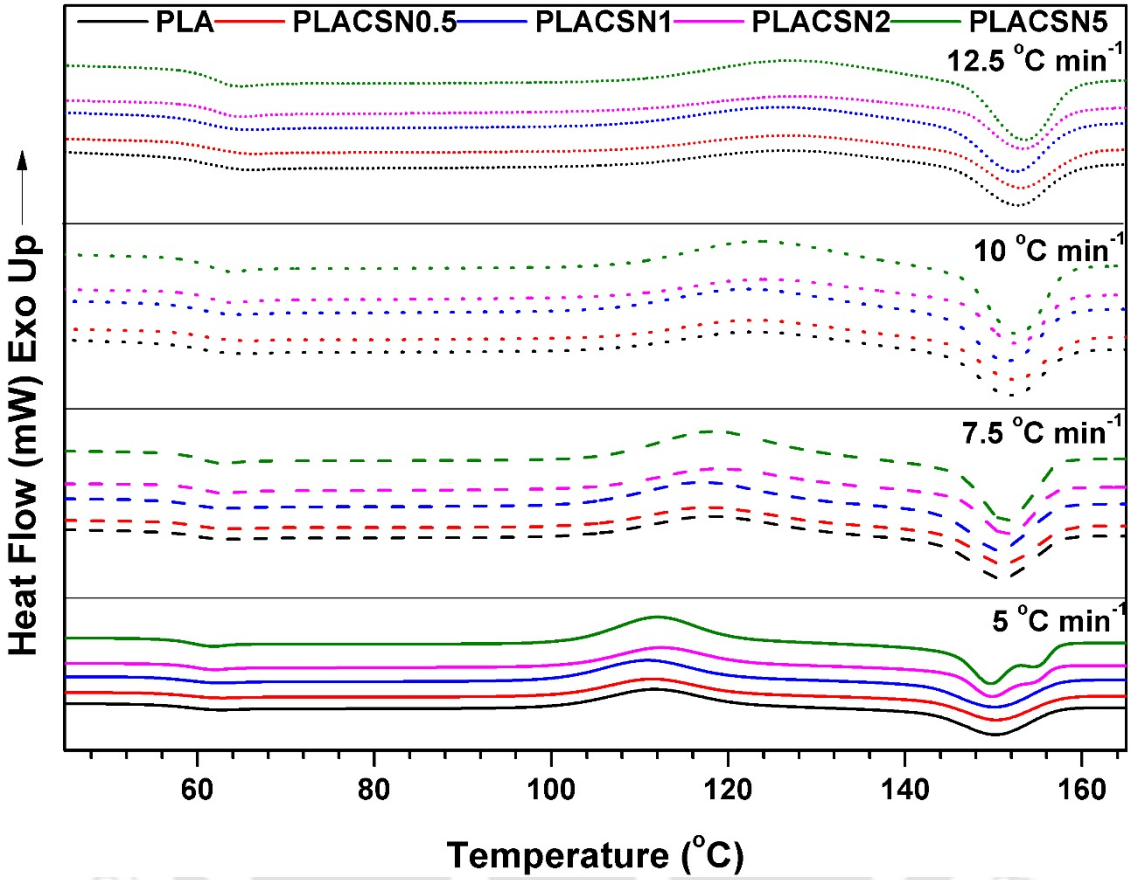

Figure 5.2: DSC thermographs at different heating rates of 5, 7.5, 10 and 12.5 °C/min for PLA and PLA/CSN bionanocomposites (second heating cycle).

5.4.1.3 Relative crystallinity

The plots of X_t versus t for PLA and PLA/CSN bionanocomposites at different heating rates are shown in Figure 5.3. It can be observed that all curves have an identical sigmoidal form, these curves progress becomes stagnant due to impingement offered by the already grown spherulites. With increasing heating rates, the sigmoidal curves shift progressively towards shorter times with higher temperatures. The crystallization half times ($t_{0.5}$) can be obtained when the X_t equals 50% and the values are tabulated as Table 5.2. The values of $t_{0.5}$ can be a direct indication for crystallization rates, a lower half-time means a faster crystallization rate. The crystallization half-times invariably decrease for PLA and PLA/CSN bionanocomposites as the heating rates increase. In addition, X_C values for PLA/CSN bionanocomposites are higher than those of PLA at each heating rate,

suggesting a higher overall crystallization rate than PLA. Accordingly, lower $t_{0.5}$ and higher $1/t_{0.5}$ values indicate that CSN acts as a nucleating agent and facilitate the crystallization process.

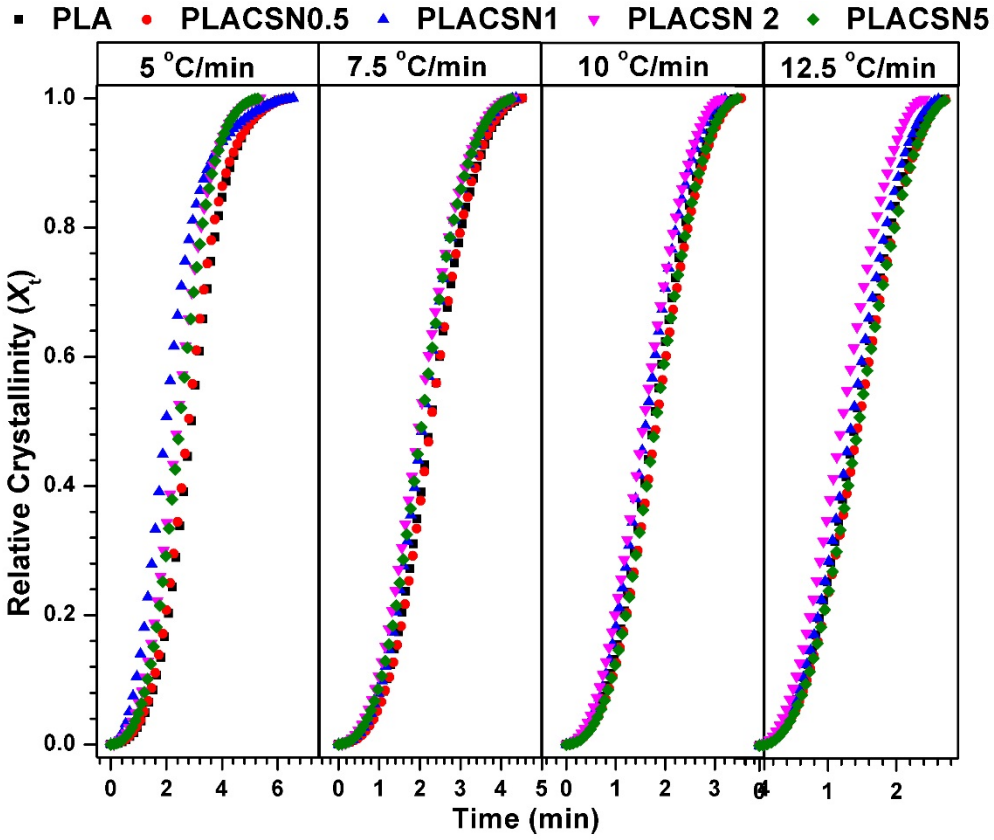

Figure 5.3: Relative crystallinity (X_t) curves of PLA, PLA/CSN bionanocomposites at heating rate of 5, 7.5, 10 and 12.5 °Cmin^{-1}.

5.4.1.4 Modified Avrami or Jeziorny's model

Modified Avrami or Jeziorny's plots for PLA and PLA/CSN bionanocomposites are shown in Figure 5.4. It can be noticed that the all plots display good linearity suggesting suitability of the theory for investigation of non-crystallization of PLA based bionanocomposites systems. The average values of Avrami exponent (*n*) for poly(lactic acid) is 2.9 while that for PLA/CSN bionanocomposites was found to be ~2.6 suggesting that the spherulite growth in bionanocomposites was imperfect or faster due to heterogeneous nucleation phenomenon occurring because of uniformly dispersed CSN.

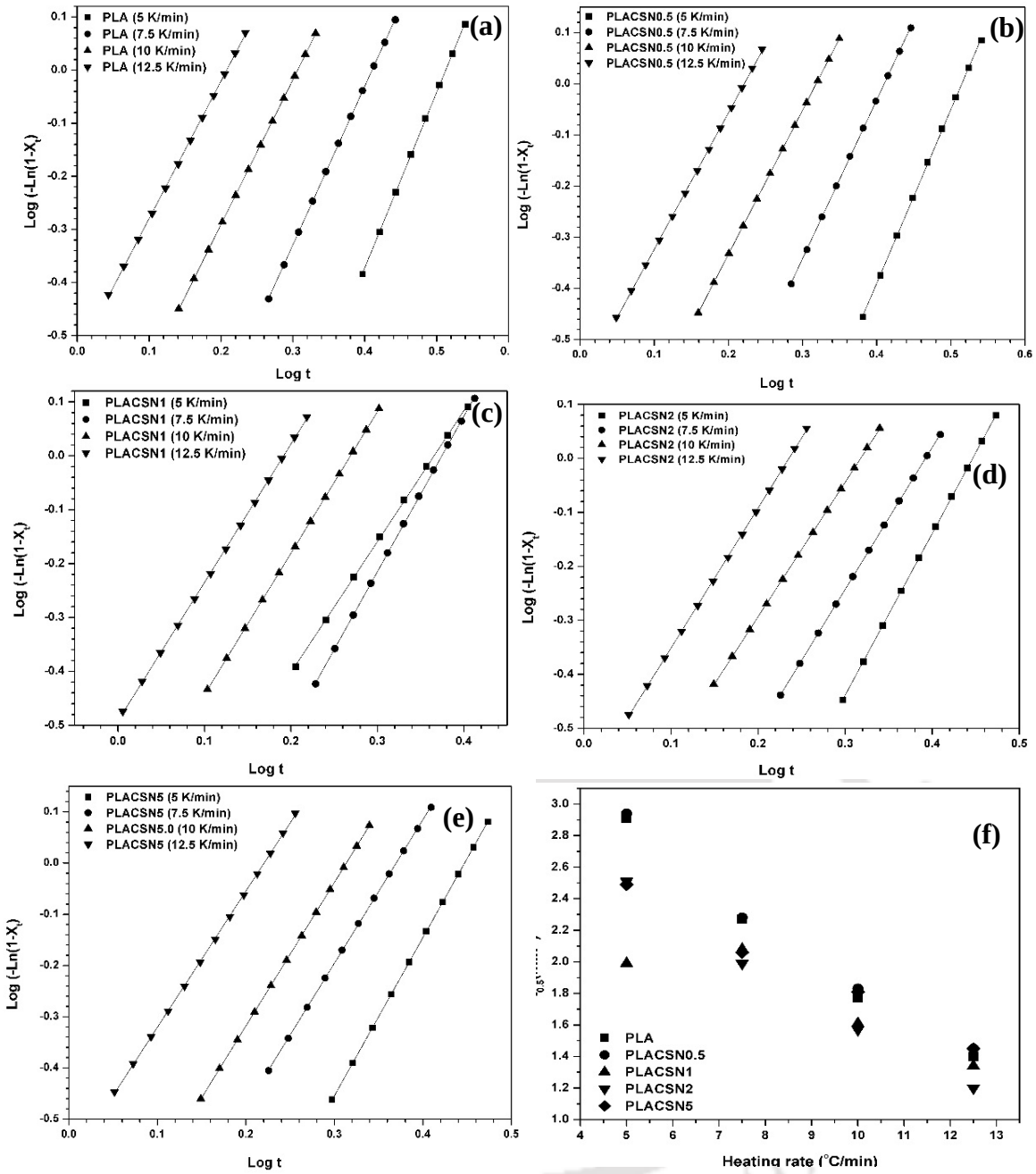

Figure 5.4: Avrami plots for non-isothermal cold crystallization of (a) PLA, (b) PLACSN0.5, (c) PLACSN1, (d) PLACSN2, (e) PLACSN5 and (f) half-time ($t_{0.5}$) for PLA and PLA/CSN bionanocomposites.

The values of k and Z_c for both PLA and PLA/CSN increases as the heating rate is increased but interestingly, Z_c values are higher for PLA/CSN bionanocomposites as compared to neat PLA which corresponds to faster crystallization rate. The crystallization half-time ($t_{0.5}$) and crystallization growth rate ($1/ t_{0.5}$) values are summarized in Table 5.2.The crystallization half-time values are less for PLA/CSN bionanocomposites as compared to PLA.

Table 5.2: Parameters from Avrami, Jeziorny, Mo and Tobin analysis.

CSN (%)	β, Kmin^{-1}	$t_{0.5}^{exp.}$ (min)	$t_{0.5}^{th.}$ (min)	$1/t_{0.5}$, min^{-1}	n	k × 10^2	Z_c × 10^3	n_T	K_T	X_t %	α	F(T)
0	5	2.92	2.91	0.34	3.3	2.0	4.1	4.4	0.009	20	1.09	11.5
	7.5	2.24	2.27	0.44	3.0	5.9	7.9	4.1	0.031	40	1.21	17.0
	10	1.76	1.77	0.56	2.7	14.6	14.6	3.8	0.107	60	1.27	22.4
	12.5	1.4	1.40	0.71	2.6	28.9	23.2	3.7	0.266	80	1.32	30.2
0.5	5	2.81	2.94	0.34	3.4	1.8	3.6	4.3	0.011	20	1.15	12.0
	7.5	2.29	2.28	0.44	3.1	5.3	7.1	4.3	0.026	40	1.26	17.8
	10	1.81	1.83	0.55	2.8	12.7	12.7	3.9	0.086	60	1.35	25.1
	12.5	1.45	1.45	0.69	2.7	25.7	20.6	3.8	0.223	80	1.38	33.1
1	5	1.99	1.99	0.50	2.4	13.0	25.9	3.5	0.088	20	1.12	10.5
	7.5	2.11	2.08	0.48	2.9	8.3	11.1	4.2	0.042	40	1.23	15.5
	10	1.62	1.61	0.62	2.6	19.7	19.7	3.7	0.158	60	1.33	21.9
	12.5	1.34	1.34	0.75	2.6	32.2	25.8	3.7	0.315	80	1.26	27.5
2	5	2.4	2.51	0.40	3.0	4.36	8.7	4.0	0.028	20	1.1	9.3
	7.5	1.99	1.99	0.50	2.6	11.36	15.1	3.8	0.069	40	1.22	14.1
	10	1.57	1.57	0.64	2.5	22.6	22.6	3.6	0.185	60	1.29	19.5
	12.5	1.2	1.20	0.83	2.4	44.5	35.6	3.4	0.493	80	1.33	26.3
5	5	2.51	2.49	0.40	3.1	4.16	8.3	4.4	0.018	20	1.52	12.0
	7.5	2.06	2.06	0.49	2.8	9.2	12.3	4.0	0.048	40	1.68	20.4
	10	1.82	1.81	0.55	2.8	13.2	13.2	4.0	0.087	60	1.75	30.9
	12.5	1.45	1.45	0.69	2.7	25.9	20.7	3.8	0.235	80	1.77	43.7

5.4.1.5 Mo and Liu method

For better physical and practical understanding of the overall process of non-isothermal crystallization of PLA and PLA/CSN bionanocomposites, Mo and Liu method Eq. (5.9) has been employed **(Liu et al., 1997)**. The kinetic parameter *F*(T) correlates cooling/heating rate to both temperature and time, depicting about the ease/difficulty of crystallization process. In precise terms, it is the value of cooling/heating required to achieve a certain degree of crystallinity in unit crystallization time **(Saengsuwan et al., 2011)**. The smaller *F*(T) value infers to faster crystallization rate. At a given relative

crystallinity (X_t), plots of log β against log t gives a straight line whose intercept and slope are log F(T) and α, respectively the values for which are listed in Table 5.2.

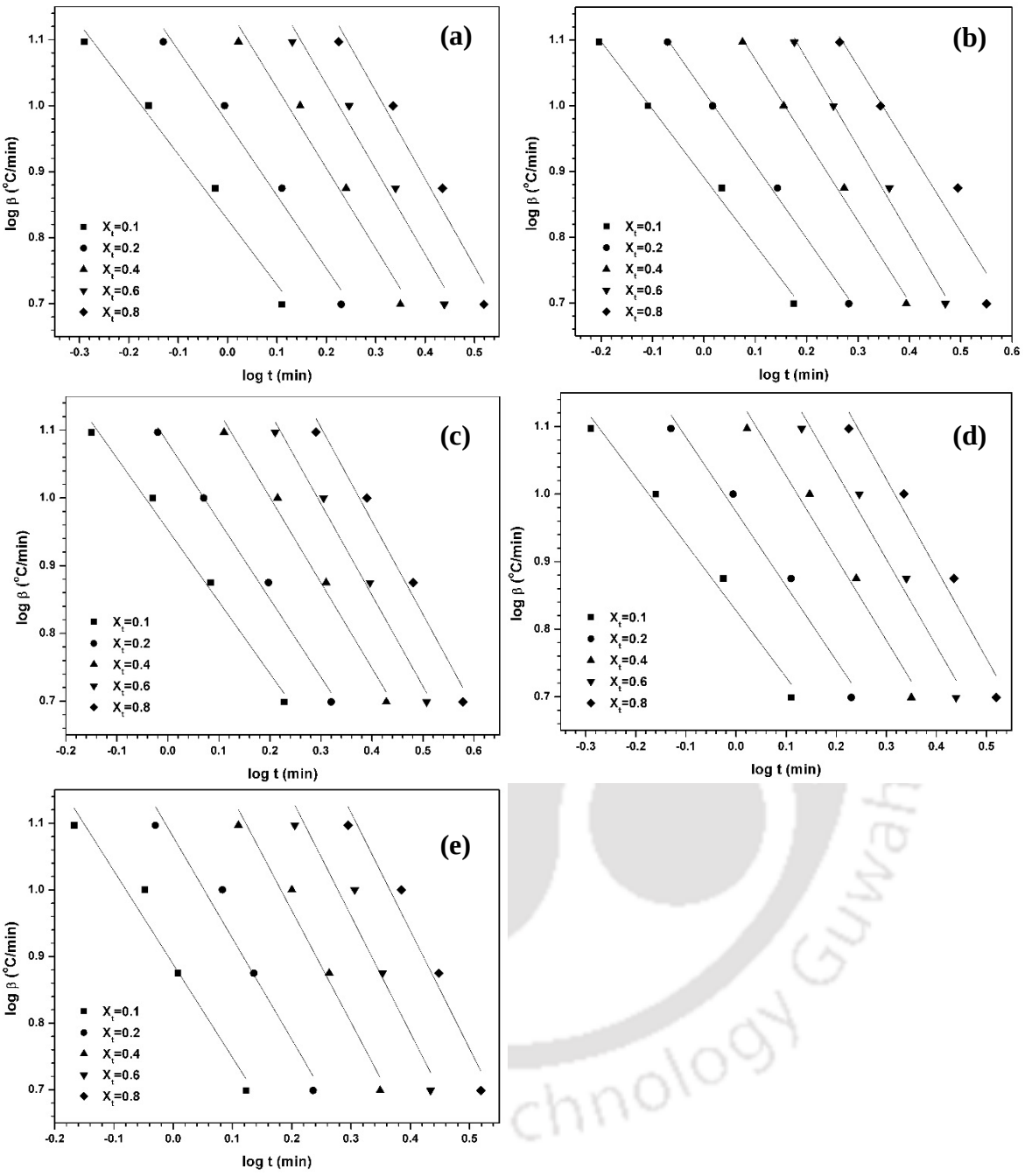

Figure 5.5: Mo and Liu plots for non-isothermal cold crystallization of (a) PLA, (b) PLACSN0.5, (c) PLACSN1, (d) PLACSN2 and (e) PLACSN5 bionanocomposites.

As seen from Figure 5.5, plots of PLA, PLA/CSN bionanocomposites show sound linearity verifying that Mo theory can be applied to the PLA and PLA/CSN system. The values of α varies from ~1.1 to ~1.4 for PLA and PLA/CSN bionanocomposites which indicate that secondary crystallization growth occurs along with the primary crystallization during the

non-isothermal crystallization. Also, PLA/CSN bionanocomposites have a higher α values as compared to PLA which shows that CSN can effectively act as nucleating agent **(Su et al., 2009a)**. The results obtained by Mo theory were found in accordance with Jezioney methods.

5.4.1.6 Tobin theory

Now, since we have an idea about nucleation effect of CSN, perhaps now Tobin theory (Eq. (5.11)) can be applied to the system which takes into account the effects of hindrance of crystallization by spherulites and secondary crystallization processes which were earlier neglected by modified Avrami theory.

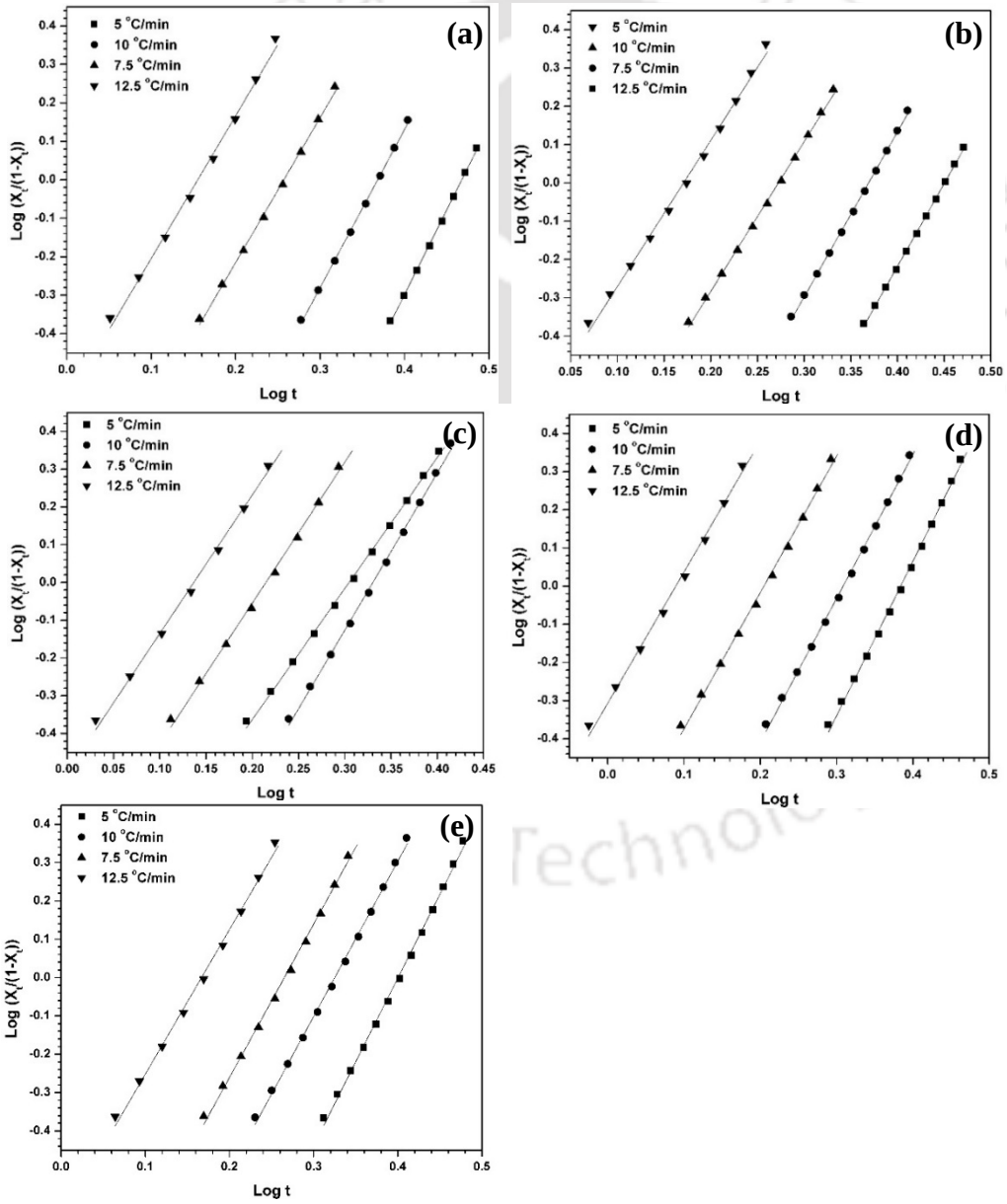

Figure 5.6: Tobin plots for non-isothermal cold crystallization of (a) PLA, (b) PLACSN0.5, (c) PLACSN1, (d) PLACSN2 and (e) PLACSN5 bionanocomposites.

The Tobin plots (Figure 5.6) are log [X_t / (1-X_t)] against log t which gives parameters n_T (slope) and K_T (intercept) known as Tobin exponent and Tobin crystallization rate constant, respectively. These values are presented in Table 5.2. It can be noticed that $\overline{n_T}$ values for PLA (~4.0) are higher than PLA/CSN bionanocomposites (~3.7) which indicate towards faster completion of crystallization or incomplete spherulitic growth. These values decrease with increase in heating rates, similar findings are reported **(Valapa et al., 2016)**. Also, the $\overline{K_T}$ values are higher for bionanocomposites, these two parameters suggest that incorporation of CSN to PLA matrix results in augmentation of crystallization rate due to the heterogeneous nucleating effect. The findings of Tobin model are consistent with the Avrami and Mo models.

5.4.1.7 Activation energy of crystallization

For estimation of the effective energy barrier (ΔE) for non-isothermal crystallization process, various mathematical models like Kissinger and Takhor models were applied. For Kissinger method, the activation energy (ΔE) required for manoeuvre of polymer chain segments to growing crystal surface is evaluated as per Eq. (5.12). The crystallization activation energy can be deduced from the slope of the plots of $ln(\beta/T_p^2)$ against $(1/T_p)$, which are shown in Figure 5.7(a). The values for activation energies are shown in Table 5.3. The values of ΔE for PLA, PLACSN0.5, PLACSN1, PLACSN2 and PLACSN5 are found to be 71.1, 72.4, 68.2, 73.8 and 70.6 kJ mol^{-1}, respectively. The PLA crystallization activation energy values matched with the values available in literature **(Wu et al., 2007)**. The PLACSN2 bionanocomposites pose hindrance to the transport of PLA chain segments towards the growing surface to a certain level during cold crystallization of PLA. This can be attributed to presence of filler. The CSN plays two roles in cold crystallization process, firstly, it behaves like heterogeneous nucleating agent to facilitate crystallization and secondly, it poses hindrance to crystallization chain movement retarding crystallization. The positive values of ΔE suggests that the rate of crystallization enhanced with increasing temperature i.e. it is the energy required for molecular chain segments for transport to the crystallizing surface. Either of the two can become dominant based on the clay content. The activation energies required for overall crystallization for PLACSN2 are higher than PLA. On the other hand, activation energy for PLACSN1 bionanocomposites is lower suggesting that CSN influence the PLA chains to crystallize easier and thus accelerating the crystallization process. This result are in agreement with modified Avrami, Mo and Tobin methods.

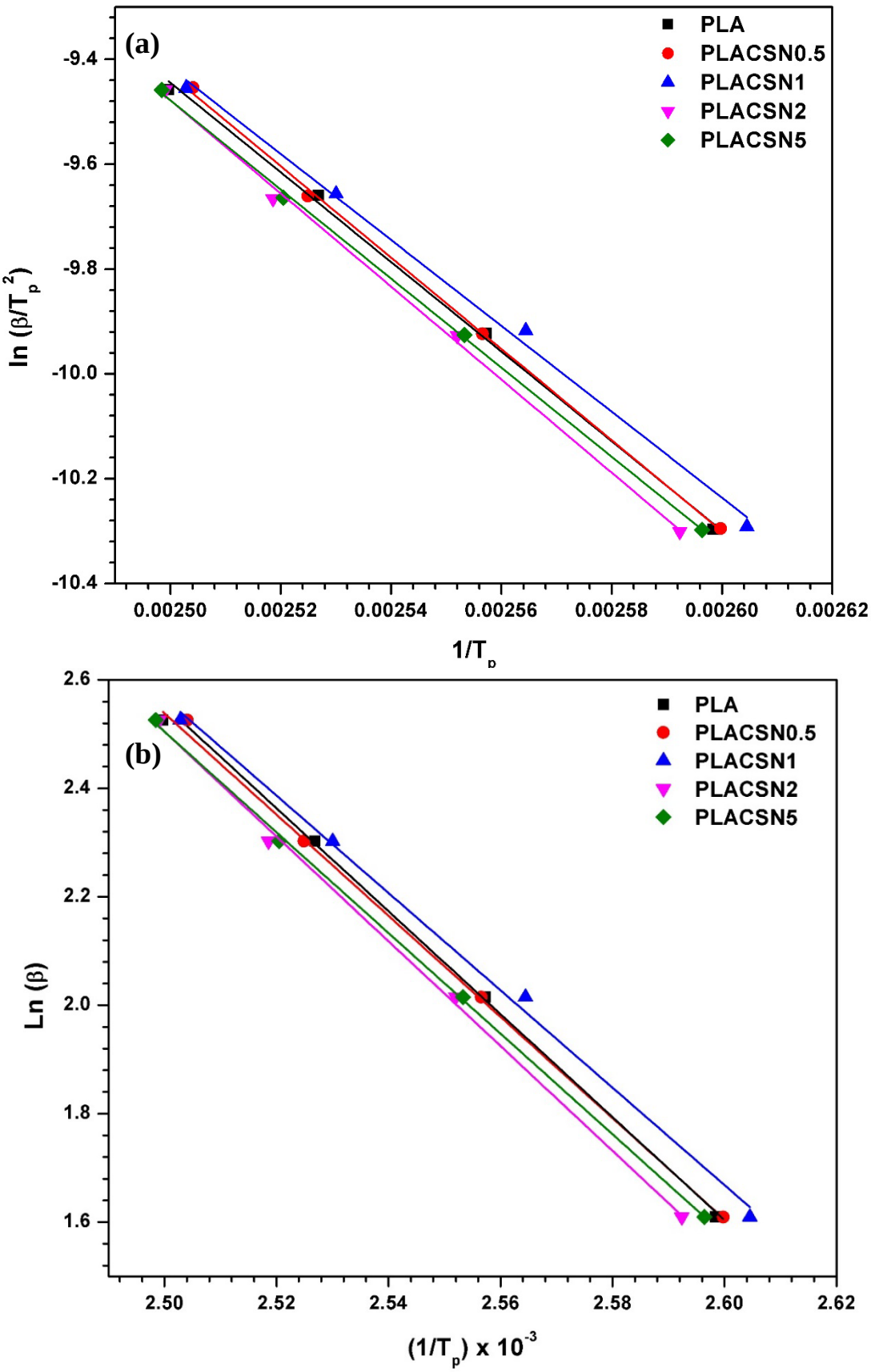

Figure 5.7: Activation energy plots for PLA and PLA/CSN bionanocomposite using (a) Kissinger and (b) Takhor model.

Takhor model (Eq. (5.13)) also showed straight lines with negative slope (Figure 5.7(b)), where CSN loading can affect the non-isothermal crystallization kinetics. Based on the above results CSN can promote crystallization phenomenon. The values of ΔE for PLA, PLACSN0.5, PLACSN1, PLACSN2 and PLACSN5 are found to be 77.6, 78.9, 74.7, 80.3 and 77.2 kJ mol^{-1}, respectively.

Table 5.3: Parameters from Kissinger and Takhor analysis.

Samples	Average Activation Energy $\overline{E_a}$ ($kJmol^{-1}$)	
	Kissinger method	**Takhor method**
PLA	71.1	77.6
PLACSN0.5	72.4	78.9
PLACSN1	68.2	74.7
PLACSN2	73.8	80.3
PLACSN5	70.6	77.2

5.4.1.8 Nucleation activity

To establish the nucleation activity of CSN, a simple estimation was applied to PLA/CSN crystallization as suggested by **Dobreva and Gutzow (1993)**. The nucleation activity (ϕ) is the factor by which the work of nucleation is reduced by the inclusion of fillers. If the filler material has a high nucleating effect its value approaches towards 0, but if it is inert the ϕ approaches to 1. Figure 5.8(a) shows nucleation activity plots for PLA and PLA/CSN bionanocomposites. The values of β and β^* for PLA and PLACSN1 calculated from the plots are 1.11 x 10^6 and 1.05 x 10^6 K^2, respectively. The nucleation factor (ϕ) was found to be 0.94, which shows that CSN has a very low nucleating effect.

5.4.1.9 Polarized optical microscopy (POM) studies

The final spherulite morphology of PLA and PLACSN1 bionanocomposite heated from room temperature to 120 °C, at a heating rate of 2.5 °C/min are shown in Figure 5.8(b-c), respectively. It is abstruse to observe the effect of CSN on the spherulite growth of PLA matrix because both materials display small-sized spherulites after non-isothermal crystallization, which is beyond the ambit for kinetic analysis. Henceforth, the non-isothermal crystallization kinetics was studied using differential scanning calorimetry (DSC) experiments.

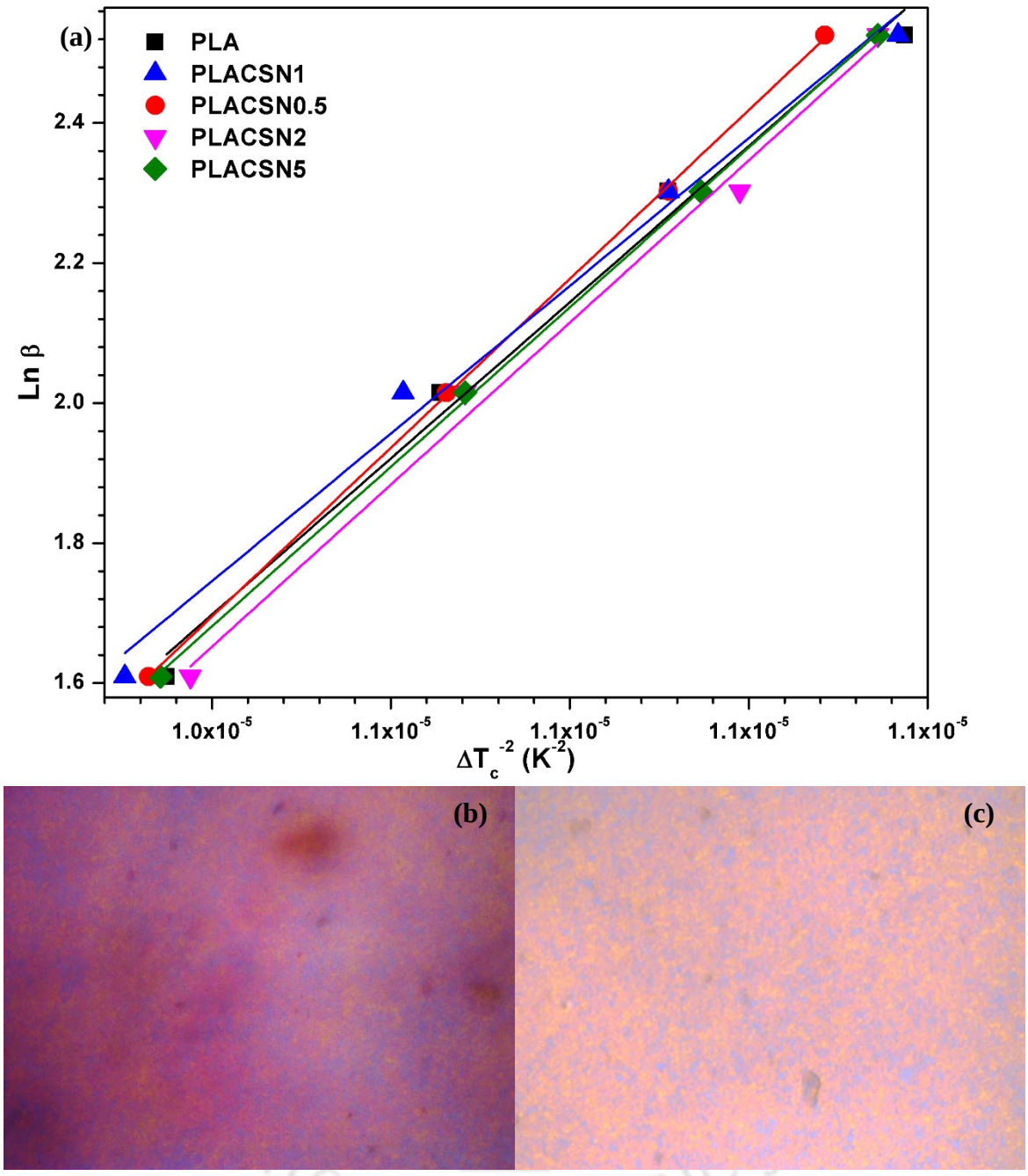

Figure 5.8: (a) Nucleation activity plots for PLA and PLA/CSN bionanocomposite, (b-c) Polarized optical micrographs of (b) PLA and (c) PLACSN1 samples after non-isothermal cold crystallization at 2.5 °Cmin^{-1} at the magnification of 500x.

5.4.2 Isothermal melt crystallization kinetics of PLA and PLA/CSN bionanocomposites

5.4.2.1 DSC analysis

The heat flow data as a function of time during isothermal crystallization exotherms of PLA and its bionanocomposites for temperatures (90–120 °C) recorded using DSC, are

shown in Figure 5.9(a-g). It can be seen that time needed to acquire the maximum crystallization depends strongly on the crystallization temperature for all samples. It is known that nucleation is better observed at lower temperatures while crystal growth can be seen better at higher temperatures, hence at 105 °C both phenomenon can be observed at optimum. This can also be supported by crystallization kinetic studies which will be conducted subsequently. As the temperature of crystallization approaches to 105 °C, The increased amplitude and sharpness indicate towards improved nucleation or crystal growth of PLA or both. While left shift shows decrease in crystallization time and increase in crystallization rate and similar observations have been reported by **Xu et al. (2015)**. These phenomena are more evident at temperatures when PLA crystallization rate is slow. This shows that crystallization performance of PLA is strongly dependent on addition of CSN which greatly reduce the required time for finishing crystallization under all crystallization temperature conditions as compared to pure PLA. Moreover, it can be seen that PLA nucleated with 5 wt. % loading showed more obvious increase of crystallization than other proportions. The progression of relative crystallinity conversion (X_t) with respect to time (t) for PLA and PLA/CSN bionanocomposites was evaluated to develop more understanding about the isothermal crystallization kinetics.

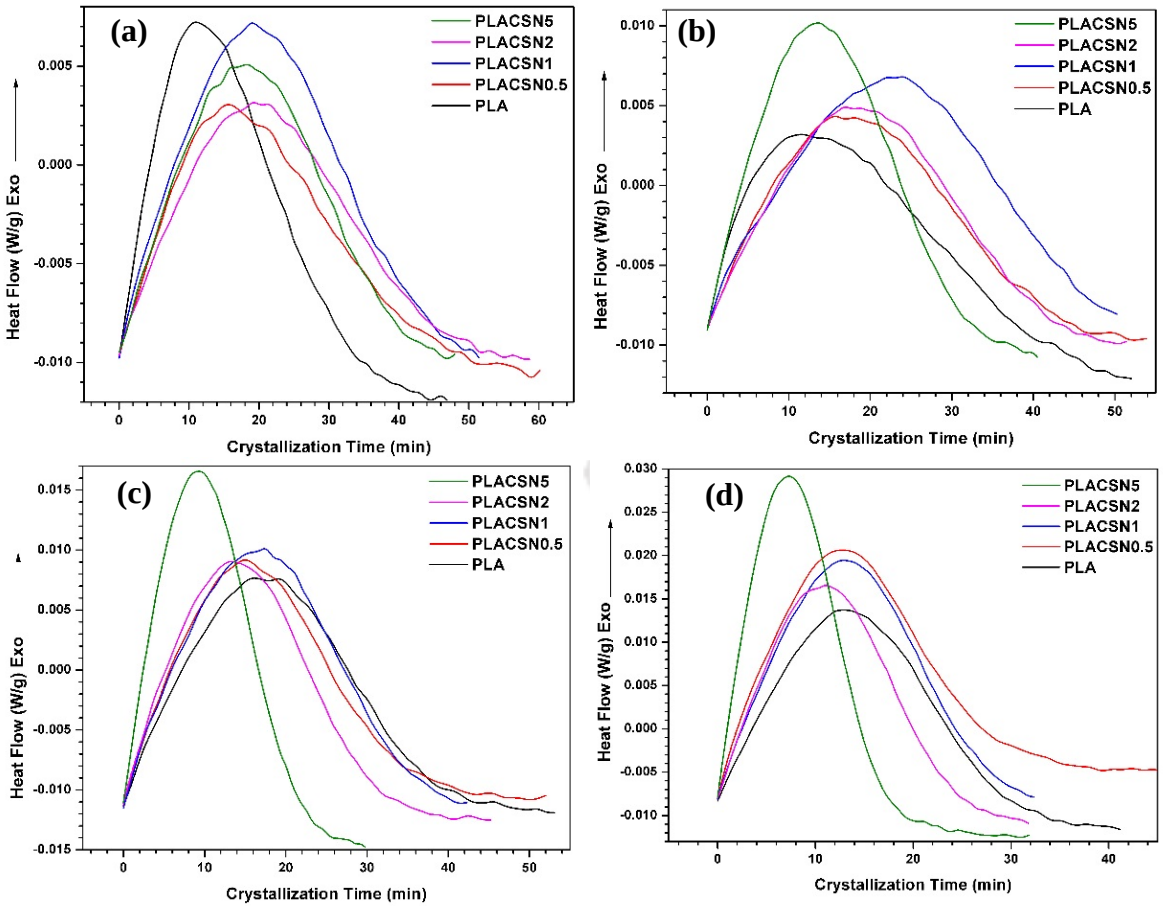

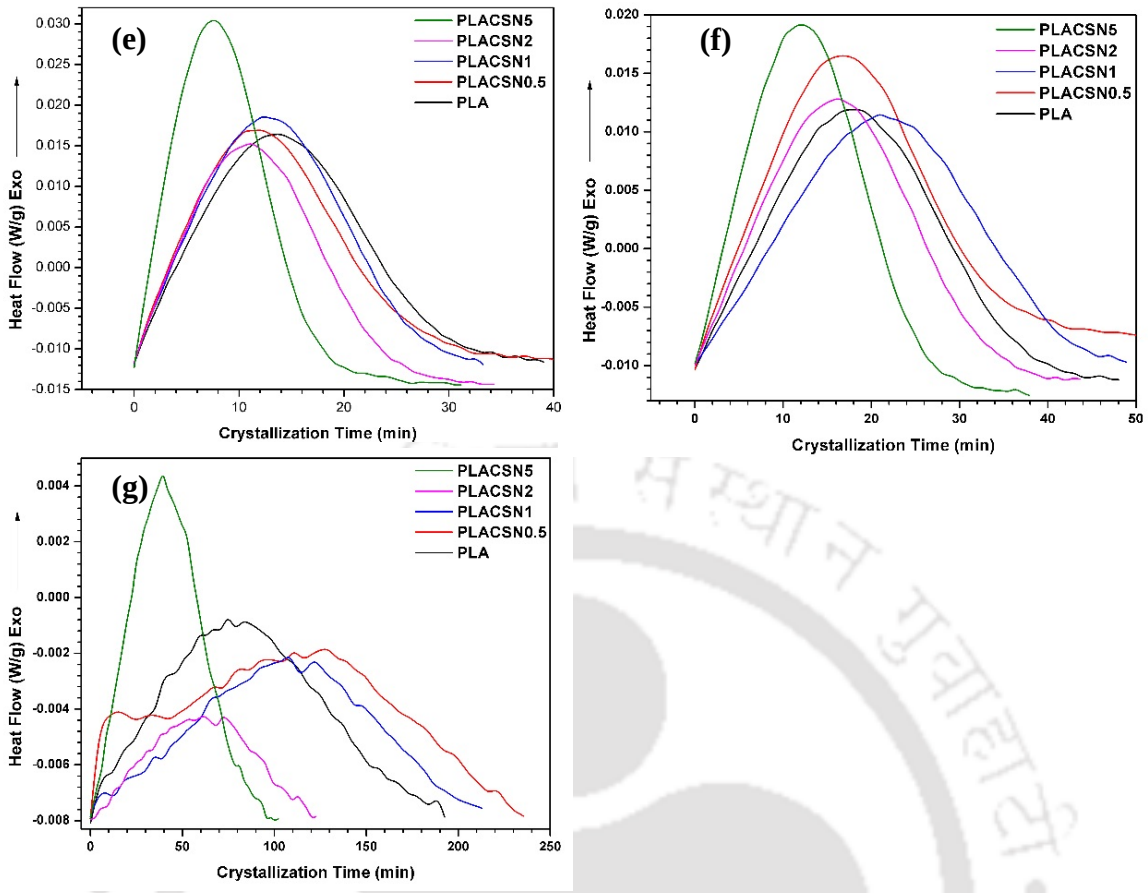

Figure 5.9: DSC isotherm for PLA and PLA/CSN bionanocomposites at various crystallization (T_c) temperatures (a) 90 °C, (b) 95 °C, (c) 100 °C, (d) 105 °C, (e) 110 °C, (f) 115 °C and (g) 120 °C.

5.4.2.2 Relative crystallinity

Calculation for relative crystallinity are based on the understanding that crystallization is an exothermic phenomenon, hence the rate of crystallization is considered to be proportional to the heat released during isothermal crystallization. Relative crystallinity of PLA and PLA/CSN bionanocomposites at different times isothermally crystallized at a certain temperature are shown in Figure 5.10(a-g), it can be noticed that the relative crystallinity plots for PLA and PLA/CSN are typically sigmoidal (S-shaped) in form and progressively shift towards lower time as the CSN content is increased. Crystallization half-time ($t_{0.5}$) can be evaluated from the relative crystallinity curves. The $t_{0.5}$ values for PLA/CSN bionanocomposites is lower as compared to PLA, for instance the $t_{0.5}$ for PLACSN5 at 120 °C, is almost halved (41.2 min) as compared to PLA (82.6 min).This shows that the crystallization rate is enhanced i.e. crystallite forming ability of PLA/CSN bionanocomposites is superior to PLA.

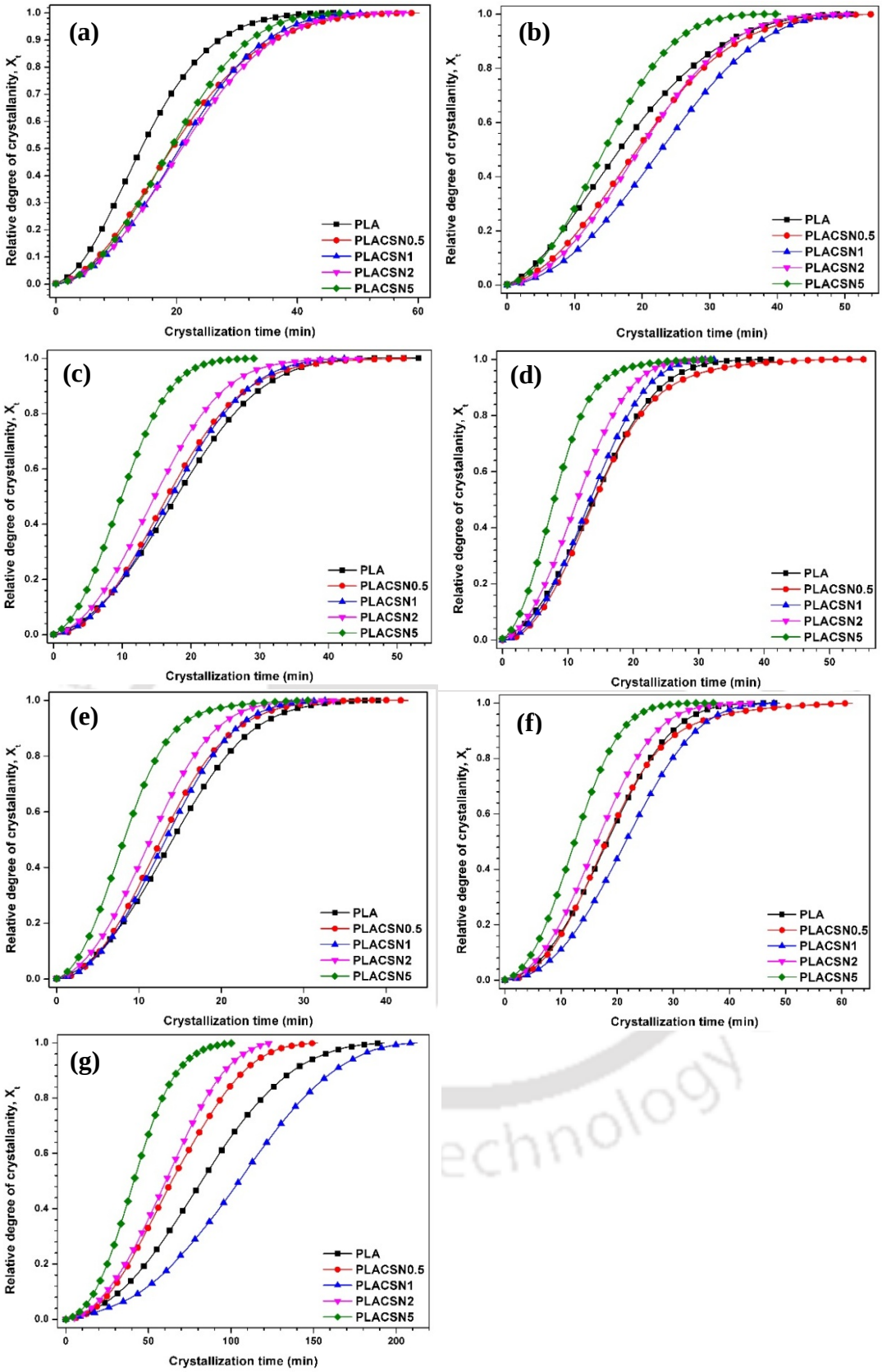

Figure 5.10: Relative crystallinity plots for PLA and PLA/CSN bionanocomposites at various crystallization (T_c) temperatures (a) 90 °C, (b) 95 °C, (c) 100 °C, (d) 105 °C, (e) 110 °C, (f) 115 °C and (g) 120 °C.

5.4.2.3 Avrami plots

The nucleation and crystallization rate are important parameters for polymer processing on industrial scale. These parameters directly or indirectly affect the properties of polymer. Out of available methods for characterization of the crystallization behavior, Avrami theory is the best-suited to analyze experimental crystallization data. In the present study, Avrami theory is applied and the plots of log [-ln (1-X_t)] versus log t for PLA and PLA/CSN bionanocomposites, as shown in Figure 5.11(a-g). The values determined from Avrami model for '*K*' and '*n*', for different isothermal temperatures are presented in Table 5.4. For simplification of calculations, secondary crystallization (spherulite impingement) is ignored and the region of primary crystallization (outward growth of lamellar stacks) i.e. 30-70% of relative crystallinity is considered, which gives linear straight line pattern **(Pal and Katiyar, 2016)**. The calculated '*n*' values are non-integral ~2, denoting the non-three dimensional structures which are a result of instantaneous nucleation regulated by diffusion. It can be noted that '*n*' values of PLA are in the range of 1.7 to 2.3. This indicates that 'n' do not depend much on crystallization temperature. These values closely matched with values reported Zhang *et al.* **(Zhang et al., 2013)**, i.e. 2.0–2.3 at T_c = 114–126 °C. The average *n* values for PLA, PLACSN0.5, PLACSN1, PLACSN2 and PLACSN5 are about 2.0, 2.1, 2.3, 2.2 and 2.1, respectively, which means that adding CSN does not alter the mechanism of PLA crystallization in the temperature range of 90–120 °C. The *k* values show an evident variation with temperature. The overall crystallization rate constant (K) of PLA show a reduction with increasing isothermal crystallization temperature (T_c) and similar effect is noticed for PLA/CSN bionanocomposites. The *K* x 10^{-3} values at 105 °C for PLA, PLACSN0.5, PLACSN1, PLACSN2 and PLACSN5 are about 3.06, 2.15, 1.93, 4.03 and 11.56 min^{-n}, respectively. For the same crystallization temperature, the crystallization rate co-efficient values (*K*) for samples with CSN are larger than PLA at >1 wt. % loadings suggesting that PLA/CSN bionanocomposites have faster crystallization kinetics compared to PLA. This implies that biocomposites crystallize faster than PLA and CSN act as active nucleating agents for augmenting the overall crystallization process. The other important parameters, $t_{0.5}$ and G values are calculated using *n* and *K* values. As seen from Table 5.4, the crystallization half-time ($t_{0.5}$) show a decreasing trend initially then starts increasing again with minima at 105 °C. This means that crystallization is hindered at higher temperatures. The reverse trend is observed for crystallization growth rate G.

Table 5.4: Kinetic parameters of PLA & PLA/CSN isothermally crystallized at 90–120 °C.

	T_c (°C)	ΔH_c (J/g)	χ_c (%)	n	$K \times 10^3$ (min^{-n})	$t_{0.5}$ * (min)	$t_{0.5}$ (min)	$G \times 10^{-2}$ (min^{-1})	ΔE_a ($kJmol^{-1}$)
PLA	90	23.2	24.7	1.8	5.4	14.2	14.1	7.1	219.6
	95	23.8	25.5	1.7	6.5	16.7	16.6	6.0	
	100	25.3	27.1	2.1	1.6	17.9	17.8	5.6	
	105	26.6	28.4	2.1	3.1	14.0	13.9	7.2	
	110	28.5	30.4	2.1	2.5	14.1	14.0	7.1	
	115	30.3	32.4	2.3	0.9	18.3	18.2	5.5	
	120	27.0	28.9	2.2	0.04	82.6	82.0	1.2	
PLACSN0.5	90	22.4	24.1	1.9	2.5	19.2	19.2	5.2	203.4
	95	22.9	24.6	2.0	2.0	19.3	19.2	5.2	
	100	26.4	28.3	2.2	1.5	16.5	16.6	6.0	
	105	27.1	29.1	2.2	2.1	14.1	14.2	7.1	
	110	28.6	30.7	2.2	2.5	12.7	12.7	7.9	
	115	30.9	33.2	2.3	0.8	18.1	18.0	5.5	
	120	29.3	31.4	2.1	0.1	59.0	64.2	1.6	
PLACSN1	90	28.3	30.6	2.1	1.1	20.5	20.4	4.9	209.5
	95	26.5	28.6	2.2	0.7	22.7	22.7	4.4	
	100	27.7	29.9	2.2	1.4	17.1	17.1	5.9	
	105	28.2	30.4	2.3	1.9	13.4	13.4	7.5	
	110	30.0	32.4	2.3	1.9	13.2	13.2	7.6	
	115	31.8	34.3	2.5	0.3	21.6	21.5	4.7	
	120	32.3	34.8	2.4	0.02	70.4	71.2	1.4	
PLACSN2	90	23.5	25.6	2.1	1.3	20.8	20.8	4.8	206.6
	95	24.2	26.4	2.2	1.2	19.6	19.5	5.1	
	100	26.3	28.7	2.1	2.3	14.7	14.7	6.8	
	105	27.9	30.4	2.1	4.0	11.6	11.4	8.8	
	110	28.9	31.5	2.1	3.9	11.5	11.4	8.8	
	115	30.0	32.7	2.3	1.1	16.3	16.4	6.1	
	120	27.7	30.2	2.3	0.1	60.4	60.2	1.7	
PLACSN5	90	23.3	26.2	2.1	1.3	18.9	18.9	5.3	199.0
	95	26.1	29.3	2.1	2.8	14.3	14.4	7.0	
	100	27.1	30.4	2.0	6.5	9.9	9.9	10.1	
	105	28.7	32.3	2.0	11.6	7.9	7.9	12.7	
	110	29.2	32.8	2.1	8.9	8.2	8.2	12.2	
	115	32.9	37.0	2.2	2.5	12.6	12.4	8.1	
	120	37.7	42.4	2.4	0.1	41.2	41.1	2.4	

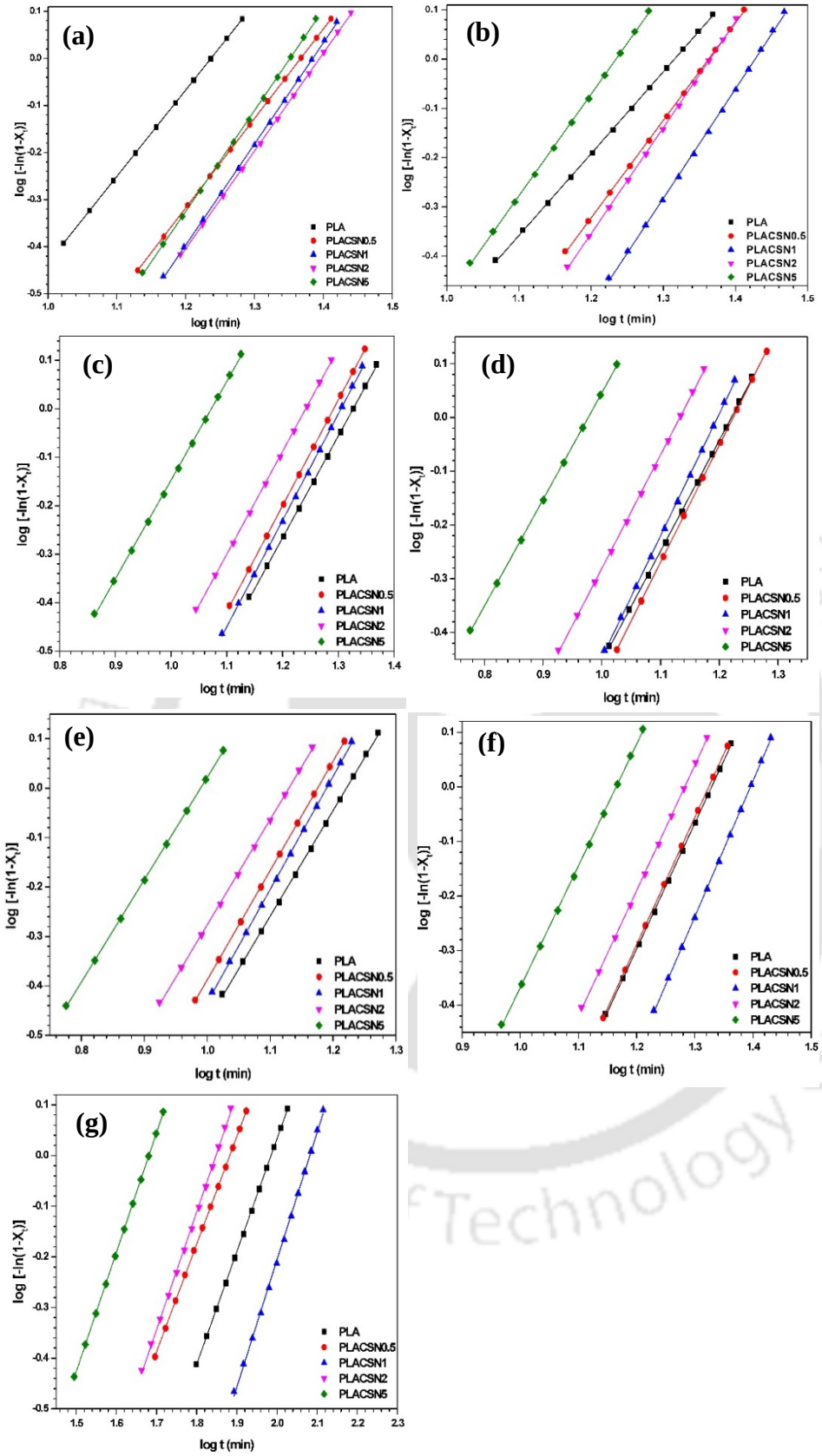

Figure 5.11: Avrami plots of *log [-ln(1-X_t)]* vs. *log t* for PLA and PLA bionanocomposites at various crystallization (T_c) temperatures (a) 90 °C, (b) 95 °C, (c) 100 °C, (d) 105 °C, (e) 110 °C, (f) 115 °C and (g) 120 °C.

5.4.2.4 Growth rate

Crystal growth rate (G) is the reciprocal of crystallization half-time ($t_{0.5}$). Figure 5.12 shows the crystallization temperature (T_c) vs. crystallization growth rate (G) of PLA and PLA/CSN bionanocomposites during isothermal crystallization, which proves the same conclusion derived earlier in section 5.5.2. A significant change in the growth rate of PLA crystals is observed upon addition of CSN, it indicates that PLA/CSN bionanocomposites had an improved growth rate under the same crystallization temperature. In addition, $1/t_{0.5}$ was highest for PLACSN5, depicting that higher loadings accelerated the crystallization process of PLA. The 'G' for PLACSN5 at 105 °C was 12.7×10^{-2} min^{-1} as compared to 7.2×10^{-2} min^{-1} for PLA. Increment in growth rate confirms the contribution of CSN in enhancing the nucleation in PLA **(Cai et al., 2011)**. The isothermal melt crystallization process of PLA and PLA/CSN bionanocomposites is thermally activated in the range of 110–120 °C.

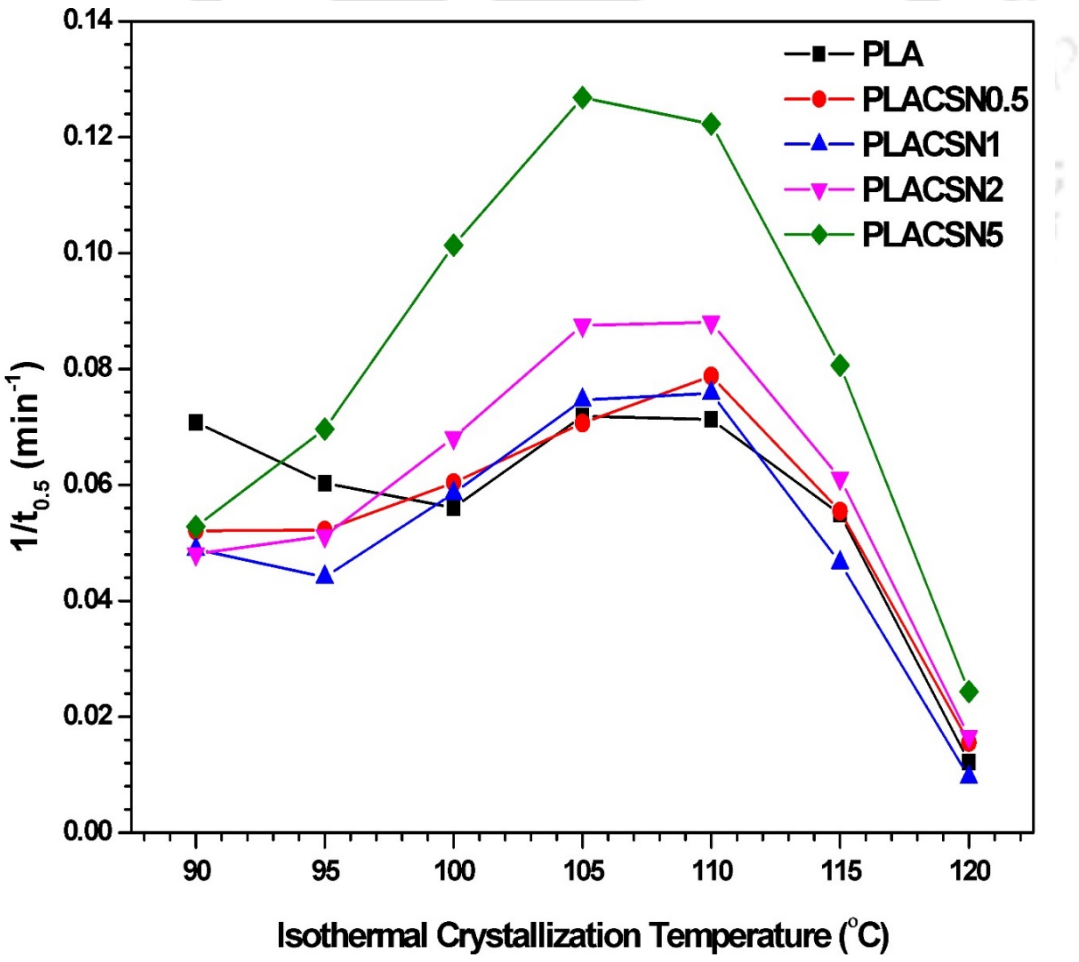

Figure 5.12: Plot of growth rate versus isothermal crystallization temperature ranging from 90–120 °C.

5.4.2.5 Apparent activation energy (ΔE_a)

The apparent activation energy (ΔE_a) for melt crystallization can be calculated from the slope of plots of (1/n) *ln K* versus $1/T_c$, as shown in Figure 5.13. The values of ΔE_a for PLA, PLACSN0.5, PLACSN1, PLACSN2 and PLACSN5 are 219.6, 203.4, 209.5, 206.6 and 199.0 kJ/mol, respectively. The value of ΔE_a for PLA matched closely with the values reported in literature **(Chu and Wu, 2007)**. The apparent activation energy required for crystallization decreases as the CSN content increases. However, all the samples show poor correlation (coefficient value much below 1) which are still comparable. Therefore, Arrhenius analysis was used to estimate the activation energies for PLA and PLA/CSN bionanocomposites. This demonstrates the increased heterogeneous nucleation and crystallization ability of CSN and also that crystallization is heterogeneous in nature and dominated the overall crystallization rate.

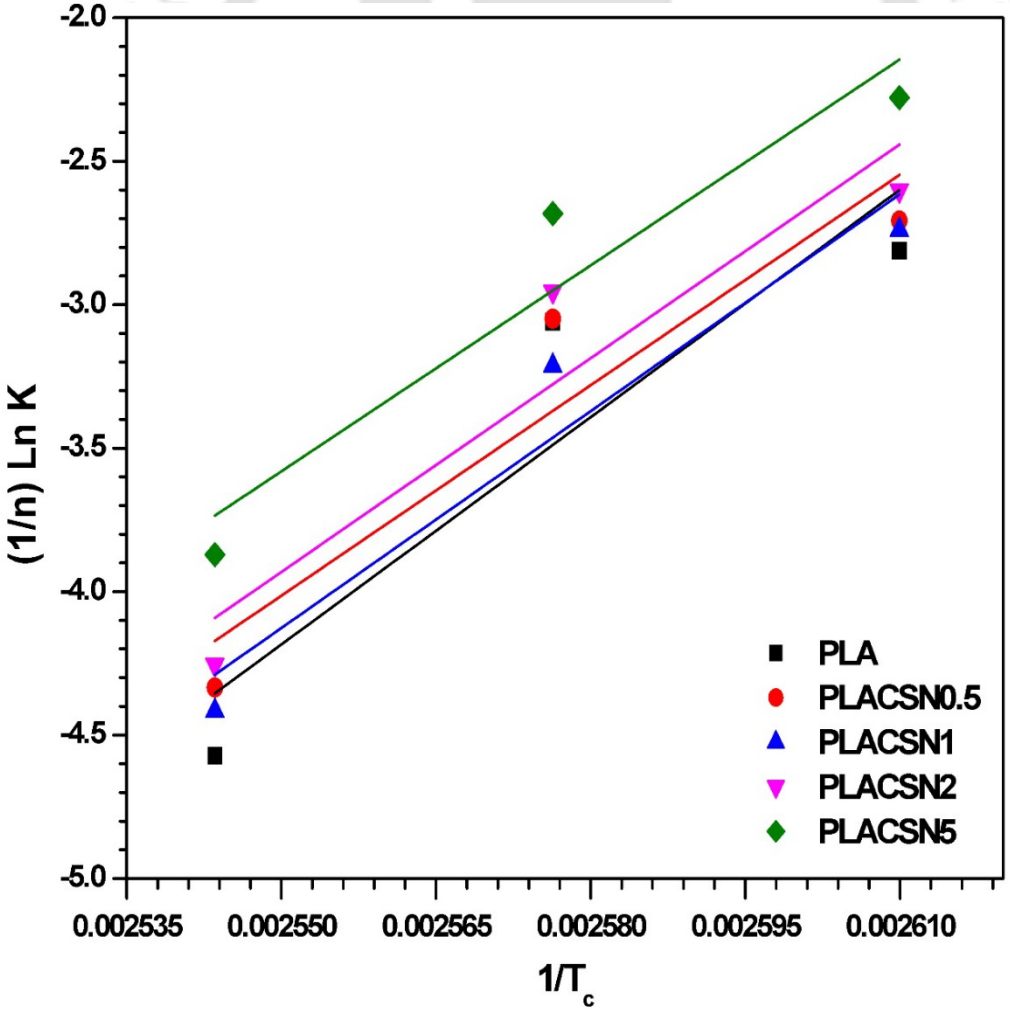

Figure 5.13: Slope of plots of *(1/n)ln K* against $1/T_c$ for estimation of apparent activation energy (ΔE_a).

5.4.2.6 Effects of CSN on crystallization morphologies of PLA

Nucleating agents can not only alter the crystallization rate but also the morphology of PLA spherulites, which had been confirmed by POM. Figure 5.14(a-g) shows POM micrographs for pure PLA and PLA nucleated with different CSN content during isothermal crystallization taken at different time intervals for a total duration of 30 min. PLA as well as PLA/CSN bionanocomposites form typical α-spherulite (Maltese cross) morphology, which implies that the three dimensional growth of PLA crystals is unchanged by the presence of CSNs **(Bhasney et al., 2017)**. Furthermore, pure PLA formed larger spherulites ~10 μm, while the size of spherulites decreased remarkably and crystallization sites have increased with the loading of CSN. The spherulite size decreased remarkably with the addition of CSN.

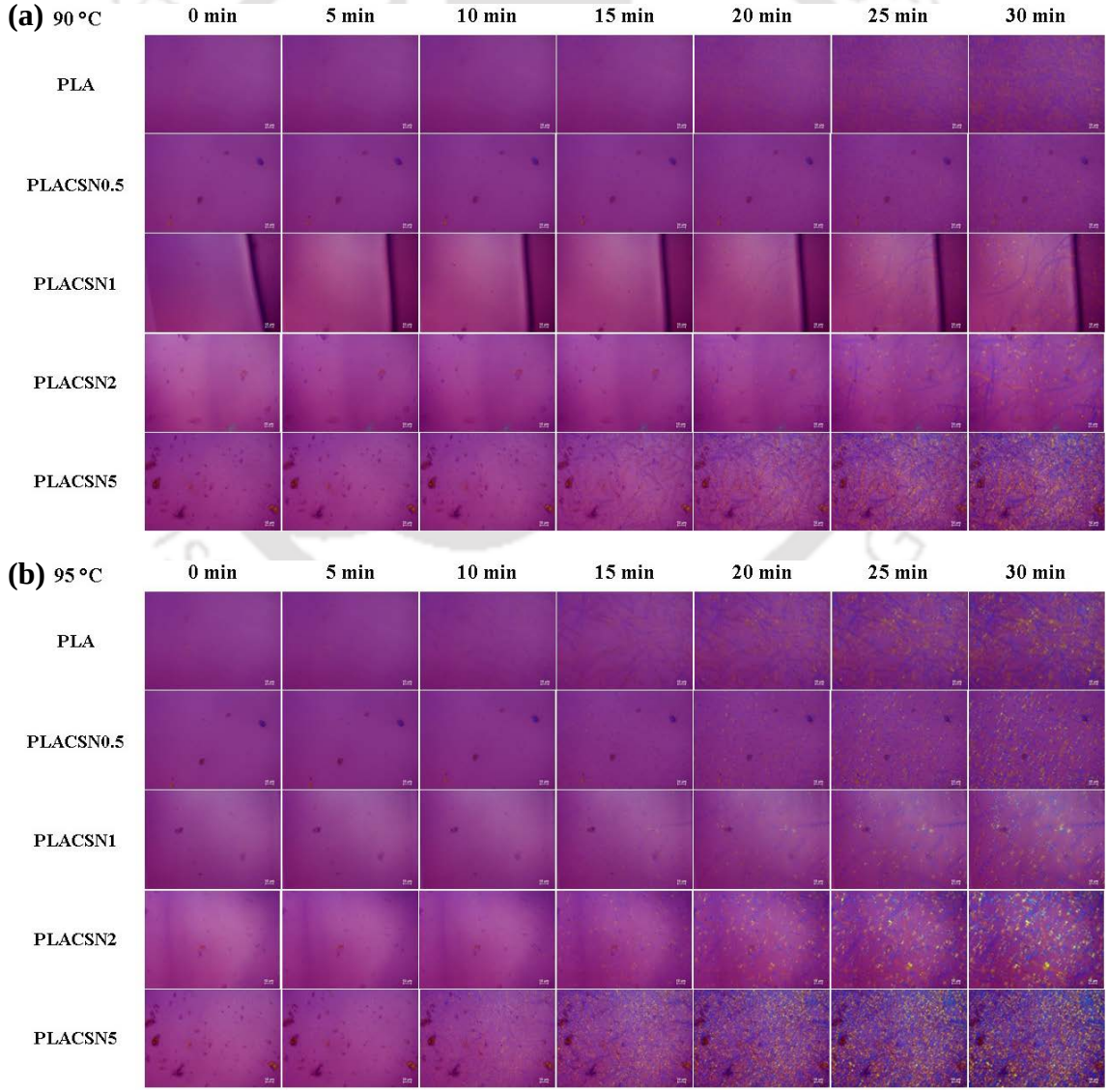

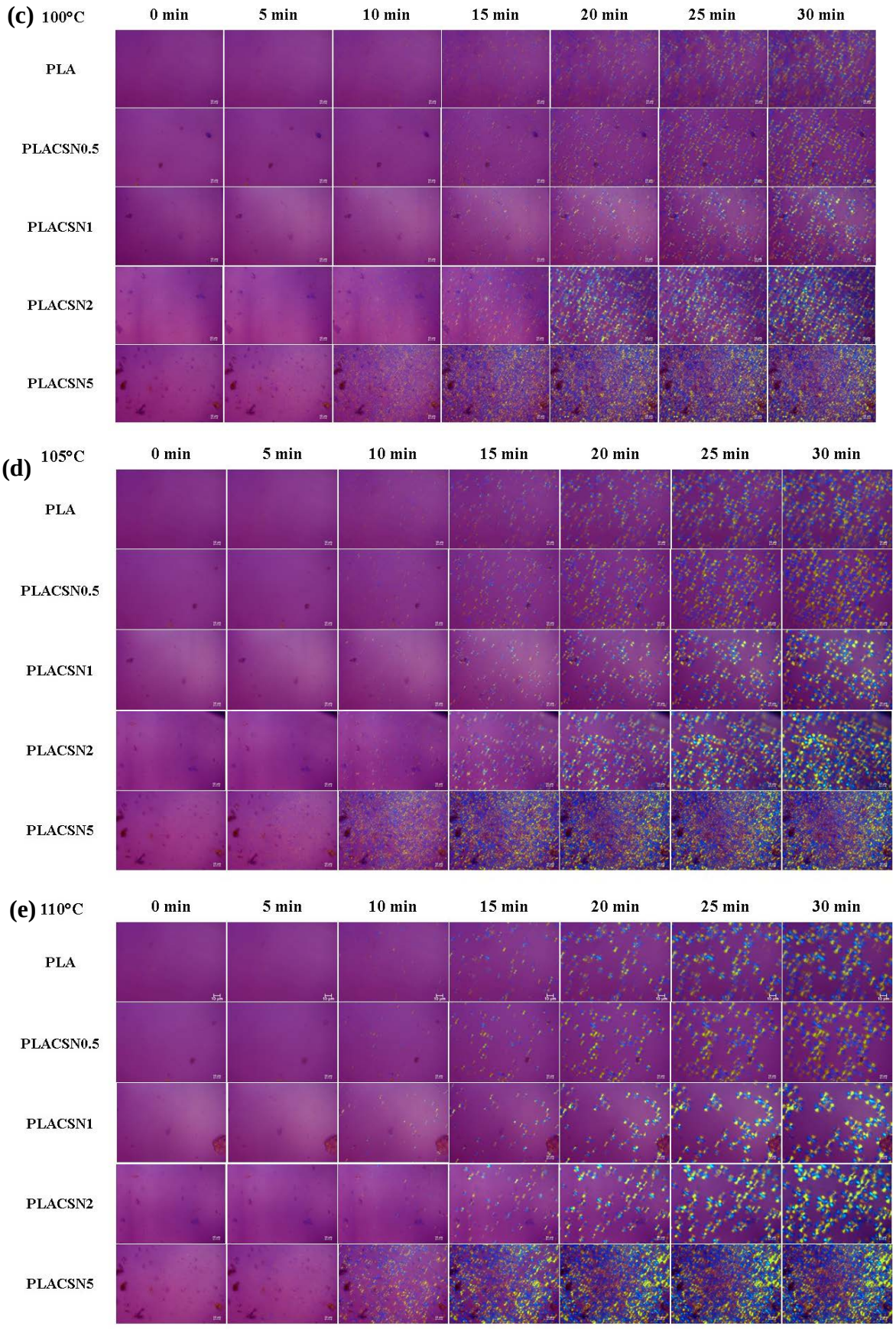
(c) 100°C
0 min
5 min
10 min
15 min
20 min
25 min
30 min
PLA
PLACSN0.5
PLACSN1
PLACSN2
PLACSN5
(d) 105°C
0 min
5 min
10 min
15 min
20 min
25 min
30 min
PLA
PLACSN0.5
PLACSN1
PLACSN2
PLACSN5
(e) 110°C
0 min
5 min
10 min
15 min
20 min
25 min
30 min
PLA
PLACSN0.5
PLACSN1
PLACSN2
PLACSN5

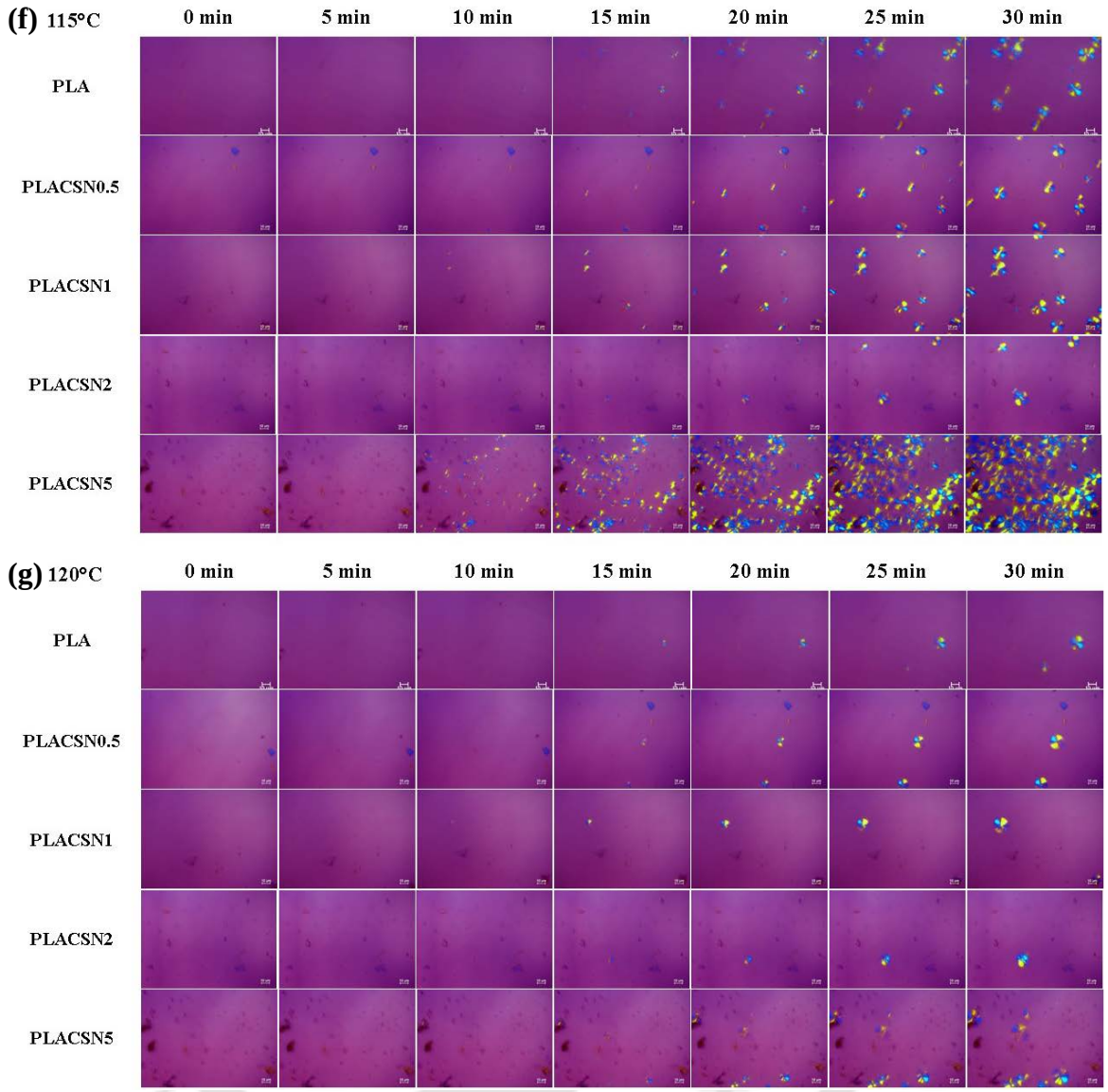

Figure 5.14: POM micrographs of PLA and PLA/CSN bionanocomposites taken at various time intervals crystallized isothermally at (a) 90 °C, (b) 95 °C, (c) 100 °C, (d) 105 °C, (e) 110 °C, (f) 115 °C and (g) 120 °C (scale bar: 10 μm).

5.4.2.7 Crystal growth rate

Nucleation rate as well as crystal growth rate both determine the crystallization behavior of a material. After CSN addition number of nucleation sites are increased, resulting into accelerated spherulite growth, as shown in Figure 5.15(a-f). The crystallization growth rate (G) of PLA spherulites increased a little by 0.5 and 1 wt. % CSN loading but considerably boosted with the addition of 2 and 5 wt. % CSN (bio-filler).

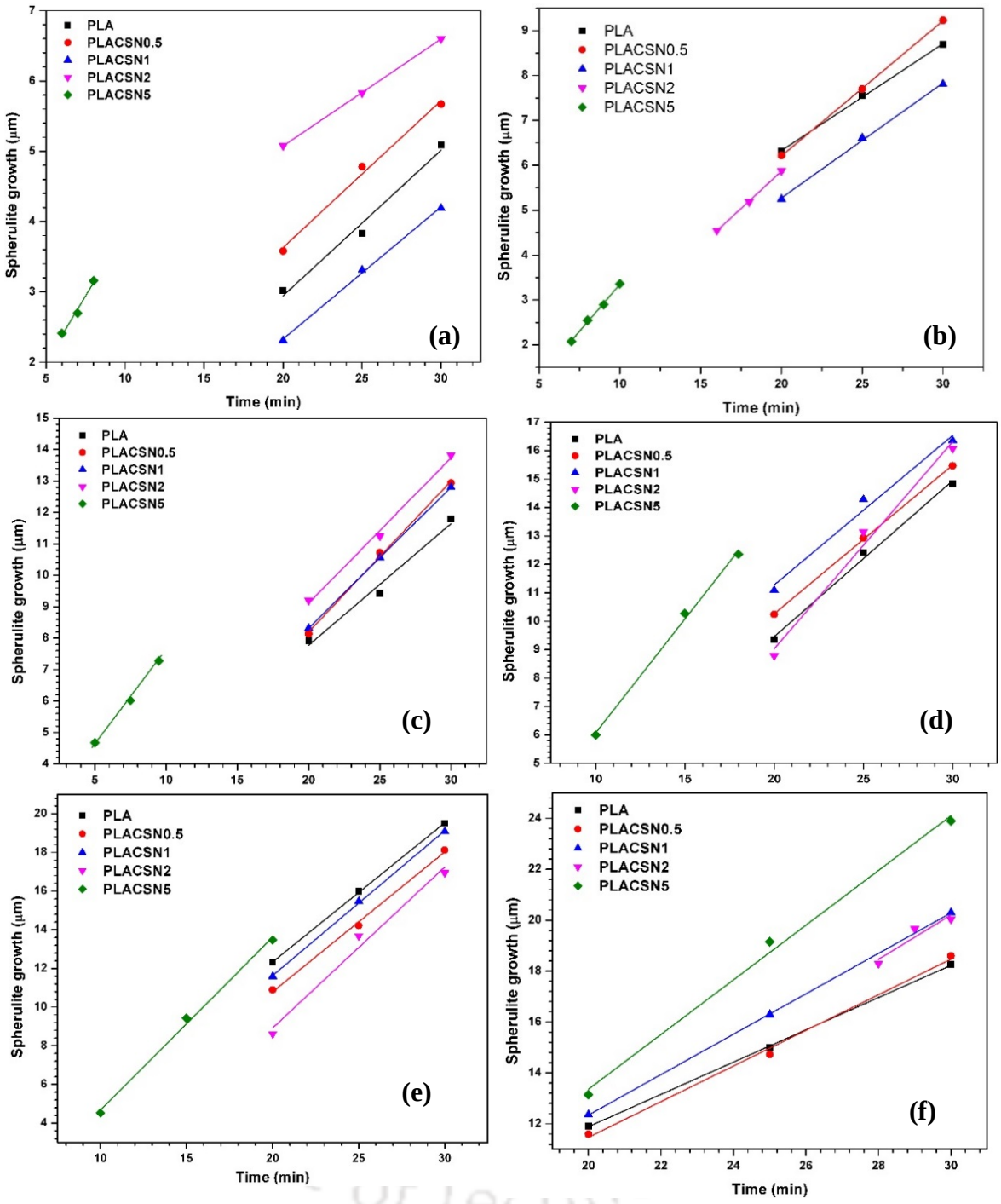

Figure 5.15: Spherulite growth rate of PLA and PLA/CSN bionanocomposites crystallized isothermally at (a) 95 °C, (b) 100 °C, (c) 105 °C, (d) 110 °C, (e) 115 °C and (f) 120 °C.

5.4.2.8 Nucleation density

It is known that addition of nucleating agents results in initiation of PLA chain folding which results in increased growth of crystals **(Tesfaye et al., 2017)**. Nucleating agents are generally 3-dimensional nano- or microparticles which act as hindrance to the freely

moving polymer chains and can allow polymer chains to come in contact with itself and result in chain folding. Similarly, PLA/CSN bionanocomposites show higher number of crystals (nucleation density) and lower crystal size as compared to PLA. This means that after certain period of time, the area covered by crystals in PLA/CSN bionanocomposites will be more than that of PLA, albeit the adjoining CSNs also act as nucleation site, thus promoting more crystals to grow thus stunting the crystal size. It can be noticed that due to the presence of numerous inclusions, size of spherulites is much smaller as compared to those in PLA which results in improvement in spherulite density as seen in Figure 5.16. This indicates that the overall crystallization rate is faster in the presence of CSN which is also corroborated by DSC experiments.

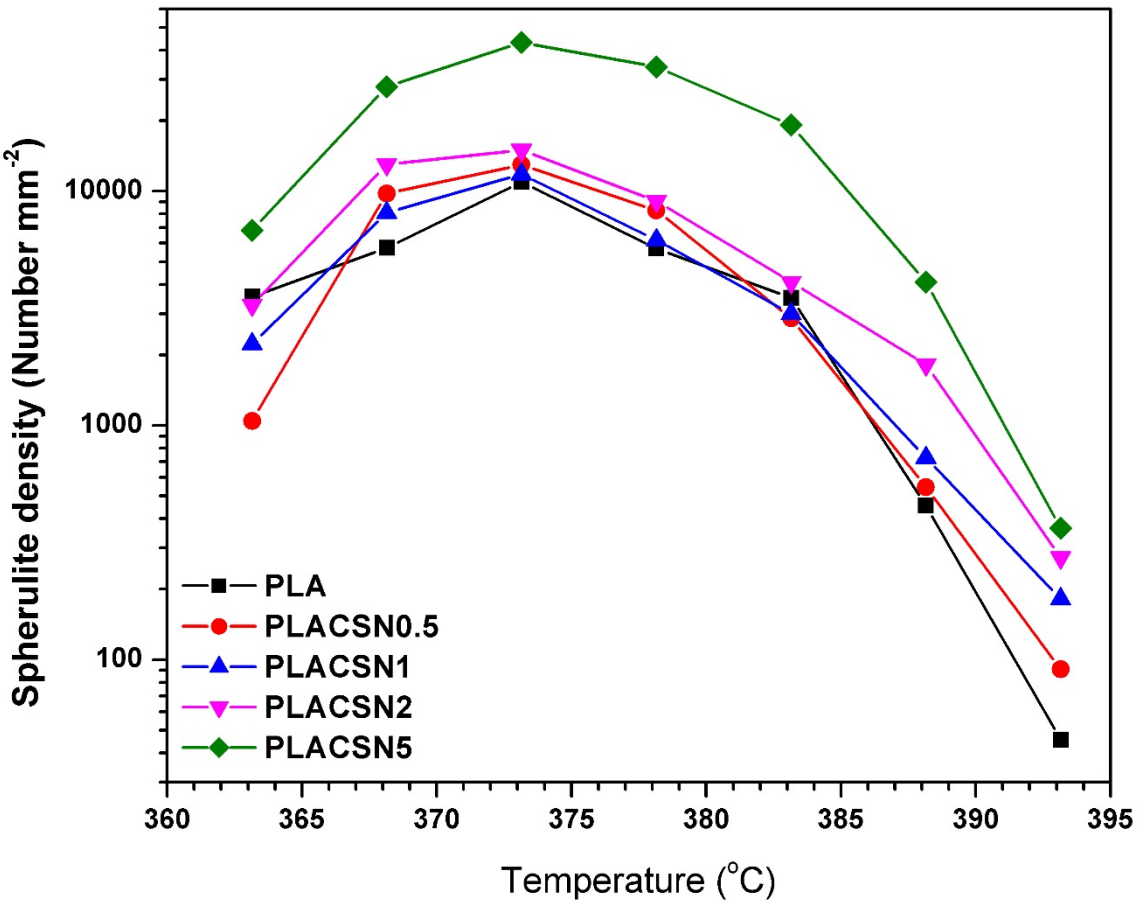

Figure 5.16: Nucleation density as a function of temperature for PLA and PLA/CSN bionanocomposites.

5.4.2.9 Hoffman-Lauritzen crystal growth theory

Eq. (5.25) is applied to investigate about the thermodynamic parameters related to the overall crystallization process. The equilibrium melting temperature for PLA was

calculated to be 172.3 °C which is very similar to the value obtained by Wang et al. (2013**)** who have reported T_m^0 of ~165 °C. However, such long extrapolation may result in some inaccuracy in evaluation. The equilibrium melting temperature (T_m^0) for PLA is 172.3 °C, the T_m^0 decreases upon incorporation of CSN (see Table 5.5). The T_m^0 values for PLACSN0.5, PLACSN1, PLACSN2 and PLACSN5 are 175.1, 172.2, 168.1 and 169.6 °C, respectively. This results into imperfect crystals in PLA/CSN bio-nanocomposites.

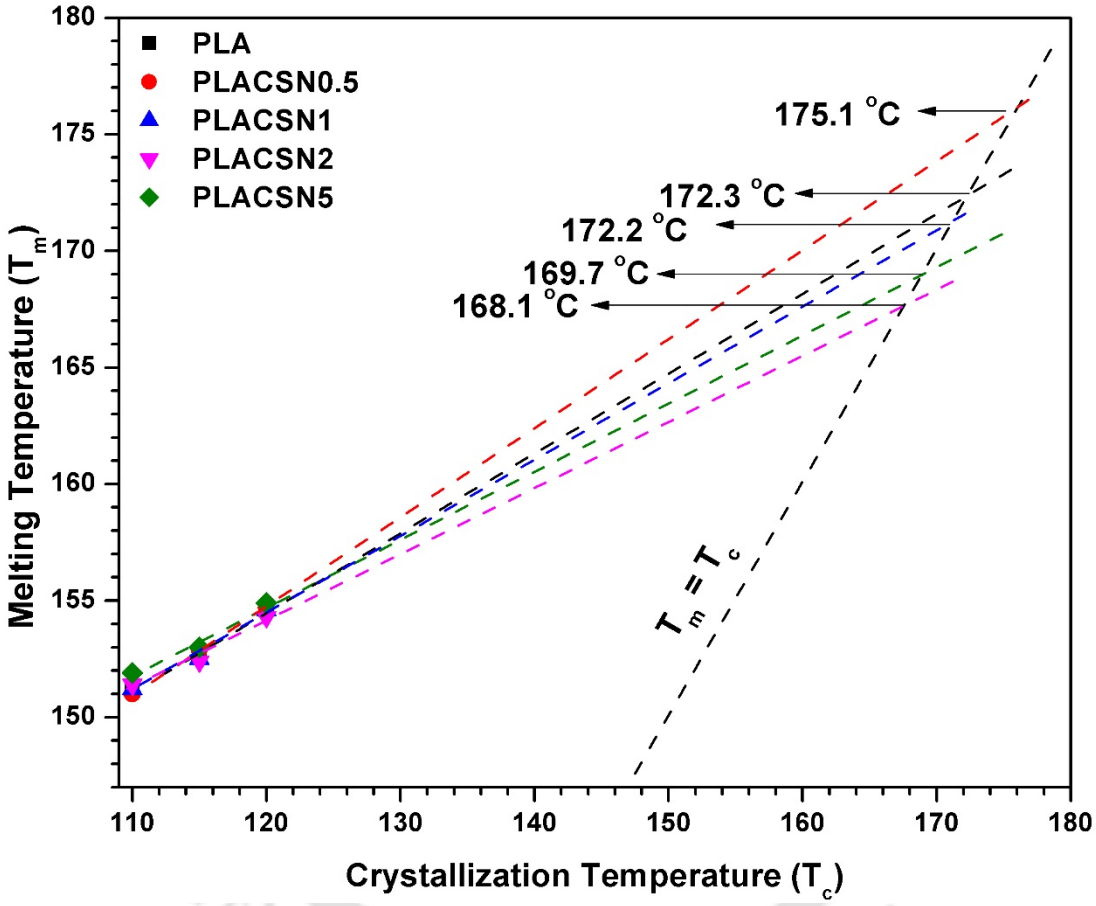

Figure 5.17: The plots for calculation of equilibrium melting point T_m^0.

As shown in Figure 5.18(a), plots of $\left[\left(\ln G + (U^*/R(T_c - T_\infty))\right)\right]$ against $(1/fT_c\Delta T)$ can be used to get nucleation constant (Kg) values from the slope and calculated values are summarized in Table 5.5. The nucleation constant (K_g) values obtained for PLA (1.42×10^5 K^2) are higher than PLA/CSN bionanocomposites, 1.04×10^5 K^2 in case of PLACSN5. This indicates that presence of CSN can reduce the chain mobility of PLA segment thus CSN loading may accelerate the crystallization process. The 'K_g' is dependent of The K_g values obtained in this study 1.0–1.42 × 10^5 K^2 are in agreement with the reported K_g values, 1.70 × 10^5 K^2 **(Cai et al., 2011)**. Using the theoretical methodology that G is proportional to $1/t_{0.5}$ and based on the Hoffman-Lauritzen theory, $1/t_{0.5}$ can be used to replace

crystallization spherulite growth rate (G). Figure 5.18(b) shows the $[ln\,(1/t_{0.5}) + (U^*/R(T_c - T_\infty))]$ of the PLA and PLA/CSN bionanocomposites as a function of $[1/(fT_c\Delta T)]$. Same values of U*, T_∞ are used which were used for POM experiments. For sake of comparison, the $1/t_{0.5}$ values from 110–120 °C were considered. Data shown in plots exists as straight lines having different slopes. Since the temperature ranges belong to regime 2, the Z values equal to 2 have been taken into calculations. The 'K_g', 'σ_e' and 'q' values for PLA are 4.4 × 10^5 K^2, 9.41 x 10^{-2} J/m^2 and 35 kJ/mol, respectively, similar values i.e. 5.7 × 10^5 K^2, 11.7 × 10^{-2} J/m^2 and 43.5 kJ/mol, elsewhere **(Miyata and Masuko, 1998)**.

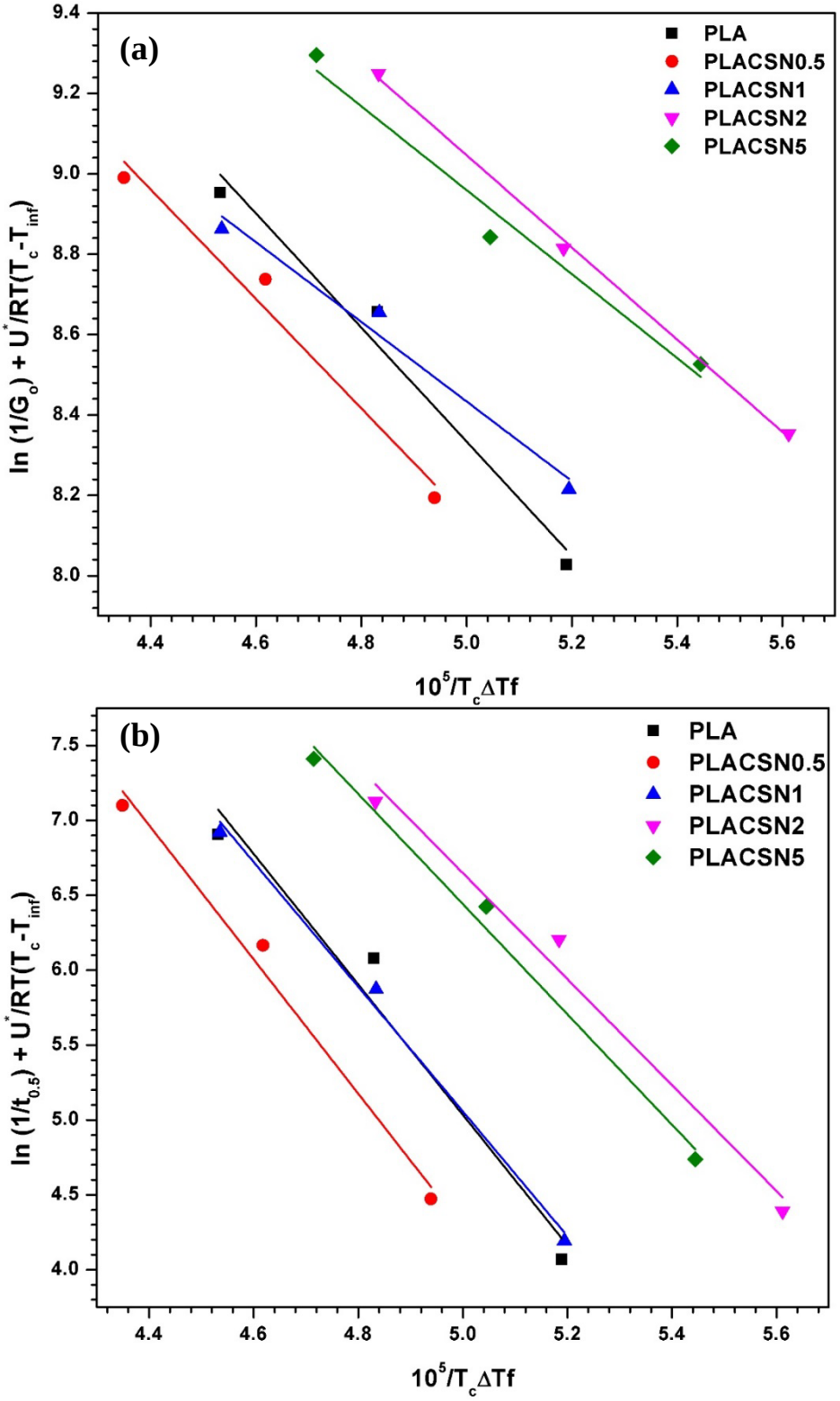

Figure 5.18: Hoffmann-Lauritzen crystal growth plots for PLA and PLA/CSN bionanocomposites using (a) DSC and (b) POM.

The 'K_g', 'σ_e' and 'q' values were calculated and are presented in Table 5.5. The values of K_g were higher than POM, but from both the analysis it can be inferred that incorporation of CSN reduces the folding free surface energies. The lesser values of the σ_e for PLACSN2

and PLACSN5 clearly indicate more regular folding of the polymer chains as compared to the other specimens. Presence of CSN reduces size of nucleus needed for the crystal growth promoting growth of the spherulite on the surface of CSN. In other words, formation of interface between filler surface and polymer chain is preferred than individual polymer crystals. This can be attributed to the CSN heterogeneous nucleation effect which reduces the energy barrier for PLA crystallization.

Table 5.5: The parameters calculated from DSC and POM.

Materials	T_m^0 (K)	Estimated from G values			Estimated from $(1/t_{0.5})$ values		
		$K_g \times 10^5$ (K^2)	$\sigma_e \times 10^{-2}$ (J/m^2)	q (KJ/mol)	$K_g \times 10^5$ (K^2)	$\sigma_e \times 10^{-2}$ (J/m^2)	q (KJ/mol)
PLA	445.4	1.42	3.07	11.4	4.36	9.41	35.0
PLACSN0.5	448.3	1.36	2.94	10.9	4.48	9.68	36.0
PLACSN1	445.4	1.00	2.14	7.97	4.16	9.00	33.4
PLACSN2	441.2	1.15	2.48	9.22	3.54	7.65	28.4
PLACSN5	442.8	1.04	3.26	8.39	3.68	7.96	29.6

5.5 Summary

CSN plays a dual role in crystallization process, firstly, it acts as a heterogeneous nucleating agent facilitating crystallization, and secondly, it obstructs the polymer chain movement. Either of the two roles, which process is dominating is decided by the filler loading. Non-isothermal crystallization showed that, T_c and $t_{0.5}$ were lower for bionanocomposite films at small loadings (~1 wt. %) as compared to PLA at all heating rates. This suggests that CSN can augment the overall crystallization rates. CSNs are also found to act as heterogeneous nucleation sites in PLA matrix. To analyze non-isothermal crystallization kinetics of samples, three kinetic models viz. modified Avrami, Mo and Tobin models were applied. The smaller exponent (n and n_T) values suggested that CSN inclusions thrust PLA spherulite formation towards unsophisticated geometries thereby, improving crystallization rates. Increased (Z_c and K_T) and smaller $F(T)$ values, for PLA/CSN bionanocomposites compared to PLA advocate towards faster crystallization processes. The crystallization activation energy based on Kissinger and Takhor methods showed smaller values for PLACSN1 bionanocomposites, indicating easier motion of PLA molecular chains in PLA/CSN system as a result of which crystallization occurs at a faster rate. Furthermore, the calculated nucleation activity of bionanocomposites show agreement between lower $t_{0.5}$, F(T) and crystallization activation energy in the bionanocomposite. The crystallization rate of PLA/CSN bionanocomposites were increased because of the high surface area of CSN. The isothermal melt crystallization behavior of PLA and PLA/CSN bionanocomposites was studied in the range of T_c between 90 and 120 °C. The sigmoidal relative crystallinity isotherms shifted towards lesser crystallization time, indicating fast crystallization behavior of PLA/CSN bionanocomposites. The crystallization kinetics of PLA and PLA/CSN bionanocomposites was studied and it was found that CSNs act as nucleating agent, thus increasing the crystallization rate and decreases the ΔE and surface energy barrier for PLA crystallization.

Chapter 6

Influence of Crystalline Silk Nano-discs (CSNs) on the Thermal and Hydrolytic Degradation Behavior of Melt-extruded PLA Films

This study investigates the effect of CSNs on the thermal stability of PLA/CSN bionanocomposites for its suitability towards food packaging applications. Samples were melt compounded with different loading of CSNs using a twin-screw extruder. The TG data revealed that incorporation of 1 wt% CSNs in PLA matrix could enhance the onset temperature (T_{onset}) upto ~10 °C in comparison to neat PLA which confirms the improvement in thermal stability due to formation of network like structures. At higher loading of 5 wt%, onset temperature T_{onset} and peak temperature (T_{max}) shifted to lower temperatures ~310 °C and ~369 °C, respectively. This can be attributed to increase in acidic sites which are responsible for acceleration of degradation rate. The apparent activation energies (E_a) of bionanocomposites, determined from Flynn-Wall-Ozawa, Kissinger-Akahira-Sunose and Coats-Redfern method, increased in comparison to PLA which confirms that CSNs impress the thermal degradation process. A possible mechanism is proposed for the thermal degradation process of PLA/CSN bionanocomposites using Criado method. Hyphenated TGA-FTIR analysis is utilized to identify the evolved gaseous products of Muga, CSNs, PLA and PLA/CSN bionanocomposites. For Muga and fabricated CSNs various volatile species were released such as different amide containing products, CO_2, CO. In case of PLA and PLA/CSN bionanocomposites similar type of major products such as CO_2, CO, cyclic oligomers, lactide, hydrocarbons and aldehydes were detected. The hydrolytic degradation rates calculated from molecular weight reduction shows that PLA/CSN nanocomposites' degradation rates are lower as compared to PLA in acidic, neutral and alkaline media, respectively, due to hydrophobic nature of CSN which are well-dispersed into the hydrophobic PLA matrix without the formation of interface to act as site for seepage of water. Strong particle-particle interaction results into formation of aggregate structures which may also reduce hydrolytic degradation activity. The crystallization fraction is increased during the hydrolytic degradation process and the degradation was suspended in presence of CSN and pH. This work provides valuable insight for the application and reclamation of PLA/CSN bionanocomposites under elevated temperature and wet working environments.

The work in this chapter is published as:

- R. Patwa, A. Kumar and V. Katiyar, "Isothermal crystallization kinetics and hydrolyticdegradation studies of poly (lactic acid)/crystalline silk nano-discs based bionanocomposites," J. Appl. Polym. Sci., vol. 135, pp. 46590-46618, May 2018, DOI: 10.1002/app.46590.
- R. Patwa, Monika, A. Kumar and V. Katiyar, "Thermal stability and non-isothermal crystallization kinetics of silk nano-discs reinforced poly (lactic acid) bionanocomposites," *Polym. Bull.* (Under review).

6.1 Introduction

From the perspectives of green origin of polymers and environment, impact of bio-based and biodegradable polymers have been on the focal point to provide alternatives against after service life utilization of conventional polymers like polyethylene (PE), polyethylene terepthalate (PET), polypropylene (PP), etc. **(Pal and Katiyar, 2016)**. Among biopolymers, poly(lactic acid) (PLA) has gained special attention because of its convenient biodegradability and analogous mechanical properties and melting temperature to many conventionally used polymers **(Gupta and Katiyar, 2017)**. It requires nearly half energy input and has low greenhouse gas emission as compared to conventional plastics. PLA possess good melt strength, transparency, UV absorption, high temperature processability and biocompatibility which makes it fit for medical, packaging and other applications **(Rasal et al., 2010)**. But inherent drawbacks like high glass transition temperatures, poor thermal stability, high costs, slow crystallization rate and brittle nature have obviated its widespread commercial usage. The aliphatic ester group present in the repeat unit is prone to thermal degradation when processed above melting point of PLA. PLA undergoes a complex degradation mechanism with a myriad of simultaneous reactions occurring during the molten state which includes random chain scission, transesterification, hydrolysis, and depolymerization, etc. **(Monika et al., 2017)**. Consequently, different strategies have been employed to enhance the thermal stability and crystallization rate by incorporation of nucleating agents such as fillers, polymer blending and stereocomplexation, etc. Among these, the use of inorganic/organic fillers such as carbon black, talc, graphene, nano-clay, etc. have been extensively studied though, these may pose health hazard at some point from manufacturing process to final disposal **(Gao et al., 2017; Molinaro et al., 2013; Pivsa-Art et al., 2016; Su et al., 2009)**. An ideal filler material should essentially be non-toxic as well as biodegradable, if the biocomposites is intended for sustainable food packaging applications because of their direct contact with the food items **(Tan et al., 2015)**. Green fillers such as cellulose, starch, chitosan, silk, etc. are low cost, abundant, light weight, biodegradable and biocompostable, etc. In view of this, much scientific research is being carried out towards exploring non-toxic fillers for PLA based bionanocomposites **(Claramunt et al., 2016; Thakur et al., 2016)**. The use of silk based organic fillers for PLA generates a new class of complete biodegradable bionanocomposites.

Thermo-mechanical characteristics of PLA decide the product performance which largely depend on thermal stability and crystallization behavior. Kinetic analysis can provide information on kinetic triplets (E_a, n, A_n) for the degradation of PLA and PLA/CSN bionanocomposite and their mechanisms of degradation. PLA thermal degradation kinetics have been studied by many researchers. **Aoyagi et al. (2002)** have calculated the PLA activation energy (E_a) values in the range of 80-160 kJ mol^{-1} which increases with conversion and suggested degradation of PLA follows a complex mechanism. In another study hydroxyapatite filled PLA showed improvement in thermal stability. The Flynn-Wall-Ozawa and Invariant kinetic parameter (IKP) methods were used to study the degradation kinetics, both methods obtained similar values. The activation energy (E_a) of PLA/g-HA (139.3 kJ mol^{-1}) was decreased as compared to neat PLA (174.7 kJ mol^{-1}). To develop a better understanding about thermal degradation behavior, apart from thermal degradation kinetic analysis, degradation mechanism and evolved gaseous product analysis are equally important. Major degradation products of PLA are cyclic oligomers, lactide, acetaldehyde, carbon monoxide, carbon di-oxide, etc. **(Liu et al., 2010)**.

PLA is susceptible to hydrolytic degradation, which limits its scope of application **(Ma and Zhou, 2015)**. Hydrolytic degradation of PLA depends upon various factors like crystallinity of matrix, temperature, degradation time and pH of the medium **(Pitt et al., 1981; Reed and Gilding, 1981)**. Efforts are being made to enhance the hydrolytic resistance of PLA to avoid deterioration of mechanical properties of PLA **(Khakbaz et al., 2015; Ma and Zhou, 2015; Stloukal et al., 2016)**. This can be done by limiting the water diffusion by incorporation of hydrophobic fillers in matrix **(Benali et al., 2015; Huang et al., 2017)**. Upon hydrolytic degradation, PLA degrades by breaking of the ester bond into monomers. In acidic or neutral media, the degradation occurs by protonation followed by formation of water molecules which eventually cleaves the ester linkage. In alkaline conditions, hydroxyl ions get attached to the carbonyl carbons leading to breaking of ester linkages **(Elsawy et al., 2017)**. Improving hydrolytic resistance of PLA for applications in wet environments motivates research on CSN loaded PLA/CSN bionanocomposite.

Recently, silk has become a suitable reinforcement for PLA due to its superior mechanical properties, biocompatibility and biodegradability. Silk has a morphologic flexibility which has opened new avenues for applications such as food packaging, tissue engineering and other biomedical engineering purposes. Silk can be used as a PLA reinforcement in form of fibers, blends and nanoparticles, etc. **Tesfaye et al. (2017)** have

performed investigations on the isothermal crystallization kinetics and thermal degradation of PLA/silk nanocrystals nanocomposites under repetitive extrusion process. Silk nanocrystals are ~100 nm spherical crystals obtained by acid hydrolysis. Another modification of silk is the crystalline silk nano-discs (CSNs), which highly crystalline nanoparticles having a well-defined discotic morphology with dimensions of ~50 nm diameter and ~2-4 nm thickness. Such materials have not been reported so far to the best of our knowledge.

In the present investigation reported here, disc like silk nano-discs, a novel bio-filler synthesis in previous section (~50 nm in diameter and ~2-4 nm in height) is used for fabrication of PLA bionanocomposites by melt extrusion. The effects of variation in silk nano-disc content on thermal stability and hydrolytic degradation of PLA/CSN bionanocomposites is investigated in detail. We have investigated thermal degradation behaviors using TGA and DSC experimental data recorded at different heating rates. To the best of our knowledge, analysis of effect of loading of silk nano-discs on kinetics of thermal degradation of PLA has not been reported. Non-isothermal degradation kinetics is carried out using different model fitting and model free methods to determine kinetic parameters such as activation energy (E_a) and regression coefficient, thus this work to understand the effect of CSN loading on PLA thermal stability is greatly needed. It is expected that the research reported herein can allow for enhancing the thermal stability and hydrolytic degradation behavior of the system to decide for potential applications. The calculated kinetic parameters using different methods are compared and discussed.

6.1.1 Theoretical considerations for thermal degradation kinetic computations

The general expression for decomposition rate may be given as Eq. (6.1):

$$\frac{d\alpha}{dt} = k(T).f(\alpha) \qquad (6.1)$$

Where, $\frac{d\alpha}{dt}$ is conversion rate, k(T) is degradation rate constant, α is the degree of conversion ($0.1 \leq \alpha \leq 0.9$) with respect to temperature ($\alpha = (w_o - w_t)/(w_o - w_f)$), w_o, w_t and w_f are the initial, at time (t) and final weight of the sample in the TGA curves, respectively, t is the reaction time (s) and f(α) is differential form of kinetic model function which depends on degradation mechanism. The degradation rate constant can be related to Arrhenius equation:

$$k(T) = A \exp\left(\frac{-E_a}{RT}\right) \quad (6.2)$$

where, 'A' stands for pre-exponential factor (s^{-1}), 'E_a' is the activation energy (kJ mol^{-1}), 'R' represents the gas constant (8.314 J $mol^{-1}K^{-1}$) and 'T' denotes the absolute temperature (K). The above two equations can be combined as:

$$\frac{d\alpha}{dt} = A \exp\left(\frac{-E_a}{RT}\right) . f(\alpha) \quad (6.3)$$

The heating rate, $\left(\beta = \frac{dT}{dt}\right)$ can be incorporated in Eq. 6.3 for the following expression:

$$\frac{d\alpha}{dT} = A \frac{1}{\beta} \exp\left(\frac{-E_a}{RT}\right) . f(\alpha) \quad (6.4)$$

Where, $\frac{d\alpha}{dt}$ is the rate of non-isothermal reactions. Generally polymer degradation is a complex degradation reaction which does not remain constant for the entire reaction duration. To address this complicated reaction mechanism it is assumed that degradation reaction follows a simple n^{th} order reaction. *f(α)* is written as $(1-\alpha)^n$, where n denotes the order of reaction. Polymer degradation can be considered as a classical example of solid state reaction, where a minimum amount of energy is needed for the atoms/molecule to vibrate and rupture the chemical bonds, this energy is known as apparent activation energy **(Yuzay et al., 2010)**. To determine the degradation kinetic parameters and degradation mechanism, thermogravimetric analysis (TGA) is considered to be the most suitable analysis technique **(Mallakpour and Taghavi, 2009)**. The kinetic parameters can be obtained by solving the above mentioned equations by integration, differentiation and approximation. Based on these approaches the models can be majorly divided into two broad categories i.e. model free or isoconversional methods and model fitting methods **(Yuzay et al., 2010)**.

6.1.1.1 Iso-conversional or model free methods

These methods are based on the principle that at a particular conversion, the rate of reaction is a function of temperature. The knowledge of exact thermal decomposition mechanism is not a prerequisite for the isoconversional methods. Such methods can be used to determine the activation energies corresponding to conversion values (α) without any model approximations. These methods use multiple heating rate TGA data **(Das and Tiwari, 2017)**.

6.1.1.1.1 Kissinger-Akahira-Sunose (K-A-S) model

This integral isoconversional model based on **Murray and White (1955)** temperature integral approximation, is also known as generalized Kissinger method and is given as:

$$\frac{d\alpha}{f(\alpha)} = A\frac{1}{\beta}\exp\left(\frac{-E_a}{RT}\right).dT \tag{6.5}$$

Integrating the above expression with the initial conditions $\alpha=0$ and $T=T_0$, to obtain the relation:

$$g(\alpha) = \int_0^{\alpha}\frac{d\alpha}{f(\alpha)} = A\frac{1}{\beta}\int_{T_0}^{T}\exp\left(\frac{-E_a}{RT}\right).dT \equiv \frac{AE_a}{\beta R}p\left(\frac{E_a}{RT}\right) \tag{6.6}$$

$$p\left(\frac{E_a}{RT}\right) \cong \frac{\exp\left(\frac{-E_a}{RT}\right)}{\left(\frac{E_a}{RT}\right)^2} \tag{6.7}$$

The crucial assumption of this approach is that 'A', 'E_a' and 'f(α)' are temperature independent, besides this, 'A' and 'E_a' are also independent of α. The term g(α) is the integral form of the model. Upon integration of Eq. (6.6) natural logarithm is taken on both sides to obtain the following relation:

$$\ln g(\alpha) = \ln\left(\frac{AE_a}{R}\right) - \ln\beta + \ln p\left(\frac{E_a}{RT}\right) \tag{6.8}$$

The final expression is of the following form **(Akahira and Sunose, 1971)**:

$$\ln\left(\frac{\beta}{T^2}\right) = -\left(\frac{E}{RT}\right) + \ln\left(\frac{AR}{E_a g(\alpha)}\right) \tag{6.9}$$

The activation energy corresponding to each degree of conversion (α) is obtained from slope of linear plots of $\ln\left(\frac{\beta}{T^2}\right)$ vs. $\left(-\frac{1}{T}\right)$, pre-exponential factor (A) can be determined from the intercept **(Aboulkas and El Harfi, 2008)**.

6.1.1.1.2 Flynn-Wall-Ozawa (F-W-O) model

Flynn-Wall-Ozawa (F-W-O) method is another integral isoconversional model where temperature measurements at different conversion values (α) at different heating rate (β) are considered for calculations **(Zou et al., 2009)**. It is assumed that conversion function f(α) does not change with the heating rate (β) for all values of the degree of conversion (α). Integrate Eq. (6.5) with condition of conversion (α) from α_0 to α_p, the following expression is obtained:

$$g(\alpha) = \int_{\alpha_0}^{\alpha_p} \frac{d\alpha}{f(\alpha)} = A\frac{1}{\beta}\int_{\alpha_0}^{\alpha_p} \exp\left(\frac{-E_a}{RT}\right).dT \quad (6.10)$$

Replacing, $x = \frac{E_a}{RT}$, integrating the R.H.S. of Eq. (6.10) we get:

$$g(\alpha) = \int_{\alpha_0}^{\alpha_p} \frac{d\alpha}{f(\alpha)} = \frac{AE_a}{\beta R} p(x) \quad (6.11)$$

Taking logarithms on both sides, the above expression becomes:

$$\log \beta = \log \frac{AE_a}{g(\alpha)R} + \log p(x) \quad (6.12)$$

Applying Doyle's approximation **(Doyle, 1958)**:

$$\log p(x) = -2.315 - 0.4567x \quad (6.13)$$

Substituting Eq. (6.13) into Eq. (6.12) to obtain final form of F-W-O model **(Flynn and Wall, 1966)**:

$$\log \beta = \left\{\log \frac{AE_a}{g(\alpha)R} - 2.315\right\} - \frac{0.4567\, E_a}{RT} \quad (6.14)$$

The activation energy is obtained from slope of linear curves of $(\ln \beta)$ vs. $\left(-\frac{1}{T}\right)$, at constant value of fractional conversion, pre-exponential factor (A) can be determined from the intercept **(Valapa et al., 2014)**. This model is generally applied to those systems where activation energy changes with time due to multiple reactions, whereas it cannot be applied when different reactions occur simultaneously **(Venkatesh et al., 2013)**.

6.1.1.2 Model fitting methods

6.1.1.2.1 Coats-Redfern (C-R) Model

Model fitting approach requires fitting the conversion versus temperature (for single heating rate). Subsequently, 'E_a' and 'n' are determined. The drawback with this approach is that if a system follows a complex thermal degradation mechanism then it gives drastic variations in Arrhenius parameters **(Othman et al., 2016)**. **Coats and Redfern (1964)** method is based on the model-fitting approach, which involves fitting various models to conversion versus temperature curves. It is an integral method that uses the asymptotic series expansion to solve the Eq. (6.6), which can be applied to TG data. The correct reaction order (n) is expected to lead the best linear fit (R^2 approach to 1), from which 'E_a' and 'A' are determined. The final form of the equation which is used for the analysis the

kinetic parameters described by the following equations **(Baloch et al., 2011; Hu et al., 2015)**:

$$Y = \ln\left[\frac{1-(1-\alpha)^{1-n}}{T^2(1-n)}\right] = \ln\frac{AR}{\beta E}\left[1-\frac{2RT}{E_a}\right] - \left(\frac{E_a}{RT}\right); n \neq 1 \quad (6.15)$$

$$Y = \ln\left[\frac{-\ln(1-\alpha)^{1-n}}{T^2}\right] = \ln\frac{AR}{\beta E}\left[1-\frac{2RT}{E_a}\right] - \left(\frac{E_a}{RT}\right); n = 1 \quad (6.16)$$

Thus a plot of (Y) vs. $(1/T)$ should result in a straight line of slope that equals to (E_a/R) for the chosen value of 'n'. The value of 'A' is calculated from intercept of the straight line, by considering the expression [1-(2RT/E_a)] equal to unity **(Valapa et al., 2015b)**. **Ramukutty and Ramachandran (2014)** reported that the positive value of 'E_a' confirmed there is no phase transition in the selected temperature range.

6.1.1.3 Prediction of degradation mechanism by Criado method

Kinetic parameters determined using the model fitting approach i.e., C-R method which takes into account single heating rate are used in Criado method **(Criado et al., 1989)**. The reaction mechanism is determined with the help of activation energy, pre-exponential factor and the apparent order of the reaction calculated using C-R method. Criado equation is given by:

$$Z(\alpha) = \frac{\frac{d\alpha}{dt}}{\beta}\,\pi(x)T \quad (6.17)$$

Where x is (E_a /RT), $\pi(x)$ can be related to P(x) by expression (6.18):

$$\pi(x) = xe^{x}P(x) \quad (6.18)$$

In this method reaction mechanism is predicted by comparing experimental values with various theoretical solid state reaction mechanisms. To determine the experimental values as a function of conversion (α) following Eq.(6.19) is used by combining Eqns. (6.17) and (6.18):

$$Z(\alpha)_{exp} = \frac{E_a}{R}\,\frac{d\alpha}{dT}\,e^{E_a/RT}\,p(x) \quad (6.19)$$

The term p(x), which is temperature dependent can be expressed in a rational form, Eq. (6.20), having a low error of 10^{-5}% (x>20) **(Senum and Yang, 1977)**:

$$p(x) = \frac{e^{-x}}{x}\,\frac{x^3+18x^2+86x+96}{x^4+20x^3+120x^2+240x+120} \quad (6.20)$$

Using Eqns. (6.17, 6.18 and 6.20), we get:

$$Z(\alpha) = f(\alpha).g(\alpha) \tag{6.21}$$

The theoretical master plots ($Z(\alpha)$ versus α) for various reaction mechanisms were plotted according to Eq. (6.22) by combining Eqns. (6.4) and (6.21). Here, $g(\alpha)$ values (see Table 6.1) are used into the below mentioned expression:

$$Z(\alpha)_{\text{theortical}} = \frac{\beta}{A}\, g(\alpha) \frac{d\alpha}{dT}\, e^{\frac{E_a}{RT}} \tag{6.22}$$

Thereafter, the experimental plots ($Z(\alpha)_{exp}$ versus α) using Eq. (6.19) is compared with master plots, Eq. (6.22) to determine the accurate thermal degradation process of all samples. As seen in Table 6.1, the algebraic expressions that represent the reaction mechanism for solid state process are divided into four broad categories nuclei formation and growth (A_n), phase boundary controlled reaction mechanism (R_n), diffusion related to heat transfer (D_n) and random nuclei degradation (F_n) for thermal degradation process **(Khawam and Flanagan, 2006a; b; Tiptipakorn et al., 2007)**.

Table 6.1: Algebraic expressions for integral form g (α) for the most frequently used mechanisms in solid state degradation process.

Solid State Degradation Mechanism	**Significance**	**Sy.**	***g*(α)**
Nuclei formation and growth	Avrami 2-D nucleation	A2	$[-\ln(1-\alpha)]^{1/2}$
	Avrami 3-D nucleation	A3	$[-\ln(1-\alpha)]^{1/3}]$
	Avrami 4-D nucleation	A4	$[-\ln(1-\alpha)]^{1/4}$
Phase boundary controlled reaction mechanisms	contracting cylinder	R2	$[1-\ln(1-\alpha)^{1/2}]$
	contracting sphere	R3	$[1-\ln(1-\alpha)^{1/3}]$
Diffusion related to heat transfer	1-D	D1	α^2
	2-D	D2	$[[(1-\alpha)\ln(1-\alpha)]+\alpha]$
	3-D, Jander Eq.	D3	$[1-(1-\alpha)^{1/3}]^2$
	3-D, Ginstlinge–Brounshetein eq.	D4	$[(1-(2/3)\alpha)]-(1-\alpha)^{2/3}$
Random nuclei	Mampel First order	F1	$[-\ln(1-\alpha)]$
	Second order	F2	$1/(1-\alpha)$

6.1.1.4 Theoretical considerations for hydrolytic degradation kinetic computations

Prior to immersion, weight of the initial sample (dried under vacuum at 37 °C) was carefully weighed. After being placed into the solution for defined time-period, the sample was taken out, washed with fresh water and dried at 37 °C for 24 h to ensure complete removal of water. Subsequently, the residual weight of the hydrolyzed sample was carefully weighed to know the weight loss of the sample during the hydrolytic degradation process. The residual weight fraction was determined using the following expression **(Girdthep et al., 2016)**:

$$\phi = \frac{W_t}{W_o} \times 100 \tag{6.23}$$

Where, 'W_o' and 'W_t' refer to the dry weight (g) of the sample, prior to and after certain time (t) of, the hydrolytic degradation process, respectively.

6.1.1.4.1 Hydrolytic degradation rate

The hydrolytic degradation rate (R, %/day) was defined according to the following relation **(Fernández and Fernández, 2017)**:

$$R = \left(\phi_{before} - \phi_{after}\right)/_{t} \tag{6.24}$$

Where, 'ϕ_{before}' and 'ϕ_{after}' are the residual weight fraction of sample before and after being hydrolyzed for a certain time (t).

6.1.1.4.2 Molecular weight degradation kinetics

The molecular weight kinetics can be studied from the relation where (ln M_w) as a function of immersion time (t), and also 'M_n' and 'M_w' are proportional to each other **(Li et al., 2017; Zhou and Xanthos, 2008)**:

$$\ln M_w = A - k.t \tag{6.25}$$

The plots of (Ln M_w) against (t) yields straight line whose slope gives value of 'k' which is degradation rate while the intercept yields a constant.

6.2 Results and discussion

6.2.1 Thermal degradation behavior of PLA/CSN bionanocomposites

To understand the influence of CSN on thermal degradation behavior of PLA, a detailed investigation was carried using Kissinger-Akahira-Sunose (K-A-S), Flynn-Wall-Ozawa (F-W-O), Coats-Redfern (C-R) and Criado's method, to gain more insight on thermal degradation kinetics of PLA and PLA/CSN bionanocomposites. The temperature dependent weight loss curve with its derivative obtained at a heating rate of 20 °C/min for PLA and PLA/CSN bionanocomposite are shown in Figure 6.1. This one step degradation from 322 to 396 ℃ is mainly due to hydrolysis by water present in trace amounts in PLA, fragmentation generating acetaldehyde, CO_2, cis-elimination producing acrylic acid and intra transesterification which forms cyclic oligomers **(Xu et al., 2016)**. The temperature, (T_{max}) at the maximum rate of mass loss is considered as point of comparison which is also a significant thermal parameter to understand the thermal degradation of polymer bionanocomposites. From the DTG profiles (Figure 6.1), the maximum decomposition temperatures for extruded PLA, 0.5, 1, 2, and 5 wt% PLA/CSN bionanocomposites are 394, 396.5, 396.5, 394 and 387.3 °C respectively. The T_{max} of PLA/CSNs samples upto 2 wt% CSN loading remain almost unchanged. It is known that polar gaseous compounds are released during degradation which cleave the PLA chains while eluting out **(Petinakis et al., 2010)**. Formation of structure among PLA/CSN leads to slow elution of degradation products resulting into thermally stable bionanocomposites, it indicated that PLACSN5 decomposes more quickly than PLA. This observation can be ascribed to presence of more acidic sites on the CSN surface which catalyze the decomposition of the bionanocomposite at a faster rate leading to short polymer chains **(Dhar et al., 2014; Valapa et al., 2014)**. At low concentrations, CSN are well-dispersed in the PLA matrix. Such well-ordered β-sheet structures when dispersed properly in the PLA matrix give rise to a labyrinth kind of network formation which provide a tortuous path. As it can be seen from TGA data at 20 °C/min, the addition of 0.5 wt% CSNs does not much alter the thermal stability of PLA matrix which might be due to hydrophobic nature of CSNs. While the presence of 1 wt% CSNs shows highest thermal stability, increasing the T_{onset} (~332 ºC) of the bionanocomposite suggesting a close interaction between the CSNs and PLA matrix. The TG result indicates that the PLACSN1 exhibits around 10 °C improvement in onset degradation temperature than extruded PLA. With further increase in loading to 2 and 5 wt%, T_{onset} shows decrease to 330 °C and 326 °C, respectively which

could be possibly due to the agglomeration of CSN nanoparticles leading to poor dispersion which upon degradation creates increased acidic sites, hence is less thermally stable. Hence, it can be inferred that there is no degradation occurring in either CSN or bionanocomposites in the temperature range 25 to 220 °C i.e. the PLA processing range.

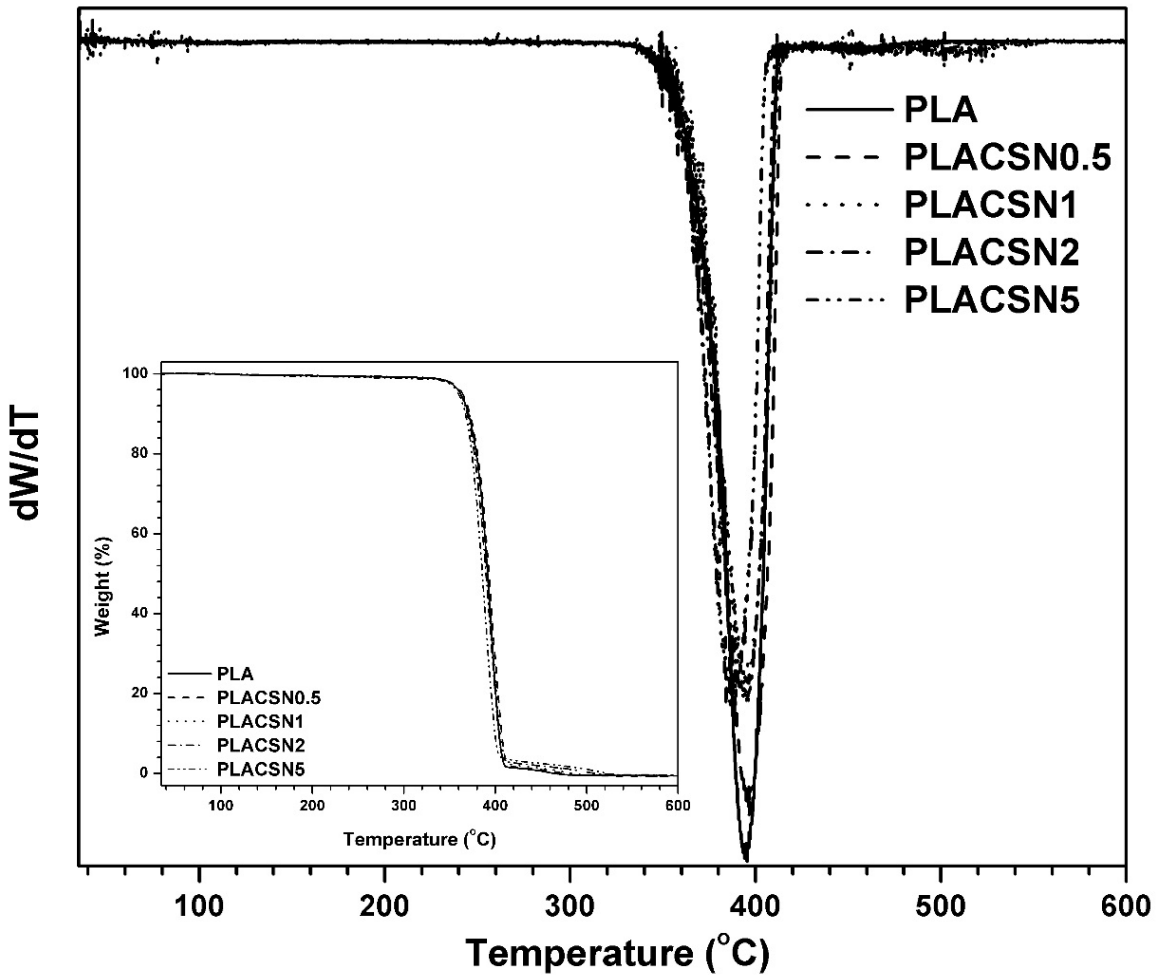

Figure 6.1: TGA and DTG thermograms of PLA and PLA/CSN bionanocomposites at rate of 20 °Cmin^{-1}.

6.2.2 Thermal degradation kinetics

The TGA and DTG thermograms for PLA and PLA/CSN bionanocomposites are obtained at heating rates of 10, 20 and 30 °C/min. It is observed that T_{onset}, T_{offset} and T_{max} show progressive increment with increasing heating rates. The values of T_{onset}, T_{offset} and T_{max} at different heating rates are listed in Table 6.2. With increased heating rates there is a faster release of gaseous products, thus resulting in elevated peak temperatures and rate curves **(Kan et al., 2016)**.

Table 6.2: TGA parameters of PLA and PLA/CSN bionanocomposites at 10, 20 and 30 °Cmin^{-1}.

Samples	10 °C/min			20 °C/min			30 °C/min		
	T_{onset}	T_{offset}	T_{max}	T_{onset}	T_{offset}	T_{max}	T_{onset}	T_{offset}	T_{max}
PLA	307.7	398.7	379.9	322.3	412.2	394.0	341.4	427.6	407.2
PLACSN0.5	315.7	401.0	381.8	326.2	417.1	396.5	345.6	429.1	409.5
PLACSN1	317.8	404.7	380.5	331.5	425.1	396.5	346.7	428.7	405.1
PLACSN2	312.0	397.6	378	330.1	417.3	394.0	342.6	424.5	403.5
PLACSN5	310.6	394.6	369	326.2	409.5	387.3	338.6	420.9	399.4

The thermogravimetric (TGA) and differential (DTG) thermal profiles for PLA and PLA/CSN bionanocomposites at different heating rates of 10, 20 and 30 °C/min are shown in Figure 6.2. For all samples, shift in thermal profiles are observed due to the influence of heating rates and filler concentration. This shift is due to the fact that at higher heating rate, the sample gets a shorter time to reach a given temperature **(Aboulkas and El Harfi, 2008)**. The aim of conducting this analysis at different heating rates is to estimate the apparent activation energies (E_a) and thermal degradation behavior of PLA and PLA/CSN bionanocomposites. The E_a and R^2 have been calculated by using isoconversional (K-A-S and F-W-O) and model fitting (C-R) methods.

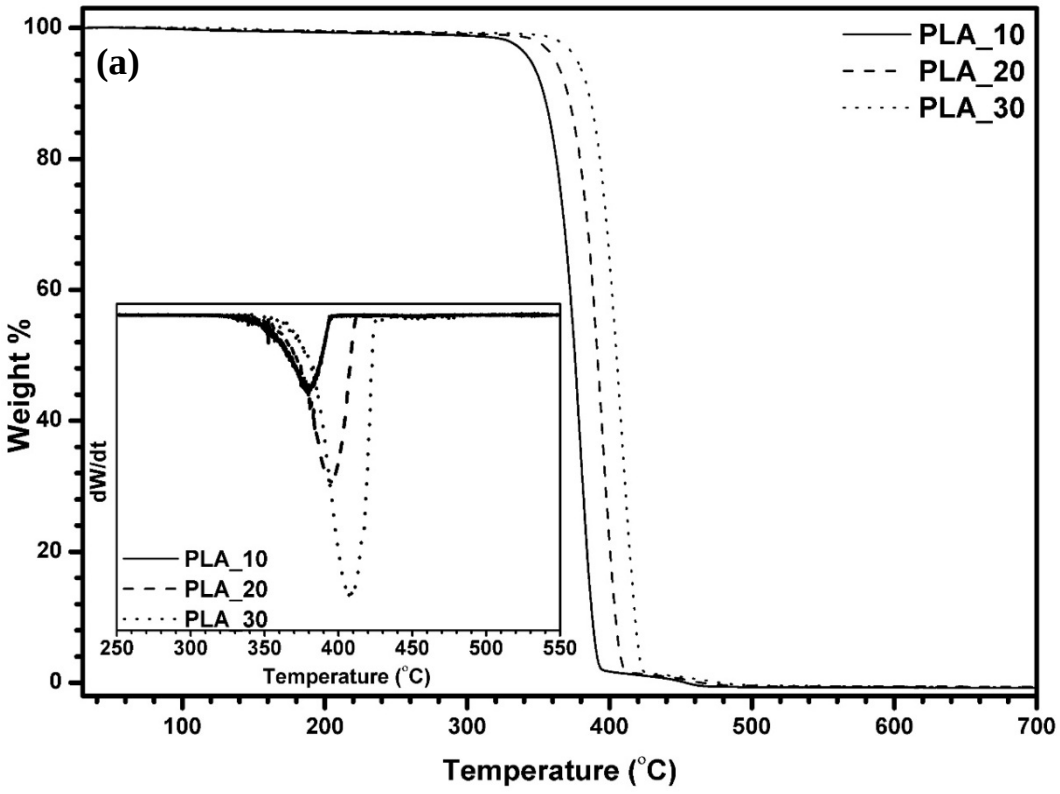

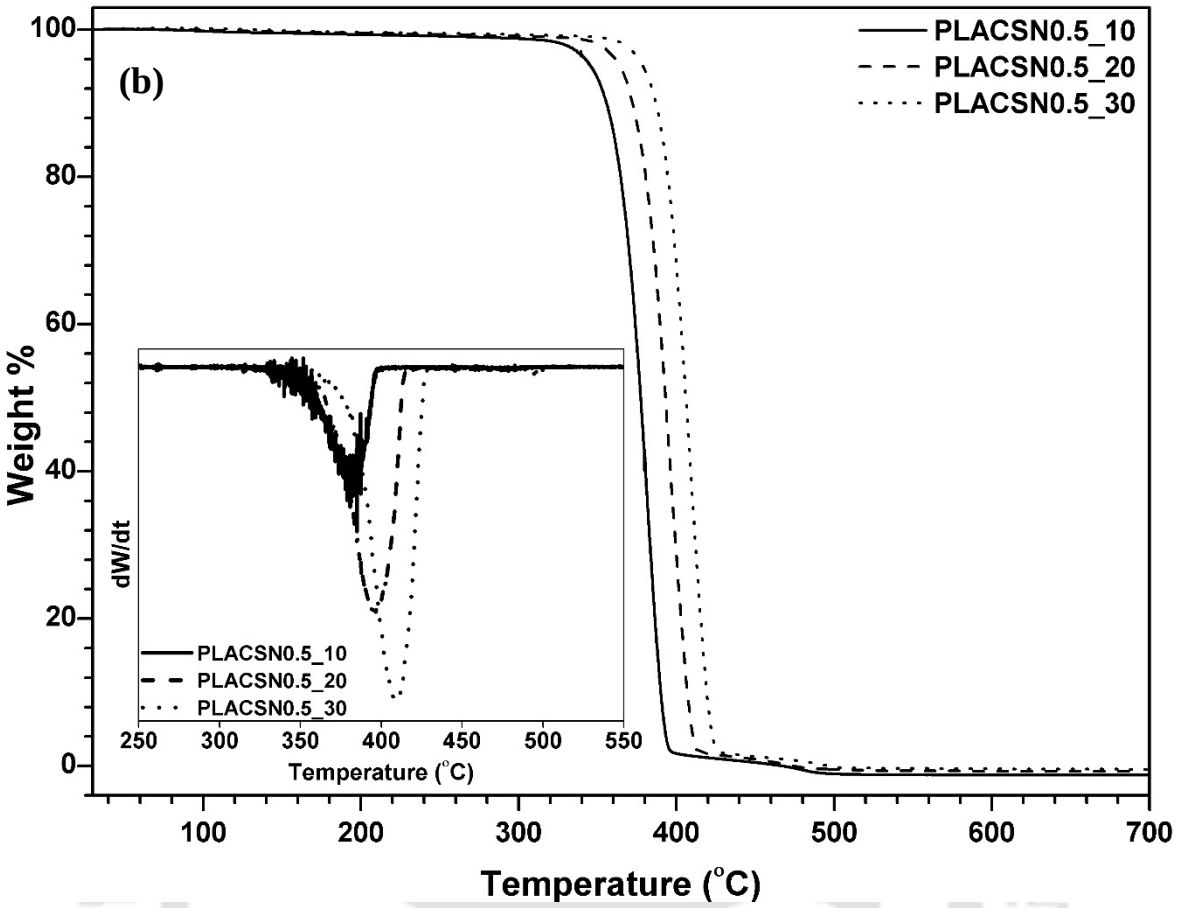
(b)
PLACSN0.5_10
PLACSN0.5_20
PLACSN0.5_30
Weight %
Temperature (°C)
dW/dt
PLACSN0.5_10
PLACSN0.5_20
PLACSN0.5_30
Temperature (°C)

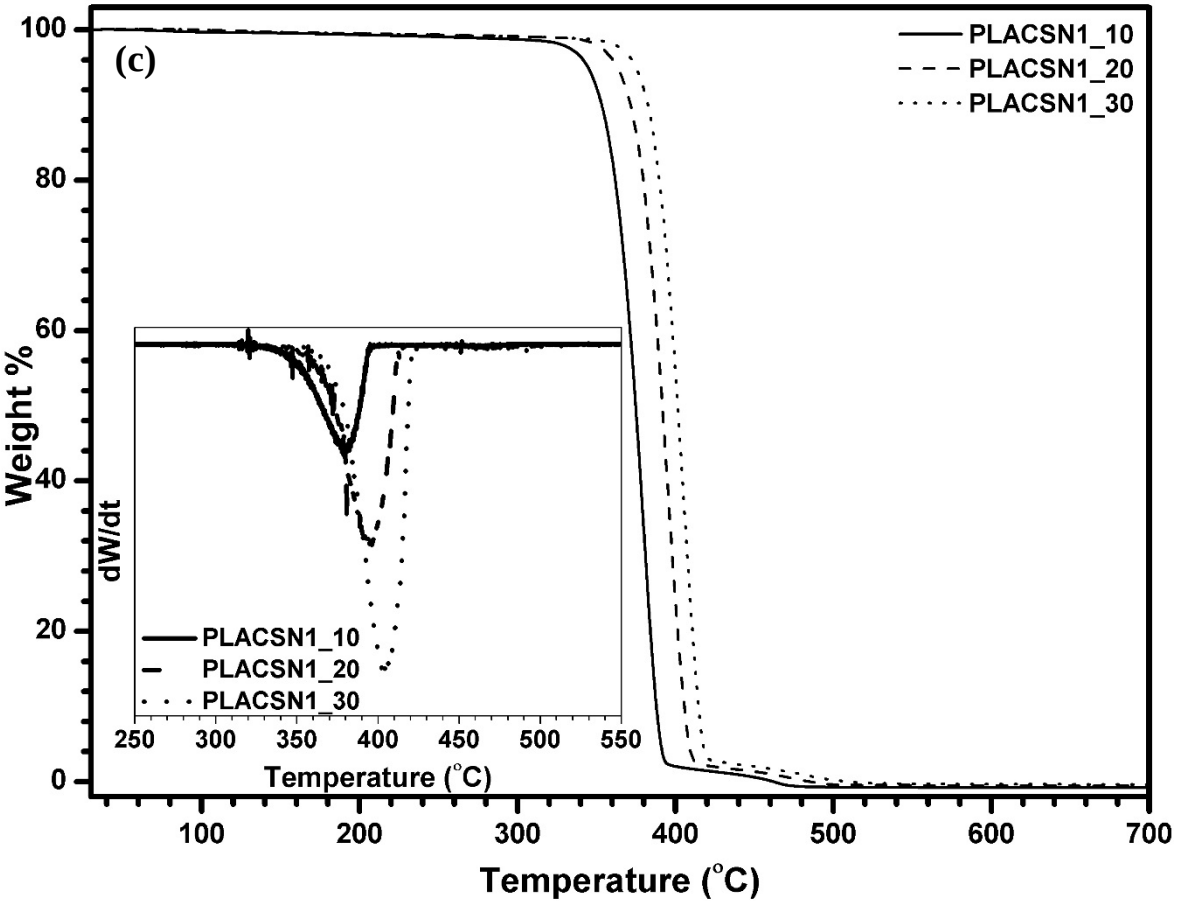
(c)
PLACSN1_10
PLACSN1_20
PLACSN1_30
Weight %
Temperature (°C)
dW/dt
PLACSN1_10
PLACSN1_20
PLACSN1_30
Temperature (°C)

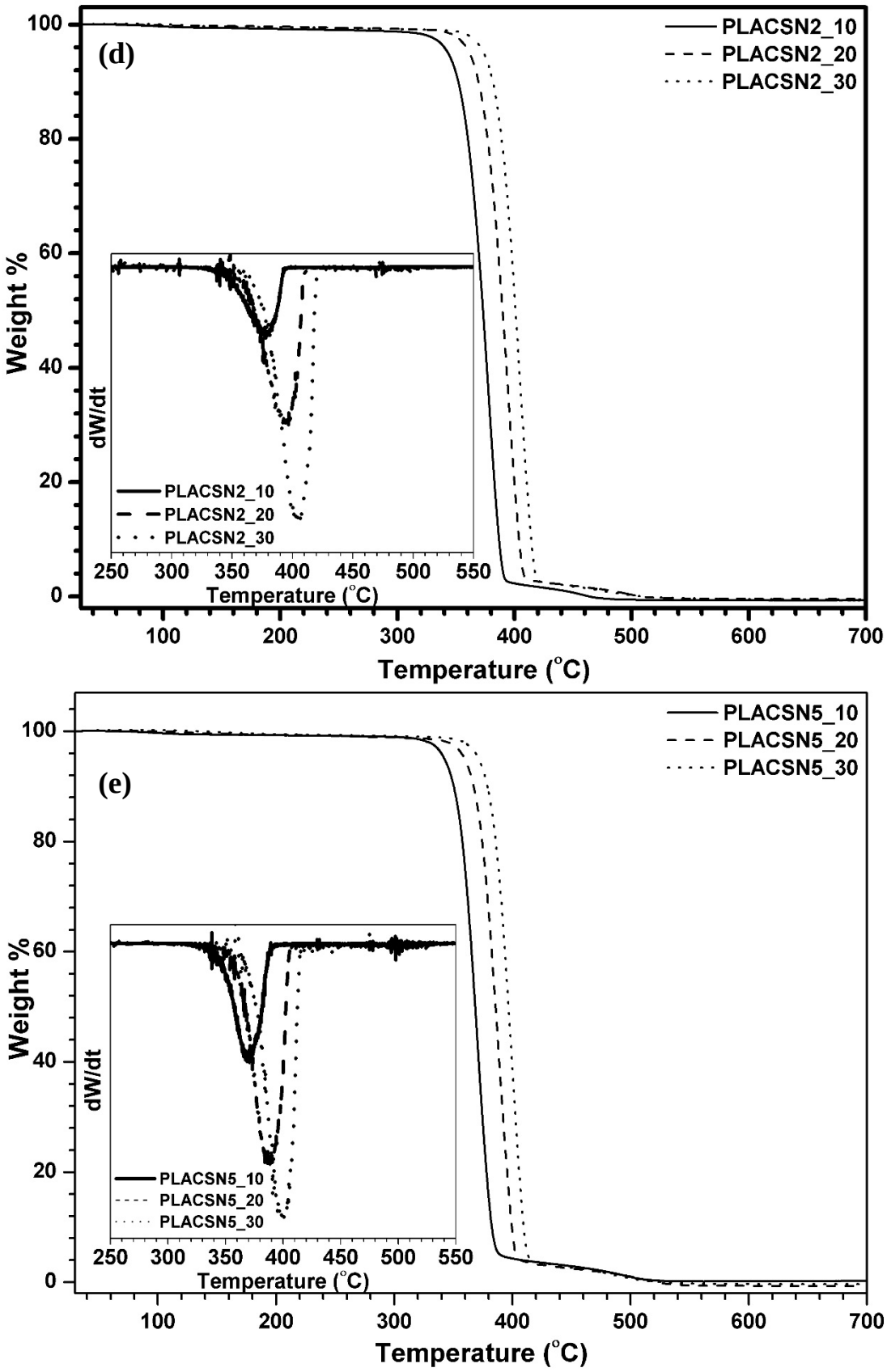

Figure 6.2: TGA and DTG curves of (a) PLA, (b) PLACSN0.5, (c) PLACSN1, (d) PLACSN2 and (e) PLACSN5 at the heating rates of 10, 20 and 30 °Cmin^{-1}.

6.2.2.1 Flynn-Wall-Ozawa model (F-W-O)

Figure 6.3(a-e) displays the F-W-O plots according to Eq. (6.14), log (β) versus -1000/T, at different conversion (α) (0.1 to 0.9) for PLA, PLCSN0.5, PLCSN1, PLCSN2 and PLACSN5. The points fall on nearly straight lines which are parallel for different heating rates, thus proving the applicability of the F-W-O method to the investigated system. The E_a for thermal degradation of PLA varies with α throughout the degradation process, indicative of a complex reaction of degradation **(Chen and Wu, 2007; Li et al., 2009; Yang et al., 2002)**. It can be observed that the activation energy for PLACSN1 has greatly improved in comparison to PLA which is consistent with the TGA (see Figure 6.1). The E_a shows increment almost linearly in the range 0.1 to 0.4 but then remained constant until complete decomposition for extruded PLA. A similar behavior was obtained by **Yuzay et al. (2010)** and the E_a value (128.1 kJ/mol) obtained for PLA in the present study is in line with the literature **(Yuzay et al., 2010)**. The addition of CSN at low concentrations i.e. 0.5 and 1 wt% causes a decrease in degradation rate for PLA bionanocomposites. This can be accounted for the network like formations between the PLA chains and CSN particles shown in previous sections. As evident from Table 6.3, apparent 'E_a' value of PLACSN0.5 (117-138 kJ/mol^{-}1) and PLACSN1 (120-147 kJ/mol^{-1}) is higher than PLA, which could signify slight improvement in the thermal stability. However, it is quite possible that it is not the thermal stability that is improved, but it is the nanoparticles interacting with the degradation volatiles that are delaying their diffusion out of the molten polymer bionanocomposite **(McNeill and Leiper, 1985; Nanda et al., 2011)**. Further loading of CSNs (2 and 5 wt%) in PLA matrix, there is decrement in activation energy. We observed that the calculated E_a for thermal decomposition of the PLACSN5 is lower than neat PLA. This means that less energy is required in the thermal decomposition of PLACSN5 in comparison with neat PLA. PLACSN5 bionanocomposite provides more actual acidic sites, this is probable reason to earlier degradation in comparison of neat PLA, because of more active end groups which have catalytic effect on PLA matrix and finally accelerate the degradation rate of PLA bionanocomposites. Another reason could possibly be the agglomerated nanoparticles fail to interact with polymer chains thus no structure formation takes place at higher concentrations.

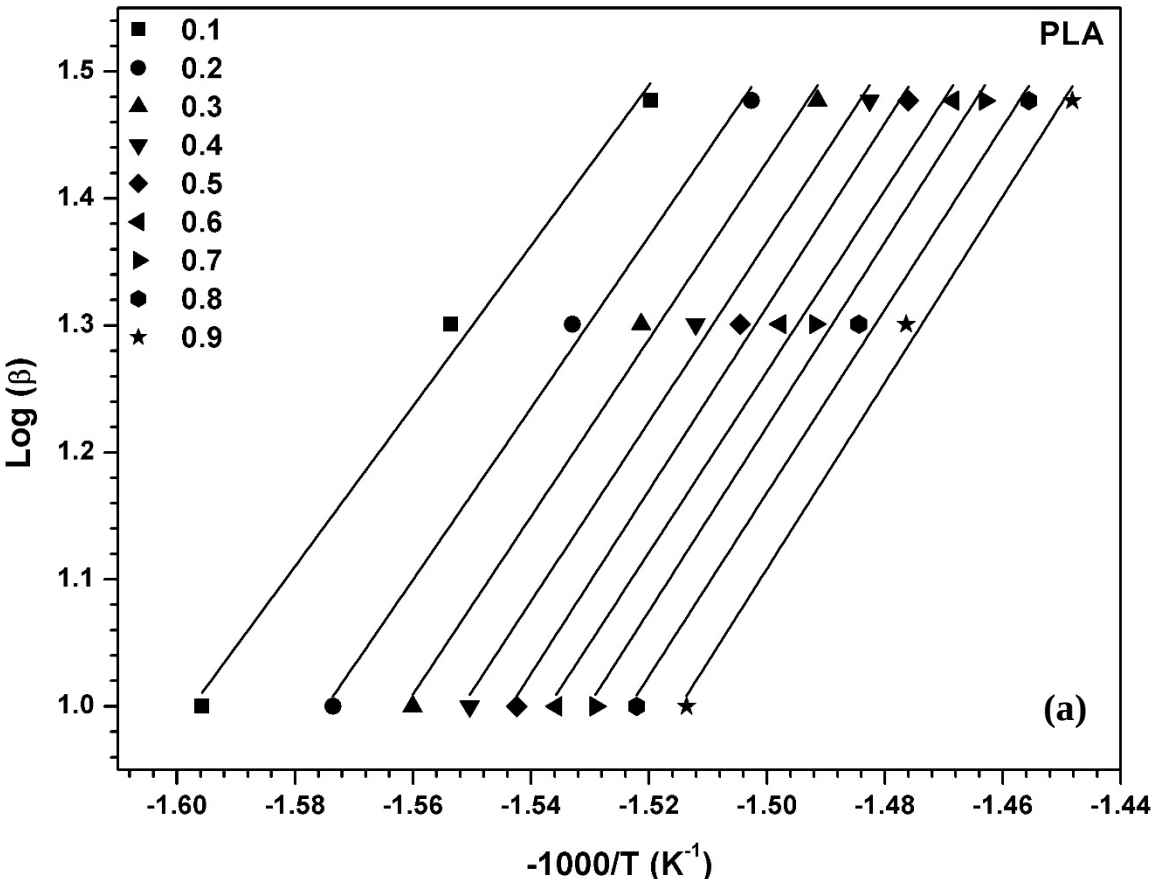
PLA
0.1
0.2
0.3
0.4
0.5
0.6
0.7
0.8
0.9
Log (β)
1.0
1.1
1.2
1.3
1.4
1.5
-1.60
-1.58
-1.56
-1.54
-1.52
-1.50
-1.48
-1.46
-1.44
-1000/T (K-1)
(a)

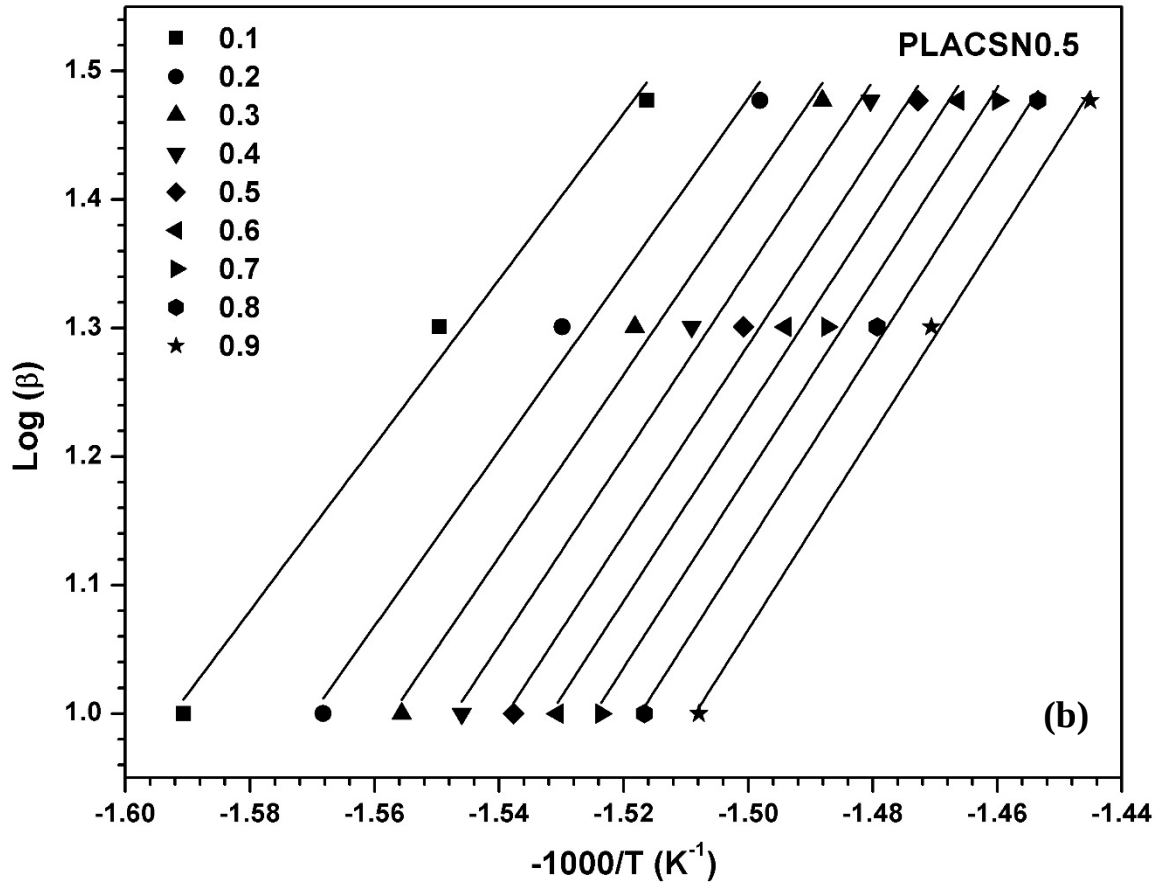
PLACSN0.5
0.1
0.2
0.3
0.4
0.5
0.6
0.7
0.8
0.9
Log (β)
1.0
1.1
1.2
1.3
1.4
1.5
-1.60
-1.58
-1.56
-1.54
-1.52
-1.50
-1.48
-1.46
-1.44
-1000/T (K-1)
(b)

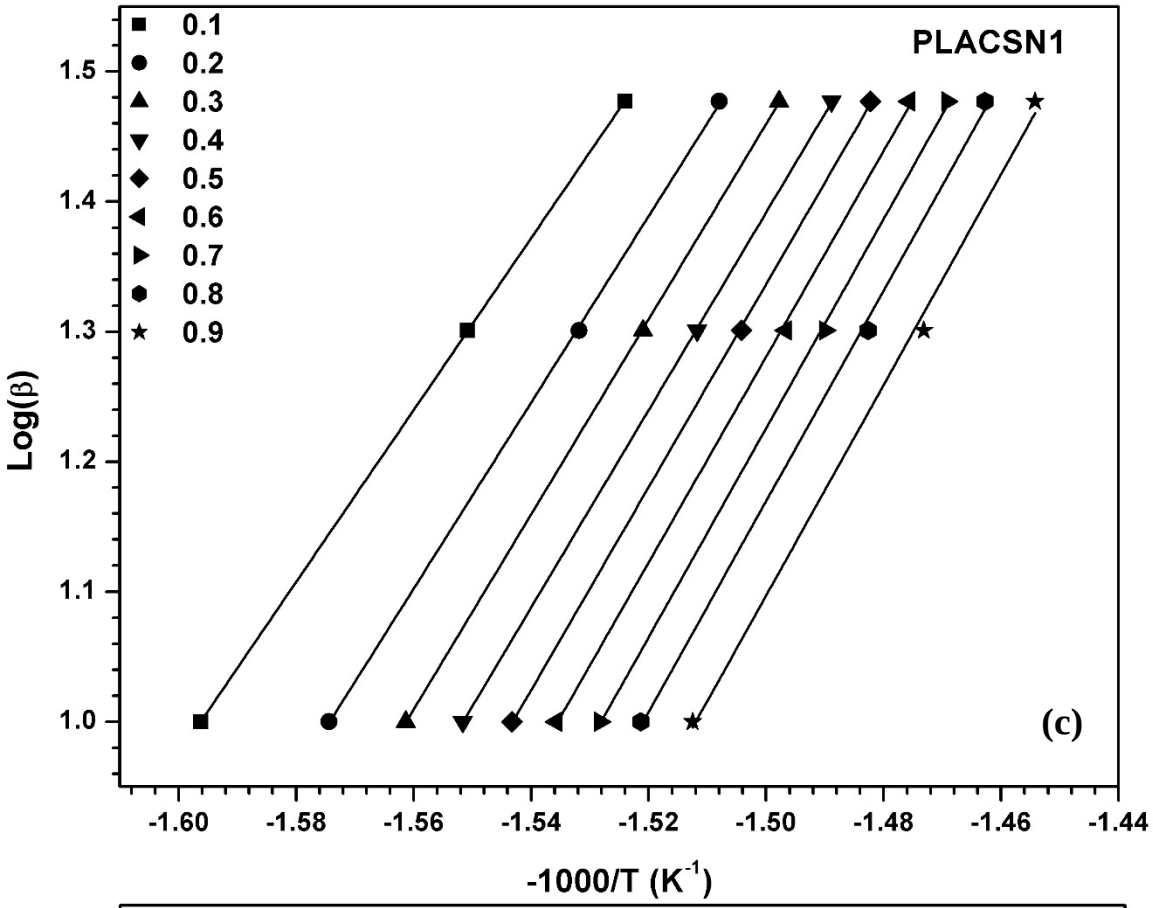
PLACSN1
0.1
0.2
0.3
0.4
0.5
0.6
0.7
0.8
0.9
Log(β)
-1000/T (K-1)
(c)

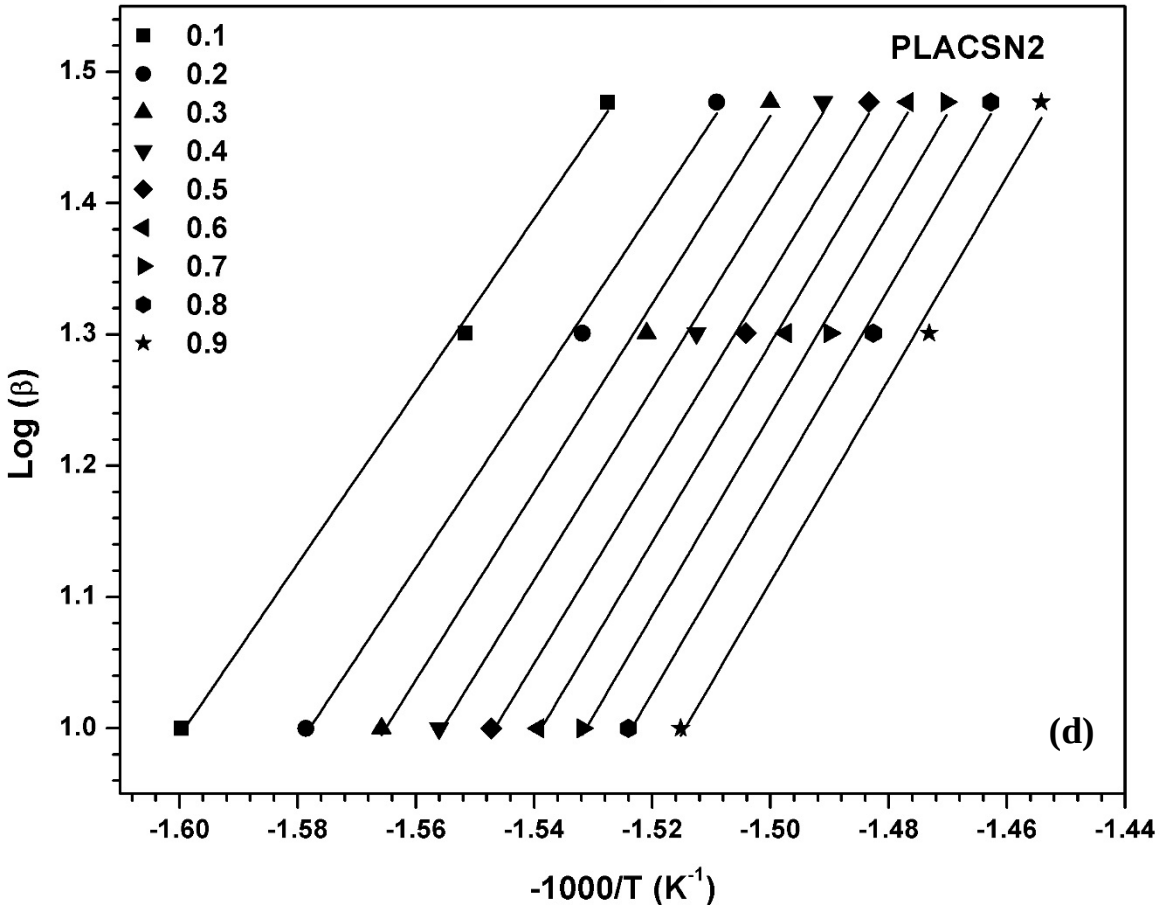
PLACSN2
0.1
0.2
0.3
0.4
0.5
0.6
0.7
0.8
0.9
Log (β)
-1000/T (K-1)
(d)

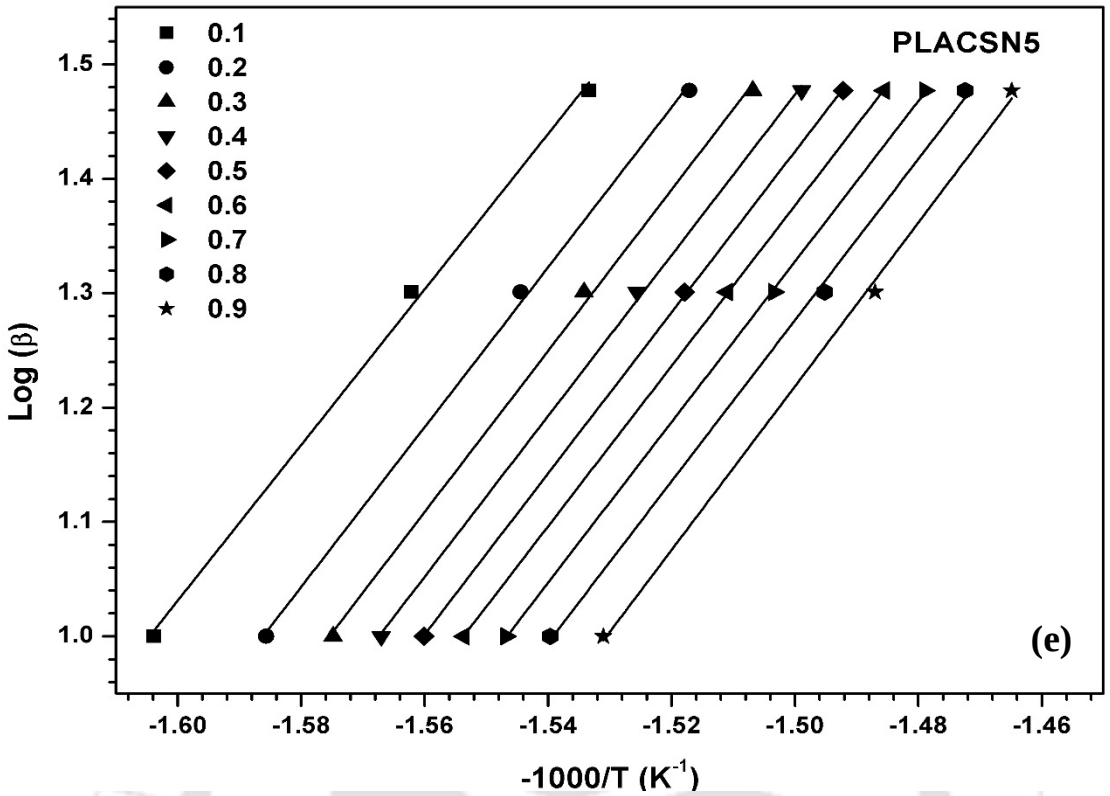

Figure 6.3: F-W-O plots of (a) PLA, (b) PLACSN0.5, (c) PLACSN1, (d) PLACSN2 and (e) PLACSN5.

6.2.2.2 Kissinger-Akahira-Sunose model (K-A-S)

In case of K-A-S method as per Eq. (6.9), plots of $[\mathrm{Ln}\,(\beta/T^2)]$ vs. $[-1000/T]$ in form of straight lines can be seen Figure 6.4(a-e). Slopes of straight lines obtained at different heating rates can be used to determine the apparent activation energies (Table 6.3). As can be observed, the parallel existence of the fitted straight lines shows the feasibility of K-A-S model. The E_a values obtained from both the methods were found to follow similar trend with respect to increase in CSN loadings. The close match between E_a values obtained from the K-A-S and F-W-O method shows that both isoconversional models are best suited models for this polymeric system. However value of E_a in K-A-S is slightly lower than those of F-W-O method. The difference in the E_a value calculated by the two methods due to different approximation is used to solve the analytical equation. It is well known that the F-W-O method based on Doyle's linear approximation while for K-A-S, Murray and White approximation is used **(Das and Tiwari, 2017)**. The correlation coefficients (R^2) values for both methods were in the range of 0.9-0.999 which implies their applicability for prediction of thermal degradation kinetic parameters of PLA and PLA/CSN bionanocomposites **(Valapa et al., 2014)**.

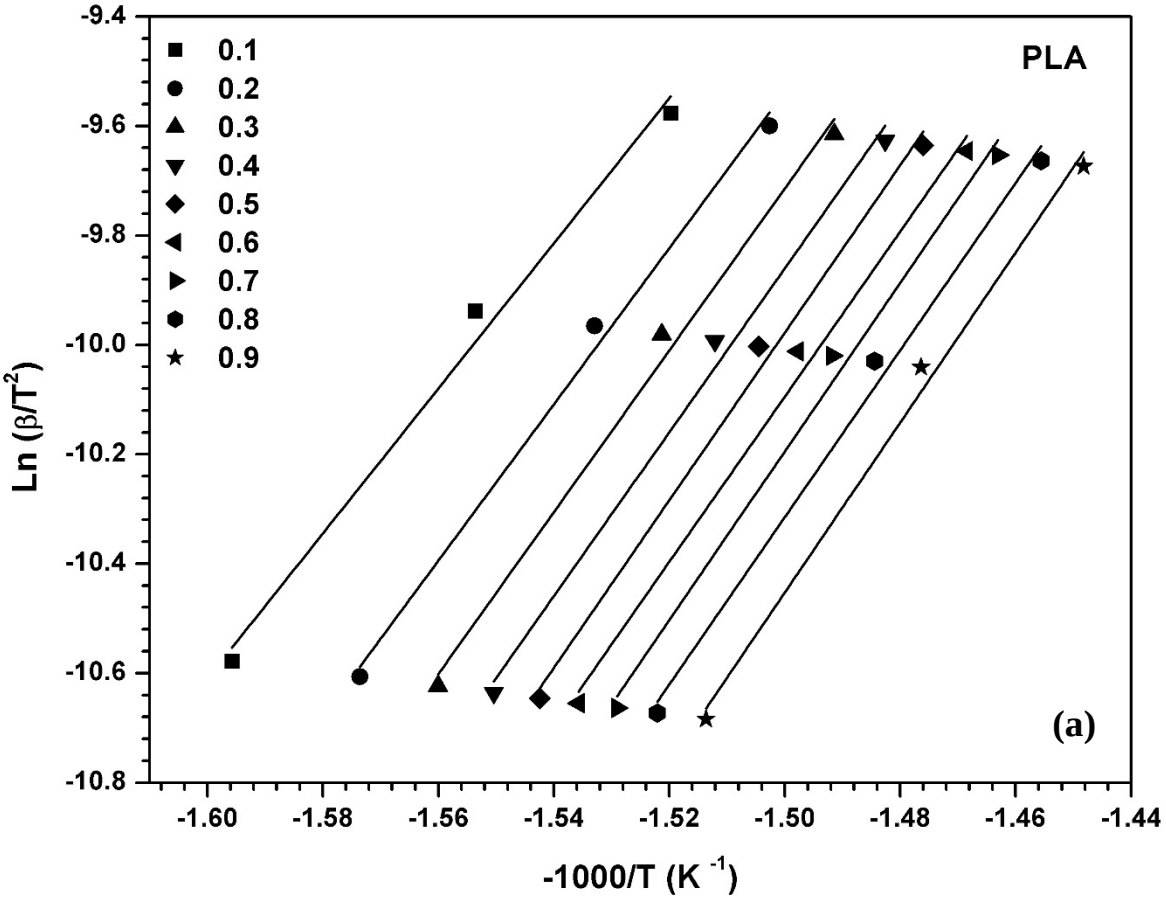
PLA
0.1
0.2
0.3
0.4
0.5
0.6
0.7
0.8
0.9
(a)
Ln (β/T²)
-1000/T (K⁻¹)
-9.4
-9.6
-9.8
-10.0
-10.2
-10.4
-10.6
-10.8
-1.60
-1.58
-1.56
-1.54
-1.52
-1.50
-1.48
-1.46
-1.44

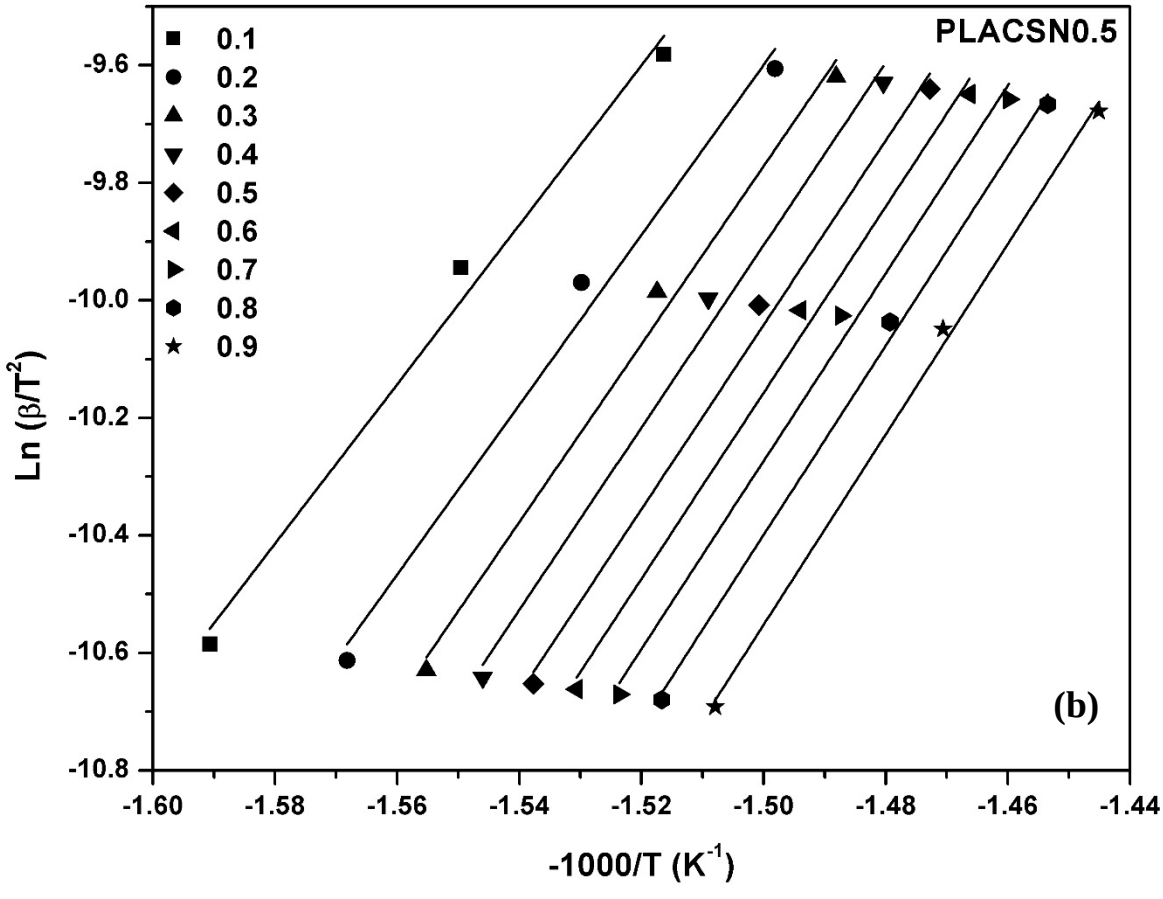
PLACSN0.5
0.1
0.2
0.3
0.4
0.5
0.6
0.7
0.8
0.9
(b)
Ln (β/T²)
-1000/T (K⁻¹)
-9.6
-9.8
-10.0
-10.2
-10.4
-10.6
-10.8
-1.60
-1.58
-1.56
-1.54
-1.52
-1.50
-1.48
-1.46
-1.44

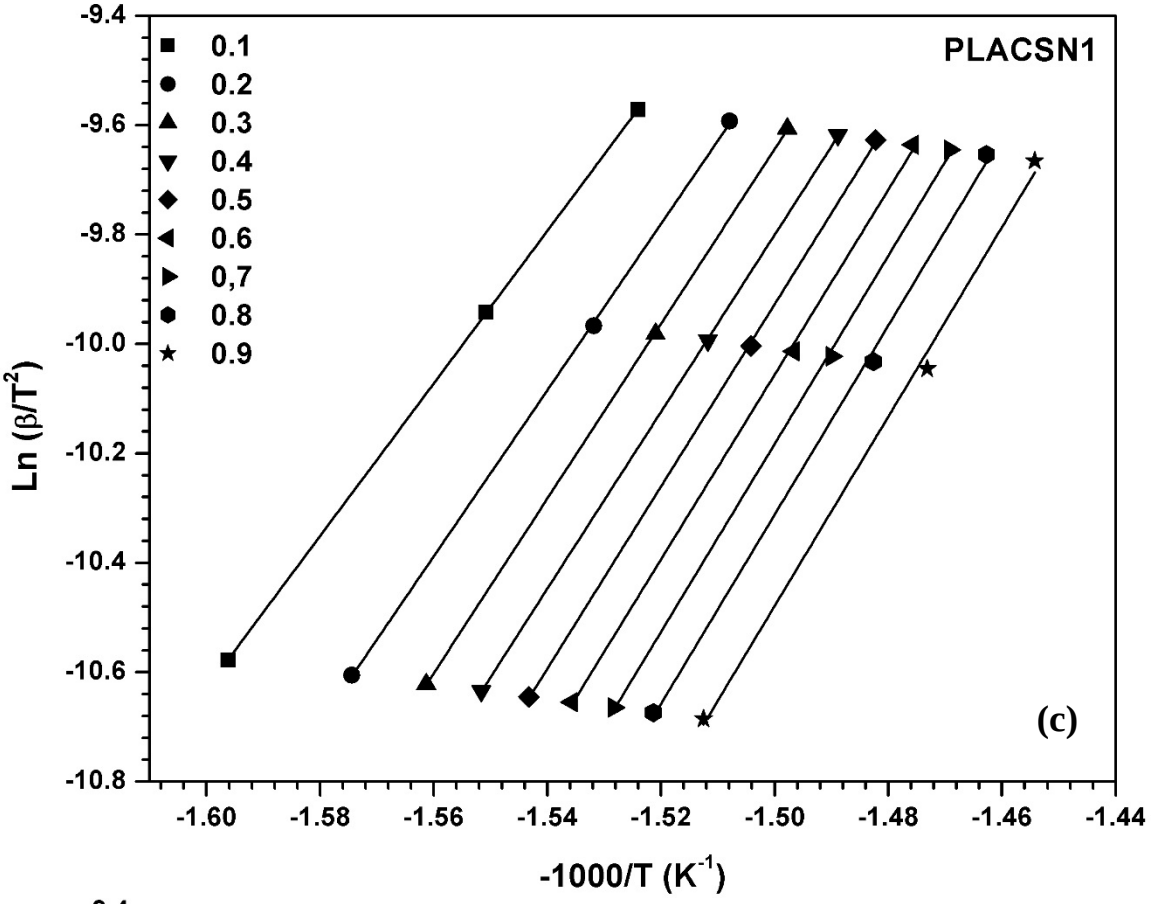
PLACSN1
0.1
0.2
0.3
0.4
0.5
0.6
0,7
0.8
0.9
(c)
Ln (β/T²)
-1000/T (K⁻¹)
-9.4
-9.6
-9.8
-10.0
-10.2
-10.4
-10.6
-10.8
-1.60
-1.58
-1.56
-1.54
-1.52
-1.50
-1.48
-1.46
-1.44

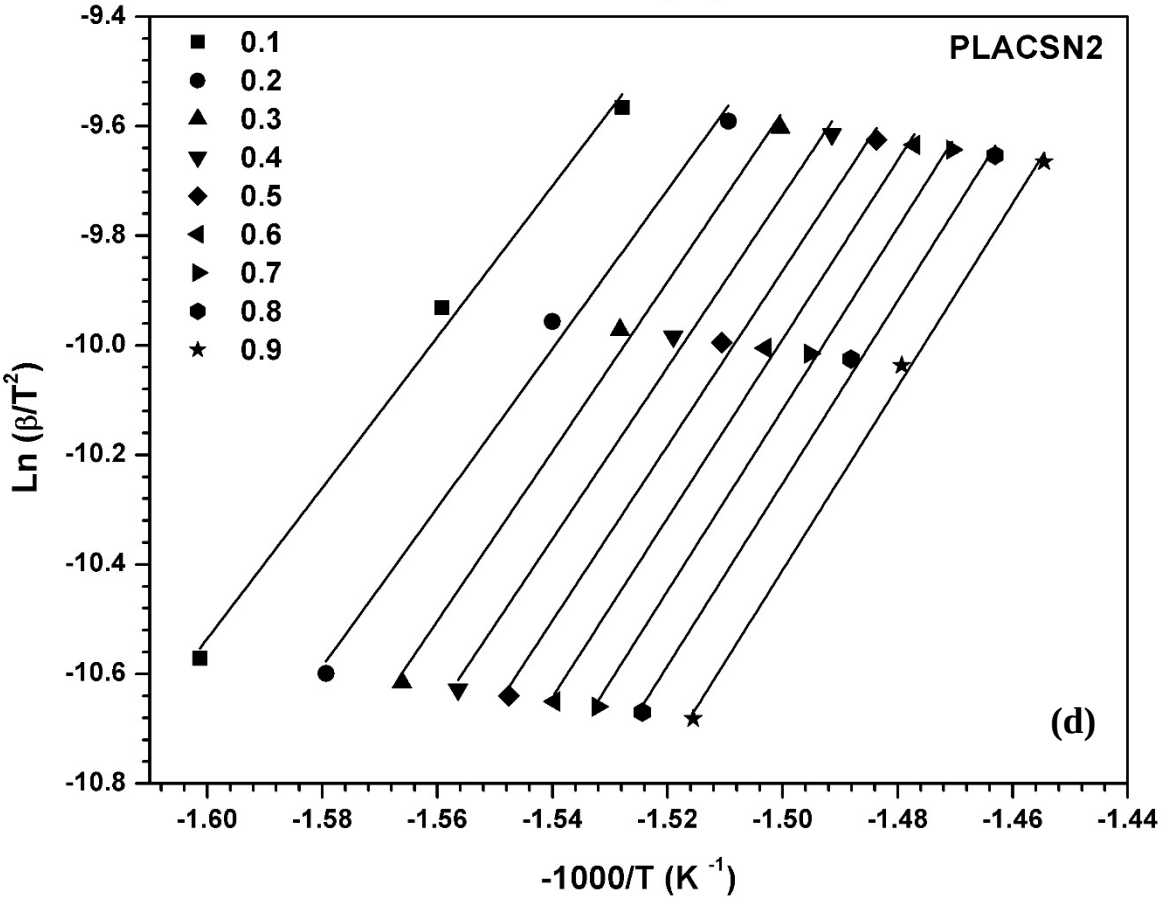
PLACSN2
0.1
0.2
0.3
0.4
0.5
0.6
0.7
0.8
0.9
(d)
Ln (β/T²)
-1000/T (K⁻¹)
-9.4
-9.6
-9.8
-10.0
-10.2
-10.4
-10.6
-10.8
-1.60
-1.58
-1.56
-1.54
-1.52
-1.50
-1.48
-1.46
-1.44

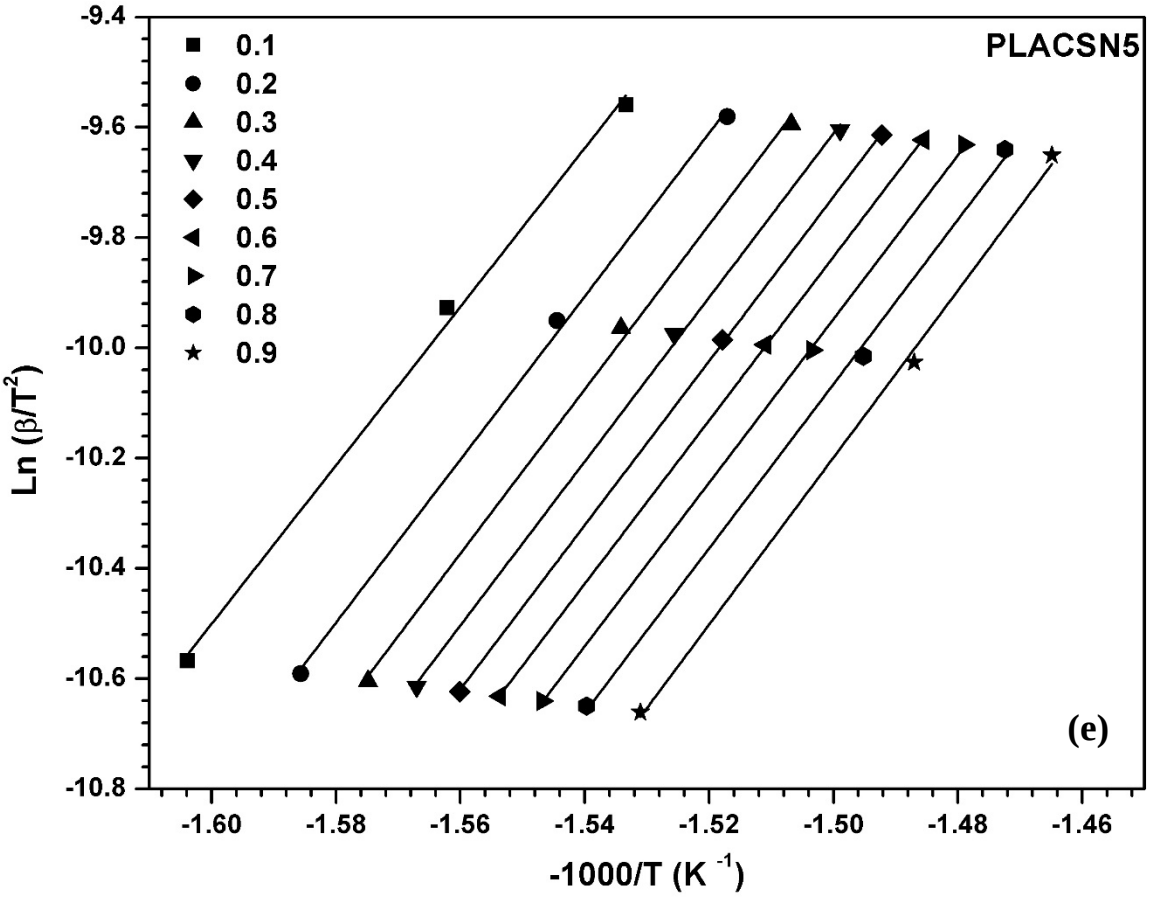

Figure 6.4: K-A-S plots of (a) PLA, (b) PLACSN0.5, (c) PLACSN1, (d) PLACSN2 and (e) PLACSN5.

6.2.2.3 Apparent activation energy vs. conversion

Activation energy (E_a) versus conversion plots have been drawn using the E_a values obtained at different conversions through F-W-O and K-A-S models as shown in Figure 6.5(a-b). Both the models show similar trends which indicates that activation energies values at each conversion values are suitable for the thermal degradation kinetics of PLA and PLA/CSN bionanocomposites. The activation energy increases almost linearly at low conversion values till α=0.3. After this conversion point, the activation energy remains almost constant. Unlike PLA, addition of biofiller, CSN shows almost linear improvement in activation energy values throughout complete degradation. Increasing the filler concentration beyond 2 wt%, again shows reduction in E_a, values lower than PLA. This can be attributed to increased acidic groups contributed by CSN, and agglomerated CSNs fail to form network like structures with PLA chains which block the eluted decomposition products leading to reduced stability. The average activation energy plots shown in inset

reveal that PLACSN1 has requires highest activation energy for degradation as per F-W-O and K-A-S models.

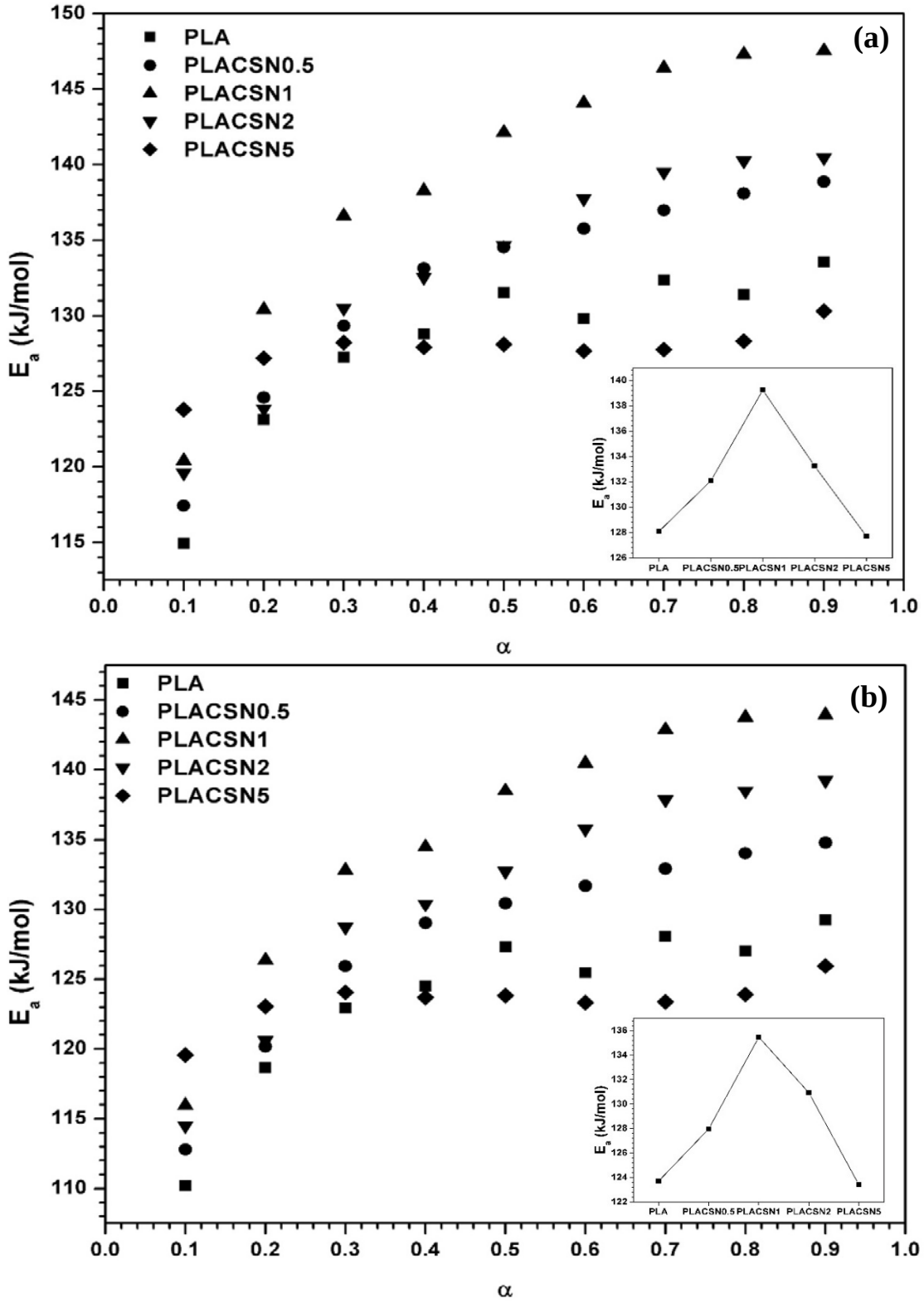

Figure 6.5: Apparent activation energy vs. conversion plots for PLA and PLA/CSN bionanocomposites by (a) F-W-O model (inset: average activation energy plot) and (b) K-A-S model (inset: average activation energy plot).

6.2.2.4 Coats-Redfern (C-R) method

In Coats Redfern (C-R) method, we obtain a single value of E_a, which is different from F-W-O and K-A-S methods where 'E_a' values dependent on conversion are required for analysis. It is well known that F-W-O and K-A-S methods are reliable to evaluate the E_a without prior knowledge of reaction model but they have some difficulties to determine 'A' and 'n'. Figure 6.6(a-o) displays the plotted graphs for neat PLA and PLA/CSN bionanocomposites for different value of n at 10, 20 and 30 ºC/min. The selection of reaction order (n) is confirmed for best fit plot (regression coefficient (R^2) ~1) **(Pilawka et al., 2014)**. According to Eqns. (6.15 and 6.16), in the present work, various reaction orders (n) are assumed from n = 0.1 to 2.0 for which correlation coefficient (R^2) values are above 0.9. The activation energies for PLACSN1 is highest amongst all samples whereas, PLACSN5 is the least. The activation energy E_a values obtained by C-R method are clearly higher than the E_a values obtained from F-W-O and K-A-S method but it can be seen that the C-R method follows the similar trends like F-W-O and K-A-S methods. The reason for such difference is that in the model fitting approach, various models are fitted to conversion versus temperature curve (obtained at any heating rate) and activation energy and pre-exponential factor are determined. The drawback with this approach is that if a system follows a complex thermal degradation mechanism then it gives drastic variations in Arrhenius parameters **(Aboyade et al., 2012)**. The apparent activation energies and correlation coefficients calculated for the three models i.e. F-W-O, K-A-S and C-R models are listed in Table 6.3.

Table 6.3: Activation energy ($0.1 \leq \alpha \leq 0.9$), average activation energies, regression coefficient for PLA and PLA/CSN bionanocomposites obtained by Flynn-Wall-Ozawa, Kissinger-Akahira-Sunose and Coats-Redfern models.

CSN (wt%)	F-W-O method			K-A-S method			C-R method			
	E_a (0.1-0.9)	$\overline{E_a}$	R^2	E_a (0.1-0.9)	$\overline{E_a}$	R^2	10 °C/min (n)	20 °C/min (n)	30 °C/min (n)	$\overline{E_a}$
0	114-133	128.1	0.994	110-129	123.7	0.987	287(0.85)	321(0.99)	355(1.1)	321
0.5	117-138	132.2	0.994	112-134	128.0	0.987	290(0.9)	326(1.1)	362(1.1)	326
1.0	120-147	139.4	0.998	115-143	135.4	0.999	294(1.0)	331(1.1)	366(1.1)	330
2.0	119-143	133.0	0.997	114-139	131.0	0.992	290(1.0)	326(1.1)	363(1.1)	326
5.0	113-132	125.6	0.999	108-128	120.9	0.999	288(0.9)	320(1.0)	348(0.9)	318

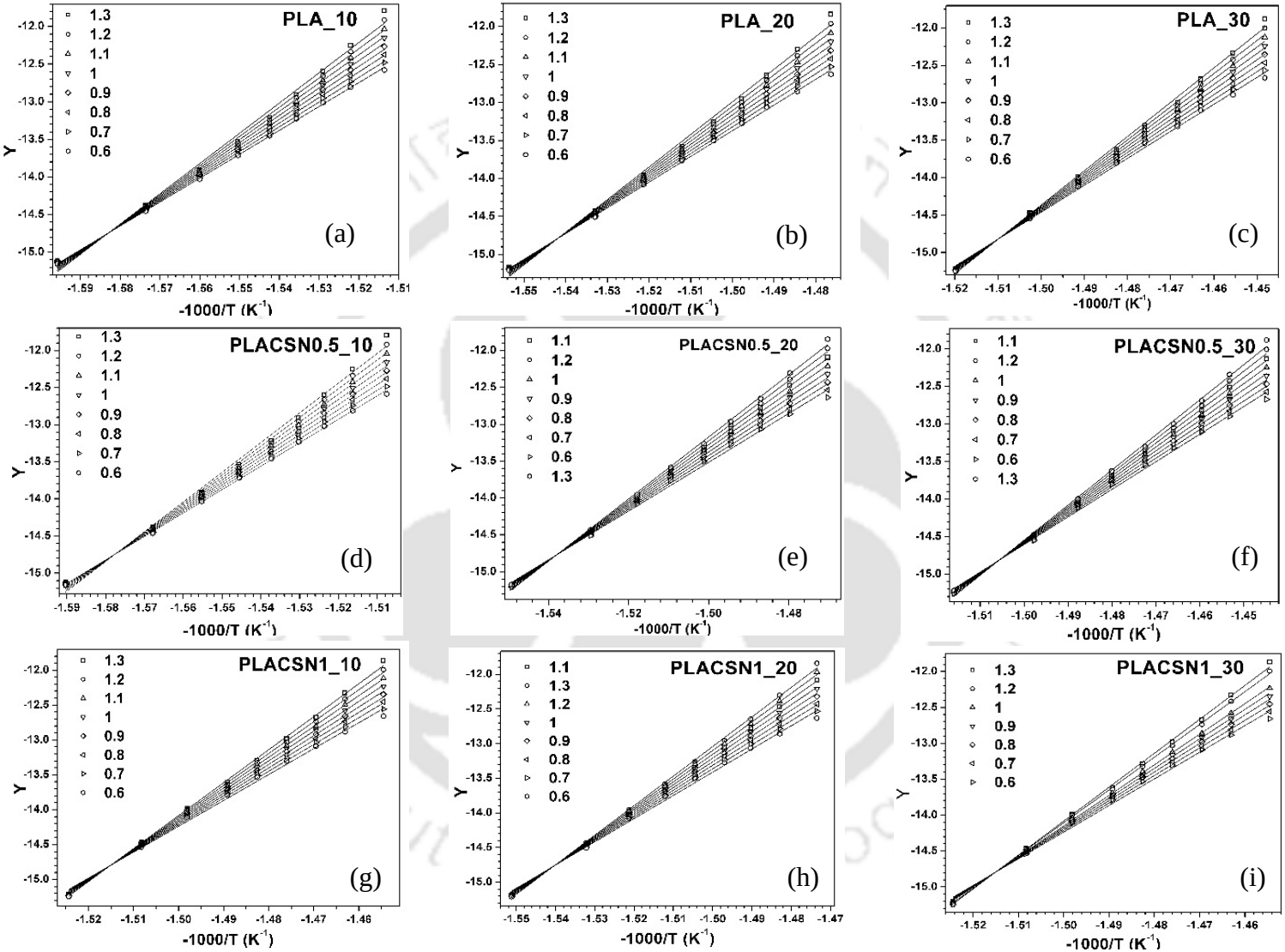
PLA_10
1.3
1.2
1.1
1
0.9
0.8
0.7
0.6
(a)
PLA_20
1.3
1.2
1.1
1
0.9
0.8
0.7
0.6
(b)
PLA_30
1.3
1.2
1.1
1
0.9
0.8
0.7
0.6
(c)
PLACSN0.5_10
1.3
1.2
1.1
1
0.9
0.8
0.7
0.6
(d)
PLACSN0.5_20
1.1
1.2
1
0.9
0.8
0.7
0.6
1.3
(e)
PLACSN0.5_30
1.1
1.2
1
0.9
0.8
0.7
0.6
1.3
(f)
PLACSN1_10
1.3
1.2
1.1
1
0.9
0.8
0.7
0.6
(g)
PLACSN1_20
1.1
1.3
1.2
1
0.9
0.8
0.7
0.6
(h)
PLACSN1_30
1.3
1.2
1
0.9
0.8
0.7
0.6
(i)
Y
-1000/T (K-1)

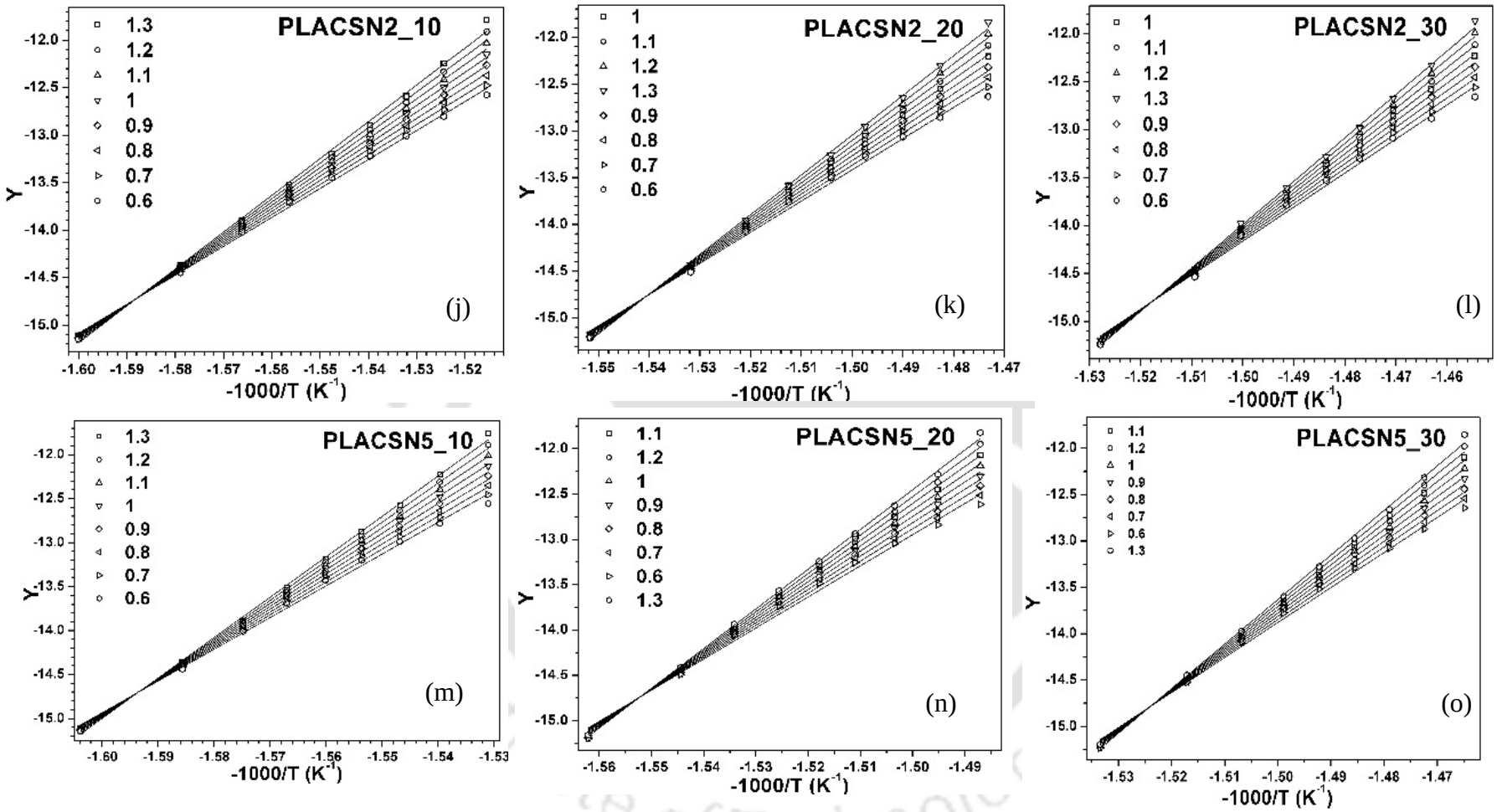

Figure 6.6: C-R plots at 10, 20 and 30 °Cmin^{-1}for (a-c) PLA, (d-f) PLACSN0.5, (g-i) PLACSN1, (j-l) PLACSN2 and (m-o) PLACSN5.

6.2.2.5 Reaction mechanism for degradation of PLA/CSN bionanocomposites

$Z(\alpha)_{exp}$ vs. α plots obtained using TGA data are depicted in Figure 6.7(a-e). Moreover, this experimental plot when compared with the master plots, provides an easy and precise determination of the degradation mechanism. It can clearly be seen that the experimental data of Z(α) vs. α for PLA are in accordance with the F1 master curve (Figure 6.7(a)) as reported earlier **(Valapa et al., 2015a)**. PLA/CSN bionanocomposites (see Figure 6.7(b-e)) exhibit degradation mechanism which is overlapped with F1 (random nucleation with one nucleus on the individual particle) mechanism, it indicates that random nucleation occur in single step. In this type of mechanism, nuclei are formed at imperfection sites due to impurities and edges, dislocation. It confirms that F1 is the rate controlling step for PLA and PLA/CSN bionanocomposites throughout the decomposition process.

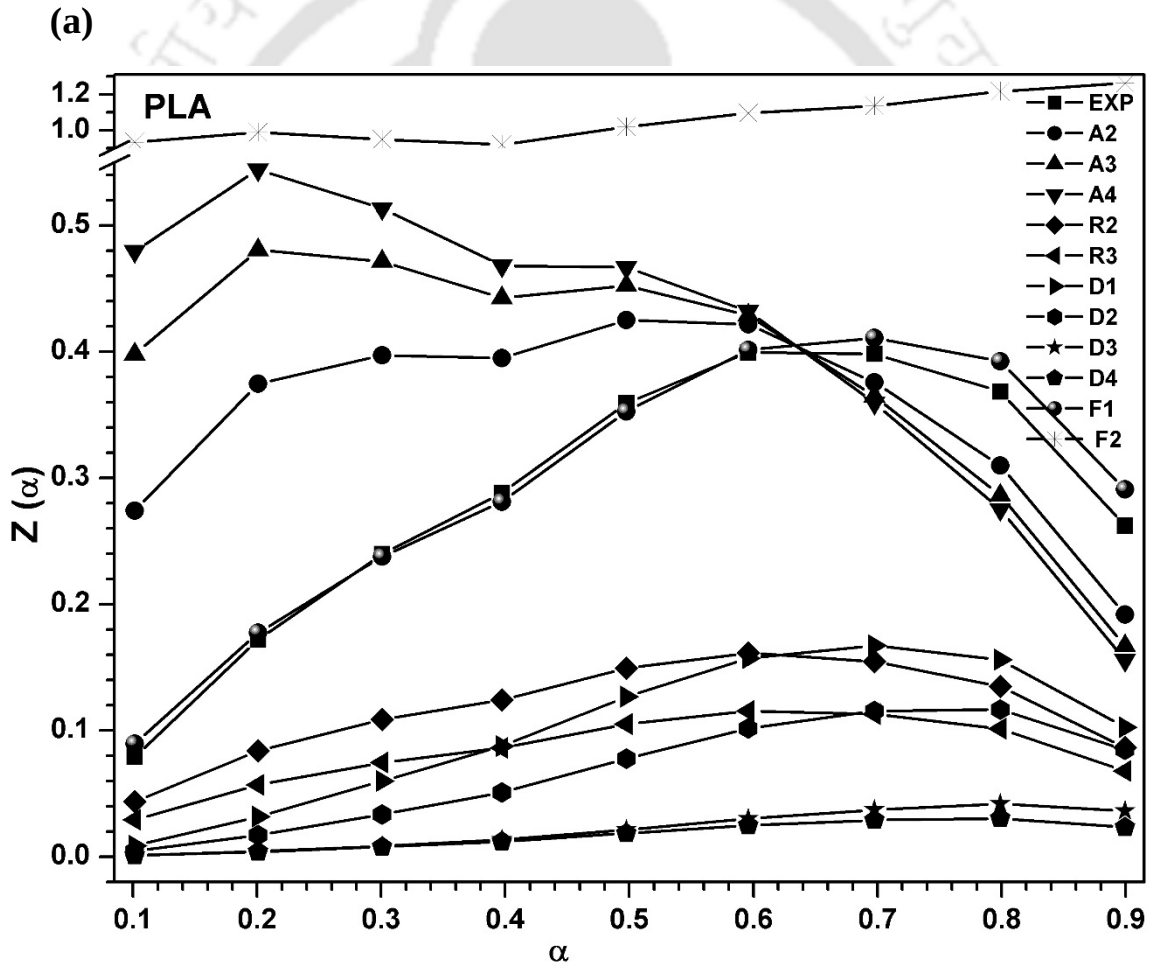

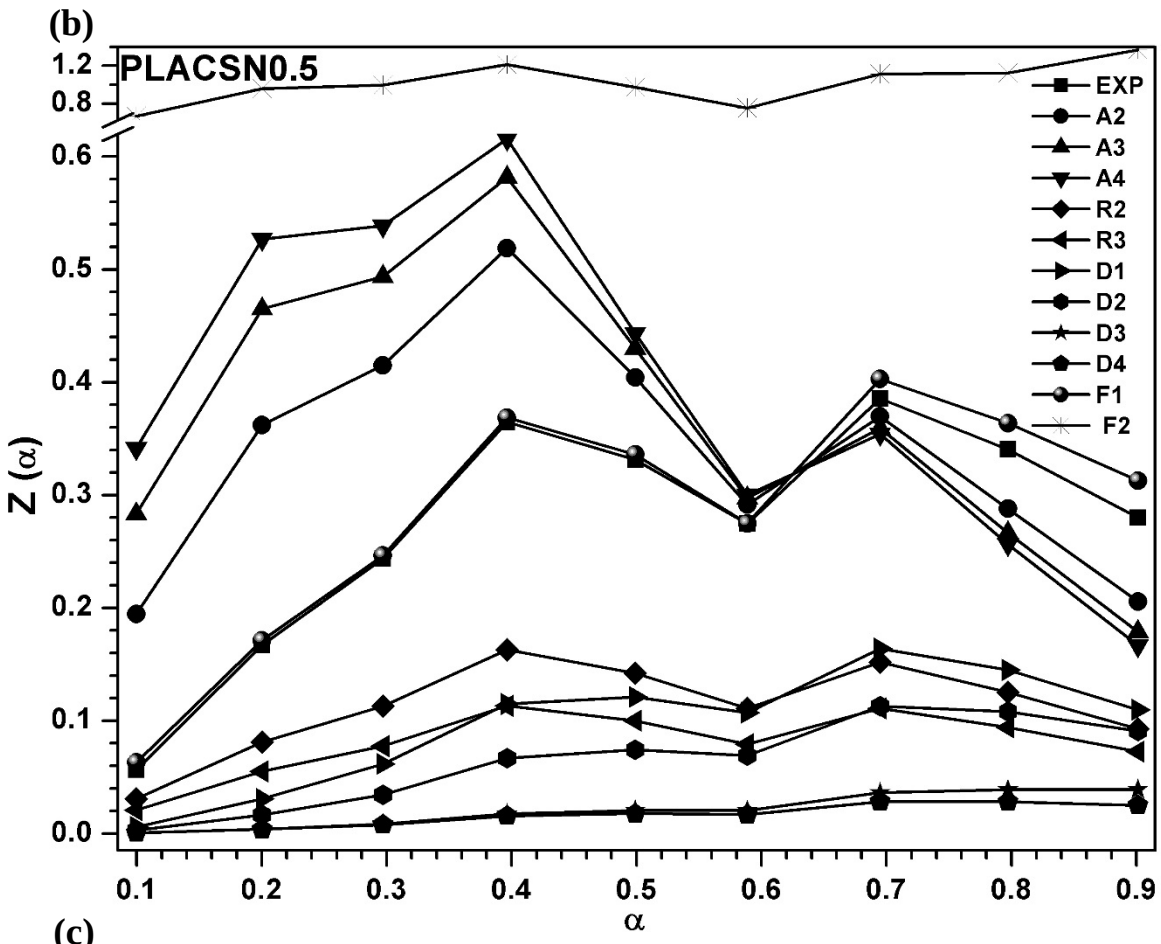
(b)
PLACSN0.5
EXP
A2
A3
A4
R2
R3
D1
D2
D3
D4
F1
F2
Z (α)
α

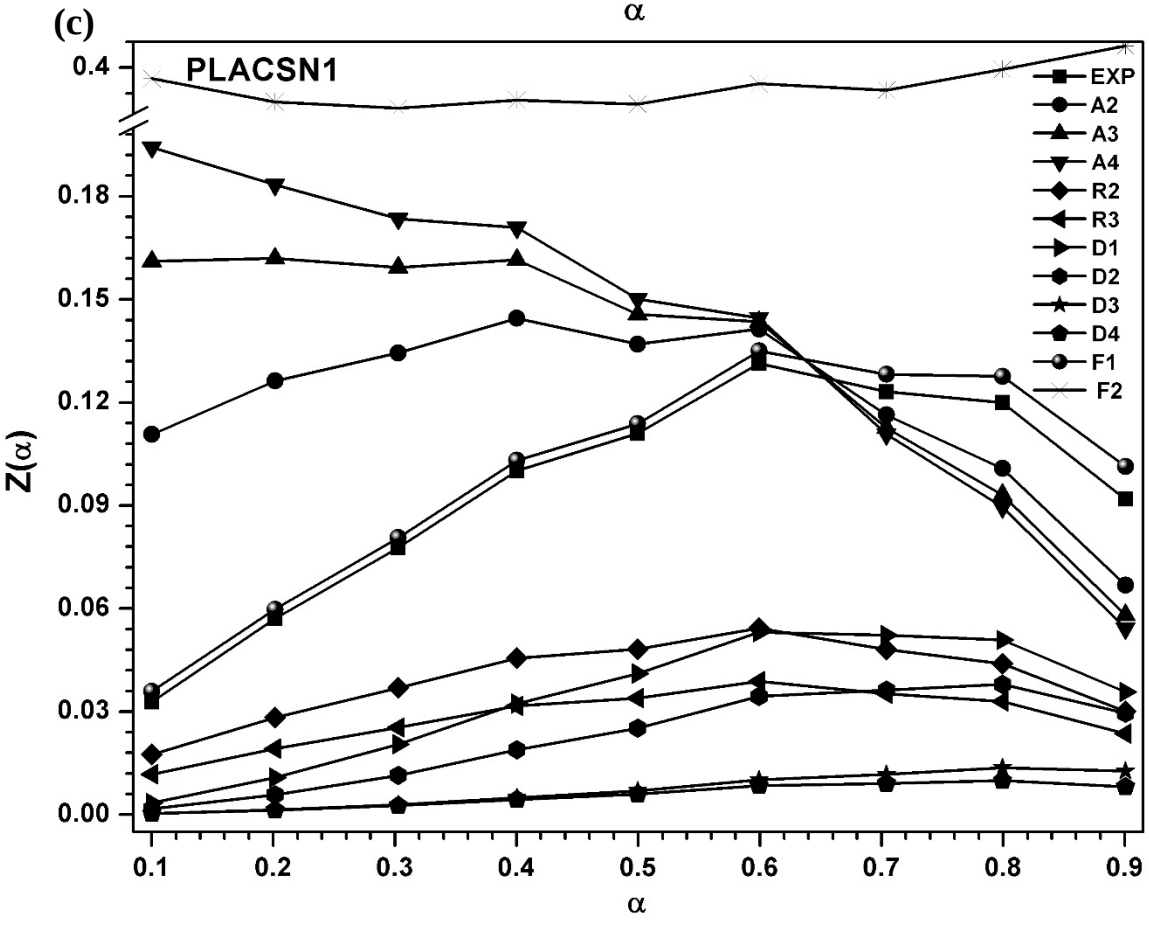
(c)
PLACSN1
EXP
A2
A3
A4
R2
R3
D1
D2
D3
D4
F1
F2
Z(α)
α

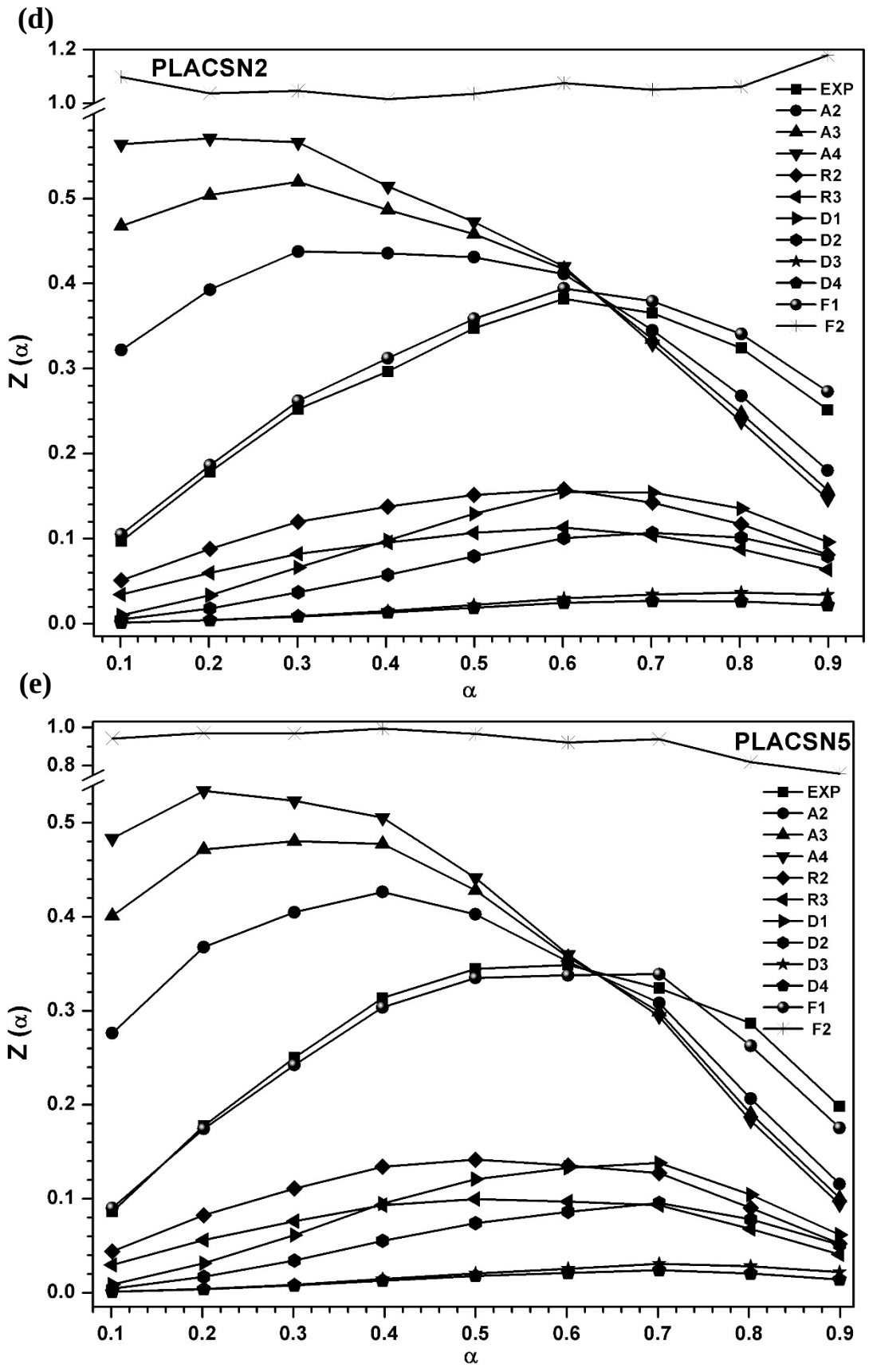

Figure 6.7: Reaction mechanism plots using Criado method for (a) PLA, (b) PLACSN0.5, (c) PLACSN1, (d) PLACSN2 and (e) PLACSN5.

6.2.3 Characterization of gaseous degradation products using TGA-FTIR

Hyphenated TGA-FTIR is a reliable technique for understanding the thermal degradation behavior of polymer and its bionanocomposite. In order to obtain information about the composition of the volatile species evolved from the TGA furnace during TGA analysis are captured in FTIR cell and continuously recorded during the dynamic heating regime with a heating rate of 10 °C/min for Muga silk, CSNs, PLA and PLA/CSN bionanocomposites, respectively. The intensity of FTIR spectra attained maximum values at temperature near to DTG peaks. The small differences that have appeared are determined by the start time difference between FTIR and TG due to the time required for nitrogen flow to fill the cell volume of spectrometer or the transport delay of volatile species through the transfer line. It is noticed that TG-FTIR technique is very sensitive tool to determine the volatile species generated during the thermal degradation of CSNs and confirm the presence of different amide peaks such as 1230–1248 cm^{-1}, skeletal modes, confirmation of polypeptide chain sequences and intensity of absorption band can well examine the type of bonds cleaved during decomposition.

6.2.3.1 Analysis of evolved gas products from degradation of Muga silk

The thermal decomposition of Muga silk is analyzed under nitrogen atmosphere. Figure 6.8(a) displays Gram-Schmidt (GS) curve, which shows a shoulder at 327 °C and two peaks at 378 °C and 624 °C. Hence 3-D and 2-D FTIR spectra of volatile species at temperatures 378 °C and 624 °C are captured as shown in Figure 6.8(b-c).

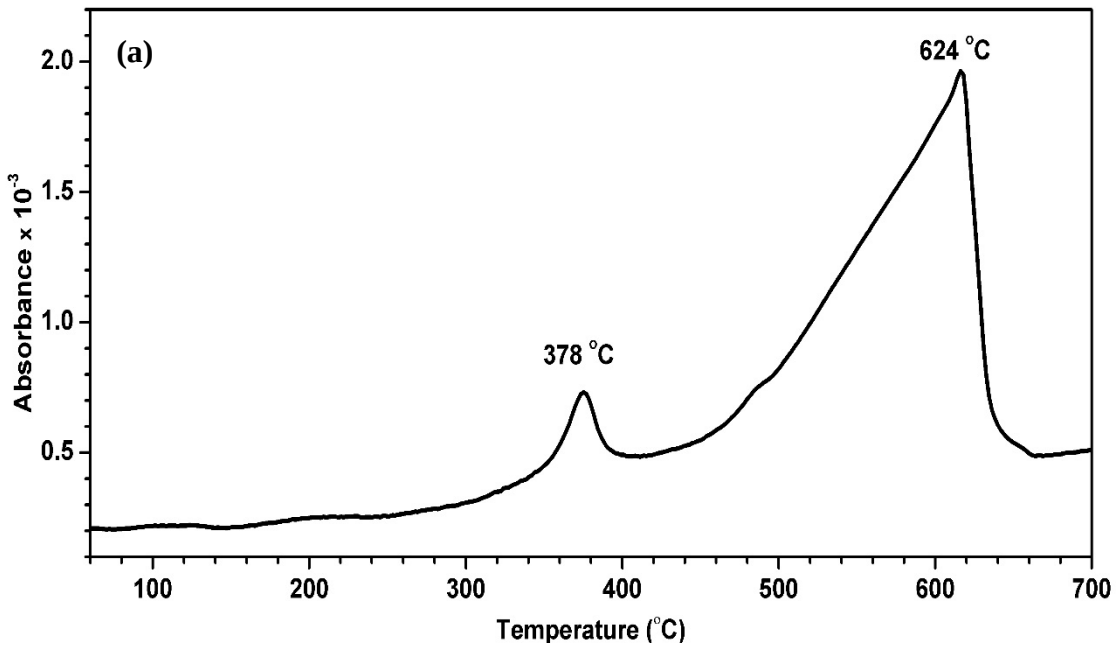

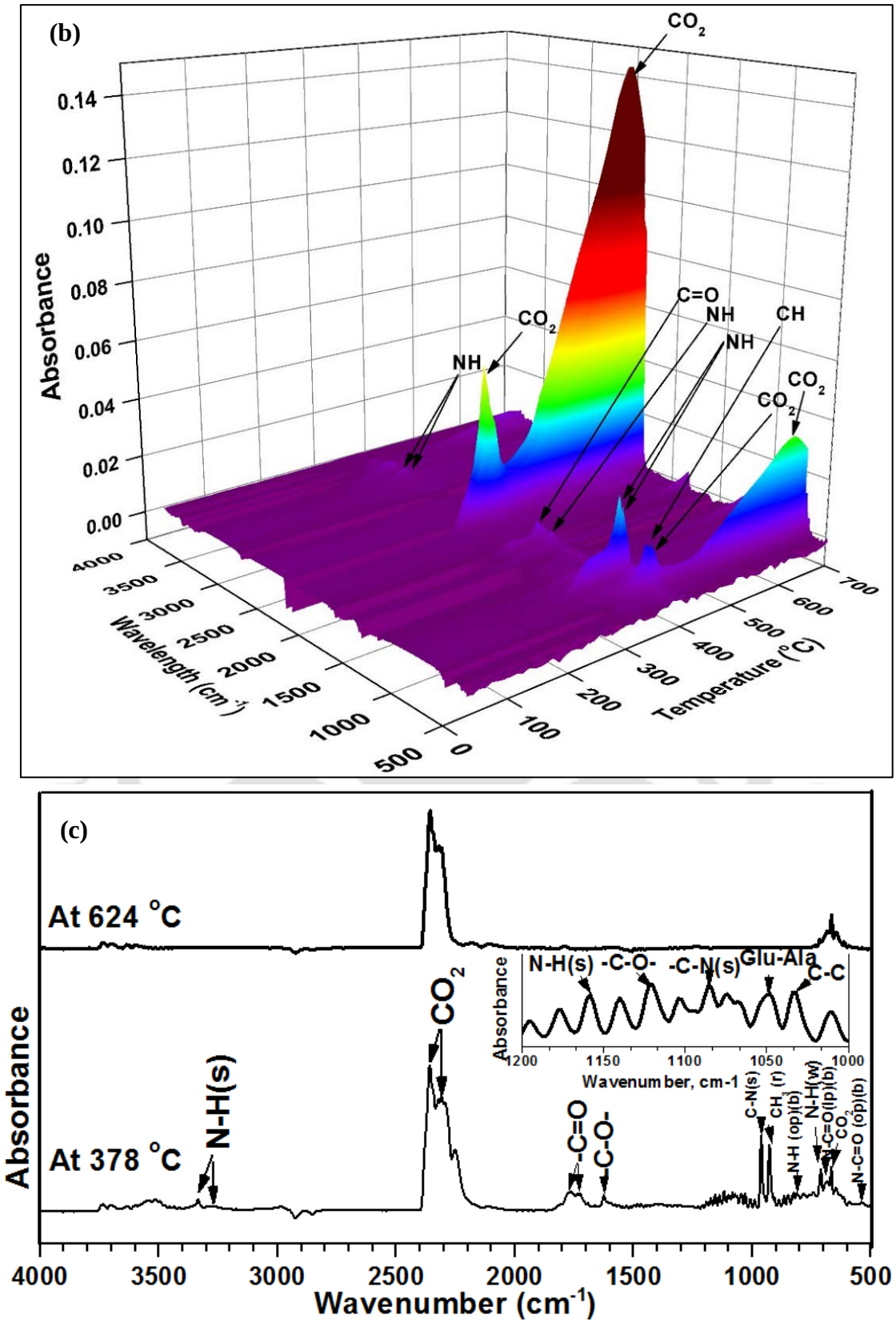

Figure 6.8: (a) Gram-Schmidt curves, (b) temperature-dependent 3-D FTIR spectra of the thermal degradation and (c) characteristic spectra recorded at maximum weight loss rates for Muga silk.

At 378 ˚C i.e. the temperature of maximum evolution of volatile products, FT-IR spectra with assigned peaks for the Muga silk show characteristic bands at 1,625 cm^{-1} (amide I) and 812 cm^{-1} (amide V) which are due to the breaking of peptide backbones in the crystalline part of β-phase (Figure 6.8(c)) **(Gogoi et al., 2011)**. The other characteristics band appears at 1048 cm^{-1}, 1010 cm^{-1}, 992 cm^{-1} and 964 cm^{-1} (amide IV) which signify the peptide chain of Muga silk, Gly-Gly linkage, Aly-Gly sequences and Ala-Ala linkages in the crystalline region of β-phase, respectively. Moreover, absorption bands located at 1,158 cm^{-1} is caused by the N-H stretching (hydrogen bonded). The presence of bands at 688 cm^{-1} (N-C=O in-plane bending, amide IV) and 540 cm^{-1} (N-C=O, out-plane bending amide VI) confirms the cleavage of alpha-form sequential alanine polymer **(Gogoi et al., 2012)**. Absorption bands at 3333 and 3272 cm^{-1} attributed to N-H stretching for amide II, peak at 1765 and 1734 cm^{-1} (C=O) is assigned to carbonyl compound, bands at 1119 and 1083 cm^{-1} for C-O stretching and C-N stretching **(Zhang et al., 2002)**. Absorption band at 923 cm^{-1} indicate the aromatic ring vibration. Carbon dioxide (CO_2) is identified by the presence of bands located at 2358, 2310 and 664 cm^{-1}, respectively. CO_2 is the main decomposition product in comparison with other volatile species which can be observed beyond 300 ˚C in nitrogen atmosphere and its band still exists when reaction further progressed during the residue decomposition stage. The evolution of CO_2 might be caused by secondary cracking of volatile species at 652 °C.

6.2.3.2 Analysis of evolved gas products from degradation of lab synthesized crystalline silk nano-discs (CSNs)

Figure 6.9(a) exhibits the GS curves of the degradation process indicates the two-step degradation of CSNs at 371 and 625 °C, respectively. Decomposition of main-chain occurred above 300 ºC, and finished at about 450 ºC. Figure 6.9(b) displayed the 3-D FT-IR spectra of CSNs and on-line evolution of volatile species with continuous mode. Figure 6.9(c) represents the characteristic spectra recorded at 371 °C with the enlarged views around (1500–1200 cm^{-1}), (1250–970 cm^{-1}), respectively. Results show that there are small differences between the Muga silk and CSNs volatile species with the major absorbance at around 3000–2900, 1800–1250, and 1200–800 cm^{-1} regions. In case of CSNs, peak intensity against various volatile components is higher than Muga silk, which confirms the higher release of volatile component. Another difference is that CSNs are more thermally stable than Muga silk and decompose later in the temperature range of 30–300 °C.

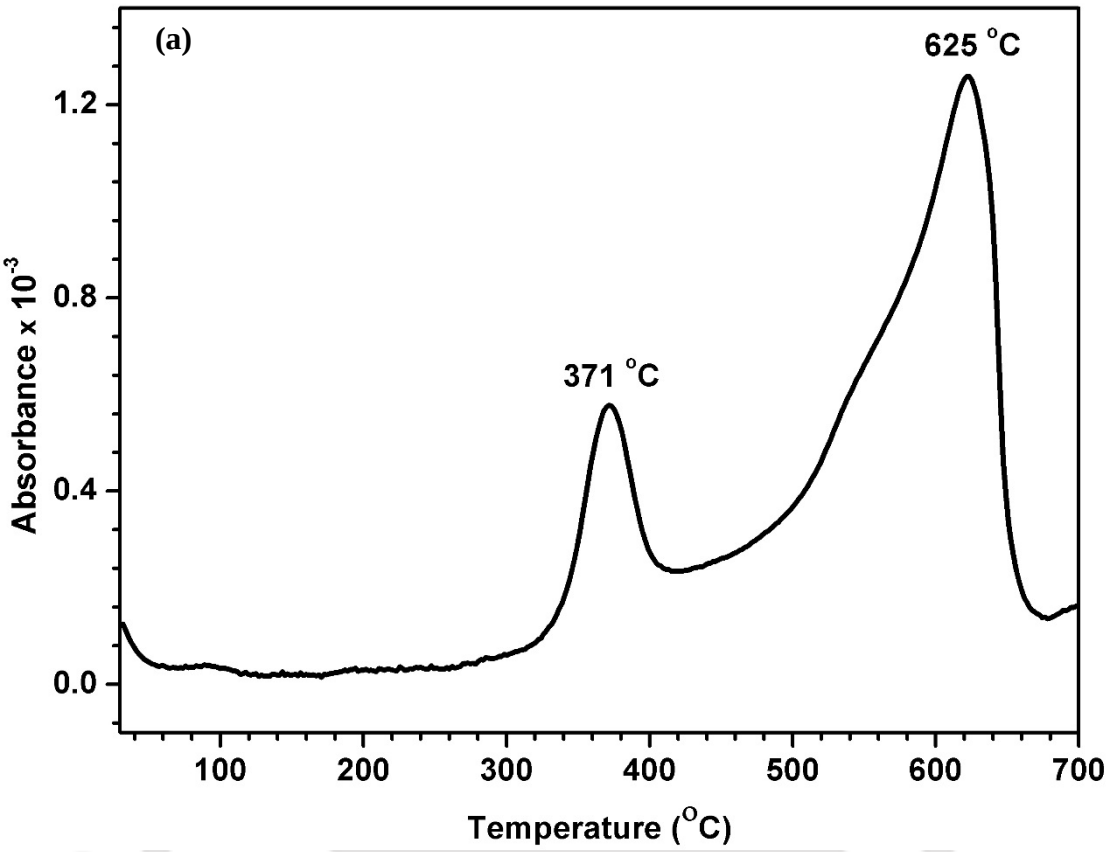
(a)
625 °C
371 °C
Absorbance x 10-3
1.2
0.8
0.4
0.0
100
200
300
400
500
600
700
Temperature (°C)

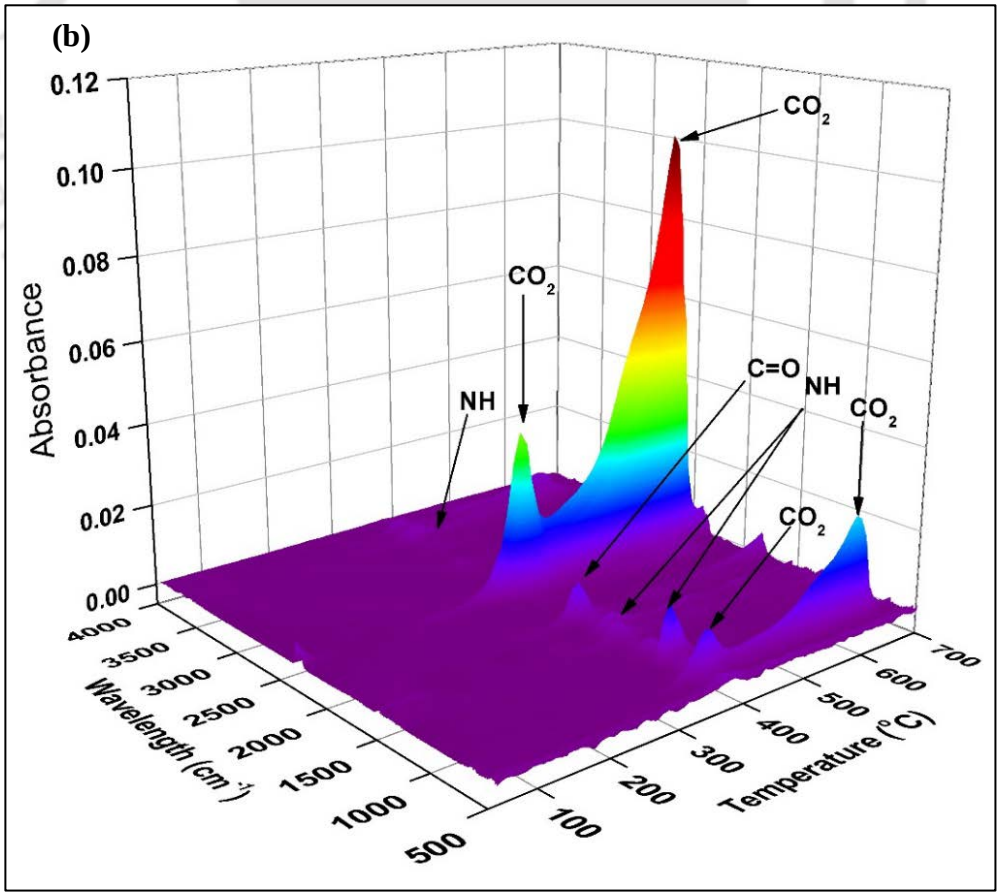
(b)
Absorbance
0.12
0.10
0.08
0.06
0.04
0.02
0.00
CO2
CO2
NH
C=O
NH
CO2
CO2
4000
3500
3000
2500
2000
1500
1000
500
Wavelength (cm-1)
100
200
300
400
500
600
700
Temperature (°C)

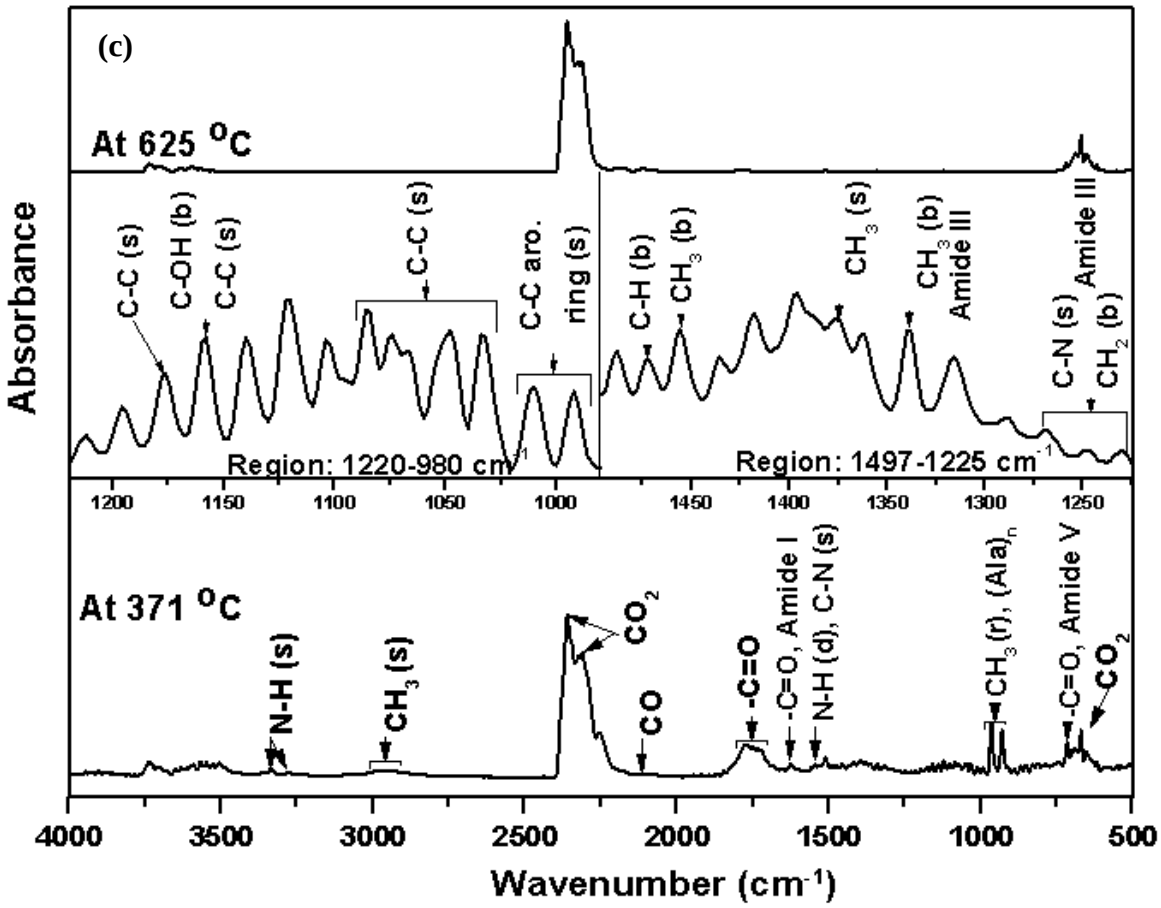

Figure 6.9: (a) Gram-Schmidt curves, (b) temperature-dependent 3-D FTIR spectra of the thermal degradation and (c) characteristic spectra recorded at maximum weight loss rates for CSNs.

The spectrum recorded at maximum evolution of volatile products (371 °C) can be assigned to the main decomposition of peptide chains, presence of Gly-Ala, Aly-Gly, Ala-Ala linkages, amide A, alkyl N-H stretching, C-O stretching, C-N stretching, ring structure related species, release of CO_2 and water as, discussed in previous section 6.2.9 for Muga silk. Additionally, β-sheet confirmation around 1230 cm^{-1}-1248 cm^{-1}(amide III) is due to C-H stretching, **(Ling et al., 2011)** absorption bands at 2982 cm^{-1}, 2940 cm^{-1} are related to C-H stretching and asymmetric stretching of CH_2 group. As seen from Figure 6.9(c), absorption band at 1070 cm^{-1} for sericin, were absent which are indicative of effective degumming in CSN whereas was present in Muga silk at 1074cm^{-1} which is submerged with band at 1083 cm^{-1}. The bands at 1486 cm^{-1}-1375 cm^{-1} are assigned to C-H bending of aliphatic groups formed by the cleaving of the main chain, band at 1375 cm^{-1} (amide III) is also assigned to amino acid group superimposed with C-H bending. The bands at 2359, 2310, 669 cm-1 and 2114 cm^{-1} imply the formation of CO_2 and CO respectively; the band at 1771 cm^{-1}, 1749 cm^{-1}, 1733 cm^{-1} confirmes the release of different type of carbonyl

compounds. The absorption band located at 1509 cm^{-1} confirms the formation of aromatic structures. When the temperature is above 371 °C, intensity of absorption band decrease with further increase of temperature during the main mass loss stage. During the second mass loss stage, when the temperature is above 622 °C, the strongest absorbance bands for CO_2 and weak bands for CO are observed, it revealed CO_2 is released in large amount due to secondary cracking of volatile species **(Liu et al., 2013)**.

6.2.3.3 Analysis of evolved gas products from degradation of Poly(lactic acid)

Conventional thermal degradation process of PLA is very complex and it usually proceeds by various reaction pathways. These degradation pathways include, transesterification (dominant degradation mechanism) of PLA at temperatures above 200 °C (see Figure 6.10(a)); cyclization, leading to the formation of cyclic oligomers, cis-elimination reactions also occur at high temperature range (300–500 °C), random main chain scission at temperatures above 180 °C, hydrolysis at a temperature between 150–215 °C **(Xu et al., 2016)**. The 3D-FTIR spectra of volatile products from the neat PLA are presented in Figure 6.10(b), as can be seen, no release of volatile components is observed up to 330 °C. Heating above 330 °C produced weak absorptions at around 2358–2310 cm^{-1}, which are related to the breakdown of PLA chains and the release of CO_2. The spectra measured at 381 °C (Figure 6.10(c)) shows significant changes, **(Tudorachi et al., 2012; Vogel and Siesler, 2008)** with strongest absorbance peaks at 1786 cm^{-1} and 1765 cm^{-1} corresponding to asymmetric and symmetric stretching of C=O group. Doublet of peaks at 2350–2310 cm^{-1} and 2178–2116 cm^{-1} are assigned to CO_2 and CO, and band at around 3568 cm^{-1} (O-H stretching) for water, bands at 2738 cm^{-1} stretching of CHO group, 1375 cm^{-1} for C-H bending of CH_3 group, 1765 cm^{-1} (C=O) are related to aliphatic aldehyde group, 3002 cm^{-1} (C-H stretching) – 2950 cm^{-1} (asymmetric stretching of CH_3 group), 1786 cm^{-1} (C=O), 1456 cm^{-1} (C-H bending for CH_3), band at 1244–1108 cm^{-1} ascribed to stretching of C-O-C and lower intensity peaks at 933 $cm^{-1}$is related to ring skeleton, these peaks are detected to lactide or cyclic oligomer. These observations supporting the data analysis of **Zou et al. (2009)** who found that thermal decomposition of PLA produces similar type of volatile species. It confirmed that the thermal decomposition of PLA is dominated by chain homolysis route and hydroxyl end-initiated ester interchange process is also involved which attribute to the formation of CO.

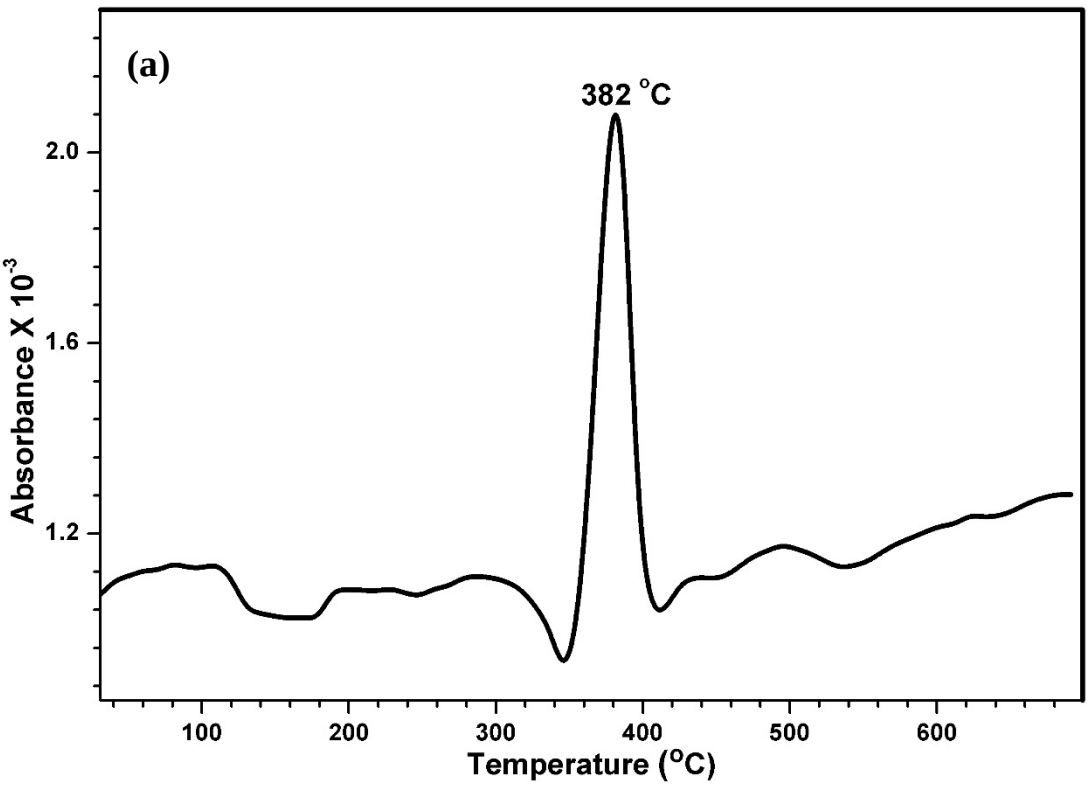
(a)
382 °C
Absorbance X 10-3
2.0
1.6
1.2
100
200
300
400
500
600
Temperature (°C)

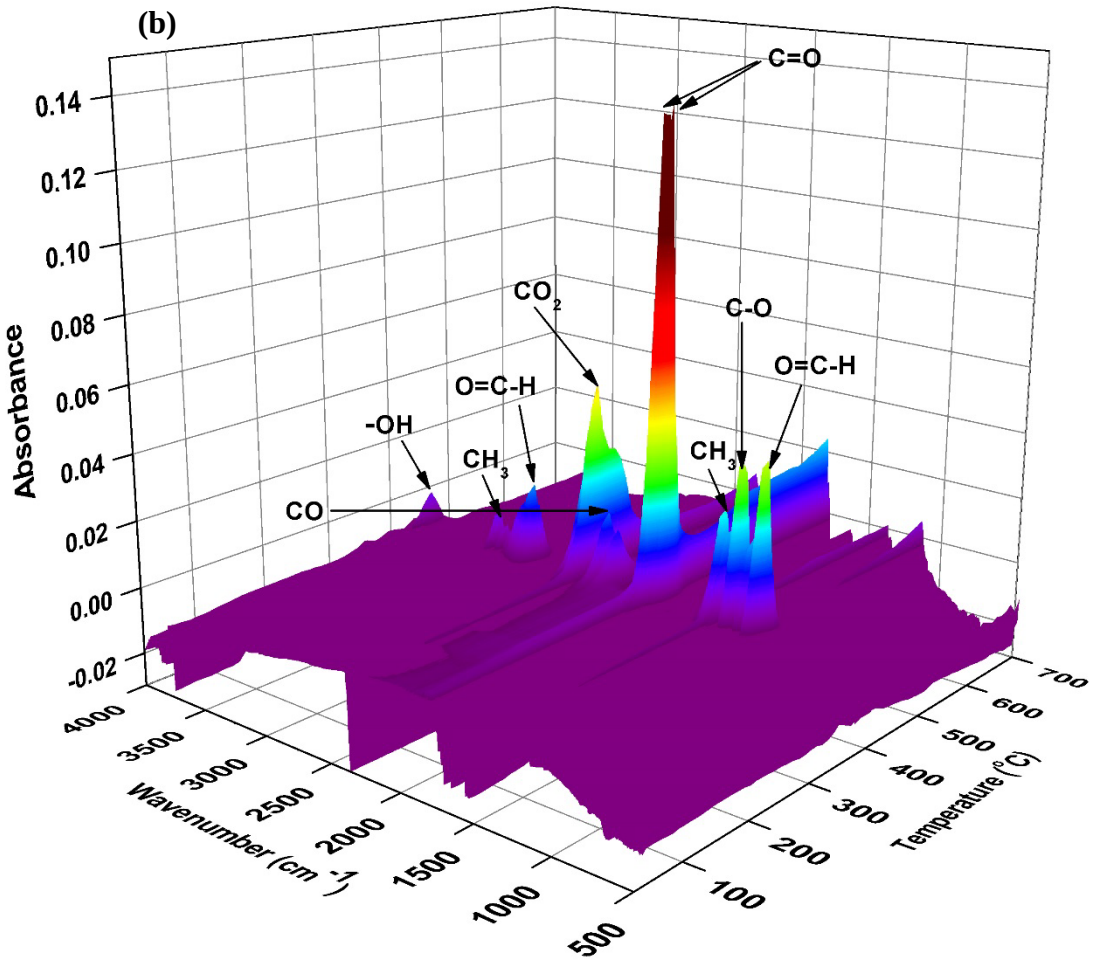
(b)
Absorbance
0.14
0.12
0.10
0.08
0.06
0.04
0.02
0.00
-0.02
C=O
CO2
C-O
O=C-H
O=C-H
-OH
CH3
CH3
CO
4000
3500
3000
2500
2000
1500
1000
500
Wavenumber (cm -1)
100
200
300
400
500
600
700
Temperature (°C)

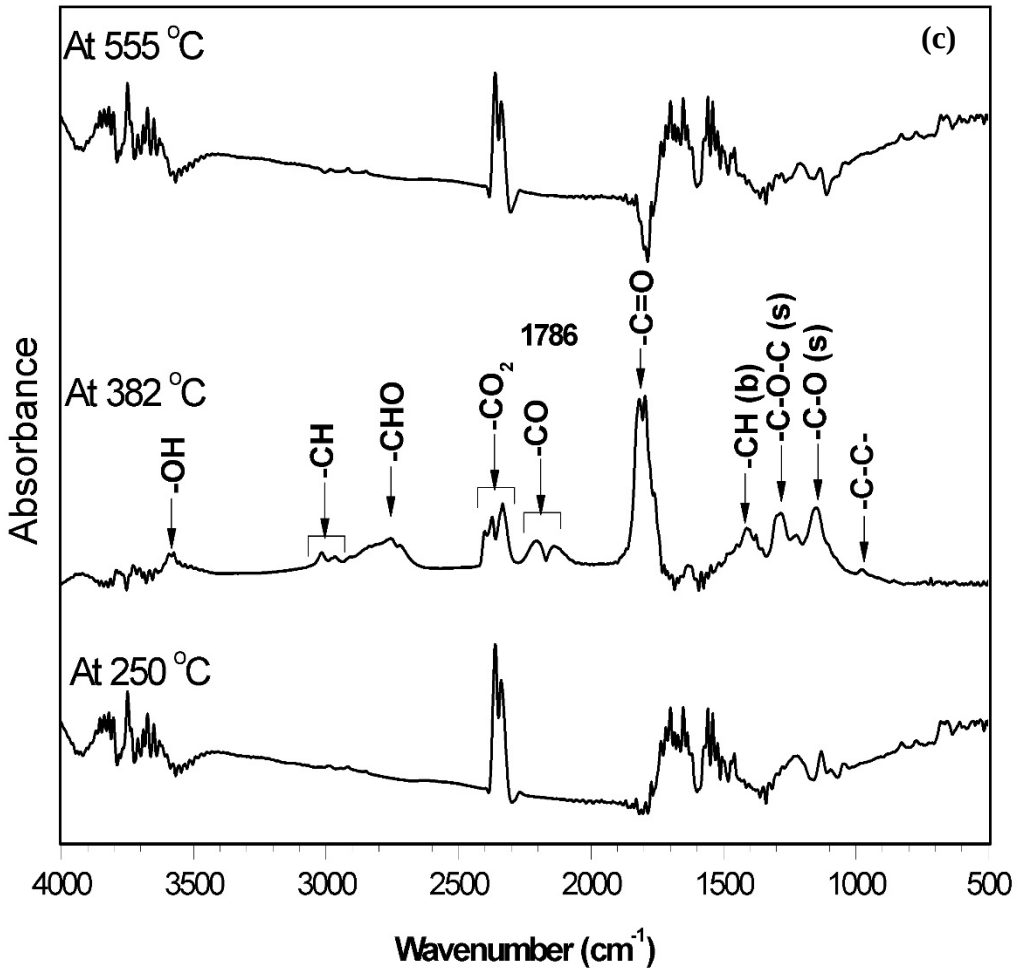

Figure 6.10: (a) Gram-Schmidt curves, (b) temperature-dependent 3-D FTIR spectra of the thermal degradation and (c) spectra recorded at maximum weight loss rates for PLA.

6.2.3.4 Analysis of evolved gas products from degradation of PLA/CSN bionanocomposites

The identification of the volatile species whose evolution is minimized or eliminated under the dynamic heating regime, is vital to elucidate the role of this bionanocomposite on the environment. The influence of lab synthesized CSNs on the thermal decomposition of PLA are shown in Figure 6.11(a-c). It is observed that the thermal degradation of the PLACSN5 is quite similar to the neat PLA. These results correspond with the GS curve (see Figure 6.11(a)) and can be used to explain the effect of this hydrophobic filler on the thermal decomposition of PLA. In comparison to pathway which involves bond rupturing and formation of new bond. This reaction will continue until degradation is completed and give higher yield of lactide monomer released **(Chiang et al., 2011; Mofokeng and Luyt, 2015)**. It is suggested that this typical reaction mechanism is more favoured by depolymerization than chain scission mechanism **(Mofokeng and Luyt, 2015)**.

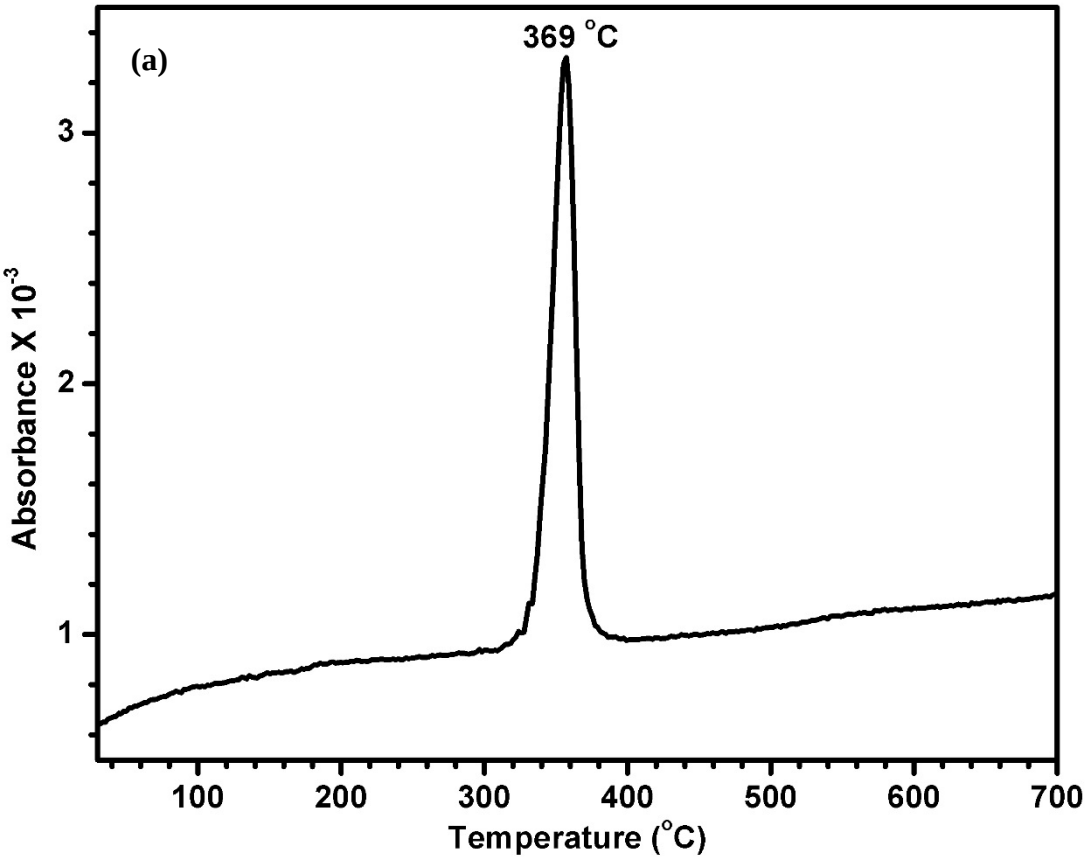
(a)
369 °C
Absorbance X 10-3
Temperature (°C)

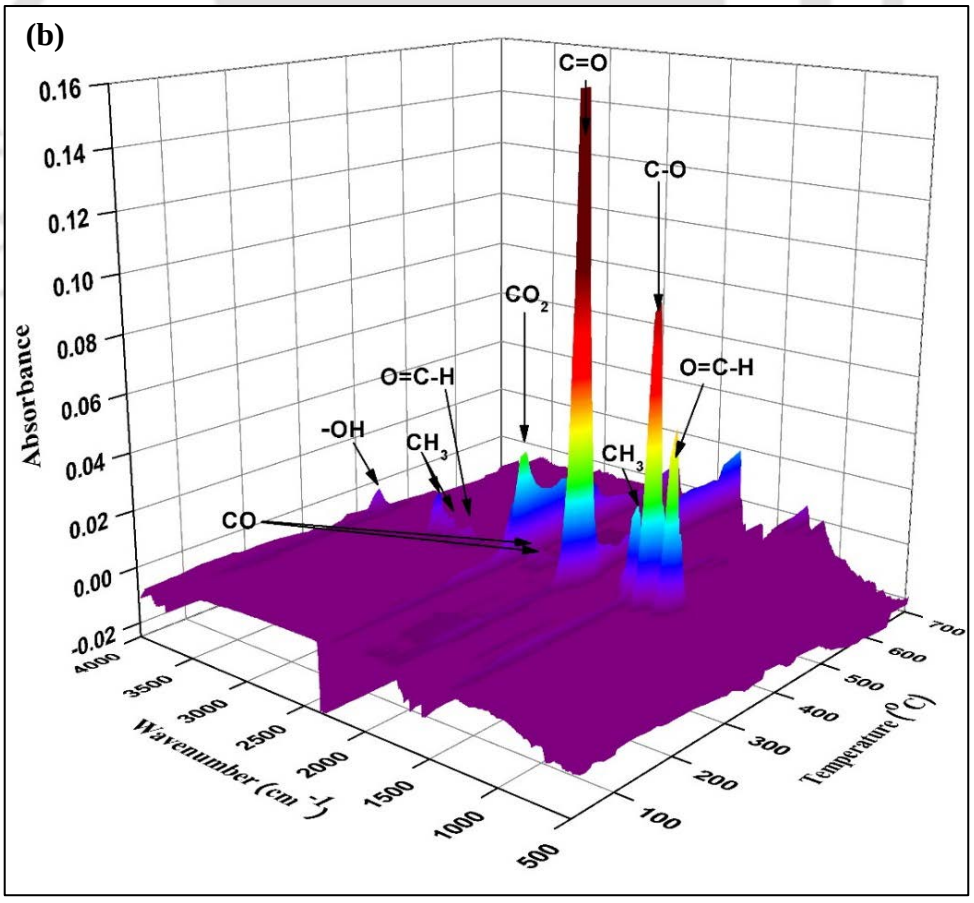
(b)
C=O
C-O
CO2
O=C-H
O=C-H
-OH
CH3
CH3
CO
Absorbance
Wavenumber (cm-1)
Temperature (°C)

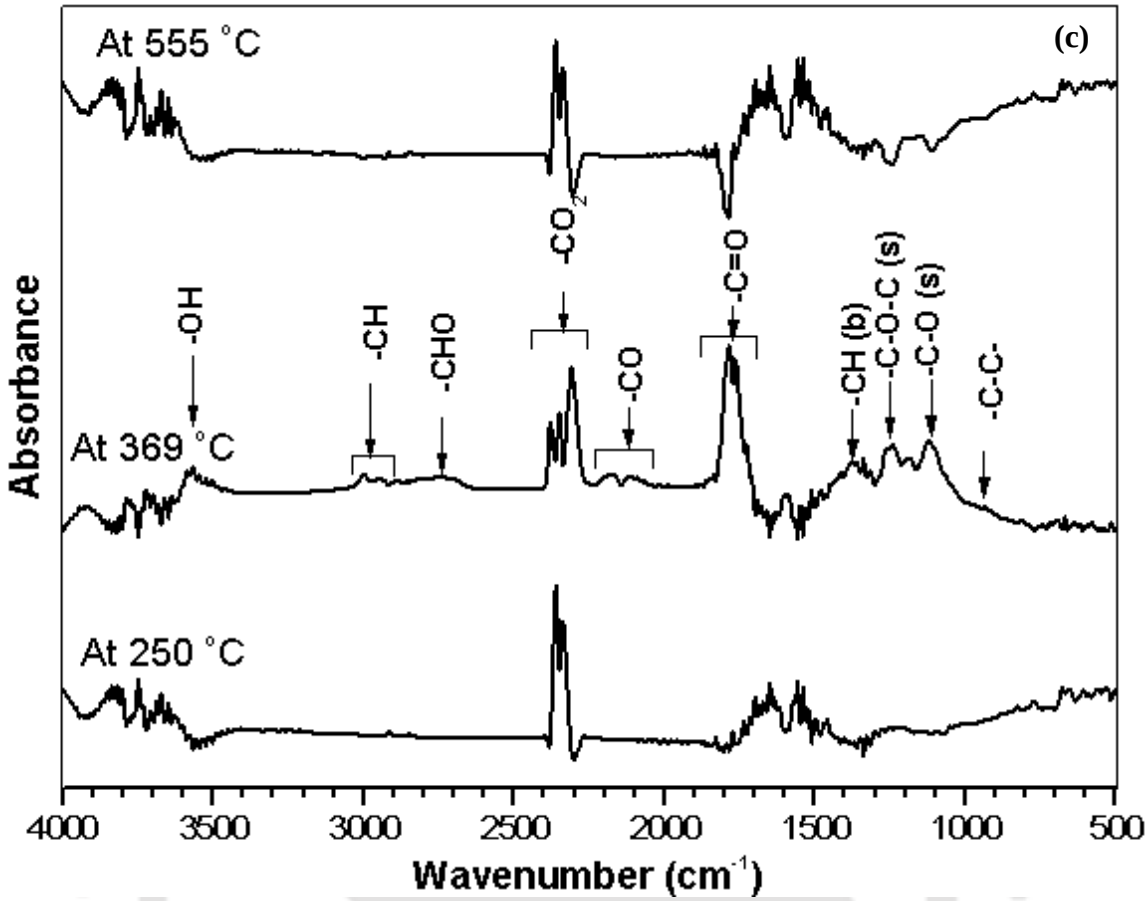

Figure 6.11: (a) Gram-Schmidt curves, (b) temperature-dependent 3-D FTIR spectra of the thermal degradation and (c) spectra recorded at maximum weight loss rates for PLACSN5.

6.2.4 Hydrolytic degradation of PLA and PLA/CSN bionanocomposites

It is indispensable to have an understanding about the hydrolytic degradation of PLA and PLA bionanocomposites. Hydrolytic degradation of non-treated amorphous PLA and PLACSN5 specimens were performed in pH solutions of 2, 7 and 12 at 37 and 60 °C. Two incubation temperatures were selected viz. 37 and 60 °C. Lower temperature (37 °C) was to simulate the process of degradation of PLA and PLACSN5 in the human body for possible uses in biomedical devices whereas, elevated temperature (60 °C) was selected as per various ASTM and ISO standards **(Fukushima et al., 2011; Gorrasi and Pantani, 2013)**. Figure 6.12 displays the plots of residual weight fraction (ϕ) of PLA and PLACSN5 bionanocomposite as a function of hydrolytic degradation duration which gives information about fraction of water soluble oligomer and monomer formed due to hydrolytic degradation which diffuse into the surrounding solution. It can be seen that the residual weight fraction (for all pH and temperature conditions studied) varies in a non-linear fashion with increasing hydrolytic degradation time.

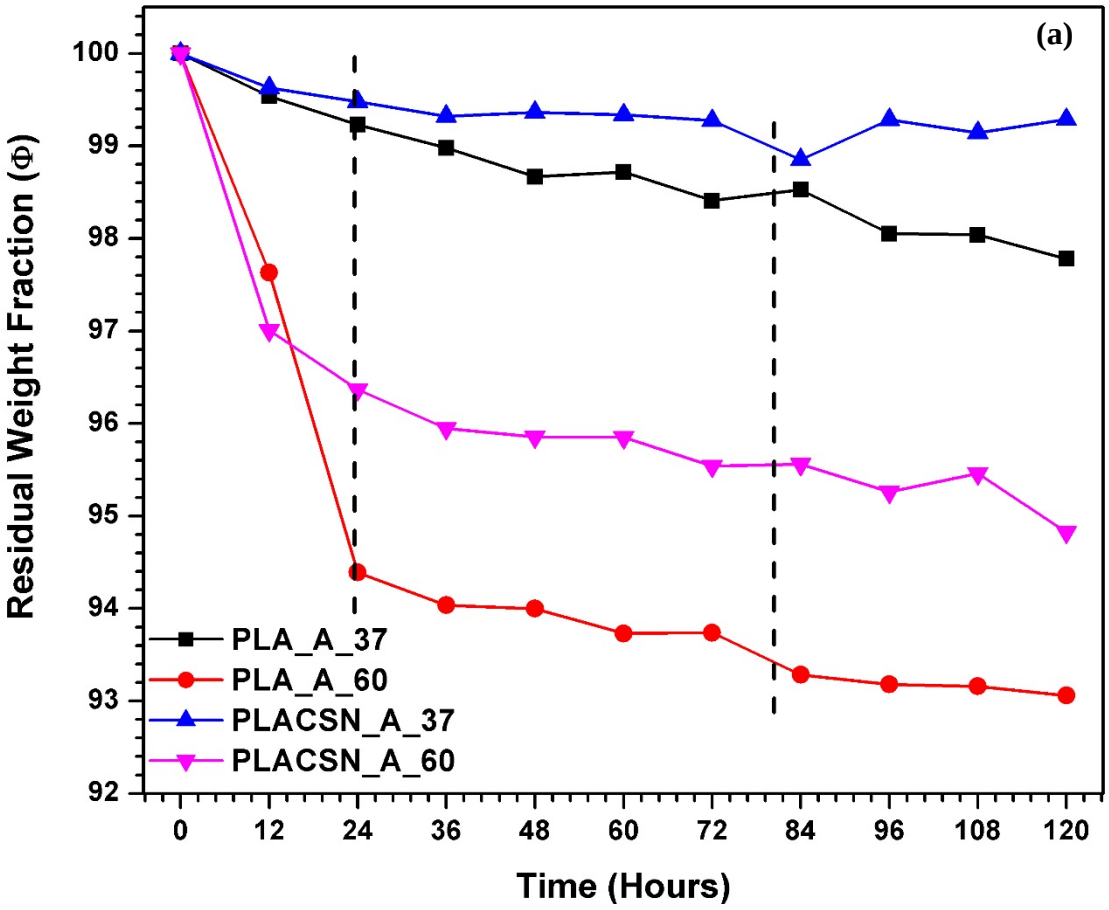
(a)
Residual Weight Fraction (Φ)
100
99
98
97
96
95
94
93
92
0
12
24
36
48
60
72
84
96
108
120
Time (Hours)
PLA_A_37
PLA_A_60
PLACSN_A_37
PLACSN_A_60

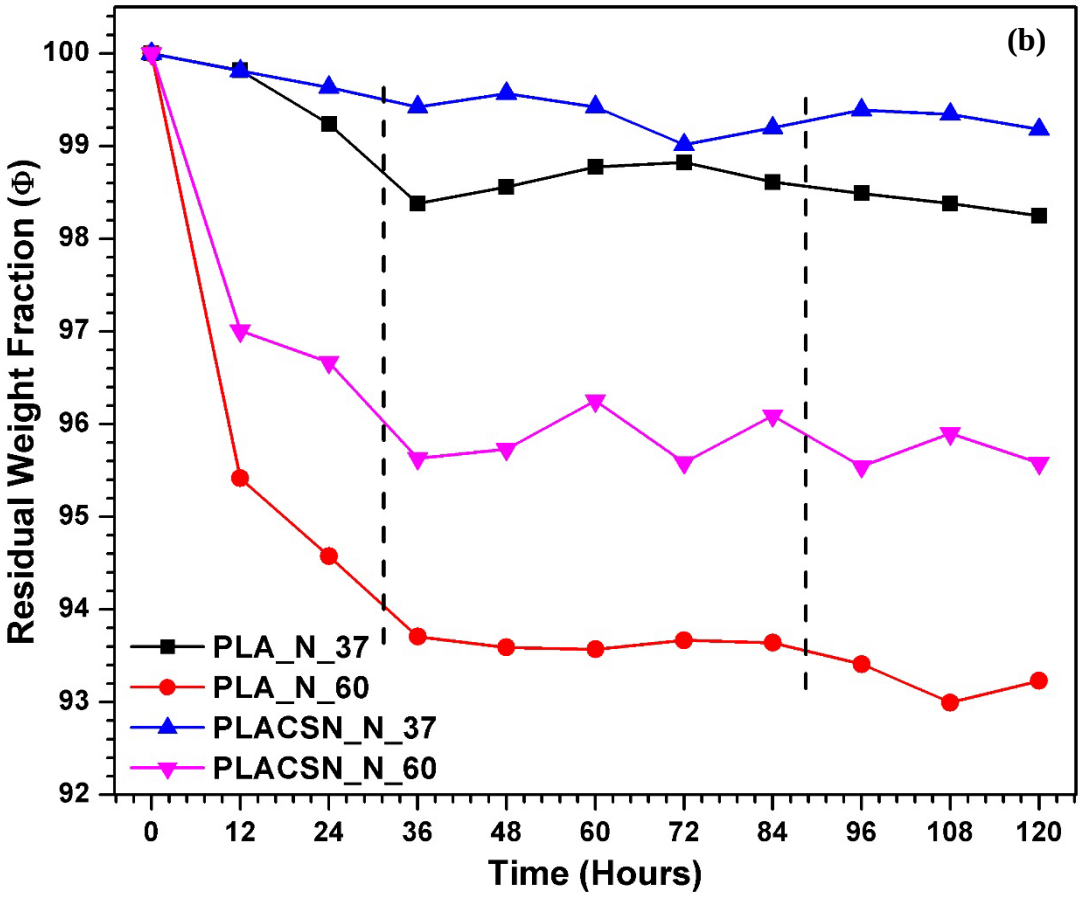
(b)
Residual Weight Fraction (Φ)
100
99
98
97
96
95
94
93
92
0
12
24
36
48
60
72
84
96
108
120
Time (Hours)
PLA_N_37
PLA_N_60
PLACSN_N_37
PLACSN_N_60

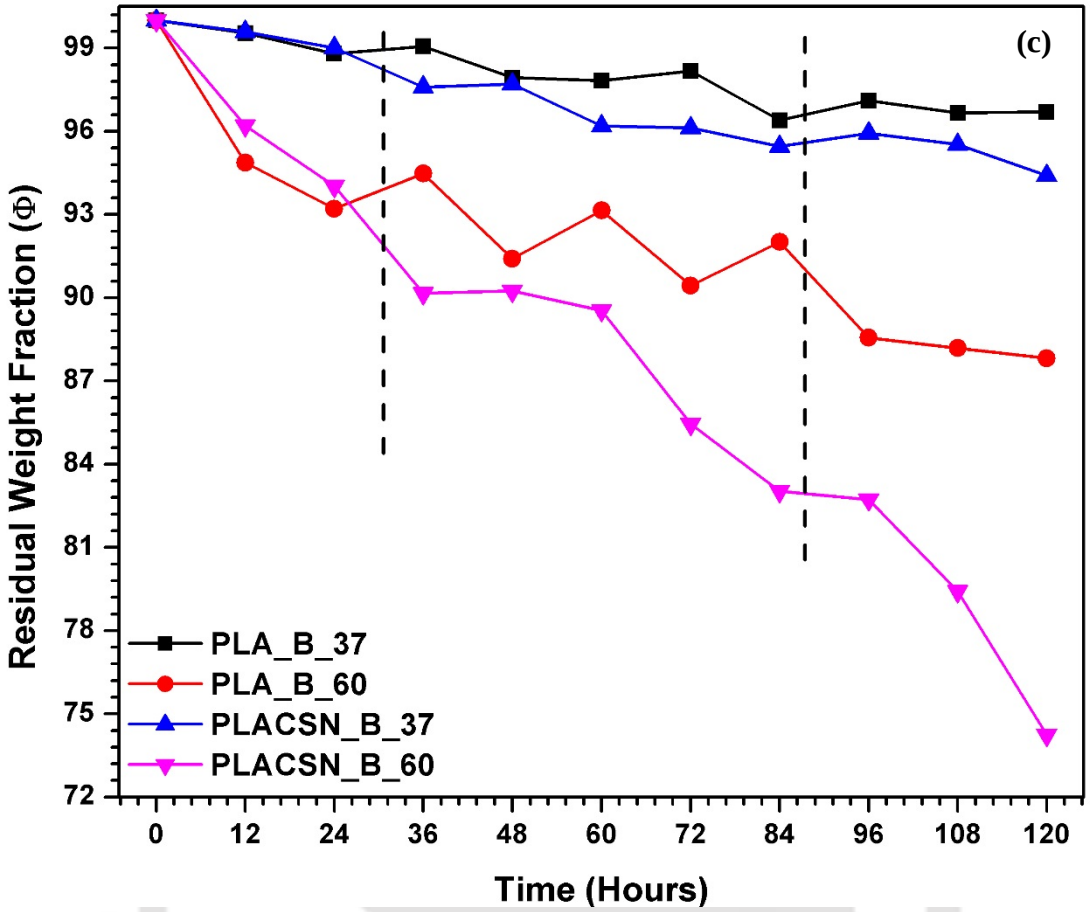

Figure 6.12: Plots of residual weight fraction (ϕ) versus hydrolytic degradation time (t) for PLA and PLACSN5 at 37 and 60 °C immersed in (a) acidic (pH=2), (b) neutral (pH=7) and (c) alkaline (pH=12) solutions.

Hydrolytic degradation can be divided into three stages, a fast initial stage, a steady mid-stage and a slower third stage, irrespective of pH and temperature conditions **(Valapa et al., 2016; Wang et al., 2016b)**. Hence, the study was conducted till 120 h only as the third stage is almost achieved for all samples investigated for hydrolytic degradation studies. It was found that the degradation rate was higher at elevated temperatures i.e. 60 °C (~$T_{g,PLA}$) as compared to 37 °C, this can be attributed to increased chain mobility which reduced the activation energy required for breaking of chains.**(Elsawy et al., 2017)**. It could be noted that weight loss was much faster in basic conditions (pH ~12) followed by acidic conditions (pH ~2). The neutral pH conditions showed least activity towards hydrolytic degradation. The –OH groups present in alkaline mediums act on the ester linkages resulting into such faster degradation rates as compared to other pH media. It can be seen that PLACSN5 impedes the hydrolytic degradation process of PLA, due to hydrophobic nature of CSN, which suppresses water absorption **(Paul et al., 2005)**. Surprisingly,

PLACSN showed accelerated degradation under basic conditions which was unexpected. This can be attributed to proper dispersion of CSN throughout the matrix, which provides additional sites for –OH groups to attack the matrix backbone.

6.2.4.1 Hydrolytic degradation rate

Figure 6.13 and Table 6.4 shows variation of hydrolytic degradation rates as calculated with Eq. (6.24). PLA degradation values are slightly lower with respect to values in literature **(Fernández and Fernández, 2017)**. It was found that unfilled PLA degrading rate was more as compared to PLACSN5 under acidic and neutral conditions. Contrary to the expected results, PLACSN5 degradation rate is higher than PLA in alkaline medium. It is known that in alkaline pH, degradation takes place through the surface whereas in acidic/neutral pH, degradation occurs at the bulk, which makes hydrolytic degradation phenomenon more observable in alkaline solutions which is aggravated by the availability of interfaces on the surface created due to the homogeneously dispersed CSN in the PLA matrix.**(Duan et al., 2016)**. The process is further amplified due to well-dispersed CSNs in the PLA matrix which creates high amount of PLA/CSN interfaces acting as additional sites for hydrolytic degradation to occur, thus eclipsing the hydrophobic nature of CSNs. To access the CSN dispersion and understand the mechanism of alkaline degradation (showing highest hydrolytic degradation rate), surface and cross-sectional morphology and other related studies such as XRD, transparency, TGA, etc is studied to support our findings, which is discussed in subsequent sections.

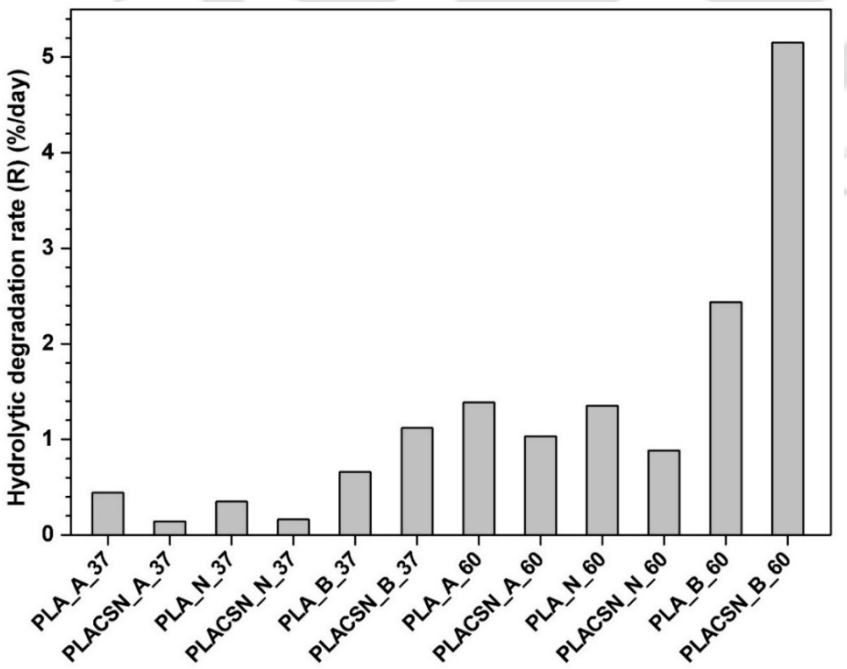

Figure 6.13: Hydrolytic degradation rate calculated from percentage mass loss.

6.2.4.2 Variation in pH

To learn about the byproducts during hydrolytic degradation, variation in pH with respect to immersion time was conducted. It can be seen from Figure 6.14 that for all the three pH solutions exhibit a decrease in pH as the time proceeds. Process of degradation proceeds by chain scission of ester bonds generating carboxylic acid end groups which further autocatalysis hydrolysis process. As the degradation proceeds, shorter PLA segments and oligomers, escape from the matrix into the surrounding media resulting in this decrease in pH **(De Jong et al., 2001)**. The main degradation product of PLA by hydrolytic degradation process is lactic acid, which has a pKa value of 3.84. As a result of which the pH of all media tends to reach this acidic pH **(Elsawy et al., 2017)**. The lactic acid released in alkaline solution is in dissociated form which accelerates hydrolysis, whereas in acidic solutions, it is in associated form which carries out hydrolysis process through auto-acceleration **(Lyu and Untereker, 2009)**.

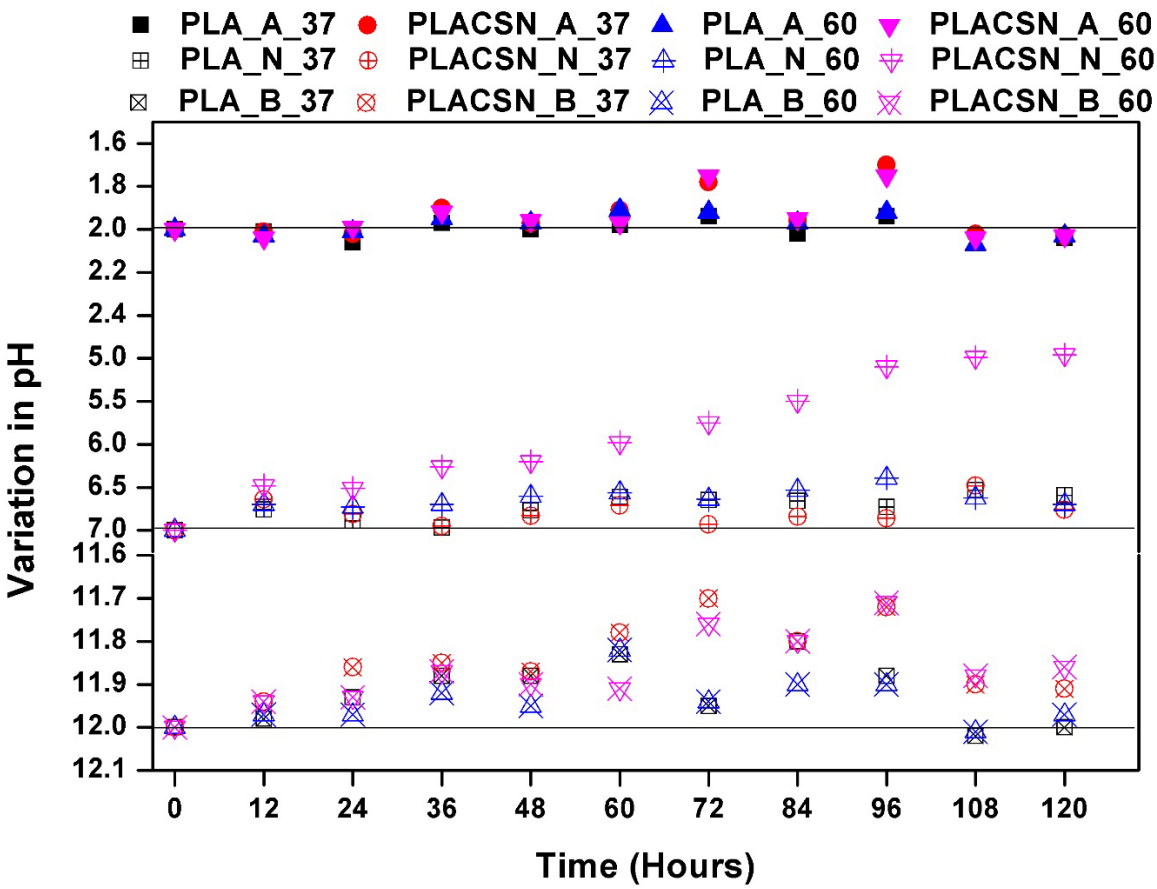

Figure 6.14: Variation in pH values recorded from 0–120 h of immersion time-period.

6.2.4.3 Morphological investigations

To develop deeper insight about the hydrolytic degradation mechanism of PLA and PLACSN5 bionanocomposites, the surface and cross-sectional morphologies for alkaline pH were examined using FESEM. Figure 6.15(a-b) shows the surface morphologies of PLA and PLACSN5 before degradation. The SEM micrographs show that the PLA surface appears to be very smooth whereas PLACSN5 surface shows rough morphology with nano-sized CSNs (shown with black arrows) homogeneously dispersed in the PLA matrix. Figure 6.15(c-d) shows surface morphologies of PLA and PLACSN5 after being immersed for 120 h in alkaline solution at 37 °C. Interestingly, the roughness of PLACSN5 is higher in comparison to PLA, this is due to the fact that homogeneously dispersed CSNs create numerous PLA-CSN interfaces which act as sites for the action of –OH ions. As already discussed, alkaline degradation is a surface phenomenon, thus the etching of polymer amorphous chains of PLA into solutions are more prone to surface erosion than crystalline regions **(Dai and Qiu, 2017; Duan et al., 2016)**. These events are more severe at higher incubation temperatures as shown in Figure 6.15(e-f). The PLACSN5 at 60 °C shows even higher surface roughness and deeper erosions as compared to PLA. Obviously, the variations of surface morphologies of samples agree well with their mass loss profiles (Figure 6.15(c)). This increased mass loss does not render increased hydrolytic degradation rate for PLACSN5 in alkaline solutions as it is the molecular weight loss and not the mass loss which is the real indication of the rate of hydrolytic degradation. This was verified by examining the cross-sectional morphologies of PLA and PLACSN5 after hydrolytic degradation at 60 °C in alkaline media. The cross-sectional morphology displayed in Figure 6.15(g-h) is quite different from the surface morphology (Figure 6.15(e-f)). The cross-sectional morphologies correspond to the bulk morphology of the specimens. It can be observed that cross-sectional morphologies appear much less eroded as compared to surface which ratifies the fact that alkaline pH is a surface phenomenon. Both samples appear smooth with appearance of small holes **(Valapa et al., 2016)**. Moreover, FESEM micrographs of PLACSN5 after being hydrolyzed shows more number of expelled CSNs (highlighted with black arrows) as compared to non-degraded sample. This clearly indicates that PLA degradation in alkaline solutions occurs at PLA-CSN interface and also PLACSN5 shows increased surface erosion and not the overall hydrolytic degradation **(Lizundia et al., 2017)**.

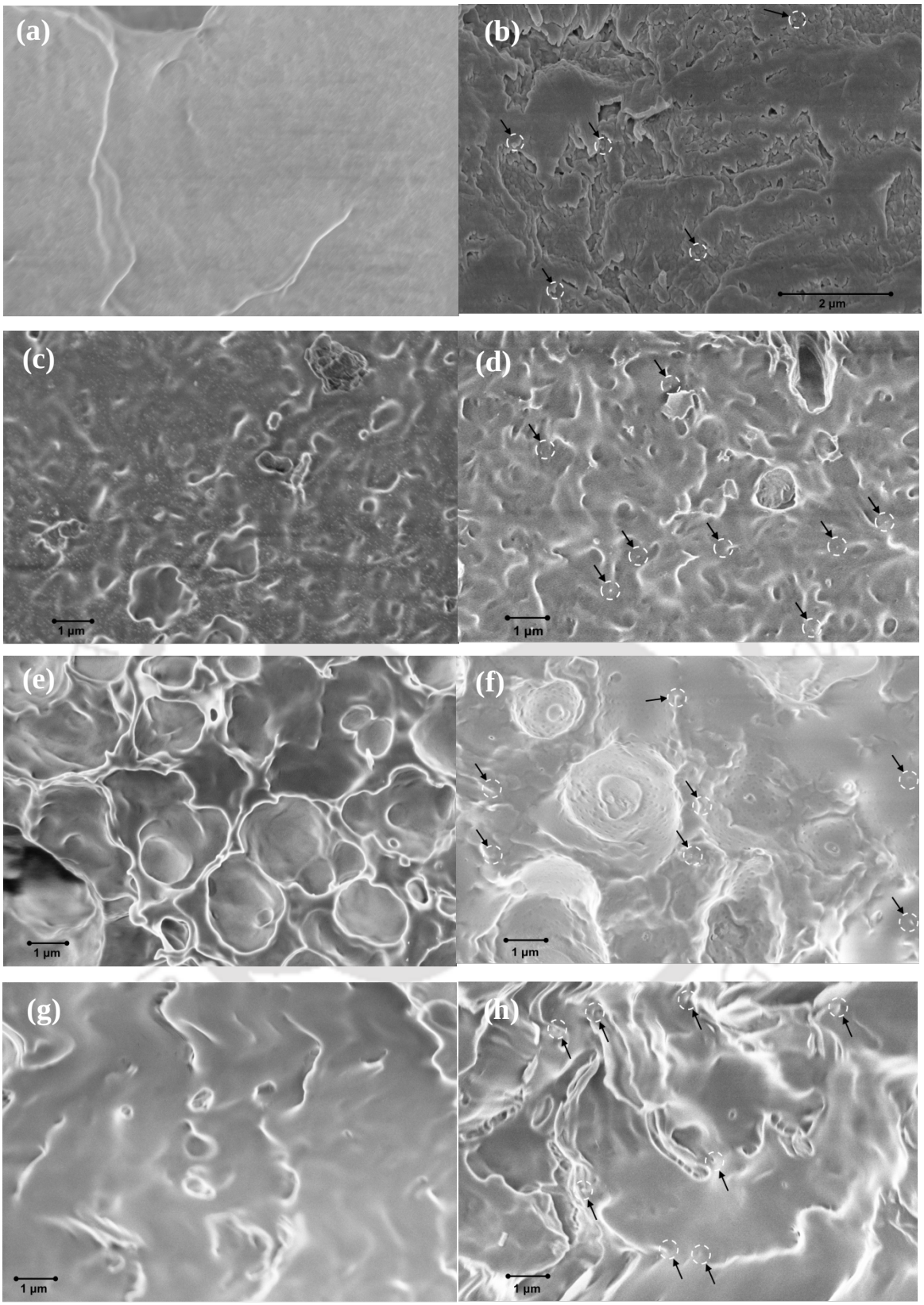

Figure 6.15: FESEM micrographs for comparison between (a, c, e, and g) PLA and (b, d, f and h) PLACSN5 bionanocomposite surface (a, b) prior to immersion and (c-h) after 120 h at pH=12 (c, d) 37 °C, (e, f) 60 °C, (g, h) cross-sectional view at 60 °C.

6.2.4.4 Changes in molecular weight during hydrolytic degradation study

In order to shed some light on the impact of hydrolytic degradation on the bionanocomposite properties, the reduction of the molecular weight (high-MW part) of PLA chains extracted from PLA and PLACSN5 samples was analyzed using GPC at different pre-determined time points after their recovery from incubation solutions. This time-period is chosen, as during this period the molecular weight loss is most prominent which attains a constant later irrespective of the time period **(Zhang et al., 2008)**. It can be seen that alkaline pH (Figure 6.16(c)) showed a higher percentage reduction in molecular weight compared to acidic (Figure 6.16(a)) and neutral (Figure 6.16(b)) pH respectively. Two inferences can be drawn from the loss of molecular weight investigations, firstly, higher incubation temperature affected the molecular weight severely and secondly the loss of molecular weights for PLA was higher in comparison to PLACSN5 owing to hydrophobic nature of CSN as seen in Figure 6.16(a-c). These findings are in line with the residual weight loss experiments. Furthermore, it can be noticed that the weight loss was much lower as compared to molecular weight reduction which was expected as upon hydrolytic degradation, shorter PLA chains and oligomers are not taken up by the pH media. It is only the dimers/trimers of lactic acid that are solubilized in pH media **(Paul et al., 2005)**. It is known that hydrolytic degradation is heterogeneous phenomenon i.e. it occurs faster inside than at the surface, because inside autocatalysis by carboxylic end groups is more prominent **(De Jong et al., 2001)**.

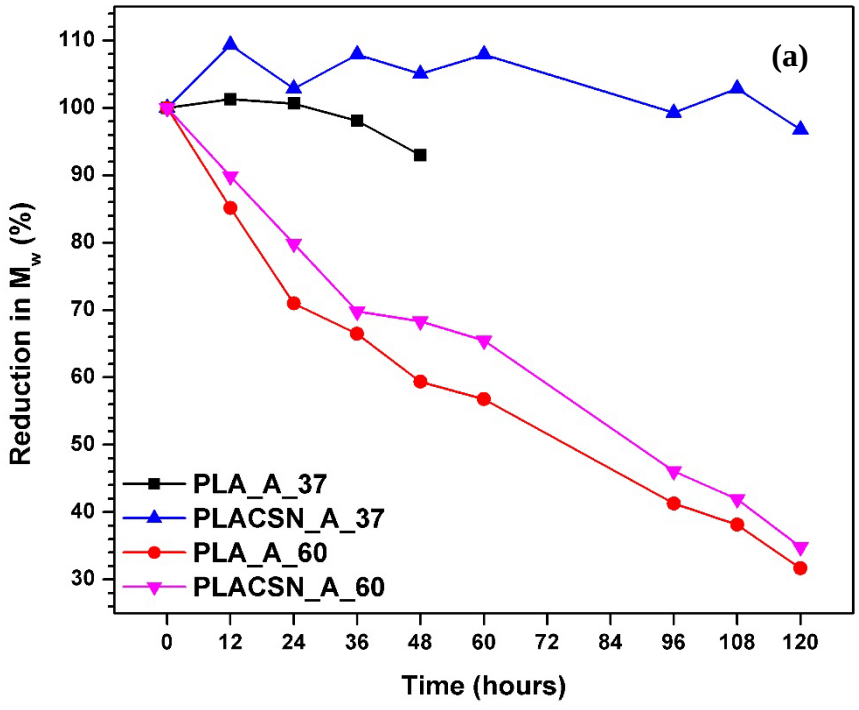

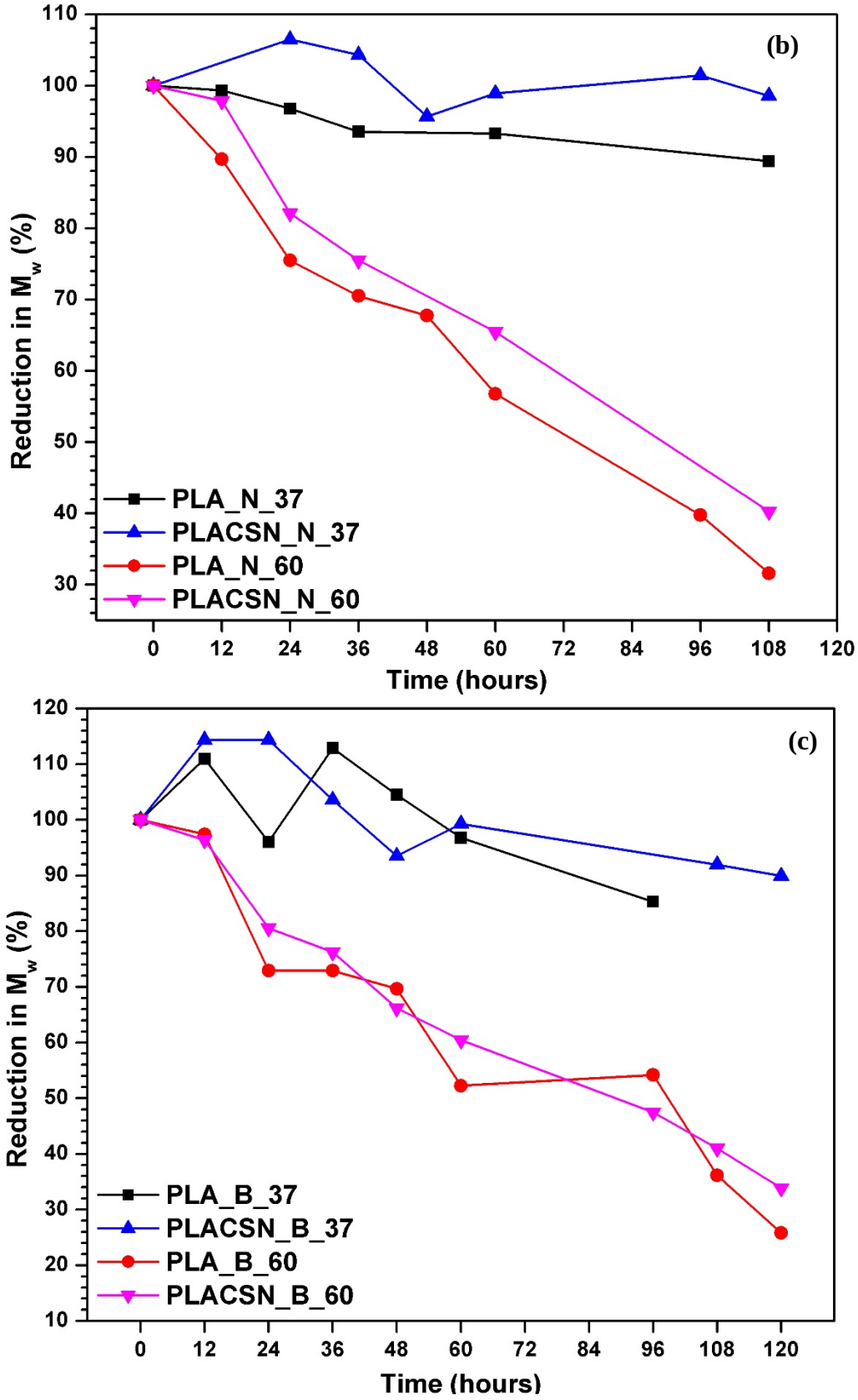

Figure 6.16: (a-c) Percentage-wise M_W reduction vs. hydrolysis time for PLA and PLACSN5 bionanocomposite with at different incubation temperature immersed in different pH solutions (a) acidic, (b) neutral and (c) alkaline.

6.2.4.5 Degradation kinetics of PLA and PLACSN bionanocomposites

PLA follows first order degradation during initial exposure to hydrolytic degradation **(Li et al., 2017)**. The relationship between logarithmic (Ln M_w) of PLA and degradation time is shown in Figure 6.17(a-b). It is observed that PLA follows first-order degradation in the pre-determined exposure time. From the slope of Ln M_w-t plots, the rate parameter k are obtained, which are presented in Table 6.4. It can be seen that degradation parameter "k" were higher for PLA in comparison to PLACSN5, which shows the hydrolytic resistance of PLA/CSN bionanocomposites. The $k \times 10^3$ values for alkaline degradation (37 and 60 °C) conditions for PLA and PLACSN5 are 4.6, 23.4 and 3.9, 20.9 g/mol.day, respectively. The k values are a little larger than the results from the study by **Li et al. (2017)**.

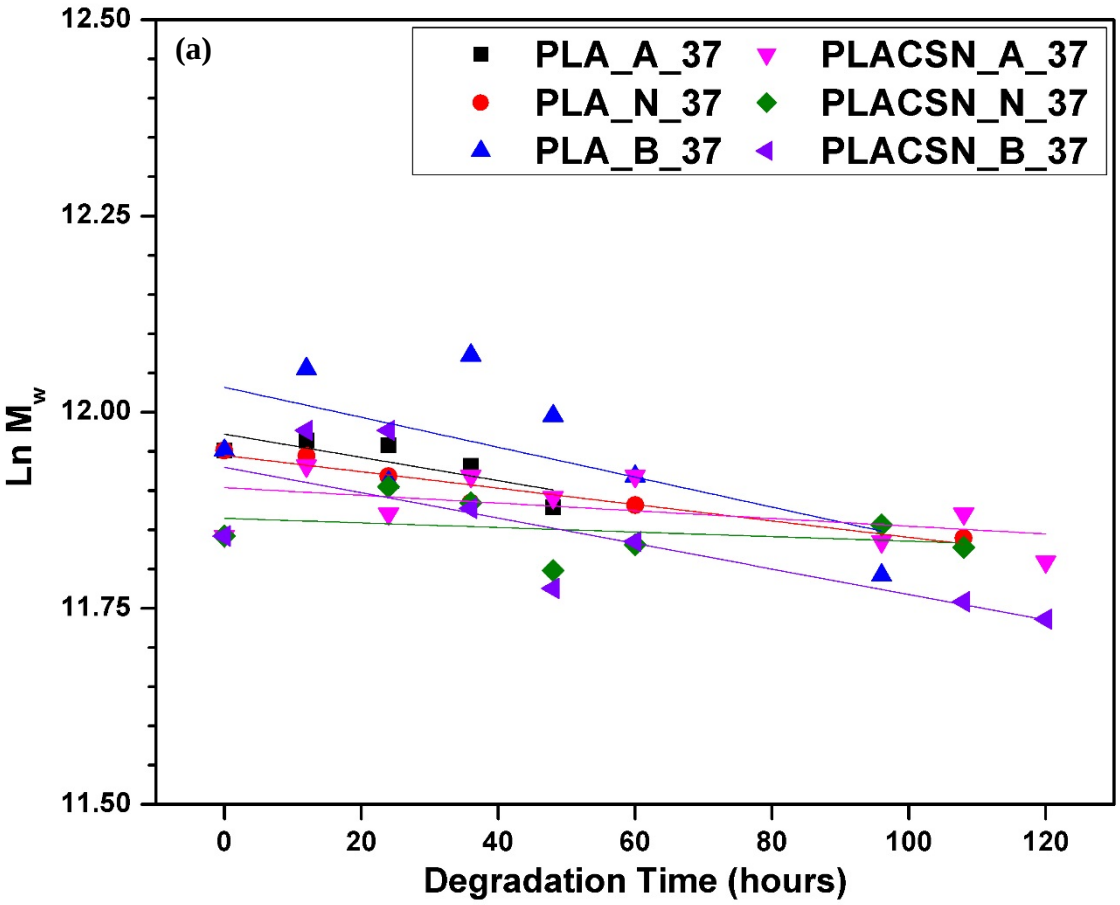

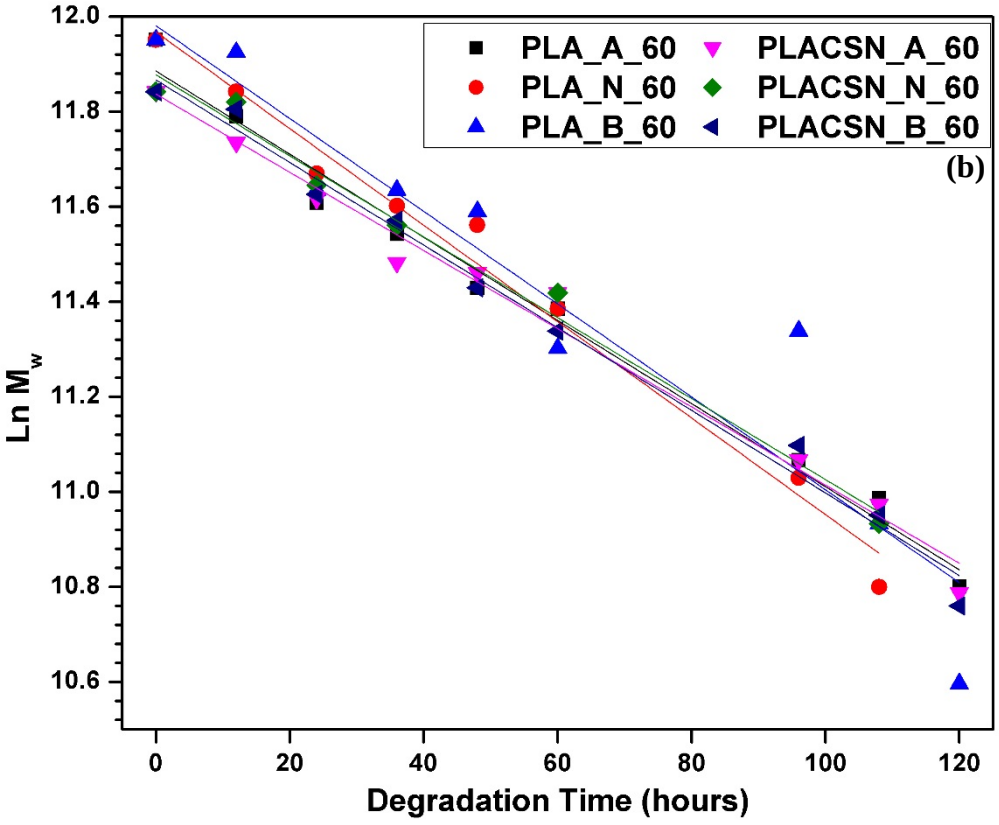

Figure 6.17: Degradation rate kinetic plots for Ln M_w vs. degradation time (t) (a) 37 °C and (b) 60 °C.

6.2.4.6 Changes in thermal stability upon hydrolytic degradation

The thermal stability of PLA and PLACSN5 was recorded by thermogravimetric analysis (TGA). The TGA traces for PLA/CSN post 120 h during hydrolytic degradation under different pH conditions and temperatures is shown in Figure 6.18(a-b). The TGA traces reveal that the thermo-degradation of submerged samples proceeds at lower temperatures as the degradation temperature increases and level of chain-cleavage. It is understood that upon hydrolytic degradation, the polymer macromolecule chains are cleaved into numerous shorter chain segments. In view of this, sample with smaller chain segments requires less energy to degrade which means it has an early onset of degradation (T_{10}). For instance the T_{10} for PLACSN5 is lowered from 280.1 to 269.1 °C when exposed to alkaline environment at elevated temperatures. (see Table 6.4 for the T_{10} values). It should be noted that all samples, irrespective of pH environment or incubation temperature display one-step degradation which ratifies that thermo-degradation occurs via intramolecular transesterification reactions **(Lizundia et al., 2017)**. Moreover, PLA shows an enhanced stability in regard to bionanocomposite film, inferring that breaking of polylactide

backbone which occurs through random scission of ester bonds, is more pronounced in samples containing CSN, suggesting that it plays role as a trigger on hydrolytic degradation of PLA.

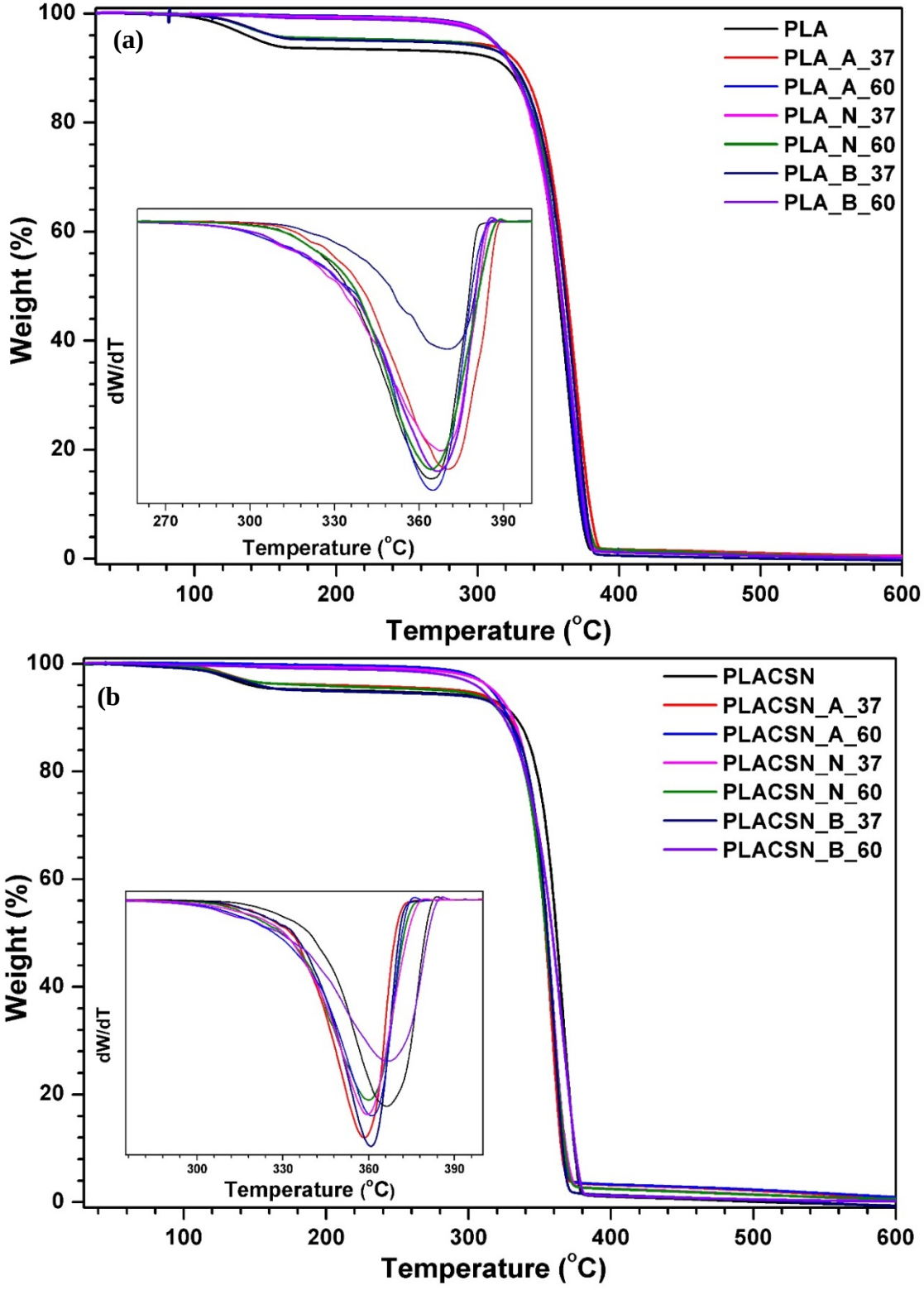

Figure 6.18: TGA thermograms of (a) PLA and (b) PLACSN5 before and after hydrolytic degradation carried for 120 h.

6.2.4.7 Changes in thermal properties upon hydrolytic degradation

Figure 6.19(a-b) shows the heating DSC traces of hydrolytically degraded PLA and PLACSN5 under different pH and temperature conditions.

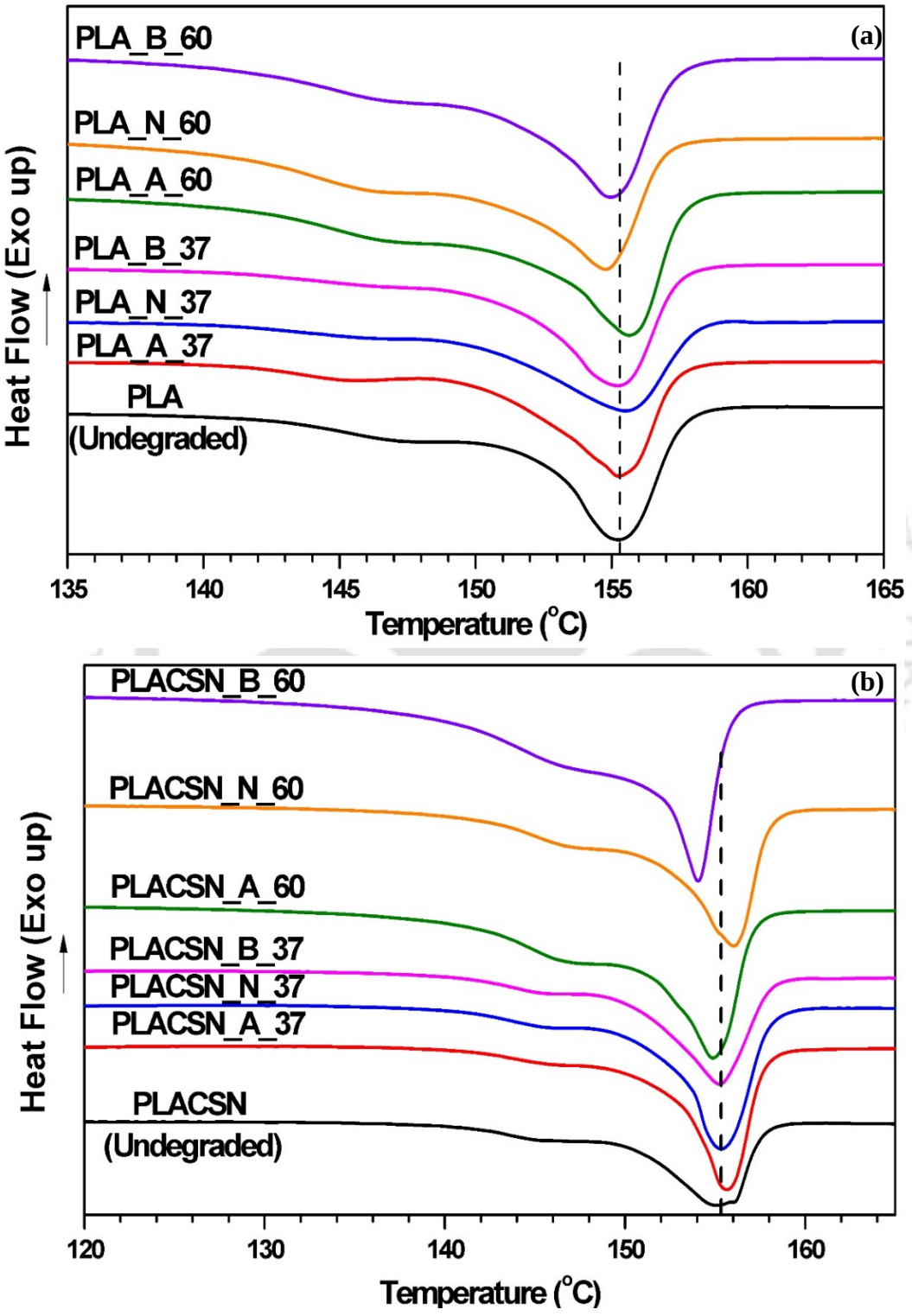

Figure 6.19: DSC thermograms of (a) PLA and (b) PLACSN5 before and after hydrolytic degradation carried for 120 h.

As presented in Table 6.4, as the degradation proceeds, the crystallization and melting point shifts to higher temperatures. The reverse trend is observed for glass transition temperature which shifts to lower temperatures due to decrease in molecular weights of the degraded samples **(Rapacz-Kmita et al., 2015)**. The crystalline fraction also improves for both materials, due to utilization of amorphous regions. These effects are more evident in PLA as compared to PLACSN5 which suggest better degradability of PLA. It could be observed that, for all studied temperature and pH conditions, PLA and PLACSN5 present thermograms characteristic to semi-crystalline polyesters having a sharp crystallization peak at ~115 °C respectively. Overall, as degradation proceeds, T_m displays a shift to higher temperatures. These changes occur at initial stages, where molecular mobility of PLA chains in increased due to hydrolytic degradation chain cleavage, allowing formation of more ordered structures **(Zhang et al., 2008)**. Hence, shorter the PLA chains become, higher T_m values are obtained combined with gradual increase in relative crystallinity.

Table 6.4: Thermal and structural properties before and after hydrolytic degradation.

Sample	R×10^2 (%/d) [a]	k×10^2 (g/mol.d)[b]	T_{10} (°C)	T_{50} (°C)	T_g (°C)	ΔH_m (J/g)	χ_c^* (%)	T_c (°C)	T_m (°C)	CI** (%)
PLA	-	-	293.7	356.7	52.3	22.2	23.7	116.5	148.7	12.0
PLA_A_37	4.4	3.6	290.3	362.7	47.9	22.9	24.5	114.0	148.0	-
PLA_N_37	3.5	2.5	275.6	357.9	48.1	34.5	36.8	117.9	148.9	-
PLA_B_37	6.6	4.6	287.5	361.1	48.5	23.1	24.6	114.9	148.9	44.5
PLA_A_60	13.9	21	275.6	358.1	48.7	31.0	33.1	117.6	148.4	-
PLA_N_60	13.5	24.4	288.6	358.7	47.9	22.5	24.1	114.0	148.4	-
PLA_B_60	24.4	23.4	270.6	358.7	48.1	32.7	34.9	120.7	149.3	52.5
PLACSN	-	-	280.1	361.9	48.0	23.7	24.0	115.0	148.4	19.5
PLACSN_A_37	1.4	1.2	277.7	353.9	47.5	22.9	23.2	114.9	148.4	-
PLACSN_N_37	1.6	0.2	280.7	355.2	49.7	32.6	33.1	115.8	148.4	-
PLACSN_B_37	11.2	3.9	281.9	355.2	46.8	23.6	24.0	116.2	149.3	50.8
PLACSN_A_60	10.3	19.8	279.5	355.0	49.1	31.5	32.0	114.0	147.1	-
PLACSN_N_60	8.8	20.4	278.2	354.4	50.2	25.1	25.4	114.9	148.4	-
PLACSN_B_60	51.5	20.9	269.1	358.6	50.0	27.8	28.2	117.6	148.4	55.3

[a]rate calculated from residual weight fraction (ϕ); [b]calculated from weight average molecular weight (M_w); [*]calculated from DSC [**]calculated from XRD profiles.

6.2.4.8 Structural changes upon hydrolytic degradation

XRD profiles of PLA and PLACSN5 films during hydrolytic degradation are shown in Figure 6.20(a-b).

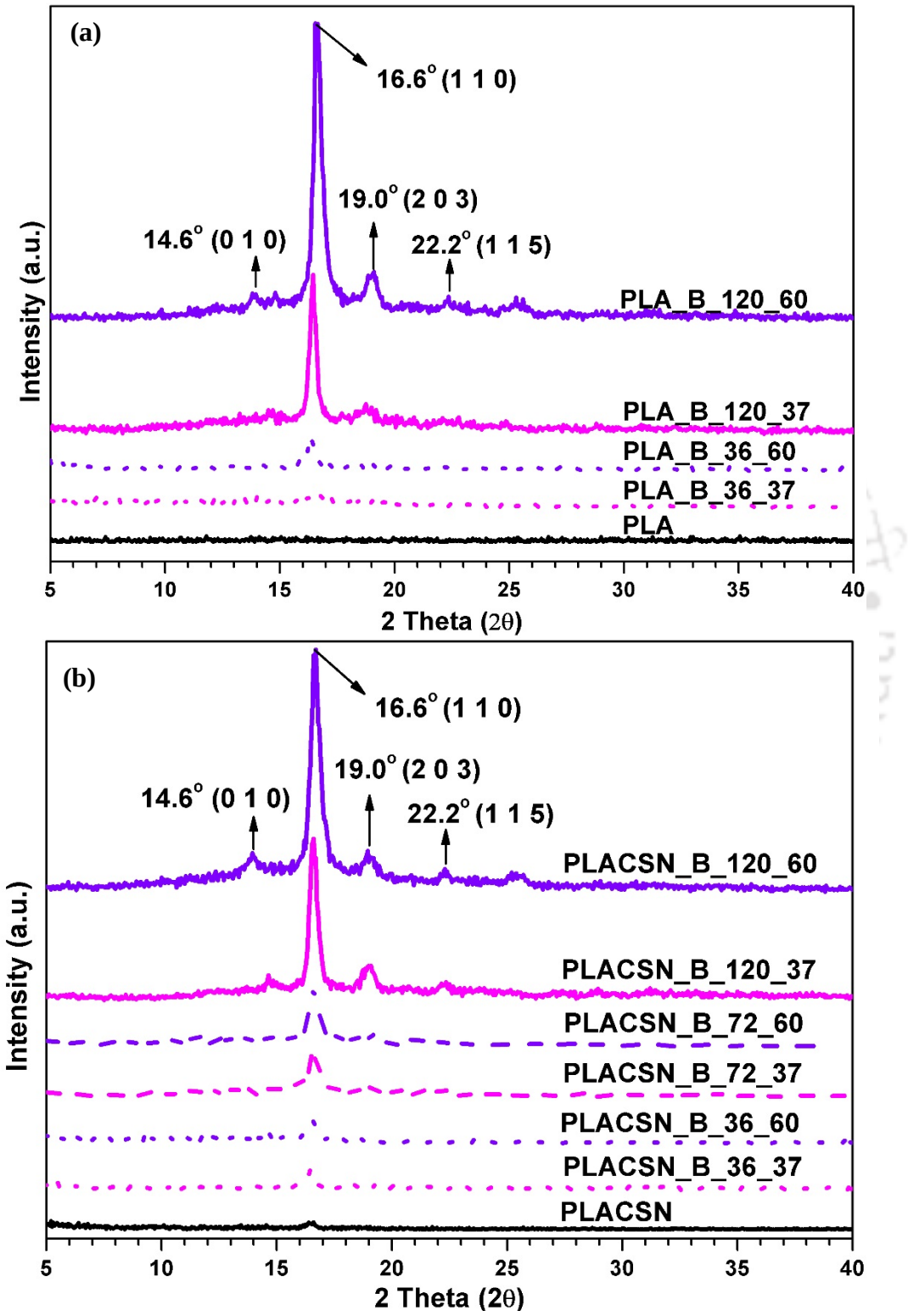

Figure 6.20: Comparison between (a) PLA and (b) PLACSN5 before and after hydrolytic degradation carried for 120 h through XRD diffractograms.

Initially, PLA appeared completely amorphous without any recognizable peaks. After 36 h, diffraction peaks appear at 2θ = 14.5, 16.6, 19 and 22.2°. The major peak at 16.6° (110) corresponds to the α-crystalline structure of PLA **(Zhang et al., 2008)**. After 120 h, the intensity of these diffraction peaks increased. Therefore, the X-ray diffraction spectra confirmed the formation of stable crystal structure during the degradation of PLA. It is well known that amorphous regions are attacked during hydrolytic degradation. This leads to increase in crystalline character of semi-crystalline polyesters. The mobile shorter chain formed during hydrolytic degradation allows for reorientation of crystalline phase which results in increment in crystallinity **(Höglund et al., 2010)**.

6.2.4.9 Physical alterations and transmittance

The impact of hydrolytic degradation can be easily judged by visual inspection. Figure 6.21 shows the specimens exposed to hydrolytic degradation under different pH and temperature environments. From visual inspection it can be seen that the degradation was more pronounced at higher temperatures 60 °C as compared to 37 °C. At elevated temperatures, considerable opacity (milky white) and extreme brittleness was achieved at shorter time period for both materials. As time proceeds samples became fragile and even lost integrity at the later stages of experiment. This opacity can be attributed to various reasons, light scattering due to water molecules present inside the films, presence of degradation products entrapped inside the films, formation of holes in the bulk as a result of hydrolytic degradation and due to development of crystallinity of the PLA matrix. As explained in previous section 6.2.20, that amorphous domains are more susceptible to hydrolytic degradation hence, increment in crystallinity seems to be the most plausible cause **(Fukushima et al., 2011)**. The light scattering ability was decreased upon hydrolytic degradation due to higher opacity in residual sample. It was observed that percentage reduction in transmittance values was higher in PLA compared to PLACSN5 which means that degradation process occurred at a faster rate in PLA. With passage of time, hydrolysis resulted in increase in relative opacity of all materials which was measured using UV-vis spectrophotometer and presented in Table 6.5.

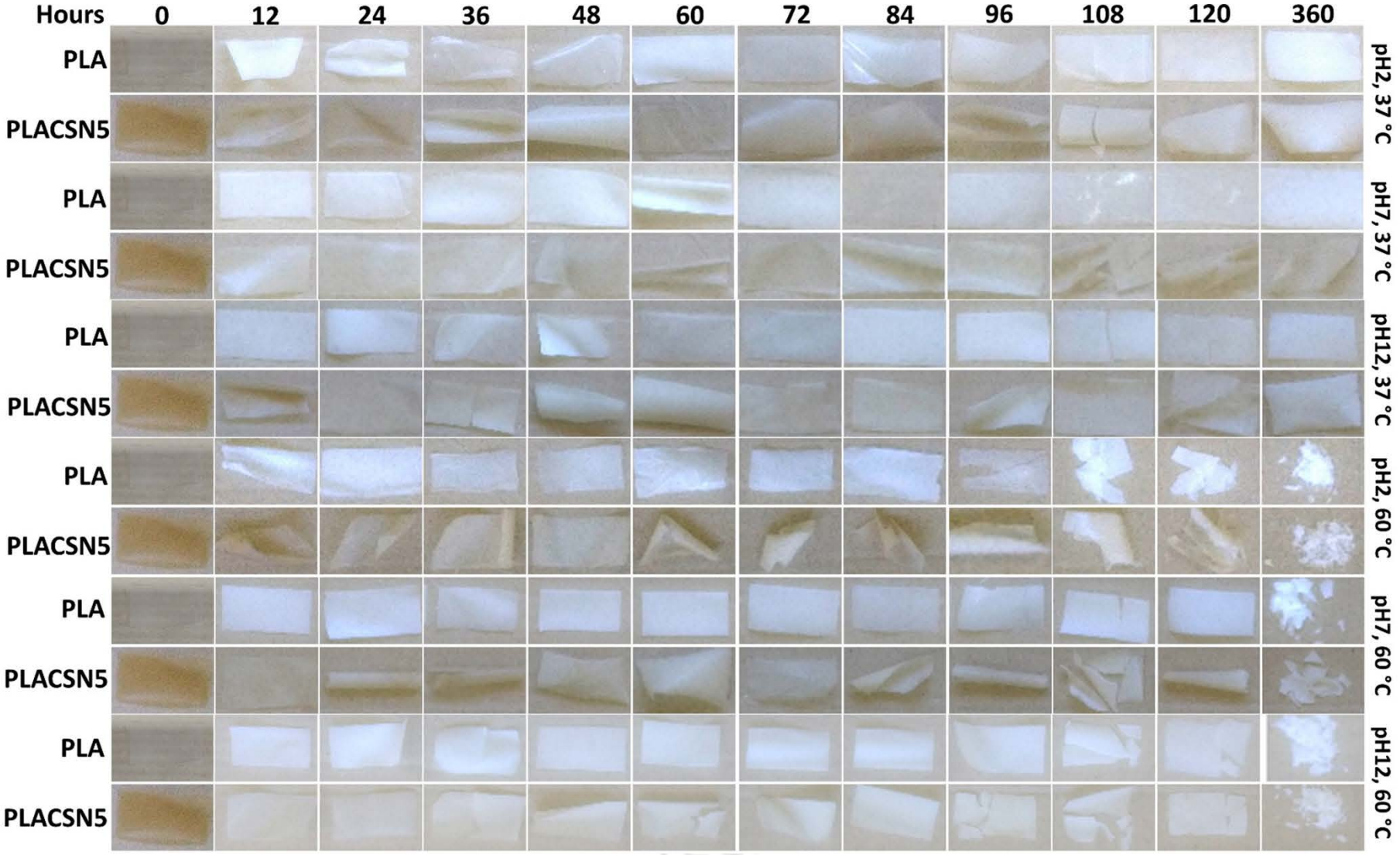

Figure 6.21: Visual appearance of PLA and PLACSN5 bionanocomposites before and after hydrolytic degradation at different time intervals.

Table 6.5: Light transmittance values with their respective reduction percentages in PLA and PLACSN5 samples.

Sample	% Transmittance	% Reduction	Sample	% Transmittance	% Reduction
PLA	56.32		PLACSN	12.99	
PLA_A_37	36.00	36.08	PLACSN_A_37	9.89	23.86
PLA_N_37	42.72	24.15	PLACSN_N_37	10.37	20.17
PLA_B_37	8.72	84.52	PLACSN_B_37	6.45	50.35
PLA_A_60	0.70	98.76	PLACSN_A_60	0.58	95.54
PLA_N_60	0.88	98.44	PLACSN_N_60	0.71	94.53
PLA_B_60	0.61	98.92	PLACSN_B_60	0.20	98.46

6.3 Summary

In this study, thermal and hydrolytic degradation of PLA and PLA/CSN bionanocomposites with varying CSNs loadings were investigated. The presence of CSNs had a pronounced influence over thermal and hydrolytic stability of PLA. TGA studies showed improvement in thermal stability at small loadings (~1 wt%) along with higher degradation activation energy, E_a than that of PLA. The network structures act as labyrinth for degraded polar molecules to escape hence slows down interaction with PLA chains, thus imparting more stability. Thermal stability was lost at higher concentration of CSN (~5 wt%) due to CSN agglomeration which lower the possibility of network formation. Thermal degradation kinetics was analyzed using two isoconversional, Flynn-Wall-Ozawa and Kissinger-Akahira-Sunose models and one model fitting model i.e. Coats-Redfern model. The models predicted higher decomposition activation energy requirement for degradation to occur in case of PLACSN bionanocomposite unlike in PLA. It was found that isoconversional models gave more realistic values for E_a, whereas model fitting C-R model gave higher values of activation energies albeit similar trend like the isoconversional methods was observed. The PLA and PLA/CSN bionanocomposites follow the F1 type degradation mechanism. The major evolved volatile products detected during TG-IR, are CO_2, CO, aldehydes, lactide and cyclic oligomers for PLA and PLA/CSNs. These results suggest that incorporation of CSNs into PLA matric enhanced thermal stability of bionanocomposite which could extend the range of applications like automobile industry and high engineering applications. The effect of *in vitro* hydrolytic degradation has been investigated by common analysis techniques. It has been observed that degradation rate is slower for PLA/CSN bionanocomposites due to hydrophobic character of CSN. The study elucidates that basic pH and higher temperature, both favour hydrolytic degradation process for PLA and PLACSN5 bionanocomposite samples. We describe, here the possibility of use of PLA/CSN bionanocomposites in moist environments. The results described here can find applications to control the degradation rate of PLA. Morphological investigations provide direct evidence on CSN-initiated PLA degradation, which is expected to occur via H_2O dissociation onto silk nano-discs, thereby breaking ester bonds of adjacent PLA chains. XRD and DSC analysis shows that crystallinity increases with due course of degradation process. GPC analysis shows reduction in molecular weight of samples as the degradation proceeds.

Chapter 7

Preparation and Characterization of PLA/CSN and PLA/MGCSN Bionanocomposites with and without Anticancer Drug (Curcumin) by Electrospinning and Evaluation for Cytotoxicity and Anti-cancer Activity

This chapter discusses the utilization of prepared crystalline silk nano-discs (CSNs) and magnetic silk nano-discs (MGCSNs) for preparation of biocompatible nanofiber based scaffolds by melt blending with poly(lactic acid) (PLA) along with silk followed by electrospinning. The prepared scaffolds are characterized for morphological, thermo-mechanical and structural properties. We assessed release behavior of curcumin from these scaffolds. Curcumin, a naturally occurring anticancer drug and found effective towards sustained release over 25 days which also shows effective cytotoxicity against human cervical cancer cells. Interestingly, alignment of CSN derived magnetic nanoparticles due to effective fiber drawing process during electrospinning could improve cytocompatibility against BHK-21 cells. *In vitro* cell cytocompatibility studies show improved cell adhesion and proliferation on the surface of bionanocomposites scaffolds which support its biocompatible nature. Combined effect of curcumin and hyperthermia reduced the growth to ~63%.

The work in this chapter is accepted as:

- R. Patwa, N. Soundararajan., N. Mulchandani, S. M. Bhasney, M. Shah, S. Kumar, A. Kumar and V. Katiyar, "Silk nano-discs: A natural material for cancer therapy," *Biopolymers*, DOI: 10.1002/bip.23231. (Accepted).

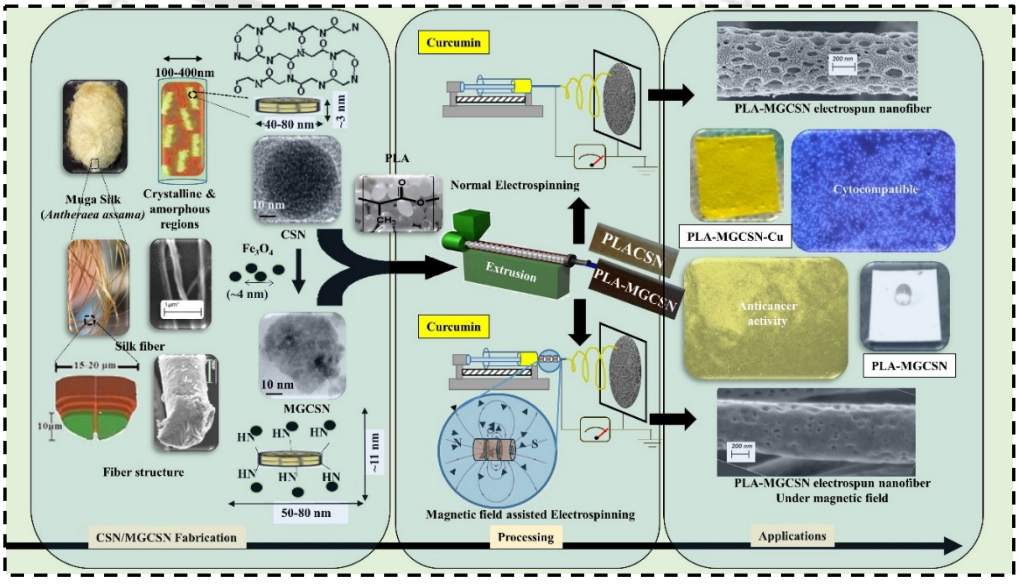

7.1 Introduction

Silk is a fibrous protein known for its combined strength and stretchability, which places it amongst the toughest biomaterials known to mankind. However, despite years of research, it is still impossible to mimic silk's unique properties which are due to self-assembly of the domains at nanoscale precision **(Keten et al., 2010)**. Moreover, silk possesses environmental stability **(Jo et al., 2017)**, ease of functionalization, favorable oxygen/water permeability, minimal antigenic response **(Babb et al., 2017)**, biocompatibility **(Shimanovich et al., 2017)**, morphologic flexibility **(Rockwood et al., 2011)** and better mechanical properties in comparison to globular proteins **(Altman et al., 2003)**, making it a viable entity in various fields of biomedical applications such as for developing sutures **(Jo et al., 2017)**, controlled drug delivery **(Min et al., 2017)**, cancer therapeutics **(Yan et al., 2016)**, wound healing **(Darshan et al., 2017)**, etc. Although a major confusion lies regarding its degradable nature, various reports suggest that silk can be degraded by proteolytic enzymes *in vivo* which over the time gets absorbed slowly **(Cao and Wang, 2009)**.

To utilize the superior properties of silk due to its unique molecular structure **(Nova et al., 2010)**, nano-level formulations of silk with polymers such as PLA, PCL, etc., can be exploited using various routes. Nanoparticles of silk fibroin can be obtained through emulsion-solvent evaporation, self-assembly, phase separation, spray drying rapid expansion of supercritical solution, electro-gelation, and salting out **(Rockwood et al., 2011)**. The above procedures utilize reconstituted silk having random coil structures which needs to be reconverted to pleated structures, hence material properties are compromised **(Rousseau et al., 2004)**. Interestingly, silk's original properties can be retained through direct utilization of silk post-degumming using mechanical attrition. Reduced morphologic flexibility, partial degradation of non-crystalline part, metal contamination and high costs are still some significant hurdles **(Wang et al., 2017)**. To improve mechanical compliance and retain morphologic flexibility, silk-based composites have been used for bone regeneration **(Shi et al., 2016)**, rope for replacement of anterior cruciate ligament **(Altman et al., 2002)**, protective gauzes for skin burn treatment **(Schiefer et al., 2017)**, silk cast films for growth of mural fibroblast and other human cells, etc. **(Wang et al., 2016c)**.

Silk-based scaffolds have detailed nano/micro internal architecture enabling them to supplement the extracellular matrix (ECM). The most commonly used techniques are solvent casting, particulate leaching, laser sintering, electrospinning, etc. **(Rockwood et**

al., 2011). Electrospinning essentially operates at high voltages, which allows the electric field to surpass the surface tension of polymeric solutions thus generating nanofibers. It can produce porous nanofibrous mats with large surface area that can withstand under continuous shear and vascular wall stretches (resembling extracellular matrix of skin tissue) and promote cell adhesion and proliferation, which are essential requirements for a material to be used as scaffold **(Wang et al., 2016d)**. To improve the case for use of silk nanoparticles for drug delivery and cancer therapeutics, magnetic functionalization is desired. Moreover, magnetic field has been found to have a positive effect on wound healing and tissue regeneration **(Meng et al., 2010)**. The mechanisms regulating wound healing can also promote cancer growth, hence a scaffold should also possess drug release abilities **(Sokolsky-Papkov et al., 2007)**. To address this, various anti-cancer drugs, both natural and synthetic, have been used. Owing to their side -effects, naturally occurring curcumin, principal bioactive component in turmeric (c*urcumina longa*) is gaining interest. Curcumin was electrospun with silk fibroin for sustained release wound dressing material **(Kasoju and Bora, 2012)**. Based on the above discussion, the present chapter outlines the preparation of electrospun, poly(lactic acid)-crystalline silk nanodiscs/magnetic silk nano-discs (PLA-CSN/MGCSN) scaffolds and their evaluation for wound healing applications, cell-cytocompatibility of these scaffolds, as well as curcumin release as a model drug. Further, the developed scaffolds are also explored for potential synergistic effect of hyperthermia and drug release on cancer cells. To our understanding, there is no study available based on the isolation of crystalline silk nano-discs by acid hydrolysis of Muga silk fibroin (*Antheraea assama*) and fabrication of magnetic nano-discs by adhering magnetite nanoparticles on the disc surface.

7.1.1 Fabrication of electrospun bionanocomposite scaffolds

7.1.1.1 Normal Electrospinning

The melt extruded strips were dissolved in a binary solvent of chloroform: dimethylformamide (Merck) (9:1) to obtain 10% (w/v) solution. The solutions were stirred overnight and were subsequently used for production of nanofibers via electrospinning using a standard electrospinning setup (E-spin, Nanotech, India). The polymer solution was taken into a 5 ml plastic syringe with a 20G SS needle. The solution was pumped with a flow rate of 0.8 ml/h with a positive voltage of 6 kV to the needle. The collector to needle distance was maintained at 15 cm. A flat plate collector was used to collect the scaffold of randomly oriented fibers at 23 °C under 35% relative humidity and the electrospinning

setup is shown in Figure 7.1(a). Curcumin (5 wt%) electrospun scaffolds were also fabricated in similar fashion. Visual image of electrospun samples is shown in Figure 7.1(b).

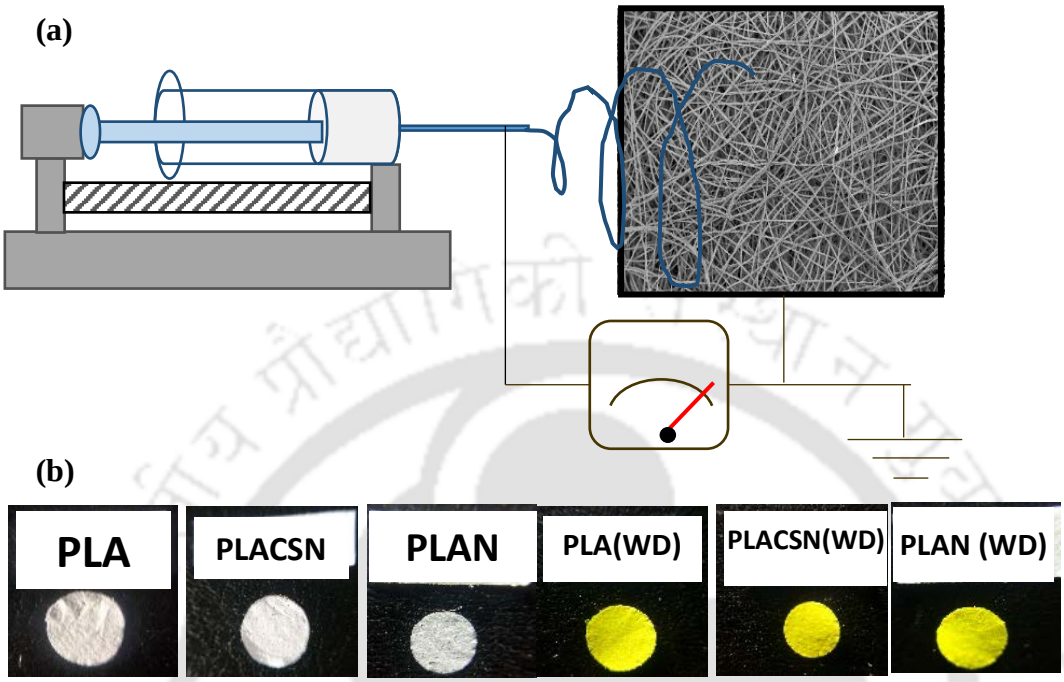

Figure 7.1: (a) Normal electrospinning setup and (b) PLA based electrospun scaffolds with and without curcumin.

Based on the above explanation, the PLA based bionanocomposites filled with CSNs/MGCSNs were prepared via electrospinning. The conventional electrospinning was used to prepare scaffolds which were labelled as PLA, PLACSN (PLACSN 5 wt%) and PLAN (PLA/MGCSN 5 wt%). Curcumin (5% w/v) loaded PLA, PLACSN, PLAN were also prepared separately under identical conditions.

7.1.1.2 Magnetic field-assisted electrospinning

Apart from standard procedure, magnetic field-assisted electrospinning was carried out with a small modification in the setup to prepare PLA based bionanocomposites filled with MGCSNs (see Figure 7.2(a)). Three tubular neodymium magnets (10 mm × 5 mm) attached back to back (Figure 7.2(b)) with central opening of around 5 mm were used. The electrospinning needle was passed through these magnets without touching them with 10 mm of needle tip protruding outside from the magnets (Figure 7.2(c)). The applied voltage was 12 kV, all other parameters were maintained the same as that in the absence of

magnetic field. Curcumin (5% w/v) loaded PLA, PLACSN, PLA/MGCSN were also prepared separately under identical conditions (Figure 7.2(d)).

The as-formed PLA-CSN/MGCSN bionanocomposite scaffolds were oven dried for 24 h at 50 °C before using for further analysis.

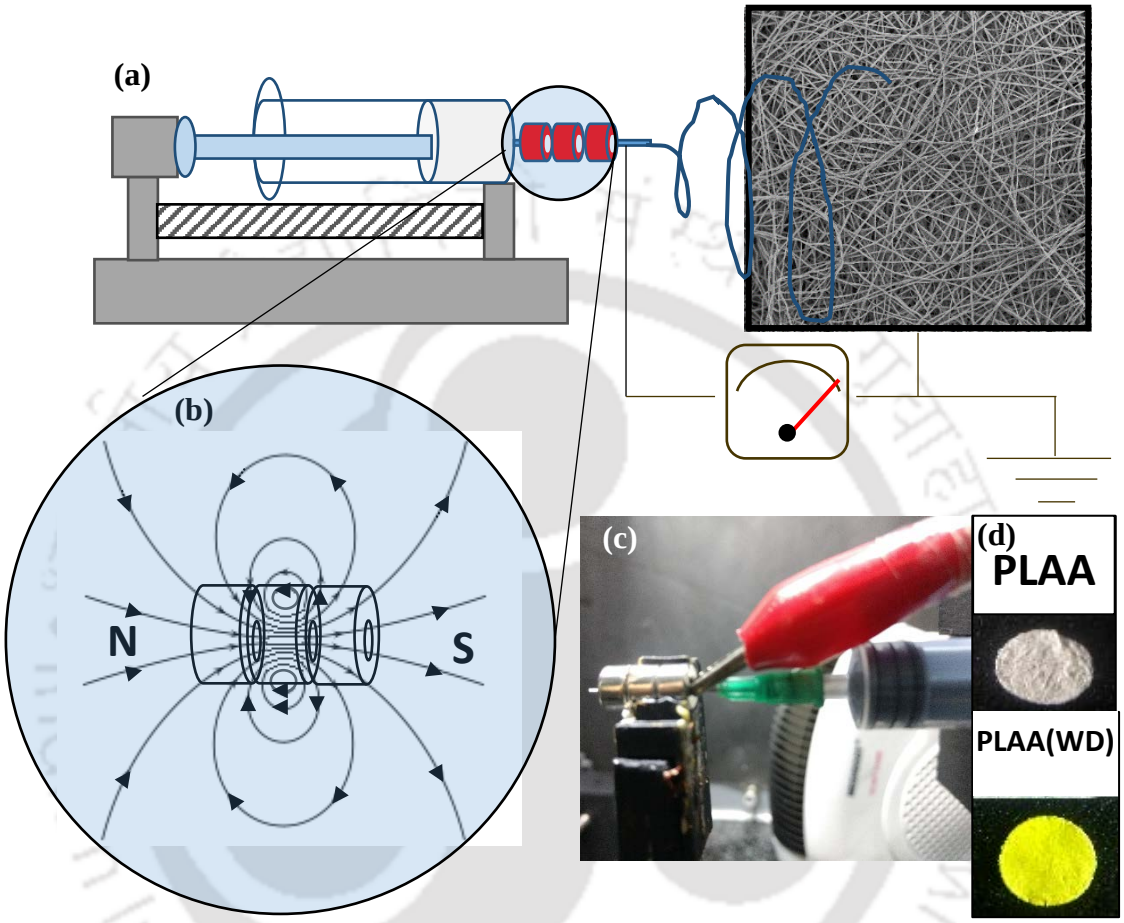

Figure 7.2: (a) Magnetic field assisted electrospinning setup, (b) magnetic field diagram of the magnetic assembly, (c) visual appearance of magnetic field-assisted electrospinning setup and (d) PLA based electrospun scaffolds under the influence of magnetic field with and without curcumin.

7.2 Results and discussion

7.2.1 Characterization of PLA/CSN and PLA/MGCSN electrospun nanofibrous scaffolds

7.2.1.1 Scanning electron microscopy (SEM)

The morphology electrospun scaffolds and the effect of external magnetic field during electrospinning was confirmed from FESEM micrographs (Figure 7.3). PLA nanofibers

were successfully fabricated without beads into porous nanofibers in the range of 1.3 ± 0.2 μm (Figure 7.3(a)).

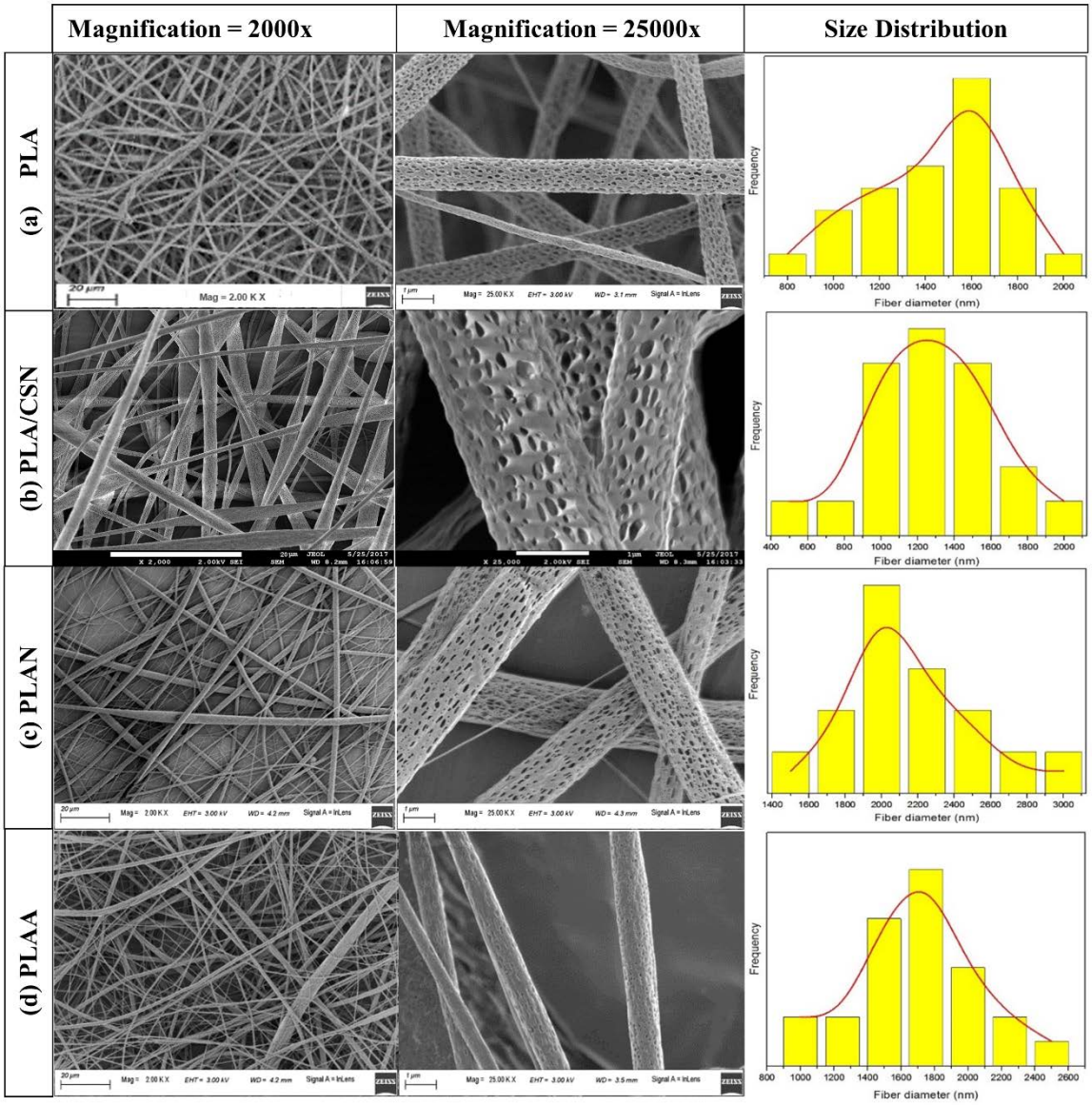

Figure 7.3: Scanning electron micrographs for (a) PLA, (b) PLA/CSN, (c) PLAN and (d) PLAA electrospun mats at 2000x, 25000x and their fiber size distribution.

The PLACSN nanofibers (Figure 7.3(b)) show increment in roughness of the fiber surface. This could possibly be due to increased porosity achieved by the incorporation of CSN into the PLA matrix. The average fiber diameter is 1.3 ± 0.3 μm, which is comparable to neat PLA nanofiber dimensions. Morphology of PLAN nanofibers was very similar to PLACSN but the average fiber diameter increased to 2.0 ± 0.3 μm (Figure 7.3(c)). The fiber diameter reduced to average 1.6 ± 0.4 μm when electrospinning of the same combination was done in the presence of external magnetic field (PLAA), the fiber

morphology changed drastically (Figure 7.3(d)). The fiber porosity reduced considerably giving it a smoother appearance. This could be attributed to the pulling effect of external magnetic field which aligns the MGCSNs to the nanofiber surface thus clogging the pores and also reducing the fiber diameter. The effect of magnetic field was applicable till solution left the needle, after that it is expected that shear-based viscous forces will become dominant on the MGCSNs as the polymer solution viscosity increases as the solvent evaporates. However, MGCSNs continued to be arranged at the surface of the nanofibers which means that the magnetic field based alignment of MGCSNs is dominant than the polymer matrix viscous forces.

7.2.1.2 Transmission electron microscopy (TEM)

Transmission electron microscopy was conducted on MGCSNs containing PLA nanofibers to confirm the alignment of MGCSNs during the magnetic field assisted electrospinning process. When electrospun without magnetic field, MGCSNs were homogeneously dispersed in the PLA matrix. As seen from Figure 7.4(a), the PLAN nanofibers is ~800 nm, which is smaller as compared to FESEM findings. When PLA/MGCSN solution was electrospun under the influence of magnetic field the MGCSNs were pulled onto the surface of the PLA nanofibers as shown in Figure 7.4(b-c). The nanofiber dimensions is approximately 400 nm, which is lower than what was measured using FESEM. It is noteworthy to mention that PLAA nanofibers have smaller diameter than PLAN. Similar observations were made using field emission scanning electron microscope (FESEM). The size of the nanoparticles present of the surface (Figure 7.4(c)) is in line with the average particle size of the MGCSNs. The nanoparticles can be seen at the outer periphery of the nanofibers which indicates that magnetic field creates a pulling effect which forces the MGCSNs to come onto the surface during the electrospinning process.

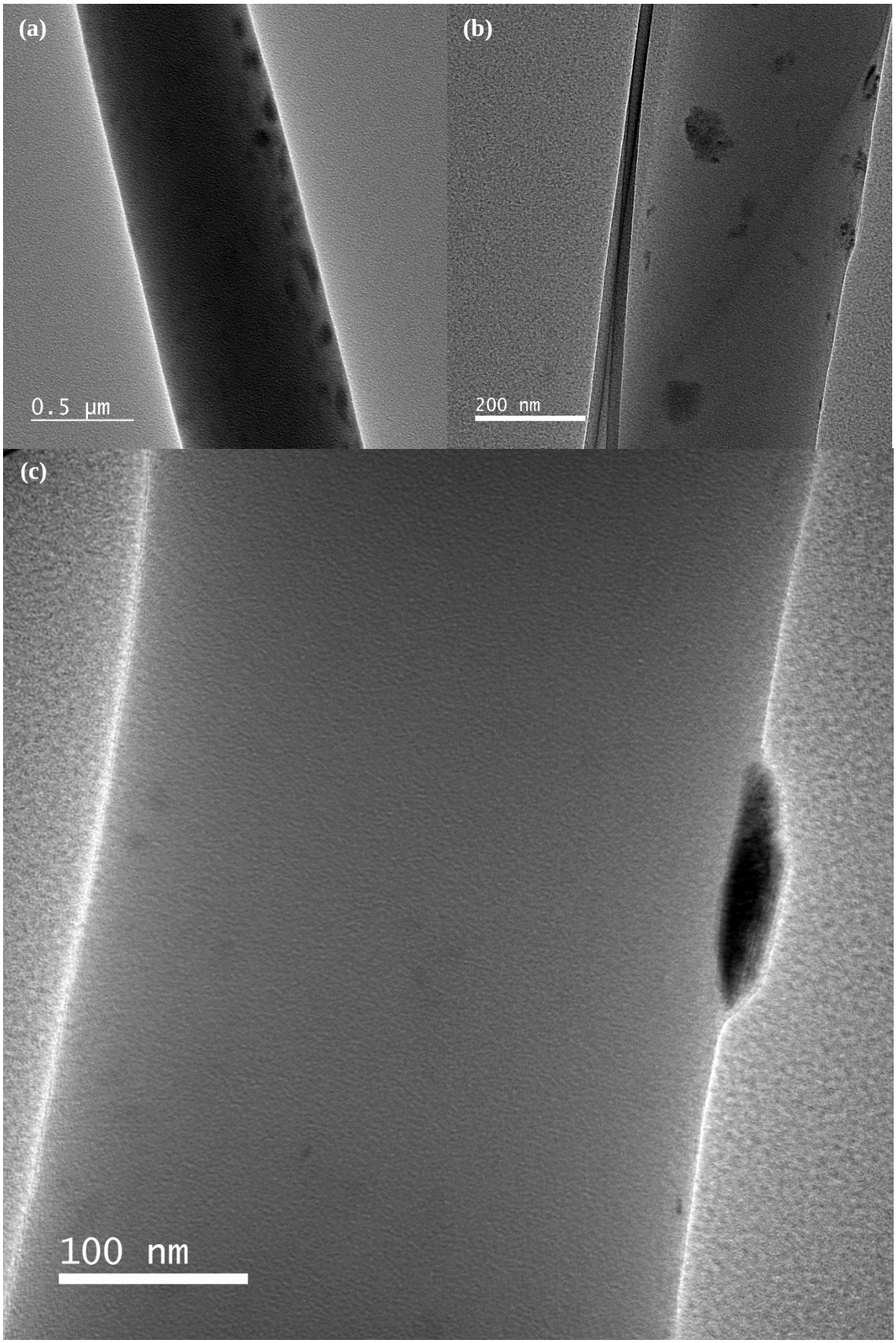

Figure 7.4: Transmission electron micrographs of (a) PLAN and (b-c) PLAA.

7.2.1.3 X-ray diffraction studies (XRD)

The effect of CSN/MGCSNs on the crystalline properties of PLA was studied using XRD analysis as shown in Figure 7.5. PLA is a semicrystalline polymer, which is evident from the amorphous hump along with the presence of small crystalline peaks at 16.7°, 19.1° and 22.3°, corresponding to α-PLLA crystallites with (110/200), (203) and (015) planes. A small peak at 15.1° (010) confirms β-form of PLA **(Gupta et al., 2017; Pal and Katiyar, 2016)**. Incorporation of CSNs into PLA led to slight increase in the intensity at 2θ =16.7°, along with the presence of amorphous hump. Characteristic peaks for crystalline silk can also be seen at 16.8° and 20.2° respectively. However, on incorporation of MGCSNs in PLA, MGCSNs which are homogeneously dispersed in the PLA matrix, act as nucleation sites for small PLA chains to assemble and form crystallites. This results in improved crystallinity PLAN as compared to neat PLA. Furthermore, there is no improvement in crystallinity when compared to PLACSN since both the fillers i.e. CSNs and MGCSNs are similar in dimensions. However, when PLA/MGCSNs were electrospun under the influence of external magnetic field, it results in movement of MGCSNs to the polymer surface which were now no longer dispersed in the matrix, resulting in reduced number of nucleation sites thus reducing the crystallinity. This can be noticed by the hump-like diffraction pattern of PLAA which is similar to PLA. A small peak at 16.8° (002), corresponding to the silk crystal structure can be observed.

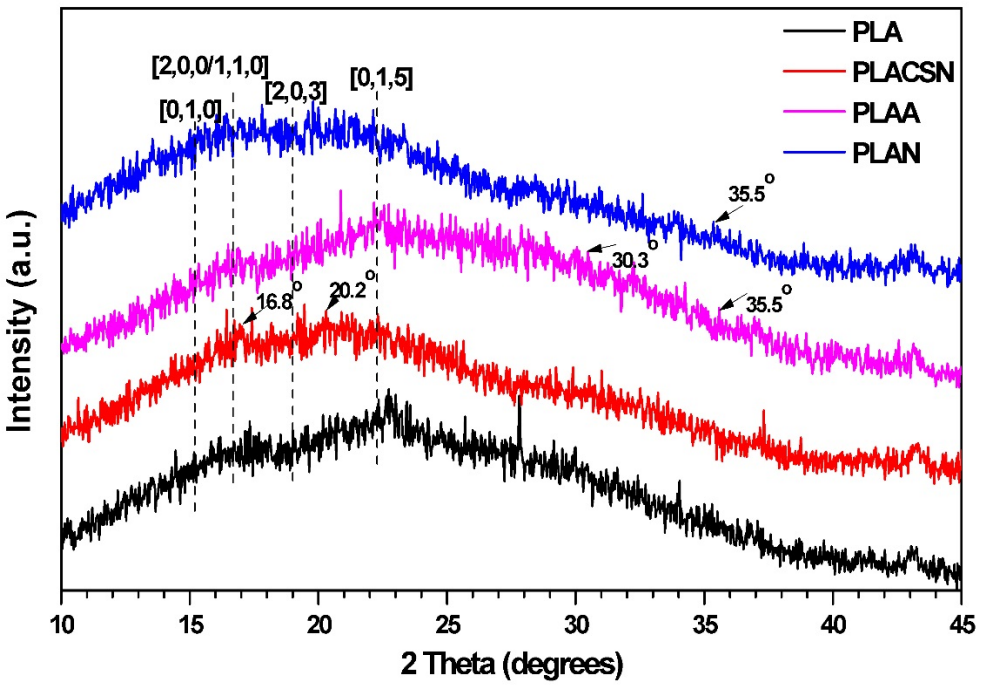

Figure 7.5: XRD diffraction pattern of PLA based electrospun scaffolds.

7.2.1.4 Molecular weight distribution by gel permeation chromatography (GPC)

The electrospun scaffolds were also checked for molecular weight by gel permeation chromatography. The number averaged molecular weight (M_n), weight averaged molecular weight (M_w) and polydispersity index (PDI) are summarized in Table 7.1.

Table 7.1: Molecular weight analysis of PLA based electrospun nanofibrous scaffolds.

Material	M_n (kDa)	M_w (kDa)	PDI
PLA (pellets)	96.1	206.9	2.15
PLA	80.4	166.2	2.06
PLACSN	111.3	201.1	1.8
PLAA	88.7	168.3	1.89
PLAN	88.9	167	1.87

As shown in Figure 7.6, the number-averaged molecular weight of PLA, PLACSN, PLAN and PLAA were 80.4, 111.3, 88.7 and 88.9 kDa, respectively. Incorporation of CSNs/MGCSNs into polymer matrix slightly improves the molecular weight which is possibly due to increase in chain length under the influence of fillers which is due to the strong attraction interaction between filler and PLA. The molecular weight of PLA/MGCSN is slightly higher when electrospun under the influence of external magnetic field.

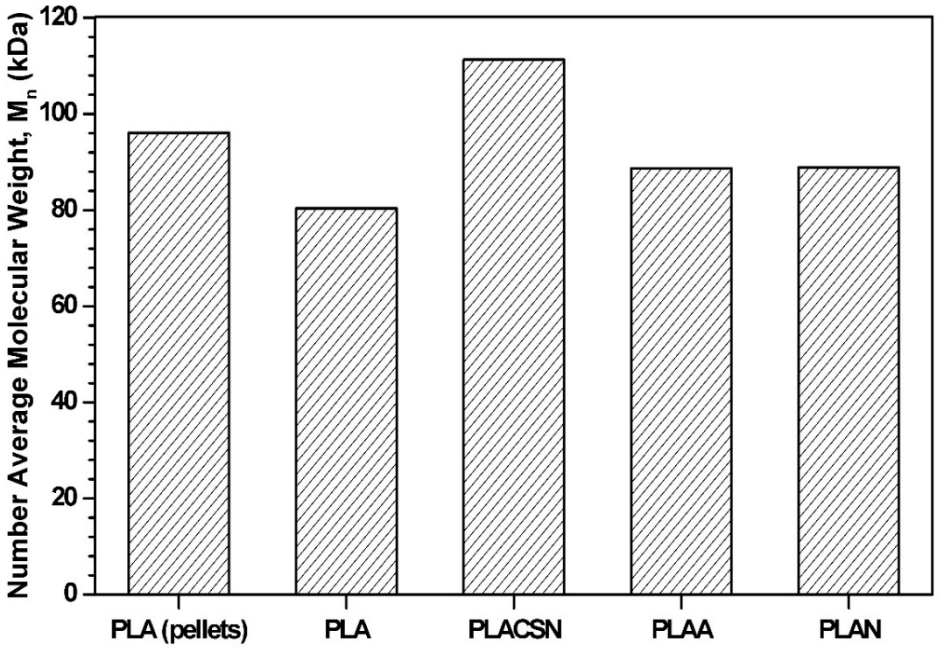

Figure 7.6: Molecular weight analysis of PLA based electrospun mats.

7.2.1.5 Mechanical properties of electrospun scaffolds

To determine the mechanical behavior of the fabricated electrospun mats were subjected to micro-tensile testing. The stress-strain curves of PLA based nanofibrous scaffolds are shown in Figure 7.7.

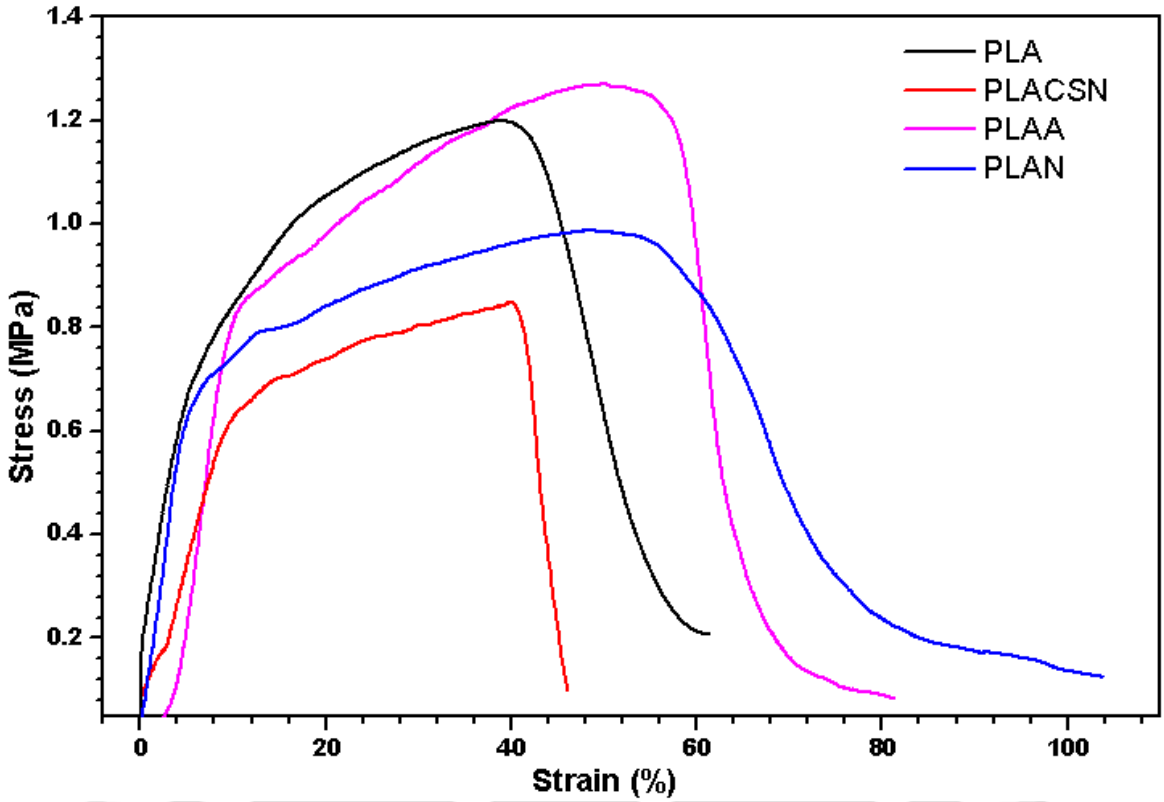

Figure 7.7: Stress-strain curves of PLA based electrospun scaffolds.

The nascent PLA mats show a Young's modulus of ~77 MPa, tensile strength of ~1.2 MPa, and stretches to ~66% elongation before failure, which is in line with the earlier reported studies **(Wang et al., 2009)**. Incorporation of CSNs (low loadings < 2 wt%) into PLA matrix improves overall mechanical properties, but at higher loadings of 5 wt%, mechanical properties were reduced obtained because of CSNs agglomeration. However, incorporation of MGCSNs, Young's modulus, strain at break (%) and percentage elongation (%E) were 122.6 MPa, 88.9% and 102.9% respectively, which was higher than PLA, as summarized in Table 7.2. Under the influence of magnetic field the electrospun mats of PLA/MGCSN showed improvement in toughness and tensile strength by 30% (1.3 MPa) and 16% (64.5 $J.m^{-3}$), respectively. Superior mechanical properties attributes to externally applied magnetic field which enhances crystallinity.

Table 7.2: Mechanical properties of PLA based electrospun scaffolds.

	Young's Modulus (YM) (MPa)	**Tensile Strength (TS) (MPa)**	**Strain at Break (%)**	**% Elongation**	**Toughness ($J.m^{-3}$)**
PLA	76.9 ± 2.2	1.2 ±0.5	65.7 ±15.9	65.5 ±15.9	63.4 ± 10.2
PLACSN	55.6 ± 12.1	0.8 ±0.1	50.4 ±5.2	53.9 ±6.9	33.7 ± 6.5
PLAN	122.6 ± 13.6	1.0 ±0.0	88.9 ±14.6	102.9 ±25.1	55.3 ± 8.7
PLAA	120.9 ± 24.1	1.3 ±0.0	75.3 ±5.1	78.6 ±3.3	64.5 ± 6.9

7.2.1.6 Thermal properties of PLA based electrospun scaffolds

Thermal properties are determined using DSC and TGA to know the effect of addition of CSN/MGCSN into PLA matrix (shown in Figure 7.8(a-b)). The first heating scans were obtained for all the nanofibrous scaffolds and it was observed that addition of fillers improved the crystallinity in all the bionanocomposites, which is observed in XRD analysis as well. The $\%X_c$ (Figure 7.8(a)) for PLA, PLACSN, PLAA and PLAN are evaluated to be 5.89, 8.5, 8.5 and 9.7%, respectively. As it was observed in diffraction studies, the PLAN were more crystalline as compared to PLAA. As compared to CSNs, MGCSNs have poor nucleating effect which can be attributed to the tendency of MGCSNs to agglomerate which results in higher crystallization temperatures (T_c) of PLAN and PLAA as compared to PLACSN. As it has been discussed in previous chapter, that CSN contributes to thermal stability of PLA. As observed from Figure 7.8(b), it is found that PLACSN (T_{max}= 373.64 °C) has a higher degradation temperature than PLA (T_{max}= 362.05 °C). Addition of MGCSNs result in reduced stability due to increased agglomeration. It is found that PLAA degrade faster (T_{max}= 325.29 °C) as compared to PLAN (T_{max}= 333.83 °C) because of the amorphous nature of PLAA. These results match with the DSC and XRD data.

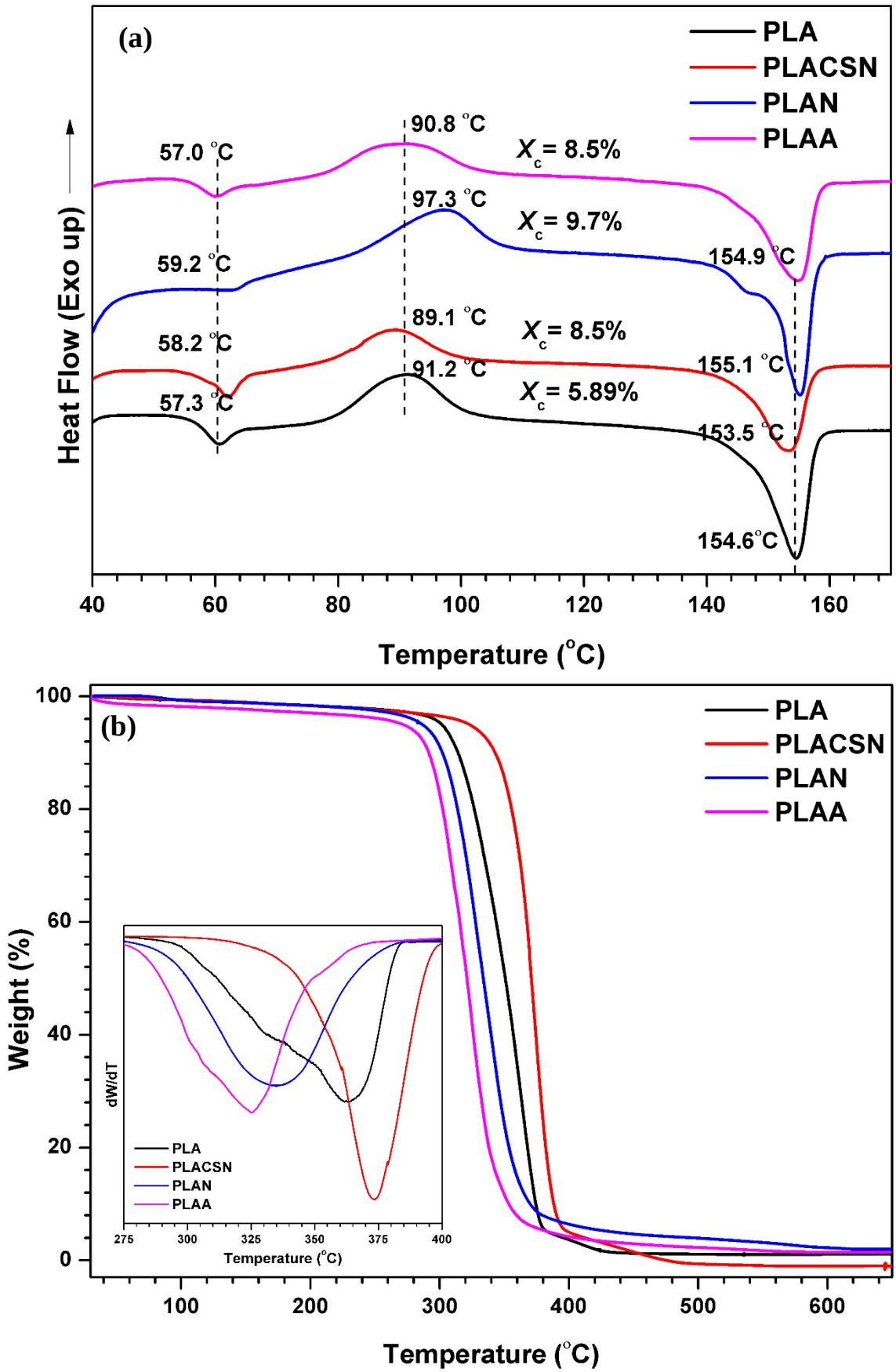

Figure 7.8: (a) DSC first heating scans and (b) TGA thermograms at a heating rate of 10 °Cmin^{-1} (inset: DTG thermograms) for PLA based nanofibrous scaffolds.

7.2.1.7 Contact angle analysis

To determine surface hydrophobicity, contact angle analysis was performed (Figure 7.9). The contact angle for neat PLA scaffolds was found to be 139.6°, which was in line with the values reported previously **(Tuancharoensri et al., 2017)**. After CSNs was added into the PLA matrix, the contact angle increased slightly to 140.2°, which can be attributed to the high porosity of PLACSN scaffolds and hydrophobic nature of CSNs. Upon incorporation of MGCSNs, contact angle increased even more (144.6°) when no magnetic field was applied which produced rough fibres with high porosity as can be seen from scanning electron micrographs shown in Figure 7.3. When external magnetic field was applied, smoother nanofibers (PLAA) were produced hence the contact angle was lesser (140.6°) as compared to PLAN scaffolds.

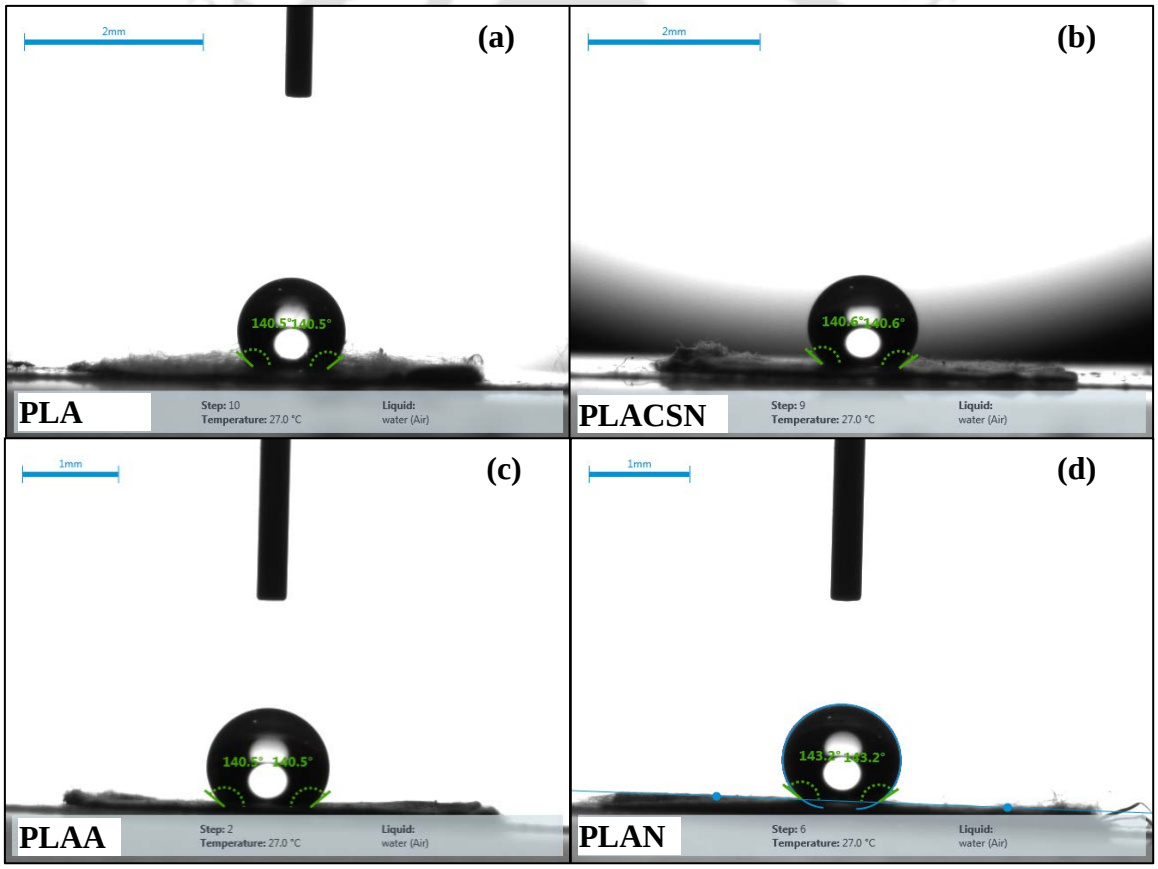

Figure 7.9: Contact angles images for PLA based scaffolds (a) PLA, (b) PLA/CSN, (c) PLAA and (d) PLAN.

7.2.1.8 Swelling characteristics

Swelling characteristics of the electrospun mats were determined (Figure 7.10) to know their ability to absorb exudates during wound healing. It was found that after a time period of 24 h, PLA/CSN showed highest swelling of ~524% in 24 h, due to increased porosity

compared to PLA (~431%). This value matched with the values reported earlier **(Suwantong et al., 2012)**. PLAN scaffolds have lower porosity and hence, showed lowered swelling percentage (~421%), comparable to PLA mats. For PLAA, swelling percentage reduced to ~58 % as its pores are clogged by MGCSN on nanofiber surface due to externally applied magnetic field.

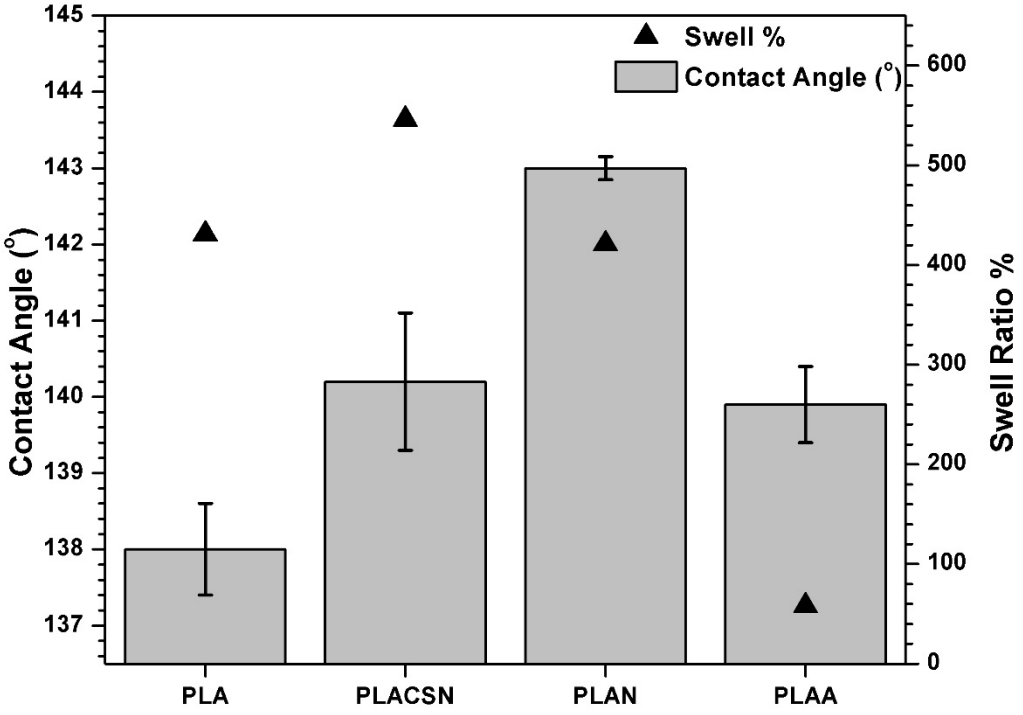

Figure 7.10: Contact angle and swelling percentage for PLA based nanofibrous scaffolds.

7.2.1.9 Moisture permeability

The moisture permeation is an important characteristic for wound dressing. Human skin has a WVTR of 204 g/m^2.day whereas water permeation of an injured skin area with a first degree burn can be around 279 g/m^2.day. For a healing (granulating) wound, water vapor permeation can be as high as 5,138 g/m^2.day. Ideally, it is observed that noted that a WVTR of 2,500 g/m^2.day should be maintained from an injury site to promote fast healing **(Queen et al., 1987)**. Such a mid-range dressing would maintain optimum evaporative water loss and also prevent the buildup of cell exudates around injury. When a wound lacks moisture it dries and forms a hard layer thus preventing the keratinocytes from necessary viable tissue. This results in more energy consumption and increases the time for wound healing. The WVTR values of PLA, PLACSN, PLAA and PLAN were found to be 1792.8, 1777.7, 1756.6 and 1813.3 g/m^2.day, respectively as shown in Figure 7.11. All the bionanocomposites have comparable permeation values and could possibly be used for as

wound dressing material in combination with some other suitable wound dressing material due to its added properties.

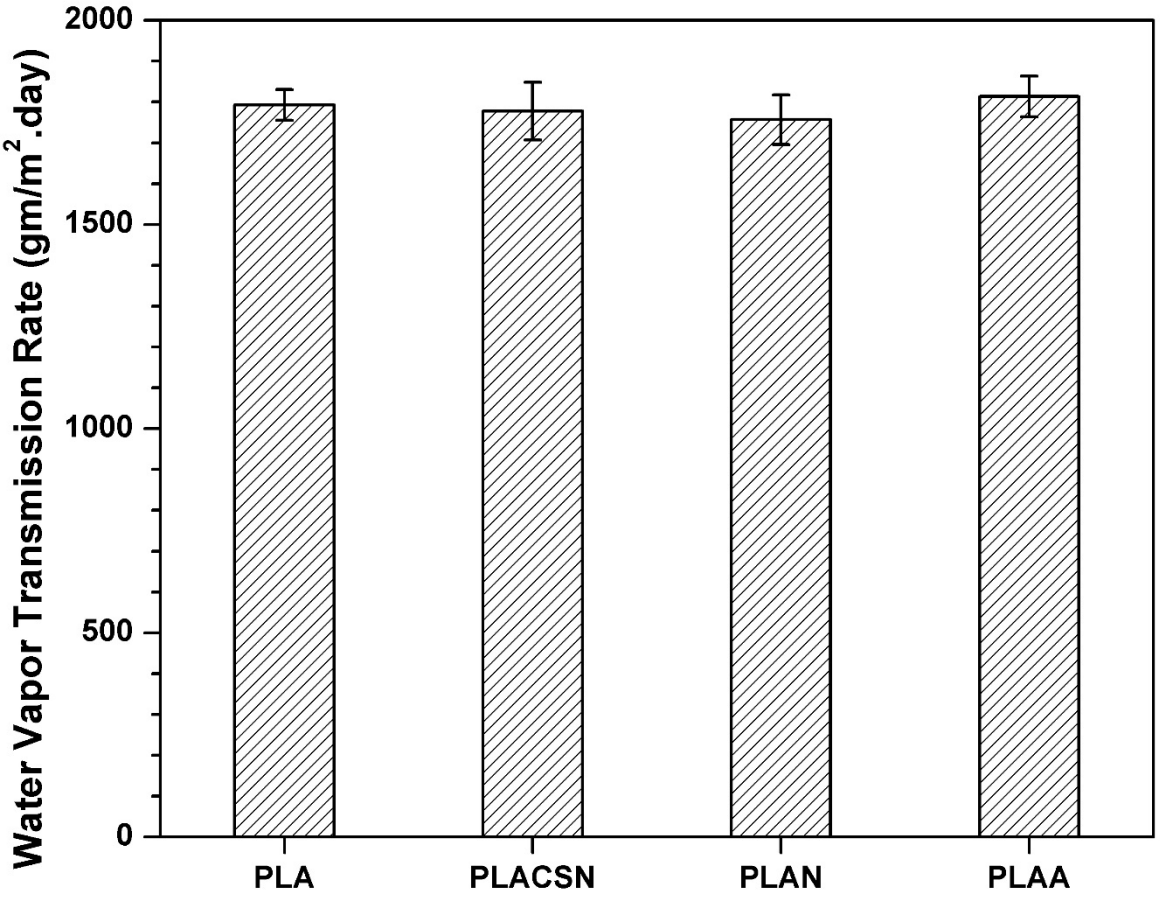

Figure 7.11: Water vapor transmission rate for PLA based nanofibrous scaffolds.

7.2.1.10 Drug release studies

Sustained drug release plays a vital role by preventing the cancer cells to developing drug resistance during cancer therapy. The *in vitro* release profiles of curcumin from electrospun mats in pH 7.4 PBS/Tween80 media at 37 °C are shown in Figure 7.12. The burst release mainly occurred for the first 12 h and could reach 10.96%, 15.84%, 18.62% and 23.62% for PLA, PLACSN, PLAA and PLAN respectively. The initial burst release owed to the loosely bound curcumin adsorbed on the nanofiber surface, this curcumin starts diffusing immediately through the pores present on nanofibers as soon as the water uptake is initiated in the scaffolds. At later stages, sustained release of curcumin is observed which can be ascribed to the release of curcumin entrapped inside the nanofibers through diffusion path filled by PBS. The hydrophobic nature of electrospun fibers is responsible for the retarded release and short burst effect. The MGCSN containing

electrospun mats showed improved release as compared to nascent PLA and PLACSN scaffolds making it as suitable candidate to be used as a novel carrier for curcumin.

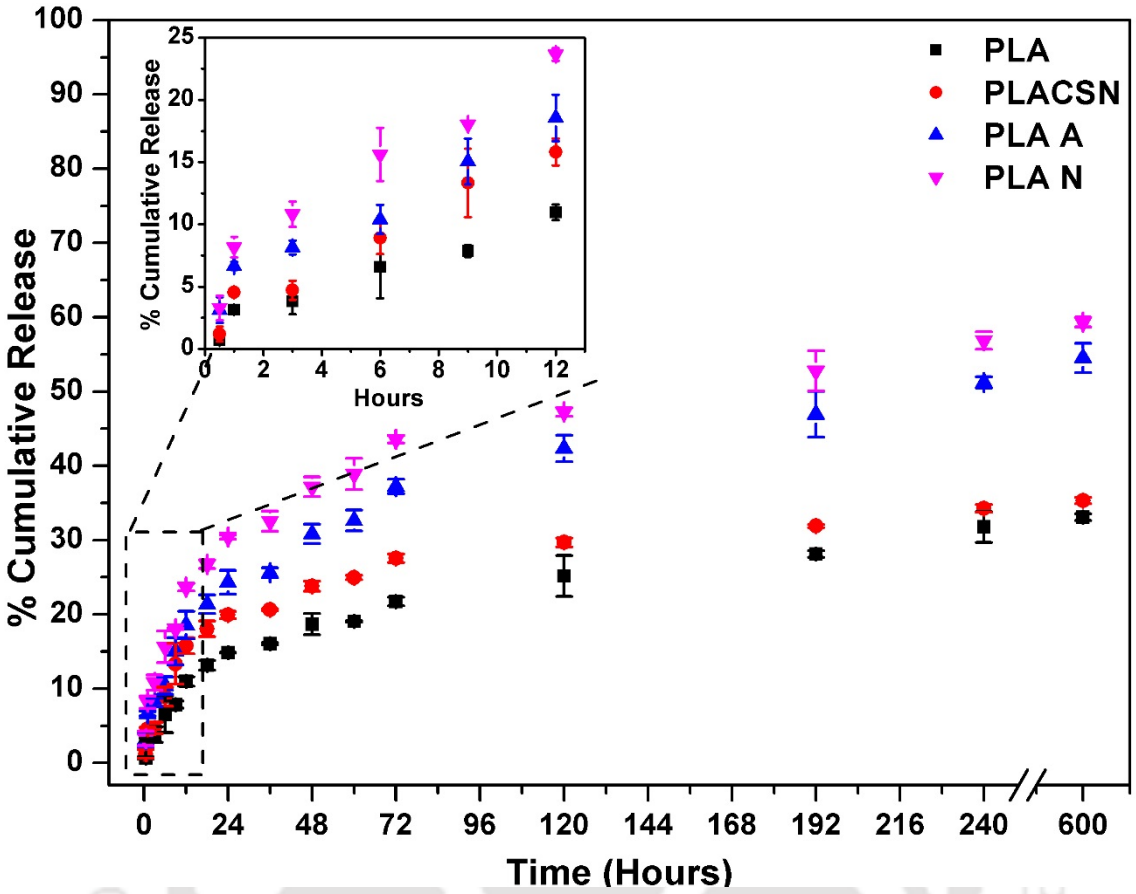

Figure 7.12: Drug release profiles of PLA based nanofibrous scaffolds (inset: burst release from 0–12 h).

7.2.1.11 Cytotcompatibility to (BHK-21) fibroblasts

The growth of cells in control (Figure 7.13) confirmed cell viability. For PLACSN scaffolds, cell growth was better than PLA owing to its higher porosity and biocompatibility. PLAA (~4%) and PLAN (~8%) scaffolds exhibited higher proliferation rate than PLA mats after 72 h period indicating that paramagnetic nanoparticles attributed to the growth of fibroblasts **(Wu et al., 2010)**. Under static magnetic field, the fibroblast proliferation rate on PLAA (~23%) and PLAN (~42%) increased markedly suggesting that applied static magnetic field augments cells' proliferation **(Meng et al., 2010)**. This gives the ability to control cell growth by tuning nanofiber characteristics, viz. type of nanoparticle, applying external magnetic field during electrospinning or applying static magnetic field during growth.

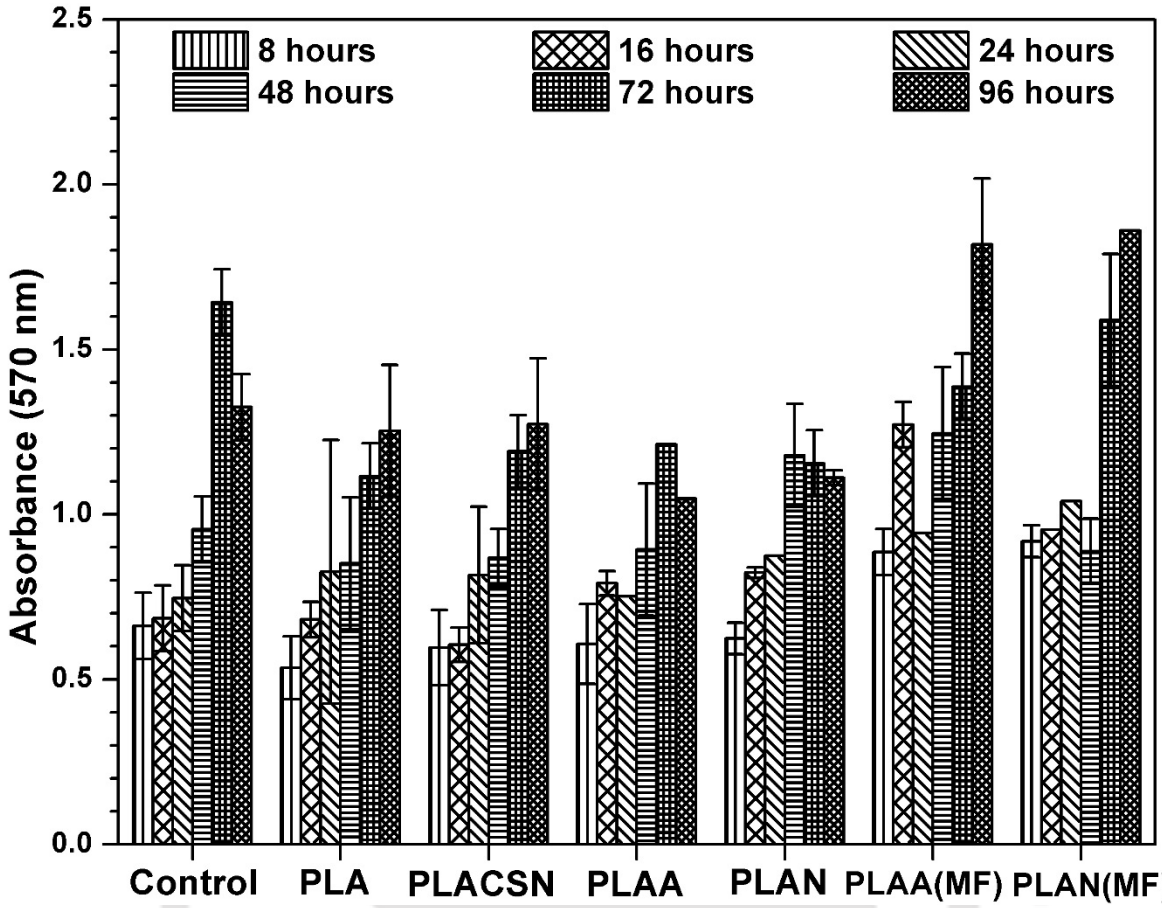

Figure 7.13: MTT assay for cell growth from 8–96 h period using BHK-21 fibroblast for group I–VI.

7.2.1.12 Cell proliferation investigations for BHK-21 fibroblasts using fluorescence microscopy

Fibroblasts nuclei can be seen as typical globular round structures which attach to the nanofibers (Figure 7.14). PLA has a non-uniform cell growth which is undesirable for fast wound healing as shown in Figure 7.14(a), whereas PLACSN provides a better environment for cells to adhere as they demonstrate uniform growth over the entire scaffold surface as can be seen in Figure 7.14(b). As discussed above, MGCSNs results in slightly stunted growth for both PLAA and PLAN conformations shown in Figure 7.14(c and d) where cells seem to grow in a concentrated area (shown in white circles). It can be seen that PLAN nanofibers are more cytocompatible due to its porous structure. Upon application of external magnetic field the cell growth is augmented as shown in Figure 7.14(e and f). However, PLAN nanofibers display dense globules of cells due to its porous structure which promotes uniform cell growth.

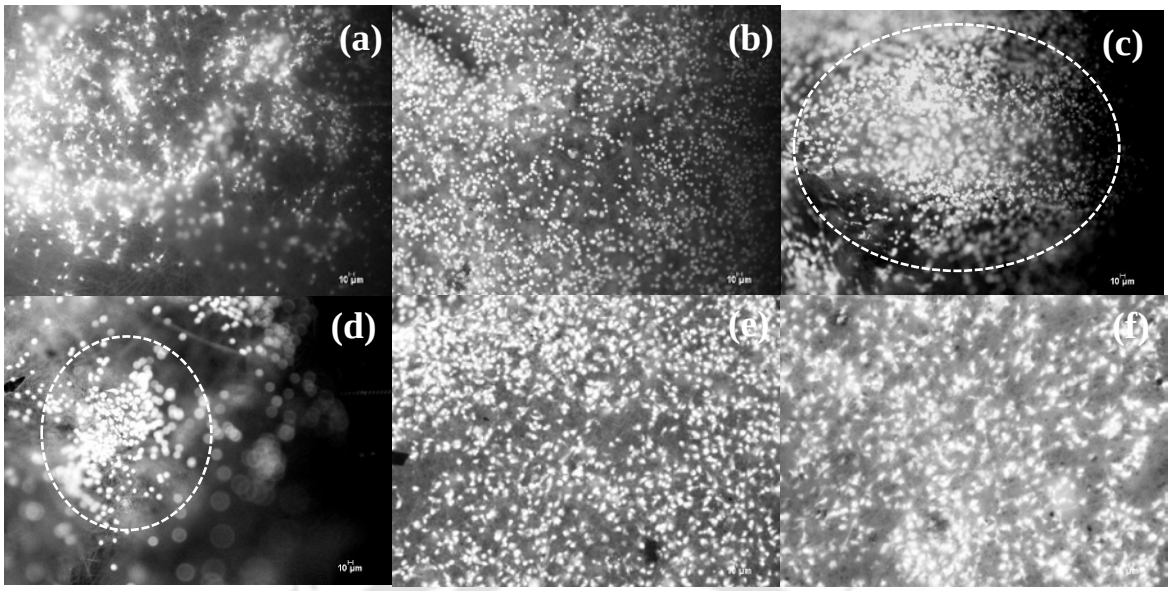

Figure 7.14: BHK-21 fibroblast cell proliferation fluorescence microscopy images (blue channel) for 96 h growth period (a) PLA, (b) PLA/CSN, (c,d) concentrated growth shown in white circles (c) PLAA, (d) PLAN, (e) PLAA (under static magnetic field) and (f) PLAN (under static magnetic field).

7.2.1.13 Cytotoxicity against cancerous (HeLa) cells

All drug-loaded scaffolds possess anti-cancer efficiency whereas PLA scaffolds without drug showed maximum cell proliferation depicting its poor anti-cancer properties (Figure 7.15(a)). Cell proliferation for PLACSN scaffolds reduced by ~14% upon 96 h incubation due to increased crystallinity. Similar phenomenon could be seen upon addition of anti-cancer drug, where PLACSN showed even lesser cell proliferation (~41% reduction) owing to higher porosity which enable it to elute higher drug dosage at a sustained rate. Out of all magnetic samples without drug (Figure 7.15(b)), group III, i.e. PLAA, showed the slowest cell growth (~11% less compared to PLAN), which could be due to nanofibers' reduced porosity of nanofibers. Interestingly, by modification of electrospinning process (applying magnetic field in this case), growth of cancerous cells can be mitigated. Scaffolds under magnetic field, i.e. group V and VI, exhibited higher proliferation rate compared to other samples suggesting that static magnetic field plays a stimulating role on cells' proliferation **(Meng et al., 2010)**. It is established that curcumin acts as a successful chemotherapeutic drug, but there is a scope for further reduction. In this regard, we tried an approach to combine the chemotherapeutic effect of curcumin with hyperthermia to be able to address concomitant chemo-radiation cancer therapy.

We found that post hyperthermia treatment, the cancer cells, succumb to high temperatures, which resulted in reduced cell counts, irrespective of presence of drug or not.

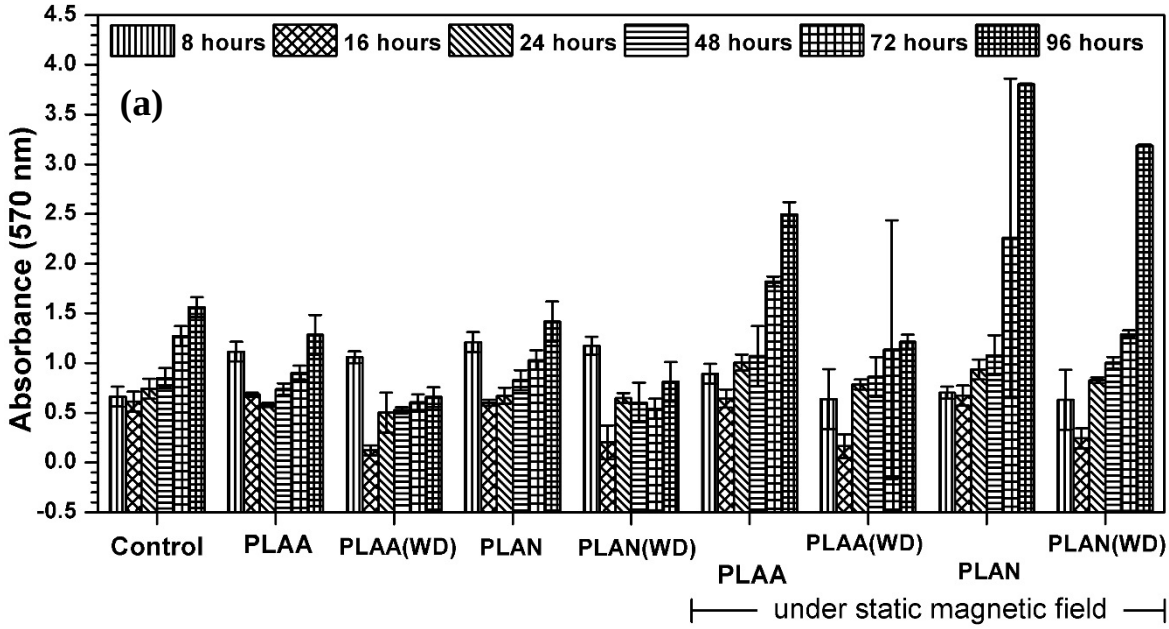

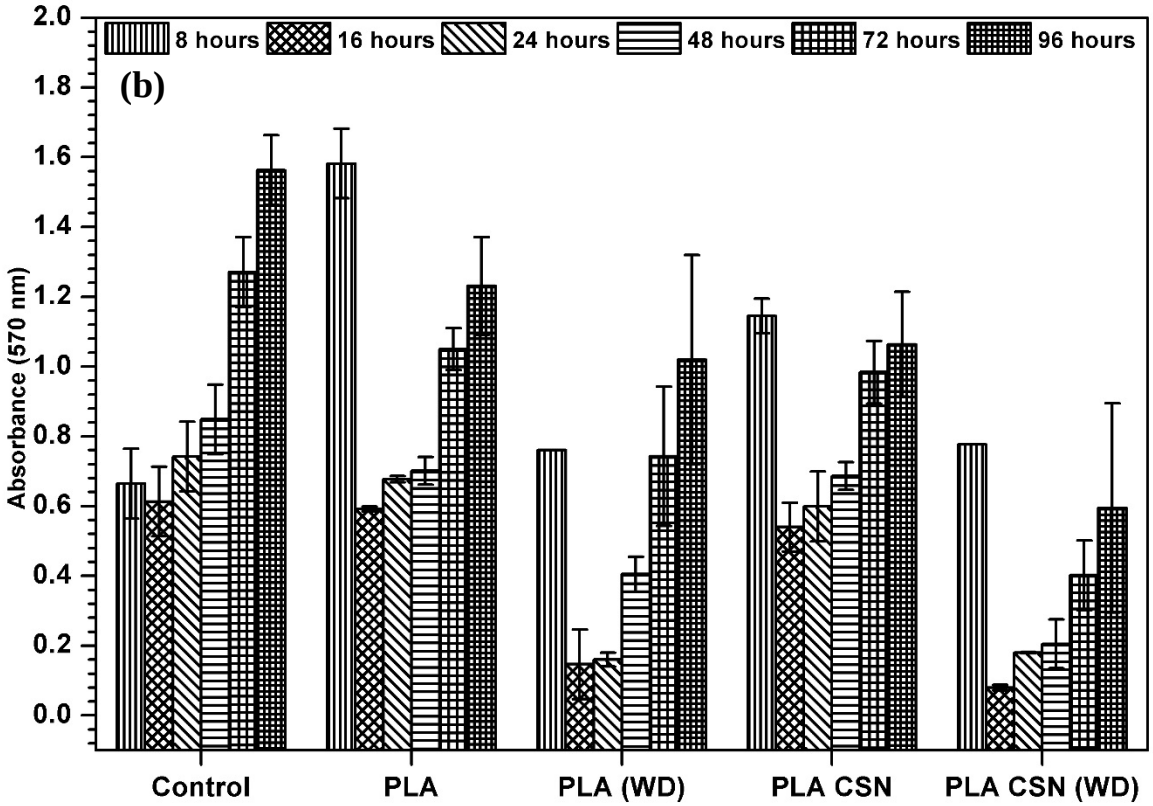

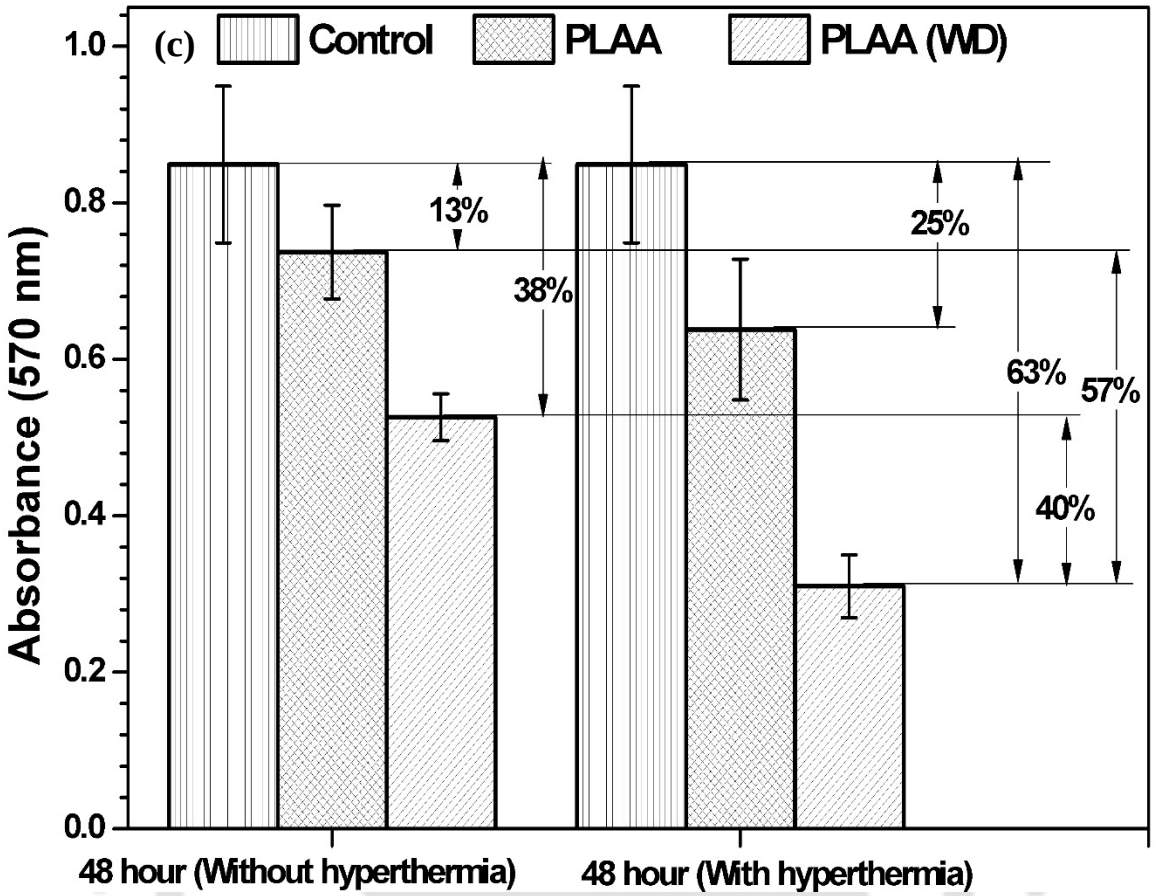

Figure 7.15: MTT assay for cell growth from 8–96 h period for HeLa cells for (a) PLA and PLA/CSN (group I–II), (b) for PLAA and PLAN((group III-VI)) and (c) post hyperthermia treatment and 24 h incubation for PLAA (group III), (WD: with drug).

By this approach magnetic nanofibers, despite their weak chemotherapeutic influence, can display remarkable improvement in cancer mitigation ability post hyperthermia treatment. In a typical example, post hyperthermia treatment (Figure 7.15(c)), PLAA nanofiber without drug showed ~25% reduction whereas drug-loaded PLAA showed ~63% reduction as opposed to ~40% decrease in cell viability when no hyperthermia treatment was done on drug-loaded PLAA. **Sasikala et al. (2016)** found a ~30% reduction in cell viability upon synergistic treatment procedure.

7.2.1.14 Cell proliferation studies for HeLa cells using fluorescence microscopy

Morphology of Hela cells on electrospun mats of group I-II (Figure 7.16(a)), III-IV (Figure 7.16(b)) and V-VI (Figure 7.16(c)) is observed for 8 and 96 h incubation period to investigate effect of fillers along with drug. Efficacy of curcumin against cancerous cells was proven by the reduction of cell counts. PLA nanofibers displayed growth of cancerous

cells as dense clusters, whereas growth lowered upon addition of CSN which was in line with MTT assay results. Upon loading of drug to PLACSN mats, the growth started depleting and by 96 h no identifiable clusters of HeLa cells were noticed.

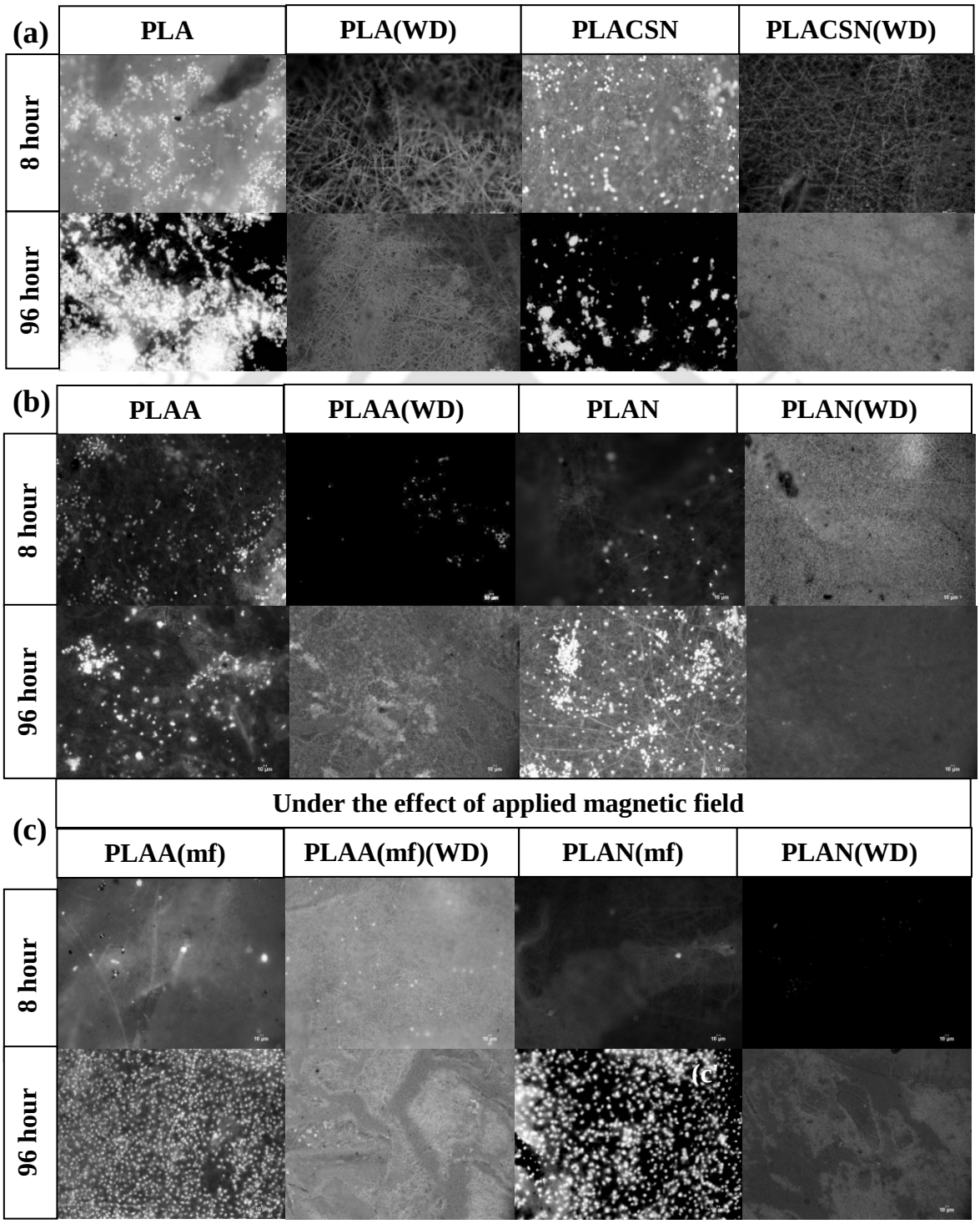

Figure 7.16: HeLa cancerous cell proliferation fluorescence microscopy images (blue channel) for 8 and 96 h growth period with or without curcumin (a) PLA and PLA/CSN, (b) PLAA and PLAN and (c) PLAA(mf) and PLAN(mf), (WD: with drug).

7.3 Summary

The electrospun bionanocomposite scaffold of poly(lactic-acid) (PLA)-CSNs/MGCSNs exhibit enhanced fibroblast proliferation due to improved nanofiber porosity with sustained drug release making it cytotoxic against cancerous cells. The aligning of magnetic nano-discs onto the nanofiber surface using magnetic field-assisted electrospinning technique can suppress the cell proliferation due to reduced porosity. Moreover, the CSN-adsorbed iron oxide nanoparticles showed unique behavior of superior cytocompatibility under magnetic field and are capable of damaging cancer cells due to hyperthermia effects. To conclude, novel cytocompatible paramagnetic CSNs synthesized from renewable resources exhibit sustained anticancer drug release with hyperthermia, which can potentially be utilized for concomitant chemo-radiation cancer therapy, tissue engineering and wound healing.

Chapter 8

Conclusions and Future Directions

This chapter elucidates the key findings and inferences drawn from the doctoral work and provides an outlook for future studies on crystalline silk nano-discs (CSNs).

8.1 Conclusions

The major conclusions drawn on the basis of overall study and major findings of this research work can be broadly classified into five subsections:

The first part focused on the extraction of silk nano-discs from Muga silk fibroin and its functionalization.

- The renewable waste such as Muga silk cocoons can be effectively converted into crystalline silk nano-discs (CSNs) and its derivatives, through strategic pretreatment and acid hydrolysis routes. CSNs fabricated from Muga silk shows distinct disc-like morphology confirmed by TEM, SEM and AFM. The average size ranging from 48.15±12.7 nm and thickness 3.1±0.9 nm. CSNs are found to have β-sheet conformation which was checked by FTIR and ss-NMR.
- Aminoacid analysis confirmed the presence of alanine (~80%), glycine (~6%) and serine (~6%) making them hydrophobic in nature. X-ray diffractograms and SAED patterns show that CSNs are highly crystalline (~94%). Thermal analysis reveal that CSNs are highly stable till 310 °C.
- Magnetic CSNs (MGSCNs) are fabricated by modification of CSN surface, where monodisperse spherical iron-oxide nanoparticles (~5 nm) were adhered onto CSNs through one-step borohydride reduction reaction. TEM images show that MGCSNs have diameter of 58.2 ± 4.6 nm and thickness of 16.0 ± 2.6 nm. MGCSN are found to have dye adsorption ability.

The second part focuses on using CSNs as reinforcement material in the poly(lactic acid) (PLA) matrix to investigate the influence of ‘CSNs’ on the structural, morphological, thermal, optical, mechanical and barrier properties of PLA bionanocomposites in order to investigate the feasibility towards food packaging applications

- ❖ XRD confirms increase in crystallinity from 30 to 45% and CSN intercalation in the PLA matrix. FTIR studies showed amide peak shift confirming the attractive interaction between CSNs and PLA.
- ❖ CSNs due to their hydrophobic nature, are well dispersed in the PLA system covering the entire matrix, corroborated through morphological analysis such as AFM and FESEM.
- ❖ This improved dispersion of filler has a positive influence on the thermal properties. DSC analysis shows that biofiller provides additional nucleation sites for the spherulitic growth of PLA crystals while thermal stability of PLA/CSN was improved ~10 °C, confirming the role of CSNs in enhancing the melt stability of PLA.
- ❖ For 1 wt% filler loading the film observed the high toughness, percentage elongation and improved storage modulus by ~70%, ~ 40% and ~12% respectively as a result of effective reinforcement of PLA by CSN biofiller. By the uniform dispersion of CSN which results in enhanced crystal nucleation density, the gas barrier properties viz. oxygen gas and water vapor permeability values were reduced to ~70% and ~28%, respectively.
- ❖ To conclude, significant property enhancements are observed upon addition of small amounts of CSN in the PLA matrix, in addition to this both CSN and PLA are derived from renewable natural resources that are abundant, non-toxic and in true sense, fit well in the class of 'green' bioplastics to replace fossil-based plastic packaging.

The third part focuses on influence of CSNs content on crystallization behavior of PLA which is studied by non-isothermal cold crystallization and isothermal melt crystallization.

- ❖ Addition of CSN significantly enhance the crystallizability of polymer matrix, which in return promotes formation of crystals. CSN plays a dual role in crystallization process, firstly, it acts as a heterogeneous nucleating agent facilitating crystallization, and secondly, it obstructs the polymer chain movement. Either of the two roles, which process is dominating is decided by the filler loading.
- ❖ Non-isothermal crystallization showed that, cold-crystallization peak temperature (T_{cc}) and crystallization half-time ($t_{0.5}$) were lower for bionanocomposite films at small loadings (~1 wt%) as compared to PLA at all heating rates. This suggests that

CSN can augment the overall crystallization rates. CSN were also found to act as heterogeneous nucleation sites in PLA matrix.

- To analyze non-isothermal crystallization kinetics of samples, three kinetic models viz. modified Avrami, Mo and Tobin models were applied. The smaller exponent (n and n_T) values suggested that CSN inclusions lead to PLA spherulite formation towards unsophisticated geometries thereby, improving crystallization rates. Increased (Z_c and K_T) and smaller $F(T)$ values, for PLA/CSN bionanocomposites compared to PLA advocate towards faster crystallization processes.
- The crystallization activation energy based on Kissinger and Takhor methods showed smaller values for PLACSN1 bionanocomposites, indicating easier motion of PLA molecular chains in PLA/CSN system as a result of which crystallization occurs at a faster rate. Furthermore, the calculated nucleation activity of bionanocomposites show agreement between lower $t_{0.5}$, F(T) and crystallization activation energy in the bionanocomposite. The crystallization rate of PLA/CSN bionanocomposites were increased because of the high surface area of CSN.
- The isothermal melt crystallization behavior of PLA and PLA/CSN bionanocomposites was studied in the range of T_c between 90 to 120 °C. The sigmoidal relative crystallinity isotherms shifted towards lesser crystallization time, indicating fast crystallization behavior of PLA/CSN nanobiocomposites. The crystallization kinetics of PLA and PLA/CSN bionanocomposites was studied and it was found that the addition of CSN into PLA induced heterogeneous nucleation, thus increasing the crystallization rate and decreases the ΔE and surface energy barrier for PLA crystallization.

The fourth part focuses on influence of CSNs content on thermal and hydrolytic degradation behavior of PLA.

- TGA studies showed improvement in thermal stability at small loadings (~1 wt%) along with higher decomposition activation energy, E_a than that of PLA. The network structures act as labyrinth for degraded polar molecules to escape hence slows down interaction with PLA chains, thus imparting more stability.
- Thermal degradation kinetics was analyzed using two isoconversional, Flynn-Wall-Ozawa and Kissinger-Akahira-Sunose models and one model fitting method i.e. Coats-Redfern model. The models predicted higher decomposition activation energy requirement for degradation to occur unlike in PLA.

- ❖ The PLA and PLA/CSN bionanocomposites follow the F1 type degradation mechanism which is found using Criado's method.
- ❖ The major evolved volatile products detected during TG-IR, are CO_2, CO, aldehydes, lactide and cyclic oligomers for PLA and PLA/CSNs.
- ❖ These results suggest that incorporation of CSNs into PLA matrix enhanced thermal stability of bionanocomposite which could extend the range of applications like automobile industry and high engineering applications.
- ❖ The *in vitro* hydrolytic degradation rate is slower for PLA/CSN bionanocomposites due to hydrophobic character of CSNs. The study elucidates that basic pH and higher temperature, both favor hydrolytic degradation process for PLA and PLACSN5 bionanocomposite samples. We describe, here the possibility of use of PLA/CSN bionanocomposites in moist environments. The results described here can find applications to control the degradation rate of PLA.

The last part focuses on utilization of CSNs and MGCSNs for the fabrication of PLA based electrospun bionanocomposite scaffolds for wound healing and concomitant cancer therapy

- ❖ PLA/CSN and PLA/MGCSN scaffolds show enhanced fibroblast proliferation due to improved nanofiber porosity with sustained drug release making it cytotoxic against cancerous cells.
- ❖ The aligning of MGCSNs onto the nanofiber surface using magnetic field-assisted electrospinning technique can suppress the cell proliferation due to reduced porosity.
- ❖ Moreover, the MGCSNs showed unique behavior of superior cytocompatibility under magnetic field and are capable of damaging cancer cells due to hyperthermia effects.
- ❖ To conclude, novel cytocompatible paramagnetic CSNs synthesized from renewable resources exhibit sustained anticancer drug release with hyperthermia, which can potentially be used for concomitant chemo-radiation cancer therapy, tissue engineering and wound healing.

8.2 Scope for future work

Based on the outcome of this work, few recommendations for future research work are presented as follows

- PLA/CSN bionanocomposite films can be fabricated by using melt extrusion technique at pilot scale, to evaluate their commercial use.
- The effect of compatibilizers and plasticizers can be explored in order to further improve the mechanical properties of PLA/CSN bionanocomposites such that it can be processed into blown film for packaging application.
- Molecular dynamic simulation study to understand the interaction of CSNs with polymer chains and validation of thermal, barrier and mechanical properties of PLA/CSN bionanocomposites using appropriate force field.
- Detailed toxicological studies, nanoparticle migration from the matrix into food material, shelf-life prediction of stored food products, anti-bacterial properties and composting of PLA/CSN bionanocomposite films can be undertaken.
- Other biopolymers such as PCL, PBS, etc. can be explored in order to produce CSN based bionanocomposites as alternate value added packaging.
- In order to further improve the properties of PLA/CSN bionanocomposites, the dispersion of CSNs in the PLA matrix need to be improved. This can be done by *in-situ* polymerization of lactic acid on CSNs followed by melt compounding can be done.
- Fabricated superparamagnetic nano-crystalline discs having non-toxic characteristics, can have huge applications in biomedical sciences as novel bioferrofluids for drug delivery vehicles and as MRI agents.
- Moreover, CSNs can be functionalized with metallic Pt and Pd nanoparticles and their application as catalyst in fuel cells can be explored.

References

Aboulkas, A. and El Harfi, K. Study of the kinetics and mechanisms of thermal decomposition of moroccan tarfaya oil shale and its kerogen, *Oil Shale*. **25**, 4, 426-443 (2008).

Aboyade, A.O., Carrier, M., Meyer, E.L., Knoetze, J.H. and Görgens, J.F. Model fitting kinetic analysis and characterization of the devolatilization of coal blends with corn and sugarcane residues, *Thermochimica Acta*. **530**, 95-106 (2012).

Acharya, C., Ghosh, S.K. and Kundu, S.C. Silk fibroin film from non-mulberry tropical tasar silkworms: A novel substrate for in vitro fibroblast culture, *Acta Biomaterialia*. **5**, 1, 429-437 (2009).

Adamson, A.W. and Gast, A.P. Physical chemistry of surfaces, *John Wiley & Sons*, New York. (1997).

Addison, J.B., Ashton, N.N., Weber, W.S., Stewart, R.J., Holland, G.P. and Yarger, J.L. β-sheet nanocrystalline domains formed from phosphorylated serine-rich motifs in caddisfly larval silk: A solid state NMR and XRD study, *Biomacromolecules*. **14**, 4, 1140-1148 (2013).

Akahira, T. and Sunose, T. Method of determining activation deterioration constant of electrical insulating materials, *Research Report (Chiba Institute of Technology), Science and Technology*. **16**, 22-31 (1971).

Alam, A.K.M.M., Shubhra, Q.T.H., Al Imran, G., Barai, S., Islam, M.R. and Rahman, M.M. Preparation and characterization of natural silk fiber-reinforced polypropylene and synthetic E-glass fiber-reinforced polypropylene composites: A comparative study, *Journal of Composite Materials*. **45**, 22, 2301-2308 (2011).

Albrecht, M.A., Evans, C.W. and Raston, C.L. Green chemistry and the health implications of nanoparticles, *Green Chemistry*. **8**, 5, 417-432 (2006).

Altman, G.H., Diaz, F., Jakuba, C., Calabro, T., Horan, R.L., Chen, J., Lu, H., Richmond, J. and Kaplan, D.L. Silk-based biomaterials, *Biomaterials*. **24**, 3, 401-416 (2003).

Altman, G.H., Horan, R.L., Lu, H.H., Moreau, J., Martin, I., Richmond, J.C. and Kaplan, D.L. Silk matrix for tissue engineered anterior cruciate ligaments, *Biomaterials*. **23**, 20, 4131-4141 (2002).

Aoyagi, Y., Yamashita, K. and Doi, Y. Thermal degradation of poly [(R)-3-hydroxybutyrate], poly [ε-caprolactone], and poly [(S)-lactide], *Polymer Degradation and Stability*. **76**, 1, 53-59 (2002).

Armentano, I., Bitinis, N., Fortunati, E., Mattioli, S., Rescignano, N., Verdejo, R., Lopez-Manchado, M.A. and Kenny, J.M. Multifunctional nanostructured PLA materials for packaging and tissue engineering, *Progress in Polymer Science*. **38**, 10, 1720-1747 (2013).

Arrhenius, S. Über die reaktionsgeschwindigkeit bei der inversion von rohrzucker durch säuren, *Zeitschrift für Physikalische Chemie*. **4**, 1, 226-248 (1889).

Asakura, T., Okonogi, M., Nakazawa, Y. and Yamauchi, K. Structural analysis of alanine tripeptide with antiparallel and parallel β-sheet structures in relation to the analysis of mixed β-sheet structures in Samia cynthia ricini silk protein fiber using solid-state NMR spectroscopy, *Journal of the American Chemical Society*. **128**, 18, 6231-6238 (2006).

Avrami, M. Granulation, phase change, and microstructure kinetics of phase change. III, *The Journal of Chemical Physics*. **9**, 2, 177-184 (1941).

Avrami, M. Kinetics of phase change. II, transformation-time relations for random distribution of nuclei, *The Journal of Chemical Physics*. **8**, 2, 212-224 (1940).

Ayoub, N.A., Garb, J.E., Tinghitella, R.M., Collin, M.A. and Hayashi, C.Y. Blueprint for a high-performance biomaterial: Full-length spider dragline silk genes, *Plos One*. **2**, 6, e514 (2007).

Babb, P.L., Lahens, N.F., Correa-Garhwal, S.M., Nicholson, D.N., Kim, E.J., Hogenesch, J.B., Kuntner, M., Higgins, L., Hayashi, C.Y., Agnarsson, I. and Voight, B.F. The Nephila clavipes genome highlights the diversity of spider silk genes and their complex expression, *Nature Genetics*. **49**, 6, 895-903 (2017).

Babu, K.M. Silk from silkworms and spiders as high-performance fibers, Structure and properties of high-performance fibers, *Woodhead Publishing*, (2016), 327-366.

Babu, K.M. Silk: Processing, properties and applications, *Elsevier Science*, (2013).

Baloch, M.K., Khurram, M.J.Z. and Durrani, G.F. Application of different methods for the thermogravimetric analysis of polyethylene samples, *Journal of Applied Polymer Science*. **120**, 6, 3511-3518 (2011).

Barghout, J.Y.J., Thiel, B.L. and Viney, C. Spider (Araneus diadematus) cocoon silk: A case of non-periodic lattice crystals with a twist?, *International Journal of Biological Macromolecules*. **24**, 2, 211-217 (1999).

Basu, A. Advances in silk science and technology, *Woodhead Publishing*, (2015).

Benali, S., Aouadi, S., Dechief, A.L., Murariu, M. and Dubois, P. Key factors for tuning hydrolytic degradation of polylactide/zinc oxide nanocomposites, *Nanocomposites*. **1**, 1, 51-61 (2015).

Bhasney, S.M., Patwa, R., Kumar, A. and Katiyar, V. Plasticizing effect of coconut oil on morphological, mechanical, thermal, rheological, barrier, and optical properties of poly(lactic acid): A promising candidate for food packaging, *Journal of Applied Polymer Science*. **134**, 41, 45390-45401 (2017).

Bhat, N.V. and Nadiger, G.S. Crystallinity in silk fibers: Partial acid hydrolysis and related studies, *Journal of Applied Polymer Science*. **25**, 5, 921-932 (1980).

Bhat, N.V., Nadiger, G.S., Paralikar, K.M. and Betrabet, S.M. Electron diffraction studies on Indian silk, *Journal of Applied Polymer Science*. **25**, 4, 635-640 (1980).

Bocchini, S., Fukushima, K., Blasio, A.D., Fina, A., Frache, A. and Geobaldo, F. Polylactic acid and polylactic acid-based nanocomposite photooxidation, *Biomacromolecules*. **11**, 11, 2919-2926 (2010).

Buehler, M.J. Tu(r)ning weakness to strength, *Nano Today*. **5**, 5, 379-383 (2010).

Cai, J., Liu, M., Wang, L., Yao, K., Li, S. and Xiong, H. Isothermal crystallization kinetics of thermoplastic starch/poly(lactic acid) composites, *Carbohydrate Polymers*. **86**, 2, 941-947 (2011).

Cai, K., Yao, K., Lin, S., Yang, Z., Li, X., Xie, H., Qing, T. and Gao, L. Poly (D, L-lactic acid) surfaces modified by silk fibroin: Effects on the culture of osteoblast in vitro, *Biomaterials*. **23**, 4, 1153-1160 (2002).

Cao, Y. and Wang, B. Biodegradation of silk biomaterials, *International Journal of Molecular Sciences*. **10**, 4, 1514-1524 (2009).

Carrasco, F., Pagès, P., Gámez-Pérez, J., Santana, O.O. and Maspoch, M.L. Processing of poly(lactic acid): Characterization of chemical structure, thermal stability and mechanical properties, *Polymer Degradation and Stability*. **95**, 2, 116-125 (2010).

Chen, E.C. and Wu, T.M. Isothermal crystallization kinetics and thermal behavior of poly(ε-caprolactone)/multi-walled carbon nanotube composites, *Polymer Degradation and Stability*. **92**, 6, 1009-1015 (2007).

Chen, S., Cheng, L., Huang, H., Zou, F. and Zhao, H.P. Fabrication and properties of poly(butylene succinate) biocomposites reinforced by waste silkworm silk fabric, *Composites Part A: Applied Science and Manufacturing*. **95**, 125-131 (2017).

Cheung, H.Y., Lau, K.T., Pow, Y.F., Zhao, Y.Q. and Hui, D. Biodegradation of a silkworm silk/PLA composite, *Composites Part B: Engineering*. **41**, 3, 223-228 (2010).

Chiang, M.F., Chu, M.Z. and Wu, T.M. Effect of layered double hydroxides on the thermal degradation behavior of biodegradable poly(L-lactide) nanocomposites, *Polymer Degradation and Stability*. **96**, 1, 60-66 (2011).

Cho, S.Y., Yun, Y.S., Lee, S., Jang, D., Park, K.Y., Kim, J.K., Kim, B.H., Kang, K., Kaplan, D.L. and Jin, H.J. Carbonization of a stable β-sheet-rich silk protein into a pseudographitic pyroprotein, *Nature Communications*. **6**, 7145-7151 (2015).

Chu, M.J. and Wu, T.M. Isothermal crystallization kinetics of poly(lactic acid)/montmorillonite nanocomposites, Experimental analysis of nano and engineering materials and structures, *Springer*, Dordrecht. (2007), 827-828.

Claramunt, J., Fernández-Carrasco, L.J., Ventura, H. and Ardanuy, M. Natural fiber nonwoven reinforced cement composites as sustainable materials for building envelopes, *Construction and Building Materials*. **115**, 230-239 (2016).

Coats, A.W. and Redfern, J.P. Kinetic parameters from thermogravimetric data, *Nature*. **201**, 4914, 68-69 (1964).

Corcione, E.C. and Frigione, M. Characterization of nanocomposites by thermal analysis, *Materials*. 5, **12**, 2960-2980 (2012).

Criado, J.M., Malek, J. and Ortega, A. Applicability of the master plots in kinetic analysis of non-isothermal data, *Thermochimica Acta*. **147**, 2, 377-385 (1989).

Crompton, T.R. Mechanical properties of polymers, Physical testing of plastics, *Smithers Rapra*, (2012).

Dai, X. and Qiu, Z. Crystallization kinetics, morphology, and hydrolytic degradation of novel biobased poly(butylene succinate-co-decamethylene succinate) copolyesters, *Polymer Degradation and Stability*. **137**, 197-204 (2017).

Darshan, G.H., Kong, D., Gautrot, J. and Vootla, S. Physico-chemical characterization of Antheraea mylitta silk mats for wound healing applications, *Scientific Reports*. **7**, 1, 10344 (2017).

Das, P. and Tiwari, P. Thermal degradation kinetics of plastics and model selection, *Thermochimica Acta*. **654**, 191-202 (2017).

Datta, A., Ghosh, A.K. and C. Kundu, S. Purification and characterization of fibroin from the tropical Saturniid silkworm, Antheraea mylitta, *Insect Biochemistry and Molecular Biology*. **31**, 10, 1013-1018 (2001).

De Jong, S.J., Arias, E.R., Rijkers, D.T.S., Van Nostrum, C.F., Kettenes-Van den Bosch, J.J. and Hennink, W.E. New insights into the hydrolytic degradation of poly(lactic acid): Participation of the alcohol terminus, *Polymer*. **42**, 7, 2795-2802 (2001).

Devi, D., Sarma, N.S., Talukdar, B., Chetri, P., Baruah, K.C. and Dass, N.N. Study of the structure of degummed Antheraea assamensis (muga) silk fibre, *Journal of the Textile Institute*. **102**, 6, 527-533 (2011).

Dhar, P., Bhardwaj, U., Kumar, A. and Katiyar, V. Poly (3-hydroxybutyrate)/cellulose nanocrystal films for food packaging applications: Barrier and migration studies, *Polymer Engineering & Science*. **55**, 10, 2388-2395 (2015a).

Dhar, P., Gaur, S.S., Soundararajan, N., Gupta, A., Bhasney, S.M., Milli, M., Kumar, A. and Katiyar, V. Reactive extrusion of polylactic acid/cellulose nanocrystal films for food packaging applications: Influence of filler type on thermomechanical, rheological, and barrier properties, *Industrial & Engineering Chemistry Research*. **56**, 16, 4718-4735 (2017).

Dhar, P., Kumar, A. and Katiyar, V. Magnetic cellulose nanocrystal based anisotropic polylactic acid nanocomposite films: Influence on electrical, magnetic, thermal, and

mechanical properties, *ACS Applied Materials & Interfaces*. **8**, 28, 18393-18409 (2016).

Dhar, P., Tarafder, D., Kumar, A. and Katiyar, V. Effect of cellulose nanocrystal polymorphs on mechanical, barrier and thermal properties of poly(lactic acid) based bionanocomposites, *RSC Advances*. **5**, 74, 60426-60440 (2015b).

Dhar, P., Vangala, S., Tiwari, P., Kumar, A. and Katiyar, V. Thermal degradation kinetics of poly(3-hydroxybutyrate)/cellulose nanocrystals based nanobiocomposite, *Journal of Thermodynamics Catalysis*. **5**, 134 (2014).

Ding, W., Chu, R.K.M., Mark, L.H., Park, C.B. and Sain, M. Non-isothermal crystallization behaviors of poly(lactic acid)/cellulose nanofiber composites in the presence of CO_2, *European Polymer Journal*. **71**, 231-247 (2015).

Doblhofer, E., Schmid, J., Rieß, M., Daab, M., Suntinger, M., Habel, C., Bargel, H., Hugenschmidt, C., Rosenfeldt, S. and Breu, J. Structural insights into water-based spider silk protein–nanoclay composites with excellent gas and water vapor barrier properties, *ACS Applied Materials & Interfaces*. **8**, 38, 25535-25543 (2016).

Dobreva, A. and Gutzow, I. Activity of substrates in the catalyzed nucleation of glass-forming melts. II. Experimental evidence, *Journal of Non-Crystalline Solids*. **162**, 1-2, 13-25 (1993).

Dong, Y., Chaudhary, D., Haroosh, H. and Bickford, T. Development and characterization of novel electrospun polylactic acid/tubular clay nanocomposites, *Journal of Materials Science*. **46**, 18, 6148-6153 (2011).

Dorgan, J.R., Williams, J.S. and Lewis, D.N. Melt rheology of poly(lactic acid): Entanglement and chain architecture effects, *Journal of Rheology*. **43**, 5, 1141-1155 (1999).

Doyle, C.D. Logarithmic thermal degradation of a silicone resin in air, *Journal of Polymer Science Part A: Polymer Chemistry*. **31**, 122, 95-104 (1958).

Drucker, B. and Smith, S.G. Structure of silk fibroin, *Nature*. **165**, 4188, 196-197 (1950).

Drucker, B., Hainsworth, R. and Smith, S.G. 30—The chemistry of silk fibroin I. The action of some proteolytic enzymes on fibroin in aqueous solution and its bearing on the molecular structure of silk, *Journal of the Textile Institute Transactions*. **44**, 10, 420-435 (1953).

Drumright, R.E., Gruber, P.R. and Henton, D.E. Polylactic acid technology, *Advanced Materials*. **12**, 23, 1841-1846 (2000).

Du, N., Liu, X.Y., Narayanan, J., Li, L., Lim, M.L.M. and Li, D. Design of superior spider silk: From nanostructure to mechanical properties, *Biophysical Journal*. **91**, 12, 4528-4535 (2006).

Duan, J., Xie, Y.N., Yang, J.H., Huang, T., Zhang, N., Wang, Y. and Zhang, J.H. Graphene oxide induced hydrolytic degradation behavior changes of poly(L-lactide) in different mediums, *Polymer Testing*. **56**, 220-228 (2016).

Elsawy, M.A., Kim, K.H., Park, J.W. and Deep, A. Hydrolytic degradation of polylactic acid (PLA) and its composites, *Renewable and Sustainable Energy Reviews*. **79**, 1346-1352 (2017).

Fan, H., Liu, H., Toh, S.L. and Goh, J.C.H. Anterior cruciate ligament regeneration using mesenchymal stem cells and silk scaffold in large animal model, *Biomaterials*. **30**, 28, 4967-4977 (2009).

Fang, G., Tang, Y., Qi, Z., Yao, J., Shao, Z. and Chen, X. Precise correlation of macroscopic mechanical properties and microscopic structures of animal silks—using Antheraea pernyi silkworm silk as an example, *Journal of Materials Chemistry B*. **5**, 30, 6042-6048 (2017).

Farah, S., Anderson, D.G. and Langer, R. Physical and mechanical properties of PLA, and their functions in widespread applications—a comprehensive review, *Advanced Drug Delivery Reviews*. **107**, 367-392 (2016).

Fawell, J.K. The impact of inorganic chemicals on water quality and health, *Annali-Istituto Superiore di Sanita*. **29**, 293-293 (1993).

Fernandez, J.G. and Ingber, D.E. Unexpected strength and toughness in chitosan-fibroin laminates inspired by insect cuticle, *Advanced Materials*. **24**, 4, 480-484 (2012).

Fernández, M.D. and Fernández, M.J. Vermiculite/poly(lactic acid) composites: Effect of nature of vermiculite on hydrolytic degradation in alkaline medium, *Applied Clay Science*. **143**, 29-38 (2017).

Flynn, J.H. and Wall, L.A. A quick, direct method for the determination of activation energy from thermogravimetric data, *Journal of Polymer Science Part C: Polymer Letters*. **4**, 5, 323-328 (1966).

Fornasiero, P. and Graziani, M. Renewable resources and renewable energy: A global schallenge, *CRC Press*, Florida. (2011).

Freddi, G., Gotoh, Y., Mori, T., Tsutsui, I. and Tsukada, M. Chemical structure and physical properties of Antheraea assama silk, *Journal of Applied Polymer Science*. **52**, 6, 775-781 (1994).

Freddi, G., Monti, P., Nagura, M., Gotoh, Y. and Tsukada, M. Structure and molecular conformation of tussah silk fibroin films: Effect of heat treatment, *Journal of Polymer Science Part B: Polymer Physics Edition*. **35**, 5, 841-848 (1997).

Fu, C., Porter, D., Chen, X., Vollrath, F. and Shao, Z. Understanding the mechanical properties of Antheraea pernyi silk-from primary structure to condensed structure of the protein, *Advanced Functional Materials*. **21**, 4, 729-737 (2011).

Fu, C., Mahadevegowda, A. and Grant, P.S. Fe_3O_4/carbon nanofibres with necklace architecture for enhanced electrochemical energy storage, *Journal of Materials Chemistry A*. **3**, 27, 14245-14253 (2015).

Fukushima, K., Tabuani, D., Dottori, M., Armentano, I., Kenny, J.M. and Camino, G. Effect of temperature and nanoparticle type on hydrolytic degradation of poly(lactic acid) nanocomposites, *Polymer Degradation and Stability*. **96**, 12, 2120-2129 (2011).

Gao, Y., Picot, O.T., Bilotti, E. and Peijs, T. Influence of filler size on the properties of poly(lactic acid) (PLA)/graphene nanoplatelet (GNP) nanocomposites, *European Polymer Journal*. **86**, 117-131 (2017).

Garlotta, D. A literature review of poly(lactic acid), *Journal of Polymers and the Environment*. **9**, 2, 63-84 (2001).

Geyer, R., Jambeck, J.R. and Law, K.L. Production, use, and fate of all plastics ever made, *Science Advances*. **3**, 7, e1700782 (2017).

Girdthep, S., Worajittiphon, P., Leejarkpai, T., Molloy, R. and Punyodom, W. Effect of silver-loaded kaolinite on real ageing, hydrolytic degradation, and biodegradation of composite blown films based on poly(lactic acid) and poly(butylene adipate-co-terephthalate), *European Polymer Journal*. **82**, 244-259 (2016).

Gironi, F. and Piemonte, V. Life cycle assessment of polylactic acid and polyethylene terephthalate bottles for drinking water, *Environmental Progress & Sustainable Energy*. **30**, 3, 459-468 (2011).

Gogoi, D., Choudhury, A.J., Chutia, J., Pal, A.R., Dass, N.N., Devi, D. and Patil, D.S. Enhancement of hydrophobicity and tensile strength of muga silk fiber by radiofrequency Ar plasma discharge, *Applied Surface Science*. **258**, 1, 126-135 (2011).

Gogoi, D., Chutia, J., Choudhury, A.J., Pal, A.R. and Patil, D. Radio-frequency ar plasma treatment on muga silk fiber: Correlation between physicochemical and surface morphology, *Journal of Theoretical and Applied Physics*. 6, 1, 39-46 (2012).

Gorrasi, G. and Pantani, R. Effect of PLA grades and morphologies on hydrolytic degradation at composting temperature: Assessment of structural modification and kinetic parameters, *Polymer Degradation and Stability*. **98**, 5, 1006-1014 (2013).

Grand view research, Lactic Acid Market Analysis By Application (Industrial, F&B, Pharmaceuticals, Personal Care) & Polylactic Acid (PLA) Market Analysis By Application (Packaging, Agriculture, Transport, Electronics, Textiles), And Segment Forecasts, 2014-2025, May (2017) https://www.grandviewresearch.com/industry-analysis/lactic-acid-and-poly-lactic-acid-market.

Gulrajani, M.L. Degumming of silk, *Coloration Technology*. **22**, 1, 79-89 (1992).

Gupta, A. and Katiyar, V. Cellulose functionalized high molecular weight stereocomplex polylactic acid biocomposite films with improved gas barrier, thermomechanical properties, *ACS Sustainable Chemistry & Engineering*. **5**, 8, 6835-6844 (2017).

Gupta, A., Prasad, A., Mulchandani, N., Shah, M., Ravi Sankar, M., Kumar, S. and Katiyar, V. Multifunctional nanohydroxyapatite-promoted toughened high-molecular-weight stereocomplex poly(lactic acid)-based bionanocomposite for both 3D-printed orthopedic implants and high-temperature engineering applications, *ACS Omega*. **2**, 7, 4039-4052 (2017).

Gupta, V., Aseh, A., Ríos, C.N., Aggarwal, B.B. and Mathur, A.B. Fabrication and characterization of silk fibroin-derived curcumin nanoparticles for cancer therapy, *International Journal of Nanomedicine*. **4**, 115-122 (2009).

Hao, X., Kaschta, J. and Schubert, D.W. Viscous and elastic properties of polylactide melts filled with silica particles: Effect of particle size and concentration, *Composites Part B: Engineering*. **89**, 44-53 (2016).

He, J., Qin, Y., Cui, S., Gao, Y. and Wang, S. Structure and properties of novel electrospun tussah silk fibroin/poly(lactic acid) composite nanofibers, *Journal of Materials Science*. **46**, 9, 2938-2946 (2011).

Hinchcliffe, S.A., Hess, K.M. and Srubar, W.V. Experimental and theoretical investigation of prestressed natural fiber-reinforced polylactic acid (PLA) composite materials, *Composites Part B: Engineering*. **95**, 346-354 (2016).

Hoffman, J.D., Davis, G.T. and Lauritzen Jr, J.I. The rate of crystallization of linear polymers with chain folding, Treatise on solid state chemistry, *Springer US*. (1976), 497-614.

Höglund, A., Hakkarainen, M. and Albertsson, A.C. Migration and hydrolysis of hydrophobic polylactide plasticizer, *Biomacromolecules*. **11**, 1, 277-283 (2009).

Holzwarth, U. and Gibson, N. The Scherrer equation versus the 'Debye-Scherrer equation', *Nature Nanotechnology*. **6**, 9, 534-534 (2011).

Hopewell, J., Dvorak, R. and Kosior, E. Plastics recycling: Challenges and opportunities, *Philosophical Transactions of the Royal Society B: Biological Sciences*. **364**, 1526, 2115-2126 (2009).

Hu, J., Chen, M., Tian, H. and Deng, W. Preparation and pyrolysis characteristics of PNIPAM-grafted SiO_2 hollow spheres loading vitamin C, *RSC Advances*. **5**, 99, 81134-81141 (2015).

Hu, X., Kaplan, D. and Cebe, P. Determining beta-sheet crystallinity in fibrous proteins by thermal analysis and infrared spectroscopy, *Macromolecules*. **39**, 18, 6161-6170 (2006).

Huang, J., Lisowski, M.S., Runt, J., Hall, E.S., Kean, R.T., Buehler, N. and Lin, J.S. Crystallization and microstructure of poly(l-lactide-co-meso-lactide) copolymers, *Macromolecules*. **31**, 8, 2593-2599 (1998).

Huang, Y., Chen, F., Pan, Y., Chen, C., Jiang, L. and Dan, Y. Effect of hydrophobic fluoropolymer and crystallinity on the hydrolytic degradation of poly(lactic acid), *European Polymer Journal*. **97**, 308-318 (2017).

Hughes, J., Thomas, R., Byun, Y. and Whiteside, S. Improved flexibility of thermally stable poly-lactic acid (PLA), *Carbohydrate Polymers*. **88**, 1, 165-172 (2012).

Imre, B. and Pukánszky, B. Compatibilization in bio-based and biodegradable polymer blends, *European Polymer Journal*. **49**, 6, 1215-1233 (2013).

Jamshidian, M., Tehrany, E.A., Imran, M., Akhtar, M.J., Cleymand, F. and Desobry, S. Structural, mechanical and barrier properties of active PLA–antioxidant films, *Journal of Food Engineering*. **110**, 3, 380-389 (2012).

Jeziorny, A. Parameters characterizing the kinetics of the non-isothermal crystallization of poly(ethylene terephthalate) determined by DSC, *Polymer*. **19**, 10, 1142-1144 (1978).

Jo, Y.Y., Kweon, H., Kim, D.W., Kim, M.K., Kim, S.G., Kim, J.Y., Chae, W.S., Hong, S.P., Park, Y.H., Lee, S.Y. and Choi, J.Y. Accelerated biodegradation of silk sutures through matrix metalloproteinase activation by incorporating 4-hexylresorcinol, *Scientific Reports*. **7**, (2017).

Kan, T., Strezov, V. and Evans, T. Effect of the heating rate on the thermochemical behavior and biofuel properties of sewage sludge pyrolysis, *Energy & Fuels*. **30**, 3, 1564-1570 (2016).

Kaplan, D., Adams, W.W., Farmer, B. and Viney, C. Silk: Biology, structure, properties, and genetics, Silk polymers, *American Chemical Society*. (1993), 2-16.

Kasoju, N. and Bora, U. Fabrication and characterization of curcumin-releasing silk fibroin scaffold, *Journal of Biomedical Materials Research Part B: Applied Biomaterials*. **100**, 7, 1854-1866 (2012).

Kasoju, N., Bhonde, R.R. and Bora, U. Preparation and characterization of Antheraea assama silk fibroin based novel non-woven scaffold for tissue engineering applications, *Journal of Tissue Engineering and Regenerative Medicine*. **3**, 7, 539-552 (2009).

Katiyar, V. and Nanavati, H. In situ synthesis of high molecular weight poly(L-lactic acid) clay nanocomposites, *Polymer Engineering & Science*. **51**, 10, 2066-2077 (2011).

Katiyar, V., Gerds, N., Koch, C.B., Risbo, J., Hansen, H.C.B. and Plackett, D. Poly l-lactide-layered double hydroxide nanocomposites via in situ polymerization of l-lactide, *Polymer Degradation and Stability*. **95**, 12, 2563-2573 (2010).

Keten, S., Xu, Z., lhle, B. and Buehler, M.J. Nanoconfinement controls stiffness, strength and mechanical toughness of [beta]-sheet crystals in silk, *Nature Materials*. **9**, 4, 359-367 (2010).

Kfoury, G., Raquez, J.-M., Hassouna, F., Odent, J., Toniazzo, V., Ruch, D. and Dubois, P. Recent advances in high performance poly(lactide): From “green” plasticization to super-tough materials via (reactive) compounding, *Frontiers in chemistry*. **1**, 32, (2013).

Khakbaz, M., Hejazi, I., Seyfi, J., Jafari, S.H., Khonakdar, H.A. and Davachi, S.M. A novel method to control hydrolytic degradation of nanocomposite biocompatible materials via imparting superhydrophobicity, *Applied Surface Science*. **357**, 880-886 (2015).

Khawam, A. and Flanagan, D.R. Basics and applications of solid-state kinetics: A pharmaceutical perspective, *Journal of Pharmaceutical Sciences*. **95**, 3, 472-498 (2006a).

Khawam, A. and Flanagan, D.R. Solid-state kinetic models: Basics and mathematical fundamentals, *The Journal of Physical Chemistry B*. **110**, 35, 17315-17328 (2006b).

Kissinger, H.E. Variation of peak temperature with heating rate in differential thermal analysis, *Journal of Research of the National Bureau of Standards*. **57**, 4, 217-221 (1956).

Koh, H.C., Park, J.S., Jeong, M.A., Hwang, H.Y., Hong, Y.T., Ha, S.Y. and Nam, S.Y. Preparation and gas permeation properties of biodegradable polymer/layered silicate nanocomposite membranes, *Desalination*. **233**, 1, 201-209 (2008).

Koh, L.D., Cheng, Y., Teng, C.P., Khin, Y.W., Loh, X.J., Tee, S.Y., Low, M., Ye, E., Yu, H.D., Zhang, Y.W. and Han, M.Y. Structures, mechanical properties and applications of silk fibroin materials, *Progress in Polymer Science*. **46**, 86-110 (2015).

Krikorian, V. and Pochan, D.J. Poly (L-lactic acid)/layered silicate nanocomposite: Fabrication, characterization and properties, *Chemistry of Materials*. **15**, 22, 4317-4324 (2003).

Kumar, D. and Kundapur, R.R. Biomedical applications of natural proteins: An emerging era in biomedical sciences, *Springer India*, (2015).

Kundu, J., Chung, Y.I., Kim, Y.H., Tae, G. and Kundu, S.C. Silk fibroin nanoparticles for cellular uptake and control release, *International Journal of Pharmaceutics*. **388**, 1, 242-250 (2010).

Kweon, H., Ha, H.C., Um, I.C. and Park, Y.H. Physical properties of silk fibroin/chitosan blend films, *Journal of Applied Polymer Science*. **80**, 7, 928-934 (2001).

Kweon, H. and Park, Y.H. Dissolution and characterization of regenerated Antheraea pernyi silk fibroin, *Journal of Applied Polymer Science*. **82**, 3, 750-758 (2001).

Lammel, A.S., Hu, X., Park, S.H., Kaplan, D.L. and Scheibel, T.R. Controlling silk fibroin particle features for drug delivery, *Biomaterials*. **31**, 16, 4583-4591 (2010).

Lasprilla, A.J., Martinez, G.A., Lunelli, B.H., Jardini, A.L. and Maciel Filho, R. Poly-lactic acid synthesis for application in biomedical devices—a review, *Biotechnology Advances*. **30**, 1, 321-328 (2012).

Lee, S.H., Wang, S. and Teramoto, Y. Isothermal crystallization behavior of hybrid biocomposite consisting of regenerated cellulose fiber, clay, and poly(lactic acid), *Journal of Applied Polymer Science*. **108**, 2, 870-875 (2008).

Leszczyńska, A., Njuguna, J., Pielichowski, K. and Banerjee, J.R. Polymer/montmorillonite nanocomposites with improved thermal properties: Part II. Thermal stability of montmorillonite nanocomposites based on different polymeric matrixes, *Thermochimica Acta*. **454**, 1, 1-22 (2007).

Li, J., Zheng, W., Li, L., Zheng, Y. and Lou, X. Thermal degradation kinetics of g-HA/PLA composite, *Thermochimica Acta*. **493**, 1, 90-95 (2009).

Li, M.Y., Zhao, Y., Tong, T., Hou, X.H., Fang, B.S., Wu, S.Q., Shen, X.Y. and Tong, H. Study of the degradation mechanism of Chinese historic silk (Bombyx mori) for the purpose of conservation, *Polymer Degradation and Stability*. **98**, 3, 727-735 (2013).

Li, X., Chu, C., Wei, Y., Qi, C., Bai, J., Guo, C., Xue, F., Lin, P. and Chu, P.K. In vitro degradation kinetics of pure PLA and Mg/PLA composite: Effects of immersion temperature and compression stress, *Acta Biomaterialia*. **48**, 468-478 (2017).

Lian, Y., Zhan, J.C., Zhang, K.H. and Mo, X.M. Fabrication and characterization of curcumin-loaded silk fibroin/P (LLA-CL) nanofibrous scaffold, *Frontiers of Materials Science*. **8**, 4, 354-362 (2014).

Ling, S., Qi, Z., Knight, D.P., Shao, Z. and Chen, X. Synchrotron FTIR microspectroscopy of single natural silk fibers, *Biomacromolecules*. **12**, 9, 3344-3349 (2011).

Liu, B., Li, Y.M., Wu, S.B., Li, Y.H., Deng, S.S. and Xia, Z.L. Pyrolysis characteristic of tobacco stem studied by Py-GC/MS, TG-FTIR, and TG-MS, *Bioresources*. **8**, 1, 220-230 (2013).

Liu, T., Mo, Z., Wang, S. and Zhang, H. Nonisothermal melt and cold crystallization kinetics of poly(aryl ether ether ketone ketone), *Polymer Engineering & Science*. **37**, 3, 568-575 (1997).

Liu, X., Khor, S., Petinakis, E., Yu, L., Simon, G., Dean, K. and Bateman, S. Effects of hydrophilic fillers on the thermal degradation of poly(lactic acid), *Thermochimica Acta*. **509**, 1, 147-151 (2010).

Lizundia, E., Mateos, P. and Vilas, J.L. Tuneable hydrolytic degradation of poly(l-lactide) scaffolds triggered by ZnO nanoparticles, *Materials Science and Engineering: C*. **75**, 714-720 (2017).

Lizundia, E., Vilas, J.L., Sangroniz, A. and Etxeberria, A. Light and gas barrier properties of PLLA/metallic nanoparticles composite films, *European Polymer Journal*. 91, 10-20 (2017).

Lucas, F., Shaw, J.T.B. and Smith, S.G. Comparative studies of fibroins: I. The amino acid composition of various fibroins and its significance in relation to their crystal structure and taxonomy, *Journal of Molecular Biology*. **2**, 6, 339-349 (1960).

Lucas, F., Shaw, J.T.B. and Smith, S.G. The silk fibroins, *Advances in Protein Chemistry*. **13**, 107-242 (1958).

Lunt, J. Large-scale production, properties and commercial applications of polylactic acid polymers, *Polymer Degradation and Stability*. **59**, 1, 145-152 (1998).

Lv, S., Liu, X., Gu, J., Jiang, Y., Tan, H. and Zhang, Y. Effect of glycerol introduced into PLA based composites on the UV weathering behavior, *Construction and Building Materials*. **144**, 525-531 (2017).

Lyu, S. and Untereker, D. Degradability of polymers for implantable biomedical devices, *International Journal of Molecular Sciences*. **10**, 9, 4033-4065 (2009).

Ma, Y.H. and Song, K.B. Physical properties of silk fibroin films treated with various plasticizers, *Preventive Nutrition and Food Science*. **10**, 2, 187-190 (2005).

Ma, M. and Zhou, W. Improving the hydrolysis resistance of poly(lactic acid) fiber by hydrophobic finishing, *Industrial & Engineering Chemistry Research*. **54**, 10, 2599-2605 (2015).

Maitz, M.F., Sperling, C., Wongpinyochit, T., Herklotz, M., Werner, C. and Seib, F.P. Biocompatibility assessment of silk nanoparticles: Hemocompatibility and internalization by human blood cells, *Nanomedicine: Nanotechnology, Biology and Medicine*. **13**, 8, 2633-2642 (2017).

Mallakpour, S. and Taghavi, M. Kinetics and thermal degradation study of optically active and thermally stable aromatic polyamides with flame-retardancy properties, *Polymer Journal*. **41**, 4, 308-318 (2009).

McNeill, I.C. and Leiper, H.A. Degradation studies of some polyesters and polycarbonates—2. Polylactide: Degradation under isothermal conditions, thermal degradation mechanism and photolysis of the polymer, *Polymer Degradation and Stability*. **11**, 4, 309-326 (1985).

Meng, J., Zhang, Y., Qi, X., Kong, H., Wang, C., Xu, Z., Xie, S., Gu, N. and Xu, H. Paramagnetic nanofibrous composite films enhance the osteogenic responses of pre-osteoblast cells, *Nanoscale*. **2**, 12, 2565-2569 (2010).

Mielke, S.P. and Krishnan, V.V. Characterization of protein secondary structure from NMR chemical shifts, *Progress in Nuclear Magnetic Resonance Spectroscopy*. **54**, 3-4, 141-165 (2009).

Min, K., Kim, S., Kim, C.G. and Kim, S. Colored and fluorescent nanofibrous silk as a physically transient chemosensor and vitamin deliverer, *Scientific Reports*. **7**, 1, 5448 (2017).

Miyata, T. and Masuko, T. Crystallization behaviour of poly(L-lactide), *Polymer*. **39**, 22, 5515-5521 (1998).

Mofokeng, J.P. and Luyt, A.S. Morphology and thermal degradation studies of melt-mixed poly(lactic acid) (PLA)/poly(ε-caprolactone) (PCL) biodegradable polymer blend nanocomposites with TiO2 as filler, *Polymer Testing*. **45**, 93-100 (2015).

Molinaro, S., Romero, M.C., Boaro, M., Sensidoni, A., Lagazio, C., Morris, M. and Kerry, J. Effect of nanoclay-type and PLA optical purity on the characteristics of PLA-based nanocomposite films, *Journal of Food Engineering*. **117**, 1, 113-123 (2013).

Monika, Dhar, P. and Katiyar, V. Thermal degradation kinetics of polylactic acid/acid fabricated cellulose nanocrystal based bionanocomposites, *International Journal of Biological Macromolecules*. **104**, 827-836 (2017).

Mottaghitalab, F., Kiani, M., Farokhi, M., Kundu, S.C., Reis, R.L., Gholami, M., Bardania, H., Dinarvand, R., Geramifar, P., Beiki, D. and Atyabi, F. Targeted delivery system based on Gemcitabine loaded silk fibroin nanoparticles for Lung Cancer Therapy, *ACS Applied Materials & Interfaces*. **9**, 37, 31600-31611 (2017).

Muller, J., González-Martínez, C. and Chiralt, A. Poly (lactic) acid (PLA) and starch bilayer films, containing cinnamaldehyde, obtained by compression moulding, *European Polymer Journal*. **95**, 56-70 (2017).

Murray, P. and White, J. Kinetics of the thermal dehydration of clays. Part IV. Interpretation of the differential thermal analysis of the clay minerals, *Transactions and Journal of the British Ceramic Society*. **54**, 204-238 (1955).

Nakazawa, Y. and Asakura, T. High-resolution 13C CP/MAS NMR study on structure and structural transition of Antheraea pernyi silk fibroin containing poly(l-alanine) and Gly-rich regions, *Macromolecules*. **35**, 2393-2400 (2002).

Nanda, M.R., Misra, M. and Mohanty, A.K. The effects of process engineering on the performance of PLA and PHBV blends, *Macromolecular Materials and Engineering*. **296**, 8, 719-728 (2011).

Narayanan, M., Loganathan, S., Valapa, R.B., Thomas, S. and Varghese, T.O. UV protective poly(lactic acid)/rosin films for sustainable packaging, *International Journal of Biological Macromolecules*. **99**, 37-45 (2017).

S. Natesh. Spider silk expressed in Bombyx mori: Can muga silk follow?, *Biotech News*, **2**, 102-103 (2011).

Neumann, A.W., Good, R.J., Hope, C.J. and Sejpal, M. An equation-of-state approach to determine surface tensions of low-energy solids from contact angles, *Journal of Colloid and Interface Science*. **49**, 2, 291-304 (1974).

Nova, A., Keten, S., Pugno, N.M., Redaelli, A. and Buehler, M.J. Molecular and nanostructural mechanisms of deformation, strength and toughness of spider silk fibrils, *Nano Letters*. **10**, 7, 2626-2634 (2010).

Numata, K., Cebe, P. and Kaplan, D.L. Mechanism of enzymatic degradation of beta-sheet crystals, *Biomaterials*. **31**, 10, 2926-2933 (2010).

O'Brien, J.P., Fahnestock, S.R., Termonia, Y. and Gardner, K.H. Nylons from nature: Synthetic analogs to spider silk, *Advanced Materials*. **10**, 15, 1185-1195 (1998).

Othman, M.B.H., Khan, A., Ahmad, Z., Zakaria, M.R., Ullah, F. and Akil, H.M. Kinetic investigation and lifetime prediction of Cs–NIPAM–MBA-based thermo-responsive hydrogels, *Carbohydrate Polymers*. **136**, 1182-1193 (2016).

Pal, A.K. and Katiyar, V. Nanoamphiphilic chitosan dispersed poly(lactic acid) bionanocomposite films with improved thermal, mechanical, and gas barrier properties, *Biomacromolecules*. **17**, 8, 2603-2618 (2016).

Palakattukunnel, S.T., Thomas, S., Sreekumar, P.A. and Bandyopadhyay, S. Poly (ethylene-co-vinyl acetate)/calcium phosphate nanocomposites: Contact angle, diffusion and gas permeability studies, *Journal of Polymer Research*. **18**, 6, 1277-1285 (2011).

Pare, B., Soni, A. and Bhagwat, V.W. Kinetics of reduction of aniline blue dye using zero-valent iron (Fe0), *Rasayan Journal of Chemistry*. **1**, 413-420 (2008).

Paul, M.A., Delcourt, C., Alexandre, M., Degée, P., Monteverde, F. and Dubois, P. Polylactide/montmorillonite nanocomposites: Study of the hydrolytic degradation, *Polymer Degradation and Stability*. **87**, 3, 535-542 (2005).

Petinakis, E., Liu, X., Yu, L., Way, C., Sangwan, P., Dean, K., Bateman, S. and Edward, G. Biodegradation and thermal decomposition of poly(lactic acid)-based materials reinforced by hydrophilic fillers, *Polymer Degradation and Stability*. **95**, 9, 1704-1707 (2010).

Pilawka, R., Paszkiewicz, S. and Rosłaniec, Z. Thermal degradation kinetics of PET/SWCNTS nanocomposites prepared by the in situ polymerization, Journal of *Thermal Analysis and Calorimetry*. **115**, 1, 451-460 (2014).

Pilla, S. Engineering applications of bioplastics and biocomposites—an overview, Handbook of Bioplastics and Biocomposites Engineering Applications, *John Wiley & Sons*, New Jersey. (2011), 1-15.

Ping, Y., Ding, D., Ramos, R.A., Mohanram, H., Deepankumar, K., Gao, J., Tang, G. and Miserez, A. Supramolecular β-sheets stabilized protein nanocarriers for drug delivery and gene transfection, *ACS Nano*. **11**, 5, 4528-4541 (2017).

Pitt, G.G., Gratzl, M.M., Kimmel, G.L., Surles, J. and Sohindler, A. Aliphatic polyesters II. The degradation of poly(DL-lactide), poly(ε-caprolactone), and their copolymers in vivo, *Biomaterials*. **2**, 4, 215-220 (1981).

Pivsa-Art, W., Fujii, K., Nomura, K., Aso, Y., Ohara, H. and Yamane, H. Isothermal crystallization kinetics of talc-filled poly(lactic acid) and poly(butylene succinate) blends, *Journal of Polymer Research*. **23**, 8, 1-8 (2016).

Plaza, G.R., Perez-Rigueiro, J., Riekel, C., Perea, G.B., Agullo-Rueda, F., Burghammer, M., Guinea, G.V. and Elices, M. Relationship between microstructure and mechanical properties in spider silk fibers: Identification of two regimes in the microstructural changes, *Soft Matter*. **8**, 22, 6015-6026 (2012).

Pluta, M., Galeski, A., Alexandre, M., Paul, M.A. and Dubois, P. Polylactide/montmorillonite nanocomposites and microcomposites prepared by melt blending: Structure and some physical properties, *Journal of Applied Polymer Science*. **86**, 6, 1497-1506 (2002).

Qiao, X., Li, W., Sun, K., Xu, S. and Chen, X. Isothermal crystallization kinetics of silk fibroin fiber-reinforced poly(ε-caprolactone) biocomposites, *Polymer International*. **58**, 5, 530-537 (2009).

Queen, D., Gaylor, J.D.S., Evans, J.H., Courtney, J.M. and Reid, W.H. The preclinical evaluation of the water vapour transmission rate through burn wound dressings, *Biomaterials*. **8**, 5, 367-371 (1987).

Rajkhowa, R., Wang, L. and Wang, X. Ultra-fine silk powder preparation through rotary and ball milling, *Powder Technology*. **185**, 1, 87-95 (2008).

Ramos, M., Jiménez, A., Peltzer, M. and Garrigós, M.C. Development of novel nano-biocomposite antioxidant films based on poly(lactic acid) and thymol for active packaging, *Food chemistry*. **162**, 149-155 (2014).

Ramukutty, S. and Ramachandran, E. Reaction rate models for the thermal decomposition of ibuprofen crystals, *Journal of Crystallization Process and Technology*. **4**, 2 71-78 (2014).

Rapacz-Kmita, A., Stodolak-Zych, E., Szaraniec, B., Gajek, M. and Dudek, P. Effect of clay mineral on the accelerated hydrolytic degradation of polylactide in the polymer/clay nanocomposites, *Materials Letters*. **146**, 73-76 (2015).

Rasal, R.M., Janorkar, A.V. and Hirt, D.E. Poly (lactic acid) modifications, *Progress in Polymer Science*. **35**, 3, 338-356 (2010).

Ravari, F., Mashak, A., Nekoomanesh, M. and Mobedi, H. Non-isothermal cold crystallization behavior and kinetics of poly(l-lactide): Effect of l-lactide dimer, *Polymer Bulletin*. **70**, 9, 2569-2586 (2013).

Reed, A.M. and Gilding, D.K. Biodegradable polymers for use in surgery — poly(glycolic)/poly(lactic acid) homo and copolymers: 2. In vitro degradation, *Polymer*. **22**, 4, 494-498 (1981).

Rhim, J.W., Park, H.M. and Ha, C.S. Bio-nanocomposites for food packaging applications, *Progress in Polymer Science*. **38**, 10, 1629-1652 (2013).

Riekel, C. and Vollrath, F. Spider silk fibre extrusion: Combined wide-and small-angle X-ray microdiffraction experiments, *International Journal of Biological Macromolecules*. **29**, 3, 203-210 (2001).

Rocha, L.K., Favaro, L.I., Rios, A.C., Silva, E.C., Silva, W.F., Stigliani, T.P., Guilger, M., Lima, R., Oliveira Jr, J.M., Aranha, N. and Tubino, M. Sericin from bombyx mori cocoons. Part I: Extraction and physicochemical-biological characterization for biopharmaceutical applications, *Process Biochemistry*. **61**, 163-177 (2017).

Rockwood, D.N., Preda, R.C., Yucel, T., Wang, X., Lovett, M.L. and Kaplan, D.L. Materials fabrication from Bombyx mori silk fibroin, *Nature Protocols*. **6**, 10, 1612-1631 (2011).

Rotabakk, B.T., Birkeland, S., Jeksrud, W.K. and Sivertsvik, M. Effect of modified atmosphere packaging and soluble gas stabilization on the shelf life of skinless chicken breast fillets, *Journal of Food Science*. **71**, 2, S124–S131 (2006).

Rousseau, M.-E., Lefèvre, T. and Pézolet, M. Conformation and orientation of proteins in various types of silk fibers produced by nephila clavipes spiders, *Biomacromolecules*. **10**, 10, 2945-2953 (2009).

Rousseau, M.E., Lefèvre, T., Beaulieu, L., Asakura, T. and Pézolet, M. Study of protein conformation and orientation in silkworm and spider silk fibers using raman microspectroscopy, *Biomacromolecules*. **5**, 6, 2247-2257 (2004).

Saengsuwan, S., Tongkasee, P., Sudyoadsuk, T., Promarak, V., Keawin, T. and Jungsuttiwong, S. Non-isothermal crystallization kinetics and thermal stability of the in situ reinforcing composite films based on thermotropic liquid crystalline polymer and polypropylene, *Journal of Thermal Analysis and Calorimetry*. **103**, 3, 1017-1026 (2011).

Sasikala, A.R.K., Unnithan, A.R., Yun, Y.H., Park, C.H. and Kim, C.S. An implantable smart magnetic nanofiber device for endoscopic hyperthermia treatment and tumor-triggered controlled drug release, *Acta Biomaterialia*. **31**, 122-133 (2016).

Schiefer, J.L., Arens, E., Grigutsch, D., Rath, R., Hoffmann, A., Fuchs, P.C. and Schulz, A. A prospective intra-individual evaluation of silk compared to Biobrane for the treatment of superficial burns of the hand and face, *Burns*. **43**, 3, 539-548 (2017).

Sen, K. and Babu, K. Studies on Indian silk. I. Macrocharacterization and analysis of amino acid composition, *Journal of Applied Polymer Science*. **92**, 2, 1080-1097 (2004).

Senum, G.I. and Yang, R.T. Rational approximations of the integral of the Arrhenius function, *Journal of Thermal Analysis and Calorimetry*. **11**, 3, 445-447 (1977).

Sezutsu, H. and Yukuhiro, K. Dynamic rearrangement within the Antheraea pernyi silk fibroin gene is associated with four types of repetitive units, *Journal of Molecular Evolution*. **51**, 4, 329-338 (2000).

Shao, Z. and Vollrath, F. Materials: Surprising strength of silkworm silk, *Nature*. **418**, 6899, 741-741 (2002).

Shaw, J.T.B. and Smith, S.G. Comparative studies of fibroins: IV. The composition and structure of chemically resistant fractions from some silk fibroins, *Biochimica et Biophysica Acta*. **52**, 2, 305-318 (1961).

Shaw, J.T.B. Fractionation of the fibroin of Bombyx mori with alkali, *Biochemical Journal*. **93**, 1, 54-61 (1964).
Shaw, J.T.B. Fractionation of the fibroin of Bombyx mori with trypsin, *Biochemical Journal*. **93**, 1, 45-54 (1964).
Shi, C., Pu, X., Zheng, G., Feng, X., Yang, X., Zhang, B., Zhang, Y., Yin, Q. and Xia, H. An antibacterial and absorbable silk-based fixation material with impressive mechanical properties and biocompatibility, *Scientific Reports*. **6**, (2016).
Shimanovich, U., Ruggeri, F.S., De Genst, E., Adamcik, J., Barros, T.P., Porter, D., Müller, T., Mezzenga, R., Dobson, C.M., Vollrath, F. and Holland, C. Silk micrococoons for protein stabilisation and molecular encapsulation, *Nature Communications*. **8**, (2017).
Shogren, R. Water vapor permeability of biodegradable polymers, *Journal of Polymers and the Environment*. **5**, 2, 91-95 (1997).
Siddaraju, G.N., Ananda, H.T., Somashekarappa, H. and Somashekar, R. Effect of electric field on mulberry (bivoltine) and tassar fibres, *Indian Journal of Fibre & Textile Research*. **37**, 4, 347-352 (2012).
Singh, N., Mondal, D., Sharma, M., Devkar, R.V., Dubey, S. and Prasad, K. Sustainable processing and synthesis of nontoxic and antibacterial magnetic nanocomposite from spider silk in neoteric solvents, *ACS Sustainable Chemistry & Engineering*. **3**, 10, 2575-2581 (2015).
Singha, A.S. and Kapoor, H. Effect of silk fibroin reinforcement on the properties of potato starch-polyvinyl alcohol blend films, *International Journal of Polymer Analysis and Characterization*. **19**, 3, 212-221 (2014).
Södergård, A. and Stolt, M. Properties of lactic acid based polymers and their correlation with composition, *Progress in Polymer Science*. **27**, 6, 1123-1163 (2002).
Sogancioglu, M., Yel, E. and Ahmetli, G. Pyrolysis of waste high density polyethylene (HDPE) and low density polyethylene (LDPE) plastics and production of epoxy composites with their pyrolysis chars, *Journal of Cleaner Production*. **165**, 369-381 (2017).
Sokolsky-Papkov, M., Agashi, K., Olaye, A., Shakesheff, K. and Domb, A.J. Polymer carriers for drug delivery in tissue engineering, *Advanced Drug Delivery Reviews*. **59**, 4, 187-206 (2007).
Sonthisombat, A. and Speakman, P.T. Silk: Queen of fibres–the concise story, วารสารวิศวกรรมศาสตร์ ราช มงคล ธัญบุรี. **4**, 1, (2003).
Sonwalkar, T.N. Hand book of silk technology, *Taylor & Francis*, (1993).
Srihanam, P. and Simchuer, W. Proteolytic degradation of silk fibroin scaffold by protease XXIII, *The Open Macromolecules Journal*. **3**, 1-5 (2009).
Stloukal, P., Jandikova, G., Koutny, M. and Sedlařík, V. Carbodiimide additive to control hydrolytic stability and biodegradability of PLA, *Polymer Testing*. **54**, 19-28 (2016).
Su, Z., Guo, W., Liu, Y., Li, Q. and Wu, C. Non-isothermal crystallization kinetics of poly(lactic acid)/modified carbon black composite, *Polymer Bulletin*. **62**, 5, 629-642 (2009a).
Su, Z., Liu, Y., Guo, W., Li, Q. and Wu, C. Crystallization behavior of poly(lactic acid) filled with modified carbon black, *Journal of Macromolecular Science, Part B*. **48**, 4, 670-683 (2009b).
Suwantong, O., Pankongadisak, P., Deachathai, S. and Supaphol, P. Electrospun poly(L-lactic acid) fiber mats containing a crude Garcinia cowa extract for wound dressing applications, *Journal of Polymer Research*. **19**, 6, 9896-9905 (2012).
Takhor, R.L. Advance in nucleation and crystallization of glasses, *American Ceramics Society*: Columbus, OH. (1971), 166-172.

Tan, Y.M., Lim, S.H., Tay, B.Y., Lee, M.W. and Thian, E.S. Functional chitosan-based grapefruit seed extract composite films for applications in food packaging technology, *Materials Research Bulletin*. **69**, 142-146 (2015).

Tao, Y., Xu, W., Yan, Y. and Cao, Y. Preparation and characterization of silk fibroin nanocrystals, *Polymer International*. **61**, 5, 760-767 (2012).

Teramoto, H. and Miyazawa, M. Analysis of structural properties and formation of sericin fiber by infrared spectroscopy, *Journal of Insect Biotechnology and Sericology*. **72**, 3, 157-162 (2003).

Teramoto, H. and Miyazawa, M. Molecular orientation behavior of silk sericin film as revealed by ATR infrared spectroscopy, *Biomacromolecules*. **6**, 4, 2049-2057 (2005).

Tesfaye, M., Patwa, R., Gupta, A., Kashyap, M.J. and Katiyar, V. Recycling of poly(lactic acid)/silk based bionanocomposites films and its influence on thermal stability, crystallization kinetics, solution and melt rheology, *International Journal of Biological Macromolecules*. **101**, 580-594 (2017).

Teshome, A., Raina, S.K., Vollrath, F. and Hagedorn, H. Structure and properties of silk from the African wild silkmoth Gonometa postica reared indoors, *Journal of Insect Science*. **14**, 36 (2014).

Thakur, M.K., Thakur, V.K., Gupta, R.K. and Pappu, A. Synthesis and applications of biodegradable soy based graft copolymers: A review, *ACS Sustainable Chemistry & Engineering*. **4**, 1, 1-17 (2016).

Thomas, D.G. and Staveley, L.A.K. 573.Hysteresis in transitions in solids, *Journal of the Chemical Society (Resumed)*. **0**, 2572-2579 (1951).

Tiptipakorn, S., Damrongsakkul, S., Ando, S., Hemvichian, K. and Rimdusit, S. Thermal degradation behaviors of polybenzoxazine and silicon-containing polyimide blends, *Polymer Degradation and Stability*. **92**, 7, 1265-1278 (2007).

Tobin, M.C. Theory of phase transition kinetics with growth site impingement. I. Homogeneous nucleation, *Journal of Polymer Science Part B: Polymer Physics*. **12**, 2, 399-406 (1974).

Tripathi, N. and Katiyar, V. PlA/functionalized-gum arabic based bionanocomposite films for high gas barrier applications, *Journal of Applied Polymer Science*. **133**, 21, 43458-43465 (2016).

Tsukada, M., Freddi, G., Monti, P., Bertoluzza, A. and Kasai, N. Structure and molecular conformation of tussah silk fibroin films: Effect of methanol, *Journal of Polymer Science Part B: Polymer Physics*. **33**, 14, 1995-2001 (1995).

Tuancharoensri, N., Ross, G.M., Mahasaranon, S., Topham, P.D. and Ross, S. Ternary blend nanofibres of poly(lactic acid), polycaprolactone and cellulose acetate butyrate for skin tissue scaffolds: Influence of blend ratio and polycaprolactone molecular mass on miscibility, morphology, crystallinity and thermal properties, *Polymer International*. **66**, 11, 1463-1472 (2017).

Tudorachi, N., Lipsa, R. and Mustata, F.R. Thermal degradation of carboxymethyl starch–g-poly(lactic acid) copolymer by TG–FTIR–MS analysis, *Industrial & Engineering Chemistry Research*. **51**, 48, 15537-15545 (2012).

Tulachan, B., Meena, S.K., Rai, R.K., Mallick, C., Kusurkar, T.S., Teotia, A.K., Sethy, N.K., Bhargava, K., Bhattacharya, S., Kumar, A. and Sharma, R. K. Electricity from the silk cocoon membrane, *Scientific Reports*. **4**, (2014).

Unni, B.G., Goswami, M., Kakoty, Y., Bhattacarjee, M., Wann, S.B., Rajkhowa, G., Das, S., Devi, B.R. and Chutia, A.D. Indigenous knowledge of silkworm cultivation and its utilization in north eastern region of india, *Indian Journal of Traditional Knowleadge.* **8**, 1 70-74 (2009).

Valapa, R.B, Hussain, S., Iyer, P.K., Pugazhenthi, G. and Katiyar, V. Non-isothermal crystallization kinetics of sucrose palmitate reinforced poly(lactic acid) bionanocomposites, *Polymer Bulletin*. **73**, 1, 21-38 (2016a).

Valapa, R.B, Pugazhenthi, G. and Katiyar, V. Thermal degradation kinetics of sucrose palmitate reinforced poly(lactic acid) biocomposites, *International Journal of Biological Macromolecules*. **65**, 275-283 (2014).

Valapa, R.B., Pugazhenthi, G. and Katiyar, V. Fabrication and characterization of sucrose palmitate reinforced poly(lactic acid) bionanocomposite films, *Journal of Applied Polymer Science*. **132**, 3, 41320-41329 (2015a).

Valapa, R.B., Pugazhenthi, G. and Katiyar, V. Effect of graphene content on the properties of poly(lactic acid) nanocomposites, *RSC Advances*. **5**, 36, 28410-28423 (2015b).

Valapa, R.B., Pugazhenthi, G. and Katiyar, V. Hydrolytic degradation behavior of sucrose palmitate reinforced poly(lactic acid) nanocomposites, *International Journal of Biological Macromolecules*. **89**, 70-80 (2016).

Venkatesh, M., Ravi, P. and Tewari, S.P. Isoconversional kinetic analysis of decomposition of nitroimidazoles: Friedman method vs Flynn–Wall–Ozawa method, *The Journal of Physical Chemistry A*. **117**, 40, 10162-10169 (2013).

Vogel, C. and Siesler, H.W. Thermal degradation of poly(ε-caprolactone), poly(L-lactic acid) and their blends with poly(3-hydroxy-butyrate) studied by TGA/FT-IR spectroscopy, *Macromolecular Symposia*. **265**, 1, 183-194 (2008).

Wang, L., Qiu, J., Sakai, E. and Wei, X. The relationship between microstructure and mechanical properties of carbon nanotubes/polylactic acid nanocomposites prepared by twin-screw extrusion, *Composites Part A: Applied Science and Manufacturing*. **89**, 18-25 (2016a).

Wang, R., Pu, D., Dong, Y., Sun, Y., Fu, Y. and Ni, Q.Q. Silk fibroin powder prepared by nontoxic low-sodium salt system, *Materials Letters*. **206**, 5-8 (2017).

Wang, S., Xuan, S., Wang, Y., Xu, C., Mao, Y., Liu, M., Bai, L., Jiang, W. and Gong, X. Stretchable polyurethane sponge scaffold strengthened shear stiffening polymer and its enhanced safeguarding performance, *ACS Applied Materials & Interfaces*. **8**, 7, 4946-4954 (2016d).

Wang, S., Zhang, Y., Wang, H., Yin, G. and Dong, Z. Fabrication and properties of the electrospun polylactide/silk fibroin-gelatin composite tubular scaffold, *Biomacromolecules*. **10**, 8, 2240-2244 (2009).

Wang, X., Yucel, T., Lu, Q., Hu, X. and Kaplan, D.L. Silk nanospheres and microspheres from silk/PVA blend films for drug delivery, *Biomaterials*. **31**, 6, 1025-1035 (2010).

Wang, Y., Wang, X., Shi, J., Zhu, R., Zhang, J., Zhang, Z., Ma, D., Hou, Y., Lin, F., Yang, J. and Mizuno, M. A biomimetic silk fibroin/sodium Alginate composite scaffold for soft tissue engineering, *Scientific Reports*. **6**, (2016c).

Wang, Y.P., Xiao, Y.J., Duan, J., Yang, J.H., Wang, Y. and Zhang, C.L. Accelerated hydrolytic degradation of poly(lactic acid) achieved by adding poly(butylene succinate), *Polymer Bulletin*. **73**, 4, 1067-1083 (2016b).

Warwicker, J.O. Comparative studies of fibroins: II. The crystal structures of various fibroins, *Journal of Molecular Biology*. **2**, 6, 350-362 (1960).

Warwicker, J.O. The crystal structure of silk fibroin, *Acta Crystallographica*. **7**, 8-9, 565-573 (1954).

Wharram, S.E., Zhang, X., Kaplan, D.L. and McCarthy, S.P. Electrospun silk material systems for wound healing, *Macromolecular Bioscience*. 10, 3, 246-257 (2014).

Wu, D., Wu, L., Wu, L., Xu, B., Zhang, Y. and Zhang, M. Nonisothermal cold crystallization behavior and kinetics of polylactide/clay nanocomposites, *Journal of Polymer Science Part B: Polymer Physics*. **45**, 9, 1100-1113 (2007).

Wu, Y., Jiang, W., Wen, X., He, B., Zeng, X., Wang, G. and Gu, Z. A novel calcium phosphate ceramic–magnetic nanoparticle composite as a potential bone substitute, *Biomedical Materials*. **5**, 1, 15001 (2010).

Xiang, C., Joo, Y.L. and Frey, M.W. Nanocomposite fibers electrospun from poly(lactic acid)/cellulose nanocrystals, *Journal of Biobased Materials and Bioenergy*. **3**, 2, 147-155 (2009).

Xu, L., Yao, Q., Han, Z., Zhang, Y. and Fu, Y. Producing pyridines via thermocatalytic conversion and ammonization of waste polylactic acid over zeolites, *ACS Sustainable Chemistry & Engineering*. **4**, 3, 1115-1122 (2016).

Xu, T., Zhang, A., Zhao, Y., Han, Z. and Xue, L. Crystallization kinetics and morphology of biodegradable poly(lactic acid) with a hydrazide nucleating agent, *Polymer Testing*. **45**, 101-106 (2015).

Yan, L.P., Silva-Correia, J., Ribeiro, V.P., Miranda-Gonçalves, V., Correia, C., da Silva Morais, A., Sousa, R.A., Reis, R.M., Oliveira, A.L. and Oliveira, J.M. Tumor growth suppression induced by biomimetic silk fibroin hydrogels, *Scientific Reports*. **6**, 31037 (2016).

Yang, T.C.K., Lin, S.S.Y. and Chuang, T.H. Kinetic analysis of the thermal oxidation of metallocene cyclic olefin copolymer (mCOC)/TiO2 composites by FTIR microscopy and thermogravimetry (TG), *Polymer Degradation and Stability*. **78**, 3, 525-532 (2002).

Yathindranath, V., Rebbouh, L., Moore, D.F., Miller, D.W., van Lierop, J. and Hegmann, T. A versatile method for the reductive, One-pot synthesis of bare, hydrophilic and hydrophobic magnetite nanoparticles, *Advanced Functional Materials*. **21**, 8, 1457-1464 (2011).

Yukseloglu, S.M. and Canoglu, S. Silk fibre degradation and analysis by proteomics, Annals of the University of Oradea. *Fascicle of Textiles*. **17**, 1, 137-142 (2016).

Yuzay, I.E., Auras, R., Soto-Valdez, H. and Selke, S. Effects of synthetic and natural zeolites on morphology and thermal degradation of poly(lactic acid) composites, *Polymer Degradation and Stability*. **95**, 9, 1769-1777 (2010).

Zhang, H., Ma, X., Cao, C., Wang, M. and Zhu, Y. Multifunctional iron oxide/silk-fibroin (Fe3O4–SF) composite microspheres for the delivery of cancer therapeutics, *RSC Advances*. **4**, 78, 41572-41577 (2014).

Zhang, H., Magoshi, J., Magoshi, Y., Yoshida, H., Chen, J. and Saiki, K. Inorganic composition and thermal properties of cocoon fiber, *International Journal of the Society of Materials Engineering for Resources*. **10**, 1, 113-116 (2002).

Zhang, Q., Zhang, Z., Zhang, H. and Mo, Z. Isothermal and nonisothermal crystallization kinetics of nylon-46, *Journal of Polymer Science Part B: Polymer Physics*. **40**, 16, 1784-1793 (2002).

Zhang, R., Wang, Y., Wang, K., Zheng, G., Li, Q. and Shen, C. Crystallization of poly(lactic acid) accelerated by cyclodextrin complex as nucleating agent, *Polymer Bulletin*. **70**, 1, 195-206 (2013).

Zhang, X. and Wyeth, P. Using FTIR spectroscopy to detect sericin on historic silk, *Science China Chemistry*. **53**, 3, 626-631 (2010).

Zhang, X., Espiritu, M., Bilyk, A. and Kurniawan, L. Morphological behavior of poly(lactic acid) during hydrolytic degradation, *Polymer Degradation and Stability*. **93**, 10, 1964-1970 (2008).

Zhang, Y.Q., Shen, W.D., Xiang, R.L., Zhuge, L.J., Gao, W.J. and Wang, W.B. Formation of silk fibroin nanoparticles in water-miscible organic solvent and their characterization, *Journal of Nanoparticle Research*. **9**, 5, 885-900 (2007).

Zhao, Y.Q., Cheung, H.Y., Lau, K.T., Xu, C.L., Zhao, D.D. and Li, H.L. Silkworm silk/poly(lactic acid) biocomposites: Dynamic mechanical, thermal and biodegradable properties, *Polymer Degradation and Stability*. **95**, 10, 1978-1987 (2010).

Zhou, Q. and Xanthos, M. Nanoclay and crystallinity effects on the hydrolytic degradation of polylactides, *Polymer Degradation and Stability*. **93**, 8, 1450-1459 (2008).

Zhou, Q. and Xanthos, M. Nanosize and microsize clay effects on the kinetics of the thermal degradation of polylactides, *Polymer Degradation and Stability*. **94**, 3, 327-338 (2009).

Zou, H., Yi, C., Wang, L., Liu, H. and Xu, W. Thermal degradation of poly(lactic acid) measured by thermogravimetry coupled to Fourier transform infrared spectroscopy, *Journal of Thermal Analysis and Calorimetry*. **97**, 3, 929-935 (2009).

भारतीय प्रौद्योगिकी संस्थान गुवाहाटी • Indian Institute of Technology Guwahati •